

ADD 443222



Proceedings of Damping'89

8-10 February 1989
West Palm Beach, Florida

(Pages ICA-1 through KDC-15)

November 1989

Final Report for Period Feb 86 to Feb 89

19960611 156

Approved for public release; distribution is unlimited.



Sponsored by:

Flight Dynamics Laboratory
of the Air Force
Wright Aeronautical Laboratories

AIR FORCE SYSTEMS COMMAND
WRIGHT-PATTERSON AIR FORCE BASE, OHIO 45433-6553

DEPARTMENT OF DEFENSE
PLASTICS & POLYMERS EVALUATION CENTER
ARDEC PIGGS PENNY ARSENAL, N.J. 07806

DTIC QUALITY INSPECTED 3

5

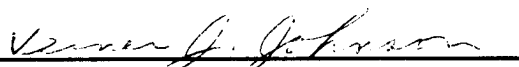
PLASTICS & POLYMERS EVALUATION CENTER
ARDEC PIGGS PENNY ARSENAL, N.J. 07806
801490-71-10140-71
99/11/89

NOTICE

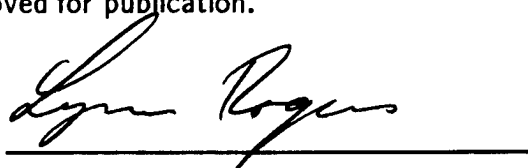
When Government drawings, specifications, or other data are used for any purpose other than in connection with a definitely Government-related procurement, the United States Government incurs no responsibility or any obligation whatsoever. The fact that the Government may have formulated or in any way supplied the said drawings, specifications, or other data, is not to be regarded by implication, or otherwise as in any manner, as licensing the holder or any other person or corporation; or as conveying any rights or permission to manufacture, use, or sell any patented invention that may in any way be related thereto.

This report is has been reviewed by the Office of Public Affairs (ASD/PA) and is releasable to the National Technical Information Service (NTIS). At NTIS, it will be available to the general public, including foreign nations.

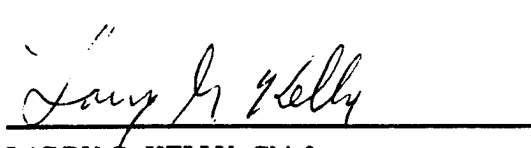
This technical report has been reviewed and is approved for publication.



VERNER J. JOHNSON, Program Manager
Advanced Metallic Structures ADPO
Structures ADP Branch



LYNN ROGERS, PhD
Advanced Metallic Structures ADP


Larry G. Kelly

LARRY G. KELLY, Chief
Structures ADP Branch
Structures Division

"If your address has changed, if you wish to be removed from our mailing list, or if the addressee is no longer employed by your organization please notify WRDC/FIBAA, WPAFB, OH 45433-6553 to help us maintain a current mailing list".

Copies of this report should not be returned unless return is required by security considerations, contractual obligations, or notice on a specific document.

-- <<ENTER NEXT COMMAND>>

-- 1 OF 4

-- 1 - AD NUMBER: A223433

-- 6 - UNCLASSIFIED TITLE: PROCEEDINGS OF DAMPING'89 HELD IN WEST PALM
-- BEACH, FLORIDA ON 8-10 FEBRUARY 1989. VOLUME 3. PAGES ICA-1 THROUGH
-- KDC-15).

--*****

ADD 443222

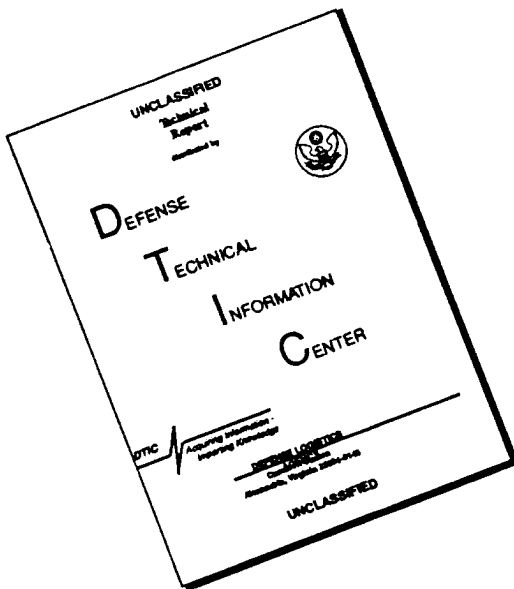
(ADD 443223 - ADD 443224)

Unclassified

SECURITY CLASSIFICATION OF THIS PAGE

REPORT DOCUMENTATION PAGE				Form Approved OMB No. 0704-0188	
1a. REPORT SECURITY CLASSIFICATION Unclassified		1b. RESTRICTIVE MARKINGS			
2a. SECURITY CLASSIFICATION AUTHORITY		3. DISTRIBUTION/AVAILABILITY OF REPORT			
2b. DECLASSIFICATION/DOWNGRADING SCHEDULE		Approved for public release; distribution unlimited.			
4. PERFORMING ORGANIZATION REPORT NUMBER(S) WRDC-TR-89-3116, Vol III		5. MONITORING ORGANIZATION REPORT NUMBER(S)			
6a. NAME OF PERFORMING ORGANIZATION Advanced Metallic Structures Adv Development Prog Office	6b. OFFICE SYMBOL (if applicable) WRDC/FIBAA	7a. NAME OF MONITORING ORGANIZATION			
6c. ADDRESS (City, State, and ZIP Code) Wright-Patterson Air Force Base OH 45433-6553		7b. ADDRESS (City, State, and ZIP Code)			
8a. NAME OF FUNDING/SPONSORING ORGANIZATION Flight Dynamics Lab. (If applicable) Wright Research Dev. Ctr.	8b. OFFICE SYMBOL (If applicable) WRDC/FIBA	9. PROCUREMENT INSTRUMENT IDENTIFICATION NUMBER			
8c. ADDRESS (City, State, and ZIP Code)		10. SOURCE OF FUNDING NUMBERS			
		PROGRAM ELEMENT NO. 63211F	PROJECT NO. 486U	TASK NO. 11	WORK UNIT ACCESSION NO. 02
11. TITLE (Include Security Classification) Damping 1989 Proceedings					
12. PERSONAL AUTHOR(S)					
13a. TYPE OF REPORT Final	13b. TIME COVERED FROM Feb 86 TO Feb 89	14. DATE OF REPORT (Year, Month, Day) 1989 November	15. PAGE COUNT 590		
16. SUPPLEMENTARY NOTATION Pages ICA-1 through KDC-15					
17. COSATI CODES		18. SUBJECT TERMS (Continue on reverse if necessary and identify by block number) Vibration damping, controls/structure interaction.			
19. ABSTRACT (Continue on reverse if necessary and identify by block number) Individual papers of Damping 89 held 8-10 February 1989 in West Palm Beach FL are presented. The subjects included: mechanical properties of polymers, experimental methods, damping in metal matrix composites, friction damping, design of damping structure, modal damping values, and applications of damping, etc.					
20. DISTRIBUTION/AVAILABILITY OF ABSTRACT <input checked="" type="checkbox"/> UNCLASSIFIED/UNLIMITED <input type="checkbox"/> SAME AS RPT. <input type="checkbox"/> DTIC USERS			21. ABSTRACT SECURITY CLASSIFICATION Unclassified		
22a. NAME OF RESPONSIBLE INDIVIDUAL Dr Lynn Rogers			22b. TELEPHONE (Include Area Code) (513)255-6622	22c. OFFICE SYMBOL WRDC/FIBAA	

DISCLAIMER NOTICE



**THIS DOCUMENT IS BEST
QUALITY AVAILABLE. THE COPY
FURNISHED TO DTIC CONTAINED
A SIGNIFICANT NUMBER OF
PAGES WHICH DO NOT
REPRODUCE LEGIBLY.**

Workshop Administration

Director

Dr. Lynn Rogers
Flight Dynamics Laboratory of the Air Force
Wright Aeronautical Laboratories

Administrative Chairman

Mrs. Melissa Arrajj
Martin Marietta Astronautics Group

Assistant Administrative Chairman

Ms. Jo Ellen Dunn
CSA Engineering, Incorporated

Session Chairmen

Dr. M. Aswani, Aerospace Corporation
LTC R. L. Bagley, Air Force Institute of Technology Wright Patterson AFB
Mr. S. D. Bigelow, Boeing Aerospace Company
Dr. A. J. Bronowicki, TRW Space and Technology Group
Dr. D. I. G. Jones, Materials Laboratory, AFWAL
Dr. M. A. Cutchins, Auburn University
Mr. M. L. Drake, University of Dayton Research Institute
Mr. P. G. Gauthier, Naval Sea Systems
Mr. R. N. Gehling, Martin Marietta Astronautics Group
Dr. J. L. Gubser, McDonnell Douglas Astronautics Company
Dr. J. P. Henderson, Materials Laboratory, AFWAL
Mr. W. Hoskins, Lockheed Missiles & Space Company
Dr. R. Ikegami, Boeing Aerospace Company
Dr. C. D. Johnson, CSA Engineering, Incorporated
Mr. L. Kelly, Flight Dynamics Laboratory, AFWAL
Dr. E. M. Kerwin, BBN
Dr. R. LeMaster, W. J. Schaffer, Association
Dr. Y. P. Lu, DTNSRDC
Mr. D. R. Morgenthaler, Martin Marietta Astronautics Group
Mr. A. D. Nashif, Anatrol Corporation
Dr. T. S. Nishimoto, Rockwell International - SSD
Mr. M. L. Parin, Anatrol Corporation
Dr. K. E. Richards, Jr., Martin Marietta Astronautics Group
Dr. S. S. Sattinger, Westinghouse R&D Center
Dr. T. D. Scharton, Jet Propulsion Laboratory
Dr. J. Soovere, Lockheed - California Company
Mr. C. V. Stahle, Jr., General Electric Company
Mr. J. A. Staley, General Electric Company
Mr. S. J. Starr, LTV Aerospace - Aircraft Products
Dr. R. C. Stroud, Synergistic Technology, Incorporated
Dr. J. Unruh, Southwest Research Institute
Mr. H. Wolfe, Flight Dynamics Laboratory, AFWAL

FOREWORD

This publication includes the individual papers of DAMPING '89 held 8-10 February 1989, West Palm Beach, Florida. The Workshop was sponsored by the Air Force Wright Aeronautical Laboratories through the Advanced Metallic Structures Advanced Development Program Office (AFWAL/FIBAA).

It is desired to transfer vibration damping technology in a timely manner within the aerospace community, thereby, stimulating research, development and applications.

TABLE OF CONTENTS

Paper No.

Damping - A Key to More, Faster, Farther, Higher (Keynote Address)	
Major General Thomas R. Ferguson, Jr.	AAA
Pioneering Damping in Space at General Electric Astro Space Division (Invited Speaker)	
C. V. Stahle, Jr.	AAB
Aircraft Modal Suppression Yaw Damper System (Invited Speaker)	
Dr. J. R. Fuller	AAC
SESSION BA—Complex Modulus	
Loss Modulus and Damping Behavior of Poly (Vinyl Methyl Ether)-Polystyrene Blends and IPN's	
J. J. Fay, Dr. C. J. Murphy, Dr. D. A. Thomas and Prof. L. H. Sperling	BAA
Time-Temperature Superposition in Multi-Component Polymer Blends	
Prof. R. E. Wetton	BAB*
Predicting Loss Factor Master Curves Using Stiffness Master Curves Derived From Transmissibility Data	
Dr. S. O. Oyadyi and Prof. G. R. Tomlinson	BAC*
SESSION BB—Aircraft Applications	
Add-on Damping for A-10 Gunbay Life Extension	
K. R. Wentz	BBA*
Development of a Damped A-10 Engine Air Inlet Ring	
D. L. Giunto and S. N. Vacca	BBB
Status of Aircraft Integral Damping Demonstration	
C. L. Rupert and R. Tate	BBC
SESSION BC—Composites	
Damping in Metal Matrix Composites - An Overview	
Dr. S. P. Rawal, Dr. J. H. Armstrong, Dr. M. S. Misra and Dr. S. G. Fishman	BCA
Highly Damped Gr/Mg Composites for Flexible Space Structures	
U. K. Kashalikar and J. Boyce	BCB

*Not available for publication.

TABLE OF CONTENTS (Continued)

Paper No.

Measured Damping and Modulus of Composite Cylinders J. B. Andriulli	BCC
SESSION CA—Electro-Rheological & Hydraulic	
The Usage of Electro-Rheological Materials in Viscoelastic Layer Damping Applications J. P. Coulter, T. G. Duclos and D. N. Acker	CAA
Analysis of a Modified Passive Hydraulic Damper with Variable Damping Characteristics H. Su, Dr. S. Rakheja and Dr. T. S. Sankar	CAB
An Experimental Investigation on the Active-Damping Characteristics of a Class of Ultra-Advanced Intelligent Composite Materials Featuring Electro-Rheological Fluids S. B. Choi, Prof. B. S. Thompson and Prof. M. V. Gandhi	CAC
SESSION CB—Damping Identification	
Identification of System Parameters in a Slewing Control Experiment E. Garcia and Prof. D. J. Inman	CBA
An Alternative to FFT for Precise Damping Estimates Prof. S. M. Pandit	CBB
Coupled Modes Resolution by an Exponential Window Prof. A. Agneni, Prof. L. Balis-Crema and Prof. A. Castellani	CBC
SESSION CC—Analysis	
Passive Damping Design Methods Using NASTRAN M. J. Matla	CCA
Application of the Ritz Procedure to Damping Prediction Using a Modal Strain Energy Approach J. C. Parekh and S. G. Harris	CCB
Formulation and Inversion of Transfer Functions of Combined Elastic/Viscoelastic Structures Prof. S. B. Skaar, Dr. G. A. Nariboli and L. Tang	CCC

*Not available for publication.

TABLE OF CONTENTS (Continued)

Paper No.

SESSION DA—Fractional Derivatives

The Fractional Order Initial Value Problem and Its Application to State Space Control Theory
LTC R. L. Bagley DAA*

The Optimal Control of Viscoelastically Damped Structures
LTC R. L. Bagley, R. Walker and R. Calico DAB

Solution Techniques for the Fractional Order Eigenvalue Problem
LTC R. L. Bagley and M. Devereaux DAC

The Rheology of Anelastic Media Studied by Means of the Observation of the Splitting of Its Eigenfrequencies
Prof. M. Caputo DAD

SESSION DB—Space Applications

A Viscous Isolator for Shuttle Hubble Space Telescope Resupply
L. P. Davis, F. Schmitt and C. L. See DBA

Constrained Layer Damping for a Space-Based Optical System
N. C. Bond and R. M. Laurenson DBB

**Hydrostatic Damper for the Space Shuttle Main Engine (SSME)
High Pressure Oxidizer Turbopump (HPOTP)**
D. G. Goggin, J. K. Scharrer and R. F. Beatty DBC

Optimized Designs of Viscoelastic Damping Treatments
Dr. W. C. Gibson and Dr. C. D. Johnson DBD

**Considerations of Synthesized System Damping in
Dynamic Analysis of Space Structures**
Dr. W. T. Tsai DBE

SESSION DC—Basics

Modal Damping – Please Stand Up
R. B. Fost, M. J. Yan and J. Reed DCA*

On Passive Spot Damping Anomalies
Dr. M. I. Young DCB

Vibration Damping Performance—What We Should Know About It
J. Chahine and P. Saha DCC

Description of Structural Damping
Prof. L. Gaul, Lt. Col. P. Klein and Dr.-Ing. S. Kempfle DCD

*Not available for publication.

TABLE OF CONTENTS (Continued)

Paper No.

SESSION FA—Complex Modulus Data

Interactive Characterization and Database Storage of Complex Modulus Data	
B. L. Fowler	FAA
Comparison of Complex Modulus Data Generated by Three Different Measurement Techniques	
M. L. Drake and Dr. A. Sircar	FAB
Frequency-Temperature Dependence of Polymer Complex Modulus Properties	
T. Lewis, A. D. Nashif and Dr. D. I. G. Jones	FAC
Complex Modulus Measurements Over a Wide Range of Frequencies and Material Characteristics Through the Confrontation of Two Instruments	
C. Chesneau, J. Y. Cavaille and J. P. Laures	FAD

SESSION FB—Structural Applications

Optimal Application of Damping to the Stanford Gravity Wave Experiment	
F. A. McLoughlin and Prof. D. B. DeBra	FBA
Viscoelastic Passive Dampers for Structures	
Dr. P. Mahmoodi and J. M. Kelly	FBB*
Large Strain Viscoelastic Dampers for Structures	
Dr. P. Mahmoodi, T. T. Soong and L. E. Robertson	FBC*
An Internal Damping Configuration for Tubes and Hollow Panels	
Dr. E. M. Kerwin, Jr.	FBD

SESSION FC—Control Structure Interaction

Active Vibration Control of Flexible Structures	
S. P. Sun, Dr. P. K. Raju and M. J. Crocker	FCA
Robust Realization/Identification of Damped Structures	
M. J. Roemer and Dr. D. J. Mook	FCB
Optimum Selection of Dampers for Freely Vibrating Multidegree of Freedom Systems	
Dr. J. J. Gilheany	FCC
Optimization of Energy Dissipation Rate in Structures	
Prof. V. H. Neubert	FCD

*Not available for publication.

TABLE OF CONTENTS (Continued)

Paper No.

SESSION FD—Non-Linear

Effect of Damping on the Predicted Fatigue Life of a Nonlinear Plate	R. N. Miles	FDA
The Role of Damping in the Suppression of Parametric Resonances in Nonlinear Systems	Dr. L. D. Zavodney and S. M. Shihada	FDB
Distributed Parameter Nonlinear Damping Models for Flight Structures	A. V. Balakrishnan and L. W. Taylor	FDC*
Non-Linear Dynamic Analysis with Frequency-Dependent Damping	F. Venancio-Filho and A. M. Claret	FDD

SESSION GA—Fluids

Fluid Inertia Effects in Squeeze Film Dampers	A. El-Shafei	GAA
A New Class of Fluid-Loop Dampers	Dr. A. M. Baz, L. Gumusel and Dr. J. Fedor	GAB
Tuned Liquid Damper (TLD) for Suppressing Horizontal Motion of Structures	Dr. Y. Fujino, B. M. Pacheco, L. M. Sun and P. Chaiseri	GAC

SESSION GB—Friction

Contact Stresses in Cables Due to Tension and Torsion	Dr. K. Kumar, Dr. J. E. Cochran, Jr., and Dr. M. A. Cutchins	GBA
Effect of Inertial Forces on Damping in a Dry Friction Joint	Dr. O. Vinogradov	GBB
Modal Damping of Suspended Cables	Prof. H. Yamaguchi	GBC

SESSION GC—Struts

Analysis, Optimization, Fabrication and Test of Composite Shells with Embedded Viscoelastic Layers	Dr. A. J. Bronowicki and H. P. Diaz	GCA
---	-------------------------------------	-----

*Not available for publication.

TABLE OF CONTENTS (Continued)

Paper No.

Passive Damping Concepts for Space Structures

With Tubular Members

Prof. Z. Razzaq and B. S. Najjar

GCB

**Design and Analysis of Viscoelastic Struts
for Large Space Structures**

Y. C. Yiu

GCC

SESSION GD—Phenomena

Increased Graphite Fiber Damping via Intercalation

G. A. Lesieutre, A. J. Eckel and J. A. DiCarlo

GDA

**Modeling Material Damping Using Augmenting
Thermodynamic Fields (ATF)**

G. A. Lesieutre

GDB

**Experimental Determination of Damping Mechanisms
in a Composite Beam**

H. T. Banks and Prof. D. J. Inman

GDC

SESSION HA—Viscous

**Experimental Investigation of a Passive, Adjustable,
Viscous Damper**

R. W. Taylor and Prof. J. M. Starkey

HAA*

Sliding Laminated Vibration Damper

M. Koleda

HAB*

**Application of Viscoelastic Damping to Reducing
a Light Motorcycle Drive-By Noise**

L. Xiaoquian, T. Xieru, C. H. Ku and R. Mingzhang

HAC*

SESSION HB—Large Space Structures

A Survey of Damping in Control of Flexible Structures

Prof. D. J. Inman and G. C. Horner

HBA

Damping of a Large Space Platform

Dr. A. S. Bicos

HBB

**Payoff of Passive Damping in Active Control
of Large Space Structures**

Dr. J. Garibotti

HBC

*Not available for publication.

TABLE OF CONTENTS (Continued)

Paper No.

SESSION HC--Intrinsic

An Experimental Study of the Complex Dynamic Modulus
G. G. Wren and Dr. V. K. Kinra HCA

A Design for Improving the Structural Damping Properties
of Axial Members
D. J. Barrett HCB

Optimization of Intrinsic Damping
Prof. R. D. Adams HCC*

SESSION HD--Joints

Damping-Like Effect of Irregularities in Nearly
Periodic Structures
C. Pierre and P. D. Cha HDA*

Study of the Damping Capacity of Structural Joints
Made of Graphite Epoxy Composite Material
M. D. Rao, Prof. M. J. Crocker and P. K. Raju HDB

Damping at a Lap Joint Interface Undergoing
Microslip Under Arbitrary Load History
Dr. A. F. Artiles and J. Walton HDC*

SESSION IA--Optimization

Simplified Analysis Approach for Optimizing
Constrained Layer Damping
S. Forness IAA*

Optimal Constrained Viscoelastic Tape Lengths
for Maximizing Damping in Laminated Composites
P. R. Mantena, Prof. R. F. Gibson and Dr. S. J. Hwang IAB

Optimum Configuration of Constrained Viscoelastic Layers
Dr. B. H. Lu and Prof. C. H. Ku IAC*

SESSION IB--Aircraft Experiment

Practical Stand-Off Damping Treatment for Sheet Metal
M. L. Parin, Dr. L. C. Rogers, M. Falugi and Dr. Y. Moon IBA

Enhanced Damping for the Sikorsky ACAP Composite Airframe
E. W. Jacobs, C. A. Yoerkie, Jr., and J. A. Moore IBB

*Not available for publication.

TABLE OF CONTENTS (Continued)

Paper No.

Damping Materials for Control of Propeller Induced Structure-Borne Noise

Dr. J. F. Unruh

IBC

Application of Constrained Layer Damping to the F/A-18 Horizontal Tail

Dr. R. N. Yurkovich

IBD

SESSION IC—Vibration Suppression

Fiber Optic Vibration Sensors for Structural Control Applications

W. B. Spillman, Jr., and B. R. Kline

ICA

Active Vibration Suppression Using NiTiNOL Sensors and Actuators

D. G. Wilson, Dr. R. Ikegami, J. R. Anderson and G. J. Julien

ICB

Damping of Structural Vibrations with Piezoelectric Materials and Passive Electrical Networks

N. W. Hagood and Prof. A. von Flotow

ICC

Passive Electromagnetic Vibration Dampers

B. W. Maxfield, J. K. Hulbert and P. Smiley

ICD

SESSION ID—Free Layer

Development of a Nomogram for Selection of a Viscoelastic Free Layer Damping Material

R. J. Dominic

IDA

Coupled Modal Damping in Transient Solutions

B. C. McFarland and Dr. A. J. Bronowicki

IDB

A Perturbation Method for the Analysis of Free-Layer Damping Treatments

S. Shen and Dr. K. K. Stevens

IDC

SESSION JA—Laminates

Damping and Vibration Control of Some Laminated Composite Beams Using Add-On Viscoelastic Materials

V. S. Rao, Prof. C. T. Sun and B. V. Sankar

PL-054107

JAA

*Not available for publication.

TABLE OF CONTENTS (Continued)

Paper No.

Classification in the Frequency-Temperature Range of Viscoelastic Materials for Damping of Flexural Waves in Sandwich Structures with Various Boundary Conditions

Dr. M. J. Ghaleb and M. Khouri

JAB

SESSION JB—Launch

The Application of Statistical Energy Analysis in the Design of Viscoelastic Passive Damping

D. W. Johnson, Dr. R. Ikegami and K. S. Hunziker

JBA

RELSAT Damped Satellite Equipment Panels - Dynamic Performance

C. V. Stahle, Jr., J. A. Staley and J. C. Strain

JBB

RELSAT Damped Satellite Equipment Panels - Analysis and Experimental Verification

C. V. Stahle, Jr., J. A. Staley and J. C. Strain

JBC

RELSAT Damped Equipment Panels - Fabrication

K. Schmidt, F. Curtis, E. Muziani and L. Amore

JBD

SESSION JC—Model Verification

Prediction and Measurement of Damping of a Laminated Beam With a Constrained Viscoelastic Layer

D. J. Segalman and Lt. P. Reamy

JCA

A New Approach to Model Determination of Large Flexible Space Systems

Dr. F. Y. Hadaegh, D. S. Bayard, Y. Yam and E. Mettler

JCB

Perturbations on Natural Modes Due to Nonproportionality of Viscous Damping

Dr. B. M. Pacheco and Dr. Y. Fujino

JCC

Measured Vibration Modes of Constrained Layer Damping Using Time Averaged Holographic Interferometry

P. R. Bernier, S. T. Fryska, C. T. Griffen and
A. M. Revello

JCD

SESSION JD—Metals

Damping Associated with Incipient Melting in Aluminum-Idium Alloys

O. Diehm, C. R. Wong and D. C. Van Aken

JDA

*Not available for publication.

TABLE OF CONTENTS (Continued)

	<u>Paper No.</u>
Damping Capacity of Aluminum 6061-Indium Alloys C. R. Wong, D. C. Van Aken and O. Diehm	JDB
Interlaboratory Study of Damping Capacity in Leaded Brass and Lead-Free Brass A. Wolfenden, T. G. Aldridge, Jr., E. W. Davis, Jr., Prof. V. K. Kinra, G. G. Wren and J. M. Wolla	JDC
A Study of the Vibrational and Acoustical Properties of Thermoset Composites, Steel and Aluminum K. M. Lombardo	JDD*
 SESSION KA—Sandwich	
Investigation of Structural Damping Combining Linear and Non-Linear Constrained Viscoelastic Mechanisms J. M. Ting, C. K. Kim and Dr. E. F. Crawley	KAA
Vibration Reduction via Constrained Layer Damping Techniques J. F. Schultze and Dr. J. B. Kosmatka	KAB
Damping Behavior of Flexible Laminates Dr. V. A. Coveney, A. H. Muhr and A. G. Thomas <i>PL-054108</i>	(KAC)
 SESSION KB—Impact	
Application of the Component Element Method to the Impact Damped Simple Harmonic Oscillation Prof. C. M. North, Jr., and R. E. Jones	KBA
Time History Study of a Classical Cantilever Beam Damped by Internal Mechanical Means Prof. C. M. North, Jr., and T. A. Nale	KBB
Nonobstructive Impact Damping Applications for Cryogenic Environments Dr. H. V. Panossian	KBC
Pendulum Impact Damper to Suppress Vibrations G. S. Chua, Y. Fujino, B. M. Pacheco and M. Ito	KBD*
 SESSION KC—Space Applications II	
Damping Treatment for Jitter Reduction on a High Power Optical Bench Dr. P. H. Chen and E. M. Austin	KCA

*Not available for publication.

TABLE OF CONTENTS (Concluded)

Paper No.

**Analysis and Testing of a Damping Treatment for a
Multi-Component Space Structure**
E. M. Austin, Dr. C. D. Johnson and L. S. Gittleson

KCB

Modal Survey of the PACOSS DTA
R. N. Gehling

KCC

**Application of Passive and Active Damping Techniques
to the PACOSS Representative System**
D. R. Morgenthaler

KCD

SESSION KD—Applications

A Damping Treatment for Resonant Test Fixtures
F. Cericola, Dr. J. D. Rogers and D. J. Segalman

KDA

**The Recent Advances in Viscoelastic Waveguide Absorbers
for Passive Vibration Control**
Dr. Y. S. Shin and K. S. Kim

KDB*

**Optimization of Dynamic Vibration Absorber –
Case of Cantilever Boring Bars**
Dr. E. I. Rivin and H. L. Kang

KDC

**Development of a Scaled-Down Inertia Brake Dynamometer to
Evaluate the Effect of Pad Damping Liners on Brake Squeal Noise**
Prof. R. Singh and R. Beer

KDD*

*Not available for publication.

DAMPING - A KEY TO MORE, FASTER, FARTHER, HIGHER

Major General Thomas R. Ferguson, Jr.
Deputy Chief of Staff for Technology
and Requirements Planning
Headquarters Air Force Systems Command
Andrews Air Force Base, Maryland

Vibration is everywhere. And where there is vibration, there is damping. Most often, vibration is bad and damping is good. There are exceptions, but since this conference is about damping, we will leave the undamping crowd to their own devices.

After getting my primer on this subject, I was reminded that damping is a complicated subject. In simple terms, vibratory response can lead to cracked structure, defocused optics, or other types of degraded performance. Historically, the damping in a vibratory system has been "take what you get", called intrinsic damping. Only in the last few years has damping been a design parameter. So let's begin with a scramble: start the engines...on take off, light the burner. In my flying experience with the B-52, it was be sure all eight were running and start the Hound-Dogs on the roll...there's a lot of noise coming out of these engines. During take-off roll, there are two paths from the engine exhaust noise to the aft structure: one is direct, the other is reflected from the runway. Take-off is typically the highest acoustic environment the structure is exposed to. The skin panel responds to sound pressure level as does a microphone and it vibrates. It can vibrate enough to literally crack and break. The skin panel also re-radiates the sound into the interior. That's called "thru transmission." That's also the technical term for being able to hear people thru the motel wall, at least the motels government per diem can afford in places like Boston and Washington.

That aircraft skin panel also transmits vibratory energy into the substructure--the stringers, frames, and bulkheads. So internal equipment also gets hit with structural-borne vibratory energy at points like mounting brackets and with acoustic energy on their covers. Internal equipment can fail, malfunction or degrade to lower performance levels. As our pilot retracts the gear and accelerates, the dynamic pressure increases and the turbulent boundary layer, especially behind protuberances, can create very high sound pressure levels. At about mach 0.9, the oscillating shocks have the same effect. When we maneuver, especially transonically, the aeroacoustic levels on the leading and trailing edges (and external stores) reach high levels. When we open weapons bay doors, the open cavity acts like a giant whistle and the internal structure and stores can be subjected to tones of extremely large amplitude. Since we fly to fight, we carry weapons; we fly at ever-higher dynamic pressures and maneuver at transonic speeds to survive: This makes the vibroacoustics problem more severe. Today, to do our engineering right, structures-and-vibration-and-damping-engineers must participate in the original design of these modern flying machines.

Vibration is also no longer an earthly problem. It is becoming a design factor in satellites as well. Launch vibroacoustics typically cause the highest vibration levels and can break equipment. There are also more vibratory disturbances in orbit than you might think. There are always imbalances in reaction wheels, momentum wheels, and control moment gyros used for attitude control. Coolant flow, shifting solar arrays, liquid slosh, gravity gradient, particle impact, to name just a few, are all vibratory disturbances which, just for example, can degrade performance of sensitive optics.

I shouldn't have to convince this audience--we know that vibration is everywhere. Although the obvious is obvious to us, let's also acknowledge that damping is a highly specialized subject. A damping engineer is a specialist because he must first be a vibration engineer, who was probably a structures engineer to start with. So, right off, we have a specialty within a specialty within a specialty. The successful damping engineer must know more than damping. He'd better know systems integration and be very conversant about the operational environment. A prime example of this is the highly successful "Damping Wrap" for the inlet guide vanes on the engines used in the F-111F fighter. So many cracks were forming so quickly that the inlet guide vane case had to be refurbished after T00 few hours of service. Air coming into the engine is turned slightly by the inlet guide vanes to get best performance from the rotating first stage compressor. The IGV case consists of titanium inlet guide vanes welded to inner and outer rings. Vibration was suspected as the cause of the cracks which were forming in the heat affected zones of the welds. The intrinsic damping was extremely low, and in this case, the dynamic magnification factors at resonances were high. Obviously, the stage was set for a damping engineer to really impress his boss. Adding damping to the inlet guide vane was easy; developing a satisfactory damper wrap for a complex systems operational environment was not. Sophisticated bonding technology was used so that the damper wrap would adhere while exposed to the air flow. The wrap had to be thin to minimize inlet blockage area, since reduced air flow would affect engine performance. Engine stall characteristics, anti-icing effectiveness, erosion, corrosion, and durability were all investigated and proven satisfactory. The point being...this was a complex interdisciplinary problem--solved very successfully. This project has estimated cost avoidance savings to the Air Force of \$50M. Spin-off damping applications in similar situations may well account for another \$200 million. Other very recent demonstrations of vibration-caused structural failures fixed by damping are the A-7 center section leading edge flap, A-10 gun bay floor and side wall, and F-111 spoilers. Once again the logistics improvements in terms of dollars were significant. I should also add these improvements lower the heart rate for our maintainers.

For the most part, successful damping treatments have been of the add-on variety. The hardware has been designed and a vibration problem rears its ugly head. A damping treatment is designed and "added to" existing structure. Once the hardware exists, add-on damping may be an extremely cost effective solution. But it's better to avoid the problem altogether and that can be done with integral damping. Commercial examples are laminated valve covers, oil pans, and timing gear covers used in automobile and diesel engines.

Integral damping is also the key to longer life, more durable aircraft structure. The objective is increased sortie generation rate and reduced maintenance cost. Since we often learn more from our failures, there's no shame to admit there have been many unsuccessful attempts to design damping solutions. I'm told you don't have to be in this business very long to have been bit. In fact, you don't earn your damping wings until you've been humbled more than once. I don't want to focus on this aspect, but during breaks and at social opportunities it also pays to discuss the failures as well as the successes.

DAMPING '89 is put together to detail the state of the art, but the keynote role allows me latitude to summarize. A baseline of damping materials and manufacturing processes is established. We can measure properties of materials fairly well. Data banks on damping materials are also established. You can analyze simply supported beams in closed form and can perform finite element analysis of damped structure to predict modal frequencies and damping limits. You can experimentally measure the modal frequencies and damping of structure. There are a growing number of successful add-on and integral damping applications and you have quantified these successes in terms, pay-off terms, that management understands. Damping, in fact, is a hot, new tool in the engineer's kit bag. But it's good not to believe as the song goes "Oh Lord it's hard to be humble when you're perfect in every way." What we already know is just a glimpse of the future. There is still great opportunity. Therefore, it's important to make good investment decisions as we plan the future.

As in most technical disciplines, the explosion in computational power, coupled with advancements in damping technology, can greatly accelerate our knowledge. Better dynamic test techniques are needed; a greater range of materials properties should be measured and catalogued; and extensions to analytical methods would really expand the range of applications. With these wishes met, let's peer in the not too distant future and I'll make some predictions:

- o Measurement of the dynamic mechanical properties of viscoelastic damping materials will be more accurate, more efficient, and have less scatter.
- o Existing materials will be screened for toxicity, flammability, outgassing, corrosion, long-term environmental stability and others. These are properties which are mandatory for system application.

- o A fully computerized data clearing center will exist soon.
- o Wide-temperature range and low-temperature damping materials will be developed.
- o Approximate closed form analysis methods will come into use for structures like thin plates and shells, brackets, pipes and tubing.
- o Approximate finite element analysis models will be developed as preliminary design tools for damped structures such as satellite equipment support structures.
- o Computer aided design will yield optimum solutions by interacting finite element analysis of damped structure with a data base of damping materials.
- o Most aircraft sheet metal will be laminated, ditto for automobiles and household appliances.
- o Interest in damped composite structural materials will rise.
- o Housings and circuit boards of avionics equipment will be damped.
- o Logistics imperatives--maintainability and reliability--will dictate much more use of damping.
- o And, some of you who think you'll be millionaires exploiting these opportunities will probably go bankrupt because of Murphy. So, maximize the opportunity this conference offers.
- o Learn!!
- o Go home and apply the technology: Be passionate...become zealots for your work and the opportunity it presents.
- o Share your successes and failures with as wide a technical community as possible.
- o Think of yourselves as a team: Academia and practitioners in commercial and military applications. All must play their roles to see the most intelligent and widespread use of this technology.

I want to conclude with some non-damping thoughts. My boss, the AFSC Commander, General Randolph, just gave a talk at the AF Association's Tactical Air Warfare Symposium. He ok'd my use of some of his remarks because the message is so important for all of us. That message is about total quality management.

In the book, "A Passion for Excellence," Peters and Austin recall the management style of General Electric's aircraft engine pioneer, Gerhard Neumann when he worked with Claire Chennault's World War II Flying Tigers. Neumann wanted make sure his maintenance people fixed aircraft engines right...the first time. So each day he used to ask a few of his squadron mechanics to "volunteer" to test fly in the Single-Seat fighter they'd just repaired. The pilot would sit on the crew chief's lap, and neither could sit on a parachute because the cockpit wasn't big enough.

Well, improvements in workmanship were dramatic! In his book, "Herman the German," Neumann writes that each night, "Way past dinnertime, the airfield looked as if it were invaded by glowworms; the twinkling came from flashlights mechanics used to check--once more--the tightness of pipes or connections they had made in case Neumann might suggest that they 'Volunteer' to ride in their planes the next day."--Now there's a guy who knew how to motivate quality. TQM's an overdue sign of a national quality revolution. It's a buzzword you see in commercials, hear at symposiums, and notice in bookstores. But don't just dismiss TQM as yet another acronym that will die off. As a term, TQM might well change over time. However, as a philosophy TQM will last, as more companies and managers come to understand what continuous quality improvement means and what it can do. Affordable price tags, fair profits and high product quality will prove TQM's merits long after the trendiness of the buzzword disappears. It offers opportunities for every person involved in research, development, test, production and operations.

TQM--is BETTER QUALITY AT LOWER COST. It's the prerequisite to good performance. AFSC's senior people have been through training seminars with W. Edwards Deming, one of the best-known quality leaders in the world. Deming's philosophy is that 85 percent of quality problems are caused by the system; just 15 percent are caused by people. Just to be sure we're communicating--you're likely to be part of the 85 percent! If the products of U.S. industry are not well liked, loved, by the customer, you are involved because you're that 85 percent of the system that designs-in-problems the manufacturing work force can't correct.

General Randolph was challenged about his intensity on this subject of total quality management. The person said it sounds as if quality issues are a matter of life and death. He said no, they're much more important than that. Think about these statistics:

If the U.S. had service suppliers who did their jobs right 99.9 percent of the time, there would still be:

- 20,000 wrong prescriptions filled each year;
- Unsafe drinking water almost one hour each month;
- 2 long or short airplane landings a day (That's an accident) at Los Angeles and New York;

- And 2000 lost articles of mail per hour every day.
- In the defense arena, given 1 million grenades, you would have 999 duds--and 1 will go off in "0" seconds.

Where is your quality meter set?

General Randolph closed his talk with this story President Kennedy would tell and I'll do the same. It's about a retired French General whose hobby was gardening. He was a very cultured man with a deep sense of history. On his 80th birthday he bought a small shrub and instructed his gardener to plant it in the garden.

"But, Sir," the gardener protested, "that plant won't flower for a hundred years!" "Then by all means," the General said, "plant it now."

The total quality we plant in our work today is FREEDOM FOR TOMORROW. We need to plant more flowers.

Fiber Optic Vibration Sensors for Structural Control Applications

W.B. Spillman, Jr.

B.R. Kline

Hercules Aerospace Company
Aircraft Systems Division
Vergennes, Vermont 05491

Abstract

In order to control the behavior of aerospace structures in real time, closed loop control systems require highly accurate measurements of the vibrational frequencies and amplitudes exhibited by structures at any given instant. Traditionally, this has meant the use of a large number of accelerometers mounted at various locations on the structure. The motion of the structure has then been inferred from these point measurements. Developments in the field of fiber optic sensing have now reached the point at which practical sensors may provide a near term ability to produce an output proportional to the integrated structural deformation along an attached or embedded optical fiber. In this paper, the principles of operation of two candidate techniques are discussed: polarimetric and statistical mode sensing. Experimental results are presented and compared with theoretical predictions. Finally, the advantages and limitations of integrating vs point vibration measurements are covered, with an emphasis on structural control applications.

Introduction

The one dimensional, flexible nature of optical fibers makes them almost ideal for use as distributed sensors. A parameter of the fiber that can be easily affected by a stimulus is the optical path length and a change in optical path length can be measured with great resolution using interferometric techniques. Figure 1 shows a two arm optical fiber interferometer that is sensitive to optical path length differences of less than a wavelength of light (<1 micron). Unfortunately, this is much too sensitive for stable operation without complex compensation schemes. The sensors described in this paper reduce the unwanted sensitivity by having all the arms of the interferometer in the same fiber.

A polarimetric sensor results when the two arms of the interferometer are the two orthogonal polarization modes of a single mode fiber. Any stimulus that induces a birefringence in the fiber will effectively cause a difference in optical path lengths. The polarimetric sensor considered here uses stress caused by bending to produce the birefringence. With a coherent light source at one end of the fiber and an analyzer at the other, a bend modulated signal is observed.

A statistical mode sensor (SMS) results when the interferometer has many arms, all coexisting as propagation modes within a single multimode fiber. When the output from a multimode optical fiber is projected upon a screen, a uniform circular pattern is observed. When the light is incoherent, there is a smooth distribution of intensity within the pattern. When coherent light is used, however, the pattern becomes very granular and consists of a very large number of "speckles" of varying intensities as seen in Figure 2. This is the complex interference pattern of a many armed interferometer. The distribution of these speckles changes slowly over time, but the intensity of the total circular pattern remains basically constant. When the optical fiber carrying the coherent light is perturbed, the distribution of the speckle intensities is seen to change with the perturbation, with some speckles becoming brighter, some dimmer, and some not changing at all. The total intensity of the pattern remains unchanged, however. A statistical analysis of the changes in the speckle pattern output from the optical fiber can then be used to obtain information about the perturbation of the fiber.

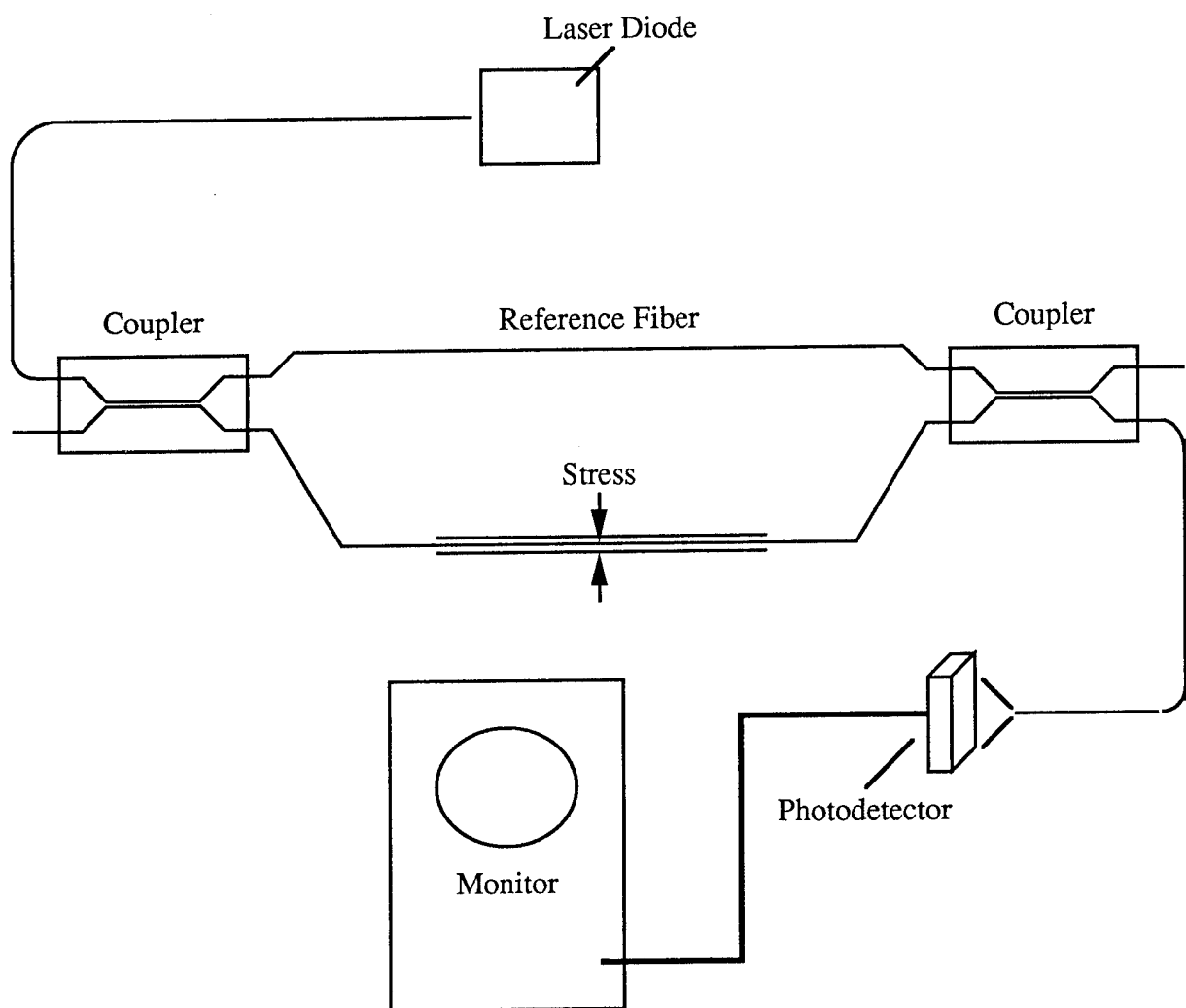


Fig. 1. Fiber optic interferometer.

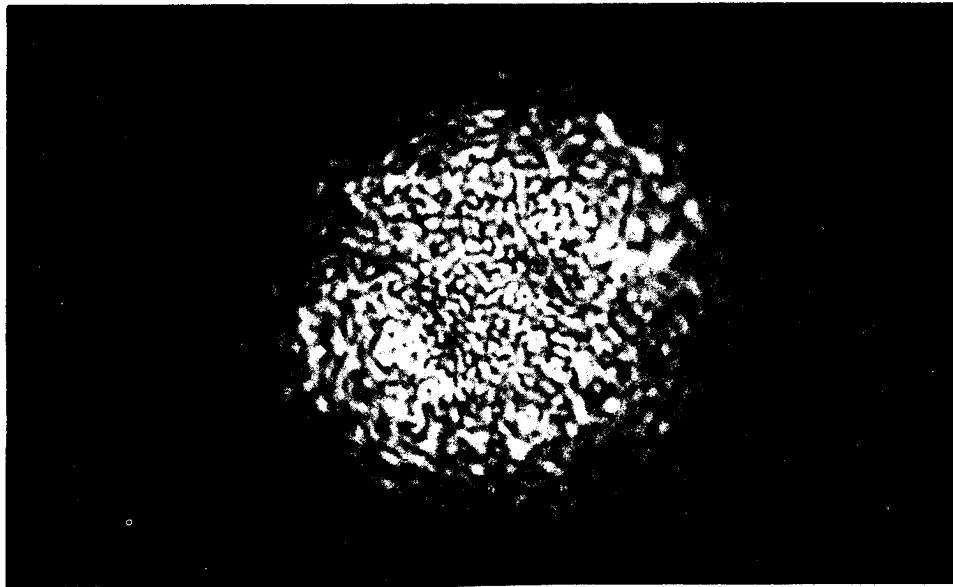


Fig. 2. Multimode optical fiber speckle emission.

There exists a body of prior work involved with investigation and use of the output speckle pattern from multimode optical fibers for a variety of purposes. Of particular interest is the work done by Claus et al. [1-2] on the vibration sensing effects using low number of modes step index optical fiber sensors. This work fills the gap between the two mode polarimetric sensor and the many mode statistical mode sensor.

In this paper, the theory and use of distributed fiber optic vibration sensors is described. In one implementation of a statistical mode sensor (SMS-A), simple spatial filtering is used to optically process the speckle pattern to provide an output related to fiber perturbation. In a second, more sophisticated implementation (SMS-B), the pattern is projected on a CCD array detector whose output is used to process changes in the pattern distribution to allow for accurate correlation with fiber perturbation. Theoretical analysis of the output modal pattern of a highly moded step index optical fiber is utilized to create a mathematical model of the SMS implementations. The mathematical model is then used to make predictions of SMS performance. Two implementations of the sensor are then simulated via a computer program. The computer simulation and actual device performance are compared with theoretical predictions. Experimental results are shown indicating the operational characteristics of the SMS units in a simple field test environment. Finally, a polarimetric sensor is described and its operation is compared to the statistical mode sensors.

Applications for distributed fiber optic vibration sensors include, but are not limited to, intrusion detection, structural vibration sensing, and acoustic sensing. A distributed sensor may be of particular importance where the alternative is a large number of point sensors such as on large space structures.

Theory: Polarimetric Sensor.

Polarimetric sensors have been well described in the literature and have been used to sense a number of different stimuli such as magnetic fields and sound waves. A concise mathematical treatment of this type of sensor is given by Beasley et al. [3] in relation to a hydrophone.

A block diagram of a polarimetric sensor is shown in Figure 3. It consists of a source of polarized light, a length of fiber with a portion exposed to a source of stress, and an output polarizer which acts as an analyzer. By choosing a coordinate system that is referenced to the applied stress, the input polarized light can be expressed (using Jones calculus) as

$$\vec{E}_{in} = \begin{bmatrix} E_x \\ E_y \end{bmatrix} = E_o \begin{bmatrix} \cos \theta \\ \sin \theta \end{bmatrix}, \quad (1)$$

where E_o is the magnitude of the field and θ is the orientation of the polarization relative to the applied stress.

The fiber itself can be modeled by the transformation matrix

$$R = \begin{bmatrix} e^{i(\alpha/2)} \cos \omega & -e^{i(q/2)} \sin \omega \\ e^{-i(q/2)} \sin \omega & e^{-i(\alpha/2)} \cos \omega \end{bmatrix}, \quad (2)$$

where q is the retardation of the coupled light, ω is the percentage of light coupled between the axes, and α is the phase difference between the two polarization modes given by

$$\alpha = \alpha_o + \frac{2\pi LC}{\lambda} (\sigma_x - \sigma_y) \quad (2a)$$

where α_o is the static component, L is the length of fiber exposed to stress, C is stress-optic coefficient, λ is the wavelength of light, and σ_x and σ_y are the orthogonal radial components of the applied stress.

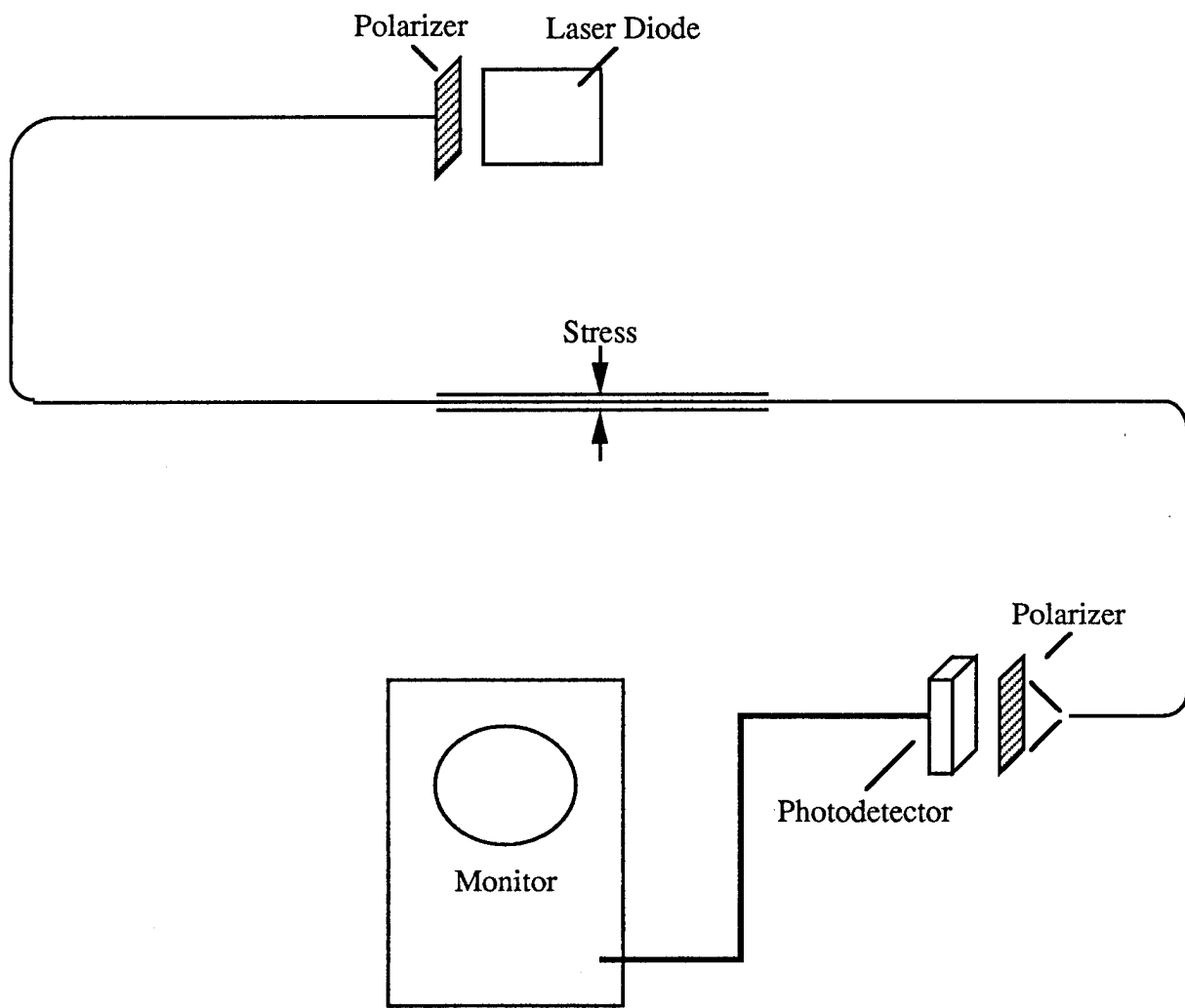


Fig. 3. Polarimetric fiber optic sensor.

Similarly, the output analyzing polarizer can be modeled by the transformation matrix

$$S = \begin{bmatrix} \cos \psi & \sin \psi \\ -\epsilon \sin \psi & \epsilon \cos \psi \end{bmatrix}, \quad (3)$$

where ψ is the angle of the transmission axis of the polarizer and ϵ^2 is its extinction ratio.

The output of the analyzing polarizer is given by

$$\vec{E}_{\text{out}} = S \cdot R \cdot \vec{E}_{\text{in}}. \quad (4)$$

Assuming there is no mode coupling in the fiber, making $\omega=0$, and that the output light is linearly polarized, making $\epsilon=0$, the output power can be expressed as

$$I_{\text{out}} = \vec{E}_{\text{out}} \cdot \vec{E}_{\text{out}}^* = \frac{E_0^2}{2} (1 + \cos 2\theta \cos 2\psi + \sin 2\theta \sin 2\psi \cos \alpha). \quad (5)$$

Simplifying further by setting the input polarization angle and the analyzing polarizer angle to $\pi/4$ reduces the equation to

$$I_{\text{out}} = \frac{E_0^2}{2} (1 - \cos \alpha). \quad (6)$$

From equation (4), it can be seen that stress on the fiber which alters the birefringence which changes the factor α , will in effect modulate the light intensity. This modulation can be made fairly linear if the stress perturbations are small and if the fiber is prestressed so that α is centered about $\pi/2$.

Theory: Statistical Mode Sensor.

Assume that the light in a multimode fiber is coherent, and linearly polarized, with the direction of propagation along the z-axis, and the electric field oriented along the x-axis. Assume each speckle has an intensity that depends upon modal interference of the coherent light in the fiber. Assume that each speckle is projected upon a photodetector element and converted to an electrical signal. The changes in this signal may then be processed to obtain information about perturbations of the optical fiber. If each individual speckle intensity is given by I_i , the total intensity is roughly constant, i.e.

$$I_T = \sum_{i=1}^N I_i = \text{constant}, \quad (7)$$

where N is the number of speckles.

Next, assume that each of the N speckle intensities act like the output from individual interferometers and vary with the fiber perturbation. Each individual speckle intensity would then vary with time according to

$$I_i = A_i [1 + B_i \{\cos(\delta_i) - F(t) \phi_i \sin(\delta_i)\}]. \quad (6)$$

Although these interferometers are obviously related, subsequent analysis and modeling will assume that for small enough sampling areas and large enough number of samples, that individual speckles will be weakly or randomly related in phase, amplitude and modulation depth with respect

to perturbation, i.e. $\{A_i, B_i, \phi_i\}$ and δ_i are assumed to be collections of random numbers within some limits. The degree of validity of this assumption will be determined through comparison of model predictions with experimental results.

In order to allow comparison of theory and experiment, two different ways of processing the individual I_i 's are considered: (1) summing the changes of a small enough number of the signals so that statistical averaging does not produce a constant sum as shown in Figure 4 and (2) taking the sum of the absolute value of the changes in all of the signals as shown in Figure 5.

In the first case, the sum of $n < N$ components is taken. In addition, only the time varying components are considered. In that case,

$$\Delta I_T = \sum_{i=1}^n -A_i B_i \phi_i F(t) \sin(\delta_i) \quad (7a)$$

may be reduced to,

$$\Delta I_T = \sum_{i=1}^n C_i F(t) \sin(\delta_i) . \quad (7b)$$

Since the $F(t)$ term is independent of the sum, it can be pulled out with the result

$$\Delta I_T = \left\{ \sum_{i=1}^n C_i \sin(\delta_i) \right\} F(t) . \quad (8)$$

This expression represents the output that could be expected from a statistical mode sensor in which the intermodal interference information is optically processed by simple spatial filtering. It should be noted that Equation (8) is also an expression of conservation of the total power contained in the speckle pattern, since as n becomes very large, the term in brackets goes to zero.

For the second case, in which the absolute values of the changes of all N pixels are summed, the basic expression for the signal output is given by

$$\Delta I_T = \sum_{i=1}^N \left| C_i \frac{dF(t)}{dt} \sin(\delta_i) \right| , \quad (9)$$

where the absolute values of the derivatives of Equation (7) have been summed. The final signal output for this case can be written as

$$\Delta I_T = \left\{ \sum_{i=1}^N \left| C_i \sin(\delta_i) \right| \right\} \left| \frac{dF(t)}{dt} \right| . \quad (10)$$

The term within the brackets sums over a large number of components so that in spite of local variations in the distribution, the sum will remain at a constant value which will be defined as C . Equation (10) can then be expressed as

$$\Delta I_T = C \left| \frac{dF(t)}{dt} \right| . \quad (11)$$

From Equations (8) and (11), response to a sinusoidal perturbation, $\sin(\omega t)$, would be

$$\Delta I_T = \left\{ \sum_{i=1}^n C_i \sin(\delta_i) \right\} \sin(\omega t) \quad (12)$$

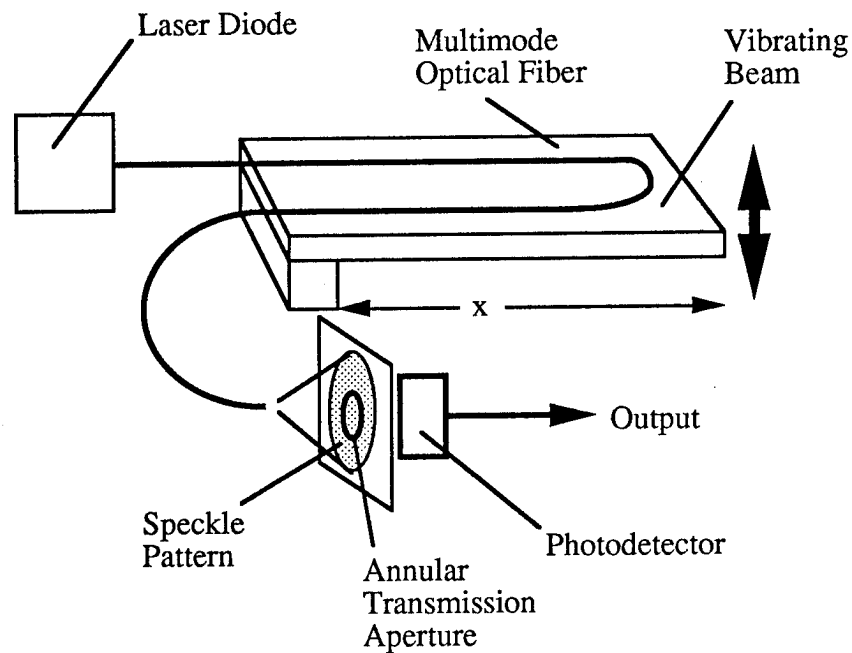


Fig. 4. SMS-A Signal Processing is accomplished using an optical spatial filter.

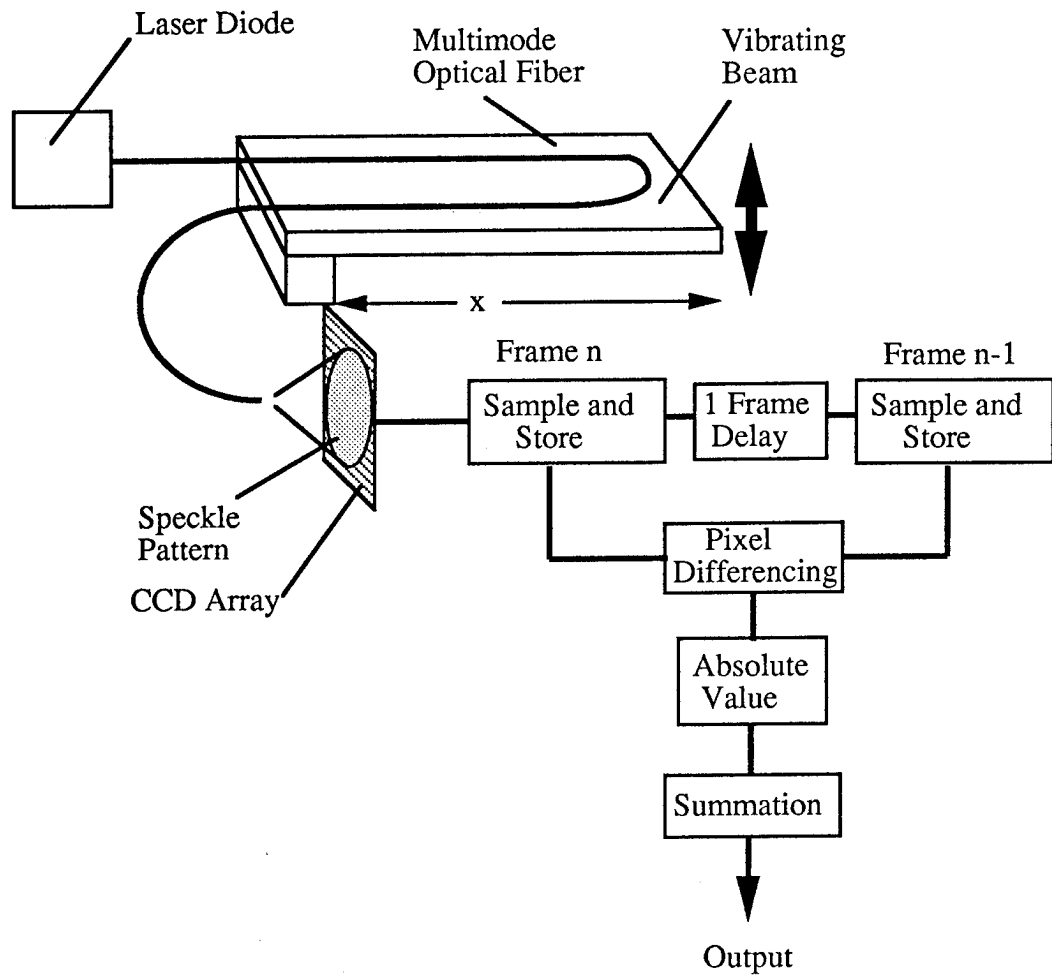


Fig. 5. SMS-B Signal processing is performed digitally by an image differentiation circuit.

for the first case, while the second case would reduce to

$$\Delta I_T = \omega C |\cos(\omega t)| . \quad (13)$$

The absolute value term in Equation (13) can be replaced by an infinite sum, or

$$\Delta I_T = \omega C \left[\frac{2}{\pi} + \frac{4}{\pi} \sum_{k=1}^{\infty} \frac{\cos(2k\omega t)}{(4k^2-1)} \right] . \quad (14)$$

Based on Equations (11) and (14), SMS device performance when the two different processing schemes are used can be predicted. For the first case, a signal should be present at the same frequency as the perturbation and either in phase with the perturbation or π out of phase. The amplitude of the signal could range from some maximum value down to zero. For the second case, the signal has no component at the perturbation frequency, a large component at twice the perturbation frequency, and smaller components at integral multiples of twice the perturbation frequency. Although harmonic distortion exists, the signal should exhibit good amplitude and phase stability due to the statistics involved in summing the absolute value of a very large number of speckle intensity changes. In addition, due to the differentiation inherent in the second case, for constant amplitude and varying frequency perturbation, the SMS signal should exhibit a linear fall off of amplitude with decreasing frequency.

Computer Model of Statistical Mode Sensor

In order to determine the characteristics of a number (N) of interferometers with randomly related coefficients $\{A_i, B_i, \phi_i\}$ and $\delta_i\}$, a computer model was developed in the C language to simulate the expected output from the two different processing schemes for the statistical mode sensors. The program was written in the Lightspeed C implementation of the language and run on a Macintosh Plus computer. The language random number generator was used to provide N sets of values $\{A_i, B_i, \phi_i\}$ and $\delta_i\}$ to correspond to the N randomly related interferometers. The allowed ranges for the interferometer parameters were: $0.5 \geq A_i \geq 0$, $1.0 \geq B_i \geq 0$, $\pi/8 \geq \phi_i \geq 0$, and $2\pi \geq \delta_i \geq 0$. The random number generator provided the same output every time, so that any $N > n$ set of interferometers always included the set of n interferometers generated for the smaller number.

The computer modeling produced the results shown in Figure 6. In Figure 6(a), one cycle of perturbation is applied and the normalized sums of 5, 50 and 500 pixels (interferometers) are taken. The normalization factor is the average of the sum of the pixel intensities over the one cycle. As can be seen, the fractional modulation of the pixel intensity sum decreases with increasing number of pixels, so that for 500 pixels, the modulation is negligible. Figure 6(b) depicts the result when the absolute value of each pixel change is summed over one cycle of modulation and normalized to the sum of the pixel intensities over the cycle. In this case, the signal does not change significantly as the number of pixels is increased with a modulation of ~2%.

Device Design and Fabrication

In order to test and compare the polarimetric and statistical mode sensors, three prototypes were constructed. A polarimetric sensor and two SMS signal processing designs were implemented, the SMS-A using spatial filtering to perform optical processing of the signal, and the SMS-B, which used much more sophisticated electronics in conjunction with a CCD detector.

The polarimetric sensor was assembled as shown in Figure 3 in the laboratory for comparison purposes. It consists of a laser diode light source, an input polarizer to assure a source of linearly polarized light, a length of single mode fiber of the type used for communications, an output analyzer polarizer, and a photodetector. Since the single mode fiber used was not polarization preserving, the orientations of the input and output polarizers were simply adjusted to give the best

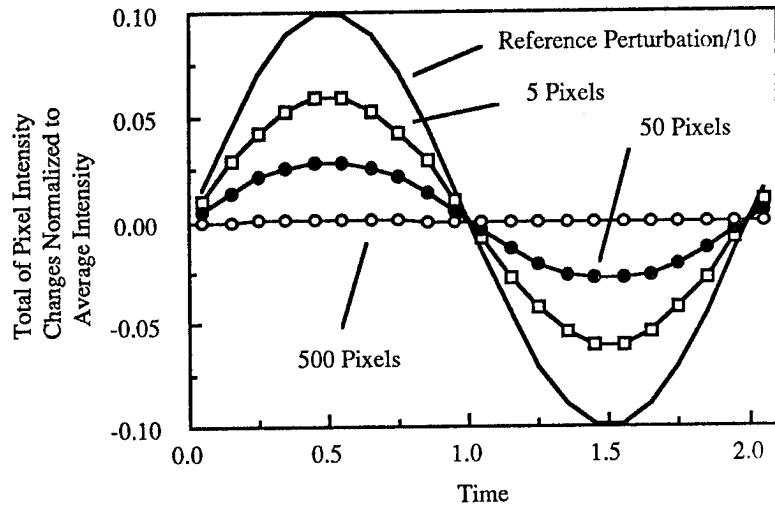


Fig. 6(a). Simulated SMS-A sensor output.

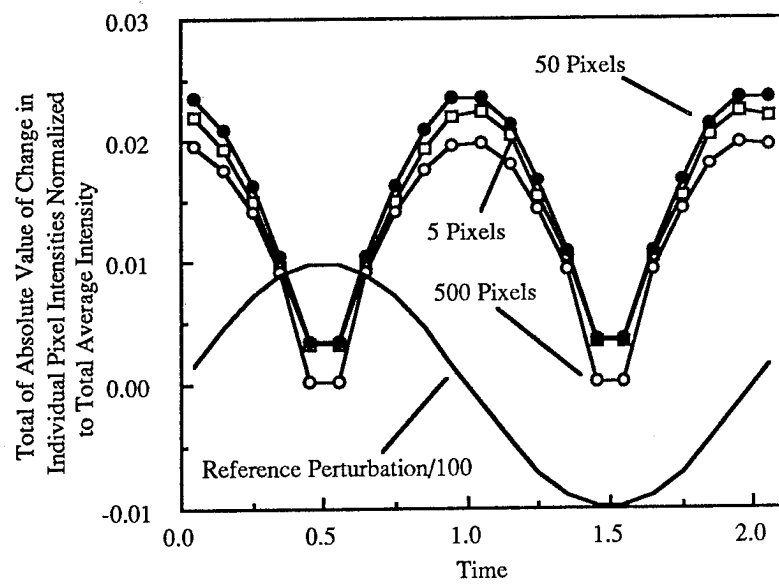


Fig. 6(b) Simulated SMS-B sensor output.

light modulation. The only signal processing required consisted of an AC coupled amplifier; a great deal of gain was needed because of the low sensitivity of the sensor.

Of greater interest were the statistical mode sensors. The SMS-A and SMS-B were designed and packaged for both lab and field use.

For the SMS-A unit, most of the speckle intensity processing is done optically, as can be seen from Figure 4. A simple amplifier for the photodetector would give a working system. Ideally, though, the output of the sensor would be much more stable and repeatable if the random effects of A_i , B_i , ϕ_i , and δ_i could be reduced. This can be done by assuming these terms vary more slowly than the perturbation signal so that they can be filtered out. Assuming a sinusoidal perturbation $F(t) = \sin(\omega t)$, and summing Equation (6) over all speckles gives a total intensity

$$I_T = \sum_{i=1}^n A_i + \sum_{i=1}^n A_i B_i \cos(\delta_i) - \sum_{i=1}^n A_i B_i \phi_i \sin(\omega t) \sin(\delta_i). \quad (15)$$

Simple high pass filtering will remove the first two terms leaving Equation (12). Because the unwanted bracketed term in Equation (12) is a gain term rather than additive, an automatic gain control (AGC) circuit is used. The control signal for the AGC circuit is derived from the inverse of the terms that were filtered out by the high pass filter. This does not provide complete compensation but A_i is completely removed and experience verifies that stability is improved. Figure 7 is a photograph of the SMS-A unit.

In the SMS-B sensor, all of the signal processing occurs in electronics as shown in Figure 5. The detector was a 128 x 128 array of photodiodes which capture an image of the speckle pattern called a frame. Each photodiode contributes one picture element, or "pixel", to the frame. Each pixel is digitized and stored in a digital memory called a frame buffer. Just before a new pixel is stored in the frame buffer, the old pixel data is removed and both old and new pixel data are passed to an arithmetic circuit. The arithmetic circuit finds the absolute value of the differences between the old and new pixels. All of the absolute values of the differences for the entire frame are then accumulated and normalized to give a single value. This single value represents the amount of change in the speckle pattern that occurs over the period of time between captured frames. For convenience, the digital value is converted back to an analog signal for display on an oscilloscope or strip chart recorder. A prototype of the SMS-B sensor is shown in Figure 8. Bandwidths in excess of 1 MHz can be attained by giving each pixel its own arithmetic circuit operating in parallel. However, to keep circuit size within reason, the photodiode array must be made much smaller. A more economical and slower method is to process the pixels serially through a single arithmetic circuit or computer. The actual implementation shown in Figure 5 clocked the pixels out of the array at 8 MHz through a pipelined "hardwired" circuit to attain a frame rate of approximately 275 Hz. The prototype unit also has an output that bypasses the final summation stage so that external signal processing may be used.

Results and Discussion

The polarimetric and the two SMS implementations were tested in a preliminary fashion in the laboratory. The tests were carried out using a communication grade single mode fiber and a 100/140 μm step index multimode optical fiber attached to a bar clamped at both ends. The fibers were attached to the bar in the same configuration as shown in Figures 4 and 5 with the single mode fiber mounted parallel to the multimode fiber. A spring weakly coupled the center of the bar to the drive piston of a Ling Dynamic Systems Linear Vibrator.

A vibrating bar was used to produce a distributed perturbation of the fiber. The choice of a bar rather than a vibrating string helped greatly with the waveform, harmonic, and phase analysis. This is because the overtones (higher modes of vibration) of a vibrating bar are not harmonic. If the overtones of the bar are excited, they would not be synchronized with the fundamental allowing them to be easily filtered out. In practice, the overtones were not present because there was no source of excitation at their frequencies. Of all the different boundary conditions for a vibrating bar

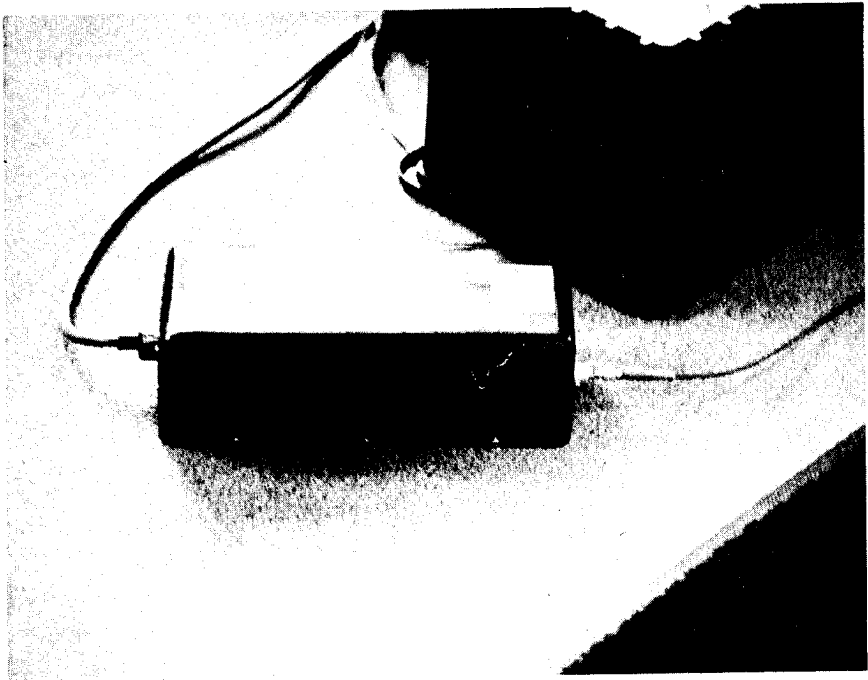


Fig. 7. SMS-A: Optical spatial filtering implementation.

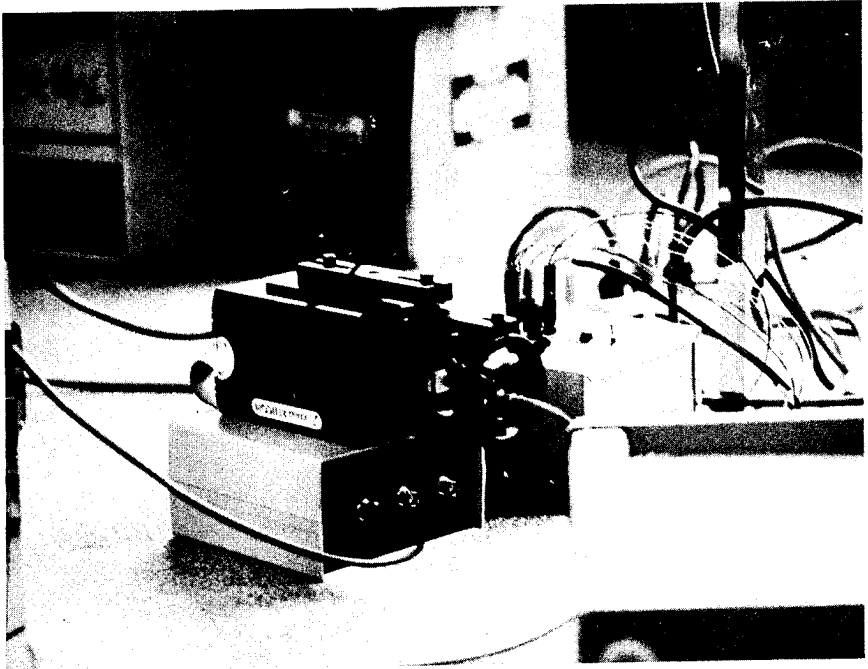


Fig. 8. Prototype SMS-B: CCD detector implementation.

(free, hinged, or clamped), the clamped - clamped configuration was chosen to avoid exciting the portion of the fiber leading up to the sensor section.

To monitor the vibrations of the bar without introducing distortions, a non-contacting fiber optic displacement sensor was used. The sensor consisted of a bundle of optical fibers whose sensing end was cleaved and polished in a uniform manner. Half of the fibers in the bundle transmitted light to the surface to be measured and the other half received the reflected light. Because the light disperses as it leaves the transmitting fiber, how much light is gathered by the receiving fibers depends on the distance to the reflecting surface.

The bar used was 74.7 cm between clamps, 0.7545 cm wide, 0.1265 cm thick, and made of steel. The fiber and glue add a little weight to the bar increasing its effective density slightly. The allowed frequencies for a bar clamped at both ends is [4]

$$v_n = \frac{\pi}{2l} \sqrt{\frac{Q \kappa^2}{\rho}} \beta_n^2, \quad \kappa = \frac{a}{\sqrt{12}}, \quad (16)$$

where l is the length, Q is Young's modulus, a is the thickness, ρ is the density, and β_n are coefficients for the allowed frequencies. For the bar used

$$a = .321\text{cm}$$

$$l = 74.7\text{cm}$$

$$Q = 19 \times 10^{11} \text{ dyne/cm}_2$$

$$d = 7.7 \text{ g/cc}$$

$$\text{and } \beta_1 = 1.5056, \beta_2 = 2.4997, \beta_3 = 3.5, \beta_4 = 4.5, \dots$$

This gives the fundamental mode at 29.4Hz which agrees with experiment. The shape of the bar as it vibrates is of the form $(1-\cos(x))$.

The bar was first perturbed in such a way as to provide a sinusoidal output from the reference displacement sensor. This output is shown in Figure 9 along with the output from the polarimetric sensor. The three signals from the polarimetric sensor indicate the result of varying the input conditions to the fiber on the vibrating bar by wrapping the input fiber around mandrels of (a) 3.2 cm, (b) 3.8 cm, and (c) 4.4 cm. As can be seen, the polarimetric sensor is fairly immune to input conditions. As long as the bending of the input fiber does not cause enough stress to move α significantly away from $\pi/2$, Equation 6 predicts that the amplitude and phase of the output should track the excitation.

Similarly, the output from the reference displacement sensor is shown in Figure 10 along with the output from the SMS-A. The three signals from the SMS-A indicate the result of varying the input conditions to the fiber as in the previous test. By changing the input conditions, the amplitude and sign of the sum term in Equation (8) have been modified so that curve (a) is π out of phase with the bar displacement with large amplitude, curve (b) is π out of phase with the bar displacement with lower amplitude, and curve (c) is in phase with the bar displacement and has large amplitude. These results indicate that the mathematical model used to predict the behavior of SMS type sensors has reasonable validity.

Following these tests, the SMS-B sensor was tested using the same optical source, sensing fiber, and excitation configuration. These results are shown in Figure 11. In this case, the frequency of the SMS-B sensor is twice the excitation frequency, precisely in accordance with prediction but out of phase by 31° . When the input conditions were varied in exactly the same manner as for the SMS-A sensor, the resulting output did not change in either amplitude or phase. These results provide additional demonstration of the validity of the simple mathematical model of device operation developed in this paper.

As Figure 11 shows, although the SMS-B maintains a constant phase, this phase is not $\pi/2$ as predicted. The large phase lag is actually a fixed time delay caused by the pipelined architecture of

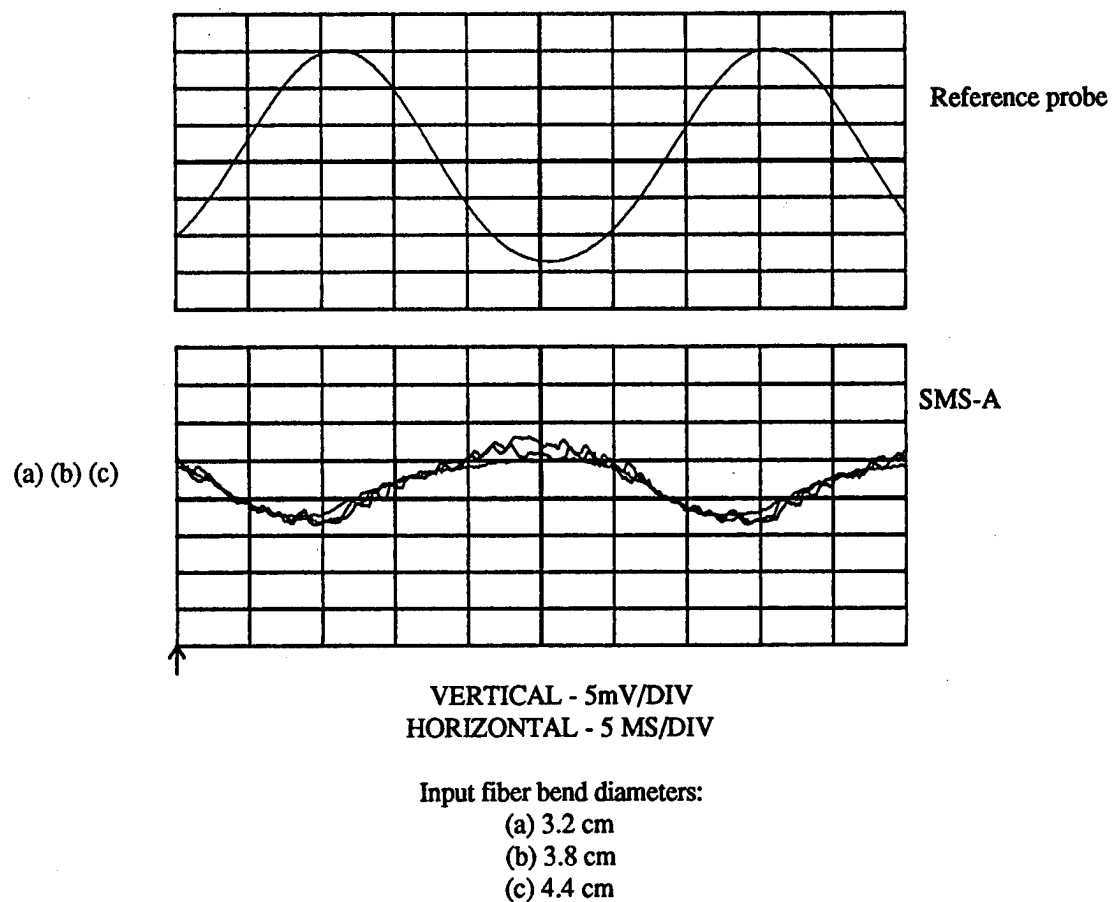


Fig. 9. Effects of varying input conditions to polarimetric sensor.

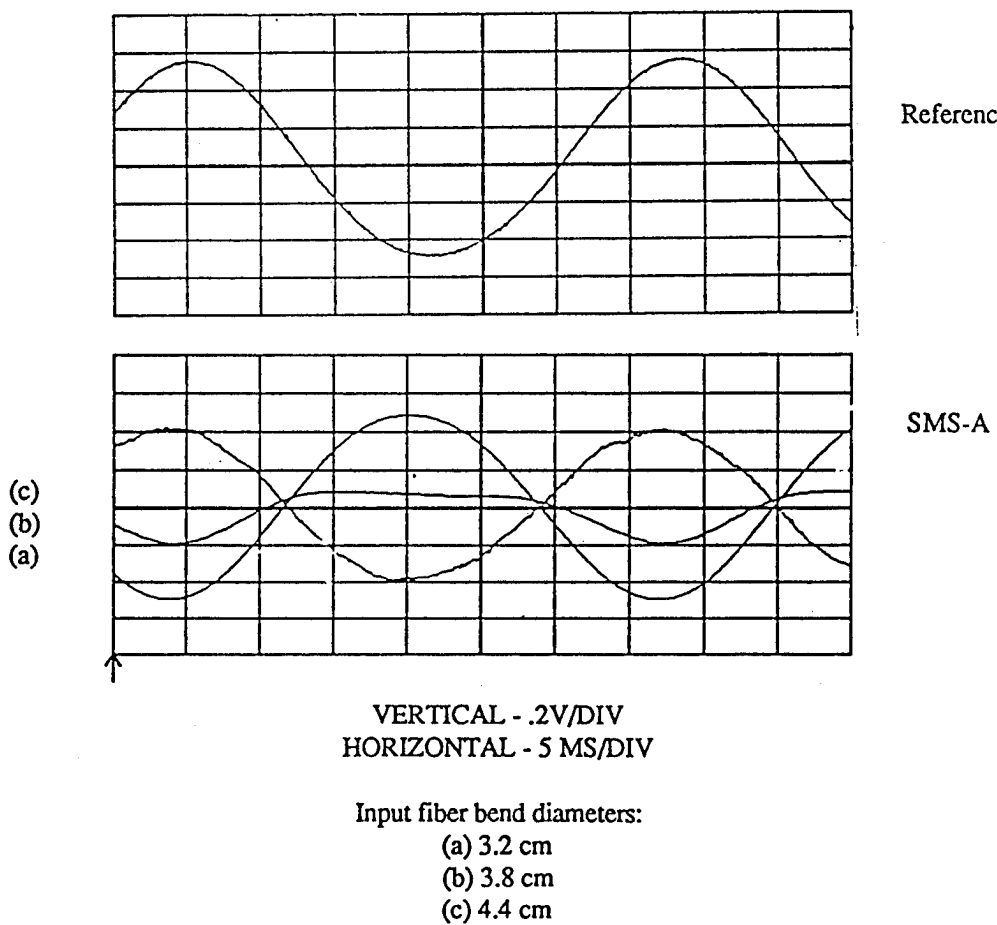


Fig. 10. Effects of varying input conditions to SMS-A.

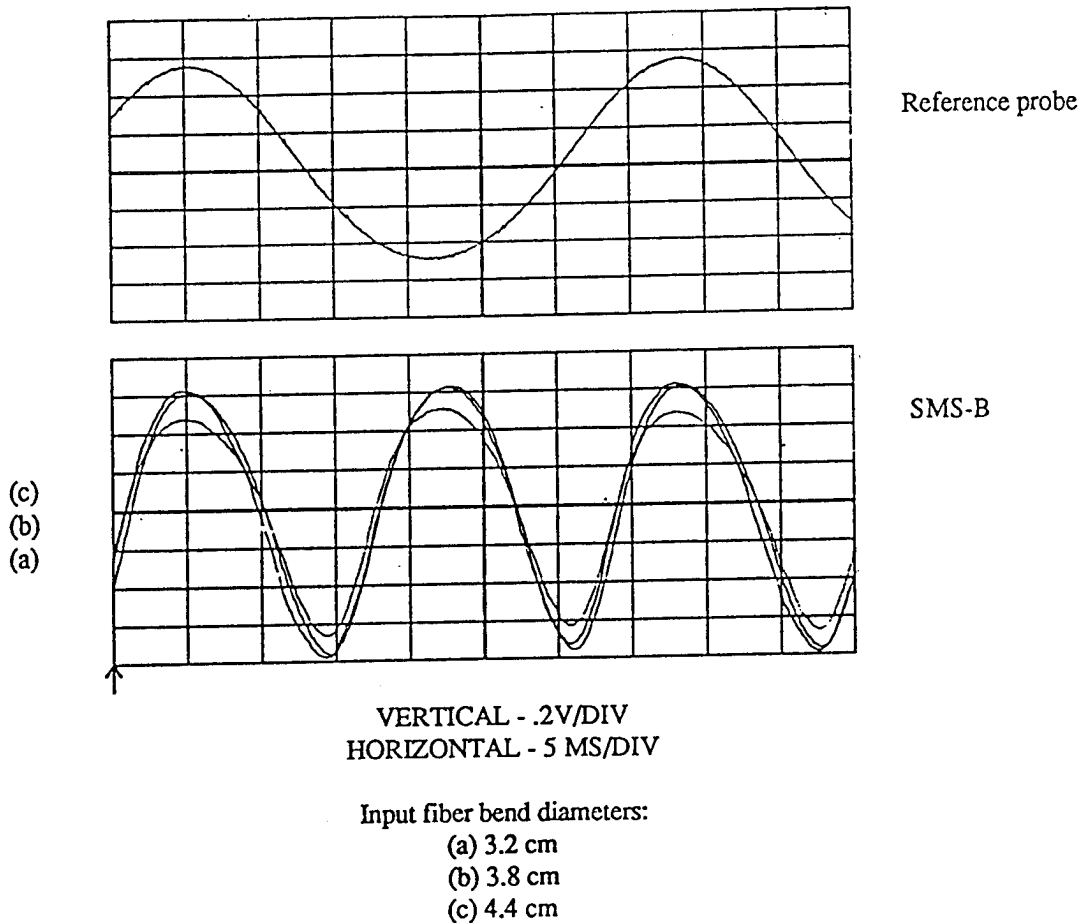


Fig. 11. Effects of varying input conditions to SMS-B.

the arithmetic circuit. The camera of the SMS-B quantizes the speckle image into frames, a complete frame taking 3.975 ms. There is a delay of approximately 3 frames from the photodiode input to the analog output. This accounts for all of the measured phase delay within the SMS-B electronics unit to within $\pm 2^\circ$. The SMS-A electronics unit has no source of large phase shift and measurement confirmed this to within $\pm 2^\circ$.

The amplitude variation of the SMS-B signal at 60.8 Hz as a function of the change in amplitude of the vibrating bar as measured by the reference sensor is shown in Figure 12. The dependence is linear as expected. Finally, Figure 13 shows the ratio of the SMS-B signal output at 2ω to the reference sensor output at ω as a function of ω . As can be seen, there is a falloff at frequencies above 65 Hz due to the frame processing rate of the SMS-B and a falloff at low frequencies due to the explicit ω dependence of the SMS-B signal as indicated by Equation (13).

A spectrum analysis of the outputs of the SMS devices was carried out under different conditions of amplitude of bar vibration. It was found that the SMS-A was very sensitive to optical input lead configuration, so that for one lead position, the fundamental frequency component virtually disappeared, leaving nothing but higher frequency harmonics. For large amplitude vibrations (4 mm), the harmonic distortion varied from 7% to 540%. Reduction of the amplitude of the vibrations by a factor of 4 (to 1 mm) resulted in a significant reduction of the harmonic distortion in roughly the same proportion although the exact numbers are not quantifiable due to the sensitivity of the SMS-A to the optical fiber lead configuration. When the SMS-B sensor was tested, it was found that the harmonic distortion ranged from 15% to 43% at the larger amplitude excitation and from 10% to 14% at the 25% excitation level.

Summary and Conclusions

Two methods of sensing vibration with integrating fiber optic sensors have been demonstrated. Mathematical models have been developed which have shown good agreement with observed sensor behavior. For the sensors examined, the sensing technique is compatible with off-the-shelf components and fiber cable and even allows for simultaneous telecommunication and sensing using the same optical fiber cable.

The results of the preliminary testing of the distributed sensors have been very encouraging. The ability to sense vibration has been demonstrated in the laboratory. Table 1 outlines the relative merits of the three sensors investigated.

Basically, the polarimetric sensor features simple construction and good amplitude, and frequency information and, with calibration, good phase response. Its main drawbacks are its low sensitivity to the type of bending stress used in our tests and the expense of coupling a laser to a single mode fiber. This sensor also exhibits a limited dynamic range because of its inherently nonlinear response as seen in Equation (6). The sensor must be adjusted to operate about a linear portion of its response curve and the excitations must be kept small to avoid amplitude errors and harmonic distortion.

The SMS-A type sensor offers the advantage that it is relatively simple and cost effective to implement. Spectrum analysis of its output can be used to determine the vibrational frequencies of whatever the sensing fiber is attached to or embedded in. This type of sensor is limited in that it can only be used to provide accurate information about vibrational frequencies, information about phase with an ambiguity of π , and no consistent information about amplitudes. Amplitude and phase of the output signal are very sensitive to the spatial configuration of the input and output optical leads to the sensing region, even if they are stationary, so frequent calibration is necessary if these parameters are needed. Like the polarimetric sensor, the SMS-A type sensor has a limited dynamic range because of its nonlinear response, however because of its statistical nature, the errors are not as bad (but neither are they adjustable).

The SMS-B type sensor improves upon the performance of the SMS-A sensor in two ways. First, like the polarimetric sensor, it is possible to obtain very accurate information about vibrational amplitudes, but with much greater sensitivity. However, the sensitivity is proportional to the signal's frequency which limits the band width and must be compensated for in subsequent

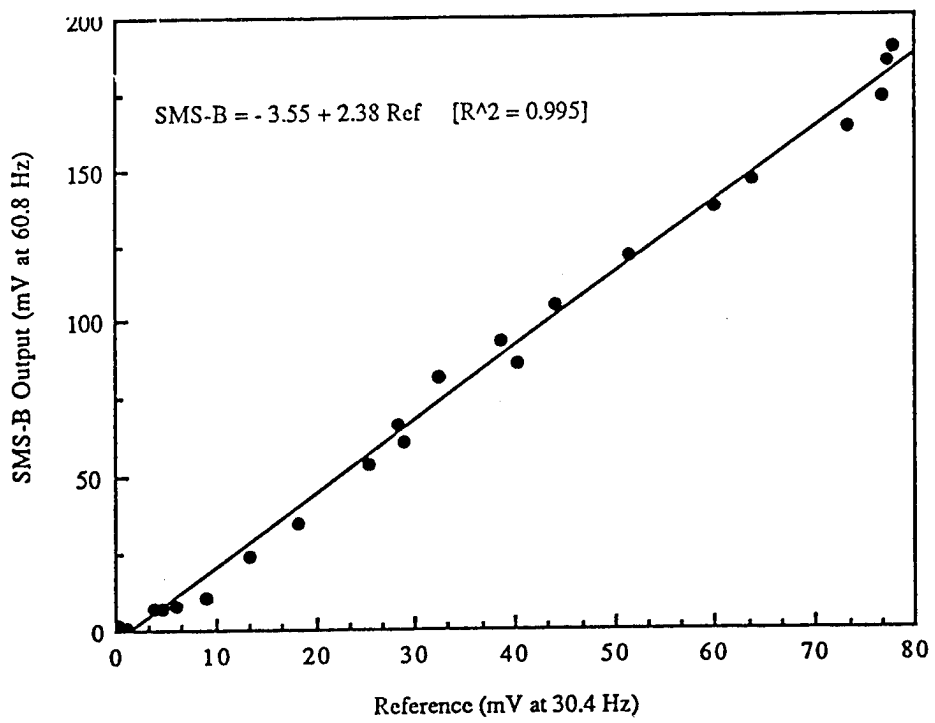


Fig. 12. SMS-B output vs. reference sensor output at constant frequency.

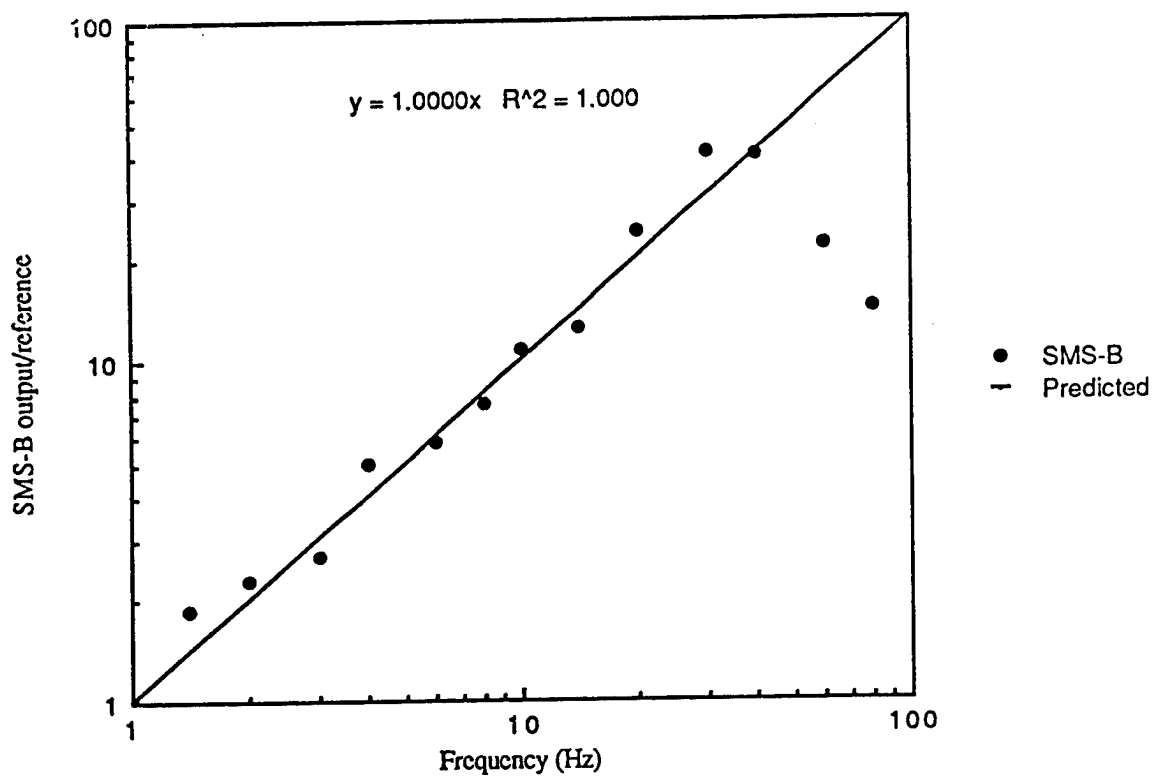


Fig. 13. SMS-B output vs. external perturbation frequency.

		Parameters					
Sensing Techniques	Sensitivity	Frequency Response	Amplitude Response	Phase Response	Harmonic Distortion	Calibration Needed	Relative Cost
Polarimetric	Low	Good (f)	Good	Good (after calibration)	Variable	Yes	Medium
SMS-A	Variable	Good (f)	Variable	Good (to within π)	Variable	Yes	Lowest
SMS-B	High	Good (2f)	Good (scales with f)	Good (to within π)	Low	No	Highest

Table 1: Comparison of Integrating Fiber Optic Vibration Sensors.

processing. Second, also like the polarimetric sensor, this type of sensor is not sensitive to the spatial configuration of the input and output optical leads to the sensing region as long as they are relatively stationary. Unlike the polarimetric and SMS-A type sensors, the dynamic range of the SMS-B type sensor is relatively large because its response is linear as Equation (11) shows. The principal limitation of the SMS-B sensor lies in the fact that it also provides phase information with an ambiguity of π because its output is frequency doubled. The phase ambiguity inherent in the SMS sensors precludes them from being straightforwardly used to provide error signals in closed loop structural control systems. Their use in such systems is still possible using sophisticated control algorithms based upon some a priori knowledge of the structural dynamics.

Both implementations of the SMS technique should have application for present sensing needs. Integrating sensors for the determination of vibrational structural modes could be used for active structural control in one application while another might include detection of structural damage or fatigue through detection of changes in basic structural vibration patterns. In applications where redundancy is needed for many point sensors, a distributed fiber optic sensor may be very cost effective if used to verify the operation of the primary sensors.

References

1. N. K. Shankaranarayanan, K. T. Srinivas, and R. O. Claus, "Mode-Mode Interference Effects in Axially strained Few-Mode Optical Fibers", SPIE Fiber Optic and Laser Sensors V (1987) Vol. 838.
2. K. D. Bennet, R. O. Claus, and M. J. Pinders, "Internal Monitoring of acoustic emission in graphite-epoxy composites using embedded optical fiber sensors", Proc. Quant. NDE Cof., (San Diego, Ca.), Aug 1986.
3. J. D. Beasley, D. W. Stowe, V. J. Tekippe, P. M. Kopera, and D. R. Moore, "A Sensitive Polarization Hydrophone", Proc. SPIE Fiber Optic and Laser Sensors, (Arlington, Va), April 1983.
4. P. M. Morse, Vibration and Sound, Ch. IV.15, Acoustical Society of America.

Active Vibration Suppression

using

NiTINOL Sensors and Actuators

by

David G. Wilson

Roy Ikegami

John R. Anderson

Gerald J. Julien

**BOEING AEROSPACE
Box 3999, MS 82-97
Seattle, WA 98124-2499**

ABSTRACT

This work investigates the development of NiTiNOL Shape Memory Alloys (SMA) sensors and actuators as components of an active vibration control system. Analytical and experimental models were developed and tested. The test set-up consisted of an aluminum cantilever beam with distributed NiTiNOL wires fastened along both sides. A constant amplitude control algorithm was used to provide a rate feedback force to actively suppress transient vibrations. The settling time of the beam was reduced by a factor of 15 through the use of the NiTiNOL wire sensors and actuators. Analytical simulations were developed which correlated well with the experimental results. This investigation demonstrated the feasibility of using NiTiNOL sensors and actuators for vibration suppression of structural members.

INTRODUCTION

Future large spacecraft missions will require improved structural performance to meet serious vibration and control issues. Active vibration suppression, and pointing and shape control techniques will have to be developed to accurately control and monitor these large flexible space structures in the space environment. The overall spacecraft design will rely on distributed structural control methods to minimize local vibration and jitter, and maintain the high accuracy pointing and shape requirements. Structural members which contain their own local sensors, actuators, and computational/control capabilities need to be investigated.

Current state-of-the-art sensors and actuators are being researched industry wide. New design concepts are using electro-rheological fluids[1], piezoelectric ceramics[2], and shape memory alloys as methods of actuation. Some of these same designs involving piezoelectric ceramics and shape memory alloys along with other concepts that use fiberoptics[3] and acoustic waveguides[4] are being developed for sensing.

The focus of this paper is to investigate the feasibility of using shape memory alloy materials for both local sensing and actuation to minimize vibrations of a simple structure. The preliminary results of this investigation verify that shape memory materials can be used for vibration suppression.

SHAPE MEMORY PROCESS

Shape Memory Alloy materials are generally provided in a basic shape (i.e. wire, rod, tube, sheet, etc.), from which the desired memory shape is constructed. The memory shape is physically constrained and annealed (heat treated) under a controlled environment to provide a permanent set. Once the material is annealed it is ready for operation. The SMA can be strained up to 8% of its original shape. This condition is usually known as the Martensite or soft condition. To return the SMA back to its memory set, heat is applied. After enough heat is added to reach the transition temperature the SMA will revert back to the memory shape with high energy release. This condition is usually referred to as the Austenite or hard condition. Once this transition has occurred heat is removed and the SMA can again be strained. This cycle is repeatable between soft and hard conditions.

EXPERIMENTAL TEST STRUCTURE

A thin flexible cantilever beam was selected as the representative test structure with NiTiNOL wires mounted externally along the beam for both sensing and actuation (see figure 1). The test set-up was designed for low frequency (approximately 1 Hz) testing such that the actuation of the NiTiNOL wire could comfortably be cycled without bandwidth limitations. Table 1 lists the beam properties of the test structure used. Standard 55-NiTiNOL was used for actuation. Two actuator wires are used to control the 1st bending mode of the beam. A 10-mil wire was determined to provide sufficient actuation force as reported from the literature in figure 2. For two-way memory operation the stroke is usually limited to about 3-4% of the total wire length.

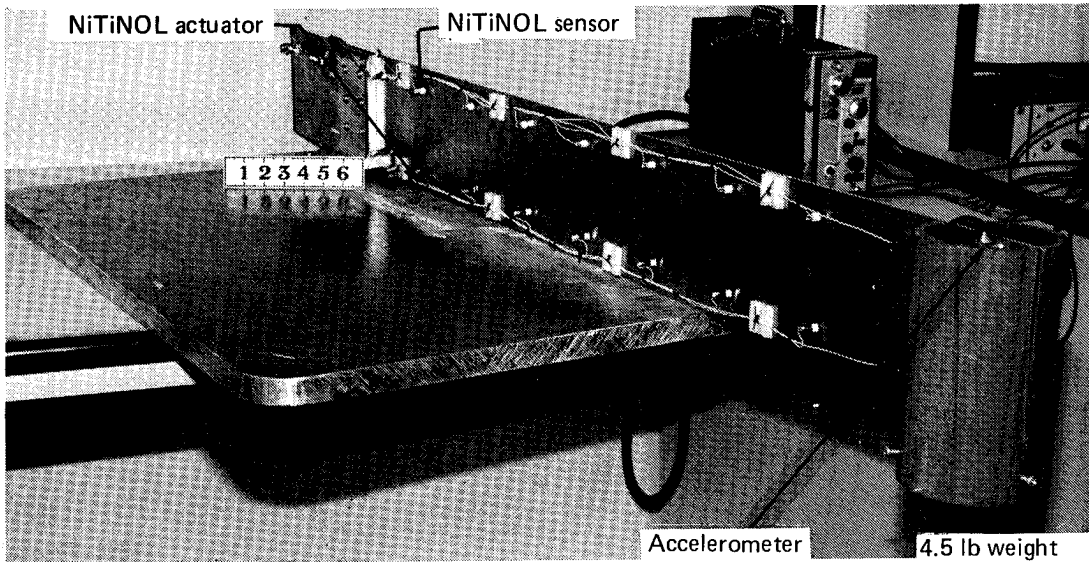


Figure 1. Cantilever Beam With NiTiNOL Wires

Material	Aluminum
Modulus	11.0 Msi
Length	48.00 inches
Thickness	0.125 inches
Width	6.00 inches
Tip Mass	4.5 lbs
Density	0.10 lb/in ²
Damping factor	0.002

Table 1. Beam Properties

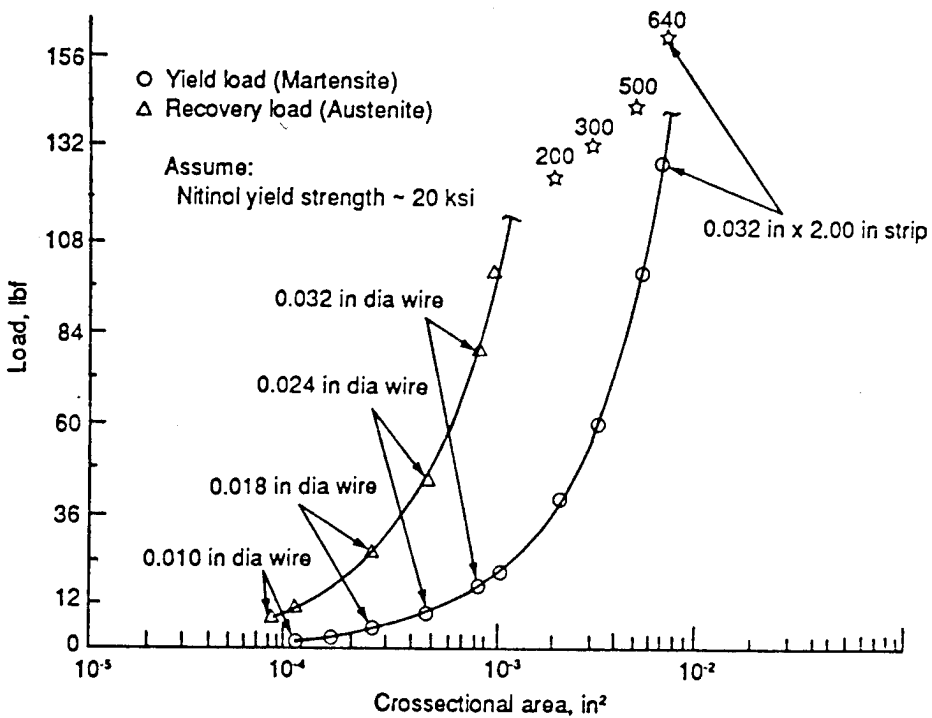


Figure 2. NiTiNOL Load vs. Cross-Sectional Area (Recovery and Yield) from the Literature

ANALOG CONTROL SYSTEM

The analog controlled NiTiNOL active damping circuit is shown in figure 3. A 10-mil diameter wire NiTiNOL sensor was activated with current from a 15v supply through an 100 ohm resistor. This provided about 100 ma of sensor current. As the beam deflected, the resistance of the NiTiNOL increased or decreased, causing a change of voltage across the sensor. The voltage across the sensor was detected with an high gain differential amplifier, the sensor was connected through capacitors so the DC voltage across the sensor would be ignored and any very slow changes due to temperature drift were also ignored. High frequency noise and spurious beam oscillations were also filtered out. Only dynamic voltage changes that correspond to the cantilever beam fundamental frequency were sensed.

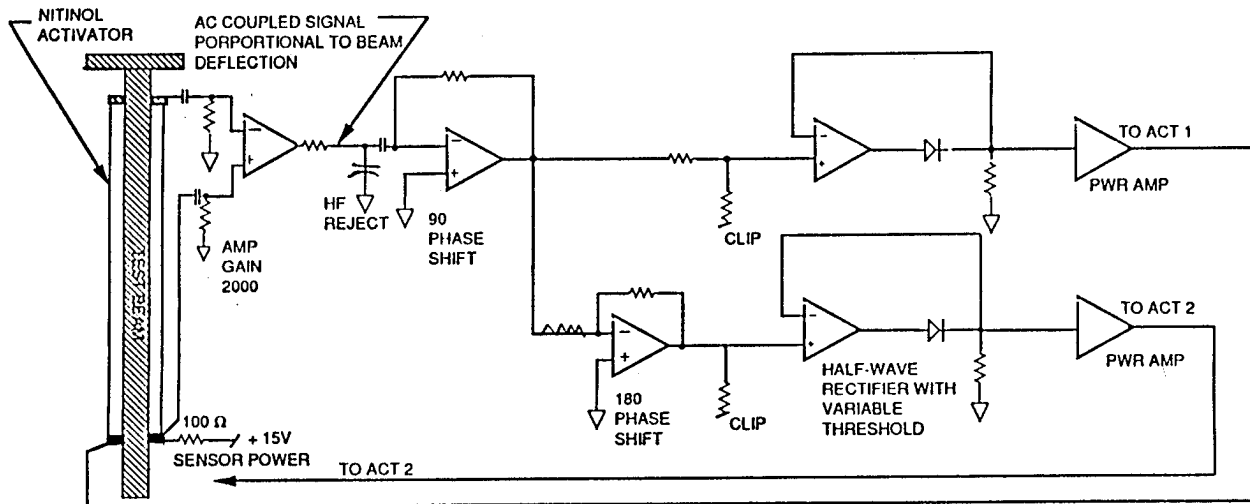


Figure 3. Analog-Controlled NiTiNOL Active Damping Circuit

The voltage out of the sensor was proportional to the length of the sensor wire or beam position. The maximum output was detected at minimum beam tip velocity. By differentiating the position signal a new signal was derived that was proportional to the velocity. In order to damp the beam oscillations, a force was applied to the beam to add a velocity vector opposite the existing beam velocity. This was intended to reduce the maximum beam velocity. Since a signal proportional to velocity was derived, it was most convenient to apply this force during the time of maximum velocity.

The velocity signal was sent to a rectifier. In parallel it was inverted and sent to a second rectifier. This circuitry provided two out-of-phase sine shaped pulse signals (see figure 4). These pulses were amplified using bench-type power amplifiers and applied to the NiTiNOL actuators. Note that power was applied alternatively to each actuator. While one was heating, the other was cooling (ambient room temperature). The clip adjustment was used to adjust the width of the heating pulses and the dead band.

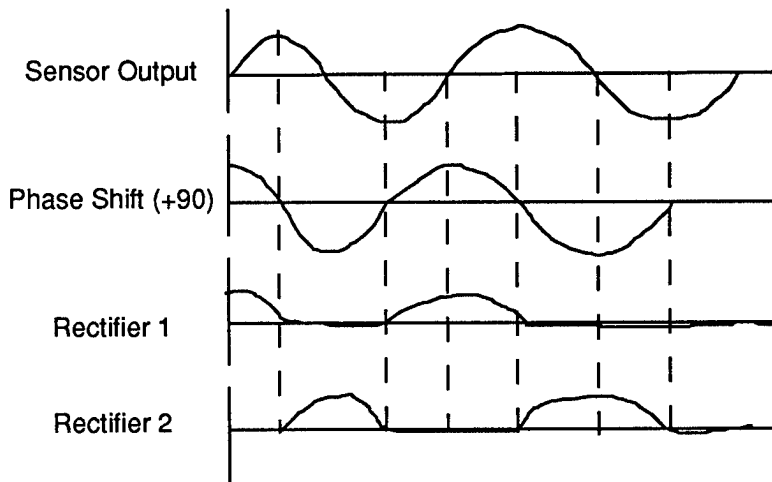
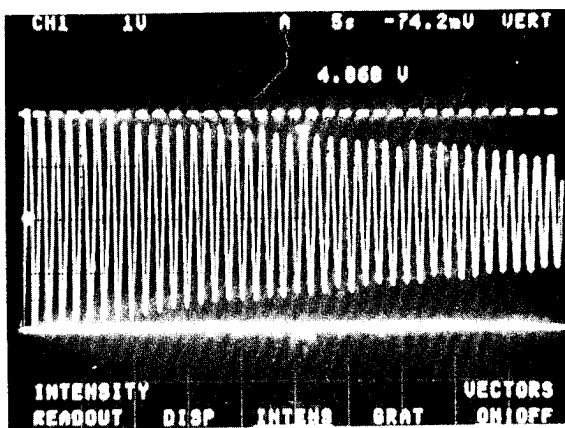


Figure 4. NiTiNOL Analog Control Signals

EXPERIMENTAL RESULTS

The effectiveness of the analog-controlled active vibration suppression circuit was evaluated by comparing the transient responses of the beam both with and without active vibration control. The tip of the beam was displaced a known distance (6 inches) and released. This test was performed first without any actuator or sensor wires attached. The beam took 7 minutes to naturally dampen out the oscillations. After the NiTiNOL wires were attached the beam was tested again and due to the high specific damping capacity of NiTiNOL [5] the beam passively damped out the oscillations in 4 minutes and 10 seconds. Figure 5 shows the oscilloscope readout of the transient response. Finally the test was repeated with the analog-controlled damping circuit activated the beam actively damped out the oscillations in 28 seconds. Figure 6 shows the oscilloscope readout of the transient response.



*Figure 5. NiTiNOL Passive Damping System,
4 min, 10 sec*

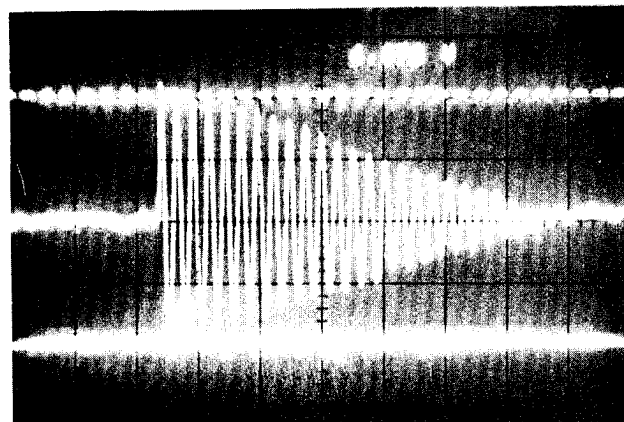


*Figure 6. NiTiNOL Activee Damping System,
28 sec*

SENSOR COMPARISONS

A standard strain gage type accelerometer was mounted at the tip of the beam. The NiTiNOL signal was differentiated twice to obtain a complimentary signal for comparison. Figure 7 shows an oscilloscope readout of transient beam vibrations using both the NiTiNOL wire sensor and the strain-gage type accelerometer. This comparison demonstrates the high level of resolution available from a NiTiNOL sensor. Because the NiTiNOL wire was strung the total length of the beam, sensor readouts could be taken at any point. To obtain this same capability using accelerometers, several would have to be placed at the desired discrete locations.

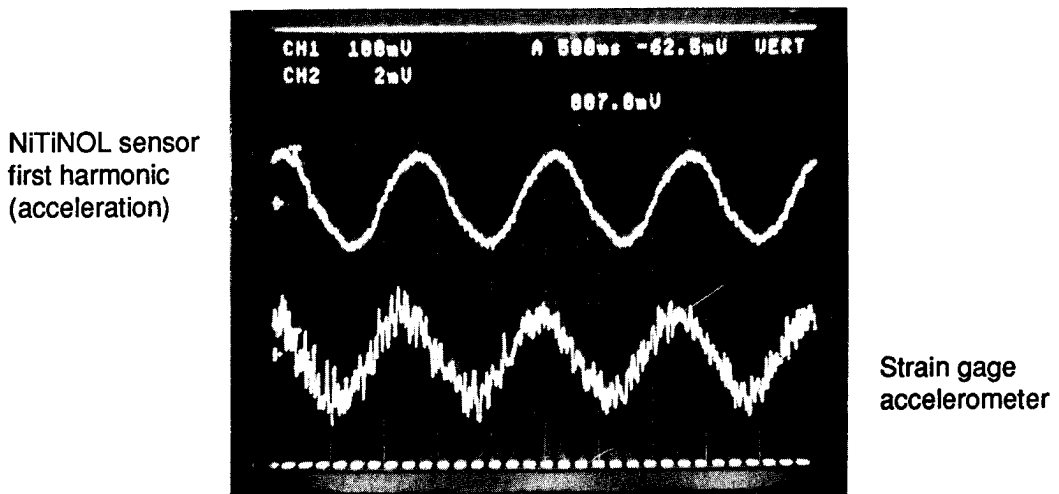


Figure 7. NiTiNOL Cantilever Beam Sensor Comparisons

SIMULATION MODEL AND RESULTS

A simple simulation model was developed to help predict the damping effectiveness that could be achieved. A 20 node NASTRAN model was used to find the eigenvalues and eigenvectors. The first two bending modes of interest were;

$$\begin{aligned} f_1 &= 0.73 \text{ Hz}, \omega_1 = 4.58659 \text{ rad/sec} \\ f_2 &= 8.20 \text{ Hz}, \omega_2 = 51.5206 \text{ rad/sec} \end{aligned}$$

The standard second order differential equation used to represent transverse vibration is given by [6]:

$$m\ddot{x} + kx = F \quad (1)$$

introduce the coordinate transformation

$$x = \phi q \quad (2)$$

where q are modal coordinates and ϕ the eigenvectors.

by substituting equation (2) into (1) and introducing modal damping yields:

$$[M] \{\ddot{q}\} + [C] \{\dot{q}\} + [K] \{q\} = \phi^T F$$

where

M is the identity modal mass matrix

C is $2\zeta\omega_i$ diagonal damping matrix $i=1,2$

K is ω_i^2 diagonal stiffness matrix $i=1,2$

Based on the experimental response the NiTiNOL actuator was modelled using dry friction;

$$F = f \frac{\dot{x}}{|\dot{x}|}$$

where

f = constant magnitude force = 7.5 lbs/NiTiNOL wire.

Figure 8 shows the predicted tip position response which agrees with the experimental data discussed previously. Figure 9 shows the predicted tip position response for 4 NiTiNOL actuator wires, with a settling time of 16 seconds. Although the 1st mode was well behaved the second mode showed no influence from the 1st mode control (figure 10). For multiple mode control, actuator distribution becomes significant.

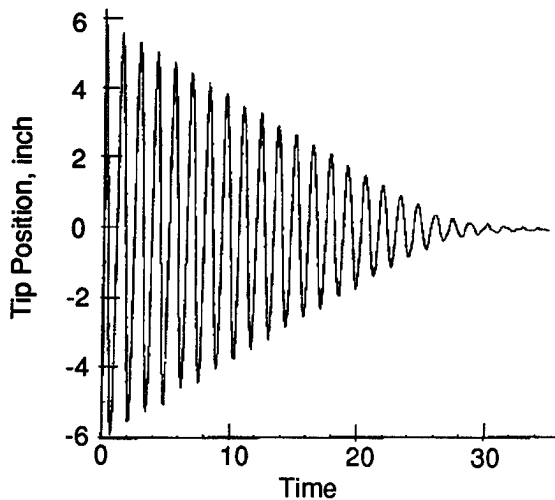


Figure 8. Two Actuator Tip Position Response

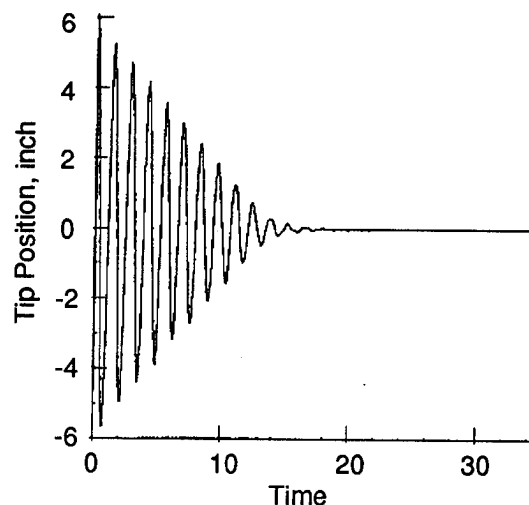


Figure 9. Four Actuator Tip Position Response

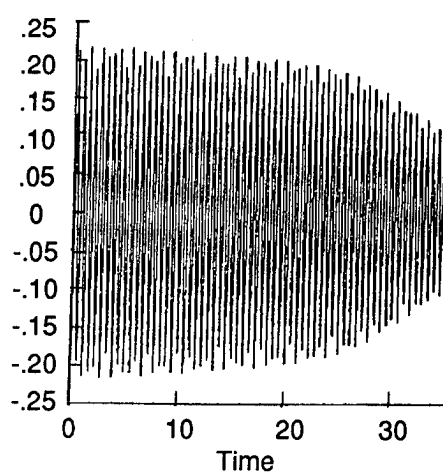
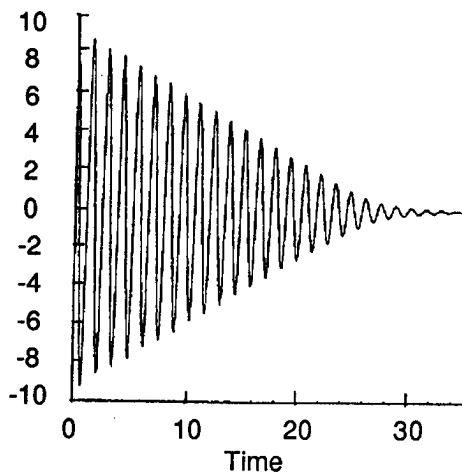


Figure 10. Flex-Response First Two Modes Two Actuator Model

OVERALL DAMPING EFFECTIVENESS

Table 2 summarizes the overall damping effectiveness. Although the transient response has approximately linear decay rate, a viscous damping or exponential decay rate was used to approximate the damping factor for comparison. As shown the active damping was found to be 15 times more effective than no control at all and the simulation model determined that by doubling the actuator authority the effectiveness could be approximately doubled.

	ζ_1^*	T_s	Effectiveness
Uncontrolled	0.002	420 sec	1
Passive	0.003	250 sec	1.5
Active			
2 NiTiNOL wires	0.031	28 sec	15
4 NiTiNOL wires**	0.054	16 sec	27

* approximated viscous damping

** model prediction

Table 2. Overall Damping Effectiveness

SMA CHARACTERIZATION

Further understanding of how SMA material provides actuation is determined by analyzing the basic parameters that characterize SMA operation. Temperature, displacement and force are all interrelated and are influenced by the power input and the environment. Characterization curves can be used to derive relationships between inputs and outputs. Relationships between parameters can help develop detailed actuator models. These models can better aide the engineer in predicting the performance and defining the limitations of shape memory alloys. The curves shown in figures 11 and 12 show the steady-state power versus temperature and temperature versus displacement curves, respectively. These two curves can be used to derive the steady-state relationship between applied power and displacement. Notice that the path is different in each direction, which is typical of thermal work cycles. These relationships help define nonlinearities; hysteresis and creep. A preliminary investigation of these types of phenomena are just starting to be understood. [7]

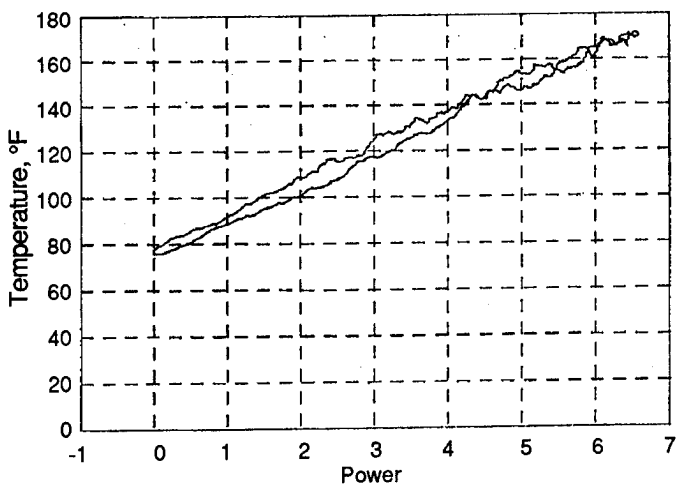


*Figure 11. Power vs. Temperature
(Constant Force Test)*

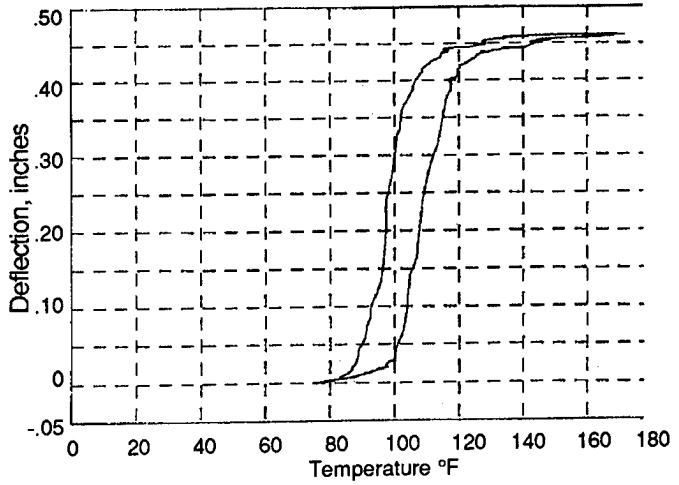


*Figure 12. Temperature vs. Displacement
(Constant Force Test)*

SUMMARY

This investigation has verified the feasibility of using shape memory alloy materials as both a sensor and an actuator to actively suppress vibrations of a flexible structure. The overall effectiveness of the active vibration control system was experimentally demonstrated to reduce the spurious vibrations of the flexible structure by a factor of 15. SMA's are an attractive material for use in actuation systems because of their large force capability for a given amount of material, however, they will probably be limited to fairly low frequency applications. Two-way actuation using SMA wires is bandwidth limited by the cooling time of the opposing wire. The SMA sensor showed high resolution along with easy signal manipulation and readily available discrete sensor locations. Finally, SMA characterization will help quantify nonlinearities, hysteresis, and creep to better understand the sensor/actuator functions.

REFERENCES

- [1] Choi, S.B., Thompson, B.S., Gandhi, M.V., "An Experimental Investigation on the Active-Damping Characteristics of a class of Ultra-Advanced Intelligent Composite Materials featuring Electro-Rheological Fluids, Proceeding of Damping 1989, Flight Dynamics Laboratory, AFWAL, Wright-Patterson Air Force Base, Ohio.
- [2] Crawley, E.F., and de Luis, Javier, "Use of Piezoelectric Actuators as Elements of Intelligent Structures," Paper 86-0878 at the AIAA/ASME/ASCE/AHS 27th Structures, Structural Dynamics and Materials Conference, San Antonio, TX, May 19-21, 1986.
- [3] Wiencko, J.A., Claus, R.O., and Rogers, R.E., "Embedded Optical Fiber Sensors for Intelligent Aerospace Structures," Sensor EXPO proceedings 1987.
- [4] Harrold, R.T. and Sanjana, Z.N., "Material Cure and Internal Stresses Monitored via Embedded Acoustic Waveguides," proceeding of ICTTE 86 Technology Shaping our Future, Pittsburgh, PA, Oct 6-8, 1986.
- [5] Schetky, L.M., and Perkins, J., "The Quiet Alloys, "Machine Design, Vol. 50, No. 8, April 6, 1978.
- [6] Bathe, K.J., Finite Element Procedures in Engineering Analysis, Prentice-Hall, New Jersey, 1982.
- [7] Cimino, W.W. and Wilson, D.G., "Working Knowledge for Shape Memory Alloys," Structures Technology, Boeing Aerospace, Kent, Wa, Internal Memo 2-3614-048/89, Feb. 1989.

Damping of Structural Vibrations with Piezoelectric Materials and Passive Electrical Networks

Nesbitt W. Hagood*, Andreas von Flotow[†]
*Space Engineering Research Center
Massachusetts Institute of Technology
Bldg. 37 Rm. 341
Cambridge, Massachusetts 02139
(617) 253-8365 (617) 253-4865*

Abstract

This paper investigates the possibility of dissipating mechanical energy with piezoelectric material shunted with passive electrical circuits. The effective mechanical impedance for the piezoelectric element shunted by an arbitrary circuit is derived. The shunted piezoelectric is shown to posses frequency dependant stiffness and loss factor which are dependant on the shunting circuit. The generally shunted model is specialized to two cases: the case of a resistor alone and that of a resistor and inductor. For resistive shunting, the material properties have frequency dependance similar to viscoelastic materials but with much higher stiffness and temperature stability. Shunting with a resistor and inductor introduces an electrical resonance, which can be optimally tuned to structural resonances in a manner analogous to a mechanical vibration absorber. Techniques for analyzing systems which incorporate these shunting cases are presented and applied to a cantilevered beam experiment. The experimental results for both the resistive and resonant shunting circuits validate the shunted piezoelectric damping models.

Nomenclature

A	= diagonal matrix of cross sectional areas of piezoelectric bar
C	= generic capacitance
C_{pi}	= inherent capacitance of the piezoelectric shunted in the i^{th} direction
d_{ij}	= piezoelectric material constant relating voltage in i^{th} direction to strain in j^{th} direction
\mathbf{D}	= vector of electrical displacements (charge/area)
E	= elastic modulus of material
\mathbf{E}	= vector of electric fields (volts/meter)
g	= real nondimensional frequency ratio = ω/ω_n
\mathbf{I}	= vector of external applied currents
K	= modal stiffness
k_{ij}	= material electromechanical coupling coefficient
K_{ij}	= generalized electromechanical coupling coefficient
L	= diagonal matrix of lengths of piezoelectric bar
L	= generic inductor
M	= modal mass
r	= dissipation tuning parameter ($RC_p^s\omega_n$)

* Graduate Research Assistant, Department of Aeronautics and Astronautics

+ Assistant Professor, Department of Aeronautics and Astronautics

R	= generic resistance
s	= Laplace parameter
S^E	= piezoelectric material compliance matrix at constant field
S	= vector of material strains
T	= vector of material stresses
U_i	= potential energy of element i
v	= velocity
V	= voltage
x^{ST}	= static displacement of a system = F/K_{tot}
Y^D	= open circuit electrical admittance of the piezoelectric (inherent capacitance)
Y^{EL}	= electrical admittance of the piezoelectric (sum of shunting admittance in parallel to the inherent capacitance)
Y^{SU}	= shunting admittance of the piezoelectric (in parallel to inherent capacitance)
Z	= generic impedance, mechanical or electrical
Z^{ME}	= effective mechanical impedance of the shunted piezoelectric
Z^{EL}	= electrical impedance of the piezoelectric (shunting impedance in parallel to the inherent capacitance)
β	= mass ratio (proof mass/system mass)
γ	= complex nondimensional frequency = s/ω_n
δ	= resonant shunted piezoelectric frequency tuning parameter, ω_e/ω_n
η	= loss factor
ρ	= nondimensional resistance (or frequency) = $RC_p^S\omega$
ω_e	= resonant shunted piezoelectric electrical resonant frequency
ω_n	= natural frequency of a 1-DOF system

Subscript

p	= piezoelectric
PP	= optimal by pole placement criteria
t	= transpose of a vector or matrix
TF	= optimal by transfer function criteria

Superscript

E	= value taken at constant field (short circuit)
D	= value taken at constant electrical displacement (open circuit)
RES	= pertaining to resistor shunting
RSP	= pertaining to resonant circuit shunting
S	= value taken at constant strain (clamped)
SU	= shunted value
T	= value taken at constant stress (free)

Introduction

There are many applications where the addition of passive vibration damping to a structural system can greatly increase the systems performance or stability. The addition of passive damping can decrease peak vibration amplitudes in structural systems and add robustness to marginally stable active control systems, Ref [1]. Structural damping can be increased by several methods the most common being the addition of high loss factor viscoelastic materials to the structure or the attachment of a mechanical vibration absorber.

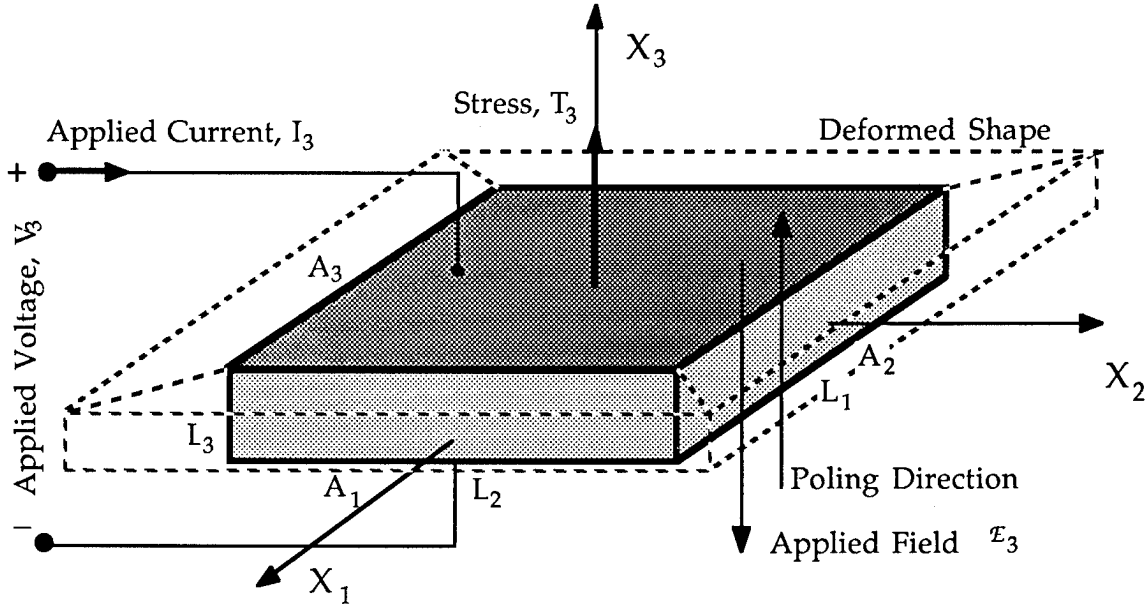


Figure 1: Assumed Geometry for a Typical Piezoelectric Material with the Top and Bottom Surfaces Electroded

In recent years piezoelectric elements have been used as embedded sensors and actuators in smart structures by Crawley and deLuis [2] and Hagood [3] and as elements of active vibration suppression system for cantilevered beams by Hanagud [4] and Hubbard [5]. They have also been used as actuation components in wave control experiments by Pines and von Flotow [6]. Within active control systems, the piezoelectrics require complex amplifiers and associated sensing electronics. These can be eliminated in passive shunting applications where the only external element is a simple passive electrical circuit. The shunted piezoelectric itself can also be used as a structural actuator in a control system.

This paper presents a new type of passive damping mechanism for structural systems which uses piezoelectric materials bonded to the structure. Piezoelectric materials possess certain properties which make them useful as dampers or control elements for structures. The first is that they strain when an electrical field is applied across them. This property makes them well suited as actuators for control systems (where the control signal is typically an applied voltage). The second is that they produce a voltage under strain. This property makes them well suited for sensing strain. In general, piezoelectrics have the ability to efficiently transform mechanical energy to electrical energy and vice-versa. It is this transformation ability which makes them useful as structural dampers.

The advantages to this type of passive piezoelectric application were first presented by Forward [7] & [8] and Edwards and Miyakawa [9] for damping applications on resonant structures. This paper establishes the derivation and analytical foundation for analysis of general systems with shunted piezoelectrics. A typical piezoelectric element is shown in Fig. (1). The fundamental constitutive relations are the relation between strain and applied field, known as the d constants, and between the charge density and the applied strain known as the g constants. Another fundamental property is the electromechanical coupling coefficient, k, which governs the energy transformation properties of a piezoelectric. The constants are explained in detail in Ref. [10].

In passive energy dissipation applications, the electrodes of the piezoelectric are shunted with some electrical impedance; hence the term shunted piezoelectrics is used. The electrical impedance is designed to dissipate the electrical energy which has been converted from mechanical energy by the piezoelectric. In the following sections, the shunted

piezoelectric's interaction with external circuits will be modeled, and the benefits that can be derived by passive circuit shunting of piezoelectrics will be quantified. First, the equivalent effective impedance of the shunted piezoelectric will be derived. This expression will then be applied to the cases of resistive and resonant circuit shunting. Expressions for the system damping will be derived, and parameters will be found which maximize this damping. An experiment verifies the accuracy of the analysis.

Modelling of Generally Shunted Piezoelectric Materials

A general expression for the material constants of a linear piezoelectric can be written from Ref. [11] as:

$$\begin{bmatrix} \mathbf{D} \\ \mathbf{S} \end{bmatrix} = \begin{bmatrix} \boldsymbol{\epsilon}^T & \mathbf{d} \\ \mathbf{d}_t & \mathbf{s}^E \end{bmatrix} \begin{bmatrix} \mathbf{E} \\ \mathbf{T} \end{bmatrix} \quad (1)$$

where \mathbf{D} is a vector of electrical displacements (charge/area), \mathbf{E} is the vector of electrical field applied to the material (volts/meter), \mathbf{S} is the vector of material strains, and \mathbf{T} is the vector of material stresses (force/area).

$$\mathbf{D} = \begin{bmatrix} D_1 \\ D_2 \\ D_3 \end{bmatrix}, \quad \mathbf{E} = \begin{bmatrix} E_1 \\ E_2 \\ E_3 \end{bmatrix}, \quad \mathbf{S} = \begin{bmatrix} S_{11} \\ S_{22} \\ S_{33} \\ S_{23} \\ S_{13} \\ S_{12} \end{bmatrix} = \begin{bmatrix} S_1 \\ S_2 \\ S_3 \\ S_4 \\ S_5 \\ S_6 \end{bmatrix}, \quad \mathbf{T} = \begin{bmatrix} T_{11} \\ T_{22} \\ T_{33} \\ T_{23} \\ T_{13} \\ T_{12} \end{bmatrix} = \begin{bmatrix} T_1 \\ T_2 \\ T_3 \\ T_4 \\ T_5 \\ T_6 \end{bmatrix} \quad (2)$$

The 3 direction is associated with the direction of poling and the material is approximately isotropic in the other two directions. These direction conventions are shown in Fig. (1). The matrix which relates the two electrical variables, electrical displacement and electrical field, contains the dielectric constants for the material. This matrix can be written:

$$\boldsymbol{\epsilon}^T = \begin{bmatrix} \epsilon_1^T & 0 & 0 \\ 0 & \epsilon_1^T & 0 \\ 0 & 0 & \epsilon_3^T \end{bmatrix} \quad (3)$$

where the superscript, $(\cdot)^T$, signifies that the values are measured at constant stress. The two elastic variables, stress and strain, are related through the compliance matrix of the piezoceramic, which has the form:

$$\mathbf{s}^E = \begin{bmatrix} s_{11}^E & s_{12}^E & s_{13}^E & 0 & 0 & 0 \\ s_{12}^E & s_{11}^E & s_{13}^E & 0 & 0 & 0 \\ s_{13}^E & s_{13}^E & s_{33}^E & 0 & 0 & 0 \\ 0 & 0 & 0 & s_{55}^E & 0 & 0 \\ 0 & 0 & 0 & 0 & s_{55}^E & 0 \\ 0 & 0 & 0 & 0 & 0 & s_{66}^E \end{bmatrix} \quad (4)$$

where the superscript, E , signifies that the values are measured at constant electrical field (eg. short circuit). Note that due to symmetry the material properties are identical in the 1 and 2 directions.

Finally, there are those terms which couple the mechanical and electrical equations by virtue of the piezoelectric effect. In the form of the equations given in (1) the coupling terms are the piezoelectric constants which relate strain to applied field. For piezoelectric ceramics, the matrix of piezoelectric constants has the form:

$$\mathbf{d} = \begin{bmatrix} 0 & 0 & 0 & 0 & d_{15} & 0 \\ 0 & 0 & 0 & d_{15} & 0 & 0 \\ d_{31} & d_{31} & d_{33} & 0 & 0 & 0 \end{bmatrix} \quad (5)$$

The first term in the subscript refers to the electrical axis while the second refers to the mechanical. Thus d_{31} refers to the strain developed in the 1 direction in response to a field in the 3 direction (parallel to the material poling).

In order to allow the use of traditional concepts of electrical admittance and impedance for the shunting analysis it is necessary to perform a change of variables. If we use the definitions for voltage and current in Ref. [10]:

$$V_i = \int_0^{L_i} \mathbf{E} \cdot d \mathbf{x}_i \quad (6a)$$

$$I_i = \int_{A_i} \mathbf{D} \cdot d \mathbf{a}_i \quad (6b)$$

and furthermore assume that the field within and electrical displacement on the surface are uniform for the piezoelectric material, then linear relationships can be defined in the Laplace domain:

$$\begin{aligned} \mathbf{V}(s) &= \mathbf{L} \cdot \mathbf{E}(s), \\ \mathbf{I}(s) &= s \mathbf{A} \cdot \mathbf{D}(s) \end{aligned} \quad (7a \&b)$$

where \mathbf{L} is a diagonal matrix of the lengths of the piezoelectric bar in the i^{th} direction, \mathbf{A} is the diagonal matrix of the areas of surfaces perpendicular to the i^{th} direction, and s is the Laplace parameter.

Taking the Laplace transform of eq. (1) and using eqs. (7a&b) to eliminate \mathbf{E} and \mathbf{D} , the general equation for a piezoelectric in terms of the external current input and applied voltage is obtained.

$$\begin{bmatrix} \mathbf{I} \\ \mathbf{S} \end{bmatrix} = \begin{bmatrix} s \mathbf{A} \epsilon^T \mathbf{L}^{-1} & s \mathbf{A} \mathbf{d} \\ \mathbf{d}_t \mathbf{L}^{-1} & s^E \end{bmatrix} \begin{bmatrix} \mathbf{V} \\ \mathbf{T} \end{bmatrix} \quad (8)$$

This equation can be further simplified by noting that the upper left partition of the generalized compliance matrix is diagonal. The elements of this partition have the form:

$$\frac{A_i \epsilon_i^T}{L_i} = C_{pi}^T \quad (9)$$

where C_{pi} is the capacitance between the surfaces perpendicular to the i^{th} direction. Noting that sC_p is the open circuit admittance of the piezoelectric material, eq. (8) can thus be written:

$$\begin{bmatrix} \mathbf{I} \\ \mathbf{S} \end{bmatrix} = \begin{bmatrix} sC_p^T & sAd \\ d_t \mathbf{L}^{-1} & \mathbf{s}^E \end{bmatrix} \begin{bmatrix} \mathbf{V} \\ \mathbf{T} \end{bmatrix} = \begin{bmatrix} \mathbf{Y}^D(s) & sAd \\ d_t \mathbf{L}^{-1} & \mathbf{s}^E \end{bmatrix} \begin{bmatrix} \mathbf{V} \\ \mathbf{T} \end{bmatrix} \quad (10)$$

where $\mathbf{Y}^D(s)$ is the open circuit admittance of the piezoelectric (the inherent capacitance with free mechanical boundary conditions). The open circuit admittance relates the voltage applied across the piezoelectric's electrodes in Fig. (2) to the external current input into the piezoelectric. The large leakage resistance of the piezoelectric material is treated as infinite in this analysis but can easily be included as a modifying term.

For shunted piezoelectric applications, a passive electrical circuit is connected between the surface electrodes as shown in one dimension in Fig. (2). Since the circuit is placed across the electrodes, it appears in parallel to the inherent piezoelectric capacitance in that direction. Since admittances in parallel add, the governing constitutive equations for a shunted piezoelectric material become:

$$\begin{bmatrix} \mathbf{I} \\ \mathbf{S} \end{bmatrix} = \begin{bmatrix} \mathbf{Y}^{EL} & sAd \\ d_t \mathbf{L}^{-1} & \mathbf{s}^E \end{bmatrix} \begin{bmatrix} \mathbf{V} \\ \mathbf{T} \end{bmatrix} \quad (11)$$

with:

$$\mathbf{Y}^{EL} = \mathbf{Y}^D + \mathbf{Y}^{SU} \quad (12)$$

The externally applied current, \mathbf{I} , is the sum of the currents flowing through the shunting impedance, the inherent piezoelectric capacitance, and the piezoelectric transformer. The shunting admittance matrix is assumed diagonal and frequency dependant with the form:

$$\mathbf{Y}^{SU} = \begin{bmatrix} Y_1^{SU} & 0 & 0 \\ 0 & Y_2^{SU} & 0 \\ 0 & 0 & Y_3^{SU} \end{bmatrix} \quad (13)$$

The top partition of eq. (11) can be solved for the voltage appearing across the electrodes.

$$\mathbf{V} = \mathbf{Z}^{EL} \mathbf{I} - \mathbf{Z}^{EL} sAd \mathbf{T} \quad (14)$$

Where \mathbf{Z}^{EL} is the electrical impedance matrix and is equal to $(\mathbf{Y}^{EL})^{-1}$. The electrical impedance matrix is also diagonal. Equation (14) can be substituted into (11) to find an expression for the strain in terms of stress and input current.

$$\mathbf{S} = [\mathbf{s}^E - d_t \mathbf{L}^{-1} \mathbf{Z}^{EL} sAd] \mathbf{T} + [d_t \mathbf{L}^{-1} \mathbf{Z}^{EL}] \mathbf{I} \quad (15)$$

This is a governing equation for a shunted piezoelectric. It gives the strain for a given applied stress and forcing current. Notice that shunting the piezoelectric does not preclude use of the shunted element as an actuator in an active control system but rather modifies the passive characteristics of the actuator. By modifying the passive stiffness of

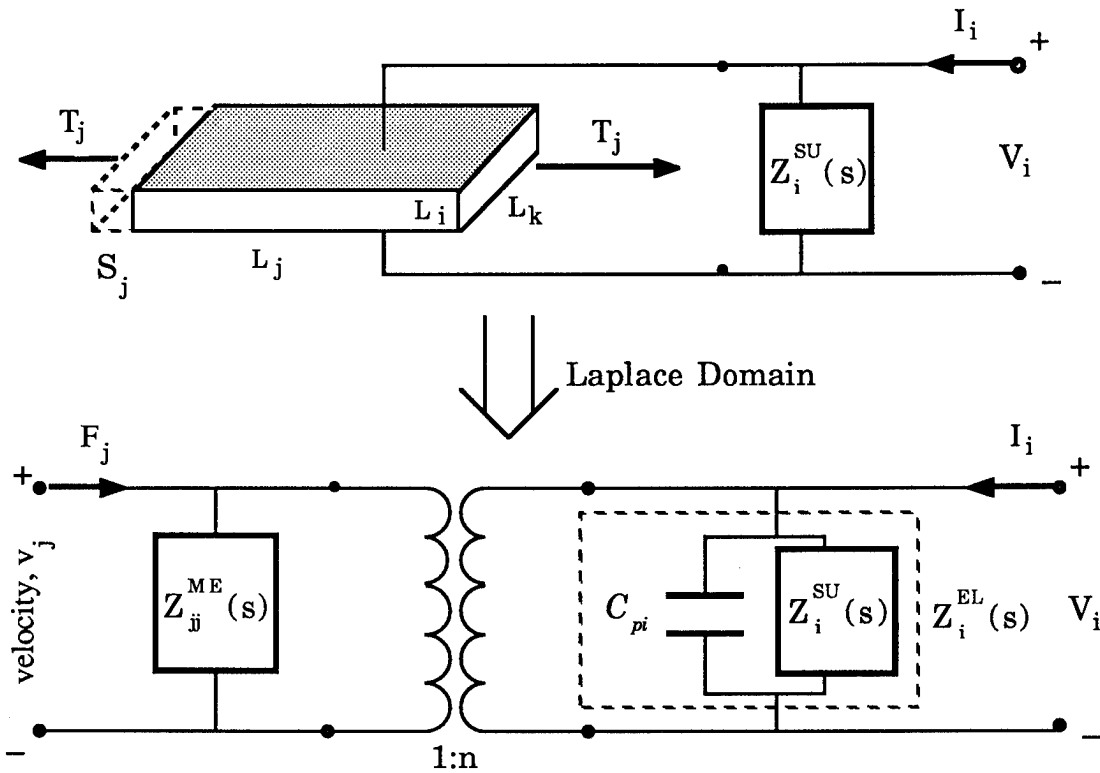


Figure 2: Simple Physical Model of a Shunted Piezoelectric and its Network Analog Showing its Ability to Transform Energy from Mechanical to Electrical and Vice Versa.

the piezoelectric to include material damping, perfectly colocated damping can be introduced into the system. This passive damping can be useful in stabilizing controlled structures in the manner of Ref. [12] in which a mechanical actuator is passively damped.

Of particular importance is the new mechanical compliance term. The shunted piezoelectric compliance can be defined from (15):

$$s^{SU} = [s^E - \mathbf{d}_t \mathbf{L}^{-1} \mathbf{Z}^{EL} s \mathbf{A} \mathbf{d}] \quad (16)$$

If we note that with constant stress:

$$\mathbf{Z}^E(s) = \mathbf{0} = \text{short circuit electrical impedance} \quad (17a)$$

$$\mathbf{Z}^D(s) = (\mathbf{C}_p^T s)^{-1} = \text{open circuit electrical impedance} \quad (17b)$$

and that:

$$s \mathbf{L}^{-1} \mathbf{\epsilon}^T \mathbf{A} = \mathbf{C}_p^T s \quad (18)$$

equation (16) can be put in the form

$$s^{SU} = [s^E - \mathbf{d}_t \bar{\mathbf{Z}}^{EL}(\mathbf{\epsilon}^T)^{-1} \mathbf{d}] \quad (19)$$

where the matrix of nondimensional electrical impedances is defined:

$$\bar{\mathbf{Z}}^{EL} = \mathbf{Z}^{EL} (\mathbf{Z}^D)^{-1} \quad (20)$$

Finally, since \mathbf{Z}^{EL} is diagonal, the electrical contribution to the compliance can simply be written as a summation over the electrical impedances:

$$\mathbf{s}^{SU} = \left[\mathbf{s}^E - \sum_{i=1}^3 \left[\bar{\mathbf{Z}}_i^{EL} \left(\frac{1}{\epsilon_i^T} \mathbf{d}_i \mathbf{d}_i^T \right) \right] \right] = \left[\mathbf{s}^E - \sum_{i=1}^3 \bar{\mathbf{Z}}_i^{EL} \mathbf{M}_i \right] \quad (21)$$

where \mathbf{d}_i denotes the i^{th} row of \mathbf{d} and for piezoelectric ceramics the \mathbf{M}_i have the form:

$$\mathbf{M}_1 = \frac{1}{\epsilon_1^T} \begin{bmatrix} 0 & 0 & 0 & 0 & 0 & 0 \\ 0 & 0 & 0 & 0 & 0 & 0 \\ 0 & 0 & 0 & 0 & 0 & 0 \\ 0 & 0 & 0 & 0 & 0 & 0 \\ 0 & 0 & 0 & 0 & 0 & 0 \\ 0 & 0 & 0 & 0 & d_{15}^2 & 0 \\ 0 & 0 & 0 & 0 & 0 & 0 \end{bmatrix} \quad \mathbf{M}_2 = \frac{1}{\epsilon_2^T} \begin{bmatrix} 0 & 0 & 0 & 0 & 0 & 0 \\ 0 & 0 & 0 & 0 & 0 & 0 \\ 0 & 0 & 0 & 0 & 0 & 0 \\ 0 & 0 & 0 & 0 & 0 & 0 \\ 0 & 0 & 0 & 0 & 0 & 0 \\ 0 & 0 & 0 & 0 & 0 & 0 \end{bmatrix} \quad (22a\&b)$$

$$\mathbf{M}_3 = \frac{1}{\epsilon_3^T} \begin{bmatrix} d_{31}^2 & d_{31}^2 & d_{31}d_{33} & 0 & 0 & 0 \\ d_{31}^2 & d_{31}^2 & d_{31}d_{33} & 0 & 0 & 0 \\ d_{31}d_{33} & d_{31}d_{33} & d_{33}^2 & 0 & 0 & 0 \\ 0 & 0 & 0 & 0 & 0 & 0 \\ 0 & 0 & 0 & 0 & 0 & 0 \\ 0 & 0 & 0 & 0 & 0 & 0 \end{bmatrix} \quad (22c)$$

These equations constitute a general expression for the compliance matrix of a piezoelectric element with arbitrary electrode placement or elastic boundary conditions. Several things are apparent from eq. (21). First, electroding and shunting the piezoelectric element in the directions perpendicular to the poling direction (3) of the piezoelectric can only effect the shear terms of the compliance. Secondly, shunting the piezoelectric in the 3 direction modifies all of the non-shear terms of the compliance matrix. Finally, the electrical shunting circuit's ability to modify the piezoelectric material properties depends on both the material piezoelectric constants and the nondimensional electrical impedance.

Specialization to Uniaxial Loading Cases

Equation (21) simplifies greatly when the piezoelectric element is loaded uniaxially with either a normal or shear stress and only one pair of electrodes are present providing an external electric field with components in only one direction. These common modes of operation can be described:

Longitudinal Case: Force and field in the 3 direction

Transverse Case: Force in 1 or 2 direction; Field in 3 direction

Shear Case: Force in 4 or 5 direction (shear); Field in 2 or 1 direction respectively

With uniaxial loading in the j^{th} direction, only a single term from the compliance matrix contributes to the material strain energy. By examining that term the energy dissipation properties of the shunted piezoelectric can be examined. For loading in the j^{th} direction and the field in the i^{th} direction the term in the compliance matrix is:

$$s_{jj}^{SU} = s_{jj}^E - \bar{Z}_i^{EL} (\mathbf{M}_i)_{jj} = s_{jj}^E - \bar{Z}_i^{EL} \frac{(d_{ij})^2}{\epsilon_i^T} \quad (23)$$

where the subscripts denote the row and column of the respective matrix.

At this point it is convenient to introduce the piezoelectric property known as the electromechanical coupling coefficient. It is defined as the ratio of the peak energy stored in the capacitor to the peak energy stored in the material strain (under uniaxial loading and sinusoidal motion) with the piezoelectric electrodes open. Physically, its square represents the percentage of mechanical strain energy which is converted into electrical energy and vice-versa. For the 3 cases of piezoelectric operation considered, the electromechanical coupling coefficients are defined in Ref. [10]:

$$\begin{aligned} \text{Shear: } k_{15} &= \frac{d_{15}}{\sqrt{s_{55}^E \epsilon_1^T}} = k_{24} \\ \text{Transverse: } k_{31} &= \frac{d_{31}}{\sqrt{s_{11}^E \epsilon_3^T}} = k_{32} \\ \text{Longitudinal: } k_{33} &= \frac{d_{33}}{\sqrt{s_{33}^E \epsilon_3^T}} \end{aligned} \quad (24)$$

or in the notation used before for force in the j^{th} direction and field in the i^{th} direction:

$$k_{ij} = \frac{d_{ij}}{\sqrt{s_{jj}^E \epsilon_i^T}} \quad (25)$$

Substituting eq. (25) into (23) we obtain:

$$s_{jj}^{SU} = s_{jj}^E \left[1 - k_{ij}^2 \bar{Z}_i^{EL} \right] \quad (26)$$

From eq. (26) we can see that the compliance of the shunted piezoelectric is related to the short circuit compliance of the piezoelectric material modified by a nondimensional term which depends on the electrical shunting circuit and the material's electromechanical coupling coefficient. From eq. (26) the relation between the short circuit and open circuit compliance of the piezoelectric can be derived by noting that in the open circuit case

$$\bar{Z}^{EL} = 1 \quad (27)$$

and thus eq. (26) reduces to:

$$s_{jj}^D = s_{jj}^E \left[1 - k_{ij}^2 \right] \quad (28)$$

which is in agreement with the relation given in Ref. [10] for the cases considered.

Equation (28) gives the change in mechanical properties of the piezoceramic as the electrical boundary conditions are changed (from short circuit to open circuit). An analogous relation can be derived for the change in the piezoelectric inherent capacitance as the mechanical boundary conditions are changed. For uniaxial field and loading (only the boundary conditions in the loading direction are varied) this relation is also dependant on the electromechanical coupling coefficient.

$$C_{pi}^S = C_{pi}^T \left[1 - k_{ij}^2 \right] \quad (29)$$

This equation will be used for nondimensionalizations in the coming sections.

Equation (28) can be used with (26) to derive a nondimensional expression for the mechanical impedance of the shunted piezoelectric. For uniaxial loading in the j^{th} direction, the mechanical impedance of the piezoelectric can be expressed as a function of the Laplace parameter, s , as:

$$Z_{jj}^{ME}(s) = \frac{A_j}{s_{jj} L_j s} \quad (30)$$

Now using eq. (30) and (26) to define the impedance of the shunted piezoelectric and eq. (28) to nondimensionalize, the final expression for the nondimensionalized mechanical impedance of the shunted piezoelectric can be derived:

$$\bar{Z}_{jj}^{ME}(s) = \frac{Z_{jj}^{SU}}{Z_{jj}^D} = \frac{1 - k_{ij}^2}{1 - k_{ij}^2 \bar{Z}_i^{EL}(s)} \quad (31)$$

where the functional dependance of the mechanical and electrical impedances is written explicitly; and the nondimensional mechanical impedance is defined as the ratio of the shunted mechanical impedance to the open circuit impedance.

Coupling Shunted Piezoelectrics to Structures

The nondimensional mechanical impedance, \bar{Z}^{ME} , can be complex and frequency dependant since it depends on the complex, frequency dependant electrical impedance. If we note that the impedance is primarily a stiffness, then we can represent the impedance as a complex modulus, as is typically done in material damping. This is especially useful if the shunting impedance is not resonant.

$$\bar{Z}_{jj}^{ME}(s) = \bar{E}_{jj}(\omega) [1 + i\eta_{jj}(\omega)] \quad (32)$$

where \bar{E} is the ratio of shunted stiffness to open circuit stiffness of the piezoelectric and η is the material loss factor. This reduction leads to frequency-dependent equations for the complex modulus of the shunted piezoelectric. Comparing eq. (32) to eq. (31) gives the frequency dependant equivalent material properties for an arbitrarily shunted piezoelectric.

$$\eta(\omega) = \frac{\text{Im}\{\bar{Z}^{ME}(s)\}}{\text{Re}\{\bar{Z}^{ME}(s)\}}$$

Loss Factor: (33a)

$$\text{Modulus: } \bar{E}(\omega) = \text{Re} \left\{ \bar{Z}^{ME}(s) \right\} \quad (33b)$$

These equations, as well as (31), can be applied to arbitrary shunting conditions for parameter optimization of the material loss factor at a critical frequency.

To find the total system loss factor, the expression for the effective impedance of the shunted piezoelectric, eq. (31) can be used along with the impedances of the other damping devices in the frequency domain system analysis described in Ref. [13]. In general, just as for viscoelastic materials, the relation between the high loss factor of a structural component and the loss factor of the total structure can be represented as an average of the system component loss factors weighted by the fraction of strain energy in the respective elements, Ref. [14]

$$\eta^{TOT} = \frac{\sum_{i=1}^n \eta_i U_i}{\sum_{i=1}^n U_i} \quad (34)$$

where U_i is the peak strain energy in the i^{th} element of the structure. Techniques for improving structural damping typically employ the damping material (shunted piezoelectrics or viscoelastics) in areas of high strain energy to take advantage of this weighting. The stiffness and loss factor of damping materials are typically frequency dependant. The high stiffness (63 GPa) of the shunted piezoelectric gives them advantages over viscoelastic materials (circa 1 MPa) since for a given strain they can store many times the strain energy of the viscoelastic and thus contribute to higher system loss factors. The piezoelectric material properties are also relatively temperature independent below their Curie temperature (temperature at which they lose their piezoelectric properties) Ref. [11]. For commonly available piezoelectrics this is typically in the range of several hundred °C.

Application: Resistive Shunting

A resistor can shunt the piezoelectric electrodes as shown in Fig. (3). In this shunting geometry, the resistor is placed in parallel with the inherent capacitance of the piezoelectric. The resistor provides a means of energy dissipation on the electrical side and thus should increase the total piezoelectric loss factor above the loss factor for the short or open circuited piezoelectric. Its exact effect on the stiffness and dissipation properties of the piezoelectric can be modelled by applying eq. (31). For the case of a resistor across the piezoelectric electrodes, the total nondimensional electrical impedance in the i^{th} direction is:

$$Z_i^{SU}(s) = R_i \quad (35a)$$

$$\bar{Z}_i^{EL}(s) = \frac{Z_i^{EL}(s)}{Z_i^D(s)} = \frac{R_i C_{pi}^T s}{R_i C_{pi}^T s + 1} \quad (35b)$$

Eq. (35b) can be substituted into Eq. (31) to give an expression for the nondimensional mechanical impedance of a resistive shunted piezoelectric.

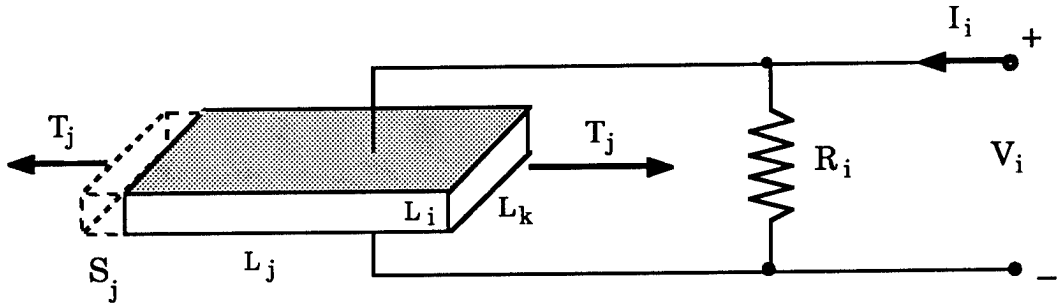


Figure 3: Resister Shunted Piezoelectric Schematic

$$\bar{Z}_{jj}^{RES}(s) = 1 - \frac{k_{kj}^2}{1 + i\rho_k} \quad (36a)$$

where ρ_k is the nondimensional frequency,

$$\rho_k = R_k C_{pk}^s \omega = \frac{\omega}{\omega_d} \quad (36b)$$

and C_{pi}^s was defined in eq. (29).

Materials Perspective

Since there are no internal resonances, it is convenient to use (33a & b) to express (36a) as a frequency dependent material stiffness and loss factor. The resistor can be thought of as changing the material properties of the piezoelectric into those of a lossy material similar to a viscoelastic in behavior. Using (33a & b) to solve for nondimensionalized expressions for η and E gives:

$$\eta_{jj}^{RES}(\omega) = \frac{\rho_i k_{ij}^2}{(1 - k_{ij}^2) + \rho_i^2} \quad (37a)$$

$$E_{jj}^{RES}(\omega) = 1 - \frac{k_{ij}^2}{1 + \rho_i^2} \quad (37b)$$

These relations have been plotted versus ρ , the nondimensional frequency (or the nondimensional resistance) in Fig. (4) for typical values of the longitudinal and transverse coupling coefficients. These curves are similar to the equivalent material curves for a standard linear solid. As illustrated in the graphs, for a given resistance the stiffness of the piezoelectric changes from its short-circuit value at low frequencies to its open-circuit value at high frequencies. The frequency of this transition is determined by the shunting resistance. The material also exhibits a maximum loss factor at this transition point. The value of this maximum loss factor can be found to be:

$$\eta_{max-ij}^{RES} = \frac{k_{ij}^2}{2 \cdot \sqrt{1 - k_{ij}^2}} \quad (38a)$$

at a nondimensional frequency of:

$$\rho_i = R_i C_{pi}^S \omega = \sqrt{1 - k_{ij}^2} \quad (38b)$$

Thus by appropriate choice of resistor, the peak of the loss factor curve can be moved to the desired frequency.

It is worthwhile to draw a comparison between resistively shunted piezoelectrics and viscoelastic materials. The form of the frequency dependence of the viscoelastic can be seen in Ref. [14] for typical damping materials. For common viscoelastic materials, the peak loss factor occurs in a narrow frequency and temperature range where the viscoelastic is in transition from its rubbery state to its glassy state. This placement is directly analogous to the peak loss factor of the piezoelectric occurring at the transition from short circuit to open circuit stiffness.

It should be noted that the loss factor curve takes the same form as the standard relaxation curve for material damping, but can lead to material loss factors as high as 8.2% in the transverse case and 42.5% in the longitudinal or shear cases for commonly available piezoelectric ceramic materials. This compares favorably to the results obtained in Ref. [9] for the effective material loss factor for a resistive shunted piezoelectric ceramic.

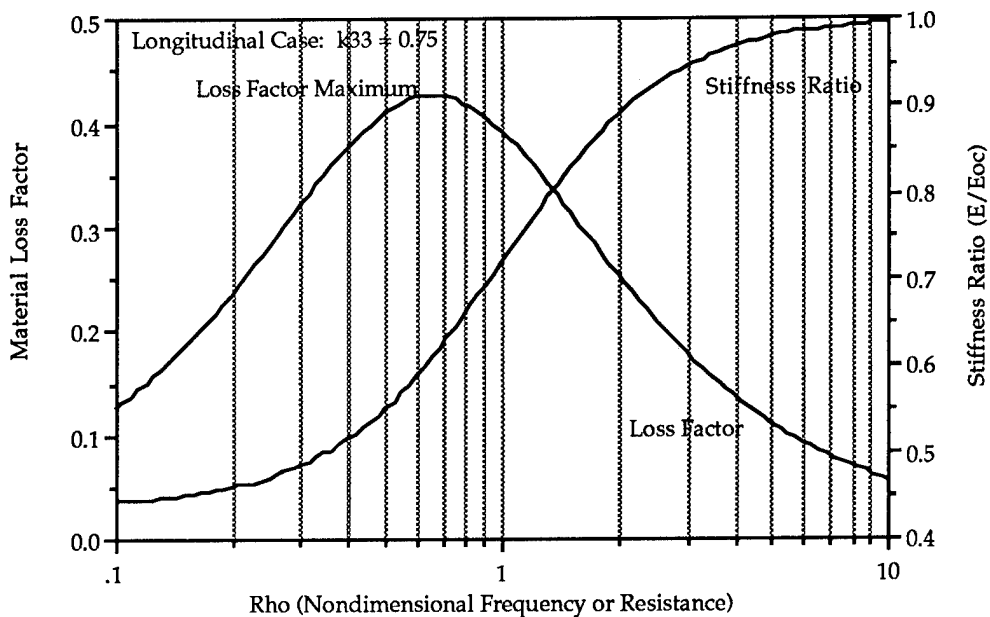
While these loss factor levels are not as high as those for viscoelastics, the piezoelectric material (typically a ceramic) has higher stiffness than most viscoelastic materials and thus stores more strain energy for a given strain. The piezoelectric ceramic material properties also have the advantage of being relatively stable with temperature over their operating range. Since their main constituent is lead, however, their density is 8 times that of water. In all, the net effect is that in most structural cases shunted piezoelectrics will provide higher total structural damping levels per unit mass with higher temperature stability. These results for the resistive shunted piezoelectrics have been validated experimentally and will be presented in a later section.

Systems Perspective for Determining Resistive Shunted Piezoelectric Effectiveness

Since the stiffness of the piezoelectric material is frequency dependant, maximizing the loss factor of the piezoelectric material does not necessarily maximize the loss factor of the total structural system of which the piezoelectric is a part. As shown by eq. (34) the total damping of the system consists of the component damping weighted by the strain energy fraction in that component. This strain energy fraction is frequency dependant for shunted piezoelectrics since the piezoelectric stiffness varies with frequency. In order to accurately model the system modal damping as a function of frequency or shunting parameters (such as resistance), this frequency dependant stiffness must be carried through the calculations.

Another method of obtaining the system modal damping which yields significant insight into the problem is to represent a single mode of the system as a simple 1-DOF system with a piezoelectric component in parallel to the system stiffness as shown in Fig. (5). The mass and stiffness in the simple system can represent the modal mass and stiffness of a multi-DOF system. In this case the modal stiffness of the piezoelectric should also be used. The modal velocity of the piezoelectric system can be expressed in the Laplace domain as:

Resistor Shunted Piezoelectric Material Properties: Longitudinal Case



Resistor Shunted Piezoelectric Material Properties: Transverse Case

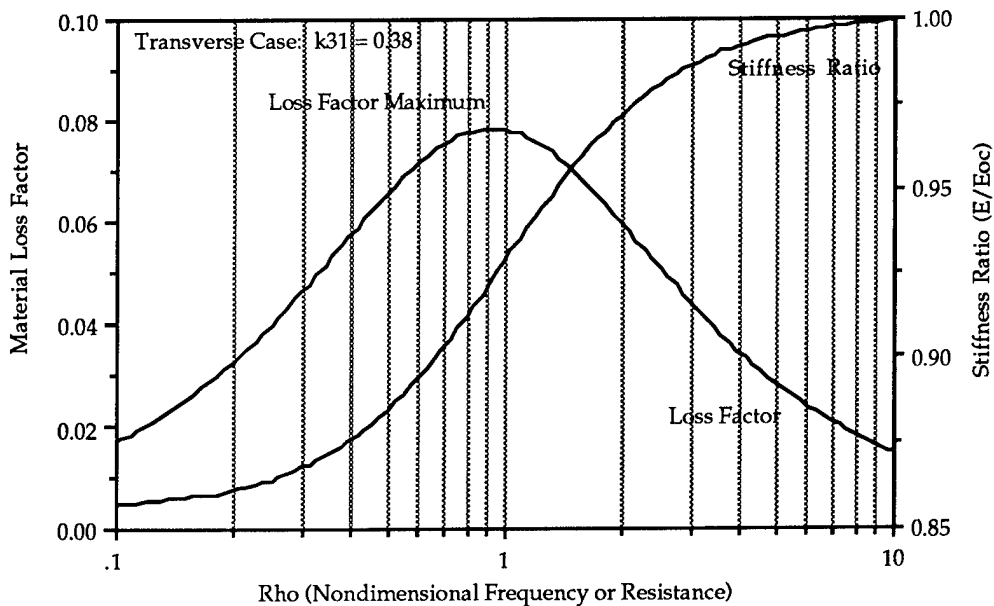


Figure 4: Effective Material Properties of a Resistively Shunted Piezoelectric in the Longitudinal (Upper) or Transverse (Lower) Cases

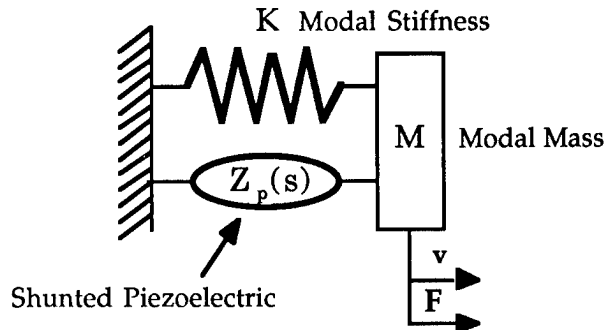


Figure 5: 1-DOF System with Shunted Piezoelectric Element in Parallel with the System Modal Mass

$$v(s) = \frac{F(s)}{Ms + \frac{K}{s} + Z_{jj}^{RES}(s)} \quad (39)$$

Where Ms is the impedance associated with the modal mass; K/s is the impedance associated with the modal stiffness; and $Z^{RES}(s)$ is the impedance associated with the resonant shunted piezoelectric's contribution to the modal mass. After reduction and nondimensionalization an expression for the position transfer function of such a mechanical system with a shunted piezoelectric in parallel with the base system stiffness and a force acting on the mass can be found from eq. (39):

$$\frac{x}{x^{ST}} = \frac{r\gamma + 1}{r\gamma^3 + \gamma^2 + r(1 + K_{jj}^2)\gamma + 1} \quad (40)$$

where x^{ST} is used for F/K_{tot} and K_{tot} is the sum of the base system modal stiffness and the piezoelectric open circuit modal stiffness. The nondimensionalization is defined relative to the mechanical system's natural frequency with the piezoelectric open circuited.

$$\omega_n^E = \sqrt{\frac{K + K_{jj}^E}{M}} \quad (41a)$$

$$\gamma = \frac{s}{\omega_n^E} = \text{nondimensional frequency} \quad (41b)$$

$$r = R_i C_{pi}^s \omega_n^E = \rho \Big|_{\omega=\omega_n^E} = \text{electrical damping ratio} \quad (41c)$$

The generalized electromechanical coupling coefficient, K_{ij} , is defined:

$$K_{ij}^2 = \left(\frac{K_{jj}^E}{K + K_{jj}^E} \right) \left(\frac{k_{ij}^2}{1 - k_{ij}^2} \right) = \bar{K} \frac{k_{ij}^2}{1 - k_{ij}^2} \quad (42)$$

where \bar{K} is the ratio of piezoelectric short circuit modal stiffness to the total system modal stiffness. The generalized coupling coefficient reflects the fact that the piezoelectric is in parallel with some other stiffness, and thus a smaller fraction of the system strain energy is converted to electrical energy. It is proportional to the fraction of the system modal strain energy which is converted into electrical energy by the open circuit piezoelectric. As such, it is a direct measurement of a shunted piezoelectric's influence on a system.

The modal damping ratio can now be found exactly by solving for the roots of the cubic equation in the denominator of eq. (40), or approximately using commonly available root solvers. The exact technique was used to calculate the modal damping of the cantilevered beam test article.

Application: Resonant Circuit Shunting

Another case of interest is to create a resonant circuit by shunting the inherent capacitance of the piezoelectric with a resistor and inductor in series forming a LRC circuit for Z^{EL} . This circuit is shown in Fig. (6). This resonant electrical circuit can be tuned in the vicinity of a mode of the underlying mechanical system and thereby greatly increase the attainable modal damping ratio, in an effect similar to the classical proof-mass damper (PMD) or resonant vibration absorber.

With an inductor and a resistor in parallel with the piezoelectric's inherent capacitance, the total electrical impedance can be written:

$$Z_i^{SU}(s) = L_i s + R_i \quad (43a)$$

$$\bar{Z}_i^{EL}(s) = \frac{L_i C_{pi}^T s^2 + R_i C_{pi}^T s}{L_i C_{pi}^T s^2 + R_i C_{pi}^T s + 1} \quad (43b)$$

where L_i is the shunting inductance and R_i is the shunting resistance. This circuit is clearly resonant with some damping due to the resistance, R_i . Equation (43b) can be substituted into eq. (31) and the results nondimensionalized to obtain the nondimensional mechanical impedance of a resonant shunted piezoelectric:

$$\bar{Z}_{ij}^{RSP}(s) = 1 - k_{ij}^2 \left(\frac{\delta^2}{\gamma^2 + \delta^2 r \gamma + \delta^2} \right) \quad (44a)$$

where the nondimensionalizations are defined relative to some arbitrary normalization frequency, ω_n

$$\omega_e = \frac{1}{\sqrt{L_i C_{pi}^S}} = \text{electrical resonant frequency} \quad (44b)$$

$$\delta = \frac{\omega_e}{\omega_n} = \text{nondimensional tuning ratio} \quad (44c)$$

and γ and r are defined in eqs. (41b & c) respectively.

Equation (44) is an expression of the effective mechanical impedance of a piezoelectric element shunted by a resonant circuit. The key parameters of (44) are the

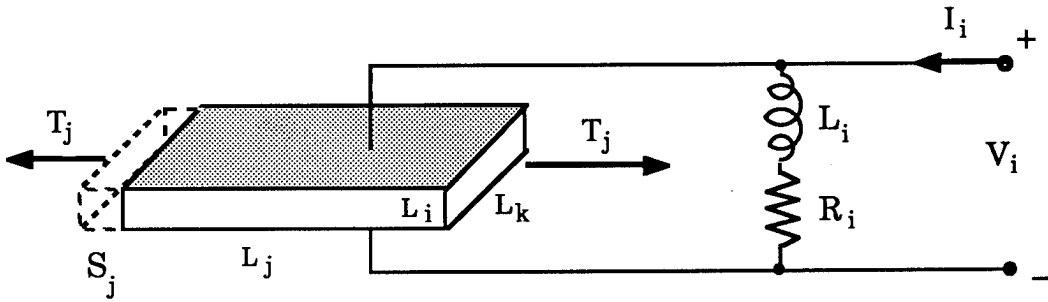


Figure 6: Resonant Shunted Piezoelectric Schematic

frequency tuning parameter, δ , and the damping parameter, r . These parameters are directly analogous to the ones used in classical proof mass damper nondimensionalization, Ref. [15]. The δ parameter reflects the frequency to which the electrical circuit is tuned, while the r parameter is an expression for the damping in the shunting circuit.

Materials Perspective

There are several ways to determine the parameters of eq. (44) which maximize energy dissipation. One of these involves treating the resonant shunted piezoelectric as a material with frequency dependant properties, in a fashion analogous to the resistive shunting case. The expression for the effective impedance of the piezoelectric can be put into a complex modulus form such as (33). This leads to complicated frequency-dependant expressions for the material stiffness and loss factor.

$$\bar{E}_{jj}^{RSP}(\omega) = 1 - k_{ij}^2 \left(\frac{\delta^2(\delta^2 - g^2)}{(\delta^2 - g^2)^2 + (\delta^2 rg)^2} \right) \quad (45a)$$

$$\eta_{jj}^{RSP}(\omega) = \frac{k_{ij}^2 \delta^2 (\delta^2 rg)}{(\delta^2 - g^2)^2 + (\delta^2 rg)^2 - k_{ij}^2 \delta^2 (\delta^2 - g^2)} \quad (45b)$$

where E^{LRC} and η^{LRC} are the effective material properties of the resonant shunted piezoelectric, and g is the real form of γ , (ω/ω_n) . These expressions can be seen plotted in Fig. (7) for common values of the parameters. They can be useful in system modelling if the values of the parameters are already known. Both the effective material stiffness and the damping vary nonlinearly with frequency and tuning parameter values, δ and r . This makes an optimization for energy dissipation difficult. The actual energy dissipated is dependant on both E and η and can be calculated for the total system using eq. (34).

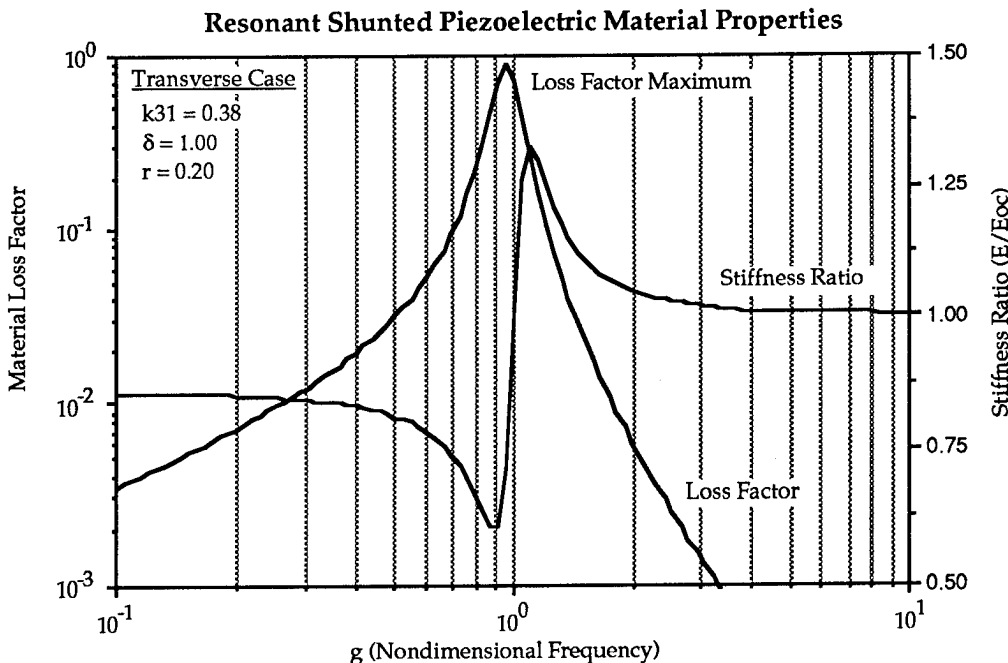


Figure 7: Effective Material Properties of a Piezoelectric Ceramic Operating Transversely and Shunted by a Resonant LRC Circuit.

Systems Perspective for Determining Resonant Shunted Piezoelectric's Effectiveness

The problems associated with the parameter optimization can be greatly alleviated by observing certain key similarities between a system containing a resonant shunted piezoelectrics (RSP) and a system containing

a proof mass damper (PMD). As illustrated in Fig. (8), the similarities in system topologies suggest that the method for obtaining the optimum parameters for the PMD can be applied to the RSP. The derivation for optimal tuning and damping of the electrical circuit parallels the technique for determining the optimal tuning and damping ratio of a PMD as outlined in Ref. [15].

These two systems can be thought of as complementary since the proof mass damper appears as a point impedance in system modeling and thus damps out only the available kinetic energy. On the other hand, shunted piezoelectrics are modeled as multi-port impedances which derive their dissipation from the relative motion of two system nodes. Thus they can be thought of as dissipating structural strain energy. This difference will reflect on the optimum placement of the actual dampers.

Following the techniques of modeling the 1-DOF system presented in the section on resister shunting, the modal deformation rate of the piezoelectric system with resonant shunted piezoelectrics can be expressed in the Laplace domain as:

$$v(s) = \frac{F(s)}{Ms + \frac{K}{s} + Z_j^{RSP}(s)} \quad (46)$$

Where Ms , K/s are modal quantities, and $Z_j^{RSP}(s)$ is the modal impedance associated with the resonant shunted piezoelectric. After reduction and nondimensionalization, an

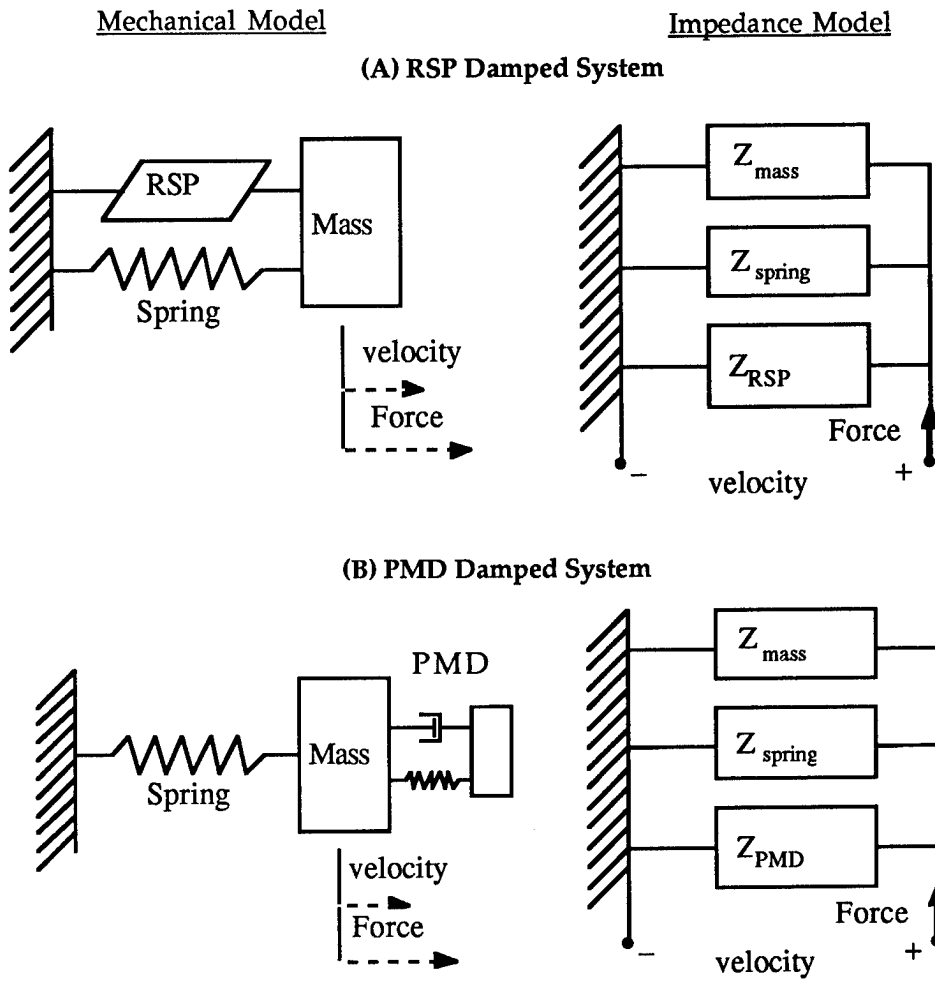


Figure 8: Comparison of Resonant Damper Topologies between an RSP Damped System (A) and a PMD Damped System (B)

expression for the position transfer function of a mechanical system with a RSP in parallel with the base system stiffness and a force acting on the mass can be found from (46):

$$\frac{x}{x^{ST}} = \frac{(\delta^2 + \gamma^2) + \delta^2 r \gamma}{(1 + \gamma^2)(\delta^2 + \gamma^2 + \delta^2 r \gamma) + K_{ij}^2 (\gamma^2 + \delta^2 r \gamma)} \quad (47)$$

where the nondimensionalization is the same as that used in eq. (44). The mechanical system's short circuit natural frequency (defined in eq. 41a) is substituted for the normalization frequency used in (44) and the generalized electromechanical coupling coefficient, K_{ij} , is defined in eq. (42).

For the tuned PMD, the transfer function expression equivalent to eq. (47) is:

$$\frac{x_1}{x_1^{ST}} = \frac{(\delta^2 + \gamma^2) + \delta^2 r \gamma}{(1 + \gamma^2)(\delta^2 + \gamma^2 + \delta^2 r \gamma) + \beta(\delta^2 \gamma^2 + \delta^2 r \gamma^3)} \quad (48)$$

with the k_{ij} used in the nondimensionalization set equal to zero and β equal to the damper mass ratio as described in Ref. [15]. By comparing the form of these two equations, (47) and (48), it is evident that the generalized electromechanical coupling coefficient for the tuned piezoelectric case, K_{ij}^2 , serves the same function as the mass ratio, β , in the PMD system.

Two techniques for determining the "optimal" tuning criteria will be presented. The first technique parallels the min-max criteria (presented in Ref. [15] for PMDs) for minimizing the maximum of the system transfer function by appropriate choice of the RSP parameters. This technique will be referred to as transfer function optimization, and the optimal parameters will bear the subscript, (\circ_{TF}) . The second technique will depend on pole placement techniques to choose system pole locations which maximize the magnitude of the real part of the system roots. The optimal parameters using this technique will bear the subscript, (\circ_{PP}) , to signify pole placement.

Resonant Damper Optimization by Transfer Function Considerations

At this point the optimal tuning parameters using the transfer function technique can be found by duplicating the argument for the PMD [15]. The first step in this process is to find the magnitudes of the transfer functions which correspond to $r = \text{zero}$ and $r = \text{infinity}$ respectively. From eq. (47) for $r = 0$:

$$\left| \frac{x_1}{x_1^{ST}} \right|_{r=0} = \left| \frac{\delta^2 - g^2}{(1 - g^2)(\delta^2 - g^2) - K_{ij}^2 g^2} \right| \quad (49a)$$

and for $r = \text{infinity}$

$$\left| \frac{x_1}{x_1^{ST}} \right|_{r=\infty} = \left| \frac{1}{(1 + K_{ij}^2) - g^2} \right| \quad (49b)$$

These two transfer functions can be equated and a quadratic expression found for the intersection points, called the S and T points in the PMD analysis. This expression is

$$g^4 - g^2 \left[(1 + K_{ij}^2) + \delta^2 \right] + \left[\frac{\delta^2}{2} (2 + K_{ij}^2) \right] = 0 \quad (50)$$

From the quadratic formula, the sum of the roots of this equation can be found to be

$$g_S^2 + g_T^2 = -\frac{B}{A} = (1 + K_{ij}^2) + \delta^2 \quad (51)$$

Equation (49b) can be solved for the magnitudes at the S and T points. This gives another expression for the sum of the two roots.

$$g_S^2 + g_T^2 = 2(1 + K_{ij}^2) \quad (52)$$

Equating (51) and (52) leads to an expression for the tuning parameter which equalizes the magnitudes of the S and T points. This is the optimum tuning parameter.

$$\delta_{TF}^{opt} = \sqrt{1 + K_{ij}^2} \quad (53)$$

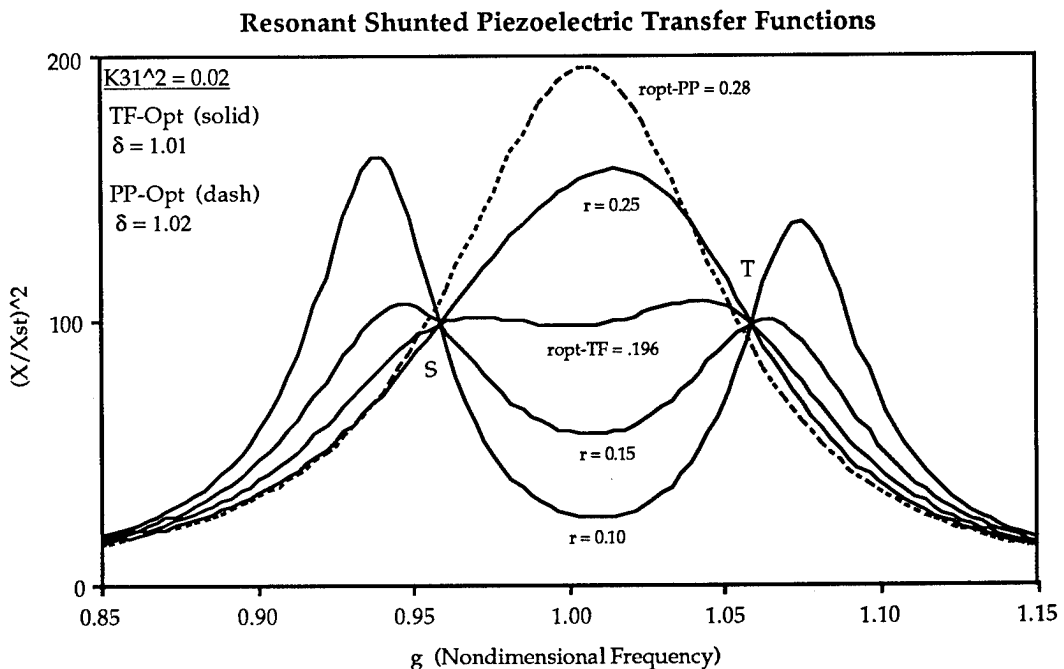


Figure 9: Transfer Function for a Single DOF System Containing a RSP at Various Values of the Damping Parameter,r

Once the optimal tuning has been found using the transfer function criteria, there are several methods for determining the "optimal" damping in the electrical circuit. One method entails setting the amplitude of the system transfer function at a chosen frequency to the amplitude of the transfer function at the invariant frequencies, the S and T points. A particularly convenient (though not technically optimal) frequency corresponds to the electrical tuning at $g = \delta$. The amplitude of the S and T points can be found by first solving equation (50) for the S and T frequencies. The roots of (50) are:

$$g_{S,T}^2 = \left(1 + K_{ij}^2\right) \pm \sqrt{\frac{K_{ij}^2(1 + K_{ij}^2)}{2}} \quad (54)$$

This expression can be substituted into (53) to yield the amplitude at S or T:

$$\left| \frac{x_1}{x_1^{ST}} \right|_{S,T} = \left| \sqrt{\frac{2}{K_{ij}^2(1 + K_{ij}^2)}} \right| \quad (55)$$

Evaluating the system transfer function, eq. (47), at $g = \delta$ and setting this amplitude equal to (55) gives an equation that can be solved for a simple expression for the "optimal" circuit damping:

$$r_{TF}^{opt} \cong \sqrt{2} \frac{K_{ij}}{1 + K_{ij}^2} \quad (56)$$

The subscript, (\circ_{TF}) , signifies that this expression was derived from transfer function considerations. The effect of various circuit resistor values at optimal tuning is shown in Fig. (9). As can be seen, the system sensitivities to damping parameter variations are essentially identical to the PMD sensitivities. As the damping parameter is increased, the two distinct system modes coalesce into a single mode which converges to the system response with open circuit piezoelectrics as the damping parameter approaches infinity.

Optimal Tuning by Pole Placement Techniques

The second technique for determining the "optimal" tuning parameters is based on s-plane methods described in Ref. [12] for PMDs and outlined in Ref. [9] for piezoelectrics. The s-plane diagram in Fig. (10) shows the root locus for the poles of the shunted piezoelectric system as the damping parameter, r , is varied. Just as in the PMD case, as the damping parameter is increased the distinct poles can coalesce into double complex conjugate pairs *only if* a special value of the frequency tuning parameter, δ , is chosen. This point of coalescence is the point of leftmost excursion in the s-plane. The pole placement method of optimization involves finding the values of the frequency tuning parameter, δ , and the damping parameter, r , which give that point on the s-plane. The poles of the system are found from the denominator of eq. (47). Assuming the coalesced poles are located at the coordinates, $s = a + ib$, $a - ib$, a series of equations for a and b can be found by equating corresponding terms of the characteristic polynomial found in the denominator of eq. (47).

$$\delta^2 r = -4a \quad (57a)$$

$$(1 + \delta^2) + K_{ij}^2 = 6a^2 + 2b^2 \quad (57b)$$

$$\delta^2 r (1 + K_{ij}^2) = -4a(a^2 + b^2) \quad (57c)$$

$$\delta = a^2 + b^2 \quad (57d)$$

These equations can be solved for the parameters, r and δ , to give the value which results in the coalesced poles:

$$\delta_{pp}^{opt} = 1 + K_{ij}^2 \quad (58a)$$

$$r_{pp}^{opt} = 2 \cdot \sqrt{\frac{K_{ij}^2}{(1 + K_{ij}^2)^3}} = r_{TF}^{opt} \sqrt{\frac{2}{1 + K_{ij}^2}} \quad (58b)$$

The subscript, (\circ_{pp}) , has been used to signify that the expressions were derived from pole-placement considerations. The transfer function corresponding to optimal tuning and this value of r is shown in Fig. (9). This method tends to give higher steady state responses than the first method presented.

As a practical point the various damper tuning criteria are indistinguishable in all but the most sensitive experimental setups. The ratios given for optimal tuning and electrical damping can now be used to add maximum damping to targeted structural modes. Use of a tuned circuit can increase the structural mode damping several orders of magnitude above simple resistive shunting at the cost of reduced damper bandwidth.

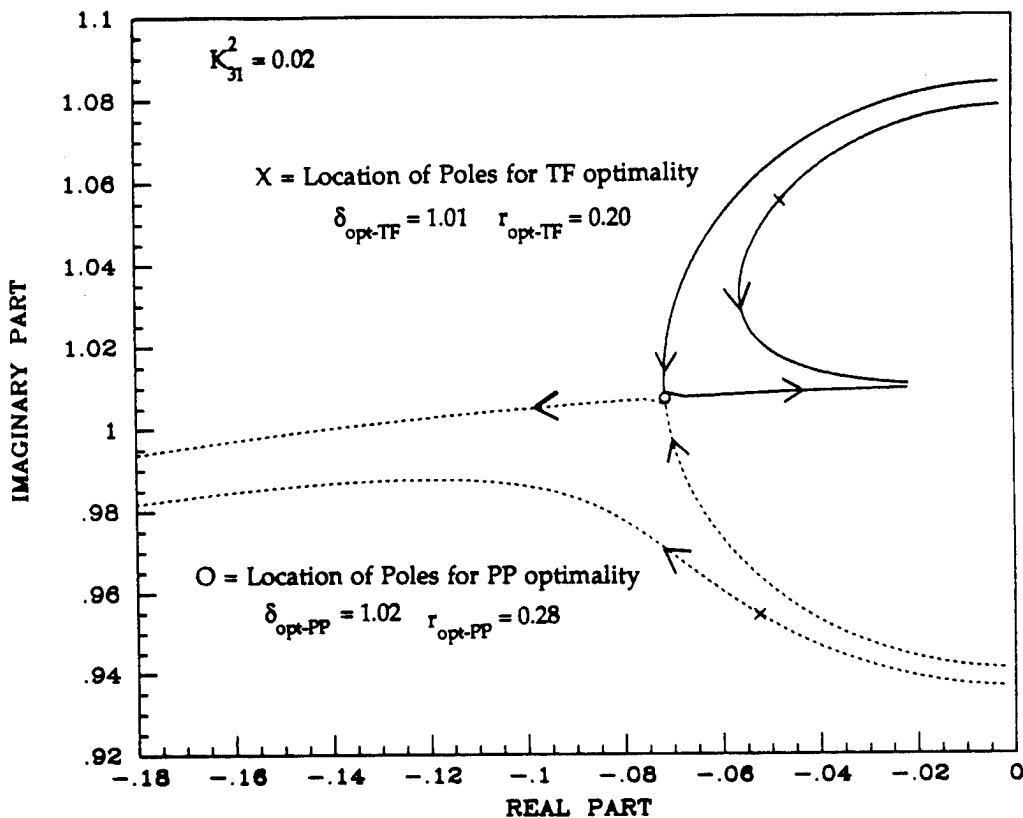


Figure 10: Root Locus for a RSP Damped System at 2 Values of δ as a Function of the Damping Parameter, r , Showing the Pole Locations for the Pole Placement (O) and Transfer Function (X) Optimal Tunings

Summary of Analytical Predictions

For resistive shunted piezoelectrics, the stiffness and loss factor of the piezoelectrics were found to vary with frequency. The loss factor exhibited a maximum at a frequency determined by the shunting resistance and the electromechanical coupling coefficient of the piezoelectric. For common piezoelectric materials this loss factor can be as high as 42.5% for the longitudinal and shear loading cases, and 8% for the transverse loading case. This high loss factor, along with the high stiffness and temperature stability of piezoelectric ceramics, makes them an attractive alternative to viscoelastic materials.

The shunted piezoelectric materials can be modeled within a structural system in two principal ways. They can be modelled as having a frequency dependant complex modulus and incorporated in the same manner as viscoelastic materials. Alternatively, their internal dynamics can be modelled using mechanical impedance and assembled into a system impedance model for dynamic analysis.

For resonant shunted piezoelectrics, the parameters of the resonant circuit can be tuned to a structural mode so as to minimize the maximum response of the mode in a fashion analogous to proof mass damper tuning. The effectiveness of the RSP damper at optimal tuning is dependant on the generalized electromechanical coupling coefficient which is a measure of the percentage of total system modal strain energy actually converted into electrical energy by the piezoelectric. For typical structures where the piezoelectric contains only a small fraction of the structural strain energy, the electrical resonance should be tuned very close to the structural resonance. The optimal damping in the electrical resonance is

also almost linearly dependant on the coupling coefficient in this case. Two sets of tuning criteria are derived, depending on minimizing the magnitude of the transfer function, or minimizing the real part of the system poles.

Description of Experiments

Experiments were conducted to test the validity of the analytical formulae for shunted piezoelectrics. The tests were designed to investigate the properties of the resistive and resonant shunted piezoelectrics.

Dynamic tests were preformed on a cantilevered beam test article with surface bonded piezoceramics and geometry as shown in Fig. (11). The cantilevered beam was 11.53" long, 1.0" wide, and 1/8" thick. Two sets of surface mounted piezoceramics were bonded to the beam. The pair closest to the base was shunted while the pair furthest from the base served to drive the beam. The shunted pair was located 97 mills from the base and extended 2.44". The piezoceramic pairs were separated by 1".

The driving and shunted pairs consisted of 10 mil thick G-1195 piezoceramic sheets manufactures by Piezoelectric Products, Inc. The pairs were poled through their thickness and actuated lengthwise, so that they were operating in the transverse mode. For both pairs, the piezoceramics were attached to the top and bottom surfaces of the beam and wired as shown in Fig. (11), so as to produce a moment on the beam if a voltage were applied as described in Ref. [2]. The piezoceramics are attached to the beam with a very thin layer of conducting epoxy. The beam is grounded and the positive electrodes are attached to the exterior electroded surfaces of the piezoceramic pairs. This produces opposite fields in the top and bottom piezoceramics (which are poled in the same direction), and thus causes the top piezoceramic of a pair to contract as the bottom expands, producing a moment on the beam. Likewise for the shunted pair, a voltage appears across the shunt if the beam is bent. The material properties of the piezoceramics are presented in Table (1). A more detailed discussion of modeling of surface bonded piezoceramics is presented in Ref. [16].

In the shunting experiments, either a resister or a resister and inductor are placed across the piezoelectric electrodes at $Z^{su}(s)$, as shown in Fig. (11). An uncorrelated, pseudo-random voltage is then applied as an input at the positive terminal to excite the beam in the vicinity of its first bending mode at 33 Hz. The white noise excitation signal is produced by a Textronix 2630 data collection system and amplified by a Crown DC-300A audio amplifier. The strain response of the beam is measured at a point 2.74" above the base a shown in Fig. (11). The amplified strain signal is collected by the Tectronix 2630 and a transfer function from input voltage to strain is computed.

In the resistive shunting experiments the shunting resistor is varied over a range of 1/10 to 10 times the theoretical optimum value for maximizing dissipation. Using eq. (38b) the optimum shunting resistance was found to be 28,680 ohms. For each resistance the damping and frequency of the first beam bending mode are identified using a 4th order

Table 1: Piezoelectric Properties of Shunted Piezoceramics

Coupling Coefficient	k_{31}	=	0.35
Elastic Modulus (free)	E_{11}^E	=	63 Gpa
Dielectric Constant	ϵ_3^T	=	1700 ϵ^o
Capacitance (clamped)	C_{pi}^S	=	0.156 μ farad
Curie Temperature		=	360°C

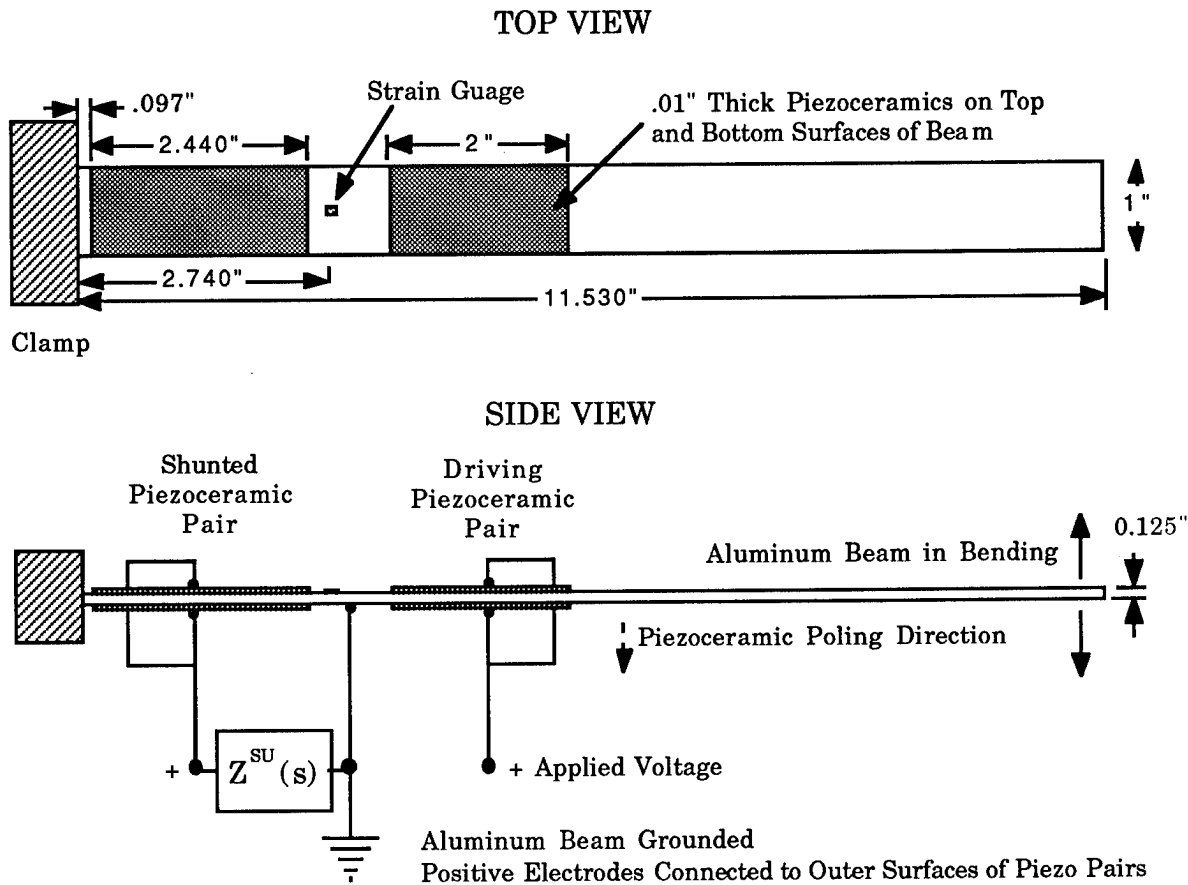


Figure 11: Cantilevered Beam Test Article with Position and Arrangement of Shunted and Driving Piezoceramic Pairs

Recursive Lattice Least Squares (RLLS) algorithm from Ref. [17] applied to the time domain data from which the transfer functions are derived.

For the resonant shunting experiments, a resistor and inductor in series are placed across the piezoelectric leads and the resistor and inductor are tuned to the first beam bending mode, in accordance with eqs. (53) and (56). The transfer function from input current to strain is then measured and compared to the theoretical response for a 1-DOF system derived in eq. (47). The resistance is further varied in the range of the optimal value to validate the behavior of the resonant shunted piezoelectric system in response to parameter changes.

Discussion of Results

The experimental first mode damping for the resister shunting case is shown compared to the analytical predictions in Fig. (12). In this figure, the experimental poles were identified from the random time domain response using the recursive lattice least squares algorithm mentioned previously. The identified damping ratio has been normalized by subtracting off the inherent damping of the beam with the piezoelectrics shorted. The curve thus represents only the damping increase afforded by the shunting process. This is called the experimental added damping.

The two analytical curves were obtained by solving for the roots of the denominator of eq. (40) exactly. The damping ratio was then found from the root location. The upper

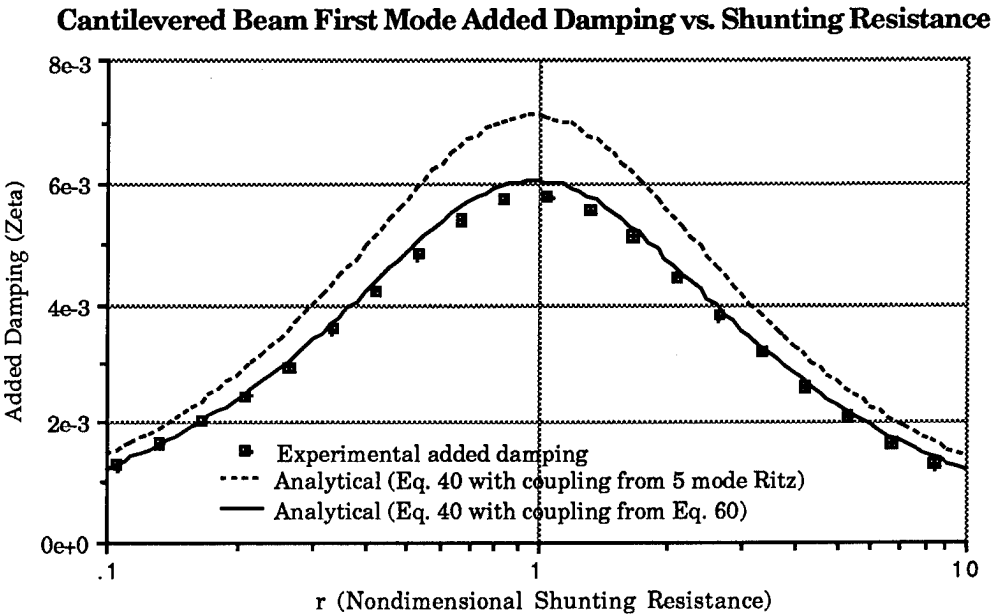


Figure 12: Comparison of Experimental and Analytical First Mode Damping Increase as a Function of the Shunting Resistance

analytical curve reflects the value of the generalized electromechanical coupling coefficient obtained for the shunted piezoceramic pair when a 5 mode Raleigh-Ritz analysis is used to calculate the ratio of strain energy in the piezoelectric to that in the structure, \bar{K} . For this curve the values of the piezoelectric material properties supplied by the manufacturer were used.

The first five bending modes of a uniform cantilevered beam were used in the 5 mode Ritz model which predicted a first resonant frequency of 35.65 Hz for shorted piezoelectrics and a generalized coupling coefficient, K_{31} , of 0.169. In this analysis, the piezoelectrics were assumed to be perfectly bonded. Details of this type of analysis for bonded or embedded piezoelectrics are presented in Ref. [16]. Since the actual beam had a first natural frequency of 33.36 Hz and the Ritz model accurately represents the system mass, it can be concluded that the Ritz model contains about 14% error in the modal stiffness of the beam. This error will effect the predicted piezoelectric performance. It can be partially accounted for by the finite thickness bond layers of the shunted and driven piezoceramic pairs. The Ritz model thus overestimates the amount of strain energy in the piezoceramic and thus the performance of the resistive shunting.

An alternative approach is to obtain the generalized coupling coefficient by a simple experiment. If it is noted that for a mode of a structure the frequency changes as the stiffness of the piezoelectric changes from its short circuit to open circuit value:

$$\omega_n^E = \sqrt{\frac{K + K_p^E}{M}} \quad \text{and} \quad \omega_n^D = \sqrt{\frac{K + \frac{K_p^E}{1 - k_{ij}^2}}{M}} \quad (59)$$

then a simple expression for the generalized coupling coefficient for a piezoelectric bonded to a structure can be obtained from the frequency change in these two cases:

$$K_{ij}^2 = \frac{(\omega_n^D)^2 - (\omega_n^E)^2}{(\omega_n^E)^2} \quad (60)$$

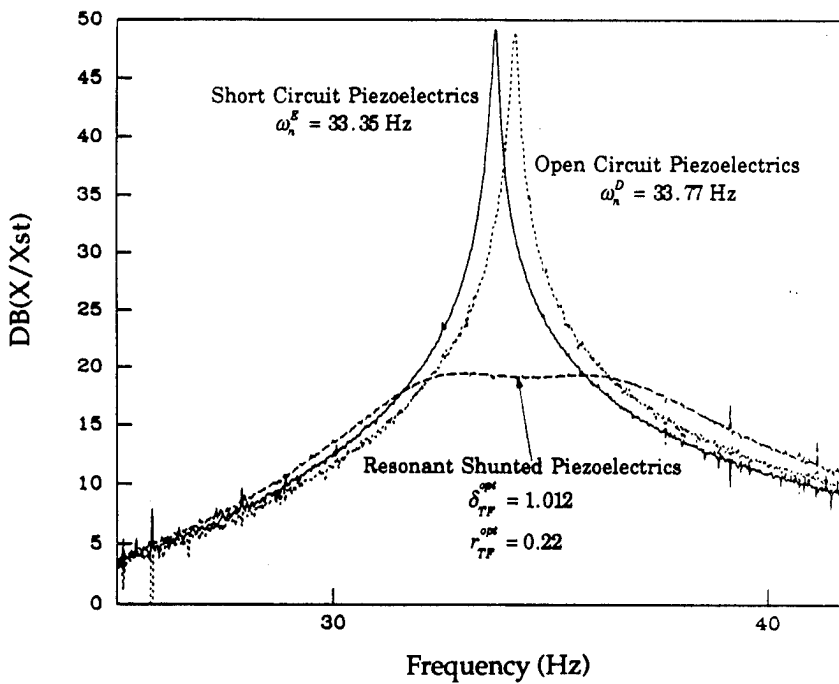
The lower analytical curve was obtained by experimentally measuring the first natural frequency of the beam with the shunted pair open or shorted and applying eq. (60) to obtain the generalized electromechanical coupling coefficient. The value obtained was 0.157. This value was then used in the denominator of Eq. (40) and the resulting roots found. As can be seen in Fig. (12), this method exhibits much better agreement with the experimentally determined added damping.

The conclusion of this analysis is that the resistive shunting piezoelectric effect is accurately modelled using the equations presented in this paper, and that the main source of error is in the mechanical models of a piezoelectric bonded to a structure. The experimental curve exhibits the form of the analytical predictions and agrees well with theory once the generalized coupling coefficient has been accurately obtained. For this particular specimen the amount of damping added is not large, because the piezoelectrics store only a small portion of the strain energy and are operating transversely.

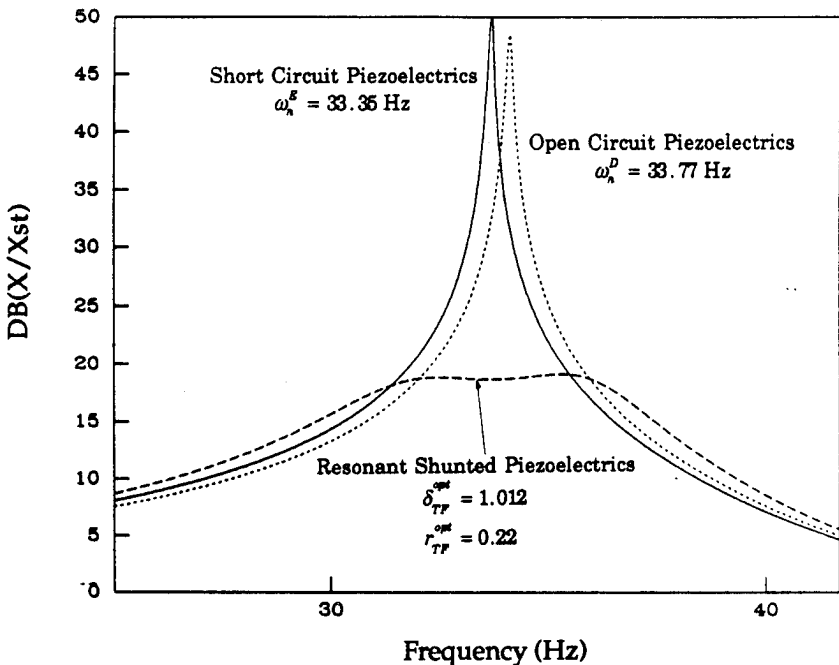
The beam transfer functions from applied voltage to strain guage with optimally tuned resonant shunted piezoelectrics are shown compared to the same transfer functions for the beam with shorted or open circuit piezoelectrics in Fig. (13). The change in natural frequency from the shorted to the open circuit piezoelectrics is clear from this figure. The optimal shunting parameter values were calculated from the transfer function criteria (eq. 53 and 56) using the value of the generalized coupling coefficient found from eq. (60). These corresponded to a 142.4 Henry inductor and a 6640 ohm shunting resistor. The large inductor was necessary to produce a low electrical resonant frequency.

The resonant shunted piezoelectric pair was found to produce a 35 db drop in peak vibration amplitude from the shorted or open circuit case. This large amplitude reduction is in good agreement with the analytical curves for a 1-DOF system obtained from eq. (47). The experimentally determined natural frequency and base damping of the beam with shorted piezoelectrics were used in the analytical curves as well as the coupling coefficient found by eq. (60). The 1-DOF system curves agree well in the vicinity of the resonance but fail (as expected) to capture the multiple mode nature of the beam. For this reason the rolloff amplitudes are not identical.

The variation in the beam response as the shunting resistor is varied away from the optimal value is presented in Fig. (14) and shown to exhibit tendencies precisely as predicted by the analytical model. This close agreement validates the resonant shunted piezoelectric model. As predicted, the system exhibits two distinct modes when the resistor is below its optimal value. As the resistance is increased these modes coalesce into a single mode which converges to the beam response with open circuit piezoelectrics.

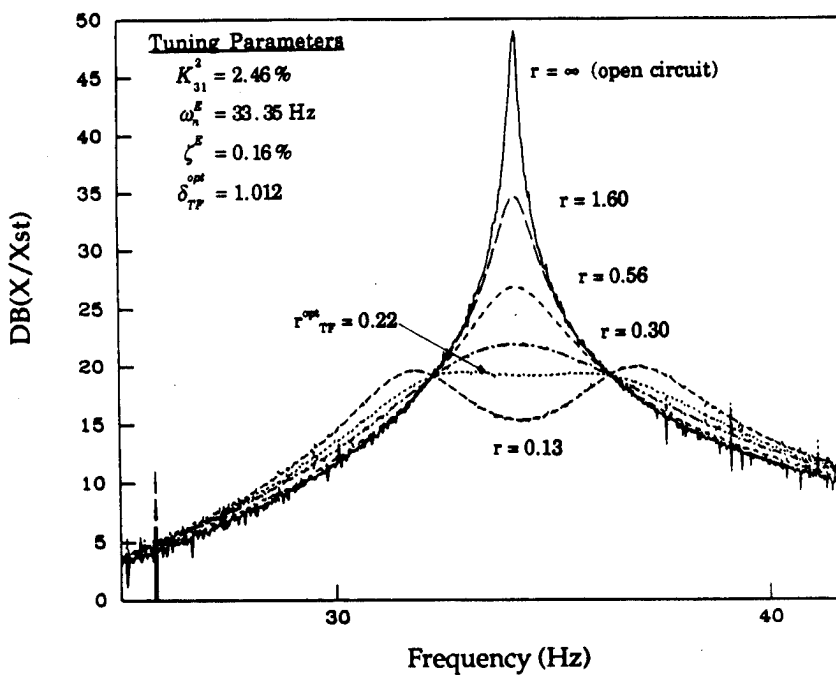


A) Experimental First Mode Transfer Functions with Open Circuit (1), Short Circuit (2), and Optimally Tuned Resonant Shunted Piezoelectrics (3)

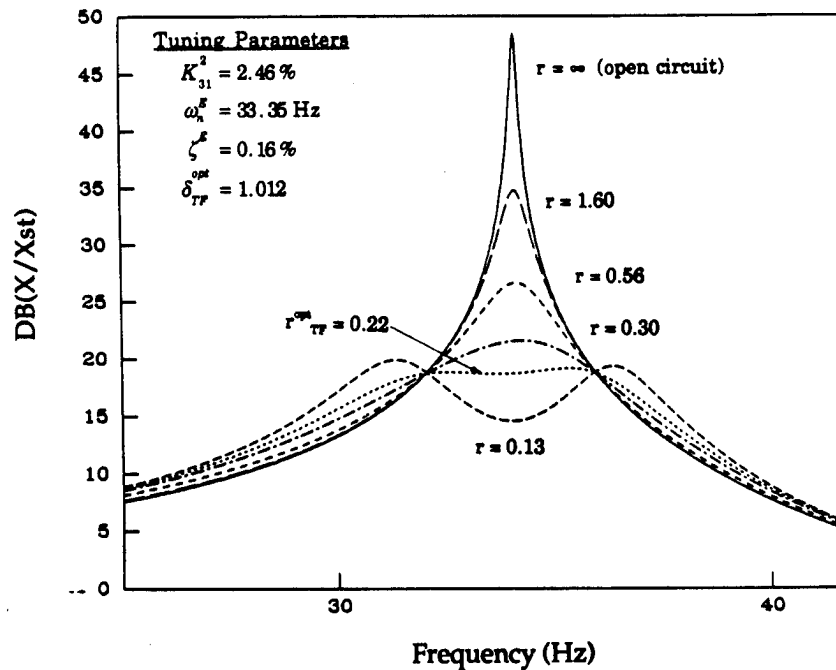


B) Analytical First Mode Transfer Functions with Open Circuit (1), Short Circuit (2), and Optimally Tuned Resonant Shunted Piezoelectrics (3)

Figure 13: First Mode Transfer Functions for Cantilevered Beam with Resonant Shunted Piezoelectric Compared to Beam with Shorted or Open Circuit Piezoelectrics: Experimental (Top) and Analytical (Bottom)



A) Experimental First Mode Transfer Functions with Resonant Shunted Piezoelectrics at Optimal Frequency Tuning and Various Values of the Dissipation Parameter, r



B) Analytical First Mode Transfer Functions with Resonant Shunted Piezoelectrics at Optimal Frequency Tuning and Various Values of the Dissipation Parameter, r

Figure 14: First Mode RSP Dissipation Parameter Variation from $r = 0.133$ (widely space modes) to $r = \infty$ (open circuit piezoelectrics): Experimental (Top) and Analytical (Bottom)

Conclusions

A new type of structural damping mechanism has been presented based on piezoelectric materials shunted by passive electrical circuits. A model for general shunting of these materials subject of arbitrary elastic boundary conditions was developed to determine the 6x6 material compliance matrix when the material is shunted. This model was found to simplify in the case of uniaxial loading and electrical field with the introduction of the material electromechanical coupling coefficient.

The uniaxial equations were then applied to the cases of resistive and resonant circuit shunting. In the resistor shunting case, the optimal shunting resistance for maximizing the piezoelectric material loss factor at a given frequency was determined. The material loss factor was found to be as high as 42% in the longitudinal loading case for commonly available piezoceramics. The high loss factor, together with the high stiffness (63 Gpa) and temperature stability, makes resistor shunted piezoelectrics an attractive alternative to viscoelastic materials in structural damping applications.

The problem of determining the global system damping was discussed in the context of the frequency dependant material properties of the piezoceramic, and two techniques were suggested. The shunted piezoelectric elements can be incorporated into the structural stiffness model via a complex modulus representation (like for viscoelastic materials), or analyzed as complex impedances and included in a complex system model (like for electrical systems). Both modelling methods yield identical results. For systems analysis, the energy transfer from the mechanical to electrical parts (and therefore the effectiveness of the shunted piezoelectric) is governed by the generalized electromechanical coupling coefficient which serves as measure of effectiveness. The square of this coefficient represents the ratio of modal strain energy which is converted into electrical energy by the piezoelectric.

Resonant circuit shunting of piezoelectrics was also modelled and shown to exhibit behavior very similar to the well known mechanical tuned vibration absorber. The analogy with the mechanical damper suggested a method of tuning the resonant shunting circuit to a structural mode to optimally damp it. Tuning criteria were developed for the shunting circuit which either minimized the peak amplitude of the system transfer function or placed the poles as far right as possible in the s-plane. The resonant shunting can have large effects on the mode to which it is tuned while the resistor shunting has a larger bandwidth.

Experiments were conducted on a cantilevered beam which validated the shunted piezoelectric models. The models developed were able to accurately predict the influence of the shunted piezoelectrics on the cantilevered beam damping in both the resistive and resonant shunting cases. In both cases, the models also correctly predicted the optimal tuning parameters and effect of variations away from the optimal parameters.

Great benefits for base system energy dissipation can be attained by shunting the electrodes of the piezoelectric material with appropriate passive circuits. The passive shunting introduces damping at the piezoelectric but does not preclude the use of shunted piezoelectrics as actuators in structural active control applications. The analytical models of the shunted piezoelectric, as well as the experimental verification of these models, provides a solid groundwork for future structural damping applications of shunted piezoelectric materials.

Acknowledgements

The authors wish to thank Mr. Walter Chung for his contributions to the experimental phases of this research. This work was sponsored under NASA Grant #NAGW-21 with Mr. Samuel Venneri serving as technical monitor.

References

1. Ashley, Holt; Edberg, Donald L., "On the Virtues and Prospects for Passive Damping in Large Space Structures," Presented at the Air Force Vibration Damping Workshop II, April 1985.
2. Crawley, E. F., deLuis, J., "Use of Piezoelectric Actuators as Elements of Intelligent Structures," AIAA Journal, Vol. 25, No. 10, Oct. 1987, pp.1373-1385.
3. Hagood, Nesbitt W.; Crawley, Edward F., "Development and Experimental Verification of Damping Enhancement Methodologies for Large Space Structures," MIT Space Systems Laboratory Report No. 18-88, September 1988.
4. Hanagud, S.; Obal, M. W.; Calise, A. J., "Optimal Vibration Control by the Use of Piezoceramic Sensors and Actuators," AIAA Paper No. 87-0959, Proc. AIAA S. D. M. Conference, 1987.
5. Bailey, T.; Hubbard, J. E., "Distributed Piezoelectric Polymer Active Vibration Control of a Cantilever Beam," *J. of Guidance and Control*, p. 605, 1985.
6. Pines, Darryll; Flotow, Andreas von, "Active Control of Bending Wave Propagation at Acoustic Frequencies," Proceedings American Control Conference, June 1989.
7. Forward, Robert L., "Electronic Damping of Vibrations in Optical Structures," *Journal of Applied Optics*, Vol. 18, No. 5, March 1979, pp. 690-697.
8. Forward, Robert L., Swigert, C. J., "Electronic Damping of Orthogonal Bending Modes in a Cylindrical Mast- Theory," *Journal of Spacecraft and Rockets*, Vol. 18, Jan. -Feb. 1981, pp. 5-10.
9. Edwards, R. H., Miyakawa, R. H., *Large Structure Damping Task Report*, Hughes Aircraft Co. Report No. 4132.22/1408, May 1980.
10. IEEE Std 176-1978, "IEEE Standard on Piezoelectricity," 1978, pp. 9 - 14.
11. Jaffe, B.; Cook, R.; Jaffe, H., *Piezoelectric Ceramics*, Academic Press, New York, NY., 1971.
12. Miller, David W.; Crawley, Edward F., "Theoretical and Experimental Investigation of Space-Realizable Inertial Actuation for Passive and Active Structural Control," *J. Guidance Control and Dynamics*, Vol. 11, No. 5, Sept-Oct 1988, pp.449-458.
13. Hagood, Nesbitt W., Crawley, Edward E., "A Frequency Domain Analysis for Damped Space Structures," 30th AIAA/ASME/ASCE/AHS Structures, Structural Dynamics, and Materials Conference, April 1989, AIAA Paper No. 89-1381.
14. Nasif, Ahid D.; Jones, David I. G.; Henderson, John P., *Vibration Damping*, John Wiley & Sons, New York, 1985, pp.69-73.
15. Timoshenko, Stephen; Young, D.H.; Weaver, W., Jr., *Vibration Problems in Engineering*, 4th Ed., John Wiley and Sons, New York, 1974.
16. Anderson, E. H., Crawley, E. F., "Detailed Models of Piezoceramic Actuation of Beams," 30th AIAA/ASME/ASCE/AHS Structures, Structural Dynamics, and Materials Conference, April 1989, AIAA Paper No. 89-1388.
17. Lee, Daniel T.L.; Morf, Martin; Friedlander, Benjamin, "Recursive Least Squares Ladder Estimation Algorithms" *IEEE Transactions on Acoustics, Speech and Signal Processing*, Vol. ASSP 29, No. 3, June 1981, pp. 627-641.

ELECTROMAGNETIC VIBRATION DAMPERS*

by

B. W. Maxfield
A. Kuramoto
J. K. Hulbert
P. Smiley

Innovative Sciences, Inc.
400 Hester Street
San Leandro, CA 94577
(415) 568-7720

ABSTRACT

A non-magnetic metal moving through a region of non-uniform magnetic field experiences a drag force. For some simple, one-dimensional or axisymmetric cases, it is possible to obtain an exact analytical solution. For more complex geometries, finite element (FE) methods are the most practical means of calculating the force between a configuration of magnets and a moving conductor. This paper describes how FE calculations can be performed and shows that good agreement can be obtained between FE calculations and the measured response. When a conducting plate, bar or rod is constrained to move near certain configurations of high energy density, permanent magnets, a large drag force proportional to the relative velocity is produced. This drag force can be used to damp mechanical motion. This paper presents several candidate magnet-conductor configurations that could be used as vibration damper assemblies. The next step is to design damper assemblies for particular modes of a specific structure and then to compare the calculated with the measured performance of these dampers.

* This work was supported in part by the Air Force Office of Scientific Research through the Small Business Innovative Research program.

1.0 INTRODUCTION

The reduction or elimination of unwanted structural motion is an ever present problem in mechanical structures. Many very clever and effective solutions have been developed to address vibration damping under a wide variety of circumstances. This paper shows that electromagnetic damping as described herein should become one of the candidate technologies that is routinely considered for adding passive damping to structures. Several modifications of the passive damping approaches discussed in this paper are also candidates for combined active and passive dampers but these are not discussed here.

2.0 GENERAL BACKGROUND THEORY

Currents are induced to flow in any conductor moving through a region of localized magnetic field; these currents and fields obey Maxwell's equations

$$\nabla \wedge \underline{E} = - \frac{\partial \underline{B}}{\partial t} \quad (1)$$

and

$$\nabla \wedge \underline{H} = \underline{J} \quad (2)$$

For non-magnetic metals such as aluminum, the appropriate constitutive equations for the moving conductor are

$$\underline{J} = \sigma \underline{E} + \sigma \underline{v} \wedge \underline{B} \quad (3)$$

and

$$\underline{B} = \mu \underline{H} \quad (4)$$

where $\underline{v}(r,t)$ is the velocity of the conductor relative to the magnetic field $\underline{B}(r,t)$, σ is the electrical conductivity and μ is the magnetic permeability. Following standard convention, solutions are developed in terms of a vector and scalar potential such that

$$\underline{E} = - \frac{\partial \underline{A}}{\partial t} + \nabla \phi \quad (5)$$

$$\underline{B} = \nabla \wedge \underline{A} \quad (6)$$

Substituting Equations (5) and (6) into Equation (3) gives

$$\underline{J} = \sigma \left(- \frac{\partial \underline{A}}{\partial t} + \underline{v} \wedge \nabla \wedge \underline{A} \right) - \sigma \nabla \phi \quad (7)$$

Under most conditions at low frequencies, the time derivative of \underline{A} will be much smaller than the velocity term and one can write

$$\underline{J} = \sigma \underline{v} \wedge \nabla \wedge \underline{A} - \sigma \nabla \phi \quad (8)$$

With no loss of generality for 2D current flow, one can take $\underline{A} = (0, 0, A)$ and $(\partial A / \partial z) = 0$. Consequently,

$$B_x = \frac{\partial A}{\partial y} ; \quad B_y = - \frac{\partial A}{\partial x} ; \quad B_z = 0 \quad (9)$$

One is free to chose the gauge such that $\nabla \cdot \underline{A} = 0$. Let us consider the special case of a conducting plate moving in the y -direction (therefore $\underline{v} = (0, V, 0)$) with the magnetic field confined to the $x-y$ plane as required by Equation (9). Combining Equations (2), (4), (6) and (8) gives

$$-\frac{1}{\mu} \frac{\partial^2 \underline{A}}{\partial x^2} - \frac{1}{\mu} \frac{\partial^2 \underline{A}}{\partial y^2} + \sigma V \frac{\partial \underline{A}}{\partial y} - \sigma \nabla \phi = 0 \quad (10)$$

Solving Equation (10) gives the magnetic field and its gradients (and hence the current density induced in the conductor).

The total power dissipated by the moving conductor is given by

$$P = \frac{1}{\sigma} \int_{\text{conductor}} \underline{J} \cdot \underline{J}^* dx dy dz \quad (11)$$

The equations developed above neglect any skin depth effects. If conditions are such that motion causes a significant screening of the inside of the conductor, then the term in $\partial \underline{A} / \partial t$ in Equation (7) must be included. The solution is straightforward but considerably more complex than the outlined given above.

3.0 FINITE ELEMENT CALCULATIONS

The standard starting point for electromagnetic finite element (FE) calculations is Equation (10) with the velocity dependent term equal to zero. It is well known that the solution of a partial differential equation (PDE) containing a term like $(V \partial \underline{A} / \partial y)$ such as in Equation (10) is difficult to solve using numerical procedures because there is a tendency to generate oscillatory solutions.

Variational calculus shows that, if a functional F' satisfies the equation

$$\frac{\partial}{\partial x} \left[\frac{\partial F'}{\partial (\partial \underline{A} / \partial x)} \right] + \frac{\partial}{\partial y} \left[\frac{\partial F'}{\partial (\partial \underline{A} / \partial y)} \right] - \frac{\partial F'}{\partial \underline{A}} = 0 \quad (12)$$

then F' is a solution to the PDE given by Equation (10). With some considerable efforts, we have shown that

$$F' = \exp(-\mu \sigma V y) \left[\left(\frac{\partial \underline{A}}{\partial x} \right)^2 + \left(\frac{\partial \underline{A}}{\partial y} \right)^2 + 2 \underline{A} \cdot \sigma \nabla \phi \right] \quad (13)$$

reproduces Equation (10) and hence can be used in the Ritz method for obtaining a FE solution to Equation (10).

Using the functional given by Equation (13), we have developed a FE solution to Equation (10). One particular case is shown in Figure 1 where an aluminum plate is moving with a velocity of 1 m/sec between the poles of a magnet that produces a maximum field of about 1 T in the gap region. It is clear that the magnetic field lines within the plate are altered substantially by current induced with the plate when it is moving.

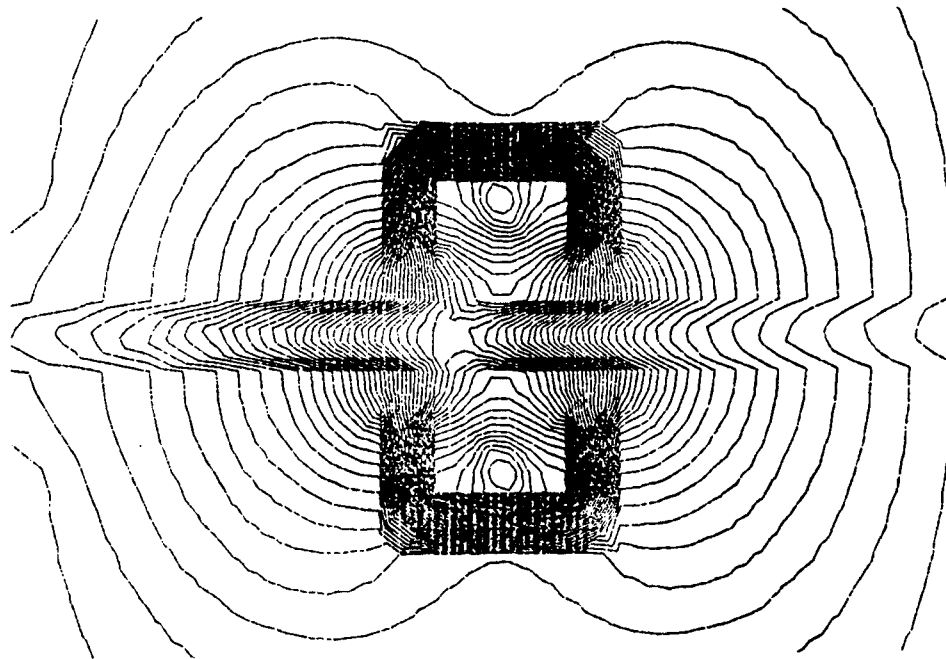


Figure 1 A finite element calculation showing the magnetic field configuration due to a non-magnetic conductor moving in a magnetic field.

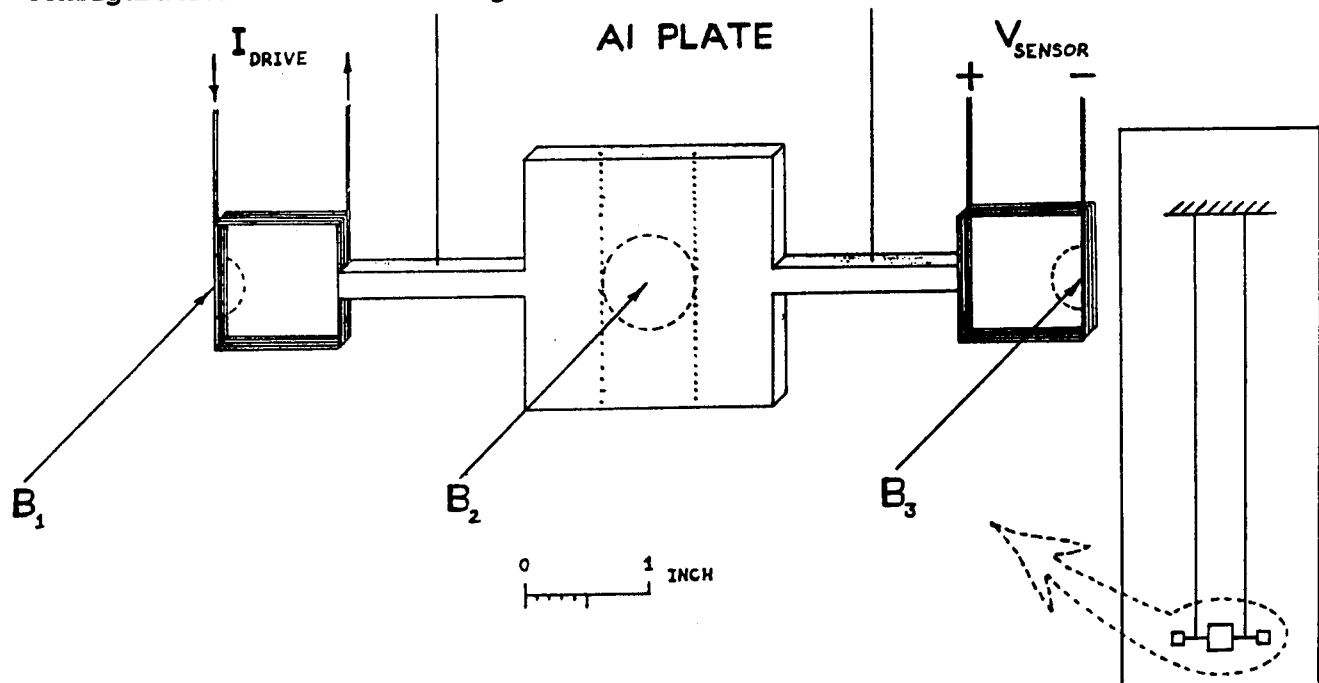


Figure 2 A pictorial illustration of the experimental arrangement used to determine the viscous drag coefficient of a conductor (Al block) moving within a reasonably localized field region, B₂. A current I (drive) through a coil that passes through a region, B₁, of reasonably constant field produces a well defined driving force on the rigid system shown in the figure. The frequency of the drive current is changed in order to map out response curves. The velocity amplitude of the response is determined by the voltage induced in a pickup coil moving in region, B₃. This coil is positioned in the field so that the pickup voltage is proportional to the horizontal velocity of the rigid system. Naturally, this voltage is also proportional to the frequency.

4.0 COMPARISON WITH EXPERIMENTS

One of the most widely studied and easily understood mechanical systems is the damped forced oscillator. This system, shown pictorially in Figure 2, was chosen for a quantitative evaluation of passive electromagnetic damping. Aluminum plates up to 6 mm thick were placed as shown at the end of a long string to form a pendulum. For the case described here, this pendulum had a frequency of 1.06 Hz. The Al plate could be driven by a linear motor shown pictorially as B, on the left hand side in Figure 2. The horizontal velocity produced by this driving force was measured using a calibrated electromagnetic velocity sensor shown pictorially on the right hand side in Figure 2.

This geometry does not satisfy all of the constraints imposed on the FE solution, namely the magnetic field in the z-direction (vertical direction in Figure 2) is non-zero in some regions. We handled this by first calculating the damping per unit volume assuming the plate to be infinite in extent and the magnetic field to be constant within the rectangular region defined by the dotted lines in Figure 2. The actual damping was calculated by using the calculated damping per unit volume and the actual volume of conductor over which there existed a magnetic field greater than 0.7 of the maximum gap field.

5.0 A DRIVEN DAMPED HARMONIC SYSTEM

A driven, damped, harmonic system is described by the equation

$$M \ddot{x} + 2b\dot{x} + \omega_0^2 x = P \sin(\omega t) \quad (14)$$

where M is the mass of the moving system, P is the peak driving force, b is the damping or drag coefficient, ω_0 is the system resonant frequency. The steady state solution is given by

$$x_0 = \frac{P/M}{[(\omega_0^2 - \omega^2)^2 + 4b^2\omega^2]^{1/2}} \quad (15)$$

The experimental setup shown in Figure 2 gives directly the peak velocity. The damping coefficient, b , can be obtained directly from these measurements. To do this, let us rewrite Equation (15) as

$$\frac{1}{(\omega x_0)^2} = \left(\frac{M}{P}\right)^2 \omega^2 \left[1 - \left(\frac{\omega_0}{\omega}\right)^2\right]^2 + 4\left(\frac{M}{P}\right)^2 b^2 \quad (16)$$

Plotting $(\omega x_0)^{-2}$ against $\omega^2 [1 - (\omega_0/\omega)^2]^2$, one obtains a straight line with slope $(M/P)^2$ and intercept of $(2Mb/P)^2$ from which one obtains b . It is also customary to define a damping constant $k = 2Mb$.

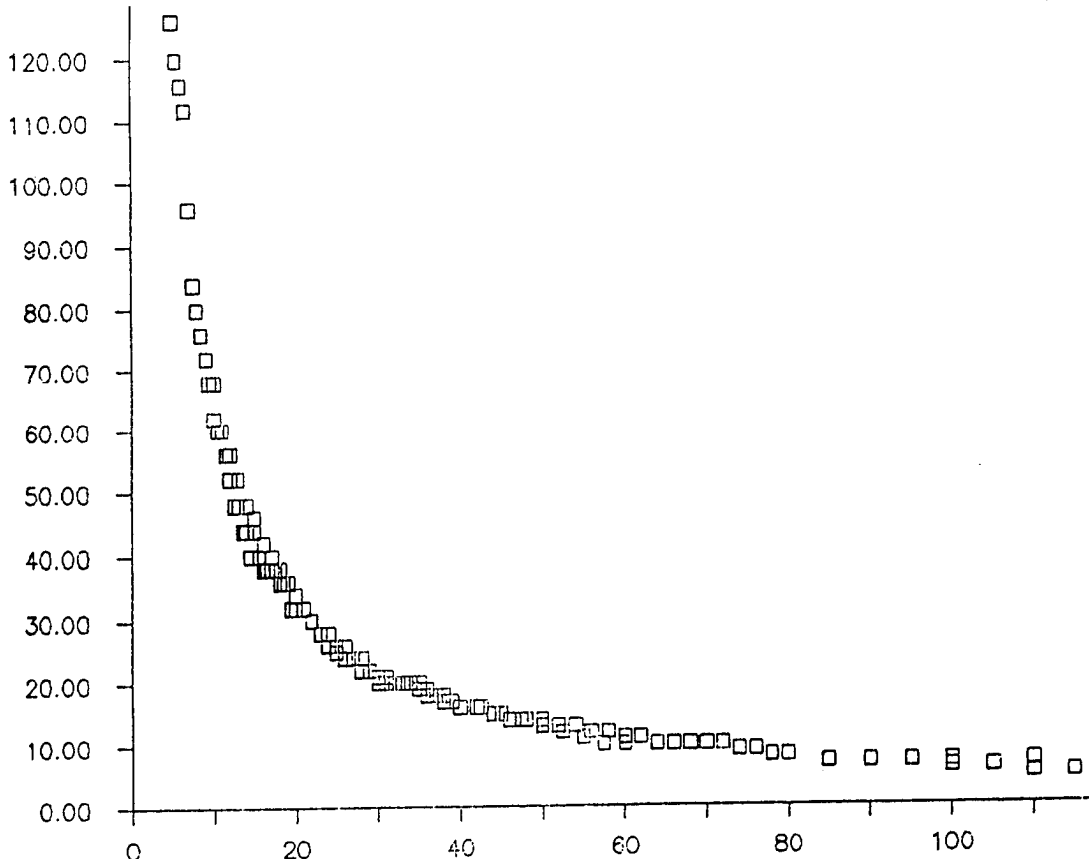


Figure 3 The velocity amplitude as a function of frequency obtained using the experimental setup shown in Figure 2.

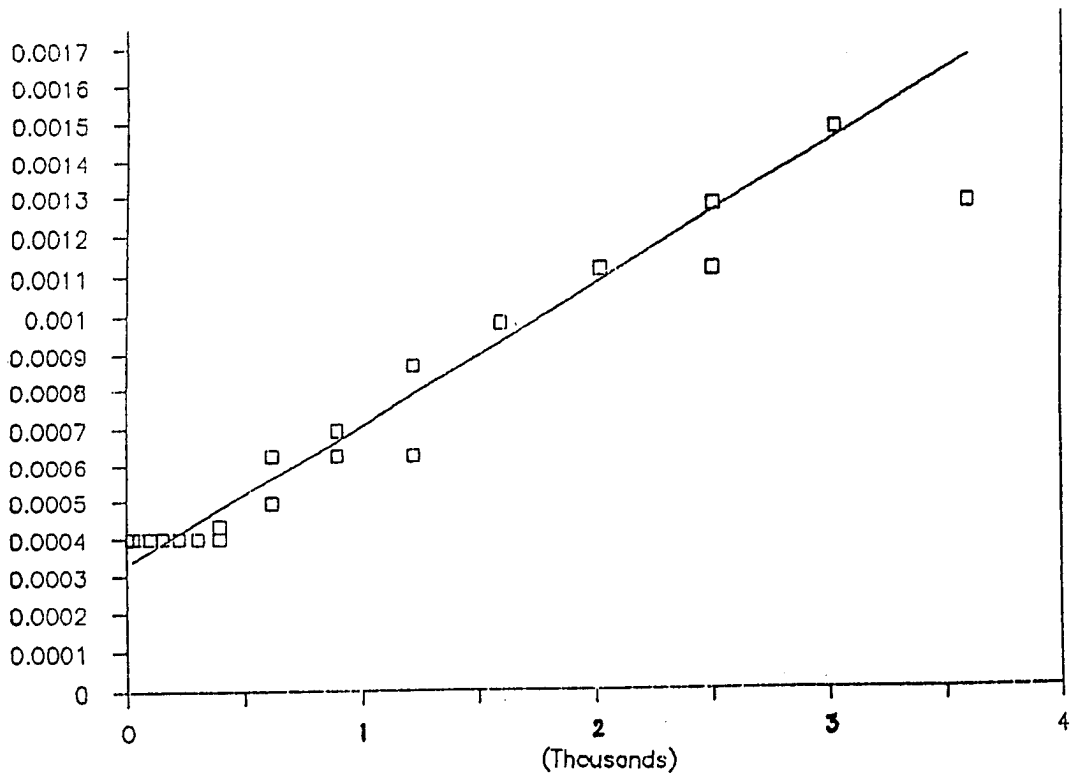


Figure 4 This shows experimental data plotted as described in the text; from the slope and vertical intercept, one obtains the experimental damping constant. The central field, B_2 , for a 0.5 inch square pole is about 1.5 T.

Figure 3 shows the velocity amplitude as a function of frequency, $f = \omega/2\pi$ for a particular value of magnetic field. When plotted as Equation (16), one obtains the graph shown in Figure 4. From this and many similar plots, one finds that, as expected, the power dissipated by electromagnetic damping is quadratic in both velocity and magnetic field. At the highest field of 1.5 T where we have the greatest accuracy in our measurements, the damping factors are

$$b(\text{EXP}) = (101 \pm 6) / \text{sec}; k(\text{EXP}) = (21 \pm 1) \text{ kg/sec}$$

A FE calculation performed as described above for this same case yields

$$b(\text{FE}) = 72 / \text{sec} ; k(\text{FE}) = 15 \text{ kg/sec}$$

We regard this as good quantitative agreement. Of course, better agreement could be obtained using a 3D FE code but this would be a great deal more time consuming to develop. A single point calibration that normalized the calculated magnetic field to the measured value in the gap would also reduce the difference between calculated and measured values for the damping.

6.0 POTENTIAL DAMPER CONFIGURATIONS

Although our example of a pendulum is an excellent case for demonstrating that there is good quantitative agreement between FE calculations and the measured behavior of a damped harmonic system, the magnet and conductor configuration that was used is not very practical. For many applications, we expect that it will be most practical to have magnets near only one surface; that is, it will not generally be practical to place the moving conductor within the gap of a permanent magnet. Figure 5 shows one magnet configuration that provides good damping. An array of rectangular permanent magnets is placed with alternating magnet poles adjacent to each other as shown in Figure 5. This magnet stack is attached rigidly to some portion of the structure that will move relative to the conductor that is adjacent to the magnet assembly. Damping results when the magnet assembly moves relative to the conductor. The dimension of the magnet pole height shown in Figure 5 determines the magnetic field liftoff coefficient or how rapidly the magnetic field decreases with distance from the pole face. This, in turn, determines the thickness and closeness of conducting material that should be used in the damper. In general, a damping constant of about 20000 kg/sec/m^2 of pole area can be obtained for each 1 mm in thickness of Al conducting material. Clearly, for the greatest damping, such a damper should be placed between two points on a structure having the largest relative velocity.

Figure 6 shows an inertial damper that is a modified version of the damper in Figure 5. The non-magnetic springs keep the damper somewhat centered. When the structure to which this damper is attached is accelerated, the magnet assembly will move relative to the support Al tube. Energy will be dissipated as long as this relative motion exists.

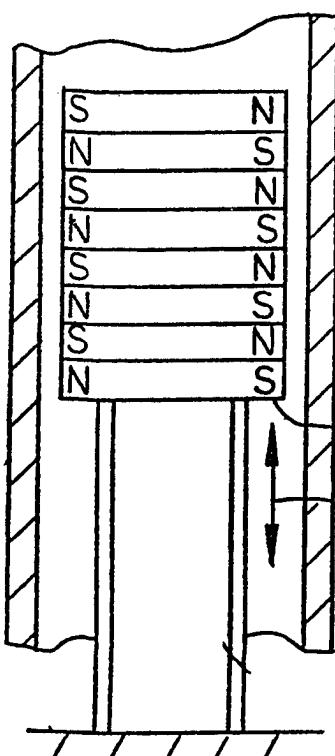


Figure 5 An electromagnetic damper that is analogous to a viscoelastic extensional shear damper. The magnet assembly is attached to one end of a tubular support strut by a very light, thin walled tube (it need only support the viscous drag or damping force between the magnets and the aluminum strut). Relative motion between the magnet assembly and aluminum strut results when the strut is lengthened or compressed due to an applied load.

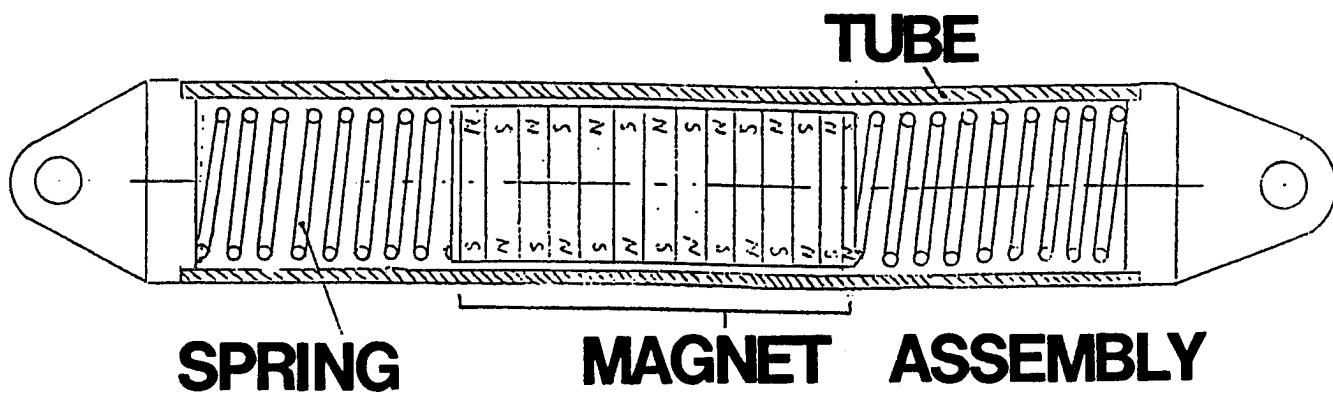


Figure 6 An inertial electromagnetic damper that operates by relative motion between the magnet assembly and the aluminum support tube. Spring constants are chosen so that the magnet assembly-spring resonant frequency is somewhat lower than the frequencies one wishes to damp. Under this condition, any acceleration of the structure (which is connected directly to the aluminum support tube) will produce relative motion between the magnet and aluminum tube. This damper is best substituted for a load bearing member although it can also be placed in parallel with structural members.

A damper assembly capable of withstanding very large loads and providing a large damping constant is shown in Figure 7.

7.0 ADDITIONAL CONSIDERATIONS

Like standard viscous damping, electromagnetic damping results from a force that is velocity dependent. This raises questions about the effectiveness of this damping at very low velocity. To evaluate the low velocity behavior in a qualitative manner, we constructed a simple loaded cantilever beam having an oscillation period of about 2 seconds. A stiff plate attached to the free end of the beam formed the moving plate of an electromagnetic damper assembly. This plate moved between the poles of an electromagnet having a pole area of 0.5 square inches and a gap field that could be as large as 1.8 T. A velocity sensor similar to the one shown in Figure 2 was used to measure the velocity of the free end of the beam. Figure 8 shows a sequence of velocity-time waveforms immediately after the beam was deflected 1 cm from its equilibrium position. Figure (8a) shows the behavior for zero applied field (about 0.05 T residual field). At a field of 0.67 T, Figure (8d) shows that one gets the most rapid return to equilibrium. Figure (8e) is very near the condition of critical damping while Figures (8f) and (8g) show that damping beyond critical damping can be achieved. Clearly, damping exists, as expected, down to the smallest measurable velocities.

8.0 SUMMARY AND CONCLUSIONS

In this paper, we have shown that the damping that results from a conducting, non-magnetic plate moving near the pole of a permanent magnet can be understood in a very quantitative manner. In addition, the expected quadratic dependence upon relative velocity (between the plate and magnet) and magnetic field has been demonstrated. Several magnet geometries that are adaptable to practical damper configurations have been suggested. To date, no quantitative measurements on any of these assemblies have been made.

Electromagnetic dampers have some advantages over other means that have been used to achieve damping. Since the energy is dissipated within an excellent thermal conductor, there is no problem in removing heat when large average powers are involved. Nearly all the temperature dependence arises from the electrical conductivity (see Equation (11)). This is a very mild temperature dependence compared to that encountered in using viscoelastic materials (VEMs). A single damper assembly could operate very well over a temperature range of several hundred Kelvin. Behavior of electromagnetic dampers (EDs) is extremely predictable under a wide variety of conditions. EDs can tolerate operating at elevated temperatures (in some cases, up to about 1000 K) and in very high radiation (neutron, gamma or X-ray) fluxes.

Although the detailed description of EDs given in this paper is only applicable at relatively low frequencies (say below 100 Hz), the basic

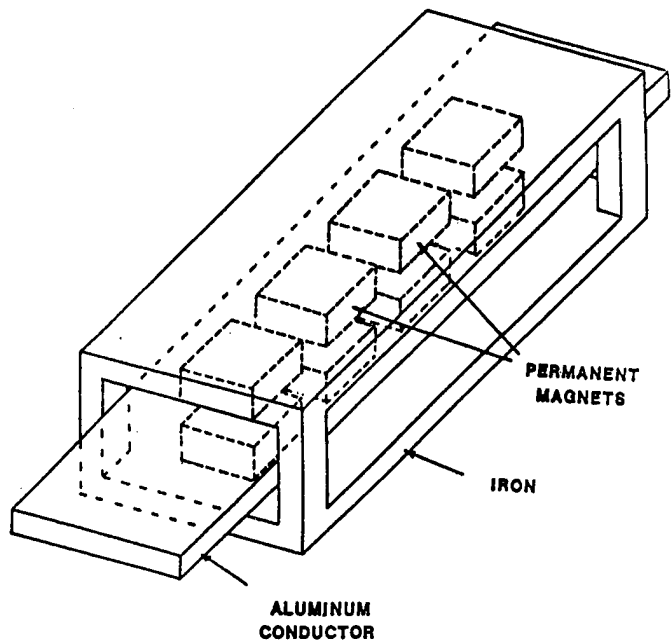


Figure 7 An electromagnetic damper that can produce large damping forces and handle large transient or steady-state loads.

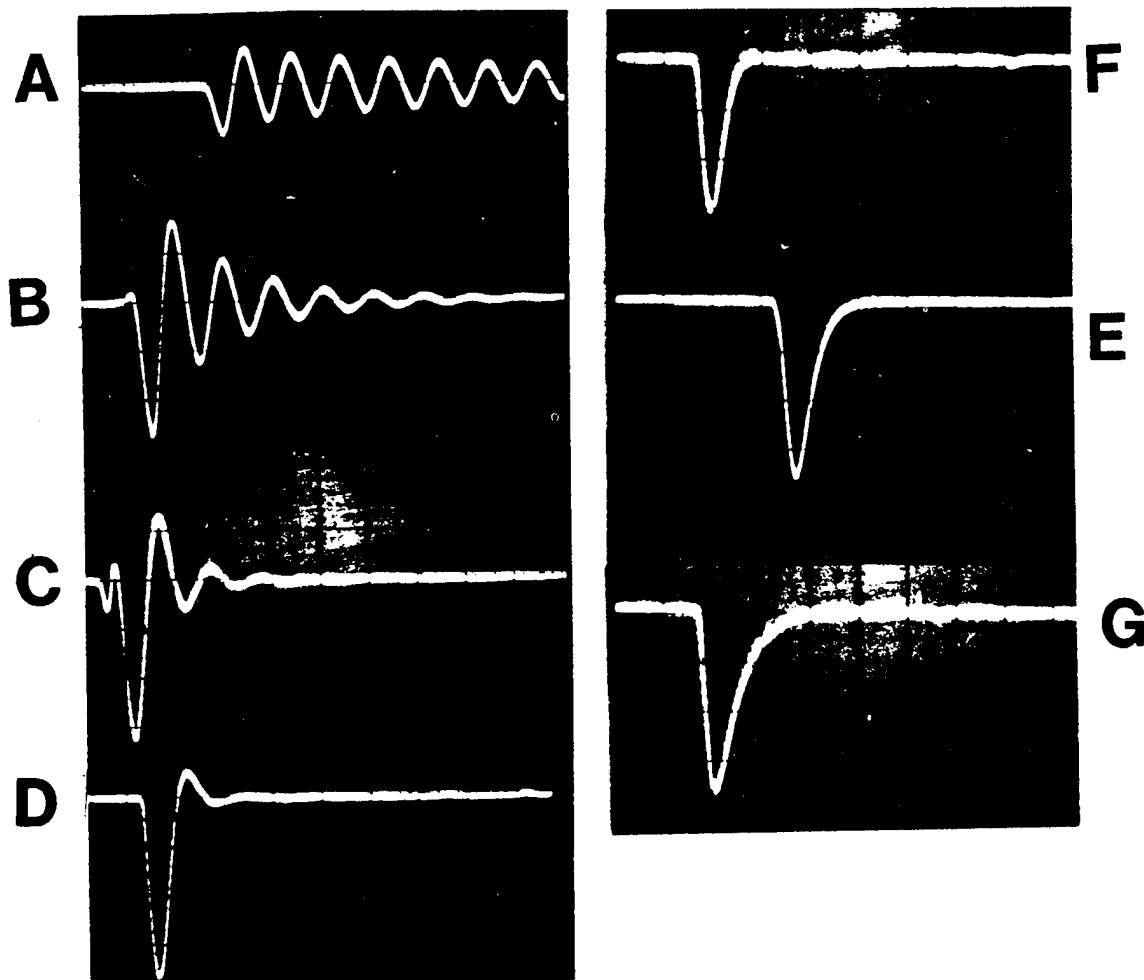


Figure 8 The output of a velocity sensor placed on the end of a vibrating, cantilever beam: (a) the damper moving in the residual field of the magnet, about 0.05 kG; (b) a damper magnetic field of 2.8 kG; (c) a damper field of 5.1 kG; (d) a damper field of 6.7 kG; (e) a damper field of 8.1 kG; (f) a damper field of 9.6 kG and (g) a damper field of 11.5 kG.

physics described by Equations (1) to (8) is valid up to several hundred megahertz. The primary effect of higher frequencies is to reduce the effective volume of conductor that is contributing to the damping. This can be overcome to some extent by using different conductor configurations. Basically, we see no problem in realizing damping up to many megahertz.

Another advantage of ED is that there is absolutely no hysteresis in either the amplitude or time behavior.

Varying the thickness of the conductor gives some degree of external control over the damper.

It should also be easy to couple the passive ED discussed in this paper with active control. For example, it is possible to embed current loops in (but insulated from) the conducting plate. Displacement or velocity sensors can be used in the conventional manner to feed current through these control loops to cancel unwanted motion. In fact, an inductive element attached to either the magnet or plate assembly can be used as the velocity sensor in this feedback loop because the time dependent fields that are produced external (or internal) to the conductor depend quadratically upon the plate velocity. These same current loops might also be used to extract small amounts of standby electrical power from the ambient mechanical noise. This standby power could be used to energize local field (velocity) sensors and thereby produce signals that could be used by the control system.

At low velocity, there can be very poor impedance matching in the sense that much more force is available for damping than is actually being used. When this is the case, ED will be improved by using a mechanical means of amplifying the displacement (velocity).

DEVELOPMENT OF A NOMOGRAM FOR SELECTION OF A VISCOELASTIC FREE LAYER DAMPING MATERIAL

By

Robert J. Dominic
University of Dayton
Research Institute
Dayton, OH 45469
(513) 229-2644

ABSTRACT

During recent years the University of Dayton Research Institute (UDRI) has implemented the concept of design, development, and production of viscoelastic damping materials to attain customer-specified damping performance. The desired damping performance may be for a new application or may be for an improvement that substantially increases the damping over that being obtained from the customer's currently used material. Usually several new candidate materials are produced in trial quantities and their damping properties are evaluated by standard vibrating beam tests. Then analytical estimates are made of their performance in the customer's system configuration. The entire procedure may be repeated several times as improvement trends due to material component ratios and processing variables are exploited. UDRI has developed a System Damping Nomogram (SDN) for free layer damping systems whereby the relative system damping performance of competing materials can be shown over a temperature range of interest by plotting data points extracted from the Reduced Temperature Nomograms (RTN) of the materials. As the new materials are characterized by vibrating beam tests, the system damping performance that results from their use can be determined and compared to previous material results by plotting appropriate data on the SDN. The development and use of the SDN will be explained.

INTRODUCTION

There are many ways to display the performance of a damping system, whether in lists or tables or graphs. We are considering here the performance of a configuration of a particular damping material installed to a structure, not the damping properties of the material itself. Those who work primarily or frequently towards the alleviation of vibration-induced noise or structural fatigue failures by use of the damping methodology usually are comfortable with any of these damping performance representations. Your boss will usually be in this category; however, your customer may or may not be in it. The system damping performance nomogram (SDN) presented here provides a clear picture of how damping material property changes affect the damping performance of a specific damping system. It is useful for convincing yourself, your boss, your customer, and especially people who are peripheral to the problem but have authority to make program decisions, that you are achieving significant system performance improvement. In the programs discussed here, the performance improvement is

obtained by formulation modifications of a damping material to improve the performance of a damping system specified by the customer.

I want to make it clear here that most of the material development work we perform for both government and industrial customers is restricted from public distribution at various security classification levels. Therefore, the example used for this paper was not a real project.

DEVELOPMENT OF THE SYSTEM DAMPING NOMOGRAM

Damping system design, as well as the development of the SDN, requires certain knowledge about the vibration problem which is being addressed. This includes:

1. the frequency of the primary vibration resonance of concern;
2. the structural temperature or temperature range at which the vibration occurs;
3. the configuration and material properties of the structural component(s) involved; and
4. the configuration of the desired damping system, or at least the configuration limitation parameters of the damping system.

When these facts are known, the best damping material currently available to solve the problem can be selected. Alternatively, a special damping material can be formulated with damping properties which fit the problem better. The parameters of the problem selected as an example are the following. The structure is a cantilevered aluminum beam and shows a high resonant vibration measured to be the second bending mode at 400 Hz in the operational temperature range of 40 to 70°F. For whatever reasons, a free layer damping system is required with the damping layer no thicker than the aluminum to which it is installed. This is, of course, a simpler problem with a more clear definition than you usually encounter.

We want to generate an SDN, specific to the problem, upon which we can plot the damping properties of elastomeric polymer materials which we might use as the free layer damping material. The SDN should show us the system damping achieved at 400 Hz over the temperature range of 40 to 70°F for each damping material under consideration. The SDN layout data can be generated easily by a damping system prediction computer program. Our program uses the beam damping equations of Ross, Kerwin, and Ungar (R-K-U Equations); and the Oberst Equation. In this case we use the free layer cantilever beam adaption of the Oberst Equation, one of the many options in the program. In addition to the configuration information, required material properties of the structure are entered to the program as are a range of the damping material properties of elastic modulus (Young's modulus) and loss factor, and also the expected density of the damping layer material. Structural dimensions may have to be varied somewhat to achieve the desired resonance mode at the structure's resonance frequency.

The computer printout for this example, showing input data and the calculated system damping loss factors and vibration frequencies, is shown in

Figure 1. The SDN is layed out from the material and system loss factor values in this list, and is shown in Figure 2. The system and material loss factor scales of the SDN usually are adjusted after evaluation of several candidate materials' damping performance.

USING THE SDN

Use of the SDN requires knowledge of the loss factor and elastic modulus, at the specified frequency and over the specified temperature range, of the candidate damping materials. This information is all incorporated in the "Reduced Temperature Nomogram" (RTN) depiction of material properties, developed by Dr. Dave Jones of AFWAL/ML with the cooperation and/or assistance of several others. It is assumed that the reader is familiar with the RTN and its use. Loss factor and modulus equations are commonly fitted to damping material test data displayed on the RTN. The equations then can be used to determine coincident values of damping material properties or they can be determined manually on the RTN. The manual method was used for this example.

Figure 3 shows the RTN of a rather poor example of a free layer damping material, for this or any other problem. The drafting construction to pick material properties values for use on the SDN are shown on this figure. The 400 Hz frequency line is drawn first. Then horizontal lines are drawn through the loss factor curve at convenient values and verticals are drawn through those intersections which extend through the 400 Hz line and the modulus curve. Then horizontals are drawn through the modulus curve intersections with the verticals to make it easy to determine modulus values. Pertinent data is the 400 Hz value, the circled loss factor and modulus data point values, and the temperature values at the intersections of the verticals with the 400 Hz line. The loss factor-modulus data points then are plotted on the SDN with the appropriate temperature noted at each data point, as shown in Figure 4. This SDN shows rather poor damping performance, though you might think otherwise if you had a part that was failing at 10 or 20 percent of its design service life. The damping performance does cover the desired temperature range, but we can do better.

COMPARISON OF TWO SIMILAR DAMPING MATERIALS

Figures 5 and 6 show the RTN's of two very similar materials which appear to be different because the nomograms are plotted with different T_0 values but identical reduced frequency scales. Figures 7 and 8 show the drafting construction to pick the data values for the SDN. That SDN is shown in Figure 9 and does indicate that the two materials are fairly close in free layer damping performance, but material A is better.

One problem with the SDN is the difficulty in following the temperature trend of the damping performance comparison at the glassy end of the transition region where elastic modulus values are high and loss factor values are low. The solution to this problem is to plot the system loss factors versus temperature over the desired temperature range. That comparison plot for these two materials is shown in Figure 10 for the temperature range of 30 to 80°F, just in case this range turns out to be different than we were told when we started. Figure 10 shows more clearly that material A provides better damping. Remember that this is not a real

problem. We can obtain three to four times this level of damping with an optimum free layer damping material formulated to fit specific problem conditions.

We have found the SDN to be useful. It is not difficult to generate or to use. It and the system damping versus temperature plot have been used to convince people that significant progress was being made. Damping performance improvements in systems using materials developed under this monitoring method have been almost exactly what the SDN predicted. The analysis is capable of predicting damping system performance on numerous beam and plate configurations for both free layer and constrained layer damping systems. Real problem solutions usually achieve considerably higher system damping levels than was shown by this example.

BEAM PARAMETERS:

BEAM TYPE: CANTILEVER
 FIRST BEAM BENDING MODE NUMBER: 2
 LAST BEAM BENDING MODE NUMBER: 2
 BEAM LENGTH: 11.000 in
 BEAM THICKNESS: .250 in
 BEAM DENSITY: .1000 lb/cu in
 BEAM YOUNG'S MODULUS: 1.000E+07 psi
 DAMPING MATERIAL DENSITY: .0600 lb/cu in
 DAMPING MATERIAL LOSS FACTOR:
 DAMPING MATERIAL THICKNESS: .250 in
 BEAM COATED ON ONE SIDE

MODE NUMBER 2
 BARE BEAM FREQUENCY IS 410.96 Hz

MATERIAL LOSS FACTOR IS .5

MATERIAL LOSS FACTOR IS 1

MATERIAL MODULUS	SYSTEM LOSS FACTOR	SYSTEM FREQUENCY	MATERIAL MODULUS	SYSTEM LOSS FACTOR	SYSTEM FREQUENCY
2.000E+06	.29167	581.2	2.000E+06	.58333	581.2
1.000E+06	.24915	480.9	1.000E+06	.49830	480.9
7.500E+05	.22325	449.3	7.500E+05	.44650	449.3
5.000E+05	.18324	413.7	5.000E+05	.36648	413.7
4.000E+05	.16110	398.1	4.000E+05	.32219	398.1
3.000E+05	.13386	381.6	3.000E+05	.26773	381.6
2.000E+05	.09985	364.0	2.000E+05	.19970	364.0
1.500E+05	.07956	354.8	1.500E+05	.15911	354.8
1.000E+05	.05654	345.2	1.000E+05	.11307	345.2
7.500E+04	.04384	340.3	7.500E+04	.08768	340.3
5.000E+04	.03025	335.2	5.000E+04	.06049	335.2
3.000E+04	.01867	331.2	3.000E+04	.03733	331.2
1.000E+04	.00640	327.0	1.000E+04	.01281	327.0

MATERIAL LOSS FACTOR IS 1.5

MATERIAL LOSS FACTOR IS 2

MATERIAL MODULUS	SYSTEM LOSS FACTOR	SYSTEM FREQUENCY	MATERIAL MODULUS	SYSTEM LOSS FACTOR	SYSTEM FREQUENCY
2.000E+06	.87500	581.2	2.000E+06	1.16667	581.2
1.000E+06	.74745	480.9	1.000E+06	.99661	480.9
7.500E+05	.66975	449.3	7.500E+05	.89300	449.3
5.000E+05	.54972	413.7	5.000E+05	.73296	413.7
4.000E+05	.48329	398.1	4.000E+05	.64439	398.1
3.000E+05	.40159	381.6	3.000E+05	.53546	381.6
2.000E+05	.29955	364.0	2.000E+05	.39940	364.0
1.500E+05	.23867	354.8	1.500E+05	.31823	354.8
1.000E+05	.16961	345.2	1.000E+05	.22614	345.2
7.500E+04	.13151	340.3	7.500E+04	.17535	340.3
5.000E+04	.09074	335.2	5.000E+04	.12098	335.2
3.000E+04	.05600	331.2	3.000E+04	.07467	331.2
1.000E+04	.01921	327.0	1.000E+04	.02562	327.0

Figure 1. COMPUTER RUN TO GENERATE NOMOGRAM LAYOUT DATA.

SDN For Free Layer on Aluminum Cantilever Beam
Damping Layer Thickness = Aluminum Beam Thickness

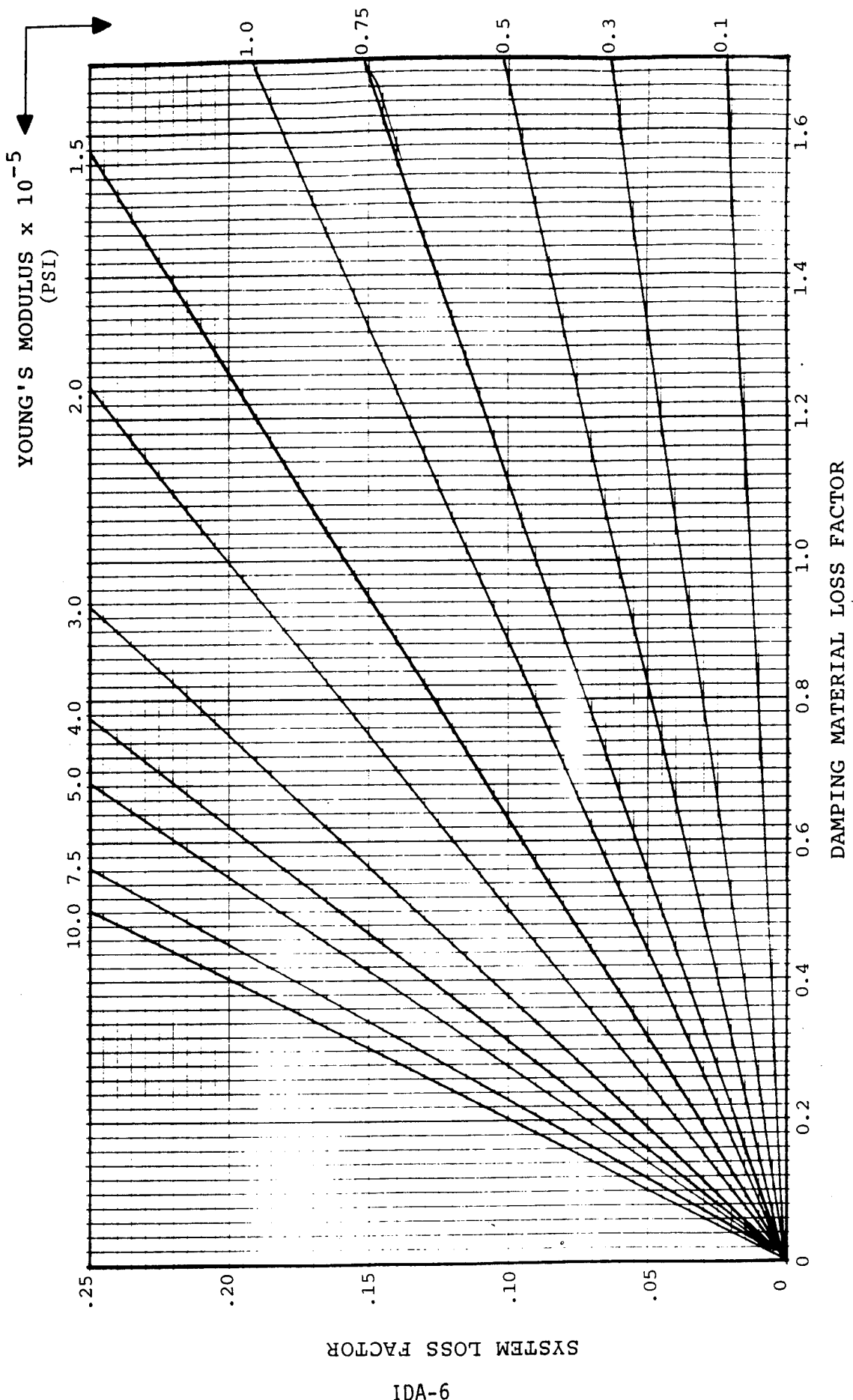


Figure 2. SYSTEM DAMPING NOMGRAM.

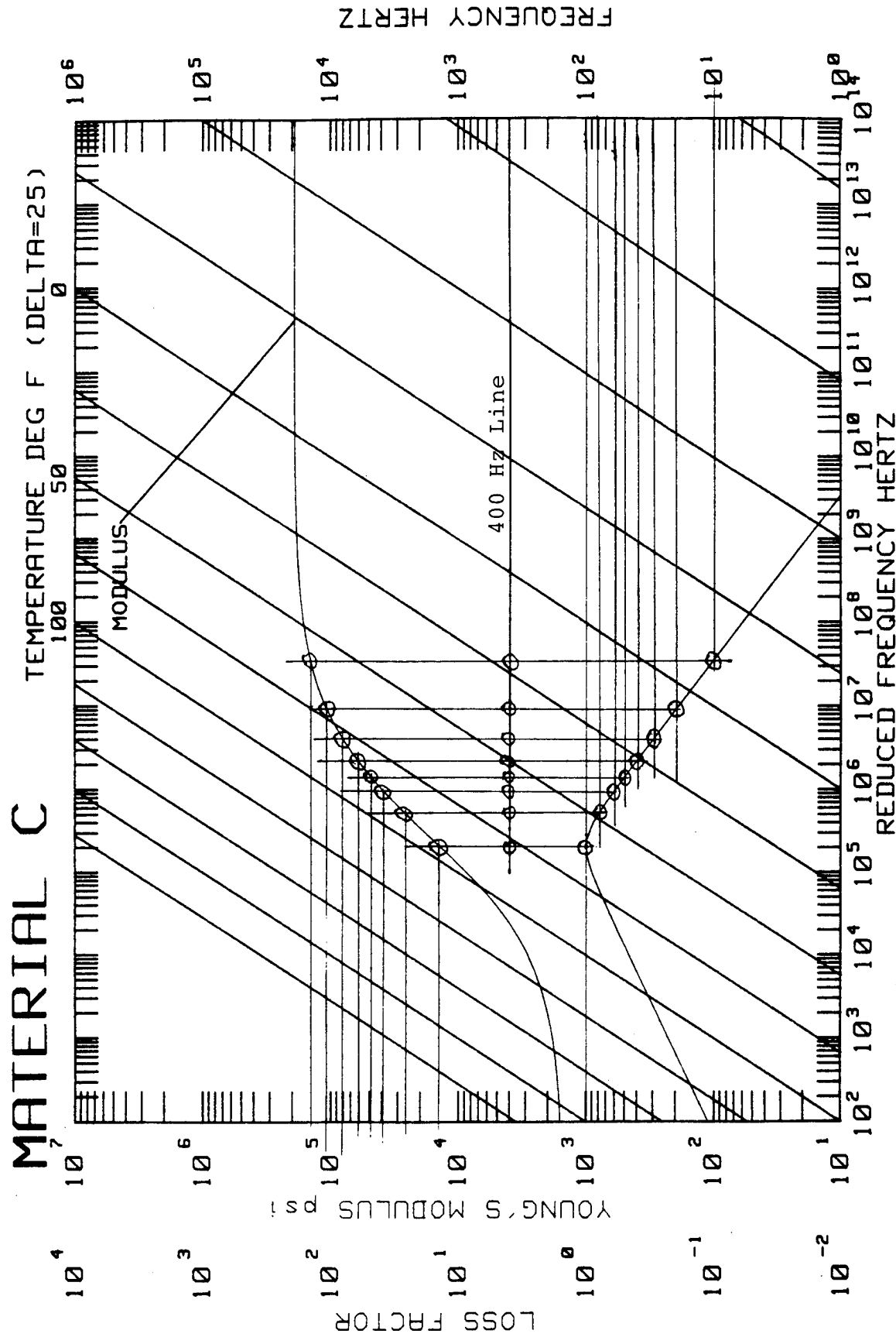


Figure 3. MATERIAL C REDUCED TEMPERATURE NOMOGRAM WITH DATA POINT LAYOUT.

SDN For Free Layer on Aluminum Cantilever Beam
Damping Layer Thickness = Aluminum Beam Thickness

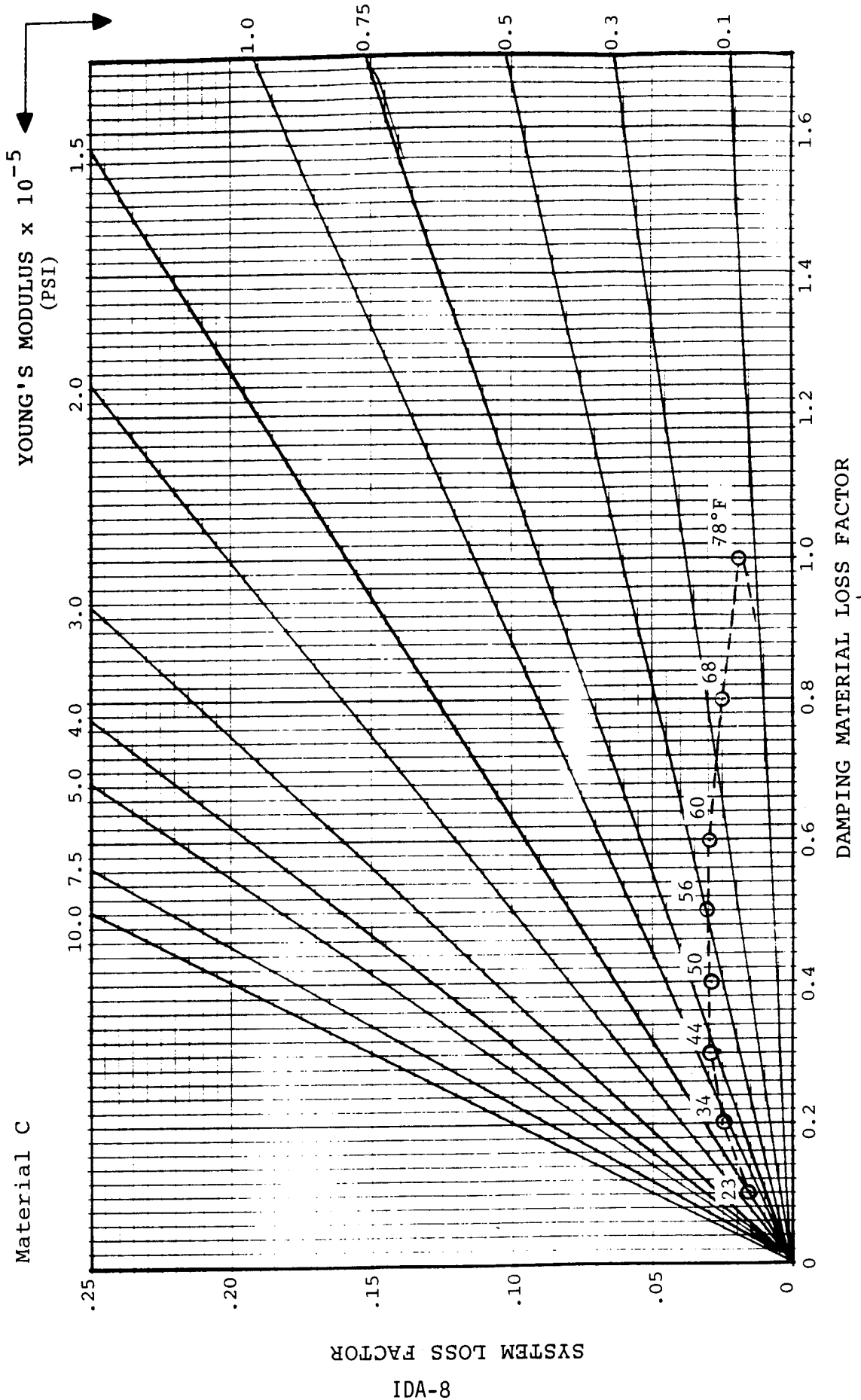


Figure 4. MATERIAL C SYSTEM DAMPING NOMGRAM FOR EXAMPLE CONDITIONS.

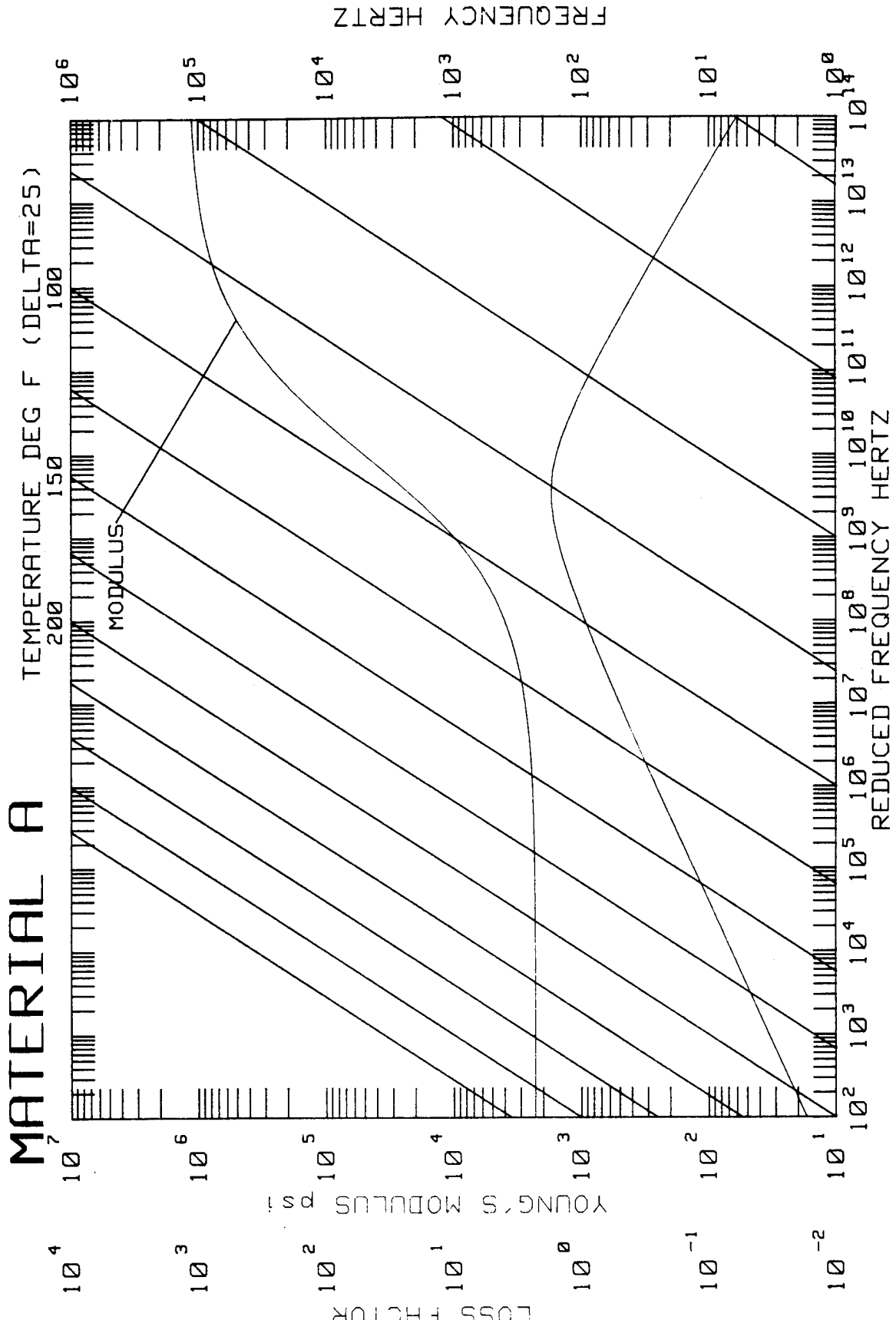


Figure 5. MATERIAL A REDUCED TEMPERATURE NOMOGRAM.

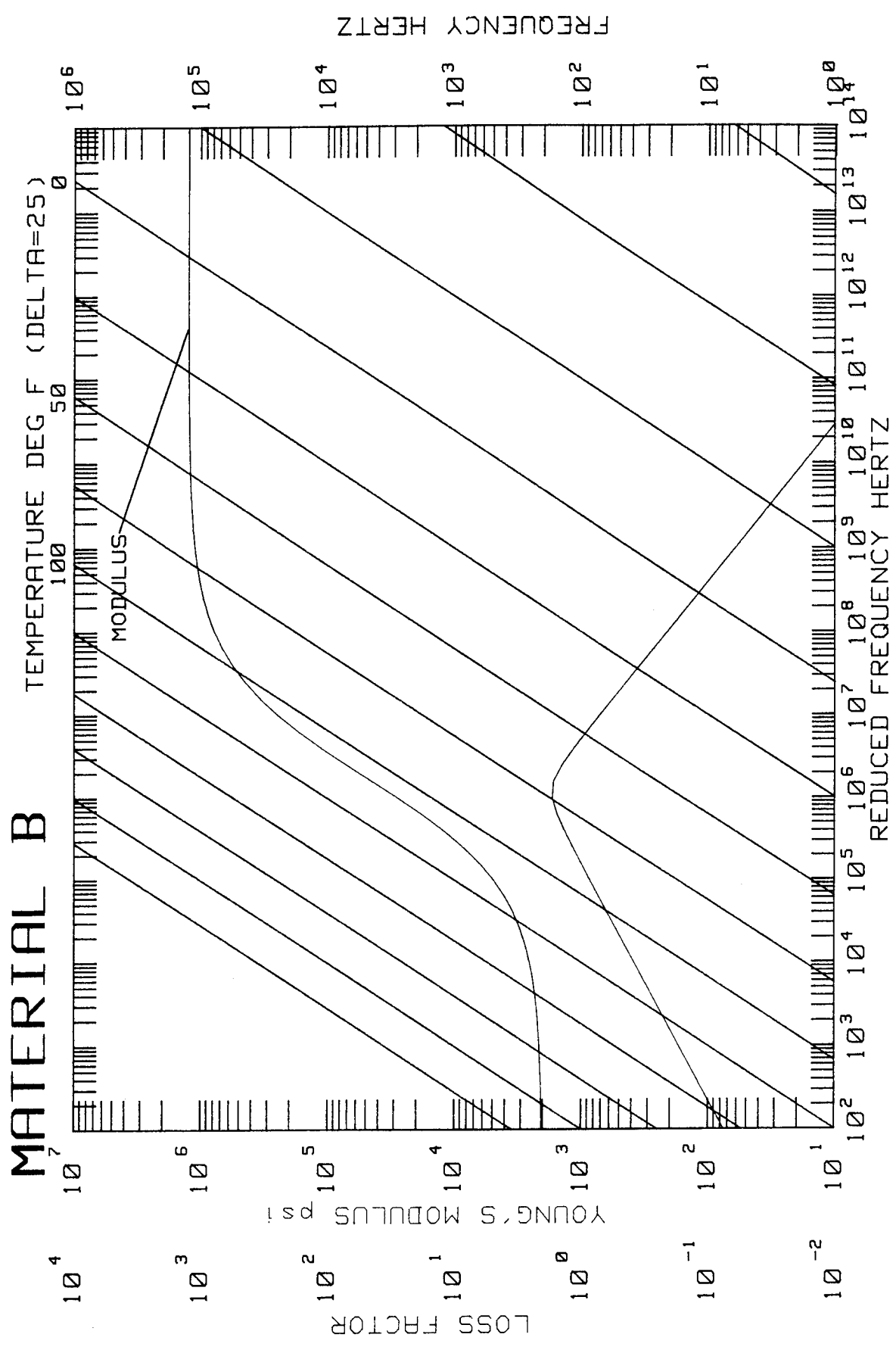
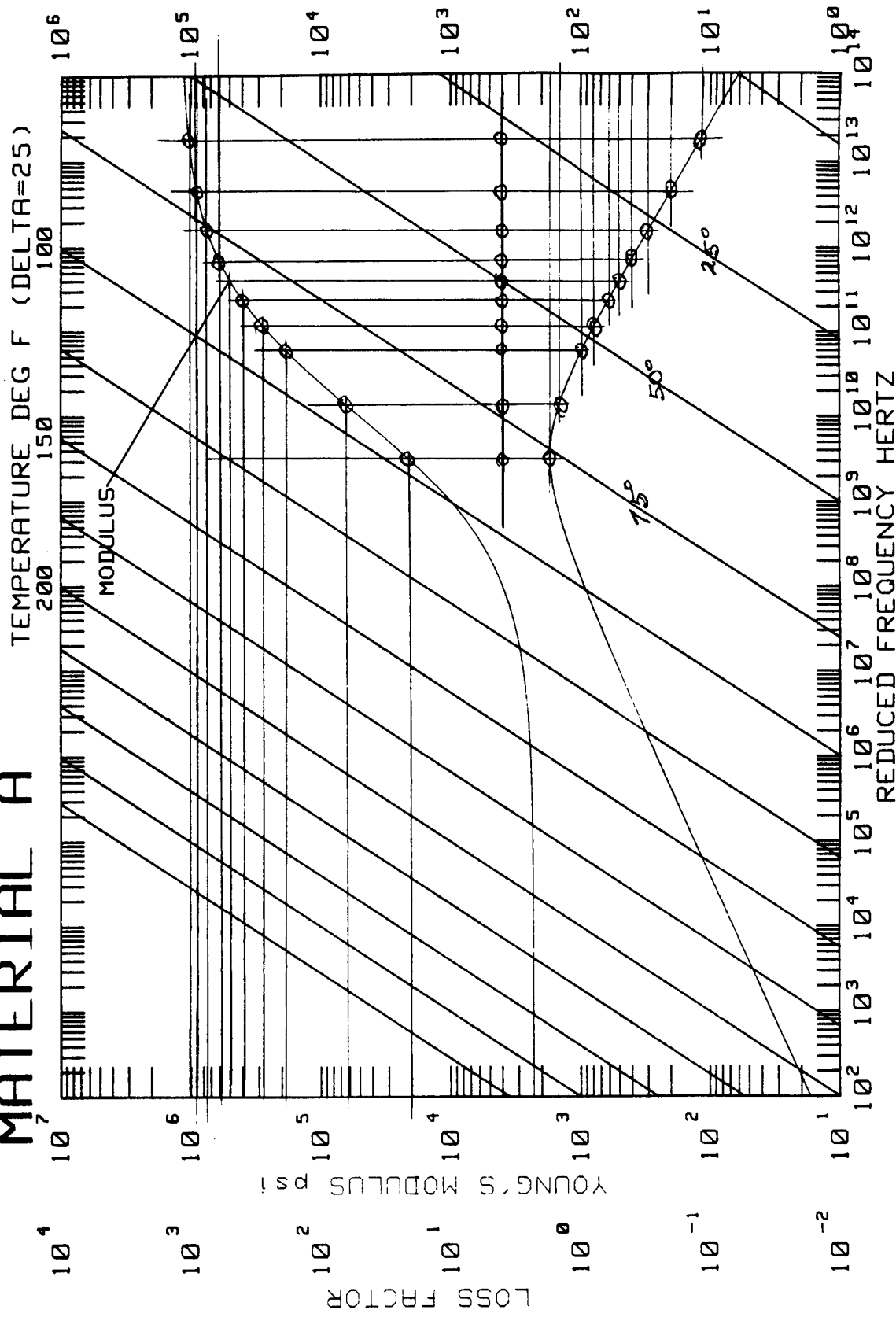


Figure 6. MATERIAL B REDUCED TEMPERATURE NOMOGRAM.

MATERIAL A



IDA-11

Figure 7. MATERIAL A REDUCED TEMPERATURE NOMOGRAM WITH DATA POINT LAYOUT.

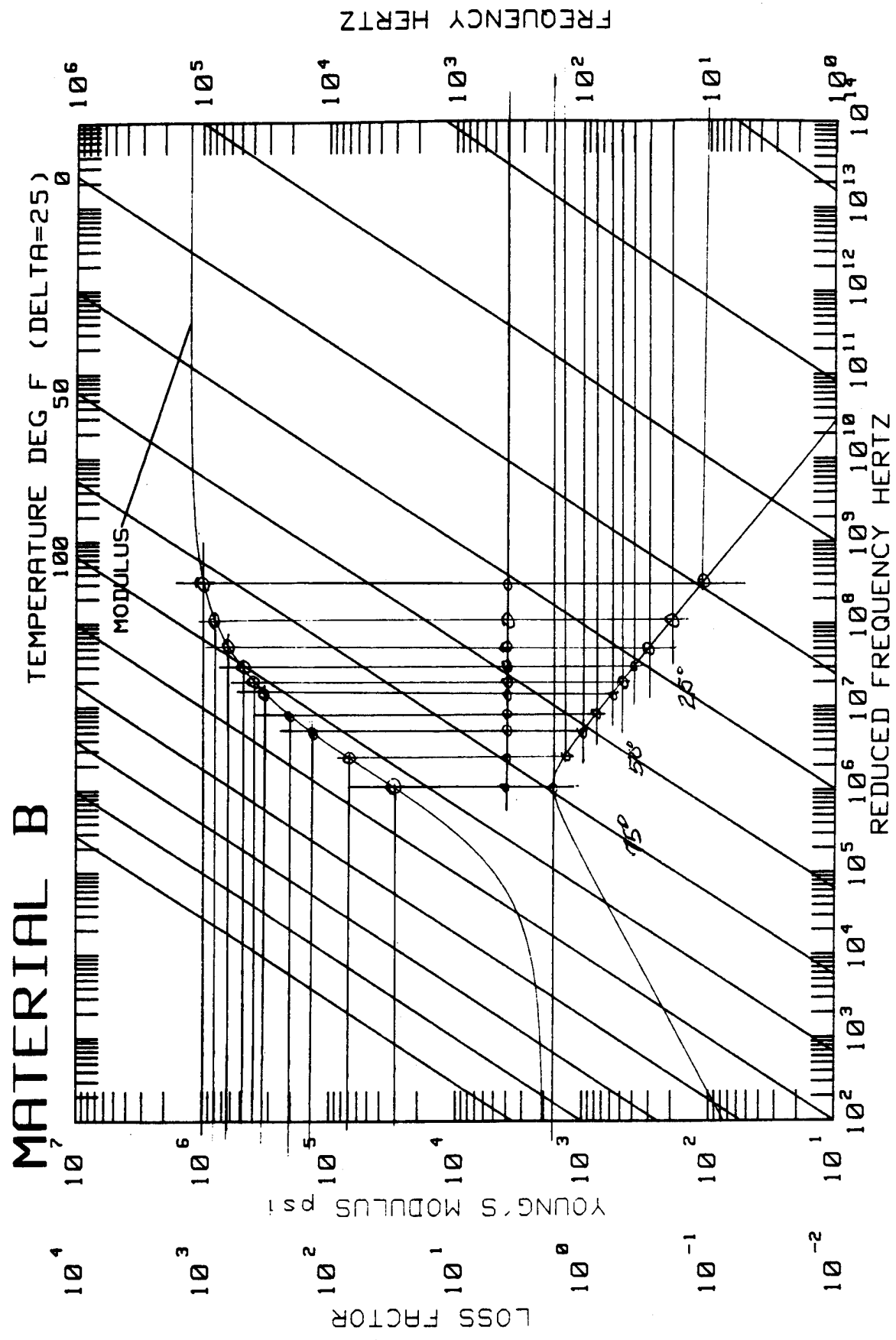


Figure 8. MATERIAL B REDUCED TEMPERATURE NOMOGRAM WITH DATA POINT LAYOUT.

SDN For Free Layer on Aluminum Cantilever Beam
Damping Layer Thickness = Aluminum Beam Thickness

Material A —○—
Material B —◇—

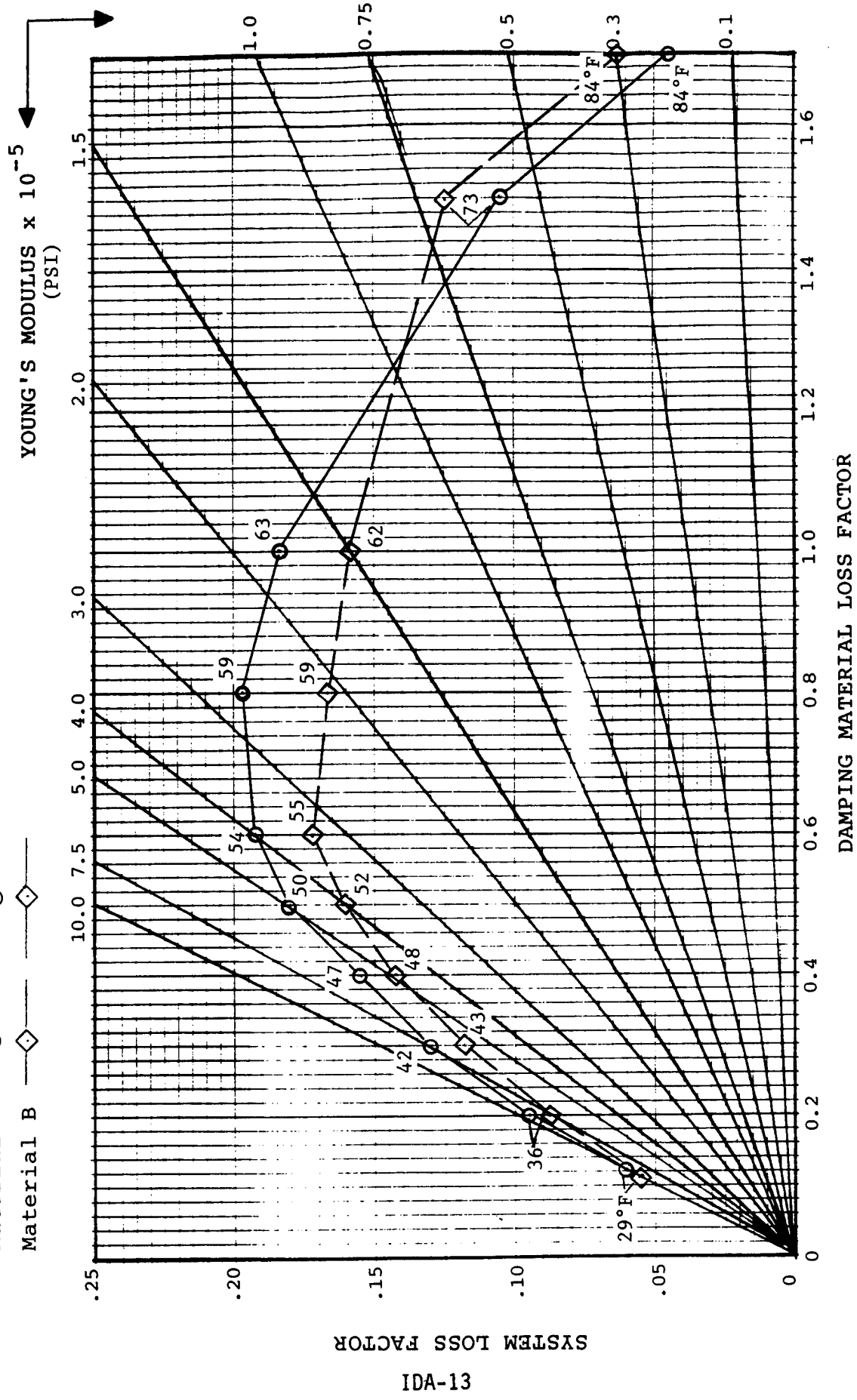


Figure 9. SYSTEM DAMPING COMPARISON FOR MATERIALS A & B FOR EXAMPLE CONDITIONS.

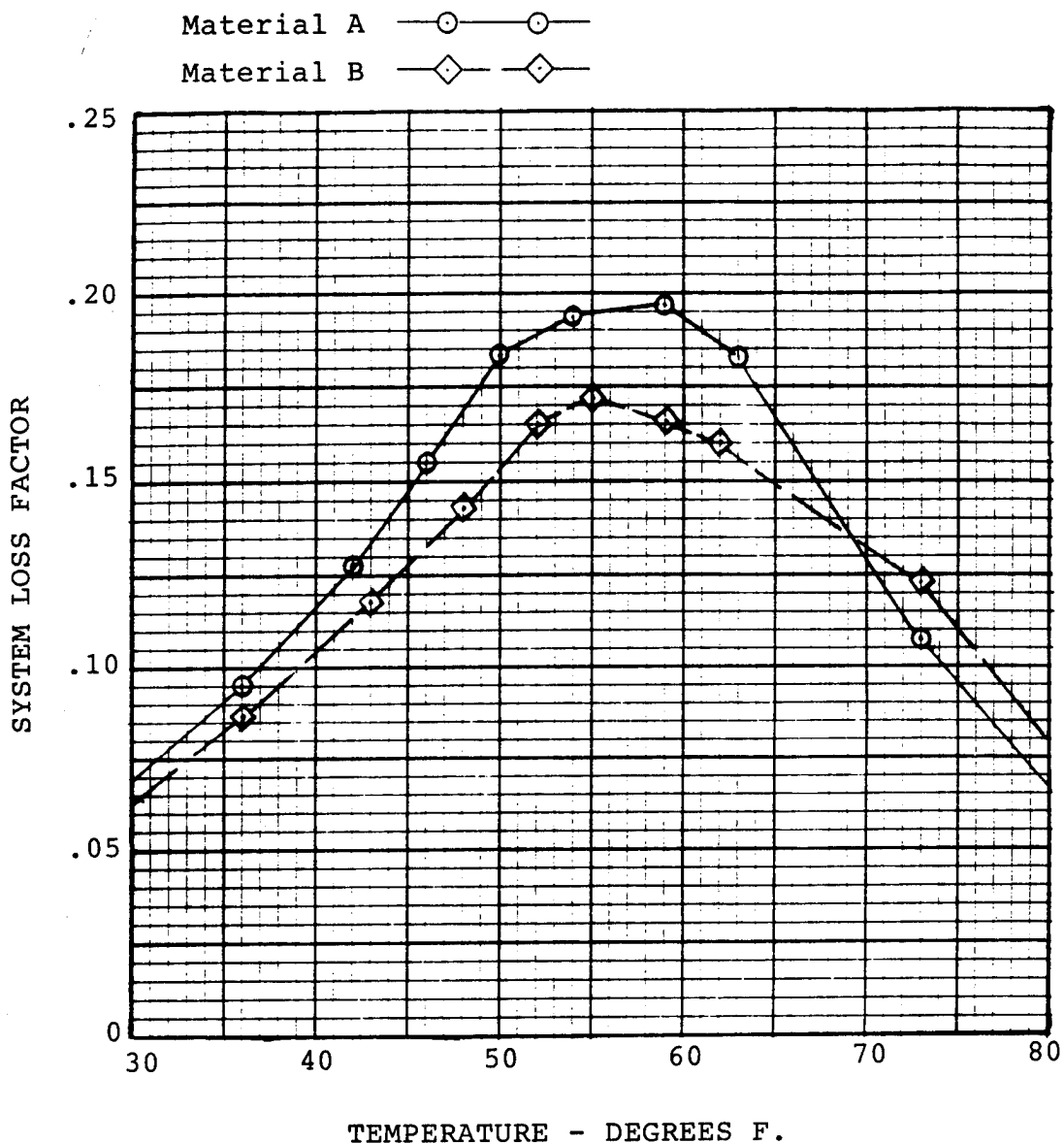


Figure 10. SYSTEM DAMPING VERSUS TEMPERATURE FOR MATERIALS A & B FOR EXAMPLE CONDITIONS.

Coupled Modal Damping in Transient Solutions

Bruce C. McFarland *

Allen J. Bronowicki†

TRW Space & Technology Group
Redondo Beach CA 90278

March 8, 1989

Abstract

The modal strain energy technique allows one to compute equivalent viscous damping ratios for real normal modes given structural loss factor data. This concept is generalized to include inter-modal coupling effects due to damping forces. Off-diagonal terms in the modal damping matrix are normalized by the geometric mean of the natural frequencies of the coupled modes. Incorporation of the damping model in a transient analysis scheme is described. The model is then demonstrated on a space structure. The effect of damping coupling is shown to be significant when damping is heavy and modal frequencies are closely spaced.

*Staff Engineer, Dynamics Department
†Head, Analytic Methods Section

1 Introduction

The modal strain energy (MSE) technique is a common means of computing equivalent modal damping values for simplified dynamic analysis of systems having structural losses. The method bases the viscous damping ratio assigned to each normal mode on the relative degree of participation in the mode of the various component strain energies, and on the material loss factors in those components. This is a rule of mixtures approach to damping. Apportionment of damping values by mode is useful since it allows one to construct a damping model in which modal damping values do not rise with modal frequency. Generation of physical equivalent viscous damping models have the undesirable effect of producing modal damping values which are proportional to modal frequency.

The technique of basing modal damping values on strain energy participation was first proposed by Ungar [1]. The method was applied to viscoelastic materials using standard finite element codes by Rogers et. al. [2]. It has since seen increasing use in the aerospace industry. The technique allows one to avoid solving a complex eigen-problem by assigning a viscous damping ratio to each real normal mode. The assumption is that damping forces are smaller than elastic forces, and hence do not affect the orthogonality properties of the modes. The standard application of this method thus does not account for coupling between the response of the modes due to the viscous forces. It was shown in Reference 3 that the effects of damping coupling between real normal modes are negligible for lightly damped structures whose modes are well separated in frequency. However, when structures are heavily damped and natural frequencies are not well separated, coupling between modes due to damping forces can be significant. The modal strain energy technique is extended in this work to account for these inter-modal coupling forces. The result is a coupled modal strain energy (CMSE) technique.

2 Damping Models

The following development works toward an equivalent viscous treatment of structural damping which includes inter-modal coupling effects. The CMSE formulation allows the computation of transient response directly, without recourse to transform techniques. An appropriate starting point for the derivation is the set of non-homogeneous equations of equilibrium in the frequency domain.

$$[-\Omega^2[M] + [K] + j \operatorname{sgn}(\Omega)[K']] \{X(\Omega)\} = \{F(\Omega)\} \quad (1)$$

The system mass, stiffness and structural damping (or loss) matrices, $[M]$, $[K]$ and $[K']$, respectively, are assumed to be real, symmetric and frequency independent. In the case of viscoelastic materials the stiffness and loss matrices actually depend on frequency. The MSE technique often employs material property data near a given natural frequency to obtain equivalent damping values for modes in the vicinity of the assumed frequency. In that case

the matrices are assumed to be piecewise frequency independent. For the purposes of this development the assumption of frequency independence is adequate. The sign function is required to ensure that the damping forces always oppose the velocity.

The stiffness and loss matrices are formed from the assembly of a number of elemental stiffness and loss matrices, $[K_i^e]$ and $[K_i^{e'}]$. The elemental loss matrices are assumed to be related to their stiffness counterparts through a simple scalar loss factor, g_i . The system stiffness and loss matrices are thus represented:

$$[K] = \sum_i [K_i^e] \quad (2)$$

$$[K'] = \sum_i [K_i^{e'}] = \sum_i g_i [K_i^e] \quad (3)$$

The nomenclature "element" may also be taken to mean component or material. The system is merely being subdivided into regions having a constant loss factor.

The objective of the following developments is to find a simple means of computing transient dynamic response which adequately matches the dynamics described by Equation 1. One could simply apply transform techniques to these equations, but the resultant response would be non-causal as discussed by Crandall [4]. A more physical approach which produces the desired behavior without introducing non-causality is desirable.

At a single response frequency, Ω_0 , one may compute an equivalent physical viscous damping matrix $[C] \equiv [K']/\Omega_0$ such that the viscous loss forces equal the structural loss forces defined in Equation 1. When the system loss matrix is strictly proportional to the stiffness matrix a set of modal damping ratios may be obtained. In that case these modal damping ratios will be linear with modal frequency. High frequency modes become heavily damped and low frequency modes are lightly damped. This is contrary to the structural damping assumption in which all modes are damped equally when the material is uniform throughout the structure. Thus equivalent viscous damping matrices formed in this simple manner are not realistic.

2.1 The MSE Technique

The MSE technique begins with real normal modes satisfying the system eigenproblem with damping terms discarded:

$$[K][\Phi] = [M][\Phi][\omega^2] \quad (4)$$

The resultant modes are normalized to give a unit diagonal modal mass matrix. The modal transformation $\{x\} = [\Phi]\{\eta\}$ is then applied. Mass-orthonormalized modes are assumed in the ensuing discussion. A truncated set of modes will generally be employed so that the number of modal coordinates, η , will be less than the number of physical coordinates, x . Time domain equations of motion in the modal space may then be defined as follows:

$$[I]\{\ddot{\eta}\} + [c]\{\dot{\eta}\} + [\omega^2]\{\eta(t)\} = [\Phi]^T\{f(t)\} \quad (5)$$

where $[c]$, the viscous damping matrix in modal coordinates, is yet to be assigned. In the MSE method the off-diagonal terms of $[c]$ are zeroed out and viscous damping ratios are assigned to each mode m as follows:

$$2\zeta_m \equiv \frac{\sum_i g_i \{\phi_m\}^T [K_i^{e'}] \{\phi_m\}}{\{\phi_m\}^T [K] \{\phi_m\}} = \frac{\sum_i g_i \{\phi_m\}^T [K_i^{e'}] \{\phi_m\}}{\omega_m^2} \quad (6)$$

where use has been made of the diagonalization of the stiffness matrix by the mode shapes. Notice that the term in the numerator can be interpreted as the sum of the elemental modal strain energies weighted by the elemental loss factors. In this manner, the modal loss factors are apportioned according to the strain energy participation of the mode in each of the materials. A diagonal modal damping matrix is obtained with non-zero elements

$$c_{mm} = 2\zeta_m \omega_m = \frac{\sum_i g_i \{\phi_m\}^T [K_i^{e'}] \{\phi_m\}}{\omega_m} \quad (7)$$

Alternately, one can employ the definition of the system loss matrix, Equation 3, to obtain an expression based on system rather than elemental quantities:

$$c_{mm} = 2\zeta_m \omega_m = \frac{\{\phi_m\}^T [K'] \{\phi_m\}}{\omega_m} \quad (8)$$

The computation using the system loss matrix rather than elemental strain energies is often simpler to perform in practice. It is instructional to view this modal damping matrix as the projection of the loss matrix on the modal space with coupling terms discarded, and then scaled by one power of frequency to reflect the additional time derivative applied to obtain modal velocity from modal displacement. The frequency scale factor allows the loss per cycle to be maintained for sinusoidal motions, assuming each mode responds only at its own natural frequency. Given broad-band excitations and low to moderate levels of damping, each mode will indeed respond primarily at its natural frequency.

When the structure is excited by a narrow-band input, it would be a better approximation to scale the modal loss matrix by a single reference frequency. That reference frequency, Ω_0 , is commonly chosen as the half-power frequency of the response power spectral density. This option of computing an equivalent viscous damping matrix, by scaling the projection of the loss matrix on the modal space by one user-defined reference frequency is available in many major finite element codes, such as MSC/Nastran.

2.2 The Coupled MSE Technique

It is proposed here that the modal damping matrix be constructed on the basis of strain energy participation without discarding coupling terms. This may be accomplished by projection on the modal space and application of a diagonal scaling transformation as shown below:

$$[c] \equiv [\omega^{-\frac{1}{2}}] [\Phi]^T [K'] [\Phi] [\omega^{-\frac{1}{2}}] \quad (9)$$

The diagonal terms which result from the CMSE damping model are identical to those of Equation 7. Coupling terms are scaled by the square root of the product of the natural frequencies of the two modes being coupled, i.e. their geometric mean, as proposed by Rogers et. al. [2]. When modes are closely spaced, and hence coupling terms are important, the geometric mean will be close to the two natural frequencies of interest.

The model is intended to be useful in cases where damping coupling is significant; where the damping forces are considered to be structural, such that the energy loss per cycle is generally independent of response frequency; and where the response is not at a single frequency, disallowing the use of a single reference frequency to scale loss terms. In other words, for want of any better knowledge, the modes are assumed to be responding primarily at their own natural frequencies. The resulting coupled damping matrix will necessitate a further eigen-solution to obtain complex modes if one wishes to diagonalize the equations of motion. Otherwise, coupled solution techniques can be applied in frequency or time domain solutions.

A physical damping matrix, $[C]$, corresponding to the assumed modal damping matrix may now be constructed. We desire a minimum norm matrix which satisfies the relation $\Phi^T C \Phi = c$. Such a matrix may be found through application of the generalized inverse [5], where $\Phi^\#$ is defined as $(\Phi^T \Phi)^{-1} \Phi^T$. A computationally efficient substitute for the generalized inverse of the eigenvector matrix for mass-normalized modes was proposed in Reference 6 to be $\Phi^T M$. Applying this quasi-inverse to both sides of the above relation results in the corresponding physical damping matrix

$$[C] \equiv [M][\Phi][c][\Phi]^T[M]^T \quad (10)$$

$\Phi^T M$ satisfies all but one of the sufficient conditions set forth in [5]; $\Phi \Phi^\#$ is symmetric, $\Phi \Phi^T M$ is not. C derived from $\Phi^\#$ will be the minimum 2-norm physical damping matrix which provides the desired modal damping matrix. Its projection on truncated modes will not be null. C derived $\Phi^T M$ provides the desired modal damping matrix and has null projection on truncated modes. A comparison has shown that transient responses resulting from use of the quasi-inverse vs. those resulting from use of the generalized inverse are within .2 percent.

3 Transient Response Analysis

Having defined an appropriate modal damping matrix, the coupled modal equations of motion may easily be solved by direct integration. It is also possible to solve a complex eigen-problem in the modal space to de-couple the equations prior to integration. If a small number of modes are being used, the coupled integration will not be a computational burden. To recover displacements a mode acceleration approach is more accurate than a mode displacement approach. To do this requires the solution of the equations of equilibrium at each time

step given the applied, inertial and viscous loads. The resultant physical displacements are

$$\begin{aligned}\{x\} &= [K]^{-1}(\{F\} - [M][\Phi]\{\ddot{\eta}\} - [C][\Phi]\{\dot{\eta}\}) \\ &= [K]^{-1}(\{F\} - [M][\Phi](\{\ddot{\eta}\} + [c]\{\dot{\eta}\}))\end{aligned}\quad (11)$$

The second, simplified expression given above was obtained by post-multiplying Equation 10 by Φ , and taking advantage of mass-orthonormality to obtain $C\Phi = M\Phi c$. By recovering displacements in this manner, it is not necessary to actually compute a physical damping matrix. The modal viscous loads are used to augment the modal inertial loads, avoiding computation of physical viscous loads. An even more simple form may be found by manipulating the expression for the real eigenproblem, Equation 4. This results in the following simple expression for displacement response due to modal inertial loads [7]:

$$[K]^{-1}[M][\Phi] = [\Phi][\omega^{-2}] \quad (12)$$

Recovery of physical displacements is then obtained in terms of applied physical loads and a summation of modal responses due to modal inertial and viscous loads:

$$\{x\} = [K]^{-1}\{F\} - [\Phi][\omega^{-2}](\{\ddot{\eta}\} + [c]\{\dot{\eta}\}) \quad (13)$$

4 Frequency Response Example

Figure 1 shows a spacecraft truss appendage supporting an optical mount. Damped tripod struts and base joint dampers are modeled with material loss factors. The tip is subjected to a lateral sine wave frequency sweep from 10 Hz to 1000 Hz. This emulates a secondary coolant disturbance. Rotations of the optical mount are monitored for the reference case with coupled imaginary stiffness, Equation 1, and for CMSE and MSE equivalent damping. These responses are shown in plots of response vs. excitation frequency in Figures 2a-2c. The CMSE viscous equivalent case shown in Figure 2b is similar to the imaginary stiffness case in Figure 2a for most the the frequency range. The difference in second mode peak response is about 10 percent. The MSE viscous equivalent case shown in Figure 2c compares well only at specific frequencies. The difference in second mode peak response between the MSE case and the imaginary stiffness reference case is 350 percent.

5 Transient Response Example

Figure 3 shows a spacecraft with solar arrays cantilevered on booms. Active damping is proposed to attenuate oscillations of the solar arrays due to spacecraft slew maneuvers. The active damping is approximated by material loss factors applied to bending strain of the booms. Boom loads recovered using displacements calculated by Equation 13 for CMSE and MSE damping techniques are shown in Figures 4a and 4b. In this example peak boom

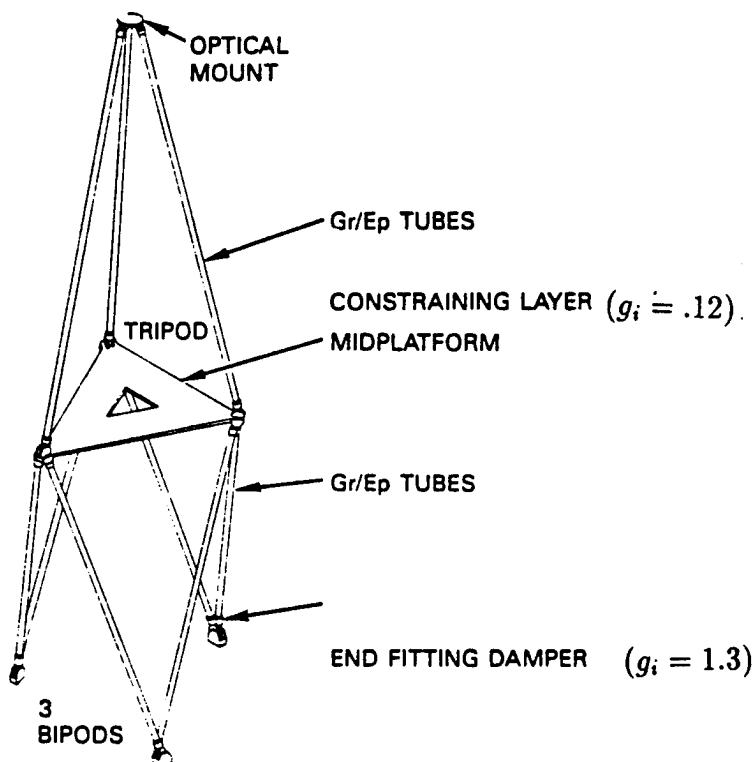


Figure 1: Damped Truss with Optical Mount

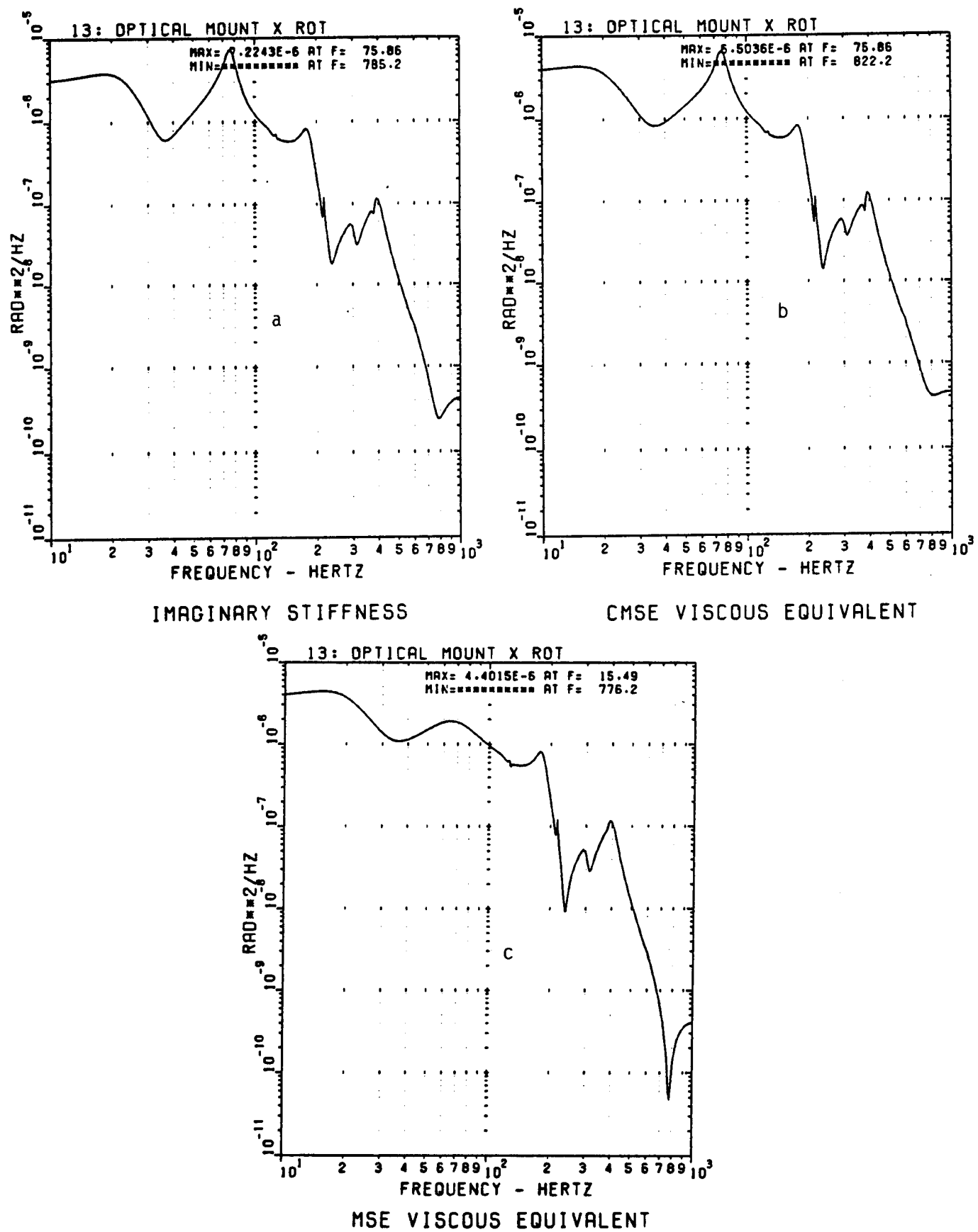


Figure 2: Optical Mount Frequency Response

bending loads are reduced by 20% when the CMSE technique is employed. A 10% increase in positive peak loads is encountered when MSE damping forces are neglected in loads recovery. This can be seen in Figure 4c. In this case neglecting damping forces in recovery improved response as compared with the CMSE reference case, but this may not be true in general. We conclude that in general additional error is incurred by neglecting large damping force corrections in loads recovery.

A more significant result is the amplitude of free vibration after the slew maneuver. At 40 seconds, response in the CMSE case is an order of magnitude greater than response in the MSE case. In this situation neglecting coupling terms in the damping matrix would lead to large errors in prediction of post-slew spacecraft performance.

SOLAR ARRAY
BOOM $g_i = .80$

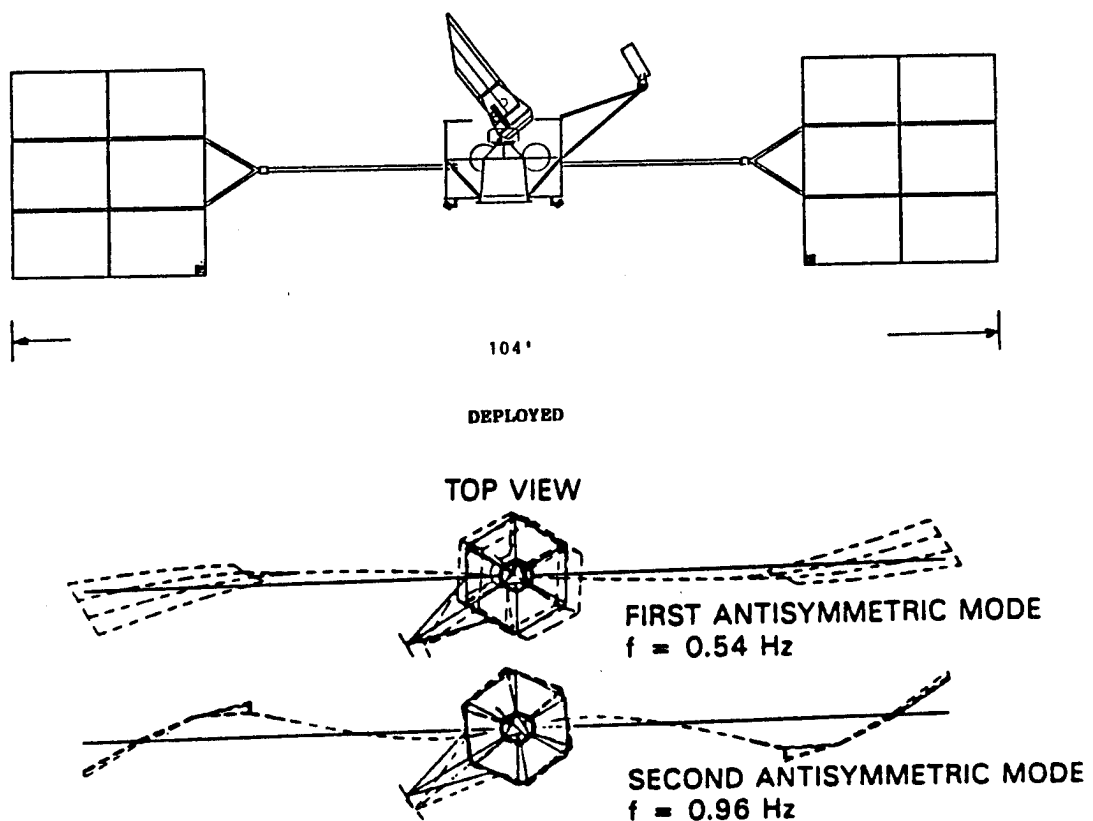
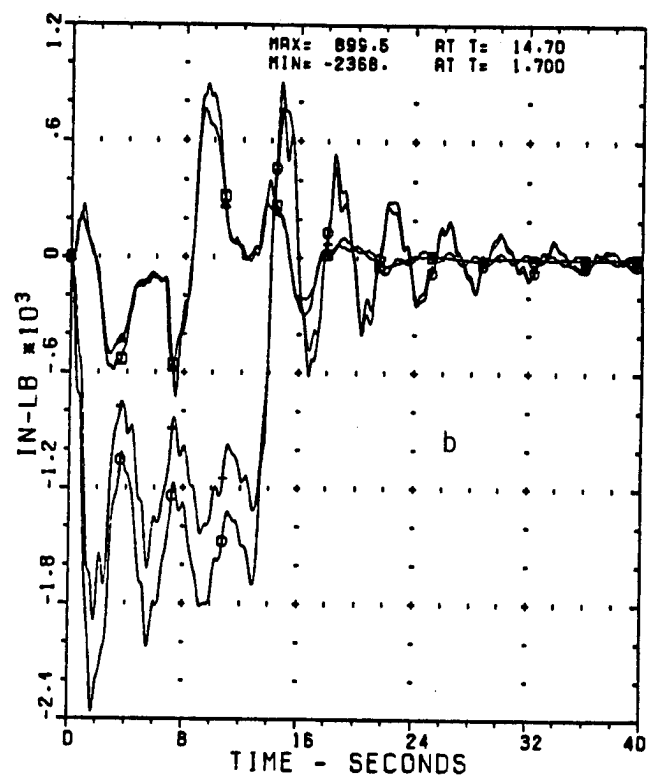
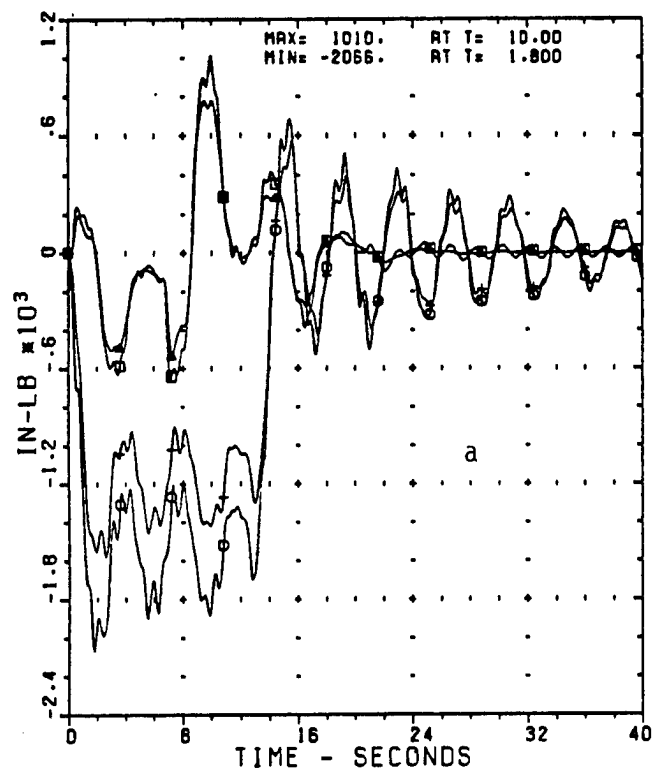
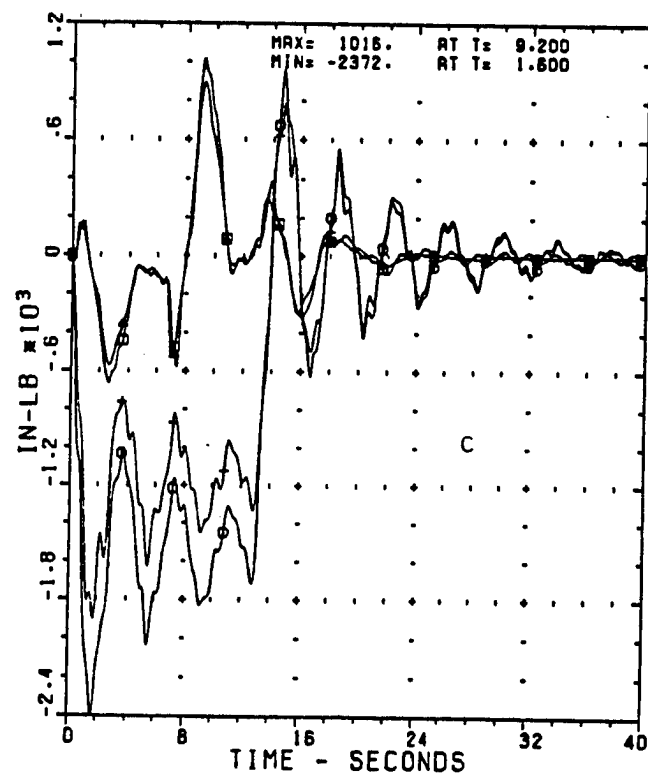


Figure 3: Agile Spacecraft with Damped Solar Array Booms



CMSE, DAMPING IN RECOVERY

MSE, DAMPING IN RECOVERY



MSE, NO DAMPING IN RECOVERY

Figure 4: Solar Array Boom Loads

6 Conclusions

The Coupled Modal Strain Energy technique allows one to build a physically reasonable structural damping model without discarding modal coupling terms. Damping models in both the modal and physical spaces were constructed. Modal coupling terms have previously been shown to be important in the case of large damping and closely spaced modes. The example presented confirms that the retention of modal coupling can have a significant effect on transient response.

References:

1. E. E. Ungar and E. M. Kerwin, "Loss Factors of Viscoelastic Systems in Terms of Energy Concepts", *Journal of the Acoustical Society of America*, Vol. 34, No. 7, pp 954–957, July 1962.
2. C. D. Johnson, D. A. Keinholz and L. C. Rogers, "Finite Element Prediction of Damping in Beams with Constrained Viscoelastic Layers", *Shock and Vibration Bulletin*, No. 51, pp 71–82, May 1981.
3. T. K. Hasselman, "Modal Coupling in Lightly Damped Structures", *AIAA Journal*, Vol. 14, No. 11, pp 1627–1628, November 1976.
4. S. H. Crandall, "The Role of Damping in Vibration Theory," *Journal of Sound and Vibration*, Vol. 11, No. 1, pp 3–18, 1970.
5. B. Noble and J. W. Daniel, *Applied Linear Algebra*, Chapter 9.6, Prentice-Hall, 1977.
6. R. W. Clough and J. Penzien, *Dynamics of Structures*, Chapter 13.3, McGraw-Hill, 1975.
7. R. R. Craig, *Structural Dynamics*, Chapter 15.3, Wiley, 1981.

A PERTURBATION METHOD FOR THE ANALYSIS OF FREE-LAYER DAMPING TREATMENTS

Sueming Shen
Graduate Student
Department of Mechanical Engineering
Florida Atlantic University
Boca Raton, FL 33431
(407) 367-3474

Karl K. Stevens
Professor
Department of Mechanical Engineering
Florida Atlantic University
Boca Raton, FL 33431
(407) 367-3474

ABSTRACT

The feasibility of using perturbation techniques to determine the effect of added viscoelastic damping treatments on the modal properties of a system is investigated. Linear perturbation equations for the changes introduced into system eigenproperties are derived and applied to several examples involving the flexural vibration of beams with varying degrees of damping treatment. Both large and small perturbations are considered. Comparison of the results with those obtained by direct solution of the corresponding complex eigenproblem shows the procedure to be accurate. The perturbation approach described can accommodate frequency-dependent material properties, and the procedures involved are illustrated in an example. The perturbation approach appears to be particularly well-suited for design situations where a number of damping configurations must be investigated.

INTRODUCTION

Addition of a viscoelastic damping treatment to a structure alters its mass and stiffness and introduces damping effects. If these changes are relatively small, addition of the damping material constitutes a small perturbation to the existing structure. This raises the possibility of using structural modification (perturbation) techniques¹⁻⁶ to analyze the effect of added damping treatments.

Perturbation techniques have the advantage that the changes in the modal properties can be expressed entirely in terms of the eigenproperties of the original system and the changes in system mass and stiffness. In the case of added damping treatments, this means that the natural frequencies, loss factors and mode shapes of the damped system can be obtained directly, without the need to re-solve the eigenvalue problem. From a computational point of view, this feature of the perturbation approach is highly attractive. Viscoelastic damping treatments often lead to nonproportional damping, with complex eigenvalues and eigenvectors. Solution of large-order complex eigenvalue problems is time consuming and costly. This is particularly true for damping treatment design, which may require consideration of a number of different damping configurations.

In this paper we explore the feasibility of using perturbation techniques to determine the effects of added viscoelastic damping treatments. Attention is restricted to free-layer treatments applied to systems whose vibratory response is described by discretized equations of motion. The basic perturbation equations are derived and applied to several examples involving the flexural vibration of an elastic cantilever beam with varying degrees of damping treatment over its length. This configuration was chosen because of its simple geometry and because of the existence of other solutions with which to compare the results of the perturbation approach.

Values of the natural frequencies, loss factors and mode shapes for the damped beam are presented for varying degrees of damping treatment. These results are shown to be in very good agreement with those obtained by direct solution of the corresponding complex eigenvalue problem. Both small and large perturbations are considered. Large perturbations are treated as a series of smaller changes. Results showing the rates of convergence of this sequential approach are presented. Also presented are results showing the optimum locations along the beam for placement of partial damping treatments. Use of the perturbation approach to account for the frequency dependence of the damping material properties also is discussed and illustrated in an example problem.

GENERAL CONSIDERATIONS

Consider a conservative vibratory system with symmetric mass and stiffness matrices $[M]$ and $[K]$. The corresponding eigenvalue problem is of the form⁷

$$\lambda_i^2 [M] \{\psi\}_i = [K] \{\psi\}_i \quad (1)$$

2

where λ_i is the eigenvalue for the i th mode of vibration and $\{\psi\}_i$ is the corresponding eigenvector (mode shape). It is assumed that the system eigenproperties are known.

Suppose, now, that a linearly viscoelastic damping treatment is added to the system. Since Eq. (1) is expressed in the frequency domain, the complex modulus is the proper representation for the properties of the damping material. Consequently, addition of the damping treatment produces a real-valued change $[\Delta M]$ in the mass matrix and a complex-valued change $[\Delta K(\omega)]$ in stiffness. Since the properties of viscoelastic materials are frequency dependent, the change in stiffness also depends upon the frequency, ω .

These changes in the system parameters give rise to a new set of eigenvalues, $\bar{\lambda}_i^2$, and eigenvectors, $\{\bar{\psi}\}_i$:

$$\bar{\lambda}_i^2 = \lambda_i^2 + \Delta \lambda_i^2 \quad (2)$$

$$\{\bar{\psi}\}_i = \{\psi\}_i + \{\Delta \psi\}_i \quad (3)$$

Except for simple structures with uniform damping treatments over the entire surface, addition of viscoelastic layers usually gives rise to a system with nonproportional damping. In this case, the eigenvectors are complex-valued and the eigenvalues are of the form⁷

$$\bar{\lambda}_i^2 = \omega_i^2 (1 + i \eta_i) \quad (4)$$

Here, ω_i is the damped natural frequency and η_i is the corresponding modal loss factor for the system.

One possibility for determining the eigenvalues and eigenvectors of the damped system is to re-solve Eq. (1) using $[M+\Delta M]$ and $[K+\Delta K(\omega)]$ as the mass and stiffness matrices. This is not an attractive proposition for large order systems, particularly if a number of different damping configurations are to be investigated. Solution of large-order, complex-valued eigenproblems is time consuming and costly.

Another possibility is to use approximate methods of analysis, such as the modal strain energy approach of Johnson and Kienholz⁸ or the Rayleigh Quotient approach of Stevens et al⁹. These approaches are relatively simple to apply and give results that are useful in many situations. However, they do not always provide all the information needed. The modal strain energy approach is restricted to problems with proportional damping and provides estimates only of the modal loss factors; the Rayleigh Quotient approach gives estimates of both the loss factors and damped natural frequencies and applies to arbitrary damping configurations. Both methods are based upon the

mode shapes of the undamped system, and neither provides information about changes in the mode shapes.

The alternative considered herein is to use linear perturbation techniques to express the changes $\Delta\lambda_i^2$ and $\{\Delta\Psi\}_i$ in the eigenvalues and eigenvectors directly in terms of the changes $[\Delta M]$ and $[\Delta K(\omega)]$ and the eigenproperties of the original system. This approach has the obvious advantage that information about all the eigenproperties can be obtained for a variety of damping configurations, while the eigenproblem need be solved only once. It should be noted that the process need not start with a mathematical model of a conservative system, as assumed in the preceding discussion. The original system can be damped. Systems whose natural frequencies and mode shapes are obtained experimentally via modal testing techniques⁷ also can be handled, provided an appropriate set of mode shapes is available.

There is one potential problem with the use of linear perturbation techniques. The density of common damping materials is of the same order of magnitude as common metals, so the changes in the mass matrix can be relatively large. A higher-order perturbation theory¹⁰ could be used, but the resulting equations are lengthy and the computations time consuming. The alternative, used in this paper, is to treat large modifications as a series of smaller ones. Changes in system stiffness usually are relatively small and cause no particular difficulties. This is because the modulus of damping materials typically in several orders of magnitude less than that of the structure to which they are applied.

PERTURBATION EQUATIONS

First-order perturbation equations for the linear eigenvalue problem can be derived in a variety of ways, and are available in various references¹⁻⁵. These derivations hold in the current case provided proper care is taken in handling the change in stiffness, which is now complex-valued. Suffice it to say that, for a system with distinct eigenvalues, the first-order approximations for the changes in the eigenproperties are:

$$\Delta\lambda_i^2 = \frac{1}{M_i} \{\Psi\}_i^T \left[[\Delta K] - \lambda_i^2 [\Delta M] \right] \{\Psi_i\} \quad (5)$$

and

$$\Delta\{\Psi\}_i = \sum_{\substack{j=1 \\ j \neq i}}^n \alpha_{ij} \{\Psi\}_j \quad (6)$$

where

$$\alpha_{ij} = \frac{1}{M_i(\lambda_i^2 - \lambda_j^2)} \{\psi\}_j^T \left[[\Delta K] - \lambda_i^2 [\Delta M] \right] \{\psi\}_i \quad (7)$$

Here the superscript T denotes a vector or matrix transpose, and M_i is the modal mass:

$$M_i = \{\psi\}_i^T [M] \{\psi\}_i \quad (8)$$

Expressions for $[\Delta M]$ and $[\Delta K]$ are given in the following Section (for a beam). Once these are known, the step-by-step procedure for applying the perturbation equations is as follows:

1. Solve the eigenvalue problem, Eq. (1), for the system without damping treatment. This gives λ_i^2 and $\{\psi\}_i$, and is the starting point for the modification steps.
2. Determine $[\Delta M]$ and $[\Delta K]$ for the damping treatment of interest. If either change is relatively large, divide it into a member of smaller changes.
3. Solve Eqs. (5) and (6) for an increment of $[\Delta K]$ and $[\Delta M]$. This determines the changes in the modal parameters.
4. Update the modal parameters using Eqs. (2) and (3).
5. Repeat steps 2 through 4 until the desired modification $[\Delta M]$ and $[\Delta K]$ is achieved.
6. Solve for the damped natural frequencies and modal loss factors using Eq. (4).

Frequency dependent material properties can be handled in a similar way¹¹. First, the eigenproperties of the original system are determined using values of the material properties at some convenient reference value of frequency. The resulting values of the natural frequencies are then used to determine updated values for the material properties and the corresponding changes in stiffness $[\Delta K(\omega)]$. Application of the perturbation equations then provides a new estimate for the natural frequencies, and the process is repeated. This iterative process is carried out mode-by-mode. Since the material properties usually are slowly varying functions over the frequency interval of interest, convergence is rapid.

Updating the mode shapes at each step of the perturbation process is a labor-intensive operation. If the mode shapes are not updated at each step, i. e., if the mode shapes of the undamped structure are used throughout, the perturbation method yields essentially the same results as the Rayleigh energy approach¹²⁻¹⁴. These approximate results may be accurate enough in many

instances. If so, the costly mode shape updating process can be avoided. For damping treatment configurations that result in proportional damping, the mode shapes are the same as those of the undamped structure⁷. Updating of the mode shapes is not required in this case.

It also is possible to minimize the calculations needed to update the mode shapes. As can be seen from Eqs. (6) and (7), a_{ij} will be small for those modes for which the values of $|i-j|$ is large. Thus, these modes contribute little to the mode shape changes and can be ignored in the updating process. This feature of updating only certain mode shapes is useful, especially for large system models. Use of the perturbation approach with condensed dynamic system models is not considered in this paper.

APPLICATIONS TO A BEAM

In this section, the perturbation approach described is applied to four examples involving the flexural vibration of an elastic cantilever beam with varying lengths of viscoelastic damping treatment on one side (Figure 1). These examples also illustrate the capabilities of the perturbation approach. The computations are based upon a finite element model of the beam, which will be discussed in more detail later. Expressions for the incremental mass and stiffness matrices $[\Delta M]$ and $[\Delta K]$ are given in the Appendix, and the dimensions and material properties used in the examples are listed in Table 1. Except where noted, all examples are for an aluminum beam with a commercially-available damping layer. Computer programs were written to perform the necessary computations.

Example 1: Accuracy of the Method

The objective of this example was to assess the accuracy of the perturbation equations. To this end, they were used to compute the damped natural frequencies and modal loss factors for a beam with damping treatments ranging in length from $x/L = 0$ to $x/L = 1$ and with thickness ratios $t_v/t = 0.2, 0.6$ and 1.0 (see Figure 1). Here, and in the following, the subscript V denotes the viscoelastic damping layer. The perturbations were carried out in ten, fifteen or thirty equal-sized increments, depending upon the thickness ratio, and the material properties were assumed to be independent of frequency.

In order to provide a basis of comparison for the perturbation solutions, the complex eigenvalue problem associated with the finite element model was solved directly using the IMSL subroutine EIGZC. The finite element model was verified by comparing results for the damped natural frequencies and modal loss factors for different numbers of elements. Results for an undamped beam also were compared with theoretical values of the natural frequencies and mode shapes. It was found that the use of ten elements gave very accurate results for the first five modes, with a variety of damping treatment lengths and thicknesses. Validation of the finite element model was essential because the main purpose of this example was to establish the accuracy of the perturbation method. Significant finite element discretization errors would have confused the issue.

The natural frequencies and loss factors of the damped beam for the first and second modes are presented in Figures (2) and (3). These results are indicative of those for all the lower flexural modes. In these figures, ω_0 is the

natural frequency of the undamped beam and FEM refers to finite element results obtained by direct solution of the complex eigenvalue problem. As mentioned previously, these results were validated carefully and can be considered to be "exact". As can be seen, the perturbation approach gives excellent results; they are indiscernible from the finite element solutions. Shear effects may be important for the thicker damping layers considered, but were neglected in this investigation.

Example 2: Rate of Convergence

Relative errors in the perturbation solutions for the damped natural frequencies and modal loss factors can be expressed as

$$e_{\omega} = \left| \frac{\omega_p - \omega_{fem}}{\omega_{fem}} \right| \quad (9)$$

$$e_{\eta} = \left| \frac{\eta_p - \eta_{fem}}{\eta_{fem}} \right| \quad (10)$$

Here, the subscript p refers to the perturbation solution and fem denotes finite element results. These errors depend upon the step size used in the perturbation solution, or, alternatively, upon the number of steps used to implement the total perturbation.

Figure (4) shows the variation of e_{ω} and e_{η} with the number of perturbation steps for the first mode. The total modification was a complete damping treatment with thickness ratio $t_y/t = 1.0$, which corresponds to a 21% increase in element mass. Again, the material properties were assumed to be frequency independent. The eigenvalues, eigenvectors, and modal mass were updated at each step.

For the particular case considered, the relative error in the loss factor is always greater than the error in the damped natural frequency. As can be seen from Figure (4), convergence is relatively rapid. With ten steps, the error in the loss factor is approximately 2%, while the error in the damped natural frequency is about 0.05%. Almost identical results were obtained for the first five flexural modes. Although the results are not presented here, the eigenvectors also were found to converge rapidly.

Example 3 Partial Damping Treatment

This example was designed to illustrate the effect of the location of a partial damping treatment along the length of the beam. The beam was divided into thirty elements of equal length, and the damping material was added to one element at a time. The thickness ratio was $t_y/t = 0.6$, and the modification was carried out in ten steps. As before, the material properties were assumed to be frequency independent.

Figure (5) shows the results for the first and second modes. As can be seen, the highest loss factors are achieved when the damping material is

placed at the nodes of the undamped member. The natural frequencies decrease the most when the damping layer is located at the anti-nodes (results not shown here). These results are as expected. At the nodes, bending strains in the viscoelastic coating are maximum. Thus, damping material located near the nodes is most effective. Placing it at the anti-nodes dissipates little energy, but adds mass to the system and lowers the damped natural frequency.

Example 4 Frequency Dependent Material Properties

To illustrate the capability to handle frequency dependent material properties, Example 1 was repeated (for $t_y/t = 1$) using the hypothetical material properties shown in Figures (6) and (7). Note that damping in the aluminum beam is now included. The dashed curves indicate the assumed variation in the material properties, while the solid lines define the reference values used in the initial calculations. The frequency dependence has been exaggerated so that its effect can be more readily observed.

Figure (8) shows the system loss factors for the first two modes. The perturbation solutions account for the frequency dependence of the material properties, while the finite element results do not. They are based upon the reference values of the material properties. Effects of the frequency dependence on the system natural frequencies were negligible for this example.

CONCLUDING REMARKS

First-order matrix perturbation methods can be an efficient means for predicting the dynamic characteristics of modified structural systems. Viscoelastic coating modifications are particularly suitable for this technique. The modifications need not be small, but, if they are not, they must be built up by a series of small modification steps. Because this technique works with discretized systems, it can be applied to structures of general shape and can be implemented along with finite element codes.

The first-order stepwise perturbation technique used in this investigation gave close approximations to the damped natural frequencies and loss factors for a beam with various configurations of complete and partial damping treatments. Relative errors in the loss factors were found to be greater than those in the damped natural frequencies. If the mode shapes are not updated at each modification step, the perturbation solution produces an approximation which is comparable to that of the Rayleigh energy approach⁹. Application to problems with frequency-dependent material properties was described and illustrated in an example problem. These same procedures also can be used for material properties that are temperature dependent.

An important factor not addressed in this paper is the question of the efficiency of the perturbation approach. Does it require more or less computational effort than a re-solution of the complex eigenvalue problem? The answer to this question depends very much upon the algorithms used to implement the perturbation equations. For example, for partial damping treatments covering only a small portion of a structure, the incremental mass and stiffness matrices consist almost entirely of zero elements. Computational time can be reduced by taking advantage of such facts. For small modifications requiring only a single solution step, the perturbation technique appears to be very effective.

REFERENCES

1. Kato, T., Perturbation Theory for Linear Operators, Springer-Verlag, New York, 1966.
2. Rellich, F., Perturbation Theory of Eigenvalue Problems, Gordon Breach Science Publishers, Inc., New York, 1969.
3. Huag, E. G., Choi, K. K., and Komkov, V., Design Sensitivity Analysis of Structural Systems, Academic Press, Inc., Orlando, 1986.
4. Chen, S., Liu, Y., and Huang, D., "A Matrix Perturbation of Vibration Modal Analysis," Proceedings IMAC 3, Orlando, FL, 1985, pp. 757-62.
5. Ma, Z., Chen, S., and Lu, Y., "Perturbation Method for Complex Eigenvalues of Damped System and its Associated Iterative Algorithm," Proceedings IMAC 4, Los Angeles, CA, 1986, pp. 1060-6.
6. Snyder, V. W., "Structural Modification and Modal Analysis - A Survey," Int. J. Analytical and Experimental Modal Analysis, Vol. 1, Jan., 1986, pp. 45-52.
7. Ewins, D. J., Modal Testing: Theory and Practice, Wiley & Sons, New York, 1984.
8. Johnson, C. D. and Kienholz, D. A., "Finite Element Prediction of Damping in Structures with Constrained Viscoelastic Layers," AIAA Journal, Vol. 20, No. 9, 1982, pp. 1284-1290.
9. Stevens, K. K., Kung, C. H., and Dunn, S. E., "Damping of Plates by Partial Viscoelastic Coatings-Part 1-Analysis," Proc. Noise-Con 81, Rayleigh, NC, pp. 445-448, June, 1981.
10. Ma, Z., Chen, S. and Lu, Y., "Perturbation Method for Complex Eigenvalues of Damped System and Its Associate Iterative Algorithm," Proceedings IMAC III, Orlando, FL, 1985, pp. 1060-1066.
11. Cao, X. S., Dai, D. P. and Ku, Ch. H., "Perturbation Method for Dynamic Analysis of Structures with Constrained Viscoelastic Layer," Proceeding IMAC IV, 1986, pp. 826-830.
12. Stevens, K. K., Martinez, M. E., and Kelly, W. J., "A Comparison of Exact and Approximate Methods of Analysis for Added Viscoelastic Damping Treatments," Proceedings IMAC VI, Orlando, FL, 1988.
13. Kelly, W. J., Jr., "An Application of Perturbation Techniques to the Vibration Analysis of Structures with Viscoelastic Coating Modifications," M.S. Thesis, Florida Atlantic University, Boca Raton, FL, 1988.
14. Kelly, W. J., Jr., and Stevens, K. K., "Application of Perturbation Techniques to the Modal Analysis of a Shaft with Added Viscoelastic Damping," Proceedings IMAC VII, Las Vegas, Nevada, 1989.

15. Weaver, W., Jr. and Johnston, P. R., Structural Dynamics by Finite Elements, Prentice-Hall, 1987.

TABLE 1. PROPERTIES FOR BEAM EXAMPLE

<u>Beam</u> (Aluminum)	$E = 70 \times 10^9 \text{ N/m}^2$
	$\rho = 2.7 \times 10^3 \text{ kg/m}^3$
<u>Damping Layer</u> (Commercially Available)	$E_V = 0.69 \times 10^9 \text{ N/m}^2$
	$\eta_V = 0.64$
	$\rho_V = 0.58 \times 10^3 \text{ kg/m}^3$

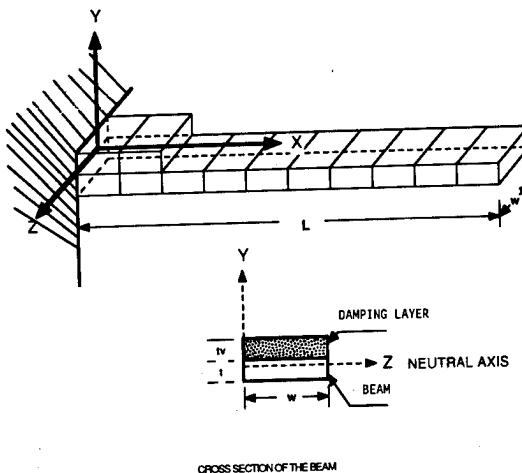


Figure 1. Cantilever Beam with a Partial Damping Treatment.

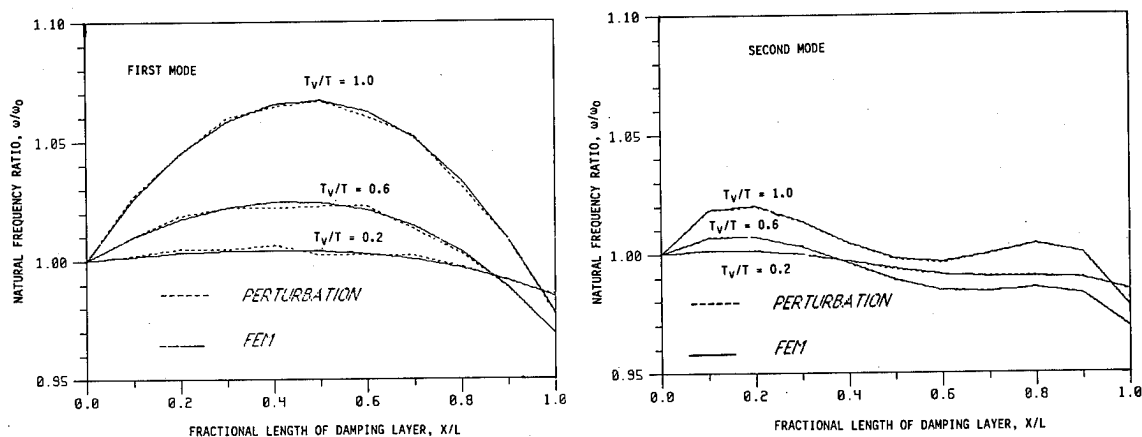


Figure 2. Effect of a Partial Damping Treatment on Natural Frequencies of a Cantilever Beam.

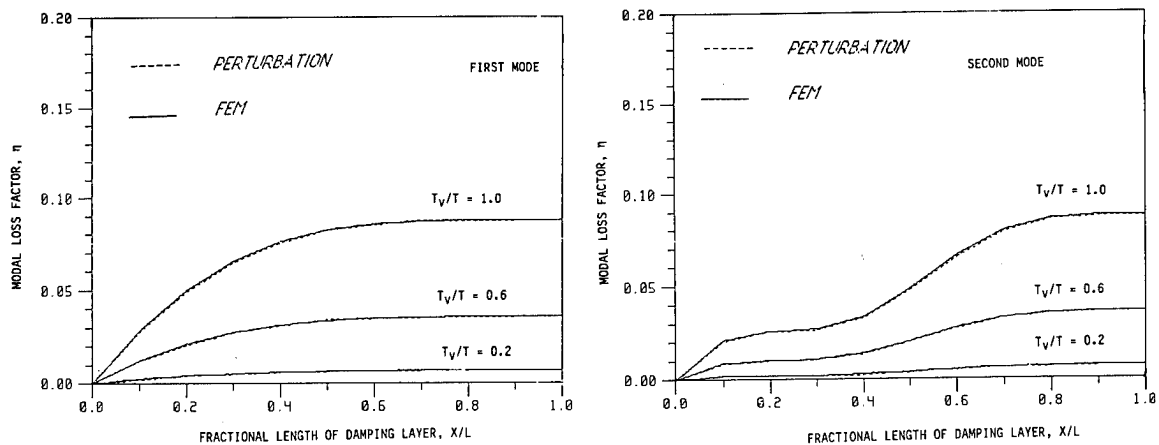


Figure 3. Effect of a Partial Damping Treatment on Modal Loss Factors of a Cantilever Beam.

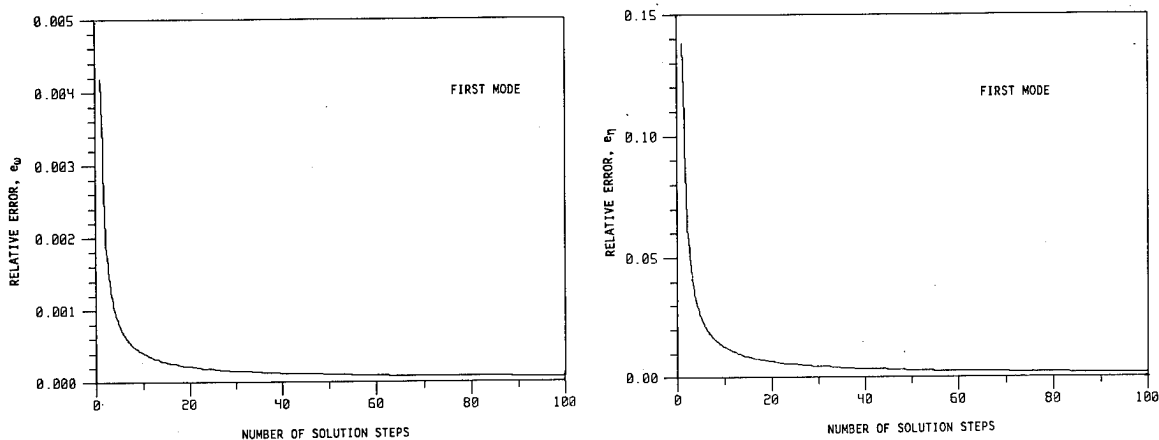


Figure 4. Rate of Convergence of Perturbation Solution.

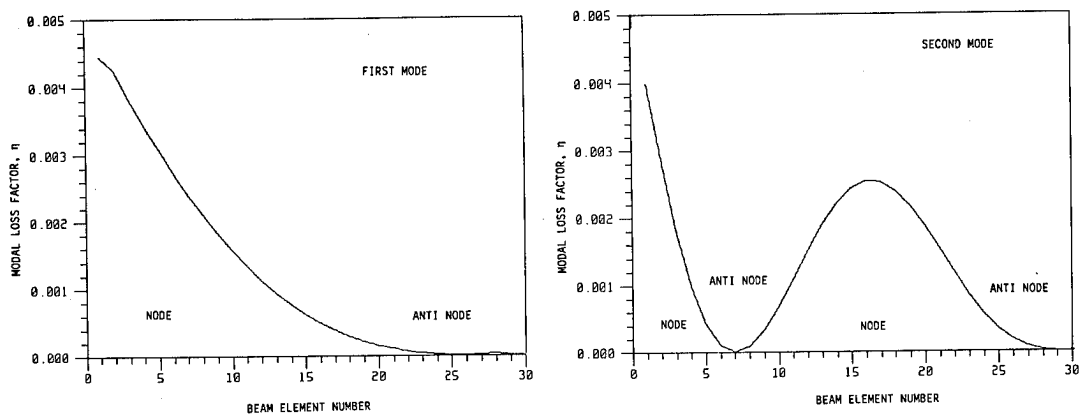


Figure 5. Loss Factor of a Cantilever Beam with Damping Treatment applied to a Single Beam Element (30 total elements).

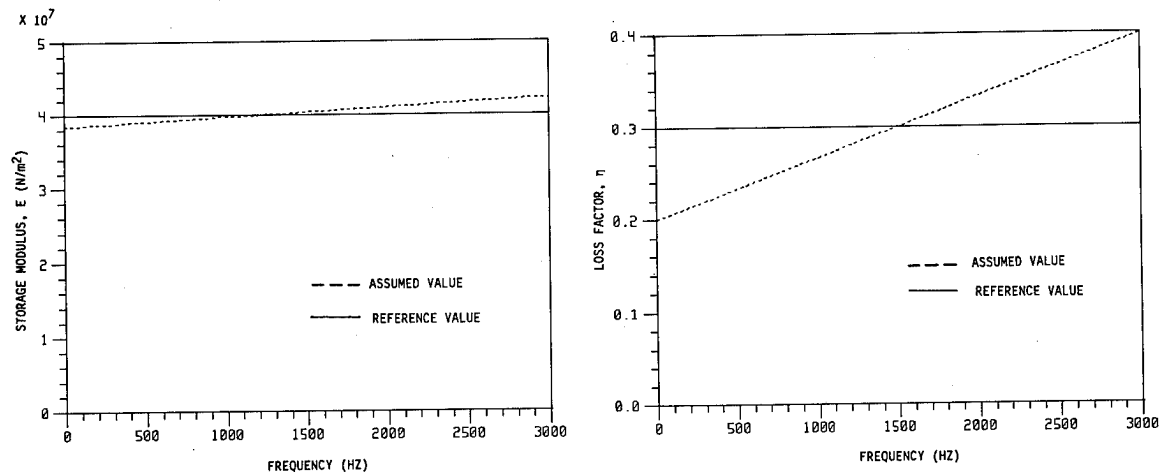


Figure 6. Properties of a Hypothetical Damping Material.

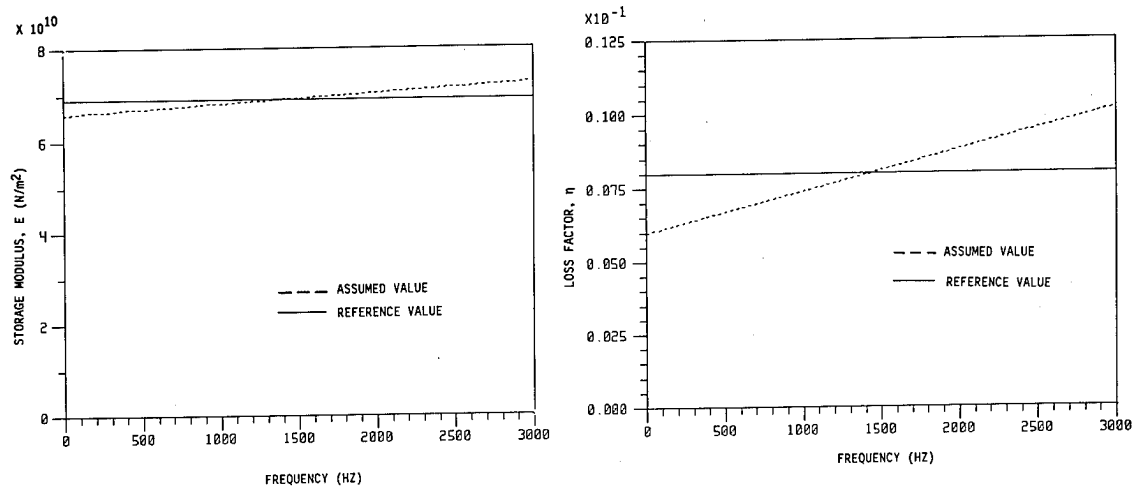


Figure 7. Hypothetical Frequency-Dependent Properties of Aluminum.

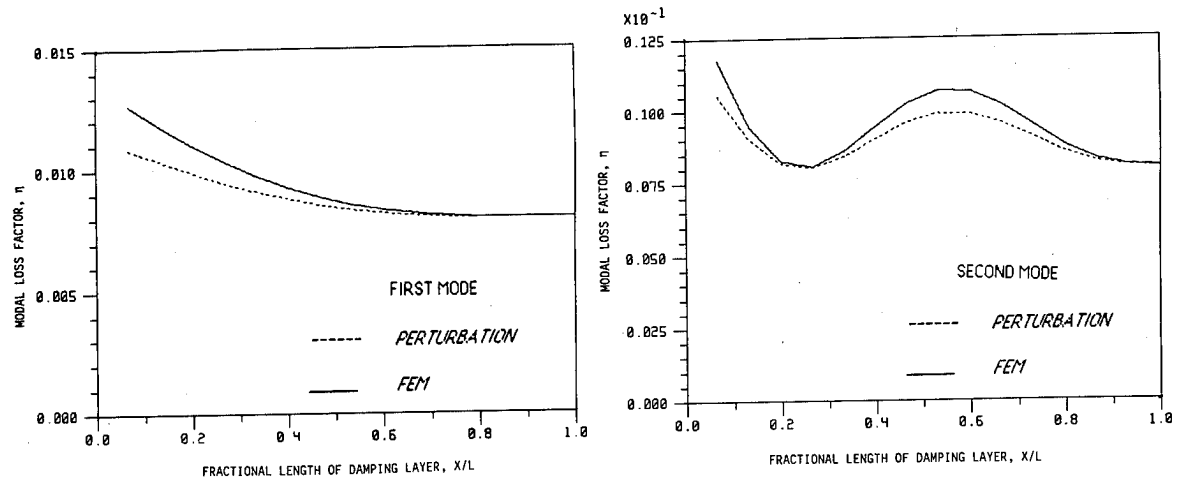


Figure 8. Effect of Frequency-Dependent Material Properties on the Loss Factor of a Cantilever Beam with a Partial Damping Treatment. (Frequency dependence not included in FEM results).

APPENDIX-BEAM EQUATIONS

Consider an elastic cantilever beam with thickness t , flexure rigidity EI , length L and elastic modulus E , with a viscoelastic damping layer of thickness t_v bonded to it over a portion of its length (Figure 1). The properties of the damping layer are described by the complex modulus

$$E^* = E_v (1+i\eta_v) \quad (A1)$$

where E_v is the storage modulus and η_v is the material loss factor. Here, and in the following, the subscript v denotes the viscoelastic damping material.

Addition of a damping layer to one side of a beam causes a shift in the neutral axis of the cross-section. Using simple beam theory, this shift can be shown to be

$$\bar{y} = y^*/t = \frac{\bar{E}\bar{t}(1+\bar{t})}{2(1+\bar{E}\bar{t})} \quad (A2)$$

where y^* is the distance between the neutral axis of the composite cross section and the midplane of the beam and

$$\bar{E} = E_v/E \quad \bar{t} = t_v/t \quad (A3)$$

Note that \bar{y} usually is small, since \bar{E} is typically small, and often can be neglected.

The mass and stiffness matrices for a beam element are available in the literature¹⁵:

$$[K] = \frac{EI}{a^3} \begin{bmatrix} 12 & 6a & -12 & 6a \\ -4a^2 & -6a & 2a^2 & -6a \\ SYM & & & 4a \end{bmatrix} = k [\bar{K}] \quad (A4)$$

$$[M] = \frac{\rho A t a}{420} \begin{bmatrix} 156 & 22a & 54 & -13a \\ & 4a^2 & 13a & -3a^2 \\ & & 156 & -22a \\ & & & 4a^2 \end{bmatrix} = m \bar{[M]} \quad (A5)$$

Here, ρ is the mass density, A is the cross-sectional area and a is the element length.

The incremental mass matrix $[\Delta M]$ due to the viscoelastic layer is given by Eq. (A5) with the beam dimensions and properties replaced by those of the layer. The incremental stiffness matrix is given by Eq. (A4), except with k replaced by k_v . Using standard finite element procedures and simple beam theory (shear effects neglected), it can be shown that

$$k_v = \frac{EI}{a^3} \left[\frac{1}{EI} + 12\bar{y}^2 + 12\bar{t} [\frac{1}{2}(1+\bar{t}) - \bar{y}]^2 \right] \quad (A6)$$

where

$$\bar{I} = I_v/I \quad (A7)$$

DAMPING AND VIBRATION CONTROL OF SOME LAMINATED COMPOSITE BEAMS
*
USING ADD-ON VISCOELASTIC MATERIALS

V. S. Rao, C. T. Sun and B. V. Sankar
Department of Aerospace Engineering, Mechanics
and Engineering Science
University of Florida
Gainesville, Florida 32611

ABSTRACT

This paper describes the development of a finite element model for laminated beams treated by a constrained viscoelastic layer. The finite element model is designed so as to represent the viscoelastic core shear accurately. An offset-beam element is developed that is specially suited for modelling such laminated beams. Element matrices are derived starting with an assumed displacement field and stress-strain relations. System damping and tip displacement are calculated analytically, and compared with those measured experimentally using the impulse-frequency response technique. Results show that dynamic response is significantly improved by use of such damping treatments.

* This work is sponsored by the Army Research Office,
monitored by Dr. Gary L. Anderson under contract No.
DAAL03-88-K0013.

Introduction

The increasing use of constrained viscoelastic materials in numerous dynamic applications have motivated the authors to develop an accurate and efficient method to estimate damping in such structures.¹ Considerable work has been done in the past few years to analyze constrained viscoelastic layer damping. Early work in the field can be found in Ross, Ungar and Kerwin's work.² Plunkett and Lee discussed the optimization of constrained viscoelastic layer damping for beams.³ The analysis assumes that the treatment is always symmetric and that the base structure is perfectly elastic. While this is reasonable for metals, fiber reinforced plastics are known to have much higher loss factors.

More recently, finite element techniques have been used to address this problem.^{4,5,6} Most of the work done so far is on damping treatment applied to metals. Advanced fiber reinforced composites are prime candidates for several interesting applications where damping is a key parameter. Improvement of damping characteristics of these materials make them even more attractive. Since most composite structural elements in military and space applications are subject to severe dynamic environments, further vibration control becomes extremely necessary. This can be achieved by using damping treatments.

High damping in a structure can often improve performance in a dynamic load environment. Efficient methods for predicting damping from a structure are required, so that means of increasing damping by design can be explored. Johnson et al. and Brockman discuss some of the finite element modeling techniques that are currently popular for modeling structures containing viscoelastic materials.^{7,8}

Much of the problems in analyzing damping in structures is due to complicated geometries; it is therefore natural to look to finite element solutions. The method considered here makes use of the correspondence principle of viscoelasticity. When applied stresses are not too large, the composite and its constituent materials exhibit linear viscoelastic behavior. For such materials, due to the correspondence principle, the Youngs modulus and shear modulus can be treated as complex qualities. The real part is called the storage modulus and the imaginary part the loss modulus.

The direct frequency response technique was used for the analytical estimation of damping and tip displacement. Experimental measurement of damping was done using the impulse-frequency response technique. In composite base structures, several factors influence system response. For example, the stacking sequence in the base structure, and the location, amount and type of treatment influence the response strongly. Parametric studies, at best, lead to locally optimal solutions; while no formal optimization was done, results show the potential for optimization.

Finite Element Analysis.

The finite element method was used to evaluate damping in the structure for different lengths of treatment of the constrained viscoelastic layer. Figure 1 shows the arrangement used for modeling the three layer sandwich. The base structure and constraining layer were modeled using a specially developed three-node, seven-degree-of-freedom, offset beam element. A key feature of this element is its ability to account for coupling between stretching and bending deformations. This allows for the beam nodes to be

offset to one surface of the beam, coincident with the nodes of the adjoining element. The viscoelastic core is modeled using a rectangular plane stress element that is compatible with the offset beam element.

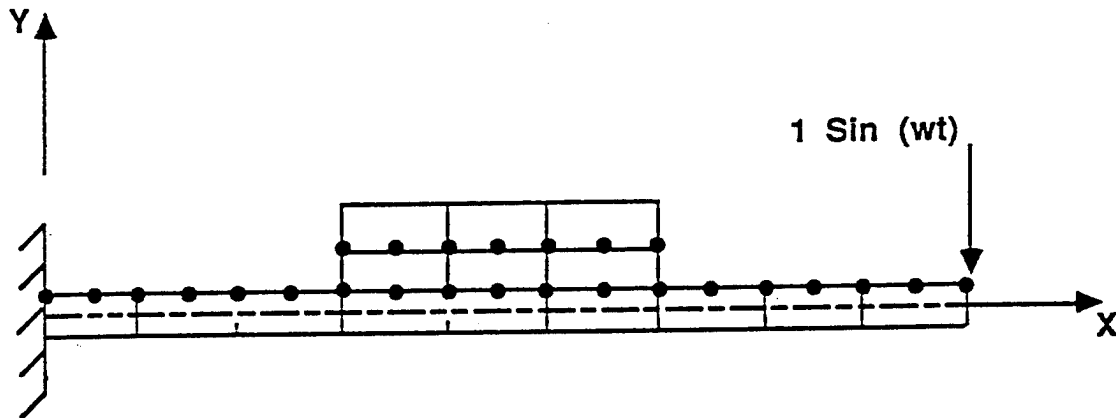


Figure 1: Typical Finite Element Mesh

Offset Beam Element

The element stiffness matrix for the offset beam element shown in Fig. 2 is formulated as follows. The different displacement components are given by,

$$\left. \begin{aligned} u(x,y) &= u_0(x) + (z - \frac{h}{2})\psi(x) \\ w(x,y) &= w(x) \\ \psi(x,y) &= \psi(x) \end{aligned} \right\} \quad (1)$$

u_0 and ψ are defined using linear interpolation functions.

$$\left. \begin{aligned} u_0(x) &= [(1-x/L_b) \quad x/L_b] [u_1^* \quad u_2^*]^T \\ \psi(x) &= [(1-x/L_b) \quad x/L_b] [\psi_1^* \quad \psi_2^*]^T \end{aligned} \right\} \quad (2a)$$

where, u_1^* , u_2^* , ψ_1 and ψ_2 are corresponding nodal displacements. w is defined using quadratic interpolation functions.

$$w = \begin{bmatrix} (1 - 3x/L_e + \frac{2x^2}{L_e^2}) \\ 4(\frac{x}{L_e} - \frac{x^2}{L_e^2}) \\ (\frac{-x}{L_e} + \frac{2x^2}{L_e^2}) \end{bmatrix}^T \begin{Bmatrix} w_1^e \\ w_2^e \\ w_3^e \end{Bmatrix} \quad (2b)$$

where w_1^e , w_2^e and w_3^e are nodal displacements.

Strains are derived from the displacement using the kinematic strain-displacement relations of linear elasticity.

$$\begin{aligned} \epsilon_x &= \frac{\partial u}{\partial x} = \frac{\partial u_0}{\partial x} + z \frac{\partial \psi}{\partial x} \\ \gamma_{zx} &= \frac{\partial u}{\partial z} + \frac{\partial w}{\partial x} = \psi + \frac{\partial w}{\partial x} \end{aligned} \quad (3)$$

The strain energy density for the system is given by

$$U_0 = \frac{1}{2} C_{11} \epsilon_{xx}^2 + \frac{1}{2} k^2 C_{55} \gamma_{xz}^2 \quad (4)$$

C_{11} and C_{55} are constants from the constitutive equations. The total strain energy for the system is given by

$$U = \int_V U_0 dv = b \int_0^{L_e} \int_{-h/2}^{h/2} U_0 dv \quad (5)$$

Using equations (2), (3), (4) and (5), the strain energy of the system is reduced to,

$$U = \frac{1}{2} \{d_e\}^T [K_e] \{d_e\}$$

where,

$\{d_e\}$ = vector of elemental D.O.F.

$[K_e]$ = element stiffness matrix

The calculations involved are lengthy, but straight forward and are not presented here. The distributed mass matrix is evaluated similarly from the kinetic energy of the system.

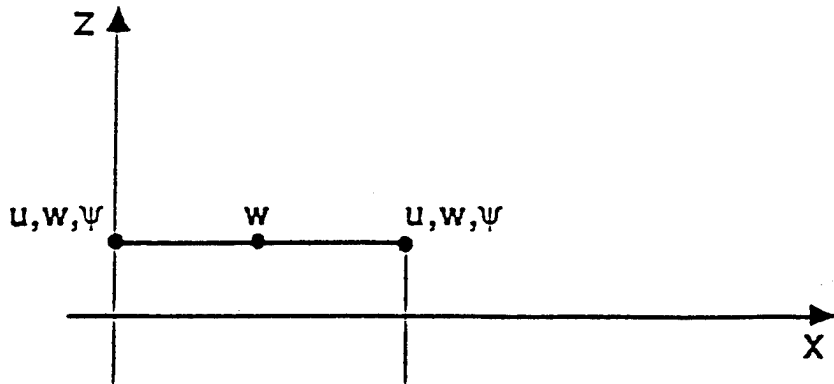


Figure 2: Offset Beam Element

Modeling and Solution Technique

As mentioned before the base structure was modeled using the three-node shear-deformable beam element. Typically, twenty elements are used to model the beam. Very large aspect ratios are common for elements used to model the viscoelastic core. Values as high as 5000 to 1 have been used successfully, and are sometimes even necessary, since the viscoelastic core is only two mils thick.⁷ Aspect ratios up to 200 to 1 were used in the present study. To validate this formulation, several calculations were made to determine natural frequencies and tip displacement of simple systems, closed form solutions to which are easily derived.

The loss factor was evaluated using the direct frequency response technique. In this method, a forced vibration at a known frequency is considered. System displacements are obtained by solving a system of complex-valued linear equations. The frequency response spectrum is obtained by plotting amplitudes over a range of frequencies. The loss factor, a measure of damping, is obtained from the real part of the response. This technique, though not the most efficient, was used for two reasons, simplicity and the relative small size of the problem in question.

The modeling method used is reasonably efficient. A three layer structure is modeled using only two layers of nodes. This technique can be easily extended to two-dimensional problems. However, alternative methods for determining system loss factor will have to be used as the problem size increases.⁸

Experimental Procedure

The most common methods used to measure damping are the free vibration decay method, the resonant dwell method, the hysteresis loop method and the frequency-response technique. For the purpose of this research the impulse-frequency response technique was used.⁹ This technique offers potential for rapid nondestructive evaluation of materials and structures.

In the impulse-frequency response technique, the specimen is excited impulsively with a controlled-impact hammer which has a force transducer attached to its head. The specimen response is sensed by a non-contacting eddy current proximity probe. The signals from the force transducer and the motion transducer are fed to a Fast Fourier Transform (FFT) analyzer which displays the frequency spectrum. A block diagram of the instrumentation is shown in Figure 3. By analyzing the resonant peaks for a particular mode, the loss factor, a measure of damping, is obtained from the real part of the response spectrum as explained in Fig. 4. In this research the improvement technique was used.⁹ Some of the features of this improved technique are the excitation level is accurately controlled, therefore, the amplitude of vibration of the specimen can be reduced to a minimum (thereby reducing air damping to a minimum). Also, the response function, which is identical in shape to the transfer function after ensemble averaging, can be used for damping measurements.⁹

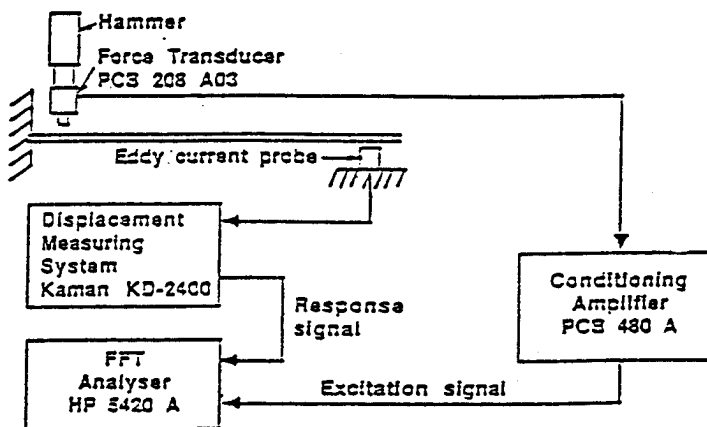


Figure 6: Variation of Loss Factor with Tape Length (Mode I)

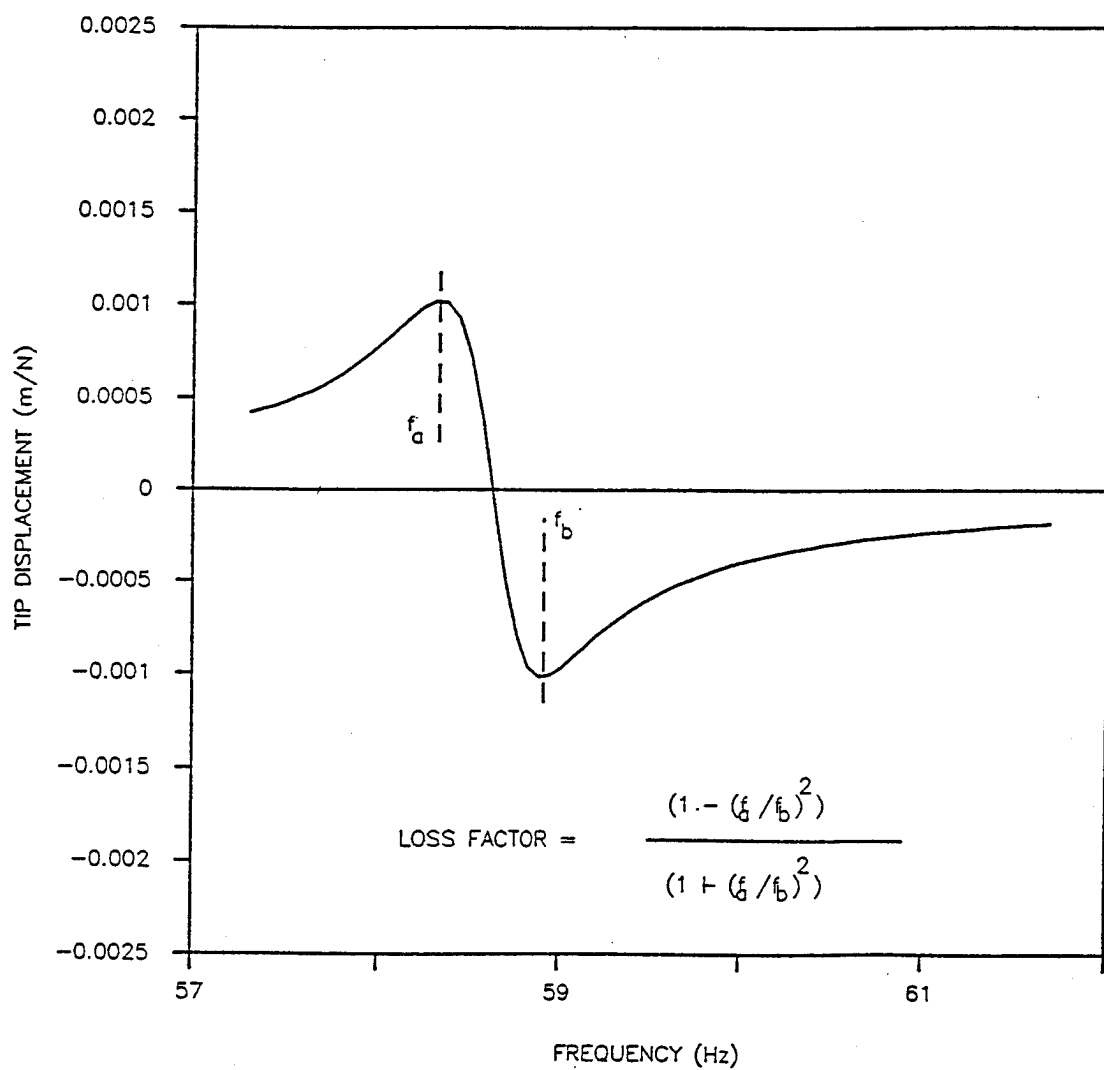


Figure 4: Real Part of the Response Spectrum

Results and Discussion

The material properties of Glass-Epoxy and the soft aluminum constraining layer are given in Table I. The damping material used was 3M's SI2052x, a class of constrained viscoelastic damping tape. The shear modulus and loss factor of the damping material, as a function of temperature and frequency are provided by the manufacturers.

Table - I Material Properties

Glass-epoxy composites (0°)							
V_f	ρ g/cm ³	E_L GPa	E_T GPa	G_{LT} GPa	ν_{LT}	η_L	η_T
0.50	1.90	38	8.80	3.0	0.28	0.0033	0.01
Constraining Layer: - Type 1100 Dead Soft Aluminum.							
ρ g/cm ³	E GPa	G GPa	ν	η			
2.76	69 GPa	26 GPa	0.32	0.005			

Structural damping with and without (taped and untaped) the add-on viscoelastic layer are evaluated experimentally, and analytically using finite element analysis. Results of the effects of different parameters such as, the quantity of treatment, location of treatment and the thickness of the damping material on the overall damping of the system are presented. Stacking sequences of the three different laminates analyzed, specimen dimensions, measured loss factors of the untaped beam and first and second mode resonant frequencies are given in Table II.

Table II - Laminates Tested**

laminate	length (mm)	thickness (mm)	frequency (Hz) Mode I	frequency (Hz) Mode II	loss factor Mode I	loss factor Mode II
[0/90] _{4s}	20.32	3.57	54.1	339.7	0.00291	0.00282
[0/90/00/90] _{2s}	20.32	3.68	49.4	309.3	0.00382	0.00346
[90/90/0/90] _{2s}	20.32	3.61	41.2	258.2	0.00428	0.00422

Figure 5 shows the real and imaginary parts, and magnitude of the response as a function of the frequency of the forced vibration for three different lengths of treatment. Corresponding structural loss factors

** Three specimens tested in each case.

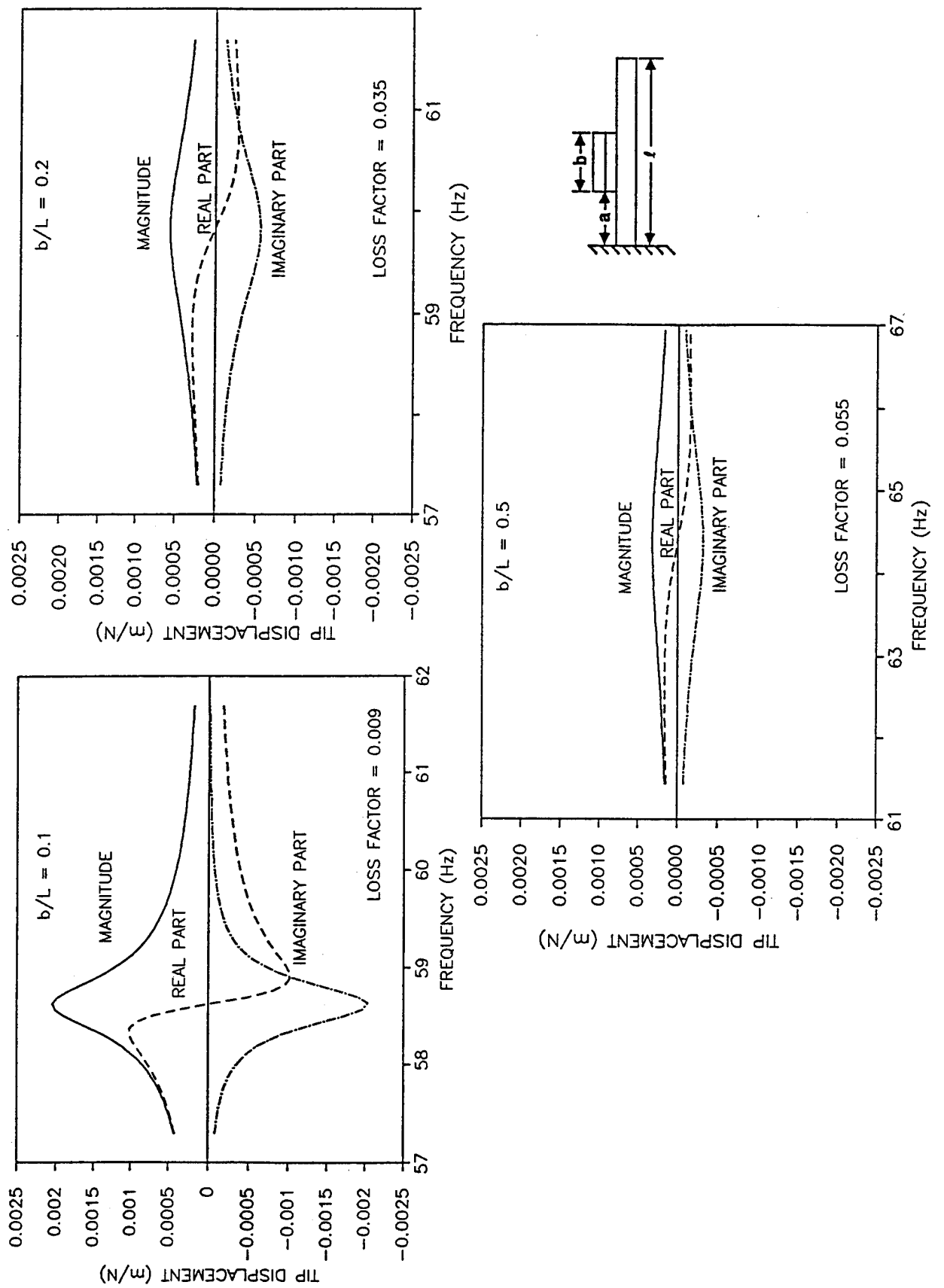


Figure 5: Analytical Results for Different Tape Lengths ($a/L = 0$)

evaluated from the finite element analysis is also shown. The change in system response due to addition of the viscoelastic material can be seen from the figure. Displacement is plotted in meters, per Newton of applied force. Large reductions in response amplitude can be seen due to application of the damping tape.

Figure 6 shows the variation of loss factor with tape length for the three different laminates for mode 1. Loss factor ratio is the ratio of the loss factor of the taped beam to the measured loss factor of the untaped beam (value in Table II). In each case the loss factor increases rapidly from $b/L=0$ to $b/L=0.4$, after which it shows a slight drop and then remains steady. The existence of a tape length, b , for which $b/L < 1$ and damping is maximized is significant. This result confirms our previous belief that shear deformation of the viscoelastic core is the primary source for energy dissipation. For lengths greater than the optimal value, the deformation of the viscoelastic core follows the extensional deformation of the surface of the beam.

Similar results are presented in Fig. 7 for vibration in the second mode. The trend observed here is different from that for mode 1. While treatment closer to the root of the beam seems to have the greatest effect on mode 1, the center of the beam seems to be the optimal location for mode 2. Figure 8 presents the experimental results for the $[0/90]_{4S}$ laminate. The trends observed are identical to those suggested by analytical results for mode 1. However, for $b/L > 0.4$ experimental results are consistently higher than analytical predictions. Mode II results show excellent agreement with analytical predictions.

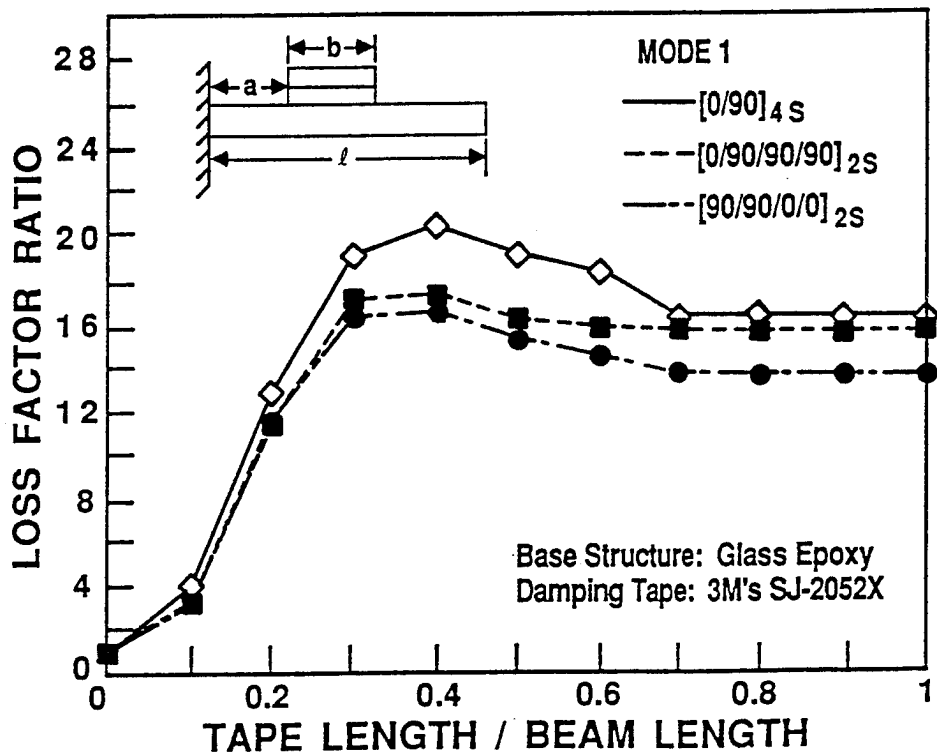


Figure 6: Variation of Loss Factor with Tape Length (Mode I)

The variation of loss factor ratio with tape length for different thicknesses of the damping material is shown in Fig. 9. The results suggest that for a given thickness of the constraining layer there exists an optimal thickness of the viscoelastic damping material (about 0.127 mm for a constraining layer thickness of 0.254 mm) for which greatest damping can be achieved. The variation of amplitude ratio with tape length is given in Fig. 10. Amplitude ratio is the ratio of the maximum tip displacement of the taped beam to that of the untaped beam. For each of the three laminates the vibration amplitude is seen to reduce dramatically with increasing damping.

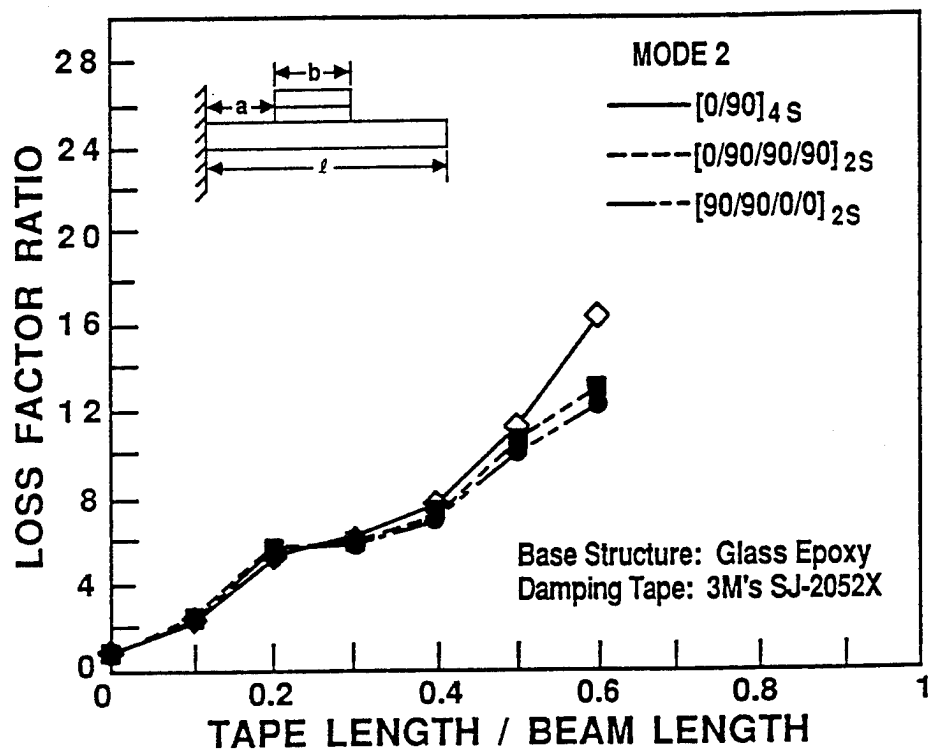


Figure 7: Variation of Loss Factor with Tape Length (Mode II)

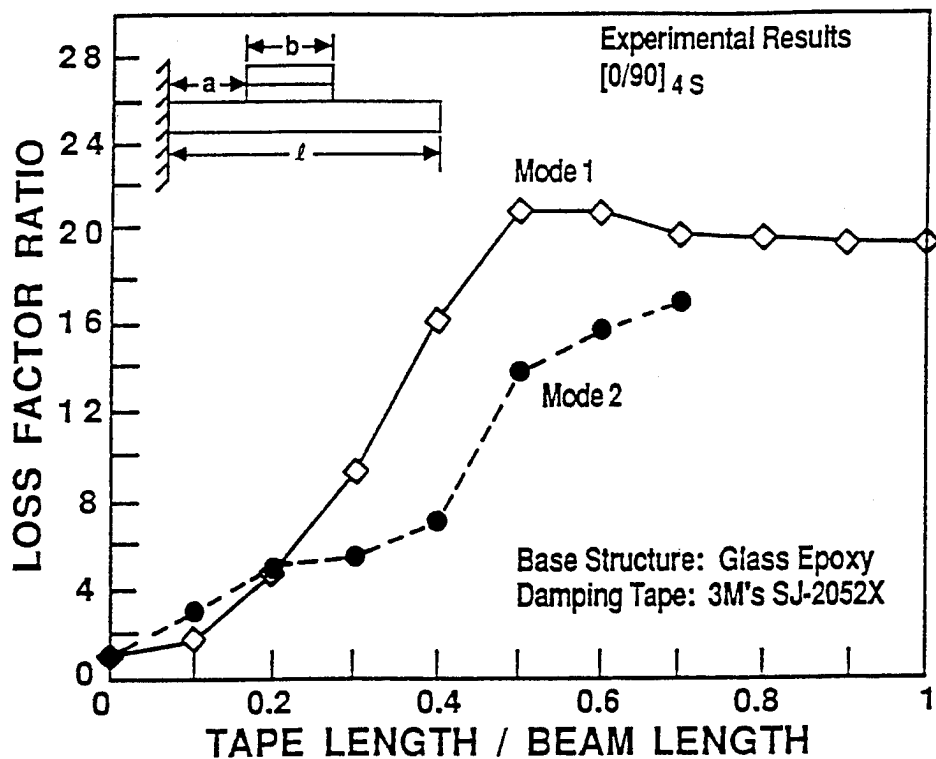


Figure 8: Variation of Loss Factor with Tape Length (Experimental Results)

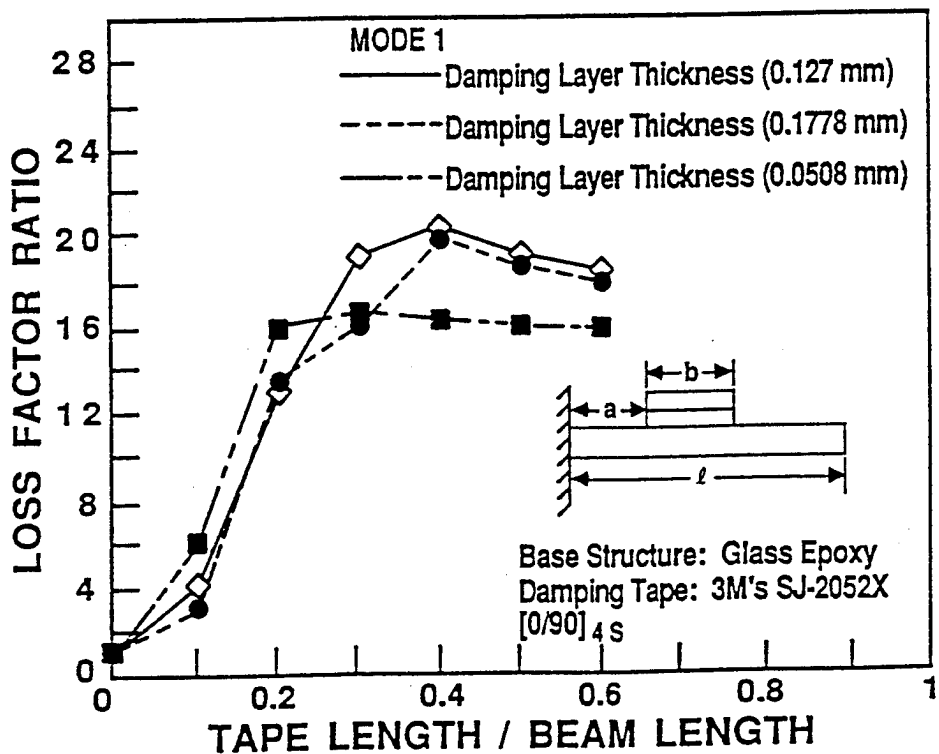


Figure 9: Variation of Loss Factor with Tape Length for Different Damping Layer Thicknesses

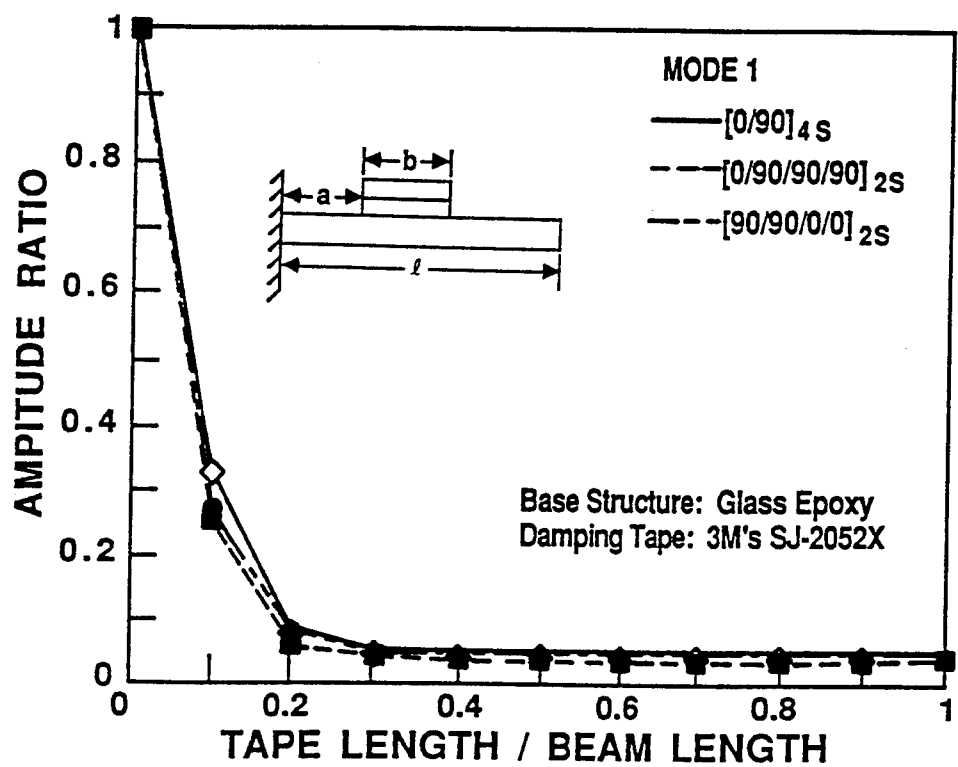


Figure 10: Variation of Amplitude Ratio with Tape Length (Mode I)

Concluding Remarks

Based on the numerical and experimental results presented, it is concluded that viscoelastic surface layer treatments can be used to significantly improve the dynamic response of structures. Increases in overall system damping and large reductions in response amplitudes are achieved using damping treatment. Results also show, for each mode of vibration, there exists a length, location and a thickness of the damping tape, for a given thickness of the constraining layer, for which the overall system damping is maximized.

In future the work will be extended to accommodate the effects of continuous variation in cross section, (this is already possible with a little modification) pre-stress, initial twisting and rotation on the system response.

References

- [1] Nashif, A. D., Jones, D. I. G. and Henderson J. P., "Vibration Damping," John Wiley and Sons, 1985.
- [2] Ross, D., Ungar, E. E. and Kerwin, Jr., E. M., "Damping of Plate Flexural Vibrations by Means of Viscoelastic Laminae," Section 3, ASME Monograph on Structural Damping 1959.
- [3] Plunkett, R. and Lee, C. T., "Length Optimization for Constrained Viscoelastic Layer Damping," Journal of Acoustical Society of America, Vol. 48, p. 151, 1970.
- [4] Johnson, C. D. and Kienholz, D. A., "Finite Element Prediction of Damping Layers," AIAA Journal, Vol. 20, No. 9, pp. 1264-1290, May 1982.
- [5] Soni, N. L. and Bogner, F. K., "Finite Element Vibration Analysis of Damped Structures," AIAA Journal, Vol. 20, No. 5, pp. 700-707, May 1982.
- [6] Soni, M. L., "Finite Element Analysis of Viscoelastically Damped Sandwich Structures," Shock and Vibration Bull., Vol. 51, pt. 1, May 1981.
- [7] Johnson, D. C., Kienholz, D. A., Austin, E. M. and Schneider, N. E., "Finite Element Design of Viscoelastically Damped Structures," Proceedings of Vibration Damping Workshop, February 27-29, pp. HH1, 1984 Workshop.
- [8] Brockman, R. A., "On Vibration Damping Analysis Using the Finite Element Method," Using the Finite Element Method," Proceedings of Vibration Damping Workshop, February 27-29, pp. 11-1, 1984 Workshop.
- [9] Suarez, S. A., Gibson, R. F., "Improved Impulse-Frequency Response Techniques for Measurements of Dynamic Mechanical Properties of Composite Materials," Journal of Testing and Evaluation, Vol. 15, No. 2, March 1987, pp. 114-121.

**CLASSIFICATION IN THE FREQUENCY-TEMPERATURE
RANGE OF VISCOELASTIC MATERIALS FOR DAMPING
OF FLEXURAL WAVES IN SANDWICH STRUCTURES
WITH VARIOUS BOUNDARY CONDITIONS .**

Dr. Marie-Josèphe GHALEB¹ and Mona KHOURY

Centre d'Etudes et de Recherches pour la Discréction Acoustique des Navires (CERDAN)
DCAN Toulon , 83800 Toulon Naval , FRANCE

Telephone Numbers : (33) 94-02-54-75 (Ghaleb) (33) 94-02-47-74 (Khoury)

Damping of flexural waves by constrained or unconstrained viscoelastic layers is considered in order to classify the viscoelastic materials according to their efficiency for given ranges of temperature and frequency . The loss factor is computed for structures of various geometries , such as beams, plates and tubes, with various materials of the constraining layers , such as steel, aluminum, fiber glass composite . The influence of boundary conditions is studied . The curves corresponding to particular loss factors are plotted in the frequency - temperature plane for a given structure, so that the efficiency of the damping treatment may be evaluated immediately for each range of temperature or frequency . A classification between different materials can then be made . An experiment giving the modes and the corresponding loss factors of free sandwich plates is presented .

¹ External consulting engineer for CERDAN .

INTRODUCTION

The damping of flexural vibrations by the mean of viscoelastic materials is a classic method involving different techniques such as extensional damping by unconstrained layers, and shear damping by constrained layers . The resulting loss factor for an elementary structure such as a beam, a plate or a tube, is given by well-known theories (Oberst, Ruzicka and Kerwin). However, one of the user's problems is the choice of the different added layers : the viscoelastic material and, eventually, the material of the constraining layer, and their dimensions.

This paper presents a method of classification of viscoelastic materials, based on their intrinsic loss factor or on the composite loss factor of damped structures in which they are involved. The principal results are curves representing a given loss factor in the temperature-frequency plane, so that the user can immediately evaluate the damping's efficiency in the ranges of temperature and frequency he is interested in. It is also possible to plot the loss factor of a composite structure versus the frequency (or the temperature) for given temperatures (or given frequencies), or versus different thickness ratios for given temperatures and frequencies.

The combination of all these possibilities helps to find the best viscoelastic material, and eventually the constraining material, and to optimize the thickness of each layer.

The utilization of the method will be illustrated with some examples of damping by five different viscoelastic materials .

INTRINSIC DAMPING .

Characterization of a viscoelastic material .

Under linear conditions, the complex modulus is a classic way to characterize the behavior of a viscoelastic material . The stress-strain relation can be written :

$$\sigma = E(f,T)(1+i\beta(f,T)) \epsilon$$

where f is the frequency, T is the temperature, and E, β are respectively the Young's modulus and the loss factor of the material .

The complex modulus $E(1+i\beta)$ is provided by experimental data giving the variations of E and β with temperature and frequency . Usually, there is an equivalence between temperature and frequency effects, so that the separate variables f and T can be combined in a single variable $f\alpha_T$ called the reduced frequency , where the 'shift factor' α_T is a non-dimensional parameter depending only on temperature . The Young's modulus E (or the shear modulus $G=E/3$) and the loss factor are then given ,in function of the reduced frequency , by the 'master curves' which characterize each viscoelastic material . Figures 1 and 2 show the master curves of two viscoelastic materials : M1 and M4 .

Classification of viscoelastic materials according to their intrinsic loss factor .

One way of comparing the efficiencies of different viscoelastic materials is to look for the frequency intervals where their loss factor is greater than a certain value, for the temperatures one is interested in. Table 1 shows the frequency intervals where $\beta > 0.5$ for five materials: M1 to M5, and for three temperatures . This method gives a first indication about the best materials available for given temperatures and frequencies .

In order to avoid tedious manipulations, the master curves of the viscoelastic materials have been stocked in a library ; the user can then compute E and β for each value of f and T by the mean of a simple program using the following method : it first computes the shift factor α_T , then the reduced frequency $f\alpha_T$, and finally E and β . The user can obtain more global results than the table above by plotting E and β versus frequency (or temperature) for the temperatures (or the frequencies) he is interested in. However, if he wants to have a general view of the efficiency of the material in order to make a first selection, the most appropriate method consists in plotting the curves corresponding to different values of β in the (f,T) plane . These curves are obtained by a program which computes β for several values of f and T, and then plots contour lines corresponding to the desired values of β . In order to have reliable results, one should consider a great number of points in f and T, and make regular subdivisions in $\log(f)$ and T . Figures 3 and 4 show the curves obtained for M1 and M4 for $10 \text{ Hz} < f < 10000 \text{ Hz}$ and $0^\circ\text{C} < T < 60^\circ\text{C}$. A comparison with the results of Table 1 or the master graphs shows that the curves give quite good results if we take into account the imprecision on the master graphs .

The different types of viscoelastic damping treatments .

There are two types of viscoelastic damping treatments :

- the extensional damping (by unconstrained layer), in which the extensional deformation of the damping layer accounts for the damping
- the shear damping (by constrained layer) , in which the energy losses due to shear motions are dominant .

We will study these two types of treatments with one viscoelastic layer and for elementary structures such as beams, plates, and tubes .

EXTENSIONAL DAMPING.

This method consists in adding a viscoelastic layer of Young's modulus $E_V(1+j\beta)$ to the base structure (Figure 5) .

The loss factor of the composite structure in the case of a damped beam or plate is given by : [1,2,3] :

$$\eta = \frac{\beta eh(3+6h+4h^2+2eh^3+e^2h^4)}{(1+eh)(1+4eh+6eh^2+4eh^3+e^2h^4)}$$

H_1, H_v : Thicknesses of the layers

$$e = E_v / E_1$$

$$h = H_v / H_1$$

$eh = E_v H_v / E_1 H_1$: Ratio of the extensional stiffnesses of the two layers

In most practical cases, $eh \ll 1$.

For a damped tube, the loss factor is :

$$\eta = \frac{\beta E_v (R_3^4 - R_2^4)}{E_1 (R_2^4 - R_1^4) + E_v (R_3^4 - R_2^4)}$$

with R_1, R_2 : Internal and external radii of the initial tube

R_3 : External radius of the damped tube

For the beam or plate as well as for the tube, the composite loss factor increases with the intrinsic loss factor, the Young's modulus and the thickness of the viscoelastic layer. The best materials for extensional damping are then those which have the greatest loss factor and extensional stiffness. Increasing the thickness of the viscoelastic layer improves the efficiency of the treatment, however there is a limit above which the damping tends to saturate and even to decrease.

For example, the material M4 is better than M1 for extensional damping (Table 1, Figures 3 and 4). In fact, M4 and M5 are used for extensional damping, whereas M1, M2 and M3 are used for shear damping.

Figures 6 and 7 show the curves $\eta(f, T)$ for a beam damped by M4 and M5. By comparing them, one can deduce that :

- M4 is less efficient than M5 for high temperatures and low frequencies, and more efficient for low temperatures and high frequencies

- M4 is more efficient than M5 for intermediate temperatures and frequencies

More precise results can be obtained by superimposing the figures 6 and 7. The best material for the particular case considered is then deduced immediately for each range of temperature and frequency.

The influence of H_v can also be studied by plotting the curves $\eta(H_v/H_1)$ for given values of f and T (Figures 8 and 9).

SHEAR DAMPING .

This treatment, which has been considered by many authors [1,2,4], consists in applying a constrained viscoelastic layer (Figures 10 and 11) . Ruzicka and Kerwin [4] have provided a simplified theory with the following assumptions :

- The considered modes are sinusoidal (simply supported structure)
- The effects of the boundary constraints are negligible
- Shear and torsional distortions of the elastic elements are negligible
- The dimensions of the different cross-sections remain constant
- There is contact without slippage at all the interfaces
- The stress-strain relations are linear in all the layers
- The axial inertial forces are negligible
- The elastic elements have zero extensional and shear loss factors
- The elastic elements are considerably stiffer in extension than the viscoelastic material
- The viscoelastic material is thin and of approximately constant thickness

The loss factor of the composite structure is :

$$\eta = \frac{\beta X Y}{1 + X(Y+2) + (1+\beta^2)X^2(Y+1)}$$

with β : Intrinsic loss factor of the viscoelastic material

X : Shear parameter

Y : Geometrical parameter

The intrinsic loss factor is deduced of the master graphs . It depends on the frequency and the temperature : $\beta (f, T)$.

The geometrical parameter Y is defined as

$$Y = \{ (EI)_\infty / (EI)_0 \} - 1$$

where $(EI)_0$ (resp. $(EI)_\infty$) is the flexural rigidity of the composite structure when the elastic elements are completely uncoupled (resp. coupled) . Another expression for Y is :

$$Y = \frac{M A_1 A_2 d_2}{(A_1 + M A_2)(I_1 + M I_2)}$$

with $M = E_2/E_1$

$A_{1,2}$: Cross sections of the elastic elements

$I_{1,2}$: Moments of inertia of the elastic elements

d : Distance between the neutral planes of the elastic elements

More generally, $Y = Y_0 x (Y/Y_0)$

where Y_0 is a function of dimension ratios and ratios of Young's moduli of the elastic layers

Y/Y_0 is a correction factor representing the influence of the viscoelastic layer

$$Y_0 = Y(H_v = 0)$$

The expressions of Y for a beam, a plate or a tube are given with figures 10 and 11 ;
The shear parameter for the mode n is given by

$$X_n = \frac{G'_v B_v d_0^2}{p_n^2 H_v Y_0 (EI)_0}$$

where G'_v , B_v and H_v are respectively the shear modulus, the mean length and the thickness of the viscoelastic layer

d_0 is the distance between the neutral planes of the elastic elements when $H_v = 0$

p_n is the wave number

The frequency of the mode n for the beam or the tube is :

$$f_n = \frac{a_n^2}{2\pi L^2} \sqrt{\frac{(EI)_n}{m}}$$

where $(EI)_n$ is the flexural rigidity of the composite structure

m is its mass per unit length

L is its length

a_n is a coefficient depending on the boundary conditions

For a simply supported structure, the modes are sinusoidal ; the wave length is related to L by:

$$\lambda_n = \frac{2L}{n}$$

and $a_n = n\pi$

The wave number p_n is then given by :

$$p_n^2 = \left(\frac{2\pi}{\lambda_n} \right)^2 = 2\pi f_n \sqrt{\frac{m}{(EI)_n}}$$

If we suppose that $(EI)_n$ is the real part of the complex rigidity $(EI)_n^*$ [4], then

$$(EI)_n = \operatorname{Re} (EI)_n^* = (EI)_0 \operatorname{Re} \left(1 + \frac{X_n^*}{1 + X_n^*} Y \right)$$

with $X_n^* = X_n (1 - i\beta_n)$

If we introduce the 'coupling parameter' :

$$Z_n = \frac{X_n(1+X_n) + X_n^2\beta_n^2}{(1+X_n)^2 + X_n^2\beta_n^2}$$

the flexural rigidity can also be written :

$$(EI)_n = (EI)_0 (1+Z_n Y)$$

Then the shear parameter for the mode n is :

$$X_n = \frac{G'_v B_v d_0^2}{2\pi f_n \sqrt{\frac{m}{(EI)_n} H_v Y_0 (EI)_0}} = \frac{G'_v B_v d_0^2}{2\pi f_n H_v Y_0 \sqrt{\frac{m}{m(EI)_0}}}$$

(the expressions of $(EI)_0$ and d_0 are given with figures 10 and 11)

For a given frequency, X_n and Z_n are obtained by an iterative method, then the loss factor is deduced.

If we consider a motion in one direction, the formulation is the same for a plate, with analogous expressions for the wave number and the frequency (Table 2).

In order to compare the effects of different constraining layers, the curves $\eta(f,T)$ have been plotted for a steel beam damped by M_1 , and constrained by steel, aluminium or fiber glass layers introducing the same added mass (Figures 12,13,14). It appears that in this case, the most efficient material is aluminium, which can provide a loss factor of 0.2. However, this is a global conclusion, and another material can be more efficient for particular values of temperature and frequency .

The influence of the viscoelastic material can be studied by considering the steel beam damped by M_1 , M_2 or M_3 , with the same constraining layer, for example steel (Figures 12, 15 and 16). It appears that, globally, the most efficient material is M_1 , which can provide a loss factor of 0.15 .

Influence of boundary conditions (free structure)

In the case of a free structure, the modes are no more sinusoidal, so that the theory is not valid . However, analogous relations for f_n and a_n may be used [5], knowing that the expression for a_n is not valid for the first five modes . If one is interested in the value of the frequency , independantly of the modal analysis, the loss factor is the same as for the simply supported plate.

EXPERIMENT

Modal damping measurements have been made on steel plates damped by constrained viscoelastic layers (with steel constraining layers). The plates were free and excited by a hammer. The measurements were made in five different points, and a modal analysis has given the modal frequencies as well as the corresponding loss factors. In the frequency range of measurement, a few flexural modes were identified. We plotted the experimental and theoretical values of the loss factors on the same curves (Figures 17 and 18). We can see that the experimental values are a little lower than the theoretical ones. However, the agreement between experiment and theory remains quite acceptable.

CONCLUSION

We have developed a program based on well-known theories and which can be of great help for the designer of damping devices with viscoelastic layers. It allows the user to visualize immediately the efficiency of damping treatments and then to choose the most appropriate. It offers different possibilities such as :

- extensional or shear damping
- beams, plates or tubes
- various viscoelastic layers, whose master curves are stocked in a library
- various constraining layers, such as steel, aluminium, fiber glass composite with different thicknesses of the added layers .

However, one has to make many tries before finding the best damping device. The program needs to be extended to an optimization program which would give the best materials with the appropriate dimensions for a given structure to damp .

	M1	M2	M3	M4	M5
T=0°C	1 1740	1 1000	1 10 000		
T=20°C	6 10 000	20 10 000	20 10 000	1 600	1 40
T=40°C	300 10 000		250 10 000	3 10 000	15 3000

Table 1 - Frequency intervals (between 10 Hz and 10000 Hz) where the intrinsic loss factor is greater than 0,5 for the viscoelastic materials considered (M1 to M5) .

	FREQUENCY OF THE MODE n	SIMPLY SUPPORTED	FREE (n>5)
BEAM/TUBE	$f_n = \frac{a_n^2}{2\pi L^2} \sqrt{\frac{(EI)_n}{m}}$	$a_n = n\pi$ $\lambda_n = \frac{2L}{n}$	$a_n = \frac{(2n+1)\pi}{2}$ $\lambda_n = \frac{4L}{2n+1}$
PLATE (motion along one direction)	$f_n = \frac{a_n^2}{2\pi L^2} \sqrt{\frac{D_n}{m}}$	$a_n = n\pi$ $\lambda_n = \frac{2L}{n}$	$a_n = \frac{(2n+1)\pi}{2}$ $\lambda_n = \frac{4L}{2n+1}$

L : Length

m : Mass per unit length / surface

$(EI)_n$: Flexural rigidity of the beam or the tube

D_n : Flexural rigidity of the plate

Table 2

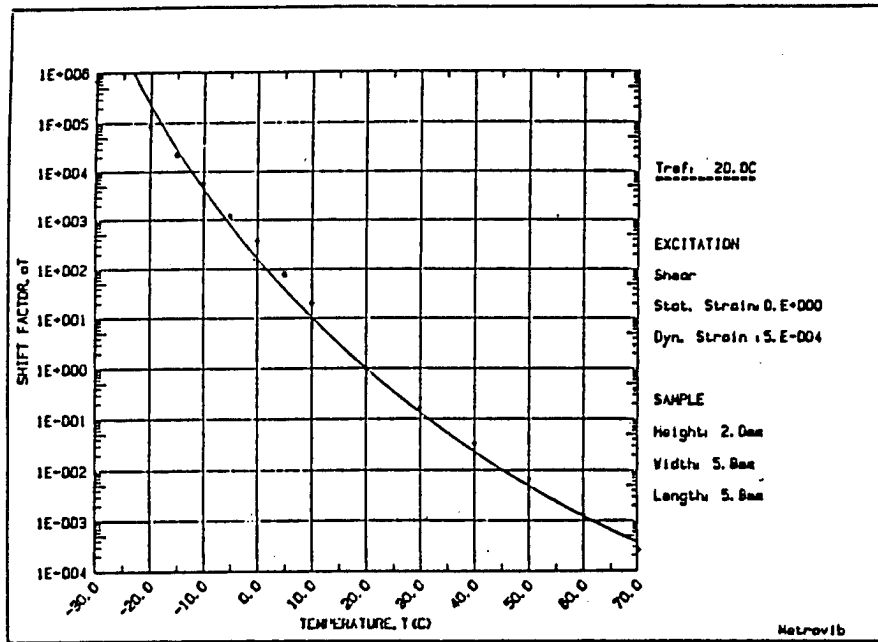


Figure 1a - M1: Shift factor

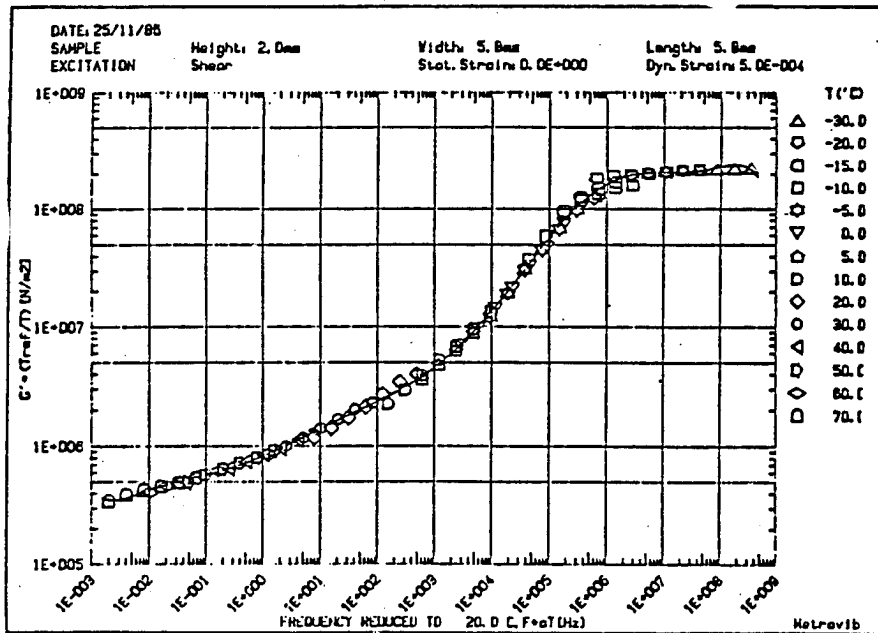


Figure 1b - M1: Shear modulus

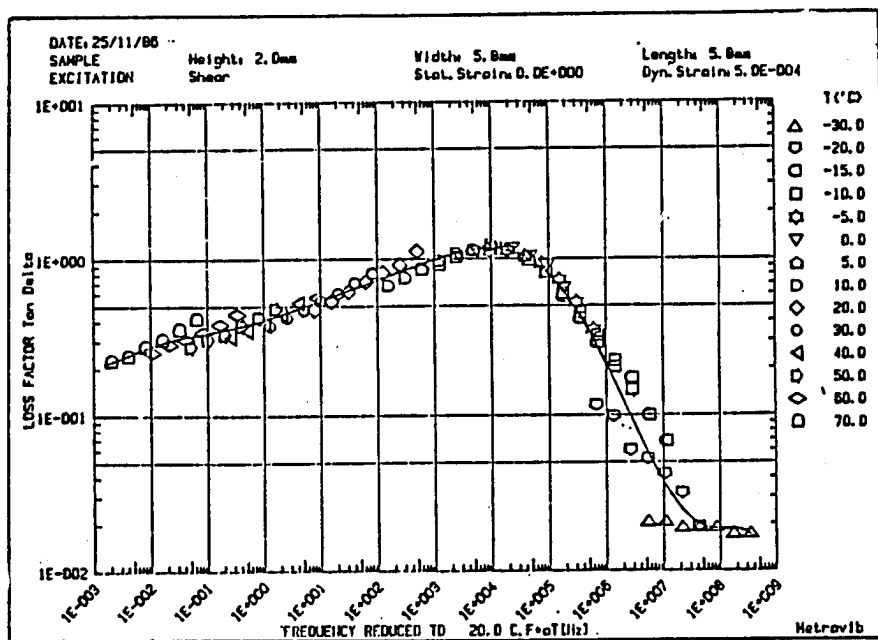


Figure 1c - M1: Loss factor

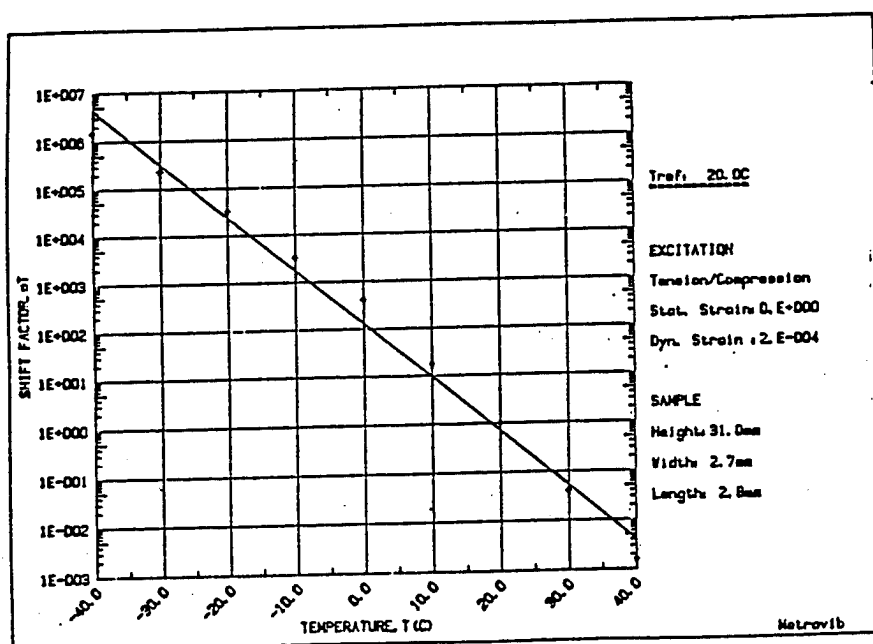


Figure 2a - M4: Shift factor

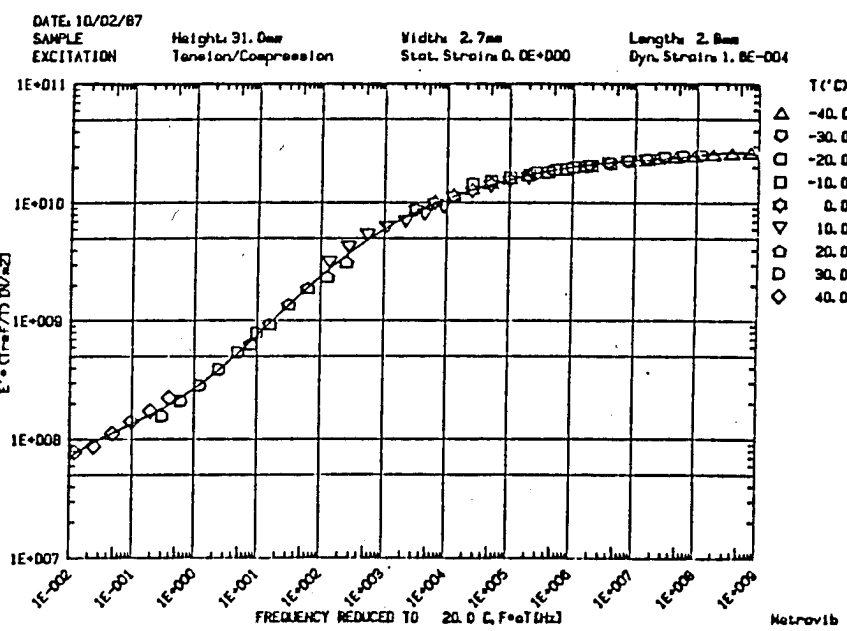


Figure 2b - M4: Shear modulus

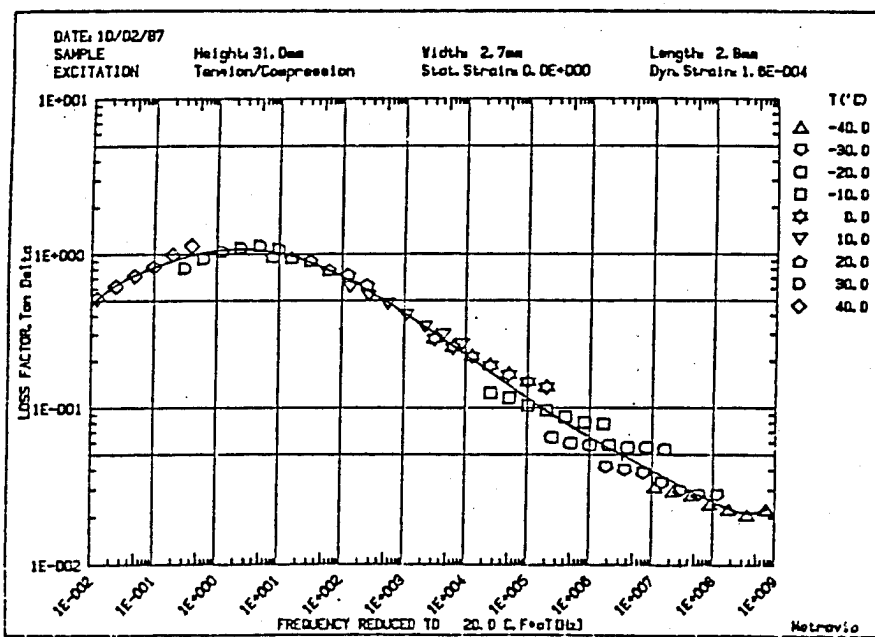


Figure 2c - M4: Loss factor

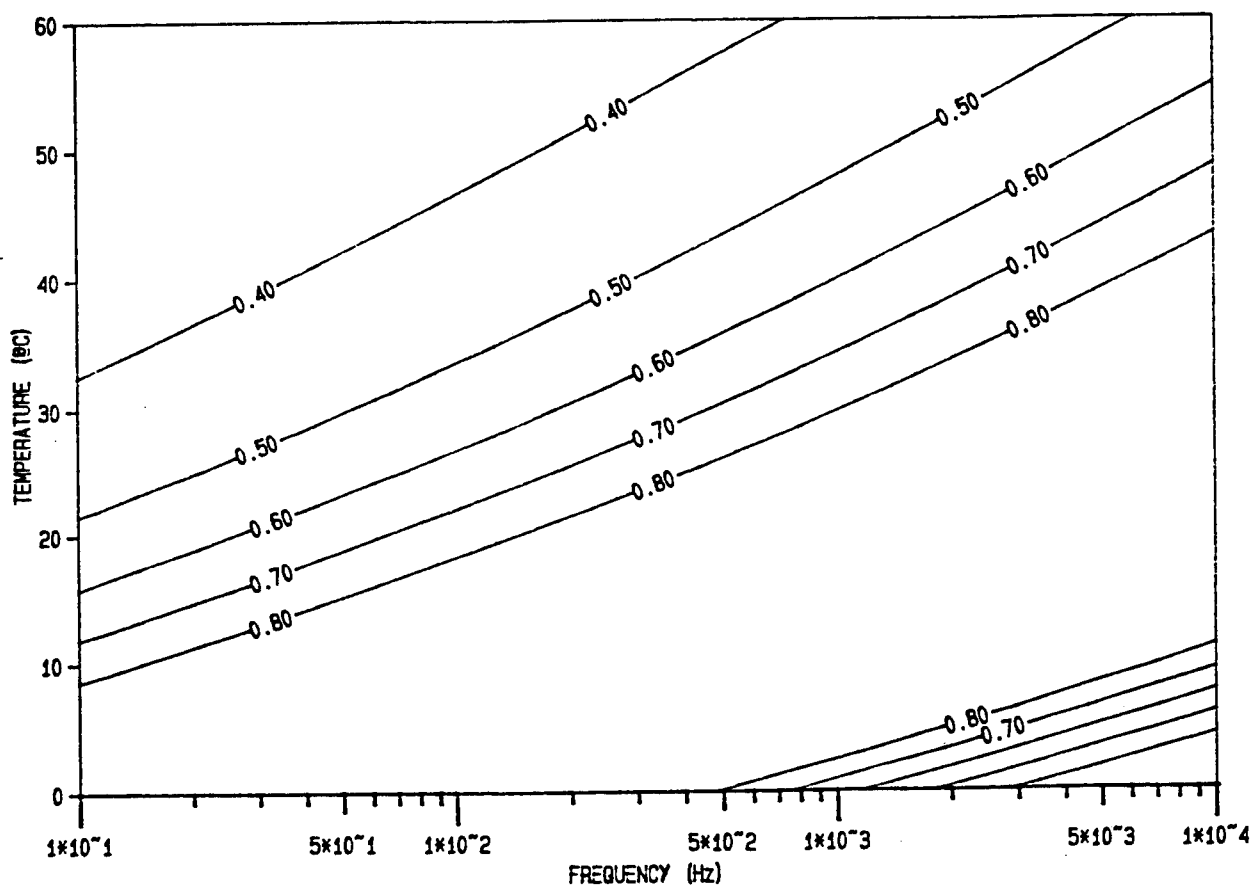


Figure 3 - M1: Contour lines for $\beta = 0.4 ; 0.5 ; 0.6 ; 0.7 ; 0.8$

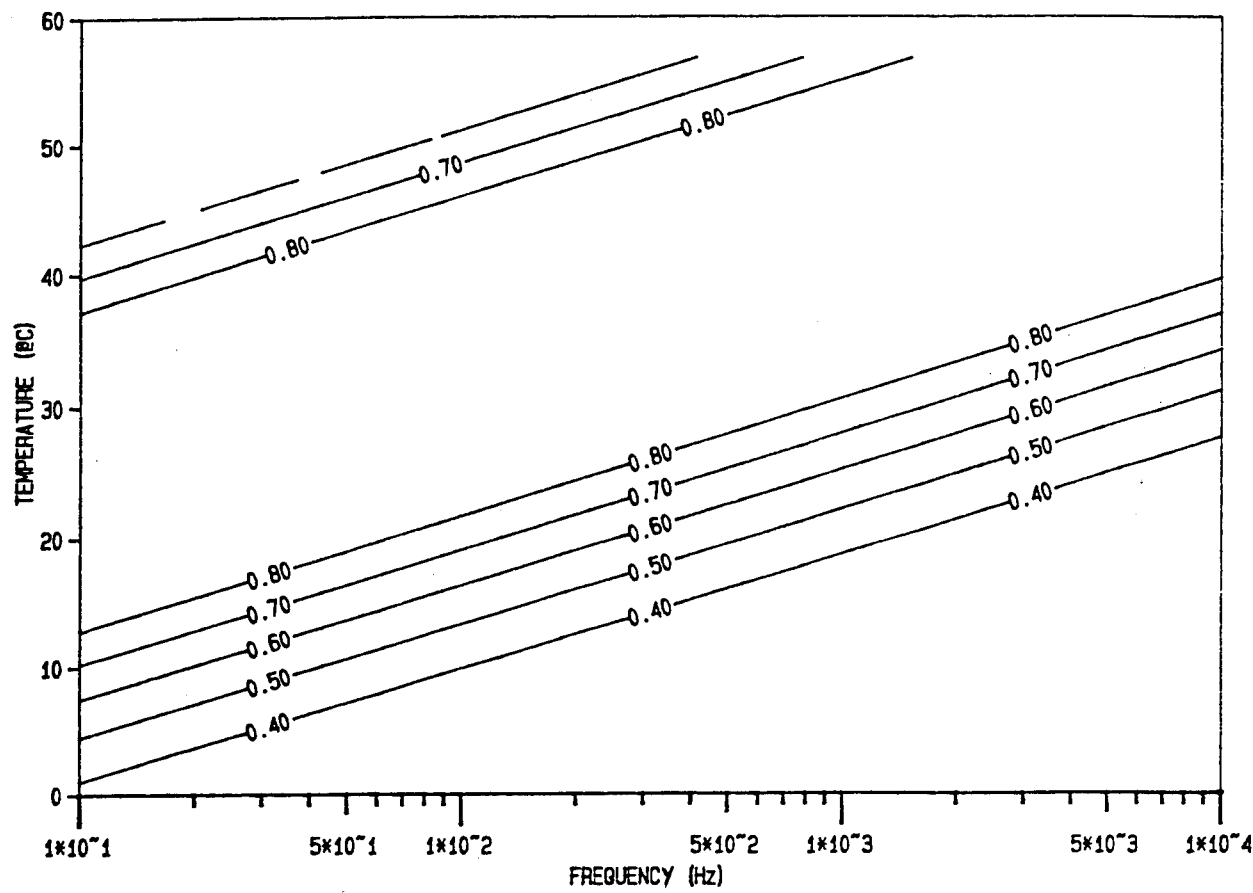


Figure 4 - M4: Contour lines for $\beta = 0.4 ; 0.5 ; 0.6 ; 0.7 ; 0.8$

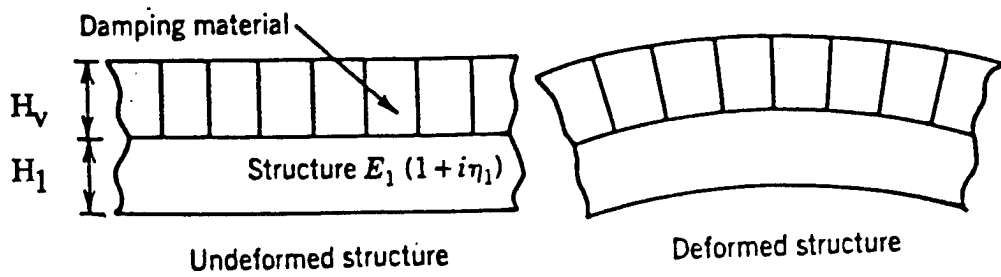


Figure 5 - Unconstrained damping treatment

Structure : $E_v(1+j\beta)$

Viscoelastic layer : $E_1(1+j\eta_1)$, $\eta_1 \ll 1$

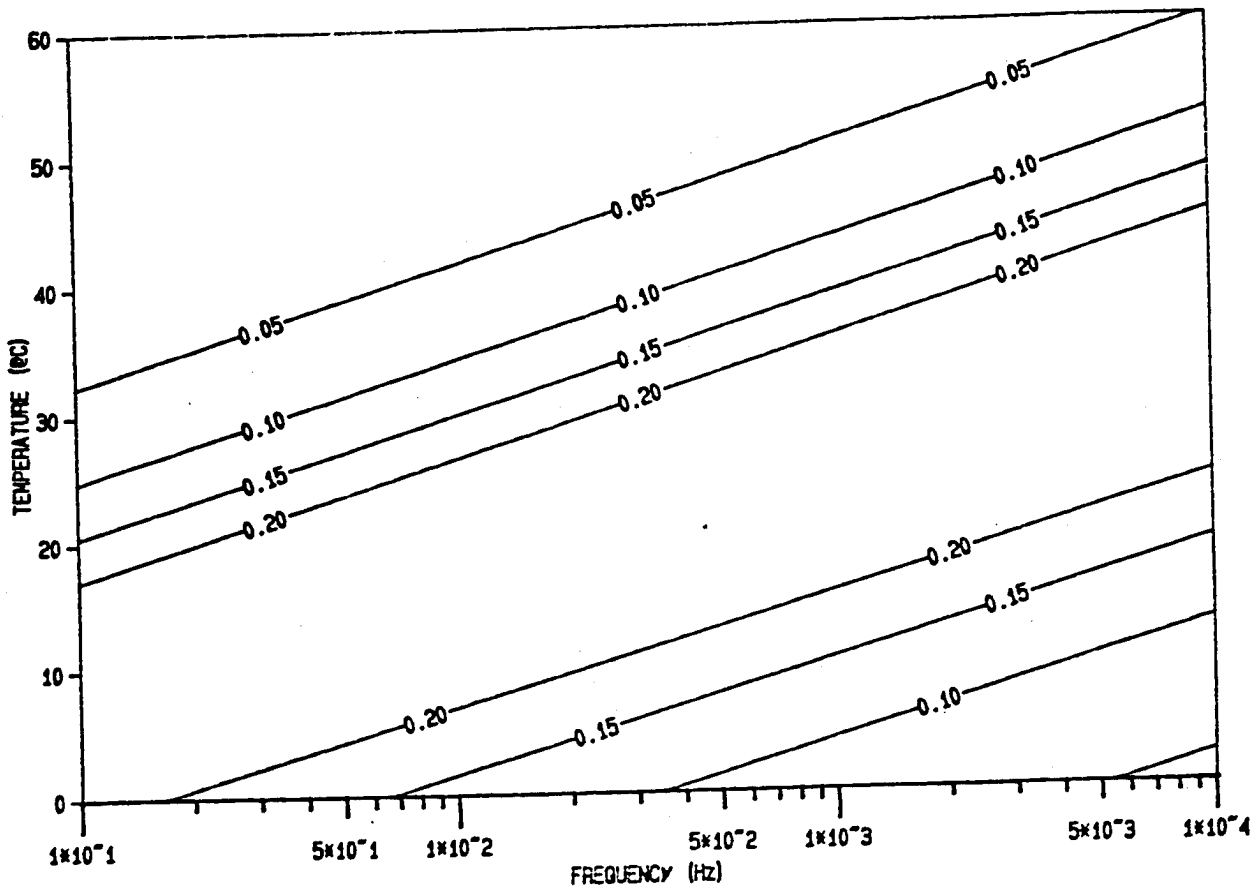


Figure 6 - Extensional damping . Contour lines for $\eta = 0.05 ; 0.1 ; 0.15 ; 0.2$

DAMPED BEAM

STEEL $H_1 = 0.01$ m

M4 $H_v = 0.02$ m

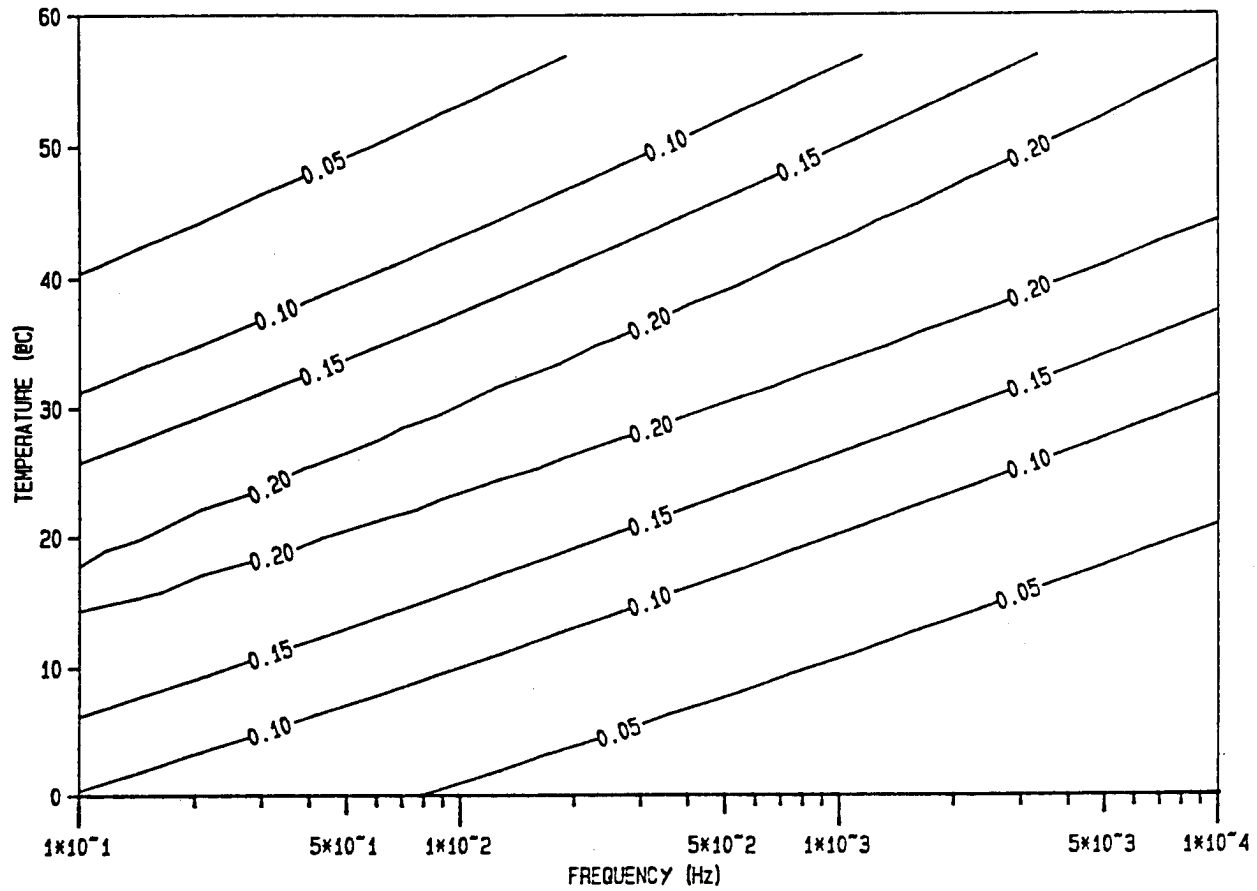


Figure 7 - Extensional damping . Contour lines for $\eta = 0.05 ; 0.1 ; 0.15 ; 0.2$

DAMPED BEAM
 STEEL $H_1 = 0.01$ m
 M5 $H_v = 0.02$ m

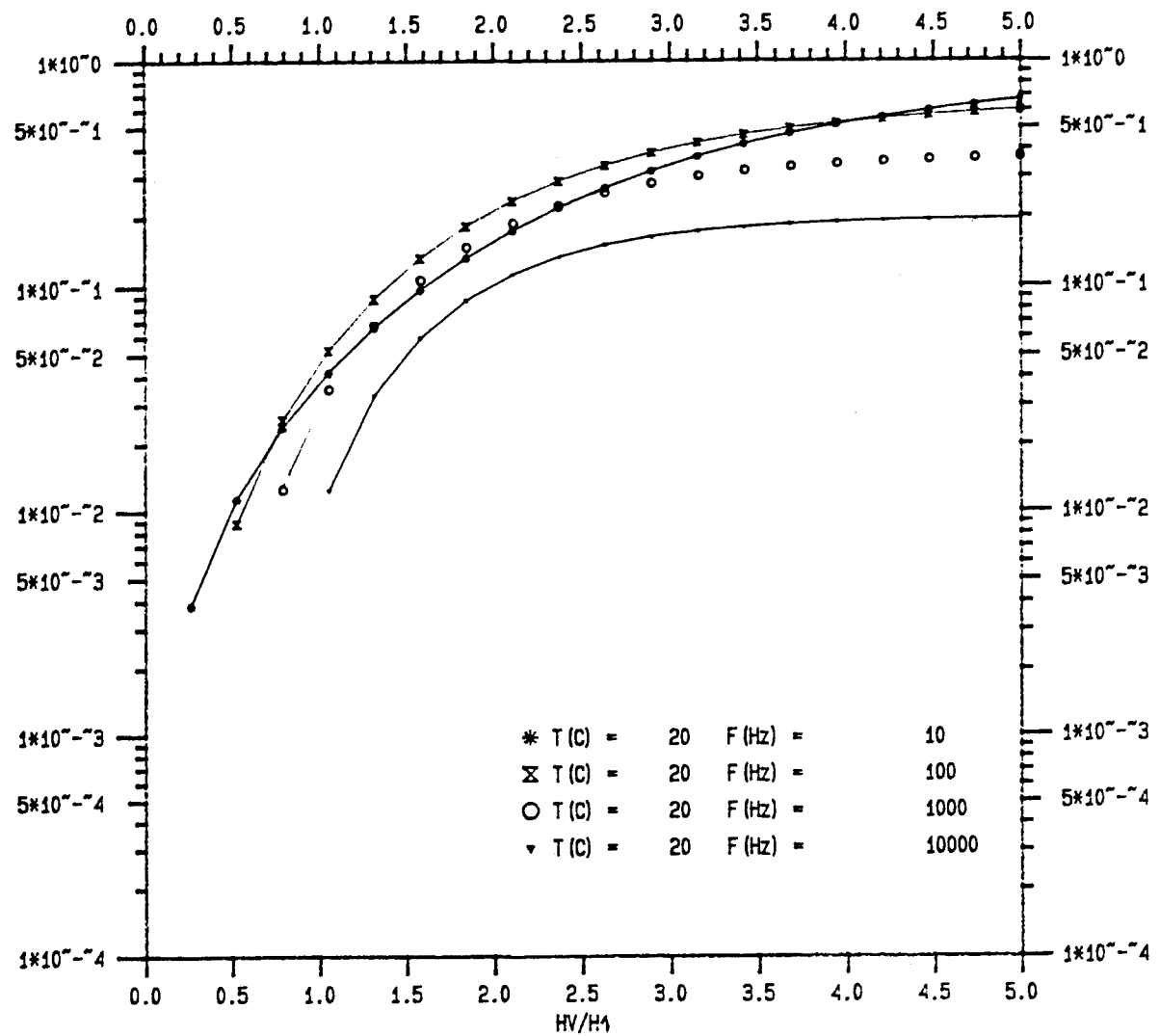


Figure 8 - Extensional damping - Composite loss factor
 DAMPED BEAM
 STEEL $H_1 = 0.01$ m
 M4

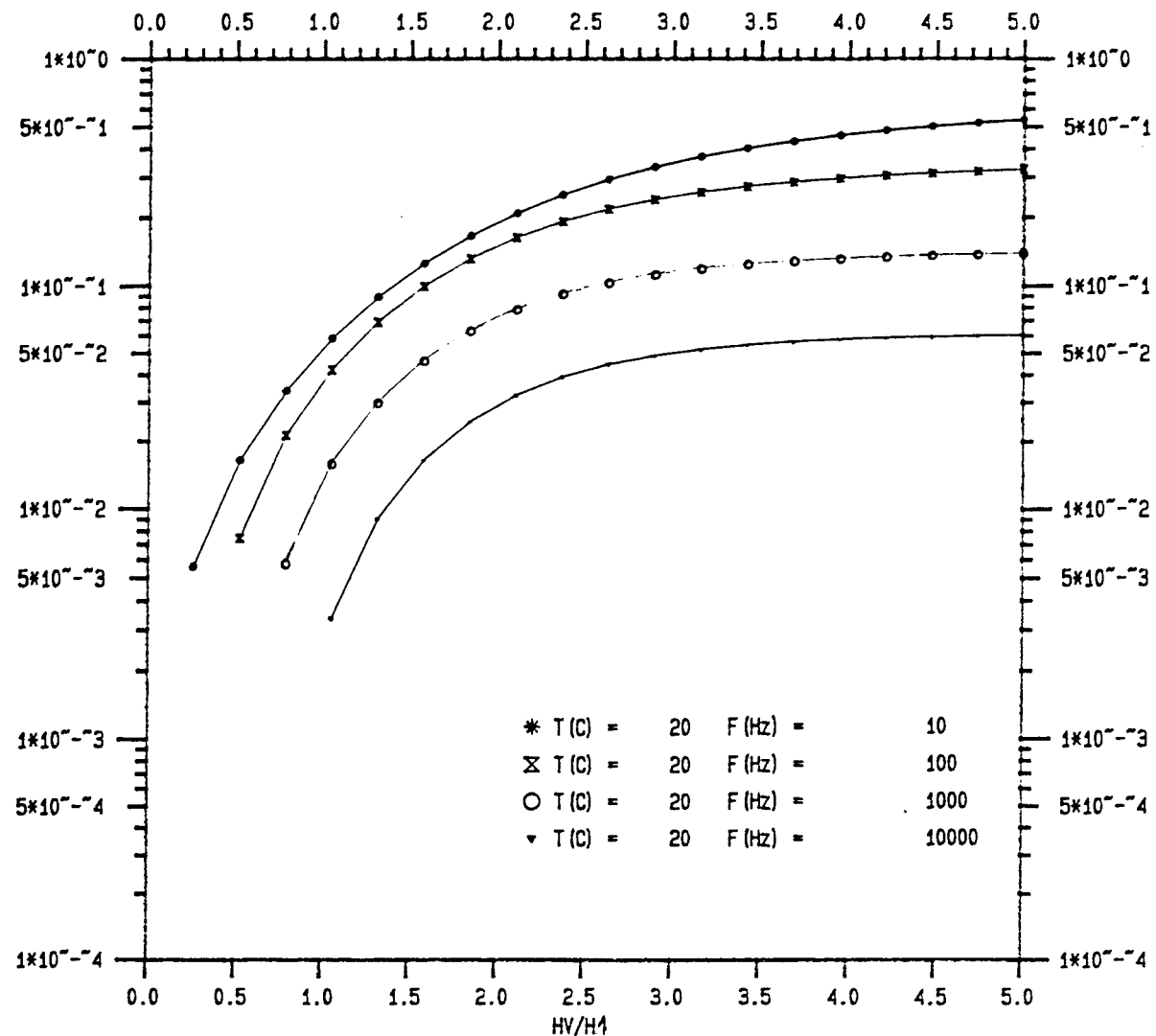
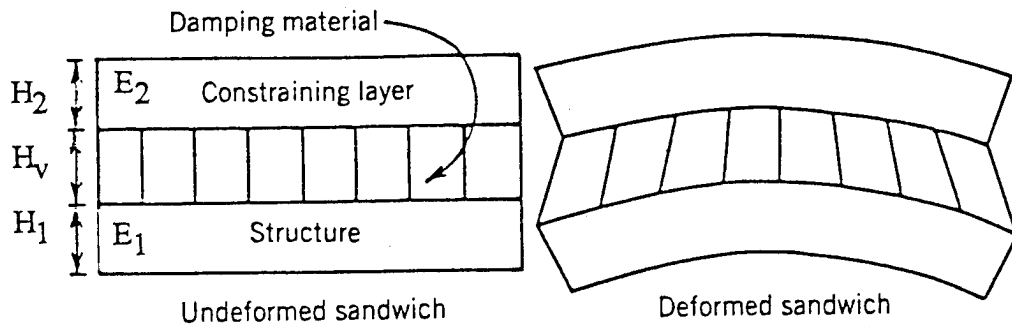


Figure 9 - Extensional damping - Composite loss factor
 DAMPED BEAM
 STEEL $H_1 = 0.01$ m
 M5



$$M = E_2/E_1$$

$$R = H_2/H_1$$

$$3MR(R+1)^2$$

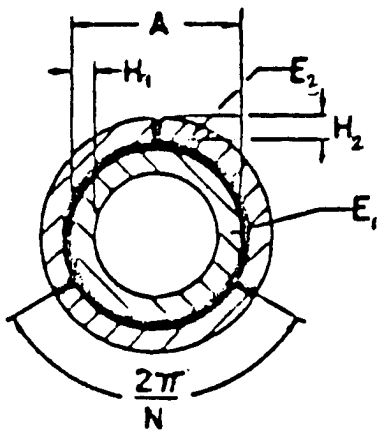
$$Y_0 = \frac{3MR(R+1)^2}{(MR+1)(MR^3+1)}$$

$$\frac{Y}{Y_0} = 1 + 2 \frac{H_v}{H_1 + H_2}$$

$$B_v = \frac{E_1 H_1^3 + E_2 H_2^3}{(EI)_0} = \frac{12}{1-v_1^2} - \frac{1}{1-v_2^2} \quad (\text{with } v_1 = v_2 = 0 \text{ for a beam})$$

$$d_0 = \frac{H_1 + H_2}{2}$$

Figure 10 - Shear damping for a plate or a beam



$$M = E_2/E_1$$

$$R = H_2/H_1$$

$$S = H_1/A$$

$$T = 1 + 2RS$$

$$8MN^2(T^3-1)^2 \sin^2(\pi/N)$$

$$Y_0 = \frac{9\pi^2(T^2-1) \{(1-(1-2S)^4) + M(T^4-1)\} - 8MN^2(T^3-1)^2 \sin^2(\pi/N)}{8MN^2(T^3-1)^2 \sin^2(\pi/N)}$$

$$Y = Y_0$$

$$(EI)_0 = E_1 A^4 \left\{ \frac{\pi(1-(1-2S)^4)}{64} + \frac{\pi M(T^4-1)}{64} - \frac{MN^2(T^3-1)^2 \sin^2(\pi/N)}{72\pi(T^2-1)} \right\}$$

$$m = (\pi/4) \{ \rho_2((A+2H_2)^2 - A^2) + \rho_1(A^2 - (A-2H_1)^2) \}$$

Figure 11 - Shear damping for a tube

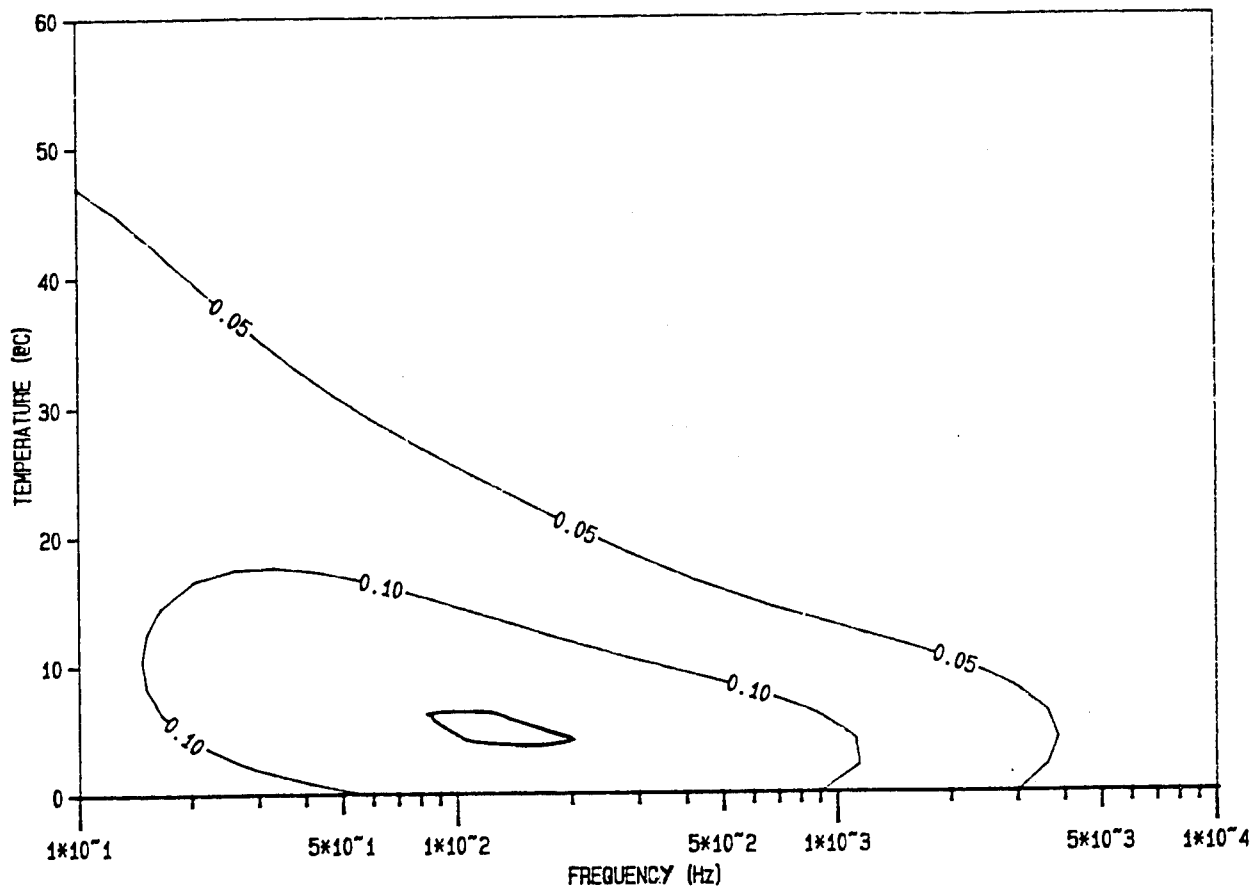


Figure 12 - Shear damping . Contour lines for $\eta = 0.05 ; 0.1 ; 0.15 ; 0.2$
 DAMPED BEAM
 STEEL $H_1 = 0.01$ m
 M1 $H_v = 0.001$ m
 STEEL $H_2 = 0.002$ m

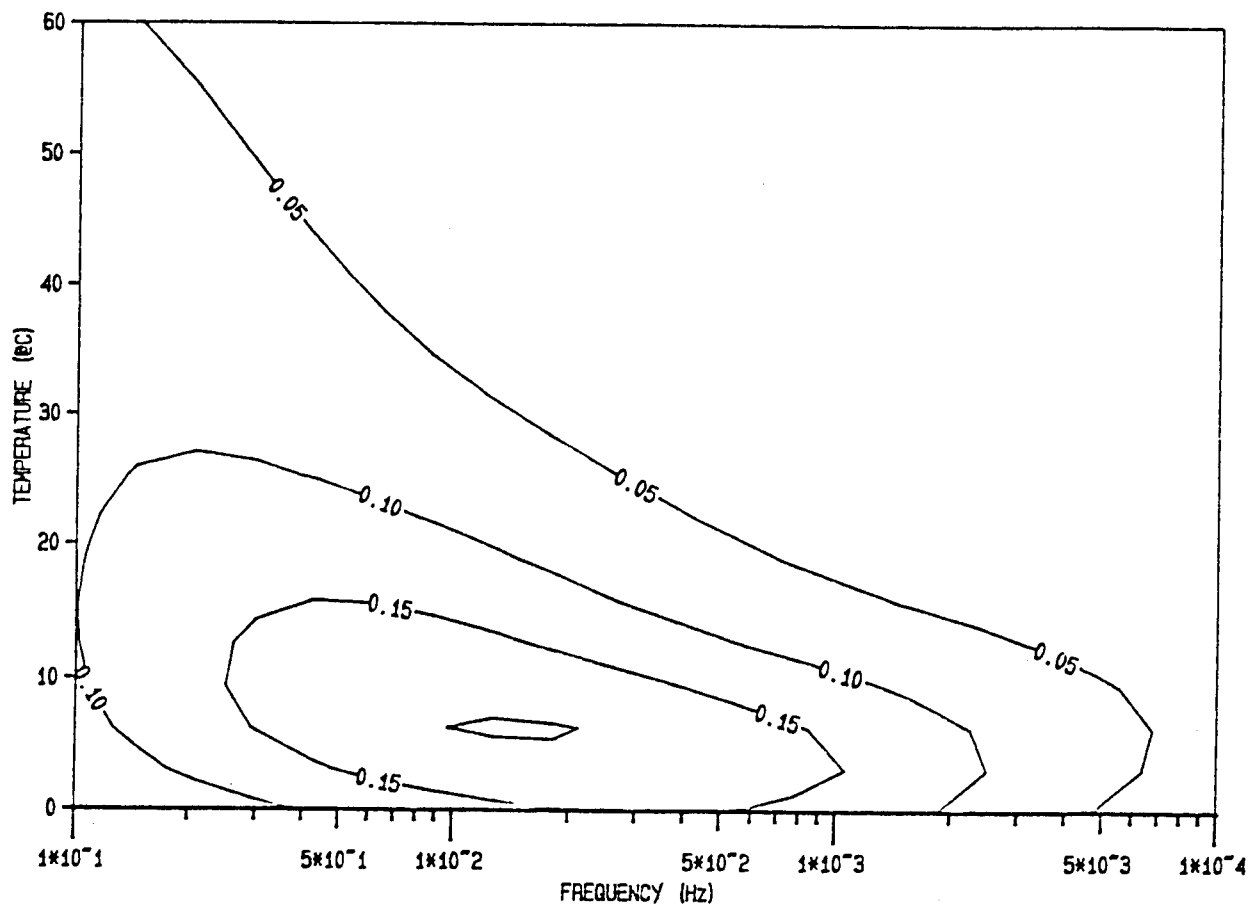


Figure 13 - Shear damping . Contour lines for $\eta = 0.05 ; 0.1 ; 0.15 ; 0.2$
DAMPED BEAM
STEEL $H_1 = 0.01$ m
M1 $H_v = 0.001$ m
Al $H_2 = 0.006$ m

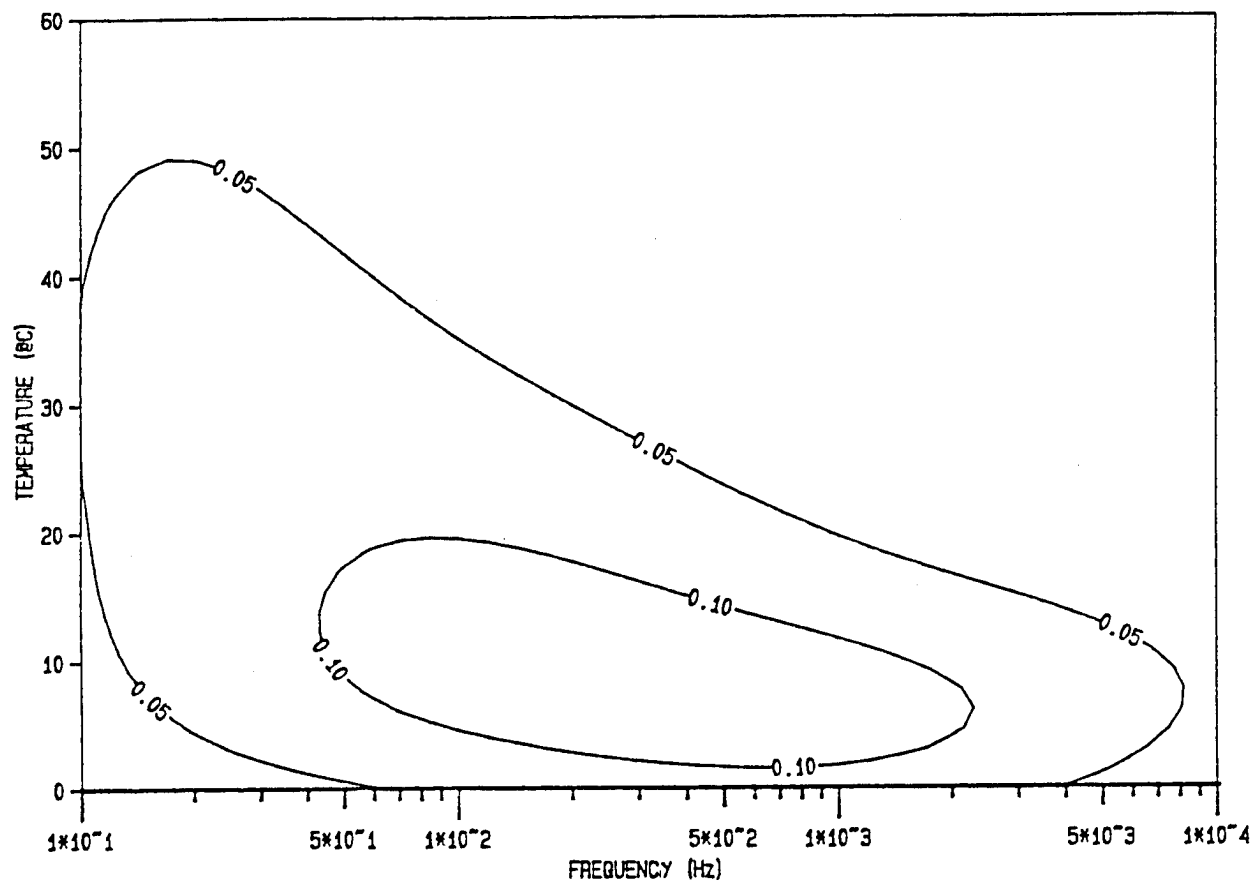


Figure 14 - Shear damping . Contour lines for $\eta = 0.05 ; 0.1 ; 0.15 ; 0.2$

DAMPED BEAM

STEEL $H_1 = 0.01$ m

M1 $H_V = 0.001$ m

CVR $H_2 = 0.009$ m

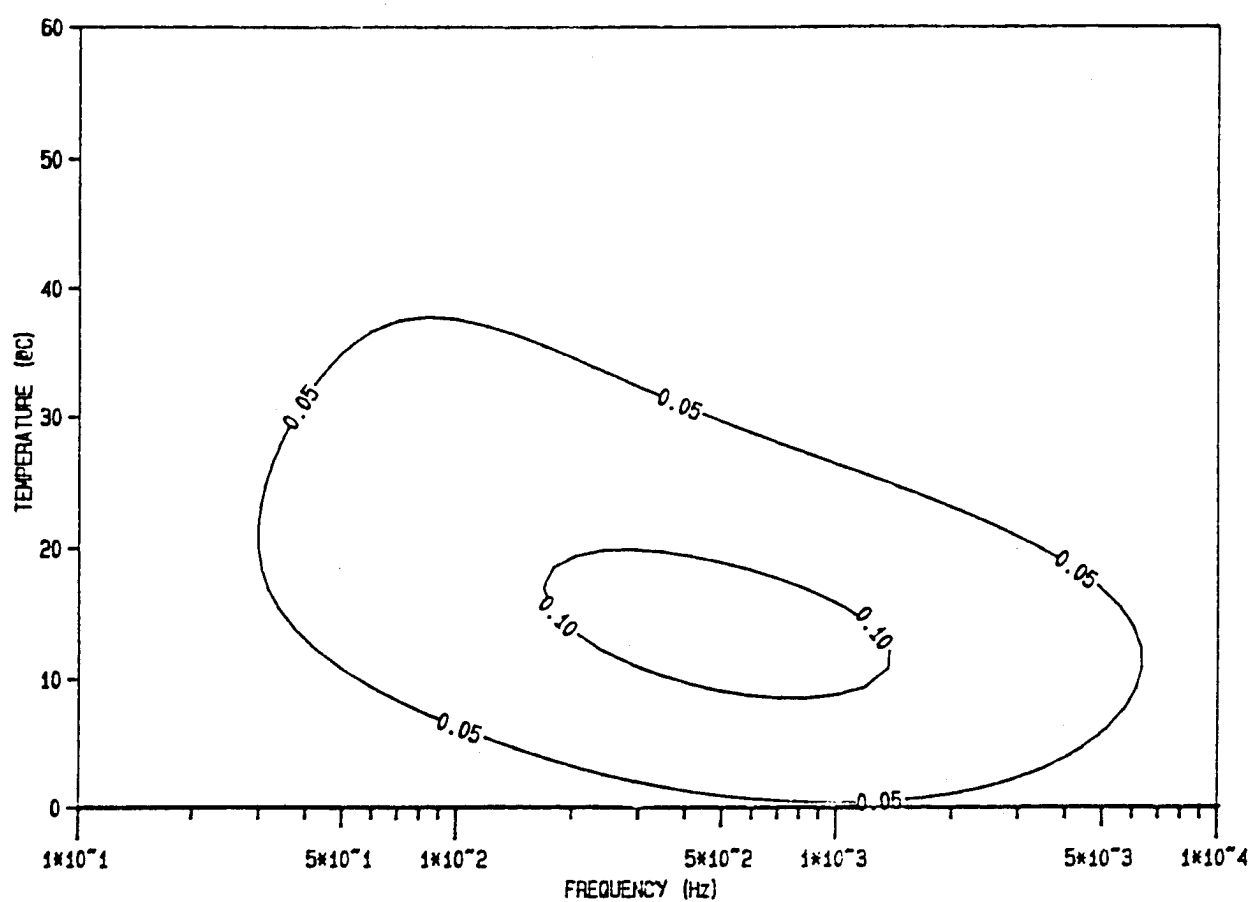


Figure 15 - Shear damping . Contour lines for $\eta = 0.05 ; 0.1 ; 0.15 ; 0.2$

DAMPED BEAM
 STEEL $H_1 = 0.01$ m
 $M_2 \quad H_v = 0.001$ m
 STEEL $H_2 = 0.002$ m

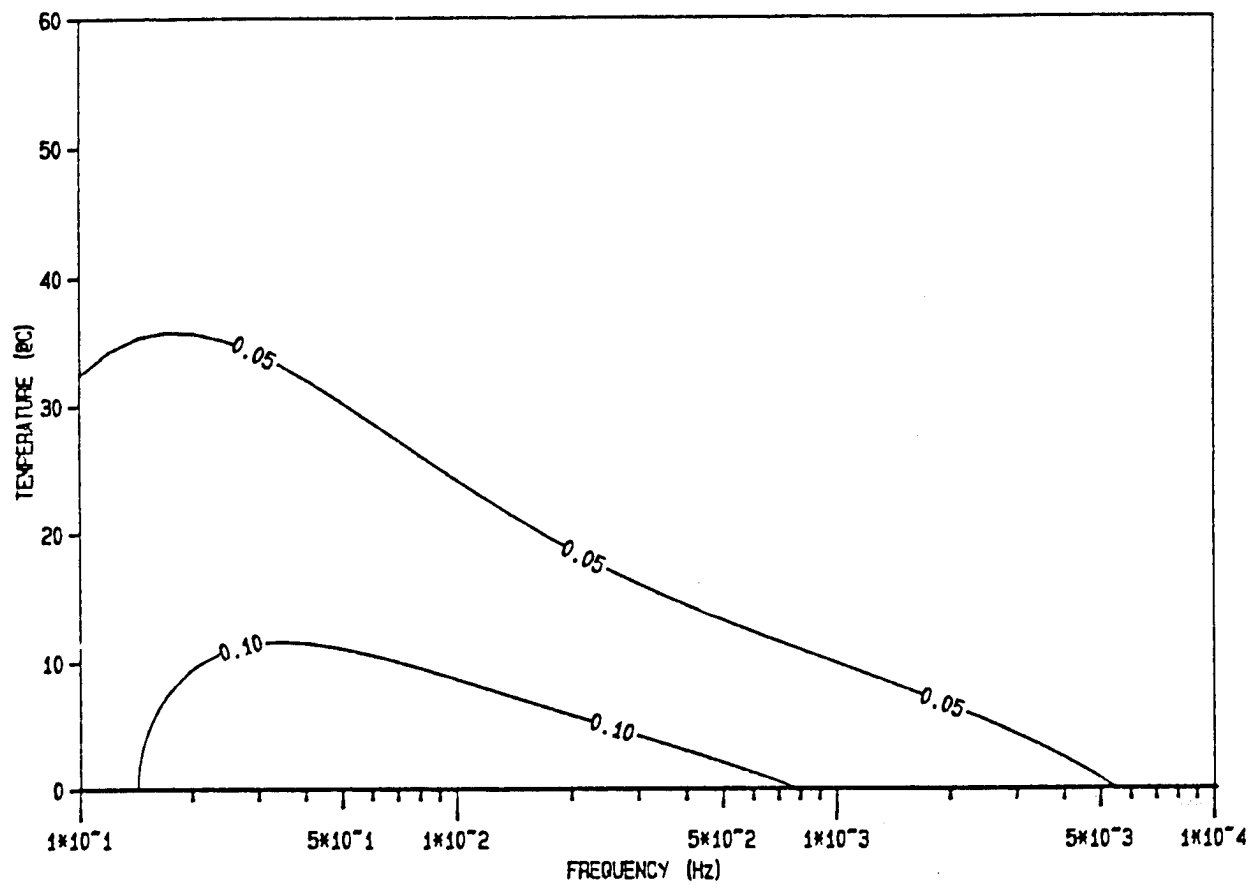


Figure 16 - Shear damping . Contour lines for $\eta = 0.05 ; 0.1 ; 0.15 ; 0.2$

DAMPED BEAM

STEEL $H_1 = 0.01$ m

M3 $H_v = 0.001$ m

STEEL $H_2 = 0.002$ m

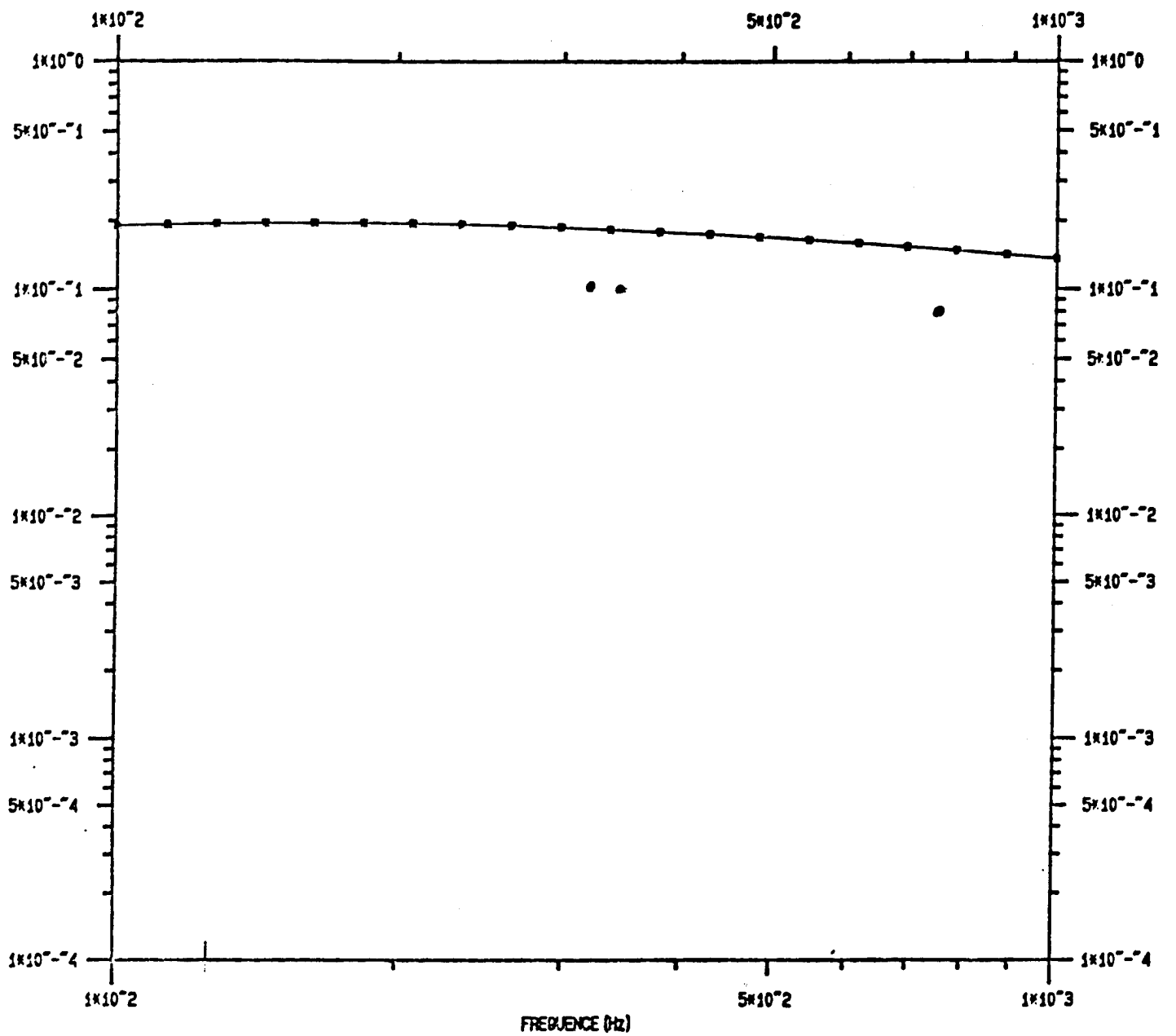


Figure 17 - Shear damping .Loss factor versus frequency for $T = 27^{\circ}\text{C}$
 Theoretical curve and experimental points (x)
 DAMPED BEAM
 STEEL $H_1 = 0.008\text{ m}$
 VISCO $H_v = 0.0017\text{ m}$
 STEEL $H_2 = 0.0025\text{ m}$

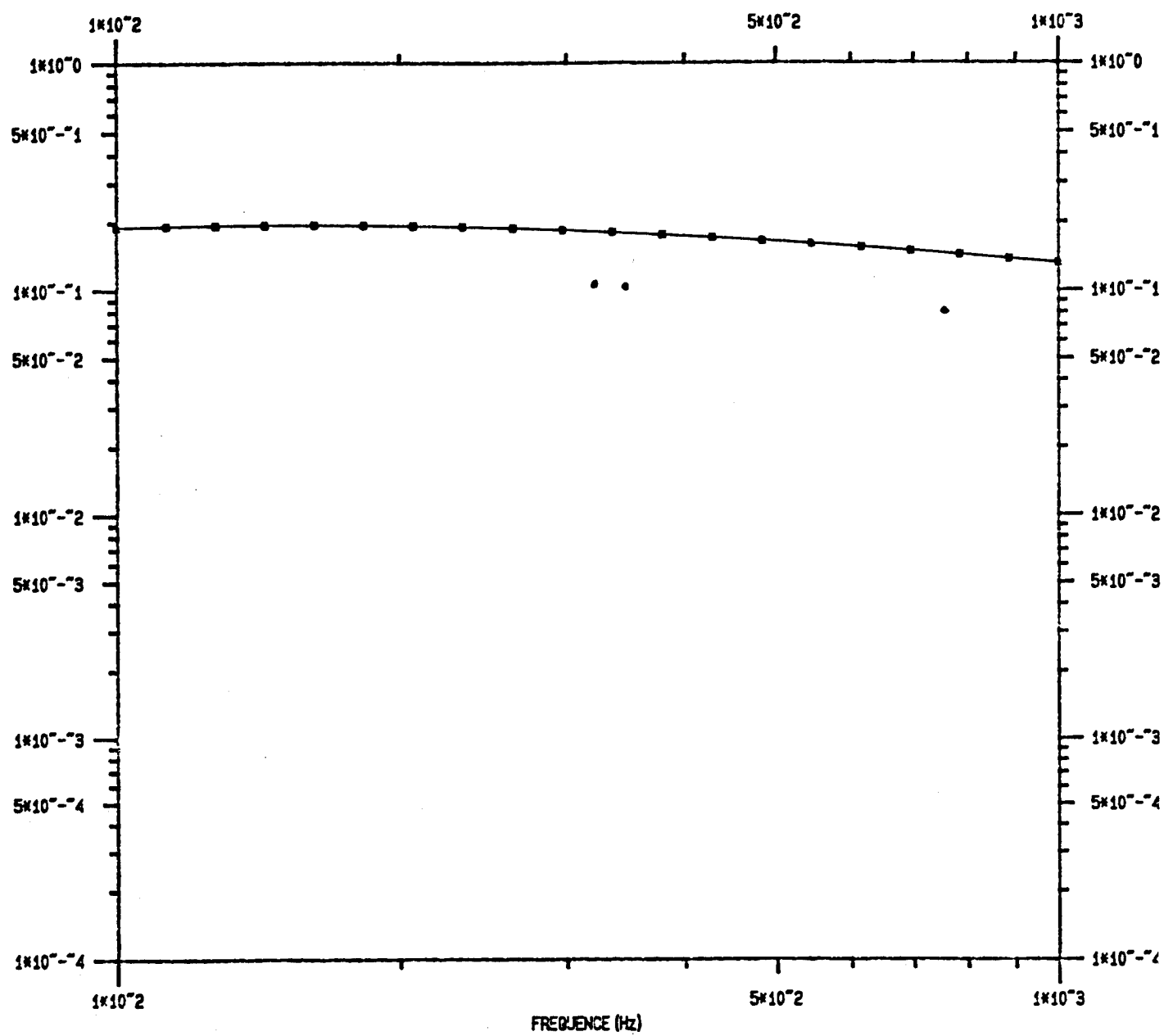


Figure 18 - Shear damping .Loss factor versus frequency for $T = 27^{\circ}\text{C}$
 Theoretical curve and experimental points (x)
DAMPED BEAM
 STEEL $H_1 = 0.008 \text{ m}$
 VISCO $H_v = 0.0025 \text{ m}$
 STEEL $H_2 = 0.002 \text{ m}$

REFERENCES

- 1 - Ahid D. Nashif, David I.G. Jones and John P. Henderson
'Vibration damping', Wiley, 1985
- 2 - D. Ross, E.E. Ungar and E.M. Kerwin,Jr
'Damping of plate flexural vibrations by means of viscoelastic laminates', Structural damping, ASME, New-York, pp. 44-88, 1959
- 3 - H. Oberst
'Ueber die Dämpfung der Biegeschwingungen dünner Bleche durch fest haftende Beläge', Acustica, Vol. 2, Akustische Beihefte N° , 1952, pp. 181-194.
(Translation by H.L.Blackford, Inc., 24 Commerce St., Newark, N.J.)
- 4 - J.E.Ruzicka, T.F.Derby, Dale W. Shubert and J.S. Pepi
'Damping of structural composites with viscoelastic shear-damping mechanisms'
NASA CR - 742, March 1967
- 5 - D.J. Mead and S. Markus
'Loss factors and resonant frequencies of encastre damped sandwich beams'
J. Sound Vib, 12(1), 99-112, 1970

The Application of Statistical Energy Analysis in The Design of Viscoelastic Passive Damping

by

Derrick W. Johnson

Roy Ikegami

K. Scott Hunziker

BOEING AEROSPACE
Box 3999, MS 82-97
Seattle, WA 98124-2499

ABSTRACT

This paper presents the results of a study to determine the feasibility of using statistical energy analysis (SEA) methods for the design of viscoelastic passive damping treatments. The primary emphasis of the study was to determine the applicability of SEA methods for predicting the response of damped structures in the high frequency, high modal density regime where modal methods such as the modal strain energy technique become inappropriate because of model complexity or uncertainties in geometry. The other area of interest was the use of SEA augmented by modal strain energy methods as a type of substructuring technique for large, complex structures. To accomplish this investigation, the VAPEPS SEA code was used to model a component test article in several damped configurations and the results were compared to available test data to determine the validity of the analysis methods. The component test article was constructed during the Reliability for Satellite Equipment in Environmental Vibration (RELSAT) program as a developmental platform representative of satellite equipment support structures which are subjected to high-level vibroacoustic environments typical of launch vehicles.

INTRODUCTION

Recent advances in the field of viscoelastic passive damping have been numerous and cover a wide variety of disciplines. They were successfully used in the "Reliability for Satellite Equipment in Environmental Vibration (RELSAT)" program to demonstrate the use of viscoelastic passive damping to control the vibroacoustic response of satellite avionics equipment (reference 1). In particular, an analysis technique utilizing finite element modeling and the modal strain energy (MSE) method is now being used to analytically predict the effects of applying viscoelastic damping treatments to structures (reference 2). Since the technique is based on finite elements, it is possible to analyze a wide variety of structural configurations, however, the size of the model required to accurately predict damping rapidly increases with the size and complexity of the structure. For this reason, a study is currently in progress at Boeing Aerospace to determine the feasibility of using finite element modeling and MSE to analyze the design of damping treatments on the substructure-level and statistical energy analysis (SEA) to evaluate the resulting changes in the vibroacoustic responses on the system level. This paper presents the approach that is being used in the study and discusses some preliminary results.

BACKGROUND

The study described in this paper is an extension of work that was performed by Boeing Aerospace on the RELSAT program. The program was started approximately 6 years ago by the AFWAL Flight Dynamics Laboratory under the direction of Dr. Lynn Rogers and was completed last year. The RELSAT program was a study to investigate the use of viscoelastic passive damping technology to reduce the structural response of typical satellite systems to high-level acoustic noise.

The approach used was to (1) design passive damping treatments into an example satellite system and (2) perform acoustic and modal survey testing on the structure to verify their effectiveness. A pictorial view of the program methodology is shown in figure 1. The Boeing Aerospace Inertial Upper Stage (IUS), which is subjected to the severe launch vibroacoustic environments of the Space Shuttle and Titan launch vehicles, was selected as the baseline satellite system. System requirements were outlined, system disturbances were identified, and a set of goals for a redesigned damped dynamic test article were established. A sketch of the IUS is shown as the first illustration in figure 1. The harshest vibrational environment endured by the IUS occurs during launch when the acoustic noise in the Space Shuttle payload bay typically reaches levels of 145 db overall from 20 to 2000 Hz. The design of damping treatments for the IUS dynamic test vehicle

(DTV) was carried out in several stages using finite element techniques and the modal strain energy (MSE) method to analytically predict the effectiveness of the designs.

To conduct the design development phase in a cost effective manner, a smaller substructure representative of the IUS DTV equipment support section was designed and fabricated. A finite element model of the substructure is shown as the second illustration in figure 1. Several design, analysis, and test cycles were performed to evaluate a wide variety of damping concepts and to establish the validity of the analysis methods. The preliminary design development on this smaller substructure proved to be very valuable in choosing damping treatments for application to the full scale DTV.

The DTV was then analyzed by breaking it into several substructures representative of critical portions of the structure. Damping treatments were designed and optimized for these substructures and then applied to the full vehicle for testing. All of the damping treatments for the DTV were designed and optimized using finite element analysis and the MSE method to predict damping levels. Figure 2 shows the finite element models and lists the damping treatments designed with each one. The global model described the entire DTV in the test configuration including a simulated spacecraft payload structure. This model was used only to design a ring damping treatment for the global ring type modes of vibration. The model was much too coarse to design damping treatments for the local substructures. The other three substructure models represent critical isolated portions of the DTV and were used to design the remainder of the damping treatments. Detailed descriptions of the damping treatments and the design optimization process are contained in reference 3.

Figure 3 shows the DTV located in the Boeing Aerospace Environmental Test Laboratory acoustic cell for testing. The acoustic testing revealed that the structural response at all equipment locations were substantially reduced by the addition of the damping treatments. A summary of the RMS response of five critical IUS avionics components is given in figure 4. Overall response levels at the avionics equipment attachment points were typically reduced by 62%. Acceleration response power spectral density (PSD) envelopes for an encrypter located on the DTV equipment support deck are shown in figures 5 - 7 before and after the application of viscoelastic passive damping. This is typical of the types of reductions achieved. Analyses and tests were also performed to assess the impact of the damping treatments on IUS system-level requirements such as vehicle weight, outgassing, strength, and heat transfer.

Although the results of the acoustic tests of the DTV showed that significant decreases in the vibroacoustic responses were achieved through application of the viscoelastic passive damping treatments, a good test/analysis correlation of predicted and measured modal damping and vibration levels could not be obtained. Due to the large size and complexity of the finite element models which include the viscoelastic damping treatments, it was not economically feasible to run a dynamic analysis with an overall finite element structural model of the DTV. Ordinary substructuring techniques based on component mode synthesis would not significantly decrease the problem size because no simple boundaries exist between the various substructures, and a large number of component modes would have to be carried to adequately predict the local deformations in the substructures.

Through the RELSAT program, it was realized that the modal strain energy method is a powerful analysis tool for damping design that is limited primarily by the ability to model the damped structure with finite elements. Extremely large, detailed models must be developed which tend to be very costly in terms of computer time to run the models and manpower to interpret the results. Areas identified for further research included the refinement of substructuring techniques and the development of an economical method to determine system-level responses from substructure-level analyses. The application of statistical energy analysis (SEA) methods was identified as a technique which should be investigated to address this issue. It was felt that SEA could potentially be a good method to track the principal energy paths of acoustic and vibration disturbances, to identify the critical substructures for the application of damping, and to envelope the system-level responses in the high-frequency 200- to 2000-Hz range.

STATISTICAL ENERGY ANALYSIS (SEA)

SEA is an analytical method to predict vibration and acoustic responses of dynamic systems by treating the structural or acoustical mode shapes and frequencies as statistical parameters. The dynamic energy is used to describe the state of the system and simple power balance equations describe the interactions between the coupled subsystems that constitute the dynamic system. Reference 4 contains a comprehensive overview of the development and engineering applications of the SEA method. As described in the reference, the general steps required in SEA to develop a model and calculate responses are outlined in figure 8. The first three steps are the development of the SEA models of the subsystems and their interactions. These steps require engineering experience and judgement. The last three steps involve computational procedures that can be performed through implementation of one of several available general purpose SEA computer codes.

For this study, the Vibroacoustic Payload Environment Prediction System (VAPEPS) code was used to perform the SEA response predictions. The VAPEPS code development was sponsored by NASA and the Air Force Space Division. The development and maintenance of the code is currently being performed by the Jet Propulsion Laboratory (JPL). In addition to the SEA option, VAPEPS provides a database of vibration and acoustic data that can be used with empirical and semiempirical techniques for determining vibroacoustic responses and test environments.

The SEA model of the IUS DTV that was developed for this study is shown in figure 9. An illustration of the DTV acoustic test configuration is shown with the associated power flow diagram for the dynamic system. The diagram describes the acoustic and structural subsystems and their interconnections. This model was used to predict the acoustic environment internal to the IUS interstage structure and the vibration response of a battery located on the interstage structure.

Equivalent plates were used for the SEA model of the interstage structure. The equivalent plate calculations are presented in figure 10. Two approaches were used in the equivalent plate calculations. The first approach included stiffening effects of the interstage rings by determining an equivalent plate thickness. The second approach considered the rings as boundary conditions.

The predicted IUS interstage internal acoustic environment is shown in figure 11 for the two equivalent plate modeling approaches. Also shown is the acoustic sound pressure level (SPL) data obtained from microphones located in the interstage internal volume during the acoustic test of the IUS DTV. Although good correlation was obtained with both approaches, the spectral levels predicted by the first approach appear to correlate better with the test data. The predicted acceleration PSD for the vibration response of the interstage battery is shown in figure 12. The PSD of the vibration responses measured by accelerometers mounted on the battery during the acoustic tests are also shown for comparison. It can be seen that the SEA prediction correlates fairly well with the test data, however, the correlation between the predicted and measured vibration responses does not appear to be as good as that obtained for the acoustic responses. One cause for this is VAPEP's inability to account for non-structural mass in its coupling and damping calculations. Currently, VAPEPS only uses non-structural mass in the conversion from energy to mean response for the entire element. This may be one area where finite element methods can be used to effectively augment the response predictions for avionics equipment and include the localized effects of a lumped mass.

SUMMARY

In summary, although the results of this study are still very preliminary, it appears that SEA may provide the means to analytically establish avionics component vibration and acoustic environments. Although the method requires an experienced user to obtain accurate results, it provides a systematic means for determining vibroacoustic responses that will be particularly useful when performing vehicle design trade studies in which predicting the absolute magnitude of the responses may not be as important as predicting the differences produced by changes in the design trade parameters. The acoustic test data obtained during the RELSAT program will be useful to correlate with SEA predictions of the differences in vibroacoustic responses produced by varying levels of substructure damping. This will be the emphasis of future efforts for this study.

During the RELSAT program, viscoelastic passive damping treatments were designed for an extremely complex structure using finite element structural modeling techniques and the MSE damping prediction method. By isolating portions of the structure down to substructures, it was possible to cost effectively design damping treatments for an otherwise intractable structure. The significant reductions in the vibroacoustic responses observed during the acoustic testing of the IUS DTV verified the viscoelastic passive damping design and analysis methodology. The MSE method was shown to be a powerful analysis tool that is limited primarily by the computational cost required to model a large complex damped structure with finite elements. This study is investigating the application of SEA methods to address this issue of economically determining system level responses utilizing the information provided by substructure level analyses. The results to date of this study and of the RELSAT program have demonstrated the use of new damping design and analysis methods and conclusively shown that viscoelastic passive damping has the potential to yield a system level payoff in the form of lower vibroacoustic environments and increased reliability for future space systems if incorporated early in the design cycle.

REFERENCES

1. Ikegami, R., Johnson, D.W., Walker, W.J., and Beck, C.J., "The Application of Viscoelastic Passive Damping to Satellite Equipment Support Structures", Jour. of Vibration, Stress, and Reliability in Design, Vol. 107, Oct. 1985, pp. 367-374.

2. Johnson, C.D. and Kienholz, D.A., "Finite Element Prediction of Damping in Structures with Constrained Viscoelastic Layers", Proc. 22nd Structures, Structural Dynamics, and Materials Conference, Atlanta, Ga., Part 2, April 6 - 8, 1981, pp 17-24.
3. Johnson, D.W., Ikegami, R., and Austin, E.M., "The Design and Analysis of Passive Damping for Aerospace Systems", Presented at AIAA 28th SDM Conference, Monterey, Ca., April 6-8, 1987.
4. Manning, J.E., "Statistical Energy Analysis - An Overview of Its Development and Engineering Applications", Proc. 59th Shock and Vibration Symposium, Vol. 1, pp 25 - 38, Oct. 18-20, 1988, Albuquerque, NM.

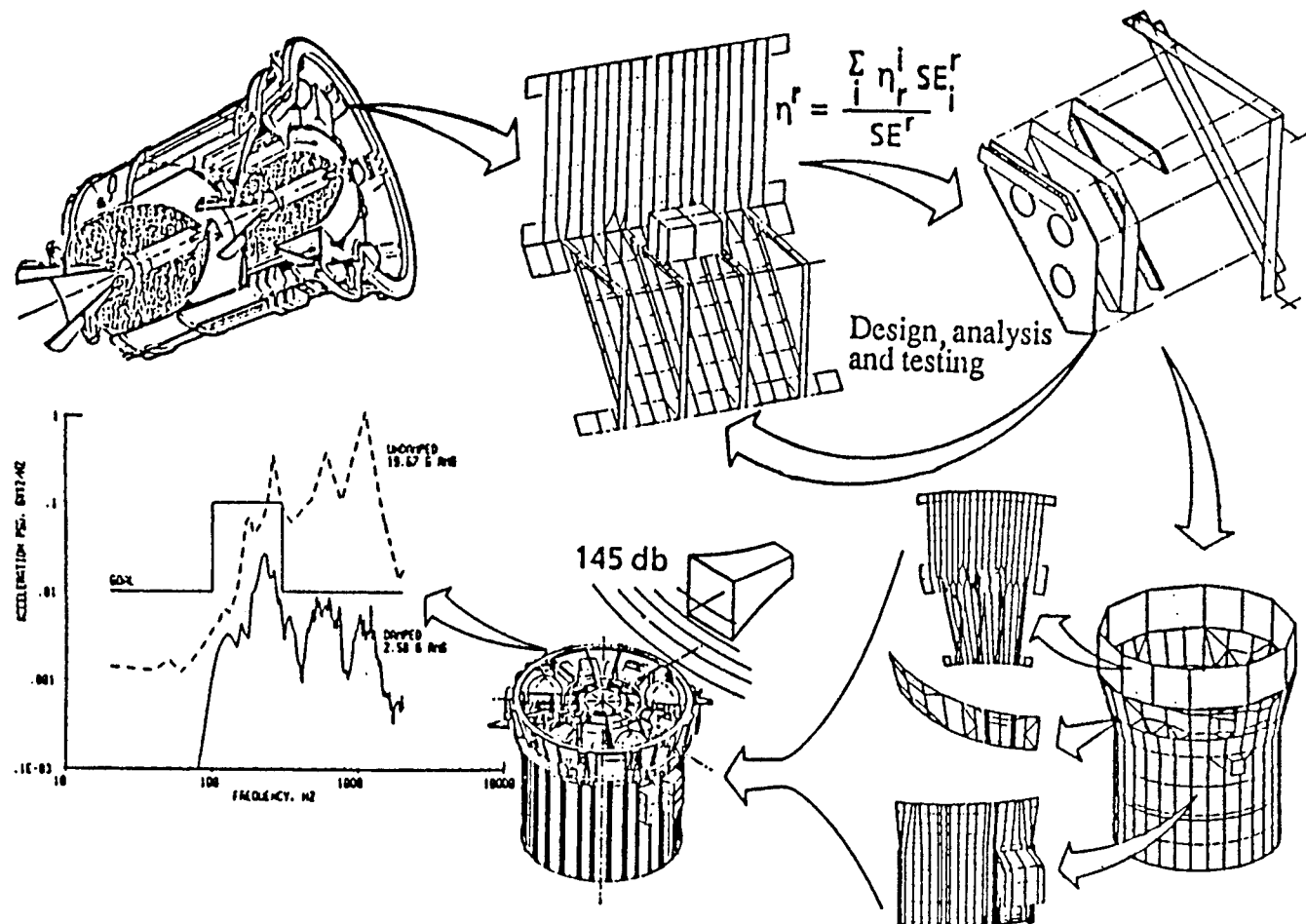


Figure 1. RELSAT Program Methodology

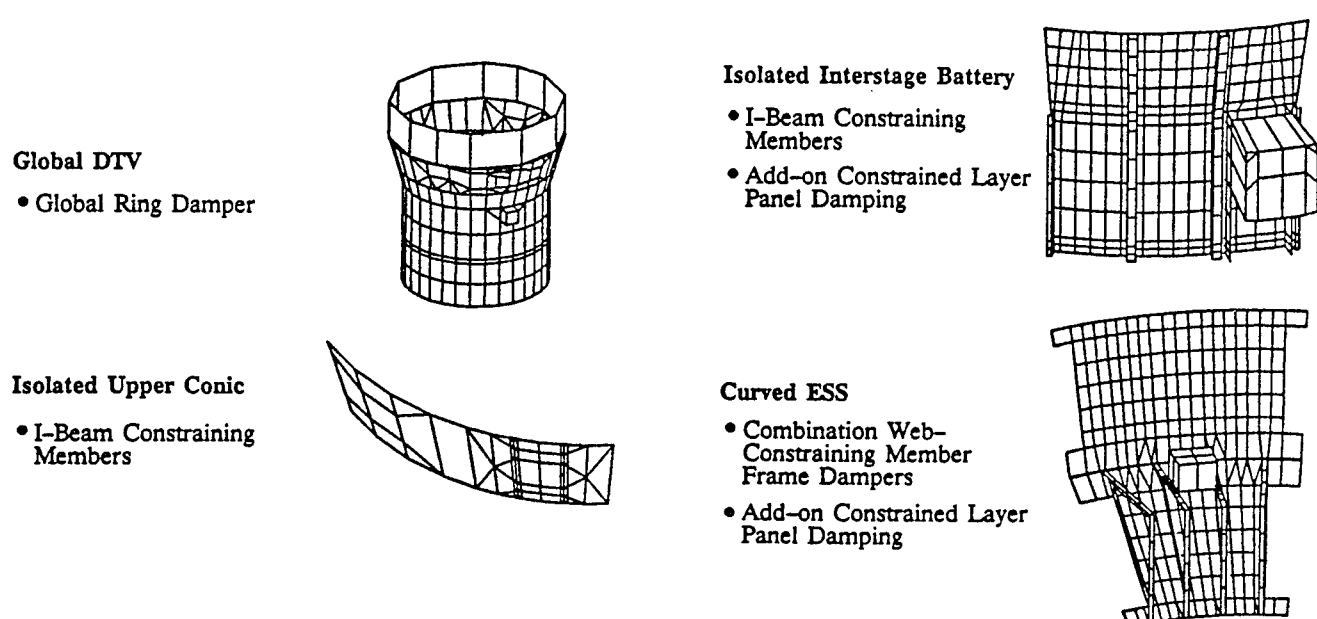


Figure 2. Summary of IUS DTV Finite Element Models and Damping Treatments

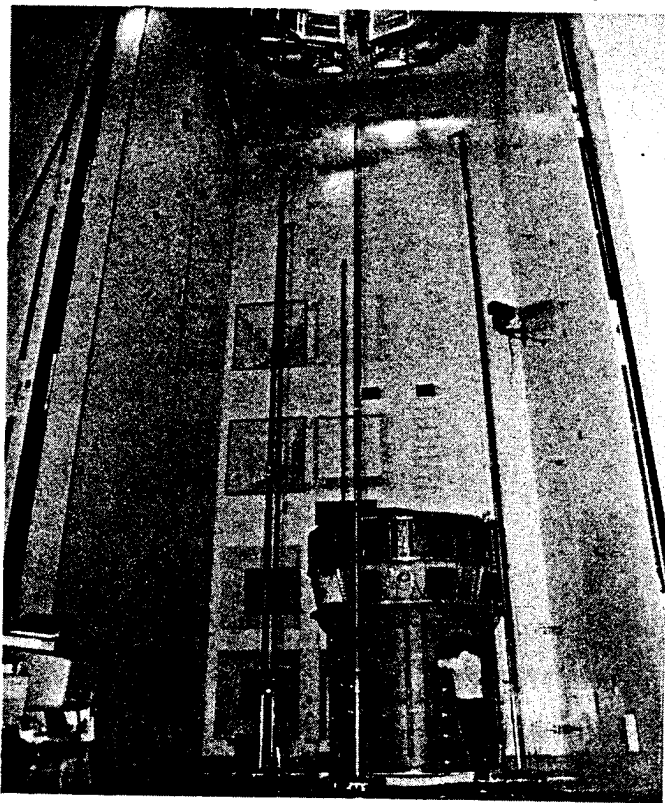


Figure 3. DTV Set Up for Acoustic Testing

Component	Direction	Undamped Response G RMS	Damped Response G RMS	Percent Reduction
Encrypter	Axial	21.83	6.47	70
	Radial	17.26	2.98	83
	Tangential	19.67	2.58	87
ESS Computer	Axial	16.27	2.40	85
	Radial	12.01	4.20	65
	Tangential	17.74	3.99	78
REM	Axial	15.78	9.75	38
	Radial	11.12	6.62	40
	Tangential	13.48	10.16	25
ESS Battery	Axial	11.84	3.81	68
	Radial	10.61	3.74	65
	Tangential	15.84	3.86	76
Interstage Battery	Axial	5.09	3.00	41
	Radial	8.63	5.51	36
	Tangential	10.08	2.83	72

Figure 4. Overall Response of Five Critical DTV Avionics Components

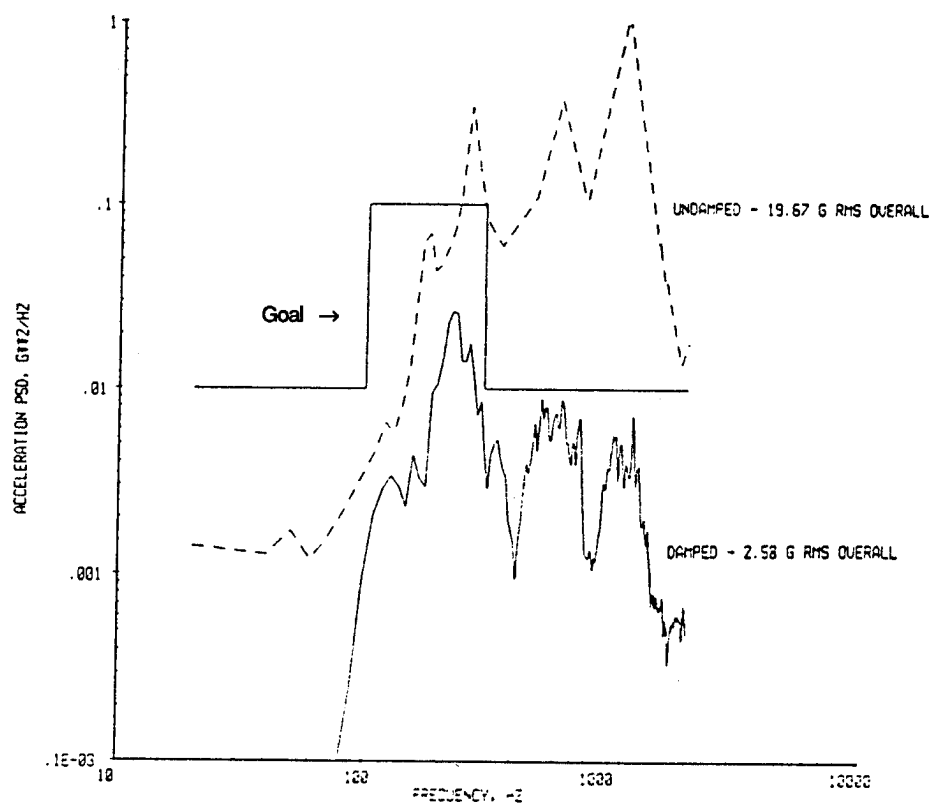


Figure 5. Envelopes of DTV Encrypter Tangential Response

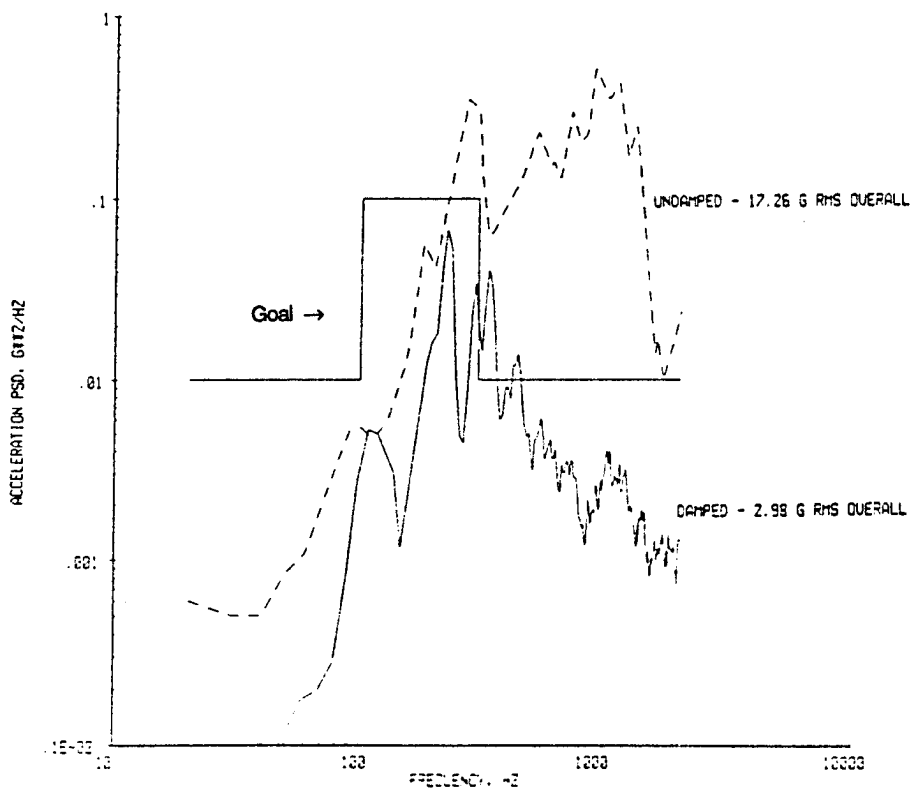


Figure 6. Envelopes of DTV Encrypter Radial Response

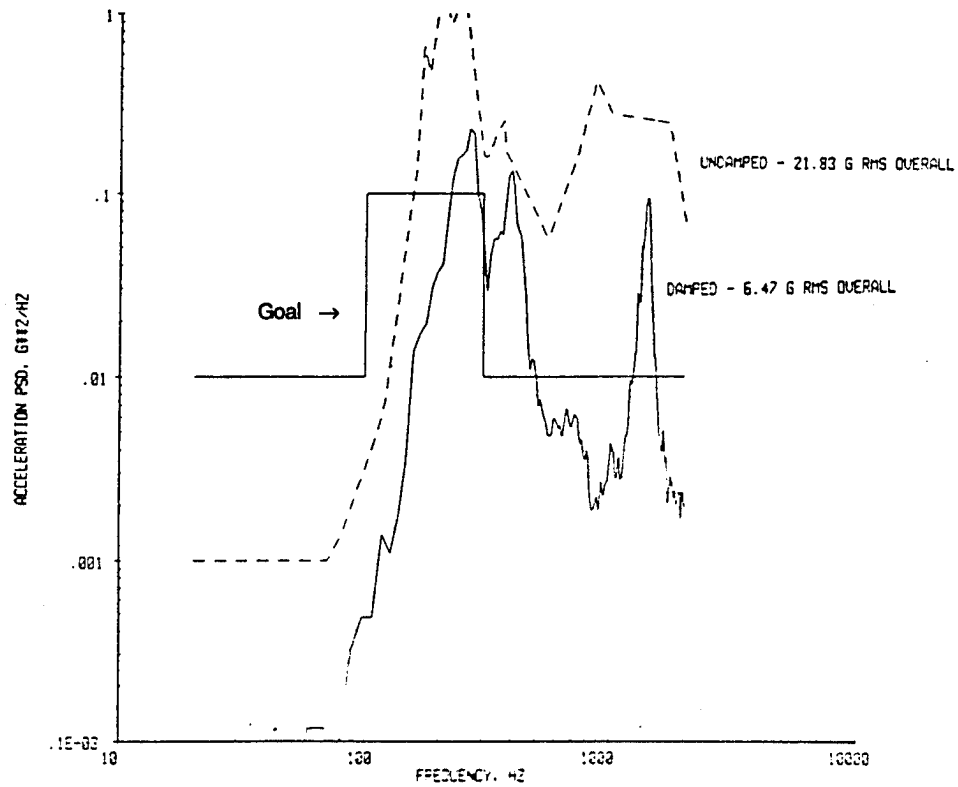


Figure 7. Envelopes of DTV Encrypter Axial Response

- Step 1: Identify SEA Subsystems
 - Substructure
 - Identify similar modes

- Step 2: Identify Junctions
 - Point, line, and area junctions

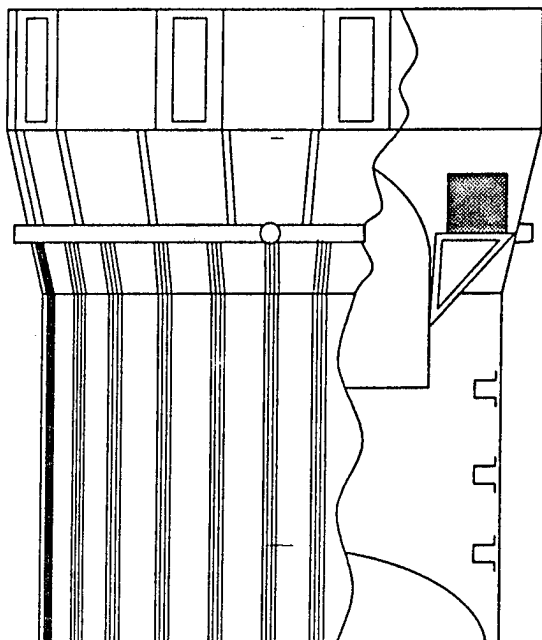
- Step 3: Compute Power Inputs
 - Impedance formulation

- Step 4: Compute SEA Parameters
 - Modal densities
 - Coupling factors
 - Damping factors

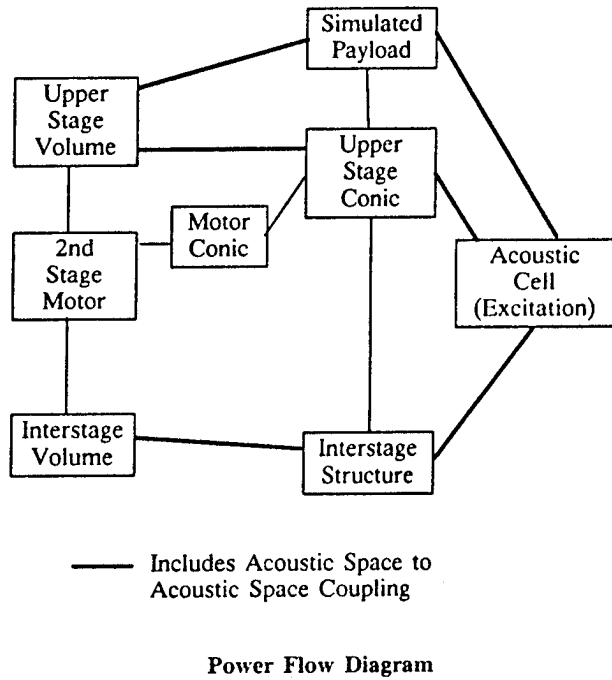
- Step 5: Power Balance Equations
 - Form matrix equation
 - Solve for modal energies

- Step 6: Response Statistics
 - Relate to modal energies
 - Mean response
 - Standard deviation

Figure 8. General Procedure for SEA

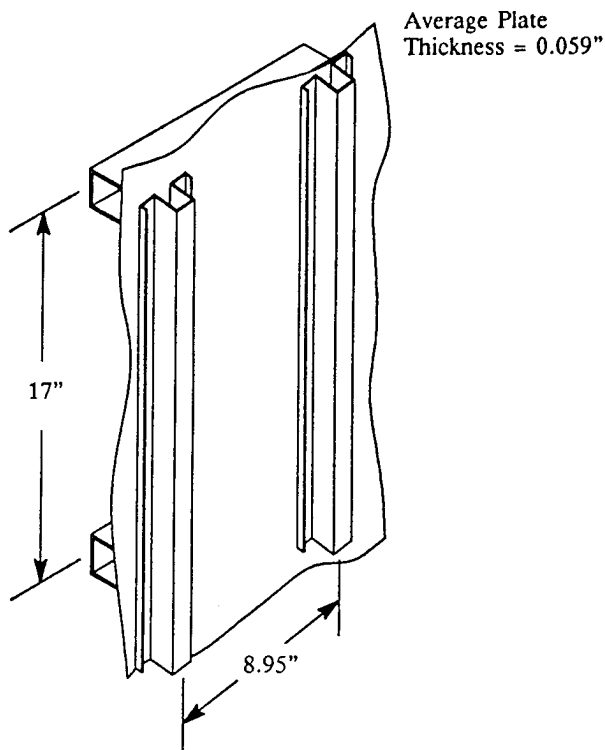


DTV



Power Flow Diagram

Figure 9. SEA Model for DTV Vibroacoustic Response Analysis



- Use VAPEPS EQPL Processor to Calculate Equivalent Homogeneous Plate Properties
- Two Possible Approaches:
 1. Include Rings in Equivalent Plate Calculation

Thickness =	2.18 in
Modulus =	7.51E+05 psi
Density =	1.90E-05 lb·s ² /in
 2. Consider Rings as Boundary Conditions

Thickness =	0.299 in
Modulus =	3.41E+06 psi
Density =	8.44E-05 lb·s ² /in

Figure 10. Interstage Panels Equivalent Plate Calculations for VAPEPS SEA Model

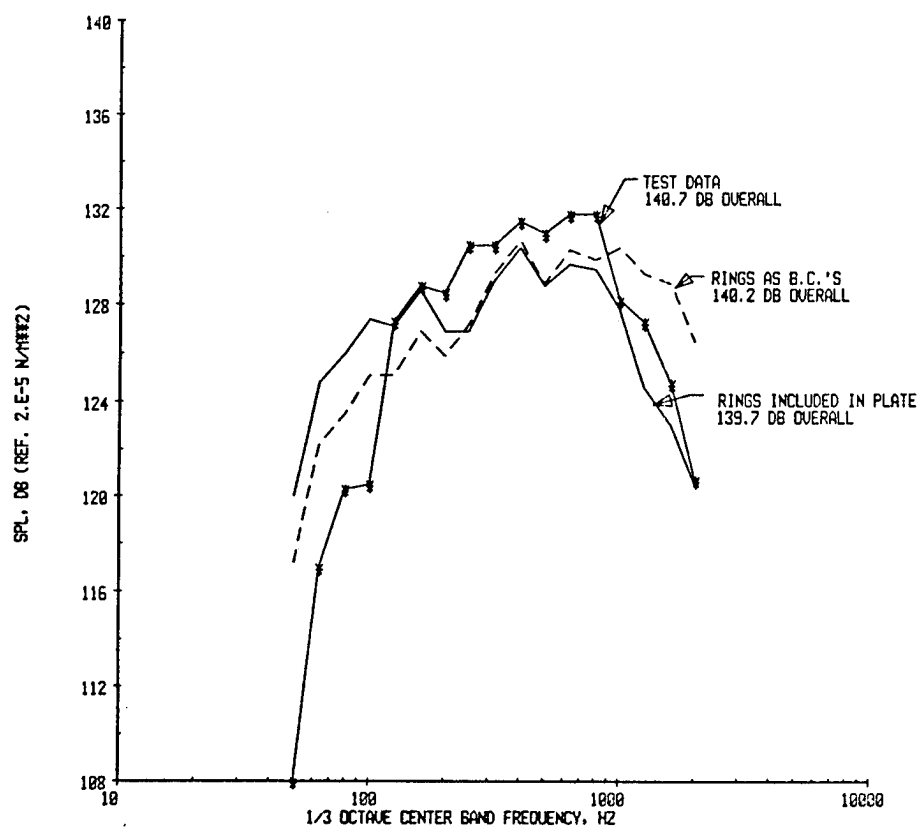


Figure 11. DTV Interstage Internal Acoustic Response

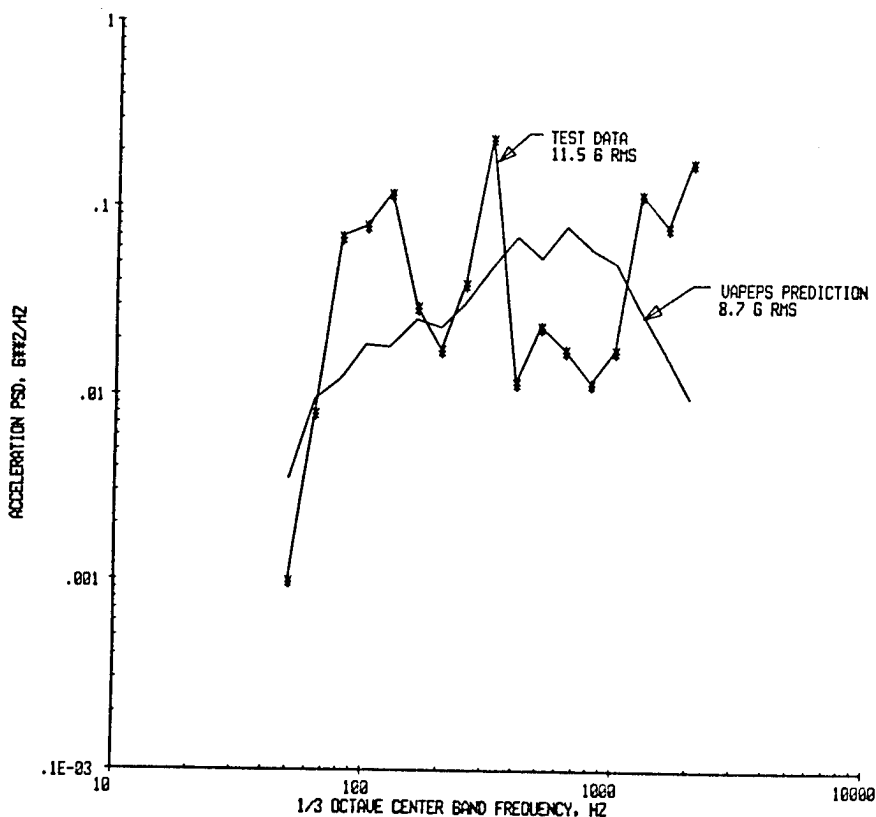


Figure 12. DTV Interstage Battery Vibroacoustic Response

RELSAT DAMPED SATELLITE EQUIPMENT PANELS - DYNAMIC PERFORMANCE*

by

C. V. Stahle, J. A. Staley, and J. C. Strain

General Electric Space Systems Division

ABSTRACT

This paper presents performance results for viscoelastically damped satellite equipment panel designs. Results show that launch vibroacoustic response acceleration power spectral densities at component mounting locations are reduced by up to 20 dB by damped panel designs. Corresponding derived component random vibration test specification PSDs are reduced by about 13 dB by damped panel designs. Component RMS response levels for the specifications for damped panels are predicted to be reduced by over 50 percent compared to baseline undamped panel designs based on a random response spectrum prediction method. Damped panel designs showed low hysteresis under application and removal of static loads. Test data show that viscoelastic material which had been in space for about four years maintained good damping and stiffness properties compared to materials which had not been in space. Viscoelastic damping treatments appear applicable to alignment critical structures because of low hysteresis under load application and removal and good property stability under long term space vacuum exposure. Results shown demonstrate the validity of methods used to design and fabricate viscoelastically damped satellite equipment panels.

*This work was performed for the Air Force Flight Dynamics Laboratory under the RELSAT (Reliability for Satellite Equipment in Environmental Vibration) Contract.

1.0 INTRODUCTION

Figure 1 shows a summary of the General Electric RELSAT program objective, approach and expected payoffs. The RELSAT program is aimed at improving satellite reliability by reducing satellite equipment failures due to effects of the launch vibroacoustic environment. The specific objective is to demonstrate the use of passive damping to control vibration of panel mounted equipment during launch. The approach is to design, fabricate, and test damped panels corresponding to Bay 3 of the DSCS (Defense Satellite Communication System) III Transponder Panel. This effort involved three major tasks: 1) evaluation of candidate damping material characteristics; 2) development and implementation of design concepts based on selected viscoelastic materials (VEMS); and 3) performing vibration, acoustic, static, and shock tests to evaluate the performance of damped equipment panel design concepts. This paper presents some of the performance results from the third task. Results from the first two tasks are reported in two other papers.^{1,2} The payoffs which are expected to result from development of damped panel designs for satellite equipment panels include: 1) improved stability and pointing accuracy for alignment critical items which might be sensitive to effects of onboard disturbances and maneuvers; 2) a 20 percent increase in the satellite reliability on orbit as a result of a 50 percent reduction in the component vibroacoustic environment during launch; 3) a reduction in the potentially large number of ground test failures by 50 percent; and 4) a reduction of the spacecraft system development and operating cost by an estimated \$40 million for a system consisting of a total of 14 DSCS III type satellites with a constellation of four satellites on orbit at any given time.

Figure 2 shows several key points relative to the RELSAT program. The DSCS III spacecraft shown is the system selected as the basis for the demonstration program. It is an Air Force communication satellite. Four are in geosynchronous orbit at any given time to give global communication coverage. The specific test article selected for study was Bay 3 of the DSCS III Transponder (North) panel. This bay has three 10 watt Traveling Wave Tube Amplifiers (TWTAs) and several smaller components mounted on it. Bay 3 is about 2 ft by 2 ft square and weighs about 50 lb including components and structure. The baseline panel structure consists of a magnesium base plate with two stiffeners. The design requirements for the panel include interdisciplinary constraints such as the need to radiate waste heat from the TWTAs through the base panel to space. Optical Solar Reflectors (OSRs) are mounted on the space side of the panel for solar radiation reflection and survivability. The panel must also have the structural integrity to withstand the steady state and low frequency accelerations during the launch phase. The center of Figure 2 shows a typical reduced temperature nomogram³ for a VEM which might be considered for design of a damped equipment panel for the baseline DSCS III. The nomogram shows VEM shear modulus and damping properties as a function of frequency and temperature. An important requirement for VEMS for satellite applications is that they be space compatible, i.e., have low outgassing characteristics.⁴ Figure 2 also indicates that the ultimate objective of the demonstration program is to develop damped stable platforms for satellite equipment and to develop damped stable platforms for satellite equipment and to demonstrate the technology for design and manufacture (fabrication) of such platforms.

2.0 DAMPING PAYOFFS

The interest in providing damping in satellite equipment panels has resulted from a history of failures after launch of a satellite and during ground development and production testing of a satellite, its subsystems, and its components. A significant number of spacecraft anomalies have been related to the launch vibration environment.⁵ Figure 3 shows flight failures or malfunctions vs days after launch. Figure 3 also shows that about 40 percent of these are related to vibration. A reduction of these failures from 40 to about 20 percent and a corresponding reduction in ground test failures is expected to result in a total savings of about \$40 million for a complement of 14 DSCS III type satellites. Vibration is also a major cause of failures occurring during ground environmental tests of spacecraft, its subsystems, and its components. Figure 4 shows that during design qualification, 64 percent of failures were related to vibration.⁶ Following qualification of the satellite design, 30 percent of failures in production acceptance tests were vibration related. With damped equipment panel designs similar to those developed under the GE RELSAT program, a 50 percent reduction in vibration/acoustic related ground test failures is expected.

A cost/reliability model which can be used to determine payoffs from equipment panel damping is available in a computer program known as OCTAVE (Optimized Cost of Testing for Acoustic and Vibration Environments).^{7,8} This computer program showed that a significant increase in reliability and decrease in satellite system cost could be obtained if the vibroacoustic responses during launch could be reduced by 50 percent. The cost and reliability improvements were based on a statistical decision theory model which in turn used a data base of cost/failure rate information for satellite components. A model of the spacecraft system was first developed which consisted of three major elements: 1) satellite housekeeping components; 2) the satellite structure; and 3) the payload (i.e., the communication system components). Various types of cost elements were incorporated in the model including direct and probabilistic cost types. Ground test options were considered which would assure that the satellite had a high reliability on orbit at optimum cost. The value of 50 percent reduction in the launch vibroacoustic environment for components was assumed due to equipment panel damping. The results showed a 20 percent improvement in reliability on orbit and a \$40 million savings for a 14 spacecraft production (DSCS III type system).

The history of increasing severity of vibration environments over the past decade for spacecraft components shows a smaller portion of spacecraft components passing vibration tests. This trend of increasing vibration environment is related to the increased acoustic sound pressure levels at launch and the need for increased vibroacoustic reliability. In particular, the Space Transportation System (STS) (or Space Shuttle) exhibits an increase in sound pressure levels in the low frequency range (below 300 Hz) compared to earlier expendable launch vehicles. Vibration requirements for new spacecraft currently being developed are higher than for previous spacecraft. Figure 5 shows: 1) a component random vibration test specification for a large diameter spacecraft being developed for launch on the Shuttle; 2) a corresponding specification for a small diameter (9 ft or less) spacecraft which was developed for launch on an expendable launch vehicle; and 3) the specification for the large diameter payload reduced by a factor of two on an RMS basis (by a factor of four or 6 dB on a PSD basis). Figure 5 shows that damping could reduce component random vibration levels for large diameter Shuttle payloads to

levels for smaller payloads developed for flight on expendable launch vehicles. Figure 5 also shows that the most significant random vibration environment is currently in the low frequency range (below 300 Hz) for shuttle launched payloads.

3. TEST PANELS

Damping materials were evaluated, damping materials were selected, damped panel design concepts were developed and evaluated, and baseline and damped panels corresponding to Bay 3 of the DSCS III transponder panel were designed and fabricated. Figure 6 shows a baseline panel consisting of a base plate with two stiffeners. Three mass simulated TWTA's are mounted directly to the base panel. Figure 7 shows a corresponding damped panel. This damped panel has damped honeycomb sandwich stiffeners. An aluminum core/aluminum face sandwich is bonded to the base plate to provide inherent stiffness of the panel independent of the damping treatment. The VEM is bonded to this honeycomb sandwich stiffener. An aluminum core/graphite-epoxy face sandwich is then bonded to the VEM to provide a constraining sandwich for the VEM. Damped panels were also made with hat stiffeners riveted to the base plate and with a VEM layer with a graphite-epoxy constraining layer bonded to the hat stiffener. Various tests were conducted on the baseline and damped panels. These included acoustic, sine vibration, static, creep, and pyro shock tests. Pyro shock test results are described briefly below. Results of acoustic tests are then discussed in some detail. Component random vibration test requirements are derived from the vibroacoustic tests for the baseline and damped panels. The implication for component random vibration test requirements are considered to be the primary result of the RELSAT satellite equipment panel damping demonstration effort.

4. PYRO SHOCK TESTS

Pyro shock tests were performed on the baseline and a damped panel. In separate tests, these panels were mounted in one bay of a dual bay simulator which is normally used to perform spacecraft separation shock tests for components mounted on the DSCS III transponder panel. The shock was produced by firing an explosive separation nut. In these tests, the separation nut was activated by a high pressure gas supply connected to the nut. This separation nut is used to separate the DSCS III from the IUS and from a second DSCS III spacecraft. Separation nuts are on bolts at either ends of the two longerons which form two ends of the DSCS III transponder panel. Three separation nut firings were made each for the baseline and a damped panel. Triaxial accelerometers were mounted at the shock source and two accelerometers were attached near the mounting locations of each of the TWTA masses on each of the panels tested. One of these two accelerometers was oriented normal to the test panel and the other was oriented in the in-plane direction of the panel in the direction of separation nut firing (in the direction of the longeron).

Figure 8 shows comparisons of damped and baseline shock spectra for the two accelerometers mounted near TWTA number 2 which was mounted in the middle of each panel. Results shown are envelopes for three firings, although results from the three firings for each panel showed little variation in the shock spectra. Figure 8 shows results for the out-of-plane and in-plane accelerometers. The figure shows that the shock spectra peak near 2200 Hz with

maximum levels on the order of 1000 g. This is above the frequency where significant damping occurs. Damping treatments were designed primarily to reduce vibroacoustic response in the out-of-plane direction in the 50 to 500 Hz range. Damping reduced the peak shock in the out-of-plane shock spectra by about 30 percent. The out-of-plane direction is the direction in which damping was intended to be provided by the damped panel design. Figure 8 shows that the peak in the shock spectra for the in-plane direction was increased by about 30 percent for the damped panel relative to the baseline. This may be due to the addition of stiffeners for the damped panel configuration which connect the longerons to the TWTA's.

5. VIBROACOUSTIC TESTS

Acoustic tests were conducted on the baseline and seven damped panel configurations. Panels with both hat and sandwich damped stiffeners were tested. The configurations included four different viscoelastic materials. Tests were conducted at temperatures ranging from 60 to 78 degrees F. Two tests were conducted with four panels suspended in the GE acoustic test facility for each test. Tests were conducted at 139.3 and 143.8 dB overall. Instrumentation on each panel consisted of 12 out-of-plane accelerometers and two in-plane accelerometers attached at component mounting locations. Thermocouples were used to monitor temperatures of viscoelastic materials. Four microphones were used to measure and control the acoustic test environment. Figure 9 shows one-third octave band qualification sound pressure levels for small diameter and large diameter shuttle payloads.^{9,10} The acoustic environment used for acoustic tests corresponded to the shape of the 9 ft payload sound pressure level curve. Test vibroacoustic levels were scaled to correspond to acoustic levels shown in Figure 9. The 9 ft diameter levels correspond to a DSCS III qualification test level.

Figure 10 shows four of the damped panels suspended in the GE acoustic test facility. Each panel was mounted to a heavy aluminum frame which was supported by a low frequency suspension system. Figure 10 shows the location of four out-of-plane accelerometers at the mounting locations for each TWTA mass. Each panel had two in-plane accelerometers. In-plane vibroacoustic responses were small compared to out-of-plane responses. For each of the panels tested, the 12 out-of-plane accelerometers were analyzed statistically to obtain a 95 percentile level. The spectral content of the data were then scaled to acoustic levels shown in Figure 9 for the 9 and 15 ft diameter shuttle payload qualification acoustic test levels. Figure 11 shows results for the 9 ft diameter payload for test data for 72 degrees F. Results are shown for the baseline and a damped panel. Results for all damped panels were very similar. Results shown in Figure 11 are for the damped panel which gave the best results for all panels tested. Other damped panel designs had similar vibroacoustic responses but were slightly higher above 500 Hz. Figure 11 shows that damping reduces response by up to 20 dB. The largest peaks for the baseline panel were reduced the most and these peaks were in the low frequency range. Damping reduced responses significantly for frequencies up to about 400 Hz. Figure 12 shows results scaled for the 15 ft diameter shuttle payload acoustic environment at launch. These results indicate that damping can provide very significant benefits for large diameter shuttle payloads.

6. RANDOM VIBRATION SPECIFICATIONS

The Random Response Spectrum (RRS) method¹¹ was used to determine component random vibration test requirements corresponding to the 95th percentile out-of-plane random vibration levels determined from the acoustic tests for the baseline and best damped panels. The RRS method is similar to the shock spectrum concept. The RRS is the RMS response of a single-degree-of-freedom oscillator to a random vibration input spectrum vs the oscillator resonant frequency. A Q of ten was assumed for the component. The objective was to generate a random vibration test spectrum which had an RRS similar to the RRS for the actual component random vibration environment, i.e., for the 95th percentile out-of-plane random vibration spectrum. Random vibration specifications were generated in this manner for the baseline and damped panel component random vibration environments. Figure 13 shows the out-of-plane random vibration spectrum and corresponding test spectrum for the 9 ft diameter payload (DSCS) baseline panel qualification level. The RRS for this specification level and the the 95 percentile out-of-plane data are also shown in Figure 13. The RRS for the specification is seen to envelope that for the actual baseline panel test data. The peak value of about 30 GRMS occurs for a component natural frequency just above 100 Hz. Note that the largest magnitudes of the test data, the specification, and the RRS are in the low frequency region (below 300 Hz). Corresponding results for the damped panel are shown in Figure 14. Damping significantly reduces the low frequency test and specification random vibration spectrum levels. The largest RRS level now occurs at about 2000 Hz for both the damped panel test data and specification. The peak GRMS at this frequency, however is now only about 13 g. Figure 15 compares the specifications for the damped and baseline panels shown previously in Figures 13 and 14. The maximum specification PSD has been reduced 13 dB using damping. The maximum GRMS has been reduced by 64 percent for the damped panel. Corresponding results for the 15 ft diameter shuttle payload are shown in Figure 16. Here the damped panel PSD is seen to be reduced by 14 dB relative to the baseline panel and the peak GRMS is reduced by 53 percent due to damping. This figure shows that major benefits from damping can be expected for large diameter payloads on the shuttle. Component random vibration test responses might be reduced from about 40 to about 20 GRMS by the addition of damping to equipment panels.

7. DAMPED PANEL HYSTERESIS AND LONG TERM VEM STABILITY

A static load test was conducted on a panel with damped hat stiffeners. A load was applied to each TWTA normal to the plane of the panel. The panel was loaded statically to an 11 g (550 lb) load in increments of approximately 1 g. The load was then removed in approximately 1 g increments. Deflections of the panel and strains in hat stiffeners were measured. Figure 17 shows a plot of strain in a hat stiffener vs total panel load for both the loading and unloading cycle. Figure 17 shows that very low hysteresis occurred. This result indicates that for the damped panel designs developed under RELSAT, viscoelastic treatments may be feasible for application to platforms requiring high alignment and pointing stability without introducing hysteresis during loading and unloading events such as launch, orbit transfer, deployments, and separations.

In April 1984, The Modular Attitude Control System (MACS) module was retrieved form the Solar Max Mission (SMM) spacecraft on a Shuttle repair mission. The SMM spacecraft was launced in January of 1980. The Attitude Control Electronics (ACE) component on the MACS module used viscoelastic materials

extensively for damping treatments. A piece of this material which had been in orbit for over four years was tested to determine its material properties after four years exposure to space environment. Figure 18 shows the measured loss factor and shear modulus (discrete data points) compared to properties of similar non-flight material (curves). The material retrieved from space is seen to have excellent damping properties (circles) which are nearly identical to the non-flight material. The shear modulus (squares) for the material which was in orbit is slightly stiffer than the similar material which was not flown. These results indicate that damping materials of the type used in the GE RELSAT damped panel designs will retain their viscoelastic characteristics for long periods of time when in orbit and could be quite useful for orbital damping applications.

8. SUMMARY AND CONCLUSIONS

The primary objective of the GE RELSAT program was to develop and demonstrate damped panel designs which would reduce the vibroacoustic response. An initial goal was to reduce the RMS response by 50 percent (6 dB). A reduction of this magnitude was estimated to result in a cost savings of \$14 million for 14 spacecraft system (DSCS type). The most significant Shuttle vibroacoustic environments are in the low frequency range. The largest deflections and stresses of components are expected here. Pyro shock tests showed attenuation of out-of-plane shock spectra due to damping but an increase was seen in the in-plane shock spectra for damped panels. Vibroacoustic responses were reduced up to 20 dB for power spectral densities in the 50 to 300 Hz range. Corresponding component random vibration specificaiton levels were reduced about 13 dB. The expected component RMS acceleration responses to derived component random vibration specifications were reduced by 50 to 60 percent by damped panel designs. Low hysteresis in static load deflection tests indicates that damping may be applicable to alignment critical structures. Data recently obtained on viscoelastic material which had been in space for four years showed that long term space exposure had little or no effect on the material damping and stiffness properties. Materials of this type appear applicable to orbital damped panel designs for alignment critical structures.

9. ACKNOWLEDGEMENTS

The work for design, development, and testing of damped RELSAT satellite equipment panels was performed under AFWAL contract F33615-82-C-3223. Technical monitors are James Eichenlaub and Lynn Rogers who provided valuable guidance and assistance. Testing and test data reduction were performed by the General Electric Space Systems Division vibration and acoustic laboratory personnel. Harold Gongloff performed statistical analyses of vibroacoustic and shock spectra data and derived component random vibration test specifications using the Random Response Spectrum method.

10. REFERENCES

1. J. C. Strain, J. A. Staley, and C. V. Stahle, "Design and Experimental Verification of Damped Spacecraft Equipment Panels," Vibration Damping Workshop II, March 1986.

2. K. A. Schmidt, F. P. Curtis, E. F. Muziani, and L. Amore, "Fabrication of Damped Spacecraft Equipment Panels," Vibration Damping Workshop II, March 1986.
3. D. I. G. Jones, "A Reduced-Temperature Nomogram for Characterization of Damping Material Behavior," 48th Shock and Vibration Symposium, Oct. 1977.
4. R. Moss, "Using the Outgassing Test to Screen Materials for Contamination Potential," SAMPE Journal, March/April 1984.
5. A. R. Timmins and R. E. Heuser, "A Study of First Day Space Malfunctions," NASA TND-6474, September 1971.
6. R. B. Laube, "Methods to Assess the Success of Test Programs," October 1982 Aerospace Testing Seminar.
7. C. V. Stahle, H. R. Gongloff, J. P. Young, and W. B. Keegan, "Shuttle Payload Minimum Cost Vibroacoustic Tests," Proc. 1977 Annual Rel. and Maint. Symp.
8. C. V. Stahle, "Cost Effectiveness of Spacecraft Vibration Qualification Testing," Proc. of Inst. of Environmental Sci., 20th Annual Meeting, May 1974.
9. "Acoustic Requirements for DoD Shuttle Payloads Launched from KSC," Doc. No. DS-YV-0093, Rev. 1.
10. C. S. Tanner, "Acoustic Environments for DoD Payloads on the Shuttle," Proc. of the Shuttle Payload Dynamic Environments and Loads Predictions Workshop, JPL D-1347, 1984.
11. C. V. Stahle and H. R. Gongloff, "Development of Component Random Vibration Requirements Considering Response Spectra," The Shock and Vibration Bulletin, August 1976.

(RELIABILITY FOR SATELLITE EQUIPMENT IN ENVIRONMENTAL VIBRATION)

OBJECTIVE

- GENERICALLY DEMONSTRATE PASSIVE DAMPING CONTROL OF PANEL MOUNTED COMPONENT VIBRATION

APPROACH

- DESIGN, FABRICATE AND TEST DAMPED DSCS-III TRANSPONDER PANEL
 - EVALUATE MATERIAL PROPERTIES
 - DEVELOP AND IMPLEMENT DESIGN CONCEPTS
 - PERFORM VIBRATION, ACOUSTIC, SHOCK AND STATIC TESTS

PAYOUTS

- STABLE PLATFORM WITH HIGH POINTING ACCURACY FOR MANEUVERS AND ON-BOARD DISTURBANCES
- 20 PERCENT INCREASE IN RELIABILITY THROUGH 50 PERCENT REDUCTION IN VIBRATION ENVIRONMENT
- REDUCE LARGE NUMBER OF TEST FAILURES BY 50 PERCENT
- REDUCE SPACE SYSTEM DEVELOPMENT/OPERATING COST BY \$40M

Figure 1. RELSAT Program

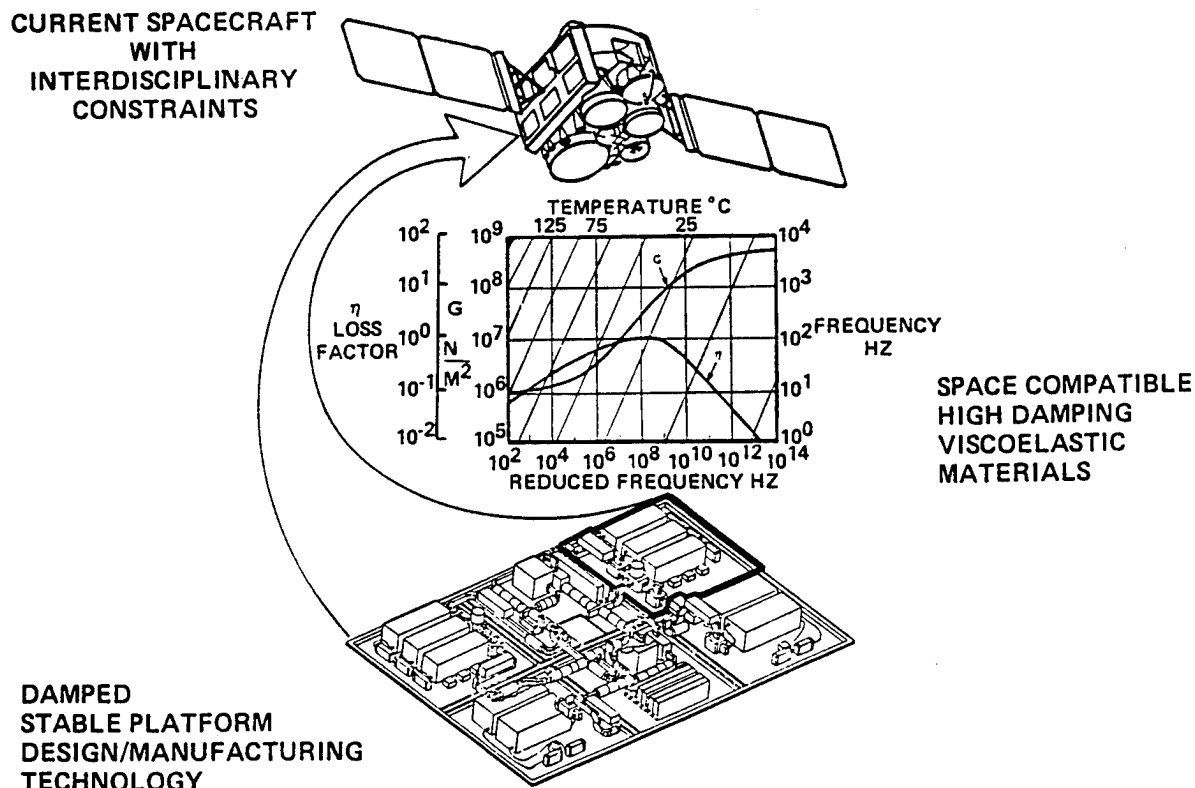


FIGURE 2. RELSAT DSCS III Baseline System

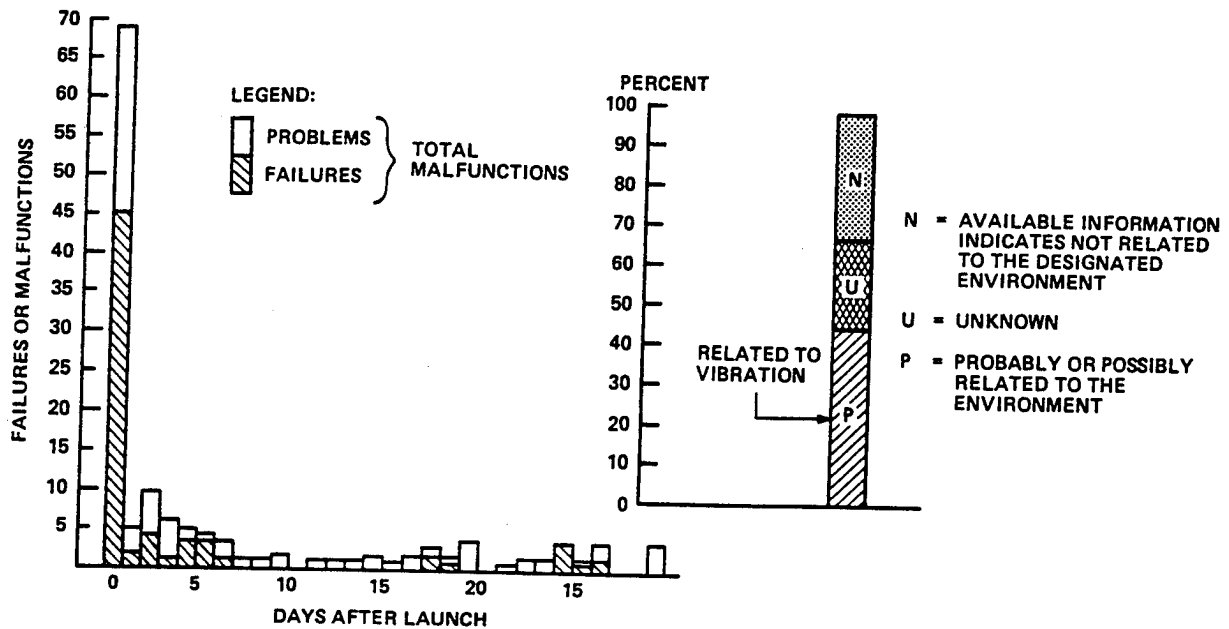
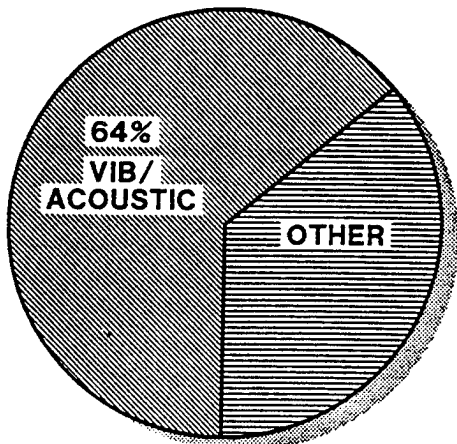


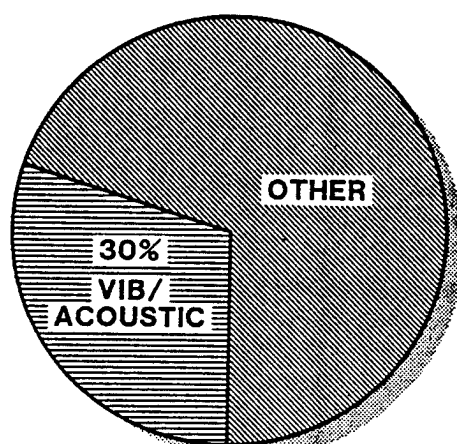
Figure 3. Spacecraft Flight Failures

DESIGN QUALIFICATION



98 TEST FAILURES/SATELLITE

ACCEPTANCE

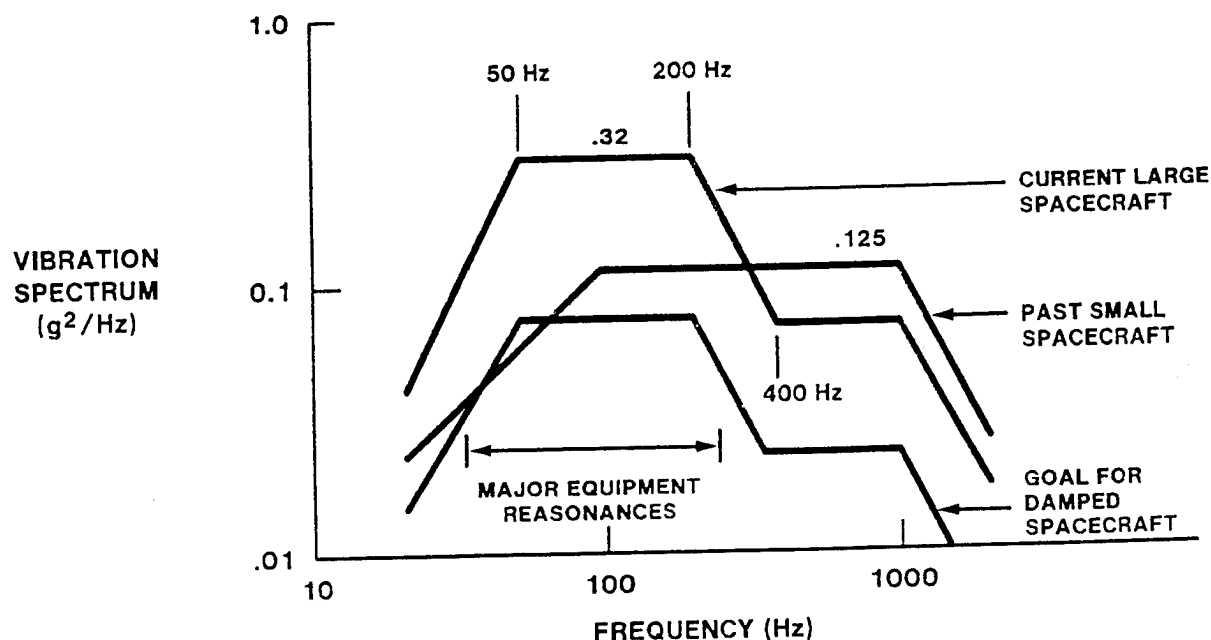


25 FAILURES/SATELLITE

REF: OCT 82 AEROSPACE
TESTING SEMINAR

A 50% REDUCTION IN VIB/ACOUSTIC
GROUND TEST FAILURES IS ESTIMATED

Figure 4. Environmental Test Failures



DAMPING COULD REDUCE Specs FOR SHUTTLE
LARGE DIAMETER PAYLOADS TO SMALL DIAMETER LEVELS

Figure 5. Equipment Random Vibration Requirements

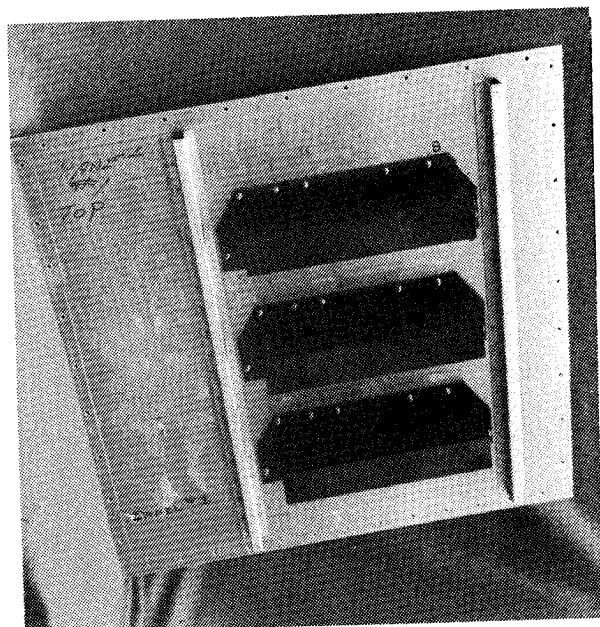


Figure 6. RELSAT Baseline Panel

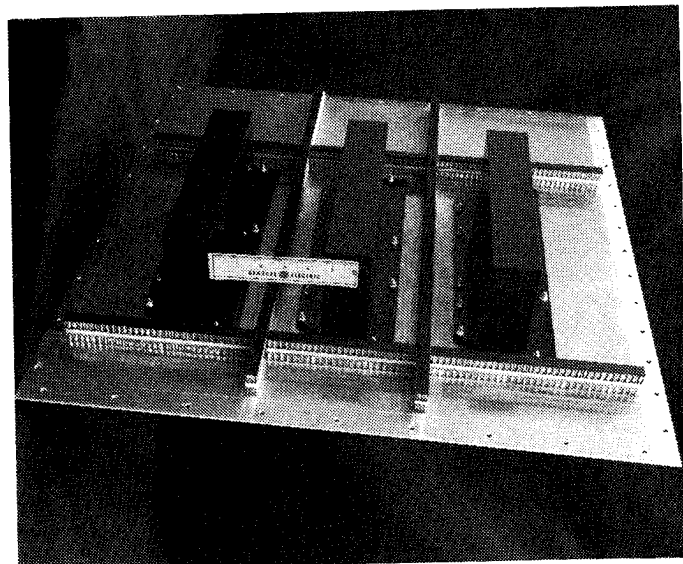
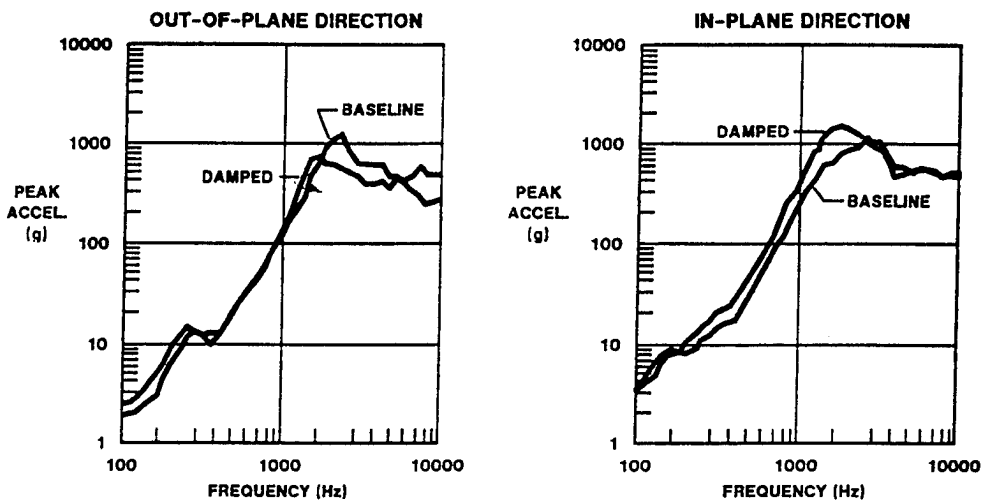


Figure 7. RELSAT Test Panel With Damped Stiffeners



DAMPING TREATMENT REDUCES OUT-OF-PLANE SHOCK SPECTRA
AND INCREASES IN-PLANE SHOCK SPECTRA

Figure 8. Pyro Shock Test Results

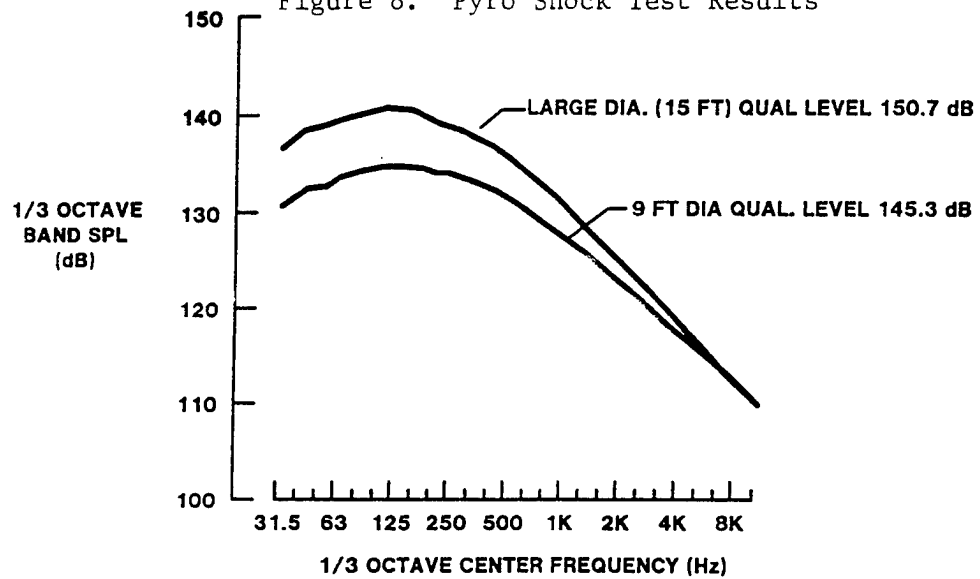


Figure 9. Qualification Sound Pressure Levels

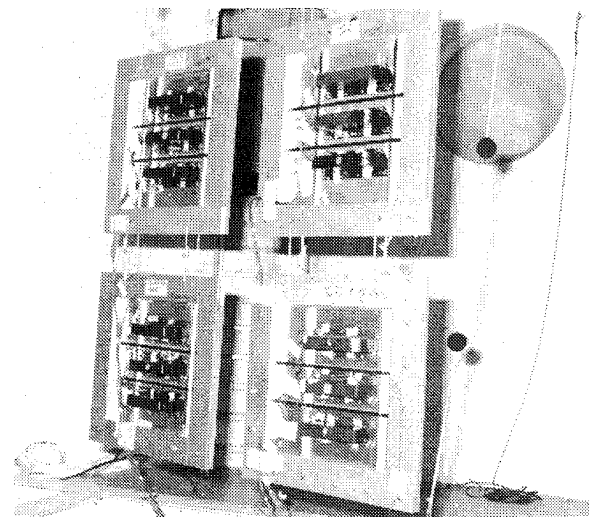


Figure 10. RELSAT Panels in Acoustic Test Facility

**95% LEVEL AT 72 DEG F
SCALED TO 145.3 dB QUAL. ACOUSTIC LEVEL**

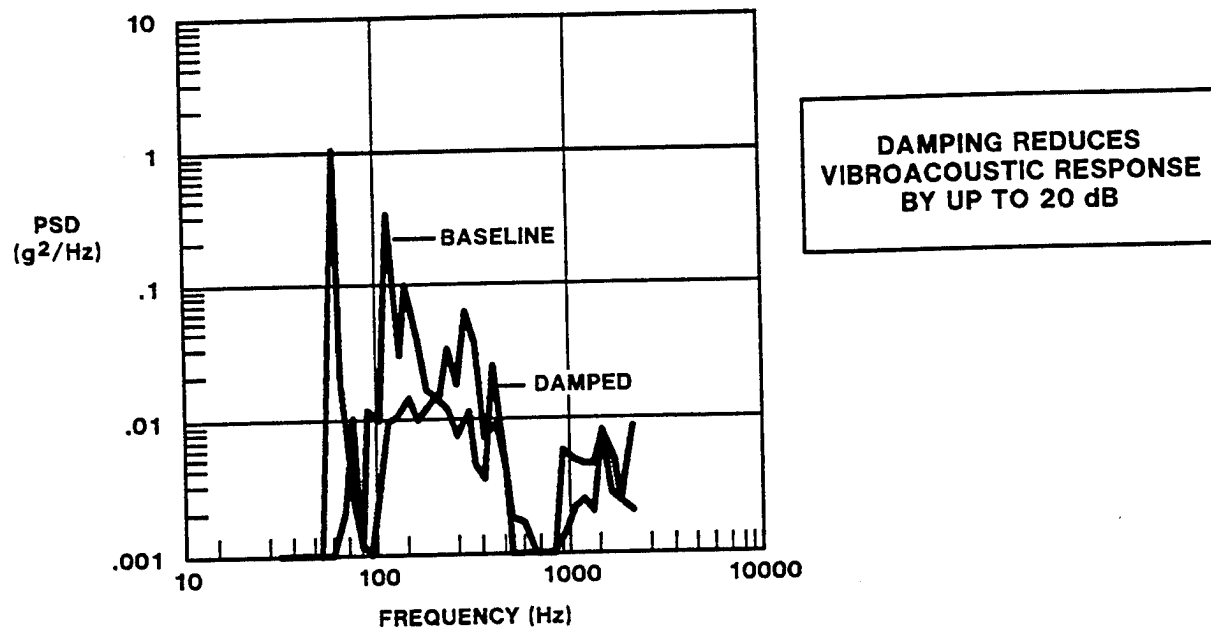


Figure 11. Out-of-Plane Vibroacoustic Response

**95% LEVEL AT 72 DEG F
SCALED TO QUAL. ACOUSTIC LEVEL - 150.7 dB**

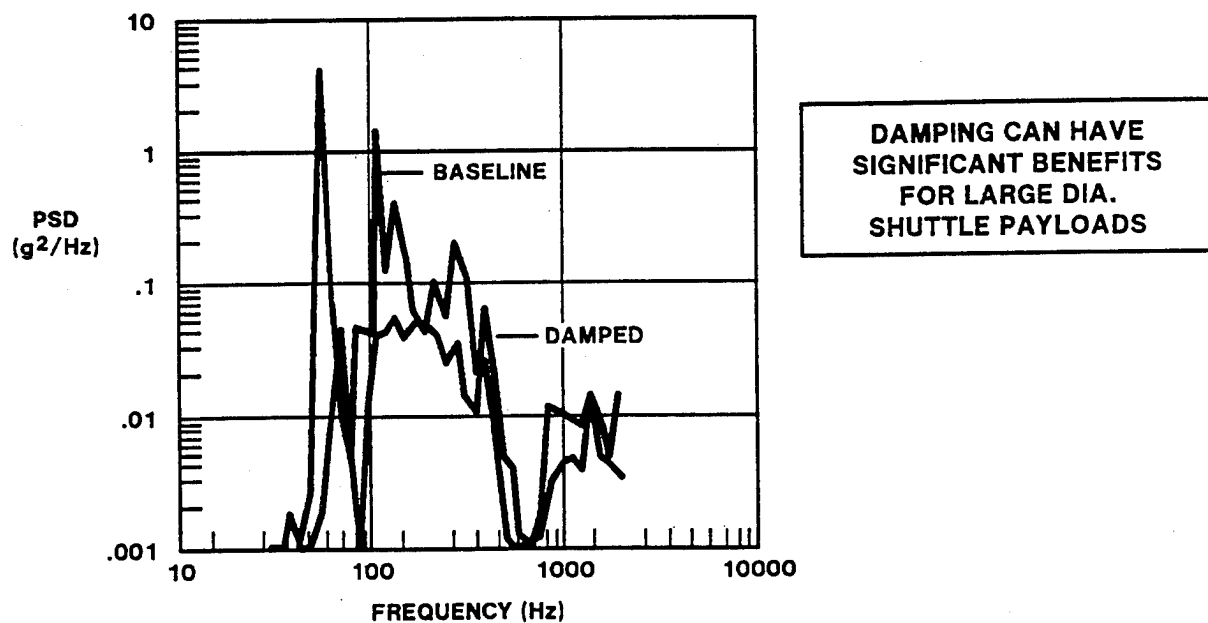


Figure 12. Vibroacoustic Response - Scaled for 15 Ft. Dia. Payload

DAMPING REDUCES
VIBROACOUSTIC RESPONSE
BY UP TO 20 dB

DAMPING CAN HAVE
SIGNIFICANT BENEFITS
FOR LARGE DIA.
SHUTTLE PAYLOADS

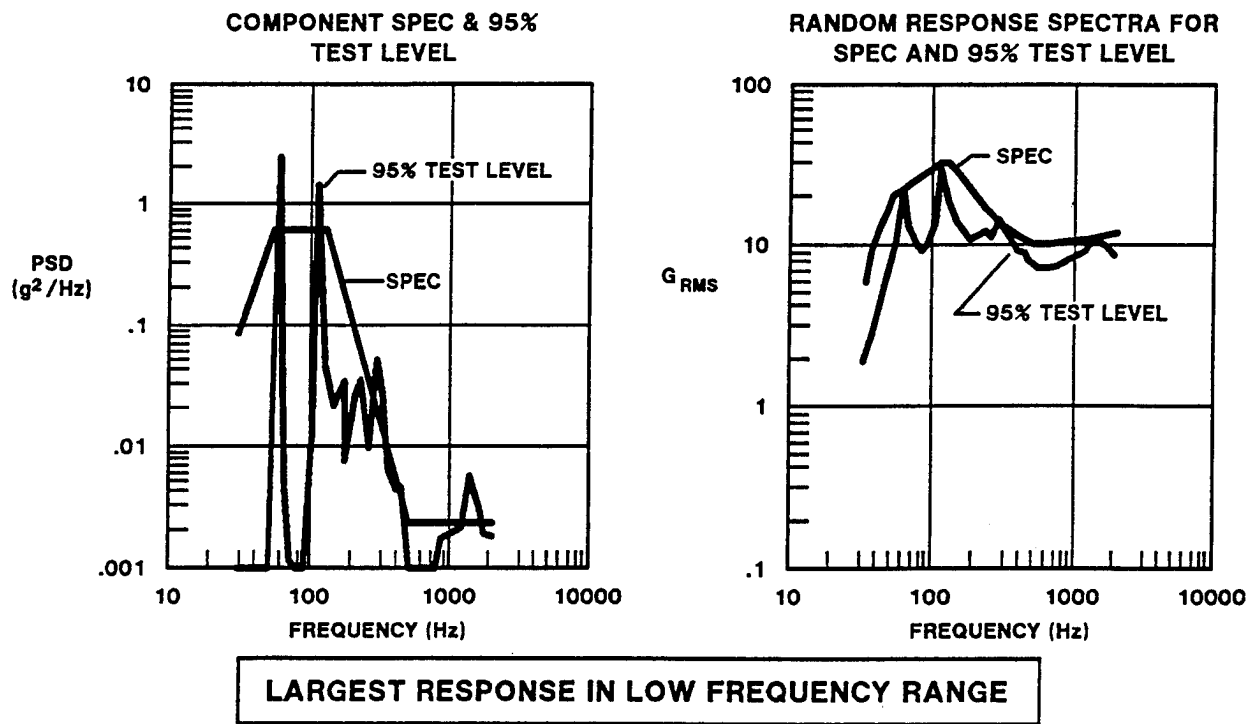


Figure 13. DSCS III Baseline Panel Random Vibration Specification

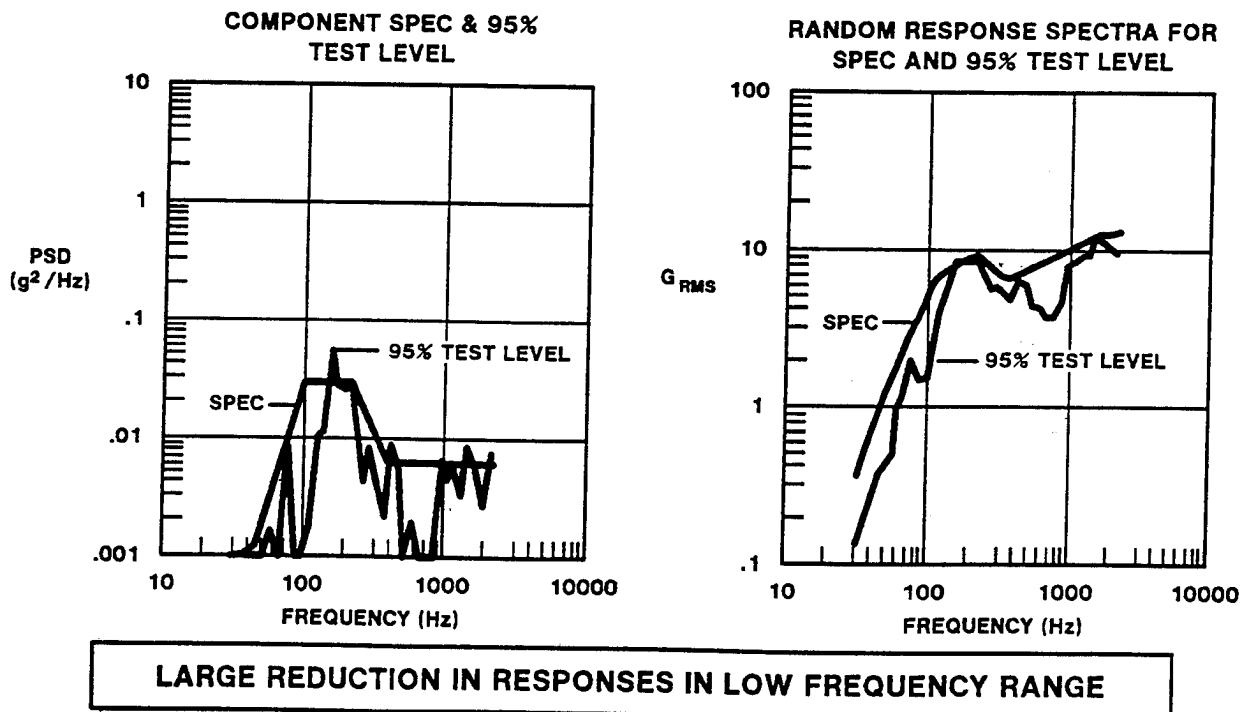


Figure 14. DSCS III Damped Panel Random Vibration Specification

OUT-OF-PLANE DIRECTION - SHUTTLE LAUNCH AT KSC

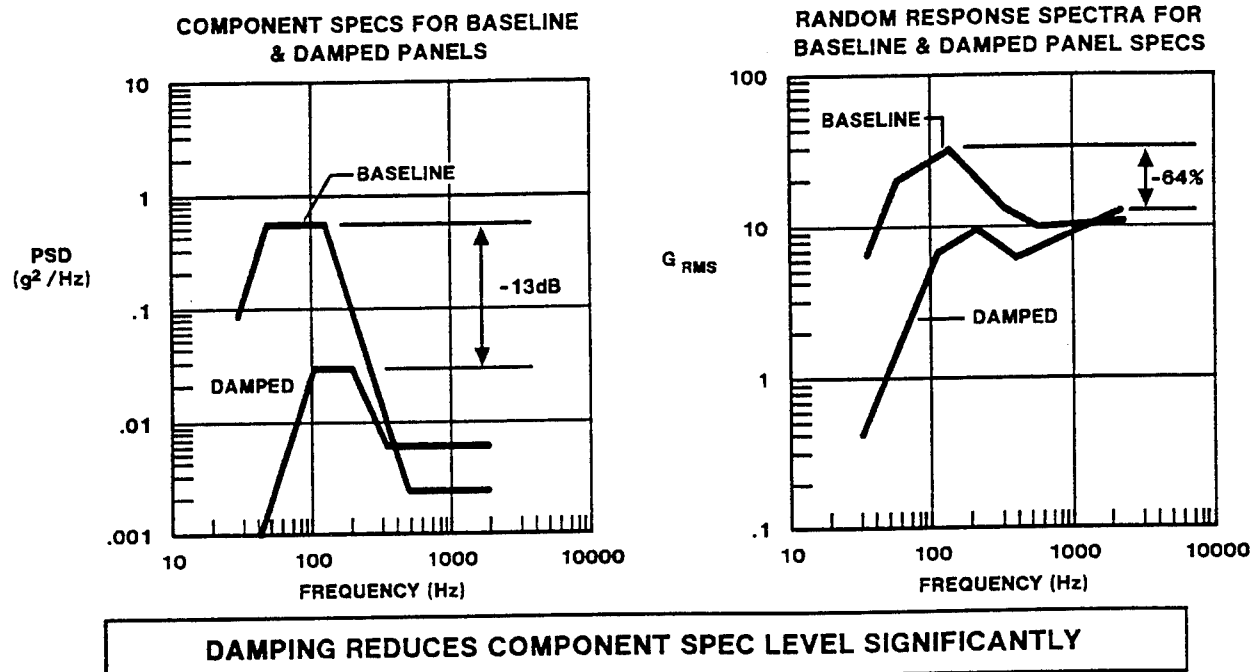


Figure 15. DSCS III Baseline and Damped Panel Qualification Level Random Vibration Specifications

OUT-OF-PLANE DIRECTION - SHUTTLE LAUNCH AT KSC

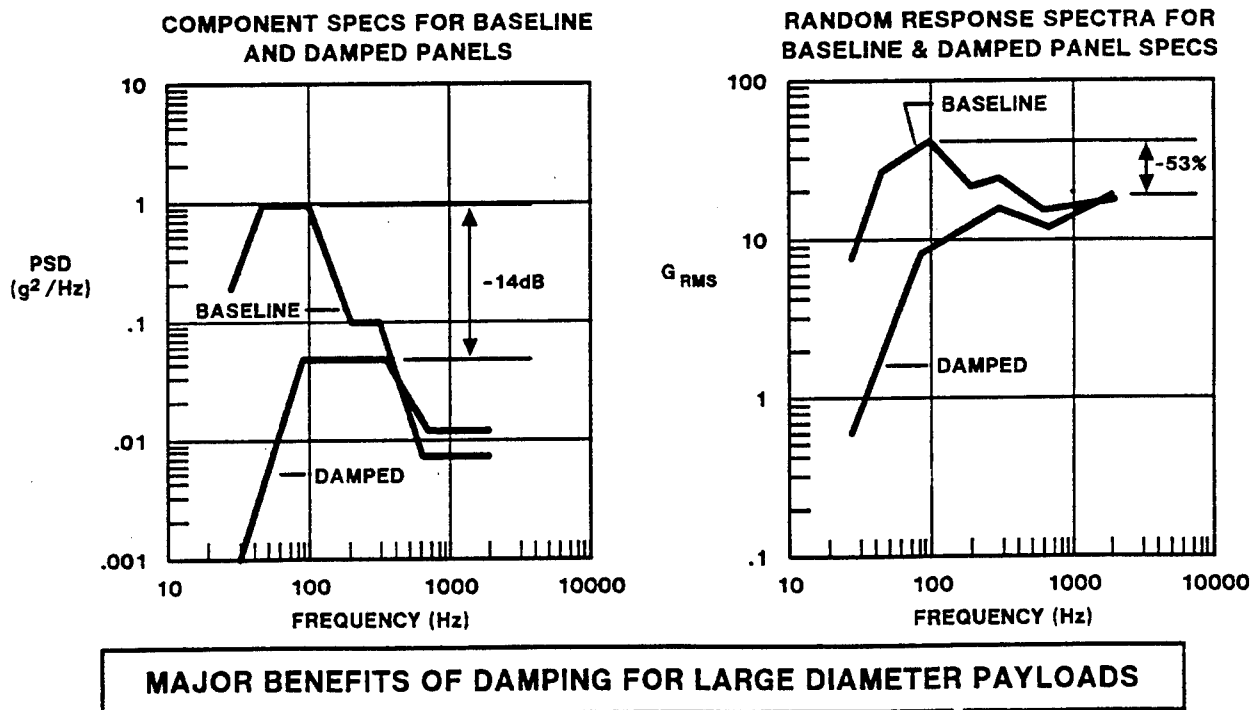


Figure 16. Random Vibration Specifications -
15 Ft. Diameter Payload

- A RELSAT DAMPED PANEL WAS LOADED STATICALLY TO AN 11g LOAD IN APPROXIMATELY 1.0g INCREMENTS
- THE LOAD WAS THEN REMOVED IN APPROXIMATELY 1.0g INCREMENTS
- VERY LOW HYSTERESIS UNDER THE STATIC LOAD CYCLE WAS INDICATED BY A STRAIN GAGE ON A PANEL HAT STIFFENER

VISCOELASTIC DAMPING TREATMENTS MAY BE FEASIBLE FOR APPLICATION TO PLATFORMS REQUIRING HIGH STABILITY WITHOUT INTRODUCING HYSTERESIS DURING EVENTS SUCH AS LAUNCH, ORBIT TRANSFER, DEPLOYMENTS AND SEPARATION

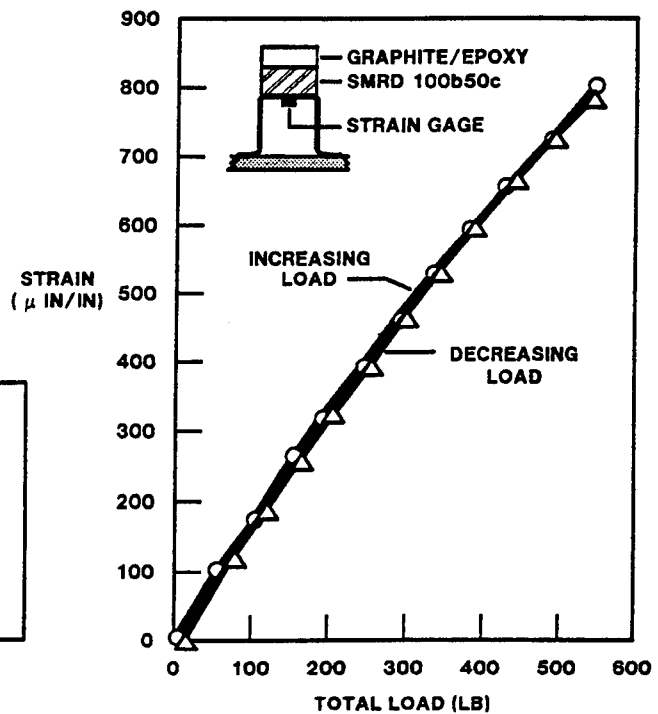
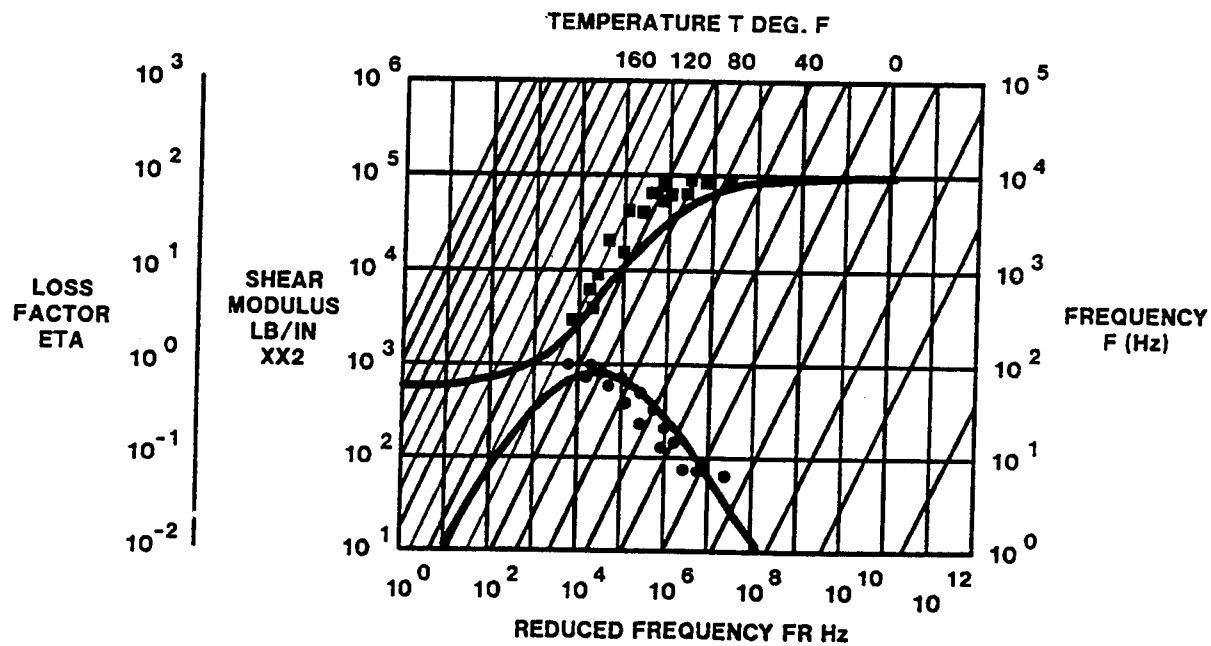


Figure 17. Static Test Hysteresis for a Damped Panel



GOOD DAMPING PROPERTIES AFTER 4 YEARS IN SPACE

Figure 18. VEM Properties After Four Years in Space

RELSAT DAMPED EQUIPMENT PANELS - ANALYSIS AND EXPERIMENTAL VERIFICATION

C. V. STAHLER, J. A. STALEY and J. C. STRAIN

General Electric Company
Valley Forge Space Center
RCA Astro Space Division
P.O. Box 8555, Philadelphia, PA 19101

ABSTRACT

The design, analysis and modal tests of viscoelastically damped spacecraft equipment panel structures are presented. The work was performed as part of the AFVAL RELSAT program and uses the DSCS III transponder panel to demonstrate the generic control of equipment vibration with passive damping. Highly effective integrally damped panel designs are achieved with small increase in structural weight. A damped stiffener approach is used that satisfies interdisciplinary constraints such as heat dissipation. Strength and deflection criteria are used that account for the load reduction and stiffness of the damped design. Two lightweight configurations are described: one using unidirectional graphite epoxy (G/E) constraining layers and the other using G/E honeycomb constraining layers with an aluminum honeycomb stiffener. Loss factors greater than 0.2 are obtained for low frequency modes using GE SMRD 100 damping materials. Damping is more than doubled in all modes below 500 Hz. The analysis uses NASTRAN finite element models with modal strain energy and can be applied to any complex design. Initial beam element tests compare analytical predictions with test results for the G/E constraining layer and honeycomb configurations using material properties from two different laboratories. Subsequent panel tests indicate damped panel analyses predict low mode resonant frequencies within 10 percent, damping loss factors within 30 percent and the temperature of maximum damping within 10 degrees F. The major source of prediction error appears to be material properties caused by measurement error, the temperature shift relation and the reference temperature. More accurate material property definition is recommended. The 20 dB attenuation of the vibroacoustic response, the material selection and panel fabrication are discussed in two other papers included in the proceedings.

*The work reported herein was performed for the Air Force Wright Aeronautical Laboratory, Contract No. F33615-82-C-3223, "Reliability for Satellite Equipment in Environmental Vibration," under the technical direction of James Eichenlaub and Lynn Rogers.

1.0 INTRODUCTION

This paper discusses the design, analysis, and modal tests of viscoelastically damped spacecraft equipment panels. Examination of early spacecraft flight anomalies has indicated a large number are caused by the vibroacoustic launch vibration. As a result, vibration requirements have been increased which has led to a large number of ground test failures during component, subassembly and spacecraft random vibration and acoustic tests. Even after qualification tests of a spacecraft design have been successfully completed, subsequent acceptance tests of production units exhibit a large number of failures indicating a susceptibility of the final designs to the vibroacoustic environment. Although damping has been used effectively within electronic packages to improve vibroacoustic reliability, its use to control equipment panel vibration has been limited and generally applied to existing designs. Because studies have shown that significant cost reductions can be obtained and that the vibroacoustic reliability can be significantly improved by reducing the random vibration environment, the RELSAT program (Reliability for Satellite Equipment in Environmental Vibration) has been initiated by AFWAL to generically demonstrate the passive damping control of panel mounted component vibration. Parallel RELSAT programs are being performed by Boeing and General Electric.

The approach used in the GE-RELSAT program is to design, fabricate and test a damped DSCS III transponder panel. The DSCS III (Defense Satellite Communication System) spacecraft was selected because the design is mature and enables interdisciplinary constraints to be readily defined. The goal is to achieve a reduction of 6 dB in the random vibration environment. As shown in Figure 1, large diameter shuttle spacecraft random vibration requirements exhibit high spectral amplitudes in the frequency range below 200 Hz where major equipment resonances occur. By obtaining a 6 dB reduction, the spectrum levels are reduced to those of current small diameter spacecraft. For any size spacecraft, the vibroacoustic reliability is significantly enhanced.

Three workshop papers are included in the proceedings covering different aspects of the GE-RELSAT program. This paper discusses the design and analysis of the panel and describes modal tests performed to verify the resonant frequency and modal damping predictions. The quantification of the cost reduction and reliability improvement, as well as the experimental results from acoustic and shock tests are presented in a second paper. The third paper discussed the selection of the viscoelastic material and describes the methods used in fabricating the damped panel.

The following sections discuss the panel design and analysis, the correlation of beam element tests with analytic predictions, comparison of panel modal test results with analytical results, and finally the conclusions reached in this portion of the RELSAT program.

2.0 TRANSPONDER PANEL DESIGN

The test article chosen for viscoelastic damping treatment was the North Panel Bay 3 of the Defense Satellite Communications System (DSCS) III, Figure 2. This equipment panel is approximately 27 inches square, constructed of magnesium thorium .18 inches thick and contains two integrally milled/riveted stiffeners. Three 10 watt traveling wave tube amplifiers (TWTA's) are mounted on it along with associated wave guides and electronics. These TWTA's place a

severe design constraint on the panel since the thermal requirement to dissipate their 30 watts of power makes the use of a lightweight honeycomb sandwich for the base panel impractical. Hence, the thick .18 plate which is required for thermal, not structural reasons.

The test articles for the RELSAT program utilize a .125 inch thick aluminum plate to simulate the stiffness of the actual .18 inch thick magnesium-thorium panel. The TWTA simulators are made of an aluminum block mounted to a steel plate. They provide the weight and center of gravity of the actual TWTA's and other components necessary to make the total panel weight equal to that of the actual flight hardware.

2.1 BASELINE UNDAMPED PANEL

This panel was designed to closely simulate the "as is" undamped North Panel Bay 3. It consists of the aluminum base plate and three TWTA simulators plus two aluminum hat section stiffeners in lieu of the integrally milled/riveted stiffeners on the flight hardware. These stiffeners were sized to provide a fundamental frequency near that of the actual DSCS panel. Figure 3 is a photograph of this test article, the NASTRAN model for which is shown in Figure 4. This model which contained 412 GRIDS and 259 ASET degrees of freedom (DOF) was constructed entirely of CQUAD4 elements with the exception of the TWTA's which were single 6 DOF nodes attached to the panel with rigid elements.

A modal test was performed on the baseline panel to provide a reference for damped panel measurements, and to verify analysis methods without the added complexity of modeling viscoelastic properties. Inaccuracies in the undamped panel model will be propagated in the viscoelastic properties used for damped panel analysis since these are very frequency dependent. These inaccuracies may result from both lack of detail in modelling, and from the unknown boundary condition.

2.2 DAMPED PANEL DESIGN

Two damped stiffener concepts were used in the designs. These were a honeycomb sandwich stiffener with a honeycomb sandwich constraining layer, and an aluminum hat section stiffener with a graphite constraining layer. Both of these concepts are illustrated in Figure 5. As in the baseline design, the aluminum hat section stiffener simulates the integrally milled/riveted stiffener on the actual DSCS III spacecraft equipment panel. The honeycomb sandwich stiffener is designed for lighter weight, and maximizes the strain energy in the viscoelastic material through a larger separation of the constraining layer neutral axis from the viscoelastic layer. One example, using each of these two concepts will be discussed in this section: a panel with honeycomb stiffeners and SMRD 100F90B damping material, and a panel with aluminum hat section stiffeners and SMRD 100B50A damping material.

A total of seven damped panels were designed for the RELSAT program. The scope of this paper is to describe the analysis used to design the panel damping treatments, and the correlation of the analysis to data from the modal test performed on one of the damped test articles.

2.2.1 DAMPED DESIGN CRITERIA

A primary objective of this effort is to demonstrate a 50% reduction of vibro-acoustic response by developing damped panel designs. A preliminary damping criteria which is expected to accomplish this is:

- 1) a minimum loss factor of 0.30 in the fundamental equipment panel mode, and
- 2) a minimum loss factor of 0.10 for all other major panel modes up to 500 Hz.

In addition to the damping criteria, structural design criteria must also be established.

A set of structural design criteria have been established for developing damped panel designs. These criteria are based on varying degrees of conservatism in the assumptions regarding: 1) the degree to which the vibroacoustic loads have been reduced, 2) limits on expected deflections, and 3) the degree to which the viscoelastic damping treatment is assumed to share in design loads for the panel structure.

Equivalent steady load factors are often used for satellite structure design. These load factors are usually composed of two parts: 1) a low frequency or quasi-steady part which consists of the nearly steady acceleration at liftoff plus a low frequency (typically of the order of two to fifty Hz) transient during liftoff; and 2) a higher frequency vibroacoustic portion induced by acoustic pressures caused by the propulsion system during launch. The sum of these two effects results in an equivalent design load factor which is used for design of secondary structures and components. The primary structure is generally designed by the quasi-steady portion only.

Three structural design criteria for the damped DTA designs are considered as shown in Table 1.

Criterion I - Baseline: Designs using this criterion represent "add-on" damping configurations. These designs consider neither the reduced dynamic loads due to damping nor the load carrying capacity of the damping treatment. For the DSCS III transponder panel the baseline structural design criterion consists of a 60 Hz minimum frequency requirement and a 35 G total load factor. The 35 G load is the sum of an 11.5 G quasi-static and a 23.5 G vibroacoustic load.

Criterion II - Conservative Integrally Damped: This criterion considers the reduction in dynamic loads due to damping, but does not allow for the load carrying capability of the damping treatment. The structural integrity of the panel is maintained by the undamped structure which is designed to a load factor which has now been significantly reduced by damping. The goal of the GE RELSAT program was to reduce the vibroacoustic portion of the dynamic loading by 50 percent. The total load factor for the criterion II design is therefore the sum of an 11.5 G quasi-steady load and a vibroacoustic load reduced to 11.8 G, or 23.3 G as compared to 35 G for the criterion I design. The stiffness of the undamped panel designed to this lower load factor will be less than that of the baseline panel, but its deflection under the combined quasi-steady and vibroacoustic load of 23.3 G will be kept the same as that of the baseline panel under 35 G's.

Criterion III - Advanced Integrally Damped: This design criterion considers not only the reduction in vibroacoustic load due to damping, but also allows for the damping treatment's load carrying capability. This will provide the lightest weight damped design. The total design load factor remains at 23.3 G as in criterion II, but allowing the damping treatment to carry part of the structural loads will result in a lower weight design. For this criterion, the stiffness of the undamped panel may be further reduced using the requirement that the deflection under 23.3 G of the damped criterion III design does not exceed that of the undamped criterion II design under the same load.

Table 2 and Figure 6 illustrate the structural weight obtainable with the three criteria. This table compares preliminary design results using all three criteria to the undamped baseline. The first three damped designs utilized an aluminum hat section stiffener, with a graphite constraining layer, while the last used a honeycomb sandwich stiffener and constraining layer. The criterion II design with hat stiffeners is seen to provide a 2% structural weight reduction from the add-on, and the criterion III design with hat stiffeners provides an additional 2% reduction. Using honeycomb sandwich stiffeners in place of the aluminum hats, reduces the weight by another 8% so that it is comparable in weight to the original undamped structure.

Final designs of the RELSAT test articles were all performed using criterion III.

2.2.2 DESIGN ANALYSIS METHODS

Design of the damped panels was performed primarily with MSC NASTRAN modal strain energy (MSE) calculations. The strain energy option in NASTRAN outputs tables of strain energy in each element of the NASTRAN finite element model, for each mode shape calculated. The viscoelastic material is modeled with solid brick elements having a shear modulus which is selected for a temperature and frequency. The ratio of the MSE in the viscoelastic elements, to the total MSE in the mode shape, multiplied by a material loss factor gives the composite loss factor. Since the resulting loss factor is correct only for the selected temperature and frequency several runs must be made using different VEM shear moduli to get results for all modes of interest. A NASTRAN direct frequency response analysis will produce sinusoidal transfer functions which account for the frequency dependence of the shear modulus and loss factor in a single run. However, if the structure being analyzed does not have modes which are well enough separated to be considered as single-degree-of-freedom responses, the equivalent normal modal characteristics cannot be readily obtained.

Of all the variables in the finite element model, the shear modulus of the VEM, which is both frequency and temperature dependent, is the most difficult to quantify. The shear modulus was obtained from VEM test data which is reduced by a least squares fit to equations for shear modulus and loss factor as a function of frequency and reduced frequency. The reduced frequency is the frequency multiplied by a shift parameter which is a function of temperatures relative to a reference temperature, T_0 . Experience has shown that this reference temperature is difficult to choose properly and that the size of typical discrepancies which often occur can produce significant differences in material properties using test data from different sources. An accurate and consistent method for choosing T_0 has been determined to be a much needed development to increase the reliability of finite element damping calculations.

Another, much simpler but often useful analysis method is that described by Abdulhadi⁸. This is a "general analysis...for three layer plates consisting of two distinct plate type facings and a core that carries shear stresses only." A sixth order equation is solved to obtain composite frequency and loss factor for various boundary conditions. Abdulhadi's method is a useful method for optimization of damping treatments for uniform beams and plates. This analysis method was used to size sub-panel dampers. These graphite epoxy constraining layer damper strips were added to reduce the acoustic response of the sub-panels, which had frequencies calculated to be between 300 and 500 Hz.

2.2.3 SMRD 100F90B DAMPED, HONEYCOMB STIFFENED PANEL

This panel uses the aluminum baseplate and three TWTA simulators previously described, as do all of the test articles. It incorporates four honeycomb sandwich stiffeners in a "criss-cross" pattern. These are made from .4 inch thick Hexcel 1/8-5052-.002 aluminum honeycomb with a 5 mil aluminum lower face sheet and 30 mil aluminum upper face sheet. The damping is provided by .25 inch thick General Electric SMRD 100F90B viscoelastic damping material between the stiffeners and a honeycomb sandwich constraining layer. The constraining layer consists of .4 inch thick Hexcel 1/8-5052-.002 aluminum honeycomb with a lower face sheet of 5 mil uniaxial HMS/CE339 graphite epoxy and upper face sheet of 80 mils uniaxial HMS/CE339. A sketch of this stiffener/constraining layer is shown in Figure 5.

The .5 inch width of the stiffeners was chosen as a result of previous parametric analysis on a stiffened end supported plate which showed this width to provide optimum damping for the lowest weight, and the desire to use as little of the panel area as possible since most satellite equipment panels are very densely filled with components.

The panel stiffener height and face sheet are designed to provide a minimum frequency to satisfy the static deflection requirements of criterion III. The constraining sandwich layer is designed to provide adequate stiffness under the transient and vibroacoustic loads of criterion III and, along with the viscoelastic material, to provide a minimum loss factor of .3 in the fundamental mode, and .1 for all important modes below 500 Hz. Figure 7 is a photograph of this panel. The NASTRAN model used for correlation with the modal test data is shown in Figure 8. This model contained 674 GRIDs and 294 ASET DOF. A more coarse model with 303 GRIDs and 78 ASET DOF was used in performing the parametric analyses.

NASTRAN Modal Strain Energy (MSE) analyses were run to determine the first mode mode loss factors for the various parametric configurations, and to give a conservative estimate of the loss factors for the higher modes. Figure 9 shows the NASTRAN MSE in the VEM plotted vs. VEM thickness, with the chosen design point circled. NASTRAN MSE calculations were made for a wide range of VEM shear modulus to give the loss factors for all modes up to 500 Hz. The calculated composite loss factors are plotted vs. frequency in Figure 10 for a temperature range of 60° F to 70° F, the temperature range during launch.

2.2.4 SMRD 100B50A DAMPED, HAT SECTION STIFFENED PANEL

This design employs four aluminum hat section stiffeners in the same pattern as the stiffeners of the honeycomb stiffener panel. These are .5 inches high, .5 inches wide, and bent up from 1/32 inch aluminum. The damping is provided by .10 inch thick SMRD 100B50A viscoelastic damping material and a constraining layer of .25 inch thick uniaxial HMS/CE339 graphite epoxy. A photograph of this panel is presented in Figure 11 and the NASTRAN model containing 367 GRIDS and 78 ASET DOF is shown in Figure 5 along with a sketch depicting the stiffener/constraining layer configuration.

NASTRAN MSE analyses were run to determine the first mode loss factors for the various parametric configurations, and to give a conservative estimate of the loss factors for the higher modes. Figure 12 shows the NASTRAN calculated strain energy in the VEM vs. VEM thickness. Constraining layer thickness and test article total weight as calculated by NASTRAN are cross plotted. The point chosen for the design is circled. The hat section was designed to meet the static deflection requirements of criterion III and the final choice of stiffener, VEM, and constraining layer was checked to ensure the satisfaction of the total deflection requirements. The calculated loss factors are plotted vs. frequency for modes up to 500 Hz. in Figure 13. Results for a temperature range of 60° F to 70° F are presented. Values for each temperature were determined from a single NASTRAN run using the shear modulus at the fundamental frequency and are therefore conservatively low in both frequency and loss factor for the higher modes. A more detailed model than the coarse one shown in Figure 11 would be required to accurately calculate loss factors for the higher modes, but since it was decided that the honeycomb stiffener panel would be used for the modal test and the analysis correlation tasks, a larger model was not justified. The more coarse model is adequate for determining the loss factor of the lower modes and performing the parametric analyses to determine the design point.

3.0 BEAM ELEMENT FABRICATION AND EXPERIMENTAL EVALUATION

Several beam elements of candidate stiffener designs were fabricated and tested to (1) verify fabrication methods planned for panels and (2) verify analytical predictions of performance. ISD112 and several GE-SMRD VEM's were used in a honeycomb sandwich configuration and in several hat stiffened configurations with unidirectional graphite-epoxy constraining layers. Results indicated ISD112 was not suitable for the stiffener configuration because of low bond strength. The SMRD materials were found to provide maximum performance close to room temperature but were slightly off on either the high or low side. Test results agreed reasonably well with analytical predictions using NASTRAN modal strain energy methods. Material properties appeared to be a major source of analysis error. Temperature was highlighted as the key variable effecting damping performance. These beam element tests are discussed in this section.

3.1 CANTILEVER BEAM ELEMENTS

3.1.1 TEST CONFIGURATIONS

A cantilever beam specimen was designed and fabricated to provide an early evaluation of candidate configurations, a preliminary correlation of analysis predictions with measured damping performance and identify unanticipated fabrication problems. The beam test article is shown in Figure 14. The honeycomb sandwich configuration was the lightest weight design using graphite epoxy (G/E) face sheets with thicknesses selected to provide inherent structural stiffness corresponding to criterion III. Honeycomb face sheet thicknesses were selected to maximize damping as discussed previously. Steel bars bonded to the bottom surface of the beam provided transverse stiffness and increased the weight so that the resonant frequencies would be in the range of panel designs. SMRD 100F90 material of 1/4 inch thickness was found to approximate the desired damping and is of the thickness used in other spacecraft applications. The beam width was arbitrary. The aluminum thickness simulates the stiffness of the DSCS III magnesium panel.

The initial viscoelastic material selected for the honeycomb sandwich was ISD112 with a 10 mil thickness. This material uses a pressure sensitive adhesive and was found to come loose as a result of surface irregularities in the honeycomb pieces. This problem combined with concerns as to the bond strength in this stiffener application resulted in a change to SMRD 100F90. The SMRD 100F90 uses a structural adhesive (HYSOL EA9309.3) known to exceed the VEM shear strength.

3.1.2 ANALYTICAL PREDICTIONS

A NASTRAN model of the Honeycomb cantilever beam configuration was used to estimate the damping and fundamental resonant frequency using the Modal Strain Energy method (MSE). The model was relatively coarse as shown in the SUPERTAB plots of Figure 15. The beam was divided into 10 spanwise segments and 7 crosswise segments using a single row of elements to represent the stiffeners and has 219 nodes. CQUAD4 elements were used for the aluminum baseplate and the honeycomb face sheets. The VEM and honeycomb core were modeled using CHEXA elements. Offsets were used in the CQUAD4 elements adjacent to the CHEXA elements so that common nodes could be used between the elements while simulating the neutral axis position. The steel bars were modeled using CBAR elements with offsets. All nodes at the cantilevered end were fixed which represented the interface with the test fixture, i.e. all DOF's at the end nodes of the plate, stiffener, VEM, and constraining layer. The model was reduced to 52 ASET DOF's of which approximately two-thirds were in the out-of-plane direction. The full mass matrix was calculated by NASTRAN using material densities for the various elements. A model check was made for the fundamental mode by increasing the number of nodes and dynamic DOF's by approximately 4; however, the much finer model results did not differ significantly from the coarse model. The Young's modulus for the G/E elements was 30E6 psi based on a 60 percent fiber volume fraction. The shear moduli for the honeycomb core were 135 Ksi and 54 Ksi representing the nominal value for 1/8-5052-.002 core material provided by Hexcel. The shear modulus of the viscoelastic material was varied over a range of values to determine the fundamental mode resonant frequency and loss factor as a function of temperature.

The analytical prediction of the fundamental resonant frequency and loss factor as a function temperature were determined by combining the NASTRAN results with the SMRD 100F90 properties displayed as a function of reduced frequency. The procedure is shown graphically in Figure 16. The VEM shear modulus, G, was varied in the NASTRAN analysis and the fundamental resonant frequency determined and plotted. The percent of modal strain energy in the VEM was also determined and plotted in the Figure. A resonant frequency was selected and the value of G determined from the NASTRAN results as indicated by Step 1. Using these values for F and G, the corresponding temperature is uniquely determined as shown. This also determines the VEM loss factor as indicated in the figure. The VEM loss factor and the NASTRAN modal strain energy are then combined as described previously to determine the composite loss factor. This procedure is repeated for various frequencies providing the analytical prediction of resonant frequency and composite loss factor as a function of temperature. The analytical results for the cantilever beam are shown in Figure 17.

The analytical results were determined using two different sets of material properties. The properties of SMRD100F90A have been determined by three different laboratories. Although the approaches used by each were similar, differences exist in the final properties. Two Reduced Temperature Nomographs are shown in Figure 18. The basic nomograms differ in shift parameters precluding direct comparison. The shear modulus and loss factor data from these two nomograms were used to define the properties at a temperature of 65 F and plotted vs. frequency in Figure 19. Also included is a third set of data measured from the same batch of VEM that was used for the Lab B measurements. The Lab A and Lab B measurements were both performed with sandwich beams and the data reduced with different α_T relations and different To constants. The Lab C measurements were obtained from a modified Oberst beam and reduced with the same α_T relation that was used for the Lab B data reduction, but with a different To.

It is apparent from the three curves of Figure 19 that more research should be performed on VEM measurement and data reduction methods. There is considerable scatter in the raw data through which these curves were faired, and the choice of constant To in the temperature shift relation α_T is of great importance. Analyses were performed using the two reduced temperature nomograms and results were compared with test results.

The accuracy of these analytical predictions depends on the accurate modeling of the overall structure as well as the accurate representation of the VEM properties. Inherent in the procedure is the assumption that the model without the VEM accurately predicts the structural behavior. If the model of the non VEM structure is too stiff, then the analytical predictions will require a lower VEM shear modulus to match the measured resonant frequency. This will ultimately result in an apparent shift in the analytic results to a higher temperature. Similarly, higher strain energy in the non VEM structure will cause the analytical composite loss factor to be low. On the other hand, inaccuracies in the VEM properties could cause the analytical predictions to vary in either direction. When correlating analytical and experimental results, structural model error sources should be kept in mind and the overall difference should not be attributed solely to the VEM modeling.

3.1.3 EXPERIMENTAL RESULTS

The cantilever beam was tested using base excitation and circle fit techniques to accurately determine the resonant frequency and damping. The beam was clamped over a two inch span at the root and bolted to a Team Hydrostatic Table which was driven with an MB C-150 shaker. Three accelerometers were mounted to the tip of the beams to determine the phase and amplitude of the beam response. A single reference accelerometer was mounted to the vibration table to measure the input. The beam was excited sinusoidally. The accelerometers were recorded on magnetic tape and processed through the HP5423A Dynamic Analyzer. The analyzer determined the resonant frequency and damping of the beams at the fundamental resonance using a circle fit to the response with the input acceleration used as a reference. Because the fundamental mode was well separated from other resonances, this technique provided an accurate estimate of the loss factor and resonant frequency. The measurements were repeatable within approximately 1% and are not subject to inaccuracies associated with bandwidth measurements. Initial tests at input levels varying from 1/2 to 2 g's indicated that non-linear effects were small compared to temperature effects. Tests were subsequently performed with a single input level.

A crude method was used in these initial tests to vary temperature. The original intent was to test the beams only at room temperature. However, as the tests progressed, it was evident that the temperature should be varied to provide adequate data to evaluate the damping performance. This was accomplished by varying the room air conditioner setting to obtain low temperatures and using heat lamps to obtain higher temperatures. A thermocouple was taped to the VEM portion of the beam to determine the test temperature. Using these techniques, the temperature varied from approximately 55° to 100° F. The test results are shown in Figure 17.

3.1.4 COMPARISON OF ANALYTICAL AND EXPERIMENTAL RESULTS

The experimental results for the honeycomb sandwich beam cover a relatively wide temperature range and indicate reasonable agreement with analytical predictions but with an apparent temperature shift. The measured fundamental resonant frequency varied from 204 to 124 Hz which compares favorably with analytical variations from 209 to 118 Hz. There appears to be a 4 to 8 degree F shift in the resonant frequency curve but this could be caused by underestimating the cantilever beam stiffness (e.g. the analytical shear stiffness of the honeycomb was lower than actual). This tends to be substantiated by the asymptotic values. A similar shift in the temperature of maximum damping is also evident. The maximum measured loss factor is within 1 to 17 percent of predicted. The difference in the VEM properties obviously has a major effect on the accuracy of the analytical predictions.

The results of these initial tests indicated the need to obtain more detailed test data to evaluate performance and to consider other damping materials. The temperature was identified as a key parameter to correlate test and analytical results. A wide, well controlled temperature variation is needed to provide data on the analytical adequacy by checking both glassy and rubbery asymptotes, with more accurate measurements in the transition region. A test of the basic undamped structure would be helpful to verify analytical model accuracy. The observed peak damping was above the temperature range of interest indicating peak performance would require a different VEM material. Some

of the differences between test and analysis can be attributed to the uneven temperature distribution in the test article caused by the heat lamps.

3.2 END SUPPORTED BEAM ELEMENTS

Following the tests of the cantilever beam specimen, two end supported beams were fabricated and tested. The objective of these tests was to obtain better analytical correlation by using end supported test articles and by using a thermal chamber over the shaker so that the temperature could be controlled more accurately. In addition, one beam used SMRD 100B50 which has a lower transition temperature than SMRD 100F90.

3.2.1 TEST CONFIGURATIONS

The end supported beam test configurations are shown in Figure 20. The beams consisted of a 10 inch wide by 17 inch long 1/8 inch aluminum plate. Five steel bars were bolted and bonded to the plate to provide chordwise stiffness and beam resonance in the frequency range of interest. A single half inch wide hat section was riveted to the center of the beam simulating a criteria III stiffener. The viscoelastic material was bonded to the stiffener and a constraining layer of G/E with uniaxial fibers was bonded to the VEM. The VEM layers were 1/4 inch thick SMRD 100F90A and 0.10 inch thick SMRD 100B50C. The beam was bolted with washer stand-offs to aluminum bars which were attached to the 30 inch diameter head of an MB C-220 shaker. The end supported configuration was felt to be more readily analyzed than the cantilever arrangement used in the initial tests. The entire shaker head was enclosed in a small thermal chamber which contained a heater, a blower and a thermostatic control. Liquid CO₂ was vented into the chamber to cool the test article below ambient temperatures. Thermocouples sandwiched within a block of SMRD and attached to the outside of the block were used to determine when the temperature of the test article had stabilized.

3.2.2 ANALYTICAL PREDICTIONS

The analyses of the end supported beams were performed using NASTRAN and the MSE method described for the cantilever beam. The SUPERTAB plot of the FEM is shown in Figure 21. The model was finer than that used for the cantilever specimens having 18 elements in the spanwise direction and 9 elements chordwise. The model used CQUAD4 elements with offsets for all but the steel bars and VEM. The steel bars were modeled using CBAR elements with offsets. The VEM was modeled using CHEXA elements as in the cantilever model. The modulus of the VEM was varied in the NASTRAN analysis and the final results presented as a function of temperature using material property curves as described previously. An additional analysis was performed for the bare beam without the VEM to correlate with test results.

The analytical predictions for the hat stiffened beam are shown in Figure 22. The resonant frequencies of the first three modes are shown for both simply supported and clamped boundary conditions. Because of the dependance of the VEM model on that of the model for the basic stiffened beam, analysis and testing of this configuration was performed. The analytical results for the two damped beam configurations are shown in Figures 23 and 24 for the 1/4 inch

SMRD 100F90 and for the 0.10 inch SMRD 100B50 respectively. For the SMRD 100F90, analytical results are presented for both Lab A and Lab B material property data. For the SMRD100B50, only one set of material property data was available.

3.2.3 EXPERIMENTAL RESULTS

The experimental results are shown in Figures 22 to 24 for the various test conditions. The tests were performed in the same manner as the cantilever tests except that the MB C-220 shaker was selected because of its larger head diameter. The major change in the procedure was the use of the thermal chamber over the test article which improved the accuracy and range of test temperatures. The instrumentation consisted of three response accelerometers: two at midspan at the center and edge and one at quarter span in the center. The input was measured at one end of the beam. The response at the center mid-span was circle fit to measure the fundamental resonant frequency and damping. The other midspan accelerometer was checked for torsion which was found to be negligible at the fundamental resonance.

3.2.4 COMPARISON OF ANALYTICAL AND EXPERIMENTAL RESULTS

The first step in correlating the analysis and test results was to compare the resonant frequencies of the basic undamped beam, Figure 22. This was done by plotting the ratio of the analysis to the test frequency for the first three bending modes. This comparison showed that there is excellent agreement in the fundamental resonant frequency when the analysis considers the beam to be clamped at the bolt attachments. There are, however, significant differences in the second and third resonant frequencies which were closer for pin constraints at the bolt attachments. In the interest of expediency, the results were considered satisfactory for analytical predictions of fundamental mode resonant frequency and damping. The decision was made to proceed but to limit comparisons to the fundamental mode only.

The analytical results for the beam with the 1/4 inch SMRD 100F90, Figure 23 agree reasonably well with test results for resonant frequency and temperature of maximum damping when Lab A material properties are used. Using Lab A material properties, the calculated temperature of maximum damping, 77° F, agreed with the test within measurement accuracy with less than 5 percent difference in the corresponding resonant frequency. The maximum damping, however, was 34 percent higher than measured. This agreement was considered to be partially the result of the accuracy of the beam-stiffener model which agreed within 2 percent of the measured resonant frequency. Using the Lab B material properties, the calculated temperature of maximum damping was approximately 77° F which was the same as predicted using Lab A properties. The analytical resonant frequency also agreed reasonably well. However, the maximum calculated damping was 21 percent higher than measured.

For the beam using the SMRD 100B50B, the analysis results agreed fairly well with measured values although only one estimate of material properties was available, Figure 24. The resonant frequency closely follows the measured values but shows a higher calculated asymptotic value at high temperature; this indicates a higher analytical stiffness of the basic beam than actual. The

temperature of maximum damping was 6° F lower than measured with the maximum calculated damping about 30 percent higher than measured. The resonant frequency of maximum damping agreed closely.

The summary of the beam test data is given in Table 3 and Figure 25 comparing the maximum loss factor and the corresponding temperature and resonant frequency. The maximum loss factor appears to be the most error prone with 30 percent variations between analysis and test. Calculated resonant frequencies and temperatures at the maximum damping point are generally within 15 percent and 3° F, respectively. The table indicates a high sensitivity of results to material properties. It will be noted that modeling errors of the basic stiffened beam are included in the calculations and the variations should not be considered to be solely VEM associated.

4.0 PANEL MODAL TESTS

4.1 TEST DESCRIPTION

The general arrangement of the modal tests is shown in Figure 26. The two test panels were the undamped baseline panel and the lightweight honeycomb configuration with a quarter inch layer of SMRD 100F90B between the inner aluminum honeycomb stiffener and the outer graphite epoxy honeycomb constraining layer. Each test panel had the simulated TWT's installed and was bolted to a test frame along its four sides. The frame, in turn, was bolted to a massive rigid base. The frame had numerous openings machined around it to permit air to flow into the opening between the panel and the base fixture. (Initial tests indicated that the air trapped between the panel and the mounting base stiffened the test panel. After the openings were machined into the frame the fundamental panel mode was found to drop to nearly half the original test frequency.) A single Unholtz Dickie 50 pound permanent magnet shaker was attached to one of the TWT's through a flexible stinger which contained a piezoelectric force transducer and accelerometer at the TWT attachment end. The shaker was attached at the outer edge of one TWT for tests of both the baseline undamped panel and the damped panel. For the damped panel, a second shaker attachment at the center of the middle TWT was also used. Analytical predictions prior to performing the test indicated that these locations would effectively excite the modes of the panel below 300 Hertz. The shaker was suspended from a bungee sling attached to an overhead crane that could readily be positioned to align the shaker with the panel.

The instrumentation for the undamped baseline panel was limited to three accelerometers while 14 accelerometers were used for the damped panel. All of the accelerometers measured vibration normal to the panel except for two accelerometers mounted to the top of the center TWT on the damped panel. While a single accelerometer at the top center of each TWT measured the undamped panel responses, four accelerometers mounted at the bottom corners of the TWT's were used to measure the out of plane TWT response on the damped panel. The temperature of the damped panel was measured with a thermocouple attached directly to the viscoelastic material.

A portable air conditioning unit was used to control the temperature by directing a flow of cooling air over the test panel. Data were obtained at 70° F. Endevco 2213 accelerometers and a Krystal force transducer were used to measure the response and excitation. Previous tests have shown negligible phase shifts between the transducers at frequencies above 5 Hz.

A pure random shaker excitation was applied over the frequency range from 20 to 500 Hertz. The force Power Spectral Density had a 6 dB/octave roll-up to improve the response signals in the higher modes. The transducer signals were analog recorded using a Spectral Dynamics multiplex system and played back for subsequent modal data processing. A shaker force of 8 pounds RMS was used to excite both the undamped and damped panel. The force amplitudes were arbitrarily selected to provide adequate response measurements.

The data were reduced using an HP5451B Fourier Analyzer with a University of Cincinnati (UCMIE) software package. The analog data were digitized and transfer functions generated using the Analyzer. The coherence was checked to assure accurate transfer function definition with zoom analysis performed to improve accuracy where needed. A typical transfer function is shown in Figure 27 and indicates the coherence was very close to unity in the resonant frequency range. Adequate frequency resolution was provided for both the undamped and damped panels. The UCMIE software option used for extracting modal parameters was the Least Squares Multi-Mode curve fit routine. This was necessary because of the large amount of modal overlap in the heavily damped modes as well as those panel modes which had closely spaced resonant frequencies. The mode shapes determined from the transfer functions were transferred by digital tape to the large mainframe computer for comparison with analytical predictions. Because of the limited number of measurements, the dot product between the test and analysis modes was used for comparison.

4.2 ANALYSIS TEST CORRELATION

The first seven out-of-plane analytical modes of the undamped panel with fixed edges are compared with the test results in Table 4. The modal dot products were calculated using only the Z motions normal to the panel for both the test and analysis modes. The dot products show good agreement between analysis and test mode shapes with those modes dominated by Z motion having values greater than 0.9. As would be expected, the agreement is not as good for modes having a large amount of rocking or X and Y motion. The resonant frequencies agree with test values to within approximately 10 percent. The test panel was bolted directly to the base plate at all locations which should have given it a nearly fixed boundary condition. The test loss factors were on the order of 0.03 or less showing the baseline structure to have relatively little damping.

The analytical predictions for the damped honeycomb panel are compared with the test results in Table 5 for a temperature of 70°F. The analysis is based on fixed boundary conditions along the four panel edges. As indicated in the Table and shown graphically in Figure 28, the resonant frequencies of the first four out-of-plane modes agree with test values within approximately 10% while larger errors are apparent in the higher modes. The coarseness of the NASTRAN model is believed to contribute to this error; however, it is apparent that the error in the resonant frequencies of the two highest modes are significantly greater than the error in undamped panel analysis. The model dot products are compared in Figure 29 and show good agreement with only two of the damped panel

modes showing values lower than those of the undamped panel. The ratio of the measured to calculated loss factors is shown graphically in Figure 30. The comparison indicates that the calculated values tend to be less than the measured values but that the measured values are generally greater than two-thirds of the calculated values. The earlier element test results gave similar results with the agreement between calculated and measured loss factors being closer when maximum values were used. Subsequent panel tests using the base excitation method were performed over a wider temperature range to better correlate the analysis and test results.

The damped panel was excited sinusoidally by exciting it through its base using the MB C-220 shaker. The temperature was varied from approximately 60° F to 90° F using the portable thermal chamber. The measured response was analyzed digitally using an HP5423A Fourier Analyzer to provide circle fits to the measured response. The input acceleration was used as the reference. Because of the overlap of the modal responses, circle fit results were only obtained for the fundamental mode. The results shown in Figure 31 agree with the previous test results and indicate that a maximum loss factor of 0.27 occurs at approximately 77° F. This is in closer agreement with the analytical predicted value of 0.35 but is shifted to a higher temperature.

The results of the modal test verify that a large amount of damping can be introduced into the panel with the damped honeycomb stiffeners. Although the maximum measured loss factors are less than the predicted values, the values agree within approximately 30 percent. The test results indicate that another viscoelastic material having a lower transition temperature would be more effective in damping the panel.

5.0 CONCLUDING REMARKS

Damped DSCS III Transponder equipment panel designs were developed using constrained layer viscoelastic materials (VEM's) on the panel stiffeners. Although preliminary studies indicated integrally damped honeycomb panels would be lighter and more effective, the damped stiffener design was selected because of thermal constraints caused by the high heat dissipating TWTA's. By using design criteria that accounted for the load reduction achieved by the damping, the weight impact was limited to 2 to 10 percent of the structural weight for the highly damped panel final designs. NASTRAN finite element analyses using Modal Strain Energy were used to systematically examine structural and VEM parameters to optimize the design. The VEM properties were represented with reduced frequency nomographs.

Reasonable agreement was obtained between analytical predictions and experimental results. Frequency and temperature were shown to govern the damping and resonant frequencies of VEM panel designs both analytically and experimentally. Analytical and measured modes shape agreement for the damped panel was nearly comparable to that of the undamped panel based on the dot product comparisons. There appeared to be shifts in the predicted temperature of maximum damping on the order of 3 to 10 degrees F. The resonant frequencies of the first seven panel modes agreed with analysis prediction within about 12 percent which was comparable to the agreement for the undamped panel. The maximum measured loss factor was within approximately 30 percent of analytical predictions with some values showing negligible variation. At specific temperatures, the measured

loss factors were on the order of one half to two thirds of analytical predictions for the final panel design. Material property variations were shown to have a major effect on analytical predictions and could account for most of the differences between analysis and test results. Boundary conditions and inaccuracies in the finite element model of the basic structure also contribute to the test/analysis difference.

Large reductions in resonant magnifications were achieved with the damped stiffener designs. The first mode magnification measured on the undamped baseline panel was 26. The constrained layer damper design of the damped modal test panel reduced this Q of 26 to only 4.3 at the temperature of the modal test, (70° F) and to 3.7 at the temperature at which the peak loss factor was found during subsequent temperature sweep testing. These values compare to the Q of 3.0 which was calculated using NASTRAN MSE with VEM properties determined from a reduced temperature nomogram.

Subsequent acoustic test results showed that the damped panels were highly effective in reducing the random vibration environment. The initial goal of 6 dB reduction in the PSD was exceeded in the low frequency range by a large amount.

The results of this study demonstrate the effective application of viscoelastic material technology to the design of equipment panel structure.

6.0 REFERENCES

1. A. R. Timmins and R. E. Heuser, "A Study of First Day Space Malfunctions," NASA TND-6474, 1971.
2. R. B. Laube, "Methods to Assess the Success of Test Programs," Proc. of the 3rd Aersp. Testing Sem., Oct. 1982.
3. J. M. Medaglia, "Dynamic Integrity Methods Including Damping for Electronic Packages in Random Vibration," 50th Shock and Vib. Bull., 1980.
4. J. A. Staley and C. V. Stahle, "Damping in Support Structures for Equipment Reliability - RELSAT," Vibration Damping Workshop, Feb. 1984.
5. C. V. Stahle, "Cost Effectiveness of Spacecraft Vibration Qualification Testing," Proc. of Inst. of Env. Sci., 20th Annual Meeting, May 1974.
6. J. A. Staley, C. V. Stahle, J. C. Strain, "Vibroacoustic and Shock Performance of Damped Spacecraft Equipment Panels", Vibration Damping Workshop II, AFWAL March 1986.
7. K. A. Schmidt, F. Curtis, E. Muziani, L. Amore, "Fabrication of Damped Spacecraft Equipment Panels", Vibration Damping Workshop II, AFWAL March 1986.
8. F. Abdulhadi, "Transverse Vibrations of Laminated Plates with Viscoelastic Layer Damping," Shock and Vib. Bull. No. 4, Dec. 1969.

Table 1 Panel design criteria

CRITERION	LOAD FACTOR (G)				DEFLECTION
	STEADY (ZERO FREQ)	TRANSIENT (2 Hz)	VIBRO- ACOUSTIC	TOTAL	
I. ADD-ON DAMPING - BASIC PANEL DESIGN- ED ASSUMING LOW DAMPING	1.0	8.5	23.5	35.0	ABOUT 0.10 INCH
II. INTEGRAL DAMPING - 50% REDUCTION IN VIBROACOUSTIC LOAD - NO LOAD CARRYING CAPABILITY OF DAMPING TREATMENT ASSUMED	3.0	8.5	11.8	23.3	ABOUT 0.10 INCH
III. INTEGRAL DAMPING - 50% REDUCTION IN VIBROACOUSTIC LOAD - DAMPING TREATMENT CARRIES TRANSIENT AND VIBROACOUSTIC LOADS	3.0	8.5	11.8	23.3	ABOUT 0.10 INCH

8. DAMPING
- FUNDAMENTAL PANEL MODE LOSS FACTOR AT LEAST 0.3
- LOSS FACTOR FOR OTHER MODES UP TO 500 Hz AT LEAST 0.1

Table 3 Summary of beam test results

TEST BEAM DESCRIPTION	MAX LOSS FACTOR ()		RESONANT FREQ		TEMPERATURE		VIBROACOUSTIC MATERIAL	
	TEST	ANAL	S DIFF	TEST (Hz)	ANAL (Hz)	D DIFF	(F)	
CANTILEVERED H/C SANDWICH	46	0.465/ 0.38	+1.1/ -17.4	137	138/ 149	-0.1/ +8.8	100 35	1/4 INCH SMRD 100F90A
END SUPPORTED HAT-1/4 IN. VEN	0.29	0.39/ 0.35	+34.5/ +20.7	82	E6/ 94	+4.9/ +14.6	77 15	1/4 INCH SMRD 100F90A
END SUPPORTED HAT - 0.10 IN. VEN	0.36	0.47	+30.6	90	91	1.1	37 6	0.10 INCH SMRD 100B50C

NOTES: 1) ANALYSIS VALUES SHOWN FOR LAB A AND LAB B 100F 90 MATERIAL PROPERTIES.
2) FUNDAMENTAL MODES ONLY.
3) VALUES OF PARAMETERS ESTIMATED FOR MAXIMUM LOSS FACTOR POINT.
4) CANTILEVER BEAM TEST TEMPERATURE NOT ACCURATELY CONTROLLED.

Table 2 Preliminary design weight summary

PANEL DESIGN	STIFFENER/DAMPER		TOTAL STRUCTURE & DAMPER		TOTAL PANEL	
	LB	%	LB	%	LB	%
BASELINE-UNDAMPED	0.86	100	8.48	100	47.5	100
DAMPED STIFFENER*	1.75	203	9.37	110	48.4	102
CRITERIA I	1.55	180	9.17	108	48.2	101
CRITERIA II	1.33	155	8.95	106	48.0	101
CRITERIA III (HAT STIFFENER)	0.72	84	8.34	98.3	47.3	99.7
CRITERIA III (HONEYCOMB STIFFENER)						

*DAMPED STIFFENER DESIGNS USE P100 GRAPHITE (E=60E6, UNIAXIAL)

Table 4 Undamped panel modal test comparison

MODE NO	FIXED ANALYSIS	TEST FREQ	FIXED FREQ	MODAL DOT PRODUCT	TEST LOSS FACTOR	MODE DESCRIPTION	
						FREQ (Hz)	(Hz)
1	55.4	49.7	11.5	1.000	.038	Z	
2	117.4	106.1	10.7	.892	.016	Y - Z	
3	123.4	110.3	11.9	.947	.022	Z - X	
4	147.5	135.2	9.1	.946	.014	Z - X	
5	210.6	213.5	- 1.4	.604	.020	X - Z	
6	247.9	251.5	- 1.4	.975	.030	Y	
7	279.8	270.3	3.5	.804	.027	X - Z	
8	286.5	280.4	2.1	.810	.022	X - Z	

NOTE: MODAL DOT PRODUCTS INCLUDE ONLY Z MOTIONS

Table 5 Modal test comparison for damped honeycomb panel

70° P

MODE	RESONANT FREQ (Hz)		MODAL VECTOR DOT PDT	LOSS FACTOR (η)	LOSS FACTOR RATIO.	MEAS CALC
	FIXED ANAL.	TEST	PERCENT FREQ ERROR			
1	60.7	62.1	- 2.3	.991	.348	.231
2	90.8	87.9	+ 3.3	.720	.261	.191
3	127.4	140.1	- 9.1	.921	.117	.081
4	157.0	157.2	- .1	.937	.290	.176
5	192.6	218.9	- 12.0	.300	.121	.036
6	216.5	195.8	+ 10.6	.775	.216	.184
7	266.9	210.1	+ 27.0	.895	.068	.054
8	298.6	248.5	+ 20.2	.978	.136	.091

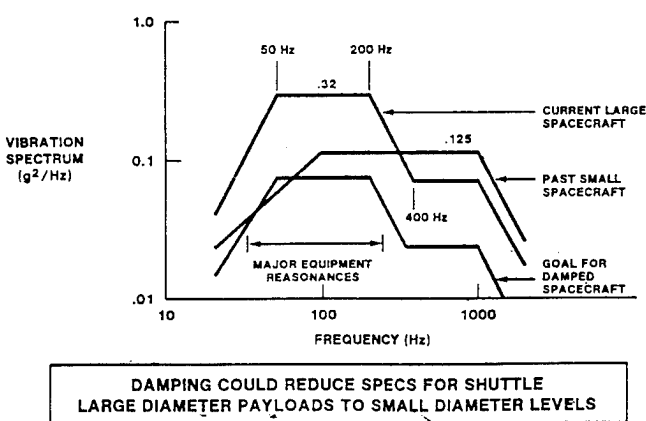


Fig. 1 Equipment random vibration requirements
with 6 dB reduction goal

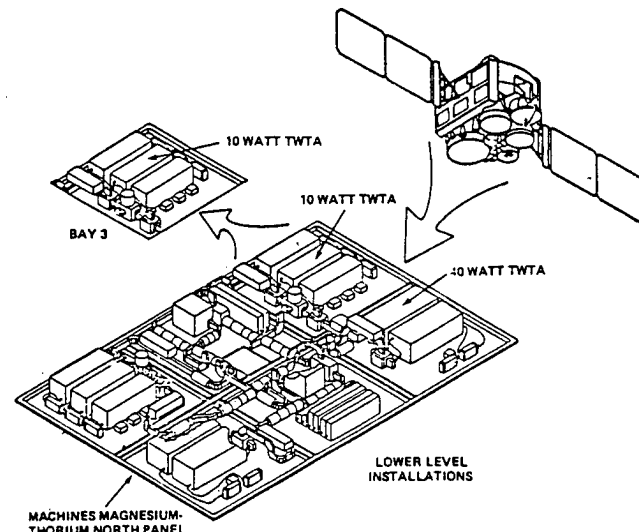


Fig. 2 DSCS-III north equipment panel

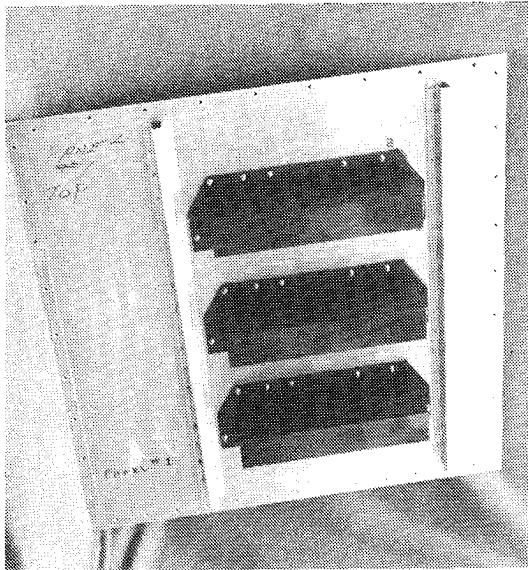


Fig. 3 Baseline panel

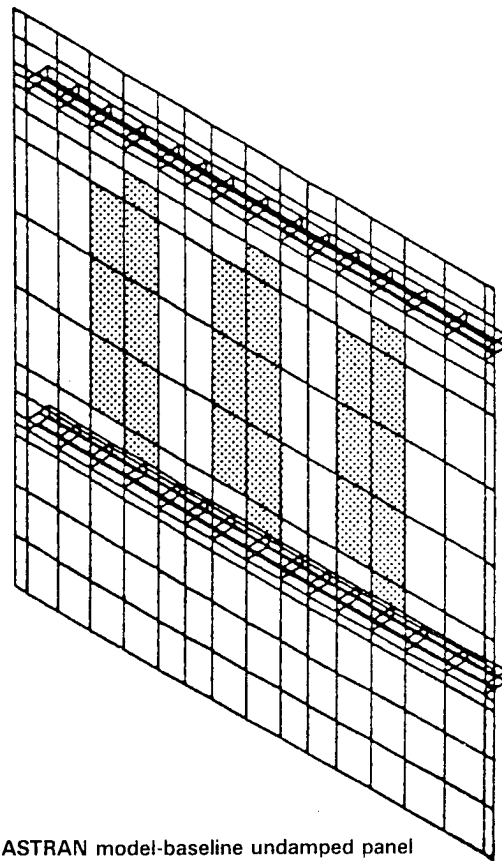


Fig. 4 NASTRAN model-baseline undamped panel

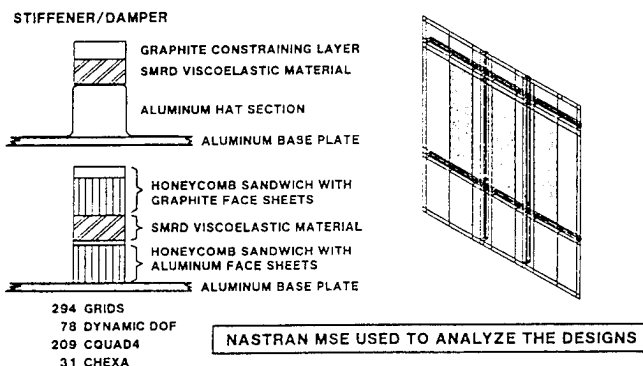


Fig. 5 Damped stiffener concept and parametric study
NASTRAN model

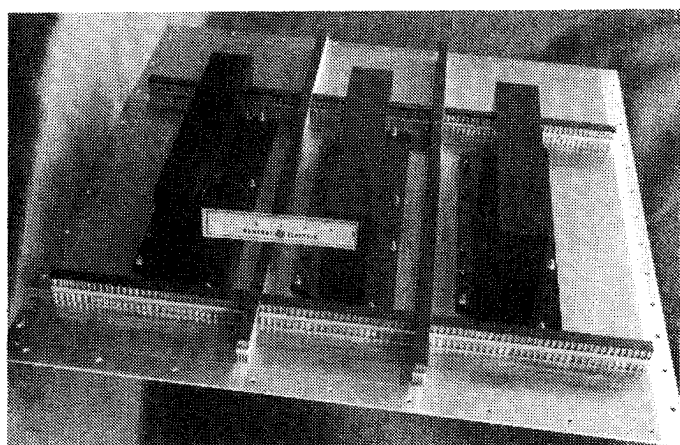


Fig. 7 SMRD100F90B Damped honeycomb stiffener panel

PANEL DESIGN	STIFFENER/DAMPER	TOTAL STRUCTURE AND DAMPER	TOTAL PANEL
BASELINE UNDAMPED	100%	100%	100%
DAMPED STIFFENER			
CRITERION I			
CRITERION II			
CRITERION III HAT AND G/E			
CRITERION III HONEYCOMB			

CRITERION III PANEL WITH HONEYCOMB SANDWICH STIFFENERS WEIGHS APPROXIMATELY THE SAME AS BASELINE

Fig. 6 Preliminary design weight summary

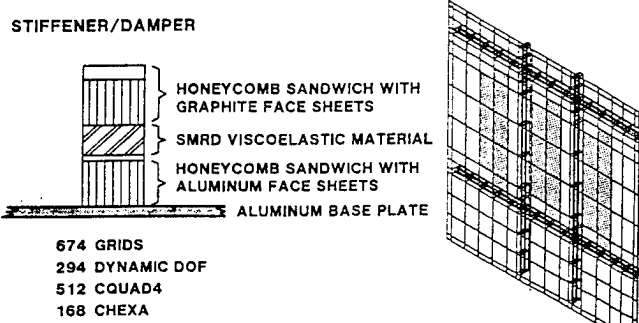


Fig. 8 NASTRAN model - damped modal test panel

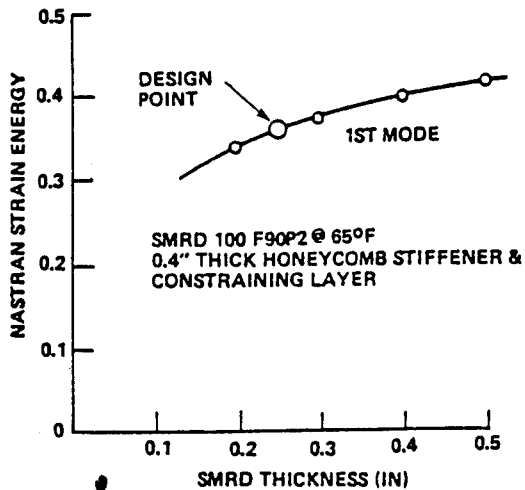


Fig. 9 Damped modal test panel-NASTRAN model strain energy vs VEM thickness

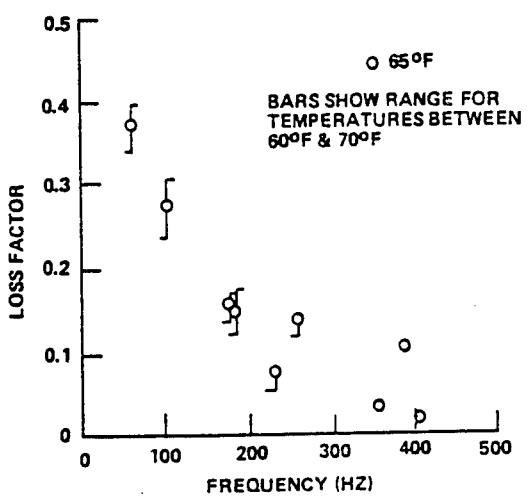
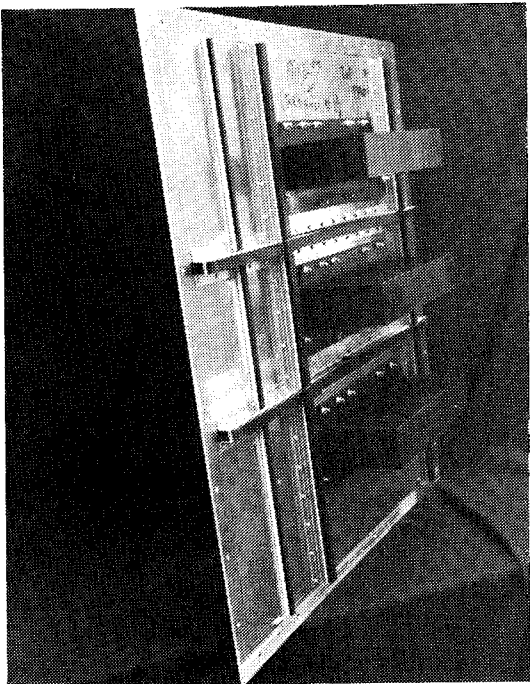


Fig. 10 Damped modal test panel - preliminary design loss factors

Fig. 11 SMRD100B50A damped hat section stiffened panel with 3 subpanel dampers

DESIGN GOAL: $\eta_c > .3$ 1st MODE
.1 HIGHER PANEL MODES

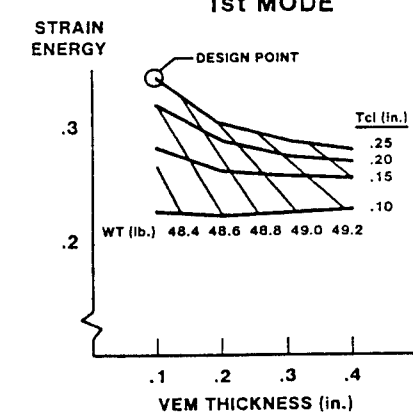


Fig. 12 VEM Strain energy vs. SMRD thickness

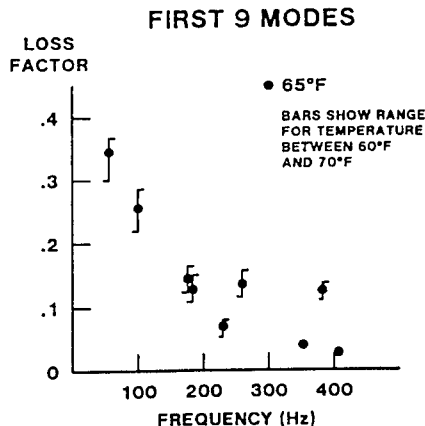


Fig. 13 Loss factor vs frequency

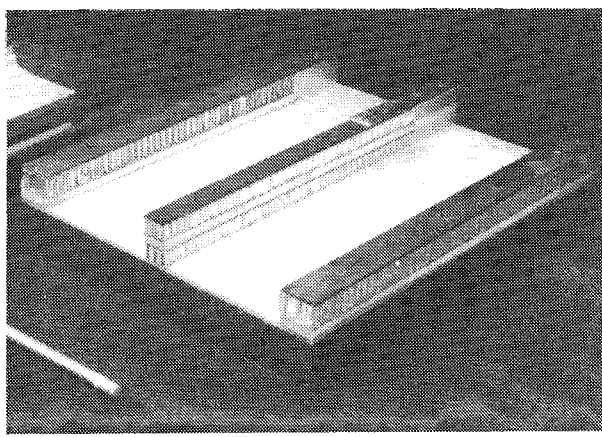


Fig. 14 Cantilever beam test element

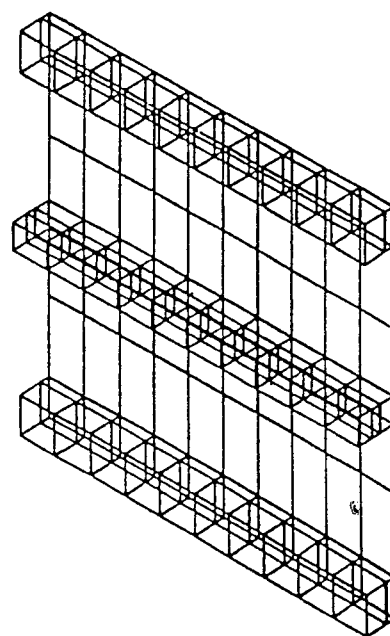


Fig. 15 NASTRAN model honeycomb stiffened panel
MATERIAL PROPERTY FOR VEM

NASTRAN ANALYSIS RESULTS

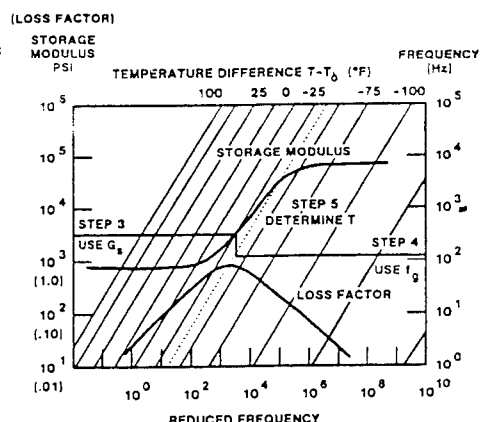
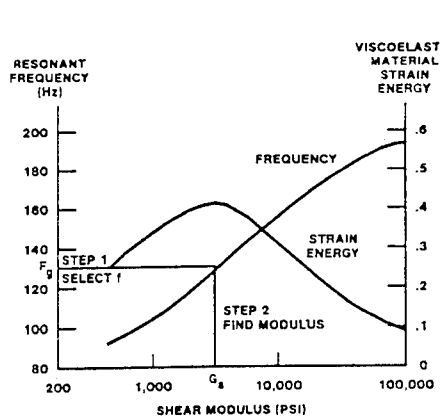


Fig. 16 Methodology for analysis/test comparison

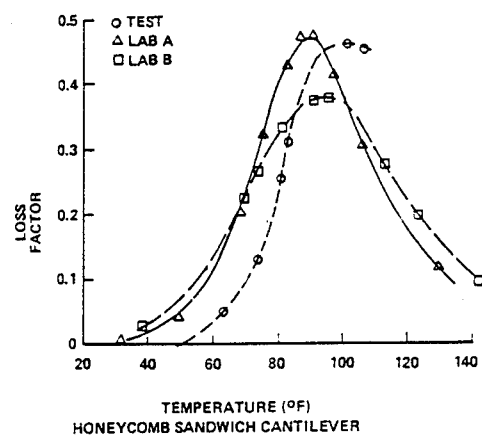
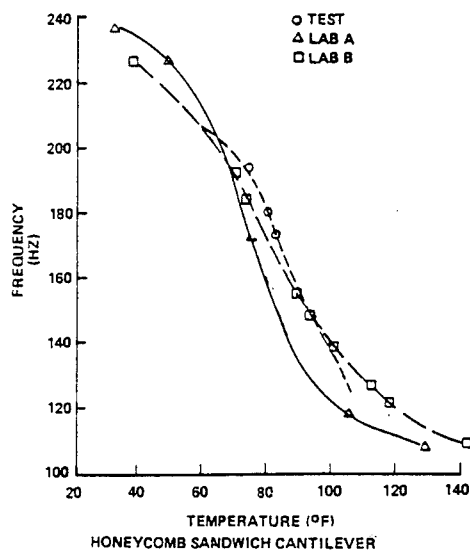


Fig. 17 Test/analysis comparison for cantilevered honeycomb stiffened beam

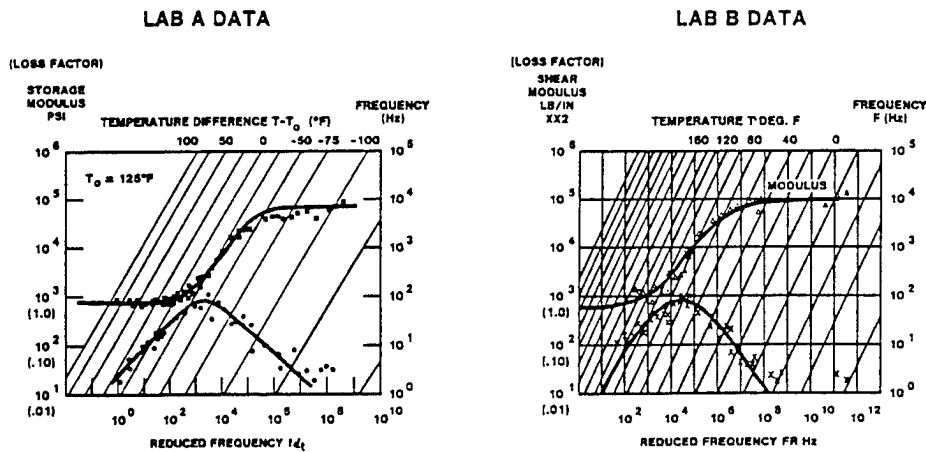


Fig. 18 Reduced temperature nomograms SMRD100F90A

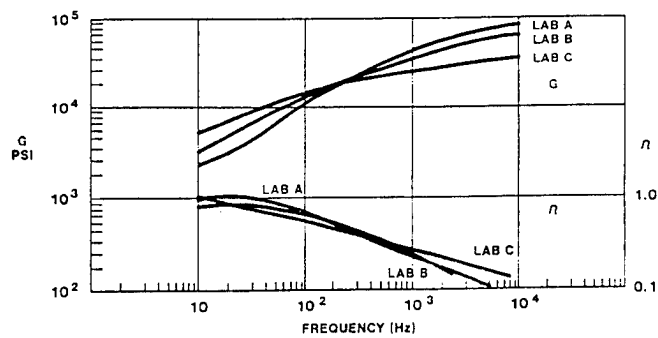


Fig. 19 VEM properties show significant variations

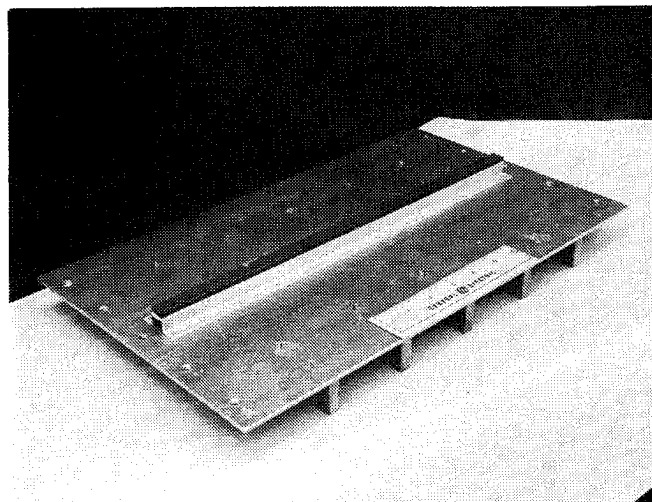


Fig. 20 End supported test element

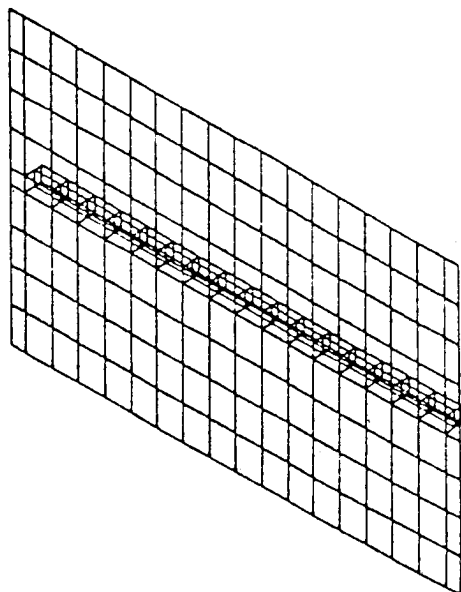


Fig. 21 NASTRAN model of hat stiffened beam

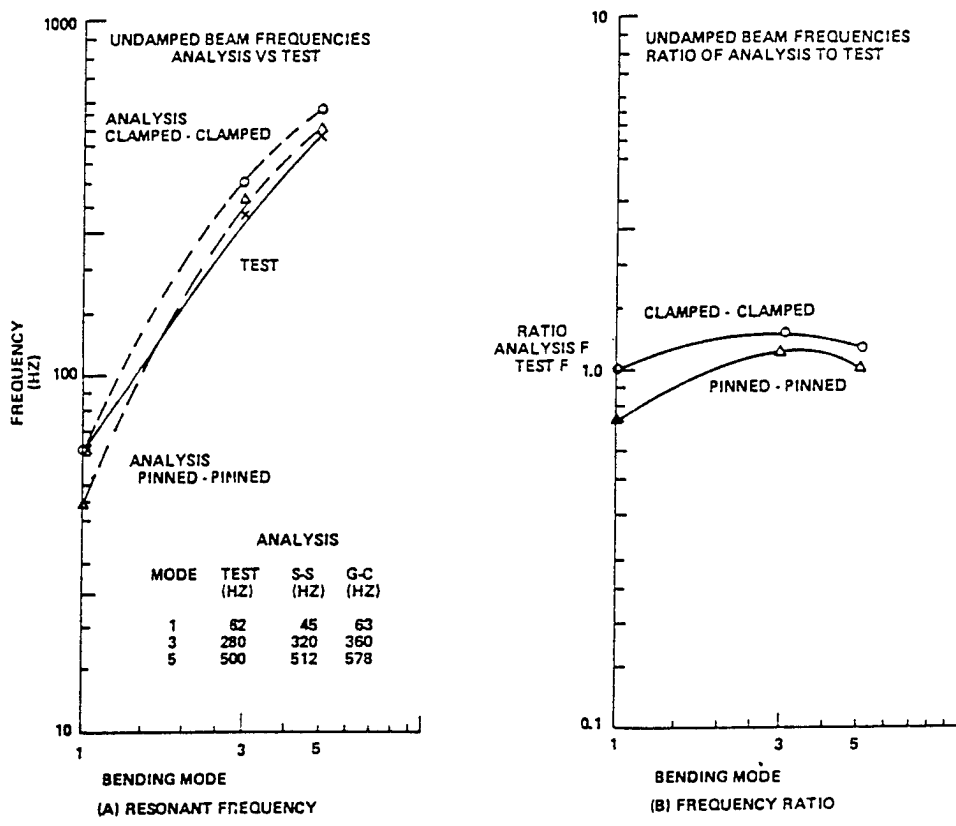


Fig. 22 Analysis/test comparison for undamped beam

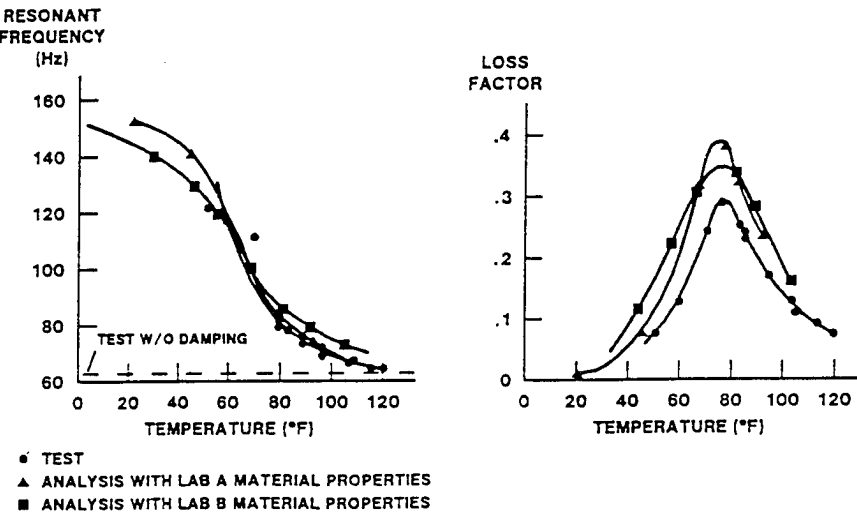


Fig. 23 Test/analysis comparison for 1/4 inch SMRD100F90A hat stiffened beam

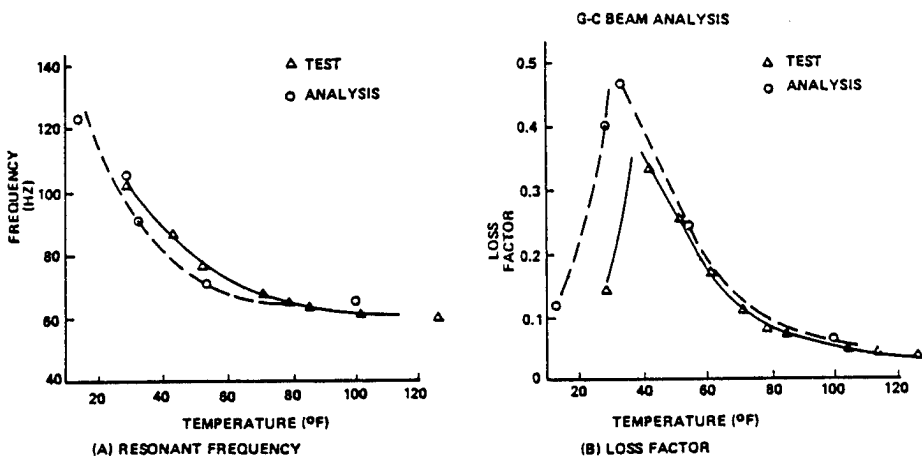


Fig. 24 Test/analysis comparison for 0.1" SMRD100B50C hat stiffened beam

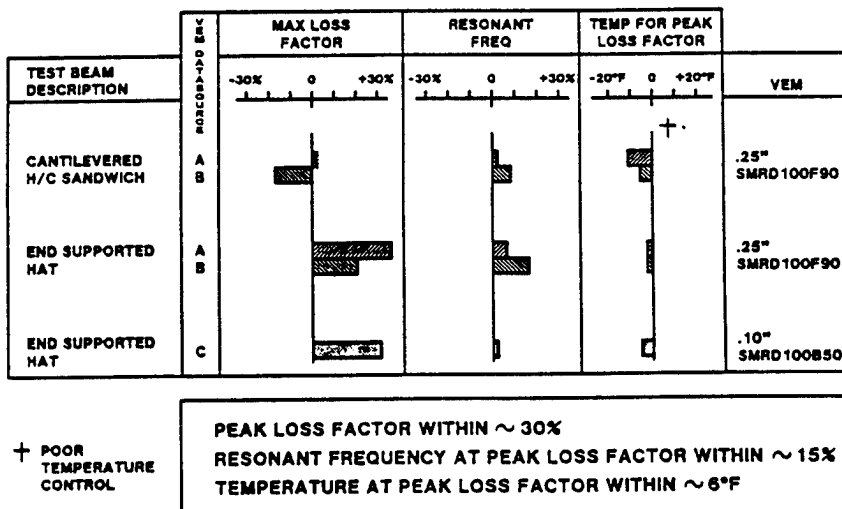


Fig. 25 Summary of elements - analysis vs test

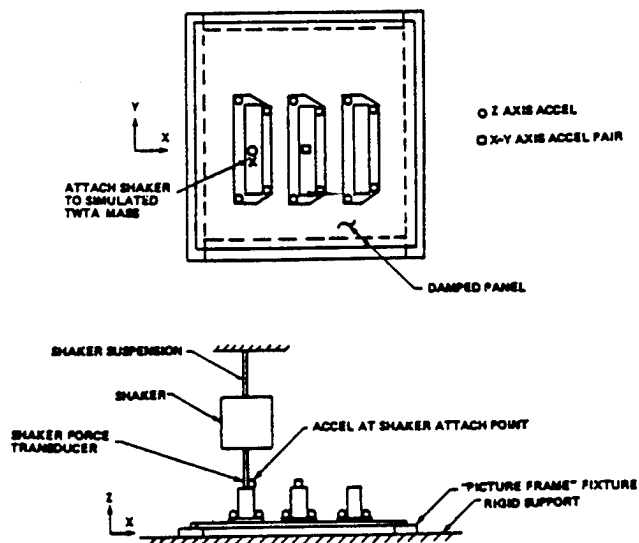


Fig. 26 Panel modal test arrangement

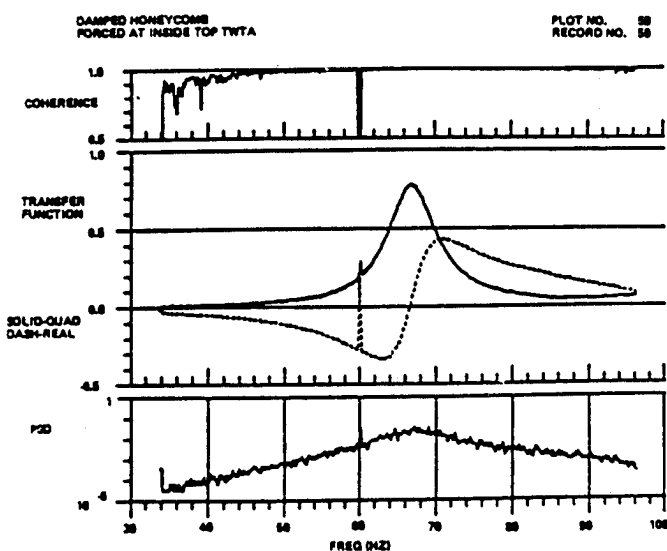
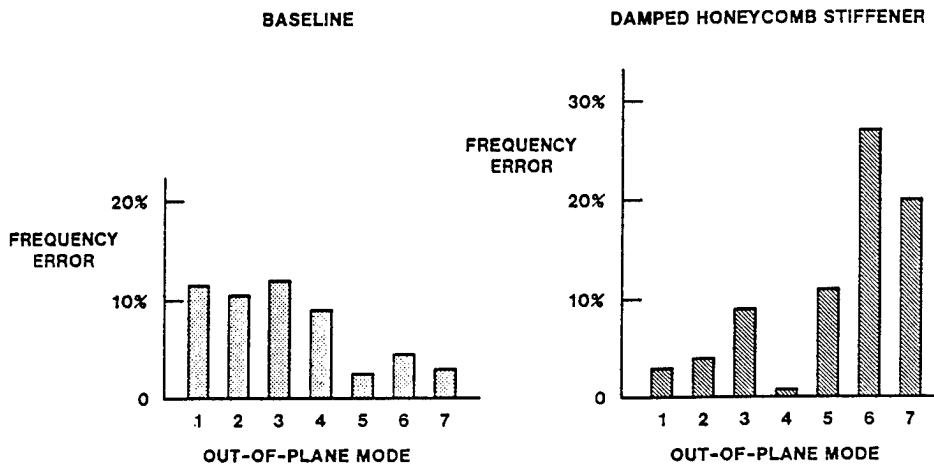
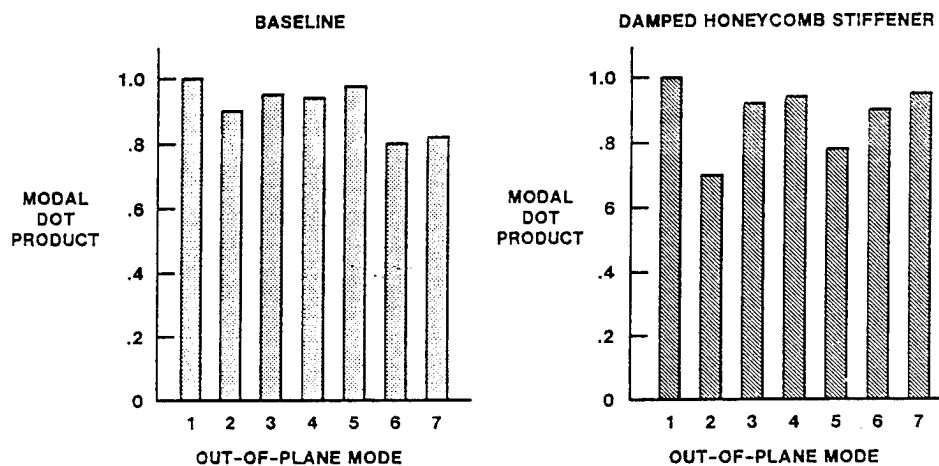


Fig. 27 Typical zoom transfer function



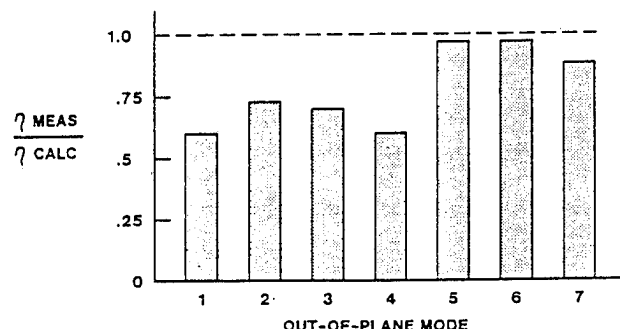
FREQUENCIES OF LOWER PANEL MODES CALCULATED WITHIN 12%

Fig. 28 Resonant frequency comparison



MODAL DOT PRODUCT > .7 FOR ALL OUT-OF-PLANE MODES

Fig. 29 Modal dot product comparison



MEASURED > 2/3 OF CALCULATED LOSS FACTOR

Fig. 30 Loss factor comparison

RELSAT DAMPED EQUIPMENT PANELS - FABRICATION*

K. SCHMIDT, F. CURTIS, E. MUZIANI, L. AMORE

GENERAL ELECTRIC SPACE SYSTEMS DIVISION
VALLEY FORGE SPACE CENTER
P.O. BOX 8555, PHILADELPHIA, PA 19101

ABSTRACT

This paper discusses the material considerations and fabrication methods used in the GE RELSAT program and describes the technology needed to produce viscoelastically damped spacecraft equipment panels. Tests of the panels presented elsewhere in these proceedings indicate the damping is predictable and highly effective in reducing the vibroacoustic environment of electronic packages. The materials technology described herein builds on more than 15 years of GE experience in damping spacecraft electronic packages and other devices using a SMRD 100 viscoelastic epoxy. Material requirements are driven by prelaunch thermal vacuum testing, launch temperature of 60 to 72 degrees F, launch vibration frequency of 50 to 500 Hertz, and the need to survive 10 years in orbit without contaminating the spacecraft. GE SMRD 100 materials were selected that satisfied these requirements and were known to maintain their excellent damping properties after 4 years in orbit. Modulus and loss factor of candidate materials are compared at the temperature of interest for frequencies from 10 to 10,000 Hertz. Standard panel fabrication methods are used except for viscoelastic material (VEM) machining which uses diamond tooling. Quality control methods needed to assure panel structural integrity and damping performance rely on X-ray and ultrasonic techniques to evaluate bonding and resonant beam measurements to determine material properties. Alternate fabrication methods that eliminate some bonding operations are presented. Because current measurements of VEM properties have a large variation, it is recommended that improved methods be investigated. Improved property measurement should address experimental errors, relations used to derive properties from test measurement, derivation of the reference temperature used in the shift relation, and VEM formulation controls that assure uniform properties.

*This work was performed for the Air Force Flight Dynamics Laboratory under the RELSAT (Reliability for Satellite Equipment in Environmental Vibration) Contract.

INTRODUCTION

This paper presents the material considerations, basic fabrication techniques and quality control measures critical to the fabrication of damped spacecraft equipment panels. In conjunction with this paper, two others have been written, which address the design and testing of Dynamic Test Article (DTA) Panels.^{1,2} The purpose of this effort, is to demonstrate the use of viscoelastic damping to reduce vibroacoustic environments for satellite equipment mounting structures in a launch environment. Research, testing and subsequent evaluation have shown that the technology and material resources are available to fabricate and implement constrained layer damping on spacecraft structures.

BACKGROUND

The formulation and application of viscoelastic materials in spacecraft has been under development at GE-SSD for over 15 years. SMRD (Spacecraft Materials Research and Development), a highly efficient damping compound developed by GE, was first flown on Landsat I Earth Observation Satellite where avionics reliability was enhanced by limiting relay panel vibrations.³ Subsequent applications include Viking Lander, Acoustic Cannisters, Gimbal, and Camera Mounts.⁴ In addition, it is used extensively on printed circuit boards, providing efficient damping and additional stiffening of the boards and/or components. Figure 1 shows a typical constrained layer damping strip installation. The board has a center strip extending from the edge to the connector and an additional strip bonded to the connector. A minimum amount of space is occupied by the strips which use unidirectional graphite epoxy constraining layers.

The constrained layer fabrication is shown in Figure 2. The constraining layers are bonded to the viscoelastic material (VEM). They are then machined to the final dimensions. Typical damping strips using SMRD 100F90 with unidirectional graphite epoxy constraining layers are shown in Figure 3 and can be made in a wide variety of shapes and sizes. Sizes range from a few inches to a few feet in length. The DSCS III spacecraft uses approximately 2000 damper strips. Most use unidirectional graphite epoxy constraining layers. The keel member shown in Figure 4 employs the use of a large damper strip to limit vibration levels so that vibration of adjacent packages stays within specified limits. This keel damper was added after acoustic tests indicated package qualification random vibration levels were being exceeded.

Currently, the concept of viscoelastic damping is being evaluated in relation to reducing vibroacoustic environments for satellite equipment mounting structures during launch. To date, testing has been conducted which has shown the damping to be highly effective in attenuating vibroacoustic response. In addition, the structural integrity of damped panels under static load, sinusoidal load and creep effects under steady state load were measured. The results of acoustic and shock tests, and the design, analysis and modal tests are presented in two other papers included in the proceedings.^{1,2} This paper discusses the viscoelastic material requirements and properties, material selection, fabrication methods and quality control procedures.

RELSAT PANEL DESIGN APPROACH

The approach used in the design of the damped panel configuration is shown in Figure 5. The original panel design provided integrally machined stiffeners with riveted flange sections to support the panel components. The damped panel design uses a similar concept with a constrained layer damper added to the flange section. Although the figure indicates the same size stiffener, the damped panel designs actually used smaller stiffeners using the VEM and constraining layers to provide added stiffness. With this concept, the thermal design of the panel is unaffected. Heat is conducted through the panel structures and the VEM effect is negligible.

MATERIAL CONSIDERATIONS

Requirements

Key requirements to be considered when selecting damping materials for spacecraft applications include space compatibility, weight, strength, stiffness and high damping in the frequency and temperature range of interest. These requirements are summarized in Table 1 for the various flight phases. Prior to launch, the material is subjected to thermal cycling for an extended period of time during subassembly and spacecraft tests. In addition, a storage capability of 2 years is also required. The launch conditions are critical for the damping performance of the material which requires high damping from 60 to 72 degrees F in the 50 to 500 Hertz frequency range. High shear strength is required so that structural integrity is assured. A wide range of stiffness values are acceptable although they influence the thickness of the damping layer. During orbital flight, the VEM must not contaminate the spacecraft during its 10 year life. This is reflected in the outgassing requirements of ASTM E-595 which requires less than 1 percent mass loss and less than 0.1 percent collectable Volatile Condensable Materials under elevated temperature and vacuum conditions. By selecting the damped panel stiffener approach, thermal conduction requirements are precluded.

Candidate Materials

The properties of candidate materials are compared in Table 2. The material density varies from .028 to .066 pounds per cubic inch which affects the weight but is not critical because of the small amount of material used. The outgassing results, however, do eliminate the AF32 (SMRD 100F90A is an acceptable material although it slightly exceeds the outgassing values).

Aging Effects

It is imperative that materials used on the spacecraft withstand the thermal vacuum conditions imposed without changing stiffness and damping properties, i.e. stability of the viscoelastic material properties is essential. In addressing this requirement, SMRD panels are post cured under vacuum for 96 hours as a stabilization process. To verify the stability of GE developed SMRD, recent events have enabled an evaluation of SMRD following four years in space. The Solar Max Attitude Control Module launched in February of 1980 and retrieved from space in April of 1984, used SMRD in its interior structure. A sample recovered from the Attitude Control Electronics (ACE) package was tested

and found to have retained high damping properties after four years in space. Figure 6 compares SMRD 100F90 retrieved from space to standard SMRD 100F90 data. The individual data points shown for the SMM material were obtained from modified Oberst beam tests. The curves correspond to the original material before extended space exposure. The comparison indicates that the properties have not changed significantly. A maximum loss factor of approximately 1.0 was measured for the SMM material. This value is in close agreement with the maximum value for the corresponding curve. The data verify the stability of the SMRD material. Similar data are not available for the other materials in Table 2.

Damping and Stiffness Properties

This section addresses material characterization of VEM damping and stiffness. This information can be readily displayed on Reduced Temperature Nomograms (RTNs). Past research has shown that there is a definite correlation between many rheological materials in regard to behavioral similarities at different temperatures and frequencies. Measurements of the stiffness, E or G, and loss factor, η , as a function of frequency for various temperatures can be obtained. Using a shift parameter, αT , and the data derived above, stiffness and loss factor information at various temperatures can be collapsed into a single curve. As a result, modulus and loss factor can then be plotted as two curves on a Reduced Temperature Nomogram.⁵ This is illustrated in Figure 7. Ultimately, this nomogram can be used to determine material properties for the temperature and frequency of interest in a particular application. Figure 7 illustrates modulus and loss factor data at an average temperature of 65 degrees F, the temperature of interest, for various frequencies. Because the RTN includes the shift parameter which is material dependent, material comparisons and selections must be made using the material property curve shown on the right of Figure 7 which is independent of the temperature shift relation.

The accuracy of the material property measurements are also indicated by the individual data points in Figure 7. The temperature shift relations can be used to translate the properties from the RTN to the material properties at a specific temperature, including the curves and the original data points. The scatter in the data points provide an indication of the accuracy of the property measurements. Although the scatter appears small on the three cycle log scale, the scatter is relatively large with factors of two or more for many points. The scatter is particularly large for the loss factor.

In essence, the goal in searching for a good damping material is to find one whose high damping properties coincide with the temperature and frequency ranges of interest. In the specific case of DSCS III launch environment, the temperature and frequency ranges of prime importance for the North Panel Structure are 60 to 72 degrees F and 50 to 500 Hertz, respectively. In an attempt to attain the required stiffness and damping under these conditions, material formula variations were researched and tested. One way to evaluate the difference in damping properties between the material candidates is to compare them in relation to glass transition temperature. Modifications were made to the standard material in an attempt to shift the transition temperature, so that peak damping would occur in the desired temperature and frequency range. Figure 8 shows that SMRD material properties can be altered to meet specific requirements. Of the three materials shown in this graph,

SMRD 100F90C performed ideally for the RELSAT application. Peak damping occurred for about 50 to 500 Hertz at 65 degrees F.

In addition to the GE-SSD material formulations, commercial damping materials were investigated. Two materials selected for initial evaluation were DYAD 601 and 3M ISD112. Both materials satisfy the outgassing requirements, however, at 65 degrees F the peak damping for DYAD 601 was at a frequency above the range of interest for the DSCS III panel. Measured material properties from beam tests are shown in Figure 9. In addition, ISD112 properties were also measured, Figure 10. It appeared to be too soft, and required very thin layers to be effective. It did not have the required bond strength for the stiffener application. UDRI 3 was also considered, but was rejected because its tacky consistency posed fabrication problems and could cause contamination of the spacecraft. The final selection of candidate materials for panel fabrication and tests were four SMRD100 materials. The material properties are compared in Figure 11. The four prime material candidates are described below:

SMRD 100F90B is a modified 100F90 formulation which has significantly better outgassing characteristics and a temperature of peak damping closer to the ranges of interest than the original formulation. It is relatively stiff with a low density, and has been used by GE-SSD for electronic packages.

SMRD 100F90C is a further modification of 100F90, formulated in an attempt to reduce the transition temperature so that peak damping would occur in the temperature and frequency ranges of interest.

SMRD 100B50A has the damping properties which appear ideally suited for DSCS III transponder panel application. The material loss factor is high over a relatively broad frequency range and is nearly unity over the frequency range of interest. It has the same base resin system as 100F90, however it is modified by the addition of a conductive filler. The temperature of maximum damping at 100 Hertz is 63 degrees F and lies within the desired temperature range.

SMRD 100B50B - This is a modification of the previous material which is stiffer. At 65 degrees F, the frequency for peak damping is shifted to about 200 Hz, and has high damping over the frequency range of interest.

The decision to use the SMRD 100 materials was based on the fact that these materials satisfy the outgassing, strength, stiffness and damping requirements established. Refer to Table 3 for material selector parameters. In addition past experience in viscoelastic damping facilitates the application of various techniques used in damped printed wire boards to those for the damped spacecraft equipment panels.

DAMPED EQUIPMENT PANEL FABRICATION

VEM Fabrication Process

Both SMRD 100F90 and 100B50 are cast and cured in teflon coated aluminum molds in thicknesses ranging from 0.1" to 0.25". The sheets are stabilized and outgassed under vacuum at 135 degrees C for 96 hours; see Figures 12 and 13. The SMRD can be used as fabricated or milled to the desired dimensions. In the past, an aluminum oxide cup wheel was used to mill the SMRD. Due to obvious surface imperfections, diamond tooling replaced the former tool. Figure 14 is a photograph of a diamond compax end mill used primarily for milling smaller sections of VEM. The diamond flycutter shown in Figure 15 mills approximately a two inch wide strip per pass as compared to 1/2 inch strip produced with the end mill. This tool is used in larger applications.

Surface Preparation

Once the materials are machined to size, the SMRD can be bonded to constraining layers such as aluminum and graphite/epoxy laminates. To obtain optimum bond strength, an effective method of surface preparation is employed. The SMRD and constraining layers are abraded using 100 grit Aluminum Oxide paper. All surfaces are thoroughly cleaned with isopropyl alcohol and allowed to air dry.

Adhesive Selection/Bonding

Proper adhesive selection is essential in terms of space application. Once again, outgassing requirements, in addition to strength under rigorous environmental conditions are critical factors which must be considered. SMRD 100F90 and 100B50 can be bonded to both graphite/epoxy laminates and aluminum using epoxy adhesives such as amine or polyamine cured epoxy resin. The adhesive selected for this application was Hysol EA9309.3 commercial grade aerospace adhesive. This material offered adequate strength and rigidity in addition to being compatible with the materials under consideration.

Finally, the actual bonding of the SMRD to the constraining layers is a simple procedure. A thin film of adhesive is applied using a fingerprint roller. The materials are mated in such a manner as to preclude excessive air entrapment. The bonded sections are then cured under pressure.

Two damped panel configurations were designed and tested, one incorporated aluminum honeycomb stiffeners and the other aluminum hat section stiffeners. Figure 16 is representative of the honeycomb stiffener panel prior to completion. Aluminum honeycomb stiffeners are bonded to SMRD which will subsequently be bonded to a graphite/epoxy honeycomb constraining layer. Traveling wave tube amplifier (TWTA) mass simulators are bolted to the aluminum panel. Figure 17 shows a completed honeycomb panel prior to test. The aluminum hat section stiffener panel shown in Figures 18 and 19 consists of aluminum hat sections riveted to the aluminum base plate. A viscoelastic damping layer is bonded directly to the hat, followed by a graphite epoxy constraining layer. TWTA mass simulators are then added for dynamic testing.

The method of damping used on these panels simulates the predicted effect of constrained layer damping on the transponder panel of the DSCS III spacecraft.

FUTURE DAMPED PANEL FABRICATION

Looking into the future of constrained layer viscoelastic damping, a technique has recently been developed to eliminate the bond between the viscoelastic material, in this case SMRD, and the graphite epoxy laminate. Figure 20 compares the interfacial bonds between the VEM and laminate for adhesive and direct bond methods.

The new procedure incorporates the bonding process into the layup of the graphite epoxy laminate. As in the current process, the SMRD must be abraded and thoroughly cleaned. The graphite/epoxy prepreg is then layed up directly onto the surface of the SMRD sheet and cured under vacuum. The damper strip assemblies can then be machined to required dimensions. The benefits of this new procedure include improved bond strength, elimination of the bonding step and surface preparation of the graphite/epoxy laminate and most importantly, it virtually eliminates the possibility of interfacial voids because of high resin flow from the graphite/epoxy prepreg and the high pressure under which the composite is cured.

QUALITY CONTROL PROCEDURES

VEM Properties Confirmation

To validate the material properties of the SMRD, several tests were conducted. Hardness, using a Shore A durometer measured the materials resistance to indentation. It is a simple and effective means of monitoring changes in material stiffness. Density was determined through weight and dimensional measurement. Finally, to determine the damping properties of the viscoelastic material, the modified Oberst beam method of test was employed.⁶ Specifically, the beams consisted of an aluminum layer sandwiched between two pieces of viscoelastic material. A series of beams were then mounted to a shaker and excited using base excitation. Damping properties of the materials under consideration, were determined over a wide range of frequencies and temperatures.

Structural Assessment

In addition to material property confirmation, non-destructive testing to determine structural integrity is critical. Delamination between the constraining layers or panel and the damping medium could cause a significant reduction in damping efficiency. As a result, it is important that non-destructive inspection techniques be employed to insure structural integrity. Three methods of test suggested are Ultrasonic Pulsed Echo techniques, Ultrasonic Impedance Plane Analysis and Real Time Radiographic Examination.

Ultrasonic and Contact Pulse Echo operates on the principle of pulsed ultrasonic waves. The waves are monitored as they interact with the material being inspected. A pulse ultrasonic beam is introduced into the part and the returning echos are monitored. This test method gives information regarding the type, size, location and depth of the defect. Figure 21 illustrates the difference between a bonded area and one with a known void. The large peak present on the photograph on the left is the back reflection of the aluminum

hat section. This peak diminishes when a voided area is contacted. Since this signal will not transmit through air, the last material the signal detects is the adhesive coated SMRD, signifying a void or debond as indicated in the photograph on the right.

Ultrasonic Impedance Plane Analysis using a Bonda Scope, is an alternate method of Non-Destructive Evaluation. The acoustical impedance plane method uses a small probe to generate a standing wave across the material thickness. The test frequency is selected to vibrate the laminate in such a fashion that the response to bondline and anomaly size is enhanced. The standing wave, which contains acoustical material information, affects the impedance value at the material surface. This value is then transformed through the probe's acoustic impedance into its electrical impedance. It is this electrical impedance which is subsequently processed for display on the acoustic impedance plane. Figure 22 illustrates a typical setup, where a bonded area appears as a dot located at the center of the grid and a non-bonded area shows up as a dot in one of the four quadrants depending upon depth and location of the anomaly.

Radiographic Examination or X-Ray, is another technique used to evaluate structural integrity. X-Rays are directed through the part being inspected and monitored with a screen or film sensitive to X-rays. Figure 23 shows an X-ray evaluation of a debonded area. Since a void will absorb fewer X-rays than a non-voided area, a dark spot will appear. Radiography can be performed through the thickness to detect anomalies or tangentially to detect delaminations.

CONCLUSIONS

As a result of this research and development effort, the following conclusions are made:

- The necessary technology is available to fabricate damped panel structures.
- Performance can be enhanced by altering material formulation to conform to application requirements.
- Key outgassing requirements can be satisfied.
- SMM damping material retains high damping properties after four years in space, verifying material stability.
- Standard fabrication methods can be used for all operations except VEM machining.
- Quality Control Methods are available to assure properties of the panel.
- The variation in measured VEM properties should be reduced.
- The VEM test method should be revised to reduce experimental errors.

- The VEM temperature shift relations should be improved.
- Material uniformity should be maintained within close tolerances.

REFERENCES

1. J. C. Strain, J. A. Staley, and C. V. Stahle, "Design and Experimental Verification of Damped Spacecraft Equipment Panels," Vibration Damping Workshop II, March 1986.
2. C. V. Stahle, J. A. Staley, and J. C. Strain, "Vibroacoustic and Shock Performance of Damped Spacecraft Equipment Panels," Vibration Damping Workshop II, March 1986.
3. C. V. Stahle and W. H. McCandliss, "Controlling Vibration of Viking Lander Electronic Packages," 44th Shock and Vibration Symposium, December 1973.
4. C. V. Stahle and J. M. Medaglia, "SMRD Damping Applications," SAMPE Series Volume 25, 1980, pp. 90-102.
5. D. I. G. Jones, "A Reduced-Temperature Nomogram for Characterization of Damping Material Behavior," 48th Shock and Vibration Symposium, Oct. 1977.
6. Ahid D. Nashif, "A New Method for Determining Damping Properties of Viscoelastic Materials," Shock and Vibration Bulletin No. 36, Pt. 4, 1967.

ACKNOWLEDGEMENTS

The authors of this paper gratefully appreciate the assistance of Art Rachild for his expert machining, John Haggerty for his assistance in fabrication and Paul Juneau for consultation.

Table 1. VEM Requirements for DSCS III North Panel

PRE-LAUNCH	
• COMPONENT/SUBASSEMBLY THERMAL CYCLING	• SPACECRAFT THERMAL CYCLING
TEMPERATURE: -34 TO 71°C	TEMPERATURE: -17 TO 60°C
VACUUM: 10^{-6} TORR	VACUUM: 10^{-7} TORR
TIME: 10 DAYS	TIME: 25 DAYS
• STORAGE-COMPONENTS AS PART OF THE SATELLITE FOR 2 YEARS	
LAUNCH	
• TEMPERATURE (SHUTTLE BAY):	60 TO 72°F
• FREQUENCY OF HIGH DAMPING:	50 TO 500 Hz
• SHEAR STIFFNESS:	100 TO 1000 PSI
• SHEAR STRENGTH:	100 TO 10000 PSI AT 100 Hz
ORBIT	
• SURVIVE ORBITAL ENVIRONMENT FOR 10 YEARS WITHOUT LOSS OF STRUCTURAL INTEGRITY OR CONTAMINATING THE SPACECRAFT	
• OUTGASSING PER ASTM E-595	
- TOTAL MATERIAL LOSS:	<1%
- COLLECTIBLE VOLATILE CONDENSABLE MATERIALS:	<0.1%
• HEAT CONDUCTION: NOT A CONCERN BECAUSE OF DESIGN APPROACH	

Table 2. Candidate Materials

MATERIAL	DENSITY (LB/IN ³)	OUTGASSING		PROPERTIES AT PEAK DAMPING		
		VCM %	TML %	G (PSI)	LOSS FACTOR	TEMP (°F) @ 250 Hz
ISD 112	.034	.02	.68	140	1.2	89
DYAD 601	.04	.01	.37	2.3K	1.0	35
AF 32	.0382	.46	1.97	78K	.9	84
UDRI 3	.034	.03	0.58	8K	1.0	62
SMRD 100F90A	.0285	.11	1.10	4.6K	1.0	98
SMRD 100F90B	.0296	.08	.81	2.7K	1.0	86
SMRD 100F90C	.0295	.05	.83	3.7K	1.0	71
SMRD 100B50A	.0613	.08	.57	4.1K	1.1	63
SMRD 100B50B	.0635	.10	1.17	4.2K	1.2	70
SMRD 100B50C	.0662	.05	.47	3.8K	1.0	74

Table 3. Material Selection

ISD 112	
• LOW BOND STRENGTH	
• FABRICATION DIFFICULTY	
DYAD 601	
• TEMPERATURE/FREQUENCY RANGE NOT MATCHED	
AF 32	
• EXCESSIVE OUTGASSING	
UDRI 3	
• FABRICATION DIFFICULTY (TACKY)	
• CONTAMINATION	
SMRD 100	
• PROPERTIES CAN BE ALTERED TO MATCH APPLICATION	
• FAMILIAR WITH FABRICATION METHODS	
• HIGH BOND STRENGTH	
• GOOD OUTGASSING REQUIREMENTS	
• STABLE AFTER INITIAL VACUUM "BAKE OUT"	
SMRD MATERIALS USE GE-SSD TECHNOLOGY BASE	

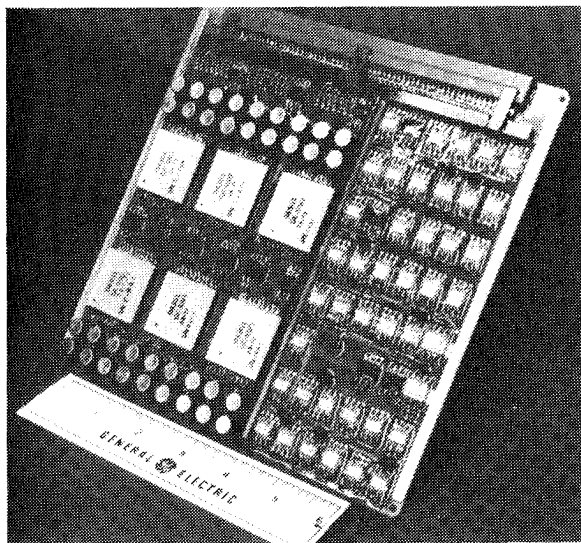


Figure 1. Typical Damped Printed Wiring Board

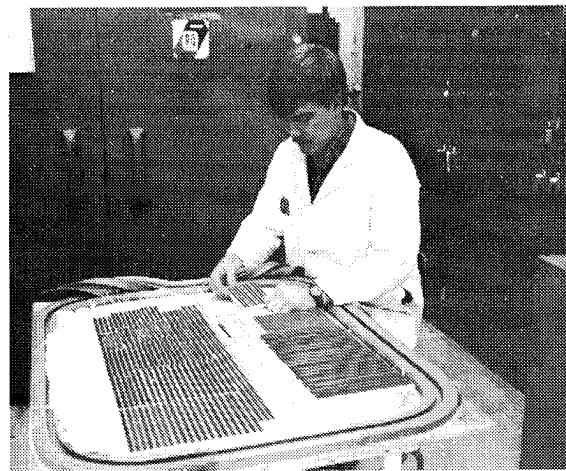


Figure 2. Constrained Layer Damper Fabrication

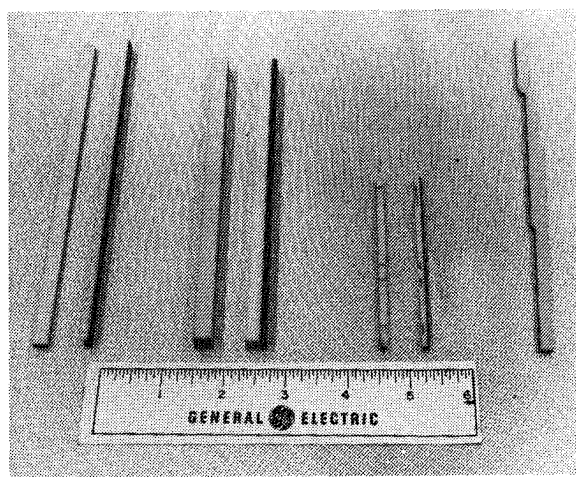


Figure 3. Typical PWB Damper Strips

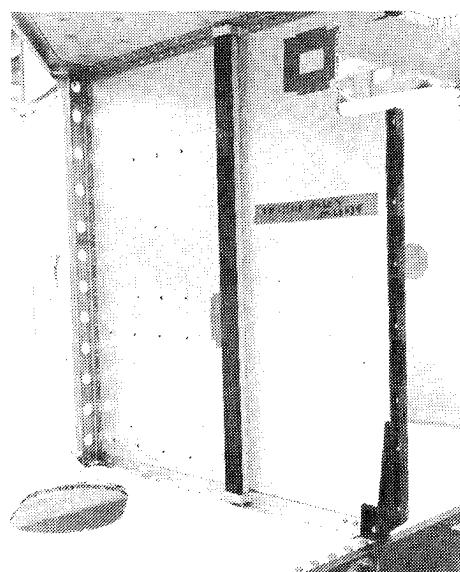


Figure 4. DSCS III Application to JLE Panel

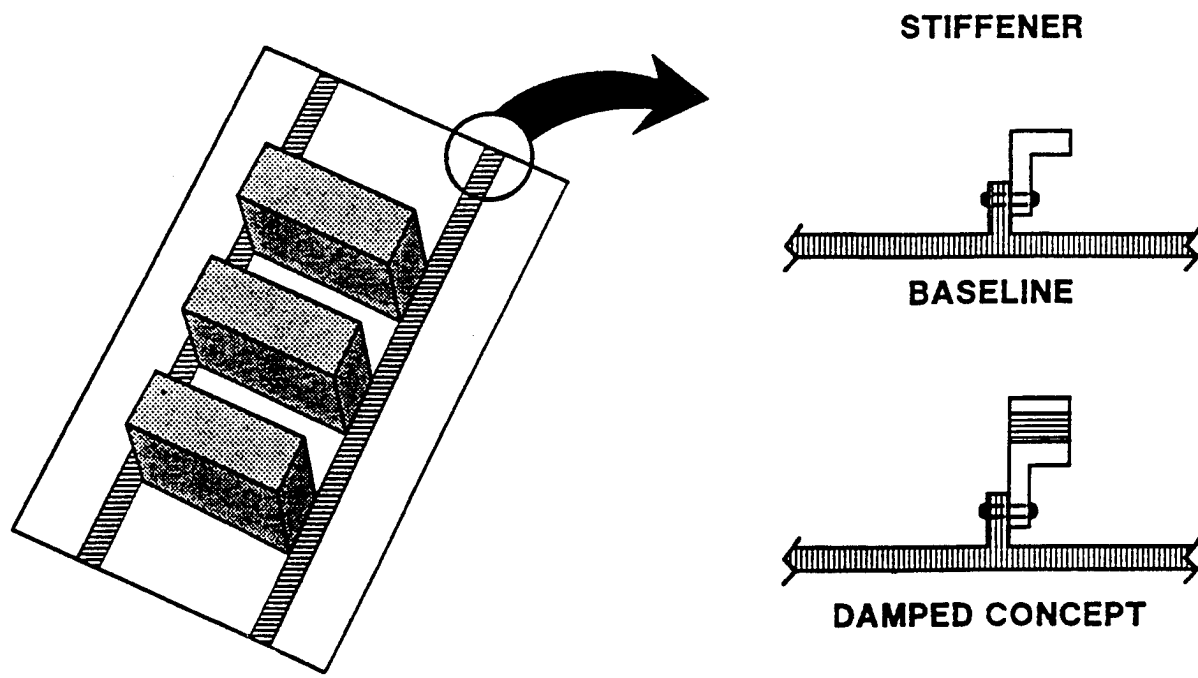


Figure 5. RELSAT Damped Panel Design Approach

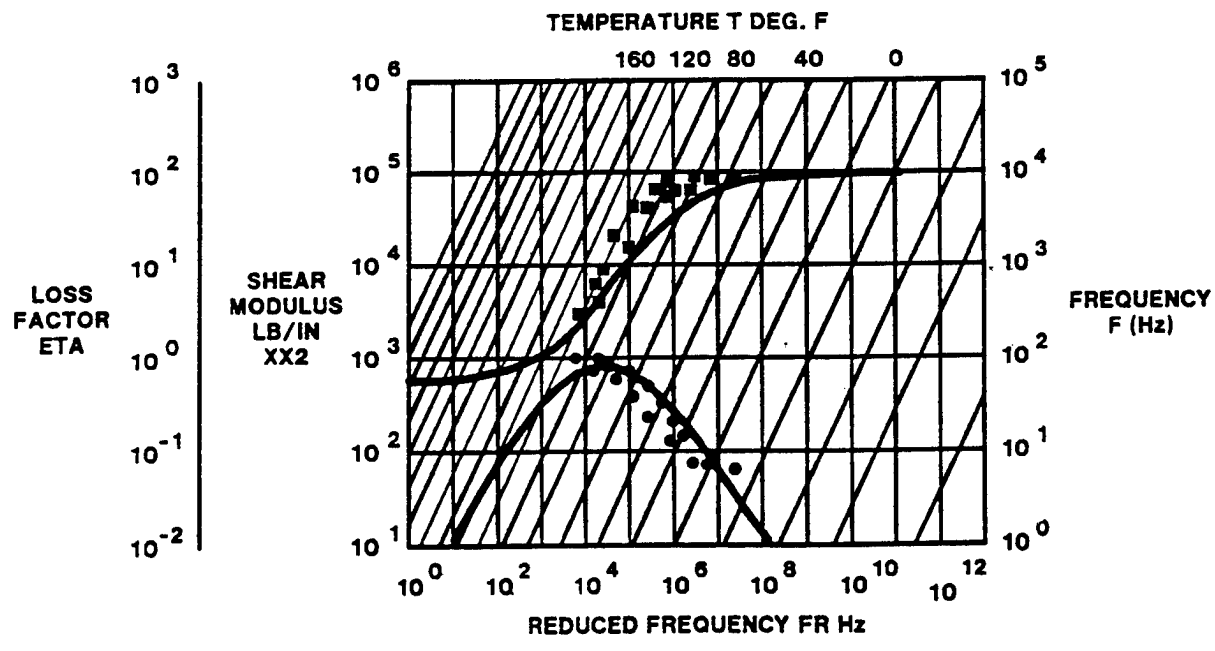


Figure 6. Comparison of SMM and Current SMRD 100F90 Properties

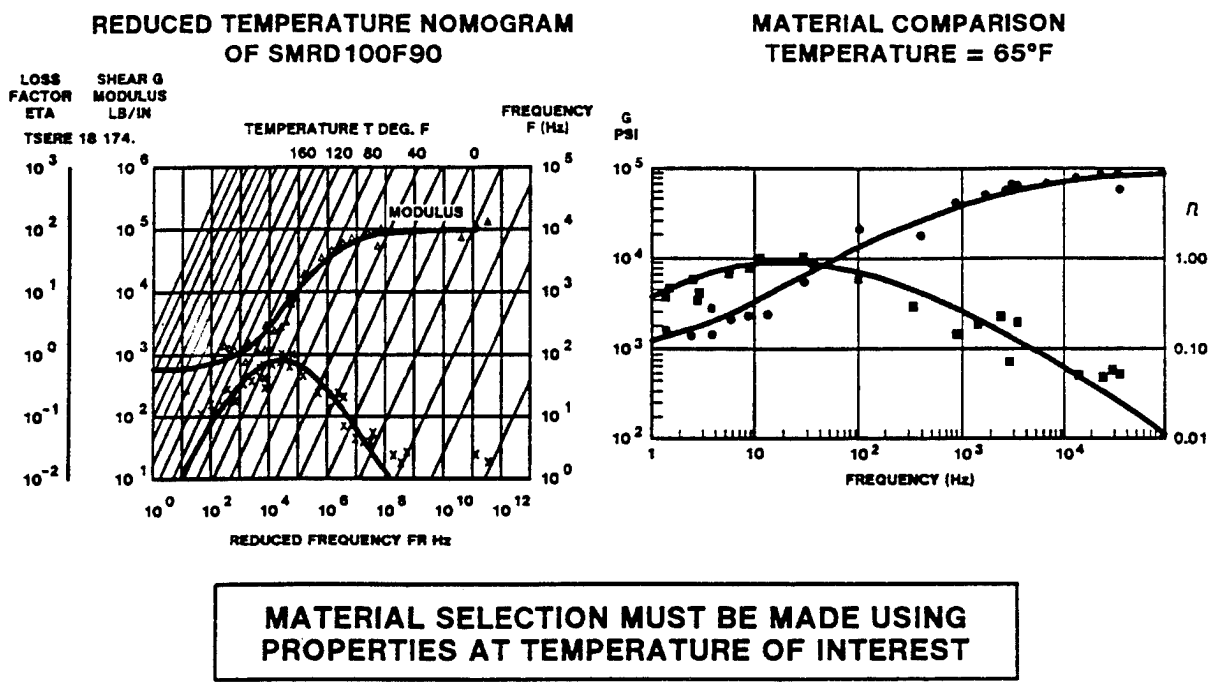
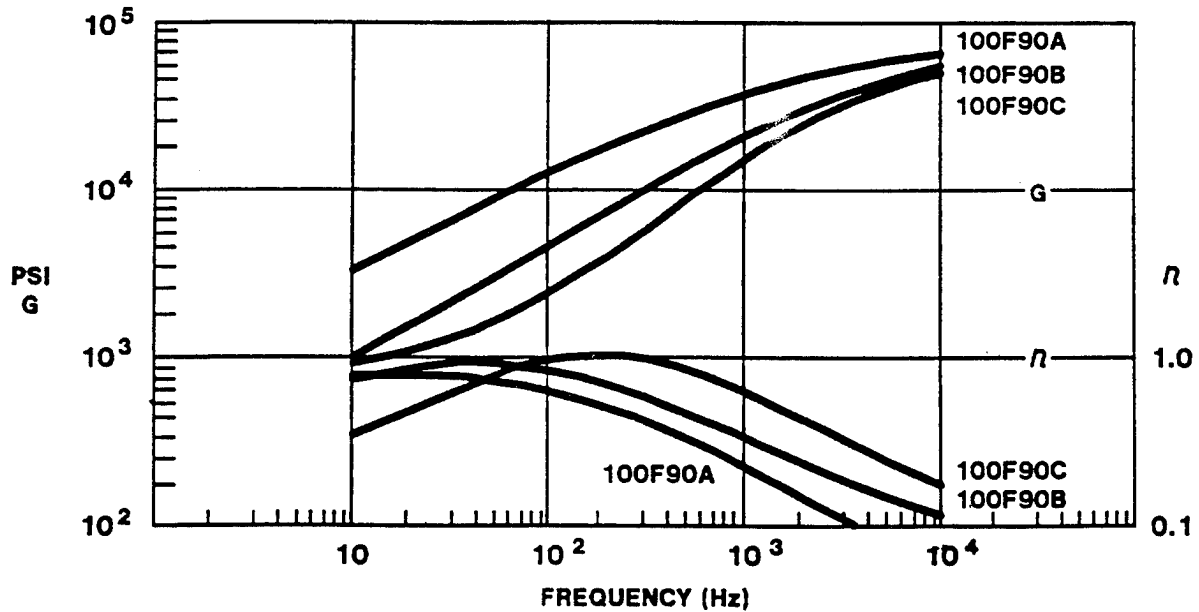
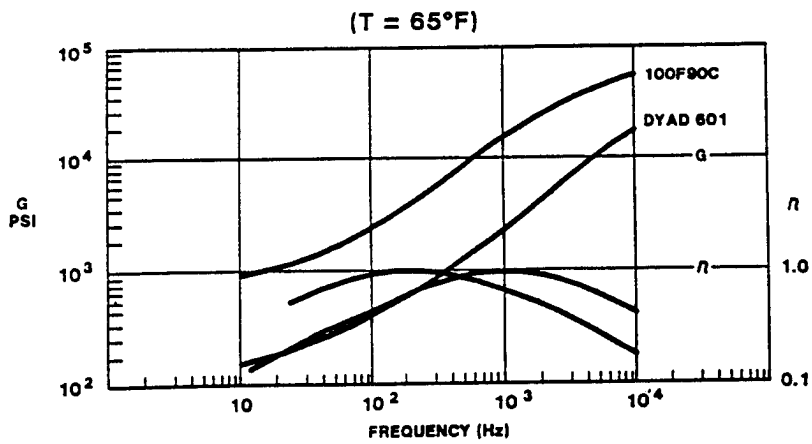


Figure 7. Material Characterization



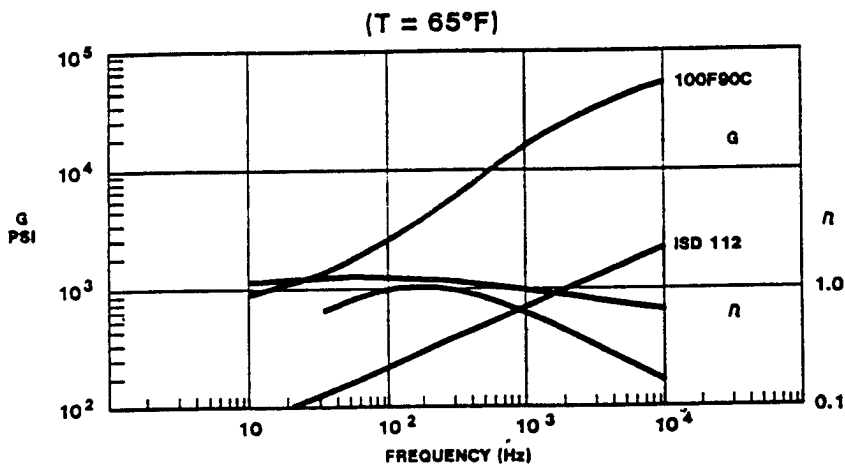
**GE MATERIAL PROPERTIES CAN BE ALTERED TO MEET SPECIFIC
REQUIREMENTS. SMRD100F90C IS IDEAL FOR RELSAT.**

Figure 8. Effect of SMRD 100F90 Formulation Changes



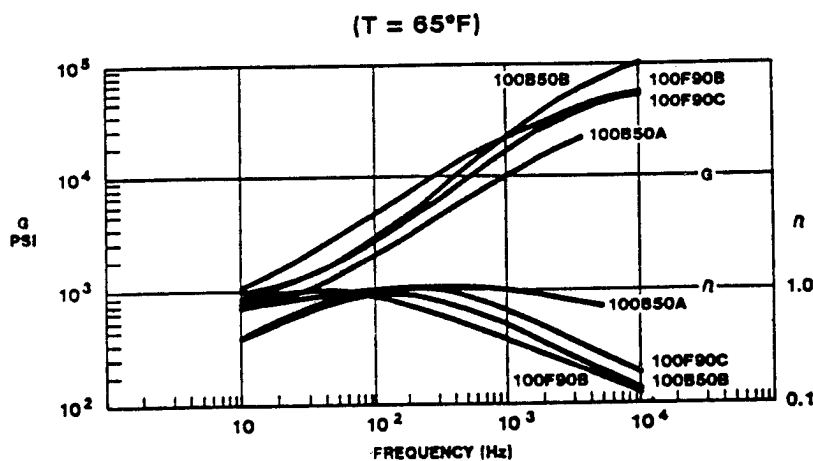
THE PEAK DAMPING FOR DYAD 601 IS ABOVE THE FREQUENCY RANGE OF INTEREST. SMRD 100F90C COMES CLOSER TO DESIRED RANGE.

Figure 9. Comparison of SMRD 100F90 and DYAD 601



ISD 112 HAS A LOW MODULUS AND, CONFORMS TO RELSAT TEMPERATURE/FREQUENCY RANGE

Figure 10. Comparison of SMRD 100F90 and ISD 112



4 SMRD MATERIALS WERE SELECTED FOR PANEL FABRICATION & TEST

Figure 11. Properties of Selected Materials at 65 Deg F

- CAST AND CURED IN FLAT SHEETS
- STABILIZED AND OUTGASSED UNDER VACUUM AT 135°C FOR 96 HOURS
- BONDED TO CONSTRAINING LAYER
- MACHINED TO FINAL DIMENSIONS
- BONDED TO STRUCTURE

Figure 12. VEM Damper Strip Fabrication Process

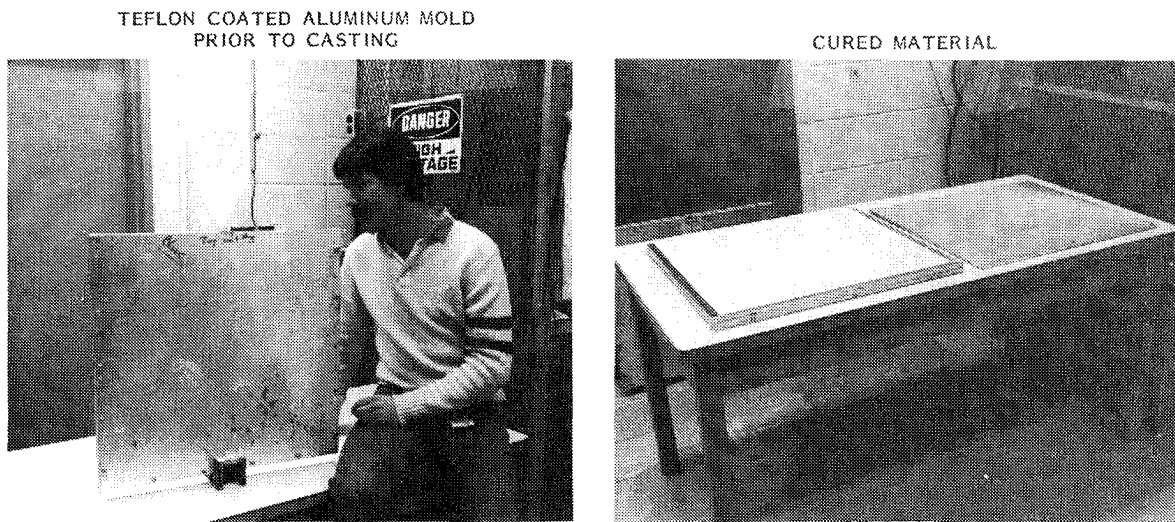


Figure 13. SMRD Fabrication

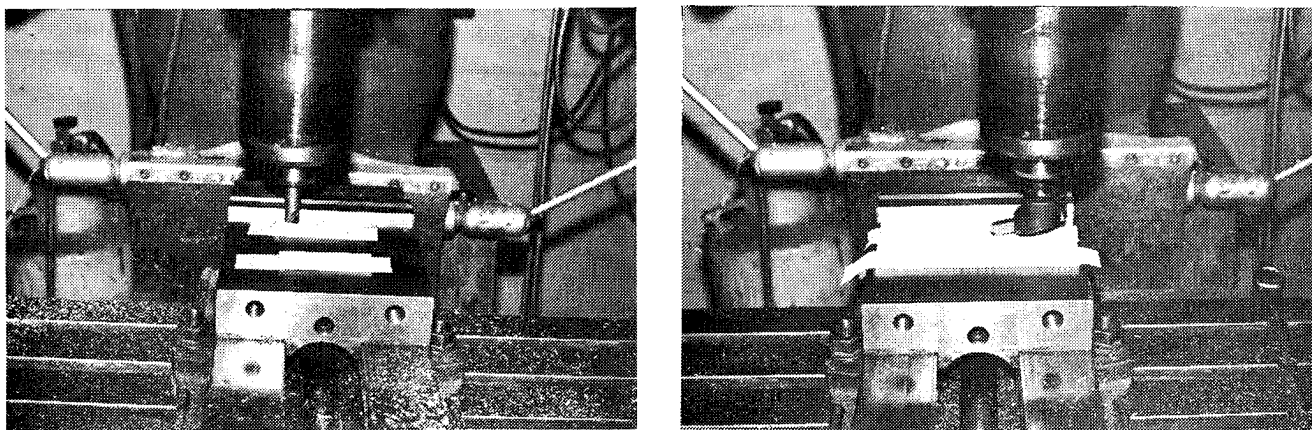


Figure 14. SMRD 100F90 Milled with a Diamond Compax End Mill

Figure 15. SMRD 100F90 Milled With a Diamond Fly Cutter

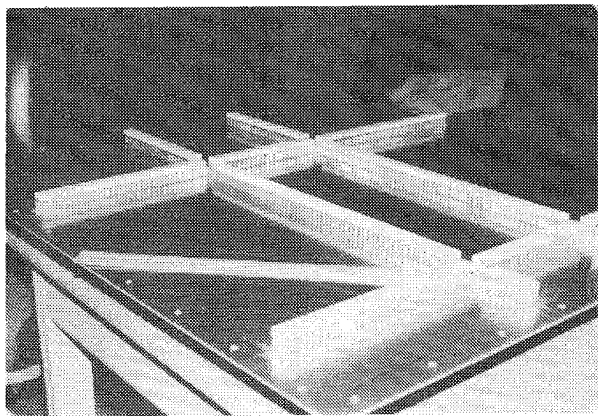


Figure 16. Honeycomb Stiffener Panel
Prior to Completion

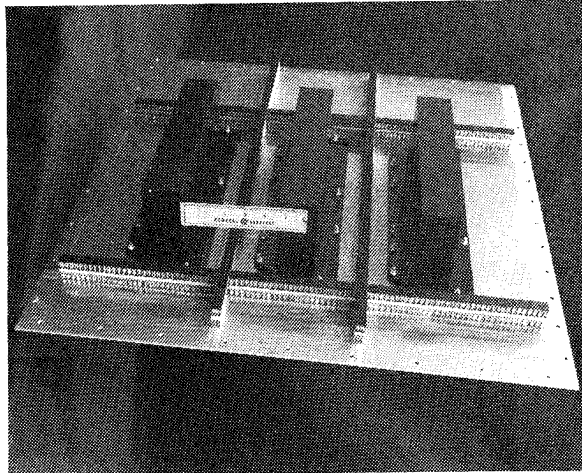


Figure 17. SMRD 100F90C Damped
Honeycomb Stiffener Panel

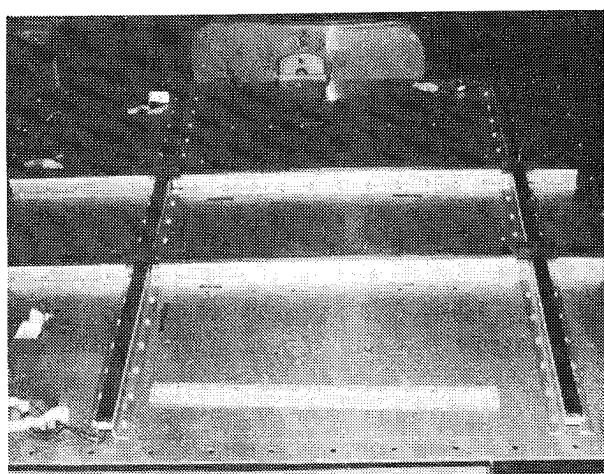


Figure 18. SMRD 100B50C Damped
Hat Section Stiffener Panel

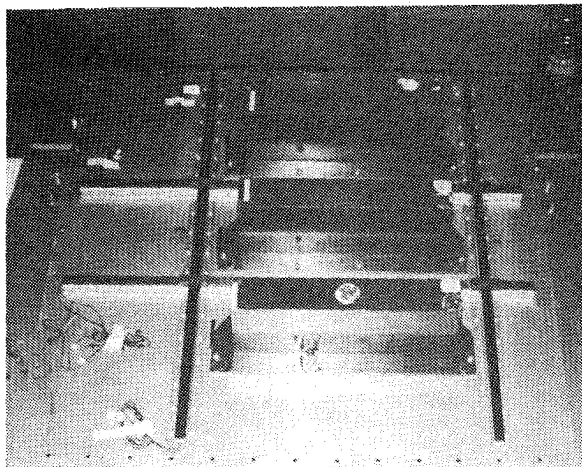


Figure 19. Completed Hat Section
Stiffener Panel

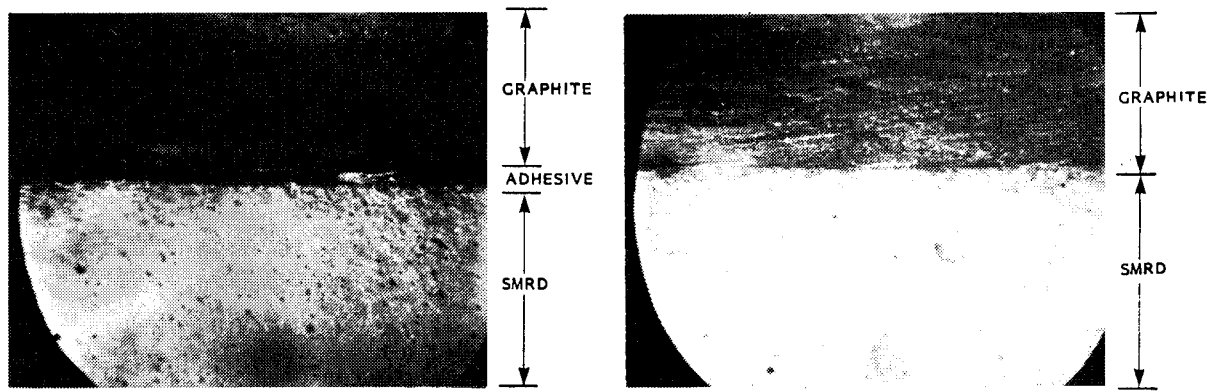


Figure 20. Direct vs Adhesive Bonding of Graphite/Epoxy Constraining Layer

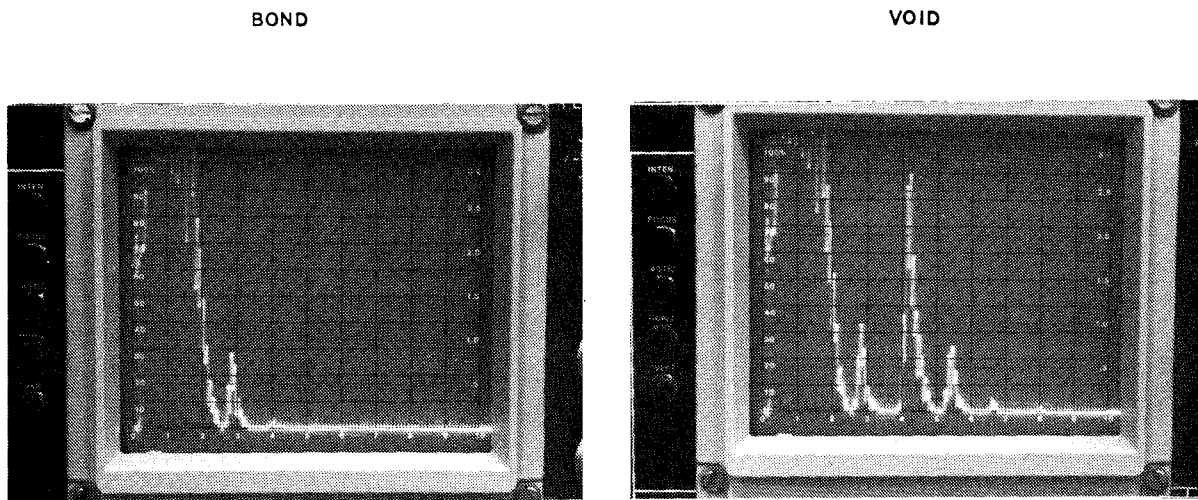


Figure 21. Pulsed Echo Ultrasonic Method for Assessing Bond

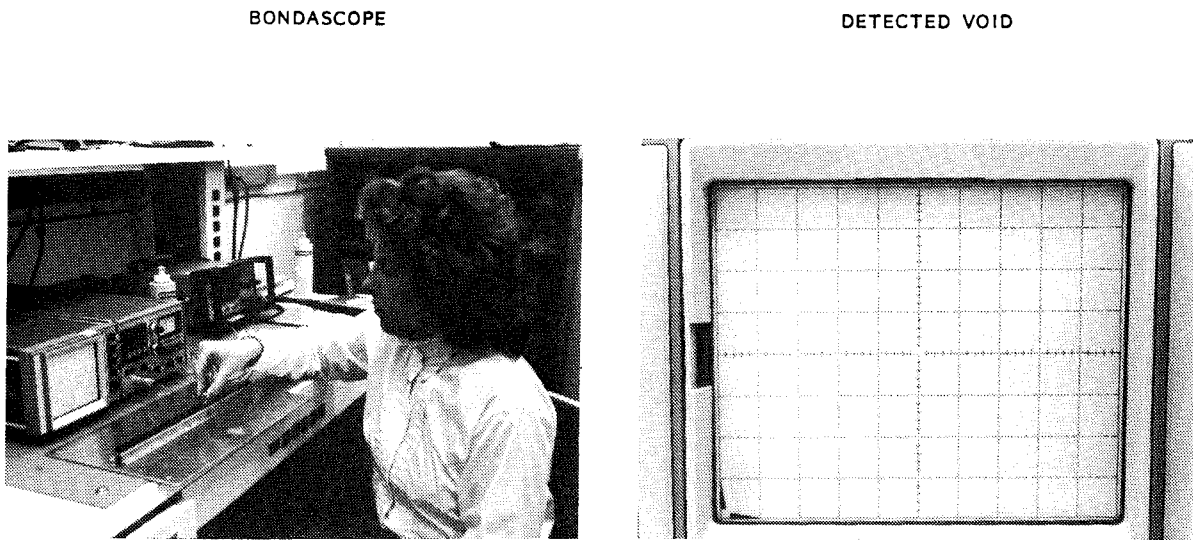


Figure 22. Ultrasonic Impedance Plane Analysis

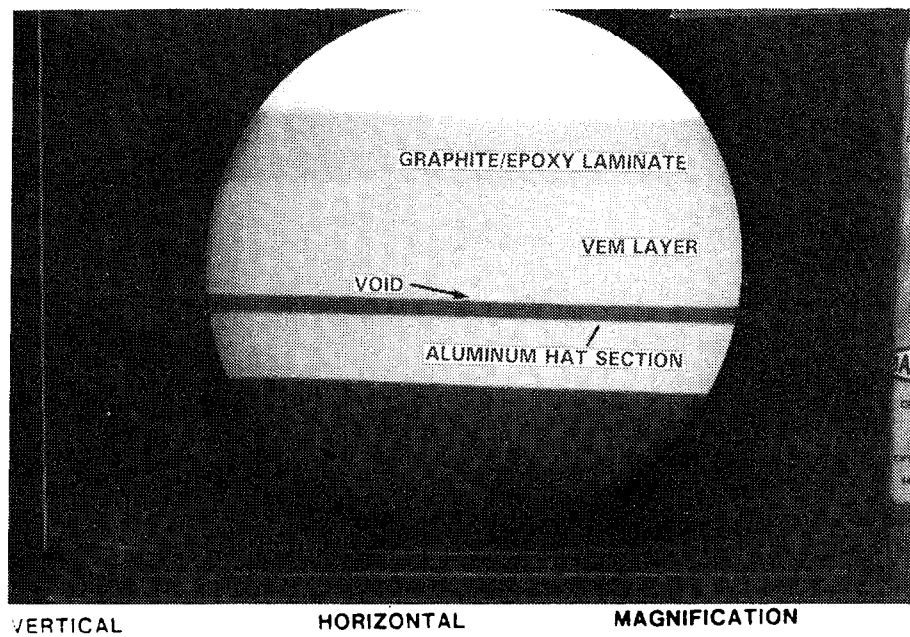


Figure 23. Bond Evaluation by Real Time X-Ray

**Prediction and Measurement of
Damping of a Laminated Beam with a
Constrained Viscoelastic Layer**

D. J. Segalman
Applied Mechanics Division I
Sandia National Laboratories
Albuquerque, New Mexico 87185
(505) 846-1899

Lt. Philip Reamy
Air Force Weapons Laboratory/ARBC
Albuquerque, New Mexico 87117-6008
(505) 844-2019

Abstract

Analytic predictions¹ for damped natural frequencies of a simple viscoelastic structure are compared with measured values². The structure studied is an aluminum channel incorporating a constrained layer of highly viscoelastic polymer. The predictive technique employs a general and systematic method for calculating damping and stiffness matrices using only measured material properties and structure geometry. These matrices are then used to predict the dynamic properties of the structure. This work constitutes the first step in the experimental verification of the analytic method.

Agreement between the predicted and measured response of the structure studied is very good, and indicating that the analytic technique used is a viable method for modeling viscoelastically damped structures.

¹The computational portion of this work was supported by Sandia National Laboratories under contract to the U.S. Department of Energy (DE-AC04-76DP00789).

²The experimental portion of this work was funded under Laboratory Independent Research Program 8722 of the Air Force Weapons Laboratory.

Contents

1	Introduction	JCA-4
2	Analytic Method	JCA-6
2.1	Formulation	JCA-6
2.2	Numerical Implementation	JCA-13
3	The Experiment	JCA-15
4	Experimental Results and Comparison with Experiment	JCA-20
5	Conclusions	JCA-28
	References	JCA-29

1. Introduction

The Role and Importance of Damping

Viscoelastic damping is a traditional method of controlling vibration and noise in structures and machinery. An example of this method of passive damping is the use of high-loss grommets in the attachment of subsystems. More sophisticated applications include the use of constrained layer damping treatments to reduce vibration in airplane shells that had previously suffered fatigue damage. Yet more advanced applications have been proposed, involving coupling viscoelastic damping with active controls in space structures.

Advanced analysis methods, particularly finite element methods, can be used to predict stresses, mode shapes, and natural frequencies adequately for guidance in the design of complex elastic structures. The utility of these elastic analysis techniques has been delineated by experimental as well as theoretical means. New methods, including that of Segalman [4], have been developed to enable corresponding calculations for viscoelastic structures. The work presented here is an experimental verification of that method.

Analytic Prediction of Damping

Inducing damping response in an otherwise elastic structure through the use of constrained viscoelastic layers is a technique that has been applied since the late 1950's. The work of Ross, Ungar, and Kerwin [1] marks the beginning of meaningful analytic methods for prediction and design of damping treatments for simple structures. Such methods are generally restricted to problems of beams and flat plates, for which closed form expressions for frequency and mode shape can be derived.

A technique for addressing constrained layer damping of more general structures was developed later as the "modal energy method" [2,3]. This method employs assumptions analogous to those underlying the Ross, Kerwin, and Ungar method for beams and plates, but generalizes them to forms that can be employed with finite element solutions for frequency and deformed mode.

The above prediction methods are restricted to problems involving primarily elastic structures with distinct viscoelastic regions. There is a further restrictive assumption embedded in those methods that the damped modes are identical to corresponding elastic modes. These restrictions sufficiently limit the application of those techniques that it is necessary to examine more general methods.

One more general method for prediction of damping in linearly viscoelastic structures was proposed by Segalman [4]. That work consisted of a purely formal derivation. The purpose of the work presented below is to test a numerical implementation of that method against measurements on a very simple viscoelastic structure. The results, shown below, provide strong encouragement to the authors to address more complex structures, for which the generality of the analytic method tested here can be demonstrated.

2. Analytic Method

2.1 Formulation

Formal Evaluation of Damping and Stiffness Matrices

The method presented in [4] begins with consideration of a nearly elastic structure, possessing only a small amount of viscoelasticity. This "slightly viscoelastic" structure consists of an underlying elastic system plus small contributions from the integral terms associated with viscoelastic material response. A perturbation expansion yields formal expressions for the complex modes and frequencies of the structure. (That expansion involves the natural modes and frequencies of the underlying elastic structure, whose elastic properties are those which would be measured in quasistatic experiments.)

A perturbation expansion is also performed on a similar but slightly damped, nearly elastic structure. This "slightly damped" system consists of the same underlying elastic structure plus small perturbations in the damping and stiffness matrices. Formal expressions for the damping and stiffness matrices of the second structure are obtained by requiring that the complex modes and frequencies of the two structures agree. The formal process described above is represented by the chart of Figure 2.1.

The strategy outlined above results in the following expressions for the damping and stiffness matrices:

$$C = \sum_{modes\ n=1}^N Im \left(\frac{1}{\omega^n} \Gamma^*(\omega^n) x^n (z^n)^T \right) \quad (2.1)$$

and

$$K = \sum_{modes\ n=1}^N Re \left(\Gamma^*(\omega^n) x^n (z^n)^T \right) \quad (2.2)$$

where $\Gamma^*(\omega)$ is the complex structural stiffness matrix of the viscoelastic structure evaluated at frequency ω .

N is the number of elastic eigensolutions retained in the calculation.

and ω^n is the n 'th eigenfrequency and x^n is the n 'th eigenmode of the elastic structure. Together, ω^n and x^n are the n 'th eigen solution to the equation:

$$[-(\omega^n)^2 M + K_0] x^n = 0 \quad (2.3)$$

FORMAL STRATEGY OF DERIVATION

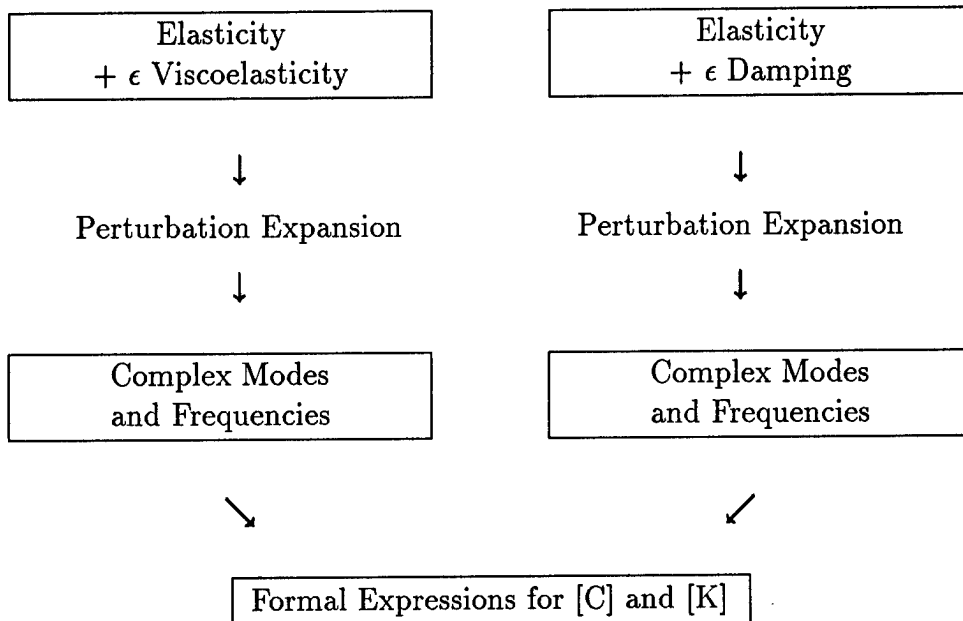


Figure 2.1. Outline of Strategy for Calculation of Damping and Stiffness Matrices for Linearly Viscoelastic Structures

The remaining quantities, z^n and K_o are defined by:

$$K_o = \Gamma^*(0) \quad (2.4)$$

$$f^n = K_o x^n \quad (2.5)$$

and

$$z^n = f^n / (x^n)^T f^n \quad (2.6)$$

(In Equations 2.1 and 2.2 and in what follows, expressions such as $x^n (z^n)^T$ are matrix-valued outer products, and expressions such as $(x^n)^T z^n$ are scalar-valued inner products.)

When the damping and stiffness terms are combined with inertial terms, a second order system of equations results:

$$M \ddot{x}(t) + C \dot{x}(t) + K x(t) = r(t) \quad (2.7)$$

where M is the structural mass matrix;

$x(t)$ is the generalized (nodal) displacement vector;

and $r(t)$ is the corresponding force vector.

Some observations should be made at this point.

- The complex stiffness matrices $\Gamma^*(\omega)$ could, in principle, be calculated in the standard manner that elastic stiffness matrices are calculated, but using the complex material properties evaluated at frequency ω rather than the corresponding elastic material properties.
- It is a result of classical linear viscoelasticity that K_o above, is the stiffness matrix that would be constructed using material properties obtained from quasistatic measurements [5].
- The vectors x^n and z^n form a biorthogonal set:

$$(x^k)^T z^l = \delta_{kl} \quad (2.8)$$

The above relationship was central to the derivation of [4].

- The elastic eigenmodes, x^k , are determined at this point only up to an arbitrary factor. They become uniquely defined when scaled so that

$$(x^k)^T M x^k = 1 \quad (2.9)$$

for each mode k . This is one of the standard forms of eigenvector normalization and from substitution of the above equation into Equation 2.3, the eigenfrequencies can be isolated:

$$(x^k)^T f^k = (\omega^k)^2 \quad (2.10)$$

This normalization becomes useful below in the extraction of complex eigenpairs for the damped system.

- Though the damping and stiffness matrices (Equations 2.1 and 2.2) of Equation 2.7 are expressed as expansions involving x^n and ω^n , these are eigensolutions of the elastic problem, Equation 2.3, and not of the damped system, Equation 2.7.
- The matrices defined by Equations 2.1 and 2.2 are, in general, full and non-symmetric. Though at first disconcerting, these features should not be unexpected: symmetric damping and stiffness matrices should be expected only where there exist elastic strain energies and Rayleigh dissipation functions. Such potentials do not exist for general viscoelastic materials.

Elastic Modal Coordinates

In order to deal with a smaller system of equations, it is useful to express displacements in terms of the elastic modal coordinates:

$$x(t) = \sum_{modes\ n=1}^N \alpha^n(t) x^n \quad (2.11)$$

(The modal coordinates $\alpha^n(t)$ are found by contracting the above equation with $(z^k)^T$ and invoking Equation 2.8 to obtain the following:)

$$\alpha^n(t) = (z^n)^T x(t) \quad (2.12)$$

Premultiplication of Equation 2.7 by $(x^k)^T$ and substitution of Equation 2.11 for $x(t)$, generates the system equations in terms of the elastic modal coordinates.

$$\hat{I} \ddot{\alpha}(t) + \hat{C} \dot{\alpha}(t) + \hat{K} \alpha(t) = \beta(t) \quad (2.13)$$

In the above, the vector $\alpha(t)$ is composed of the scalars $\alpha^n(t)$, \hat{I} is the N 'th order identity matrix, and the matrices \hat{C} and \hat{K} are defined by

$$\hat{C}_{k,l} = (x^k)^T h^l \quad (2.14)$$

and

$$\hat{K}_{k,l} = (x^k)^T g^l \quad (2.15)$$

where

$$h^k = \text{Im} \left(\frac{1}{\omega^k} \Gamma^*(\omega^k) \right) x^k \quad (2.16)$$

and

$$g^k = \text{Re} (\Gamma^*(\omega^k)) x^k \quad (2.17)$$

The components, $\beta^n(t)$, of the vector $\beta(t)$ are the contraction of $r(t)$ with each of the elastic eigenmodes:

$$\beta^n(t) = (x^n)^T r(t) \quad (2.18)$$

It should be noted that the equations of [2] and [3] result if all off-diagonal terms of Equation 2.14 for \hat{C} are dropped and the term g^l in Equation 2.15 for \hat{K} is replaced by f^l . Such a reduction of Equations 2.14 and 2.15 to obtain those of [2] and [3] is reflective of that method's assumptions that elastic eigenmodes are preserved and that strain energy is independent of frequency.

Frequency Response Matrices and Complex Eigenanalysis

Once the matrices \hat{C} and \hat{K} have been calculated, Equation 2.13 is recast as a first order system of equations in state space and the complex eigenmodes and frequencies are extracted. We have chosen to use the formalism of Newland [6] for these steps of the calculation. Letting

$$s(t) = \begin{Bmatrix} \alpha(t) \\ \dot{\alpha}(t) \end{Bmatrix} \quad (2.19)$$

Equation 2.13 becomes

$$\dot{s}(t) = A s(t) + F(t) \quad (2.20)$$

where

$$A = \begin{bmatrix} 0 & \hat{I} \\ -\hat{K} & -\hat{C} \end{bmatrix} \quad (2.21)$$

and

$$F(t) = \begin{Bmatrix} 0 \\ \beta(t) \end{Bmatrix} \quad (2.22)$$

The above state-space equation is diagonalized through introduction of a matrix, U , whose columns are the complex right-eigenvectors of A :

$$A U = U \Lambda \quad (2.23)$$

where Λ is a matrix whose diagonal terms are the complex eigenvalues, λ_k , of A and whose off-diagonal terms are zero. Since A is a $2N$ by $2N$ matrix, U and Λ are also of dimension $2N$. Both U and Λ are products of standard numerical eigensolvers.

Each complex eigenpair, (U_k, λ_k) and its conjugate, (U_k^*, λ_k^*) combine to generate real displacements:

$$s(t) = D e^{\mu_k t} [\cos(\psi_k t + \theta) \operatorname{Re}(U_k) - \sin(\psi_k t + \theta) \operatorname{Im}(U_k)] \quad (2.24)$$

where $\mu_k = \operatorname{Re} \lambda_k$ is the damping factor for that mode, $\psi_k = \operatorname{Im} \lambda_k$ is the damped natural frequency for that mode, and D and θ are indeterminate. The above expression transforms, through Equations 2.11 and 2.19, to corresponding expressions in terms of displacement coordinates:

$$x(t) = D e^{\mu_k t} \sum_{modes} \sum_{n=1}^N x^n [\cos(\psi_k t + \theta) \operatorname{Re}(U_k^n) - \sin(\psi_k t + \theta) \operatorname{Im}(U_k^n)] \quad (2.25)$$

and

$$\dot{x}(t) = D e^{\mu_k t} \sum_{modes} \sum_{n=1}^N x^n [\cos(\psi_k t + \theta) \operatorname{Re}(U_k^{N+n}) - \sin(\psi_k t + \theta) \operatorname{Im}(U_k^{N+n})] \quad (2.26)$$

where U_k^n is the n 'th component of the k 'th complex eigenmode. From the above, it is seen that when expressed in spatial coordinates, the k 'th complex eigenmode, x_c^k , is:

$$x_c^k = \sum_{modes} \sum_{n=1}^N x^n U_k^n \quad (2.27)$$

The complex frequency λ_k can also be expressed in the more common terms of damping ratio ξ_k and a nominal “undamped” frequency $\hat{\omega}^k$:

$$\lambda_k = \hat{\omega}^k \left[-\xi_k + i\sqrt{1 - \xi_k^2} \right] \quad (2.28)$$

where

$$\xi_k = \sqrt{\frac{(\operatorname{Re} \lambda_k)^2}{(\operatorname{Re} \lambda_k)^2 + (\operatorname{Im} \lambda_k)^2}} \quad (2.29)$$

and

$$\hat{\omega}^k = -\operatorname{Re} \lambda_k / \xi_k \quad (2.30)$$

In general, the nominal “undamped” frequency $\hat{\omega}^k$ will not equal any of the natural frequencies of the underlying elastic system, since the complex modes do not, in general, equal any individual elastic mode.

Equation 2.23 is substituted into Equation 2.20 and the result is rearranged to yield an uncoupled system of equations which can be integrated to yield $s(t)$:

$$s(t) = U e^{\Lambda t} s(0) + U \int_0^t e^{\Lambda(t-\tau)} U^{-1} F(\tau) d\tau \quad (2.31)$$

The quantity $e^{\Lambda t}$ is the diagonal matrix of terms $e^{\lambda_k t}$.

In the case of harmonic excitation forces,

$$F(t) = \operatorname{Re} \left\{ \begin{array}{c} 0 \\ \beta_0 e^{i\omega t} \end{array} \right\} \quad (2.32)$$

Equation 2.31 becomes

$$s(t) = \operatorname{Re} \left(\hat{H}(\omega) \left\{ \begin{array}{c} 0 \\ \beta_0 e^{i\omega t} \end{array} \right\} \right) \quad (2.33)$$

where $\hat{H}(\omega)$ is the frequency response matrix

$$\hat{H}(\omega) = U d(\omega) U^{-1} \quad (2.34)$$

and

$$d(\omega) = \begin{bmatrix} \frac{1}{i\omega - \lambda_1} & 0 & 0 \\ 0 & \ddots & 0 \\ 0 & 0 & \frac{1}{i\omega - \lambda_{2N}} \end{bmatrix} \quad (2.35)$$

Since \hat{H} is constructed from the eigenvectors and eigenvalues of A , and those eigenquantities occur in complex conjugate pairs, it is not surprising that there is some redundant information in \hat{H} . Only the upper right-hand quarter of $\hat{H}(\omega)$,

$$\hat{H}^{1,2}(\omega) = \hat{P} d(\omega) \hat{Q} \quad (2.36)$$

where \hat{P} is the upper half of U and \hat{Q} is the right half of U^{-1} , is necessary for calculating the displacement frequency response of the structure

$$\alpha(t) = \operatorname{Re} \left(\hat{H}^{1,2}(\omega) \beta_0 e^{i\omega t} \right) \quad (2.37)$$

Substitution of Equation 2.18 into Equation 2.37 and substitution of the result into Equation 2.11 returns the frequency response matrix for the original displacement vector $x(t)$:

$$x(t) = \operatorname{Re} (H(\omega) r_0 e^{i\omega t}) \quad (2.38)$$

where

$$H(\omega) = P d(\omega) Q \quad (2.39)$$

and

$$P_{i,k} = \sum_{modes \ n=1}^N x_i^n \hat{P}_{n,k} \quad (2.40)$$

and

$$Q_{k,j} = \sum_{modes\ n=1}^N \hat{Q}_{k,n} x_j^n \quad (2.41)$$

Evaluation of individual components $H_{i,j}(\omega)$ over ranges of ω involves far fewer calculations than would first appear since only individual rows of P and individual columns of Q need to be evaluated and stored while the diagonal matrix $d(\omega)$ is evaluated over the frequency range of interest.

2.2 Numerical Implementation

There are two parts to the numerical implementation of the formulation developed above:

- the evaluation of the damping and stiffness matrices occurring in Equation 2.13.
- the matrix operations associated with evaluation of complex modes and frequencies and the calculation of the frequency response matrix.

Evaluation of Damping and Stiffness Matrices

Evaluation of \hat{C} and \hat{K} is done through the following steps:

1. Material properties for all constituent materials are tabulated – as functions of frequency – in two distinct sets of tables: one for storage response (real part) and one for loss response (imaginary part). (With the finite element code used in this project, MSC NASTRAN [7], it is convenient to use the table formats which that code associates with temperature-dependent material properties.) For the second set of tables, the loss moduli are divided by ω so that it is actually viscosity type properties that are tabulated.

It is important that the tabulated material properties are tailored so that Lame' constants calculated from them are the real and imaginary parts of the Lame' constants of the material.

2. NASTRAN is used to formulate and solve the elastic eigenproblem of Equation 2.3. In this step, the stiffness matrix is constructed from the real part of the material response in the limit of zero frequency. This step generates quantities ω^n and x^n for the range of frequencies of interest.

NASTRAN is also used to evaluate h^n and g^n (Equations 2.16 and 2.17). For each eigenpair (ω^n, x^n) , two statics problems are directed to NASTRAN

- (a) for which the displacements are specified as x^n and the material properties are selected from the first set of tables and evaluated at frequency ω^n . The resulting force vector is g^n .
- (b) for which the displacements are specified as x^n and the material properties are selected from the second set of tables and evaluated at frequency ω^n . The resulting force vector is h^n .

The above calculations are done with procedures which are documented in the MSC literature for the solution of problems involving temperature dependent material properties.

3. \hat{C} and \hat{K} are evaluated in the manner indicated in Equations 2.14 and 2.15, by taking inner products of vectors x^k with vectors g^l and h^l , respectively. The appropriate Fortran coding is reasonably straightforward.

Complex Modes and Frequencies, Damping Ratio, and Frequency Response

1. Matrix A of Equations 2.21 is constructed in the manner indicated, and its complex eigensolutions are extracted using routines found in the SLATEC [8] library of Fortran code. Some sorting and normalization of the complex eigenvectors U_k is useful before printing. (In the case that the n 'th elastic eigenmode is preserved, the associated complex eigenvector is zero in all but the n 'th and $N+n$ 'th components.) Damping ratios for each complex mode are calculated from Equation 2.29 and printed along with the corresponding complex eigenfrequency-eigenmode pair.
2. Fortran code has also been written along the lines suggested by Equations 2.39 through 2.41 for the evaluation of complex frequency response functions for given nodal-force/nodal-displacement pairs.

The above codes generate three quantities that can be compared to experiment: complex mode shape, complex frequency (including damping ratio), and frequency response functions.

Also, though it cannot be demonstrated in this media, Fortran code has been written to evaluate Equation 2.25 to generate Patran [9] ".DIS" files which are then used to create movies of the complex modes.

3. The Experiment

AFWL/ARBC personnel performed experimental modal surveys on two test articles in support of this verification effort. The test articles were residual hardware from a previous study on damping techniques [10]. The first test article was a 68" x 2" x 1/8" aluminum C-channel extrusion. The second test article was an identical C-channel extrusion treated with constrained layer damping. This treatment which was applied to the backside of the beam, consisted of a layer of viscoelastic material(VEM), 3M ISD-112, sandwiched between the beam surface and an aluminum constraining layer (see Figure 3.1). Elastic properties for the aluminum and for the polymer are provided in Table 3.1 and the viscoelastic properties of the polymer are provided in Tables 3.2 and 3.3. The test articles were suspended using elastic bands at the two ends to simulate free-free boundary conditions in the modal testing.

This test utilized an Endevco model 23 triaxial accelerometer to measure motion of the test article and an instrumented impact hammer to apply and measure the input disturbance. The Endevco model 23 triaxial accelerometer is a very lightweight piezoelectric motion sensor, and was chosen to avoid mass-loading issues, particularly in the testing of the undamped beam. The outputs of this device were attached to three B & K model 2635 charge amplifiers, which convert the accelerometer output to a voltage and perform signal amplification. The input disturbance was provided by a PCB model 086B03 impact hammer. This hammer has a force gage built into the tip which measures the input disturbance. The output of this gage was attached to a PCB model 480D06 power unit which amplified the sensor signal.

This amplified input signal and the three charge amplifier output signals were input to the first four channels of the data acquisition system. The Modal Analysis Data Reduction And Testing System (MADRATS) was the primary testing computer for this program. This system is based on a Hewlett Packard A-900 computer, a multi-user, real-time interrupt system. This system includes a 132 Mbyte hard disk, 3 Mbyte memory and a complete data acquisition and analysis workstation. The system also includes other support peripherals such as printers, plotters, and tape drives.

The system front end is a 64 channel DIFA SCADIS data acquisition system. The DIFA SCADIS is fully programmable, either manually from the attached keypad or through the data acquisition software on the computer via an HP-IB interface. This front end utilizes programmable gain pre-filter and post-filter amplifiers and programmable bandpass filters. The SCADIS samples all channels in parallel using sample and hold buffers. This data is digitized by the SCADIS and then multiplexed into the

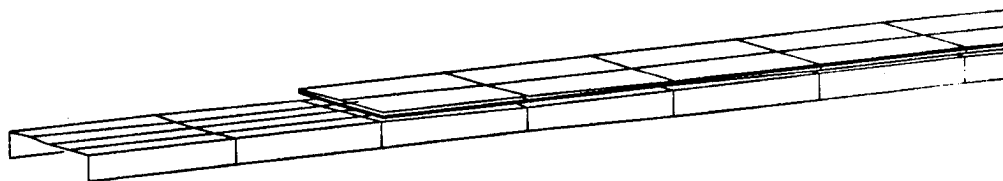
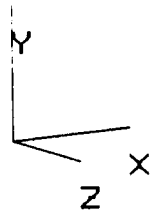


Figure 3.1. Left edge of aluminum beam with damping treatment, illustrating finite element meshing.

Material	Shear Modulus G_0 (psi)	Poisson's Ratio	Density (lb sec ² /in ⁴)
Aluminum	3.76E6	0.33	2.54E-4
3M ISD-112	60.0	0.49	1.90E-4

Table 3.1. Elastic Properties of Aluminum and 3M ISD-112

A-900 computer memory via a parallel interface. This system has a frequency range of 0.1 to 10,000 Hz and a dynamic range of 63 dB. The maximum throughput rate to memory of the SCADIS is 350 kHz.

Data acquisition is accomplished through the Leuven Measurement Systems Fourier Monitor (FMON) software package. Several modal testing techniques can be performed using FMON, including forced response, power spectrum, and impact testing. Testing can be set up and performed using menu-driven programs, user-defined command stacks or manually. The test program covered in this report utilized the menu-driven programs which allow test setups to be stored into and loaded from memory. Test setups from memory were used, requiring changes only to transducer location for the various test runs.

Data reduction is also performed on the MADRATS computer using the Leuven Measurements Systems Super Modal Analysis Package (SMAP). SMAP computes the modal parameters of a structure from the frequency response functions produced in data acquisition. This software package has several available parameter estimation techniques to tailor analysis to a specific test. The primary algorithm used in reducing the data of this test program was the Least Squares Complex Exponential Time Domain Method. In addition, a variety of curve fitters are available, including a real and imaginary fitter, circle fitters, and a Least Squares multiple degrees of freedom fitter. The least squares MDOF method was the most frequently used because of the modal density involved in these tests. The specific applications of these methods will be discussed in more detail in the Results section of this report.

The first tests were performed on the bare beam. Prior to testing, a test setup file was generated and stored on the computer. The testing consisted of a 200 Hz bandwidth, roving accelerometer impact test. The accelerometer was first attached to the beam, and the point number and direction information was entered into the computer. The structure was tapped by the impact hammer at a point at one end of the beam, 0.5 inches from the centerline, in order to perform the autoranging of the data acquisition channel amplifiers. A series of eight impacts was performed, and the data was averaged and processed to provide frequency response and coherence functions for each of the three axes at the data point. The power spectra of each impact, and the frequency response functions for the response channels were each viewed prior to

acceptance, and the resulting transfer functions were stored on the disk. This procedure was repeated for each of the 36 data points on the bare beam, and for the 36 data points on the damped beam whose data was stored under a different test identification.

The frequency response functions for the undamped beam exhibited high amounts of spectral leakage, leading to poor coherence functions. Exponential windowing was used on the response data for the undamped beam to reduce the leakage to acceptable levels. This added damping by the window can be backed out of the modal parameters calculated from data reduction. Windowing was not required or used in testing the damped beam because the higher damping exhibited by this structure greatly reduced leakage effects.

Storage Modulus $G'(f) = G_0 * (1.0 + g(f))$					
frequency f (hz)	$g(f)$	frequency f (hz)	$g(f)$	frequency f (hz)	$g(f)$
.00E+00	.00E+00	.70E+01	.18E+00	.31E+02	.68E+00
.13E+03	.19E+01	.40E+03	.46E+01	.14E+04	.11E+02
.46E+04	.24E+02	.14E+05	.58E+02	.55E+05	.12E+03
.20E+06	.24E+03	.13E+07	.46E+03	.40E+07	.62E+03
.22E+08	.81E+03	.87E+08	.98E+03	.49E+09	.12E+04
.18E+10	.13E+04	.54E+10	.15E+04	.22E+11	.16E+04
.39E+11	.17E+04				

Table 3.2. Storage Modulus of 3M ISD-112

Loss Modulus $G''(f) = 2\pi f * G_0 * h(f)$					
frequency f (hz)	$h(f)$	frequency f (hz)	$h(f)$	frequency f (hz)	$h(f)$
.00E+00	.23E-01	.23E+01	.16E-01	.67E+01	.11E-01
.21E+02	.81E-02	.42E+02	.65E-02	.11E+03	.46E-02
.24E+03	.35E-02	.49E+03	.29E-02	.65E+03	.25E-02
.13E+04	.19E-02	.31E+04	.14E-02	.96E+04	.84E-03
.28E+05	.49E-03	.64E+05	.30E-03	.25E+06	.11E-03
.14E+07	.22E-04	.77E+07	.39E-05	.46E+08	.66E-06
.33E+09	.93E-07	.24E+10	.12E-07	.11E+11	.25E-08
.41E+11	.63E-09	.54E+11	.46E-09		

Table 3.3. Loss Modulus of 3M ISD-112

4. Experimental Results and Comparison with Experiment

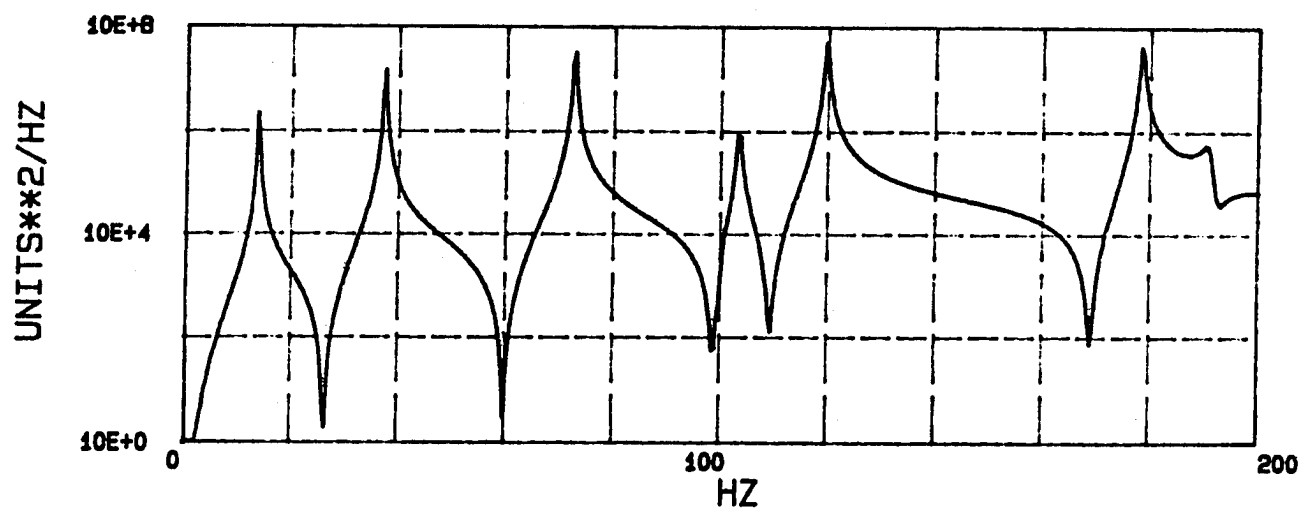
Figure 4.1 shows the driving point frequency response functions for the two beams. The driving point is at one end of the beam, 0.5 inches from the center line. The sharpness in the peaks of the bare beam transfer function graphically demonstrate the extremely low damping present in this beam. The shorter, more rounded peaks in the frequency response function of the damped beam demonstrate graphically the effect of the treatment both on the damping present in the beam and the magnitude of response at the natural frequencies. These frequency response functions also demonstrate a slight frequency shift due to the increased stiffness provided by the damping treatment. Frequency response functions similar to the driving point response function were stored on the disk for each data point on the two beams.

Data reduction was performed using the Super Modal Analysis Package (SMAP) software residing on MADRATS. The data was reduced using a Least Squares Exponential method for parameter estimation and curve fitting. This data reduction resulted in modal frequency and damping information, as well as displacement files for each mode of the structure in the 0-200 Hz bandwidth. This procedure was repeated for the data sets for each beam. Table 4.1 shows a comparison of the results from the two test articles in terms of frequency and damping.

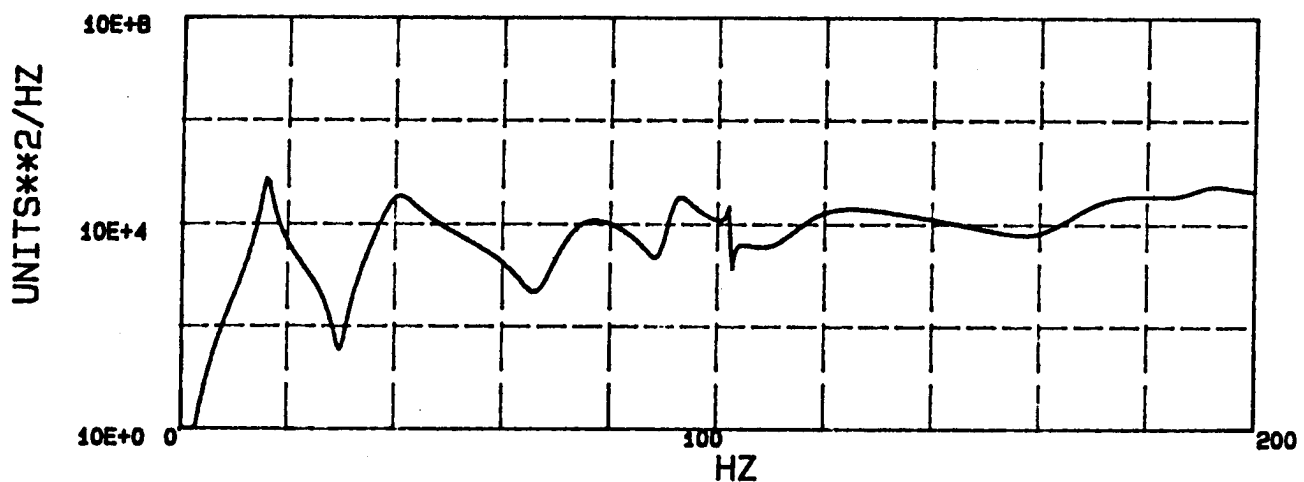
Figure 4.2 is a series of plots for the mode shapes of the damped beam. These mode shapes were produced by combining the displacement files produced by the data reduction with a geometry file. This data can also be animated to aid in the interpretation of the mode shapes.

The damping results for the final mode were not included because they were somewhat suspect. To prevent aliasing in the data, the data acquisition system filters were set to roll off at 70% of the upper frequency of a test. This last mode was so close to the upper frequency bound that most of its signal was likely below the noise floor, making it impossible for the parameter estimator to determine the damping values. This mode was retained simply as another frequency value for comparison with the analytic results.

The results of the analytic modeling and experimental testing were compared in three ways. First, a qualitative comparison was drawn between the frequency response functions developed analytically and through testing. Figure 4.3 shows an overlay of the experimental and analytic driving-point frequency response functions for the damped beam. The dashed curve is the experimental data. The impact hammer used to excite



(a) Frequency Response Function of Undamped Beam.



(b) Frequency Response Function of Damped Beam.

Figure 4.1. Driving point frequency response of damped and undamped beams

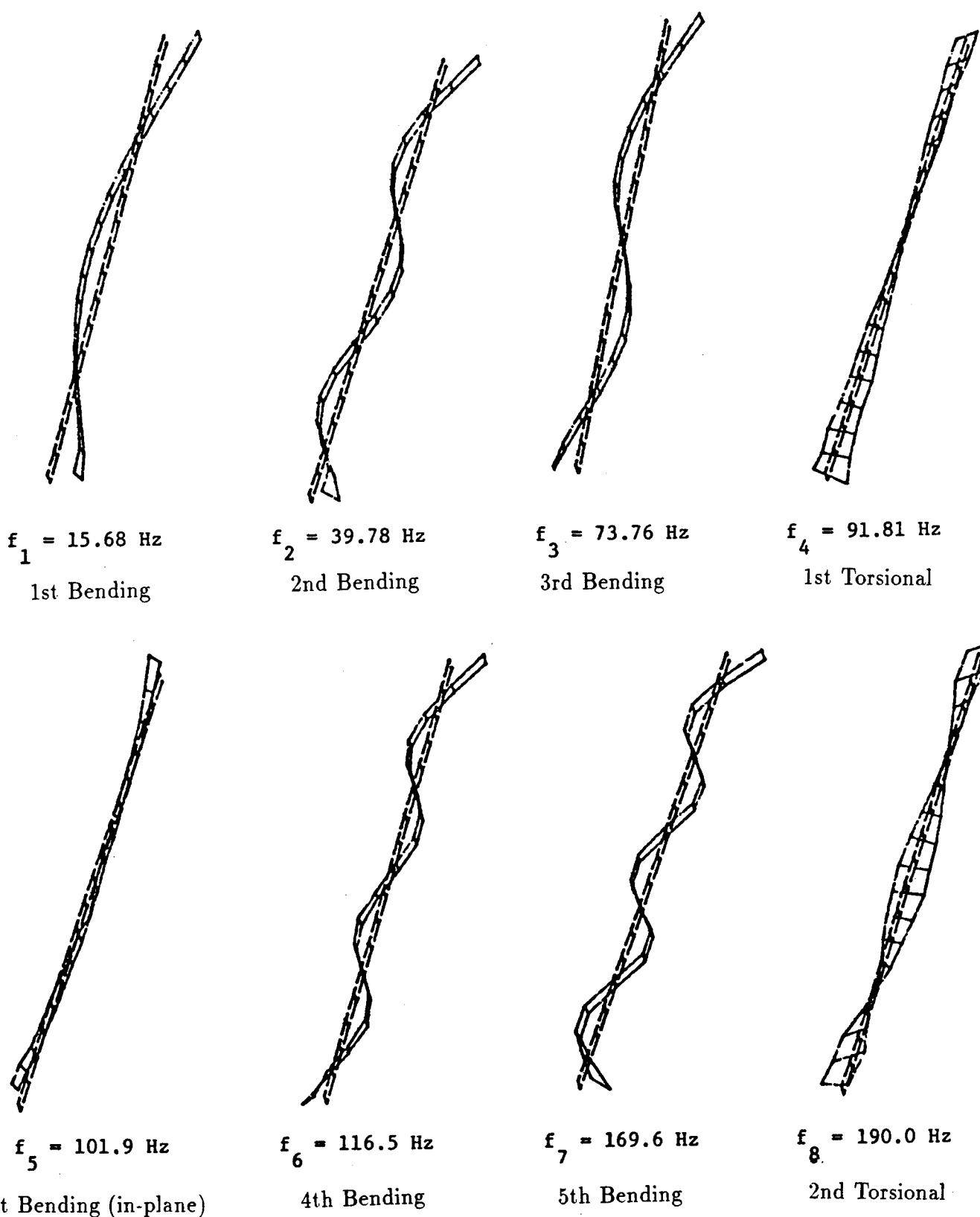


Figure 4.2. Real and Imaginary components of complex modes of damped beam.
 Imaginary components are essentially zero.

Mode	Undamped Beam		Damped Beam	
	Frequency (Hz)	Damping (% Critical)	Frequency (Hz)	Damping (% Critical)
1st Bending	13.38	0.295	15.68	5.837
2nd Bending	37.00	0.190	39.78	8.069
3rd Bending	72.12	0.156	73.76	8.489
1st Bending (in-plane)	99.77	0.278	101.95	0.204
1st Torsional	102.90	0.289	91.81	2.386
4th Bending	119.13	0.211	116.46	8.367
5th Bending	177.84	0.146	169.63	7.054
2nd Torsional	190.58	—	190.01	—

Table 4.1. Experimental Test Results

the experimental modes was uncalibrated, so the experimental curve is known only up to a multiplicative constant, corresponding to a vertical translation in the semi-log plot shown here.

Comparison of the frequency and damping information from the test data and modeling results provides a more quantitative method of comparison. Tables 4.2 and 4.3 contain these results for the two test articles. Note that both prediction and experiment for the damped beam show a reordering of the first torsional and the first in-plane-bending modes.

The comparison of the first test article results was used to gain confidence in the NASTRAN model of the beam prior to modeling the damping treatment. As one can see from the results presented in this table, nearly identical results were achieved through testing and modeling of the undamped beam, particularly in the bending modes. The larger differences in the natural frequency values for the two torsional modes have been attributed to fundamental torsional characteristics of the plate elements used in the modeling.

The second test article was compared using damping as well as natural frequency results. As indicated in the table, the frequency values are again nearly identical, with the largest variance being less than seven percent, and all of the bending modes being within five percent. The damping results were not predicted as well as the frequencies, but this is expected considering the relative difficulties in both measurement and prediction. The agreement between measured and predicted damping values is encouraging since they agree to within the uncertainty of viscoelastic properties of the polymer.

The difference for the in-plane bending mode damping was the highest, but it is

C.L.Damped Channel Section
Amplitude of Freq. Resp (Acceleration)
Node 142, DOF 2 & Node 142, DOF 2

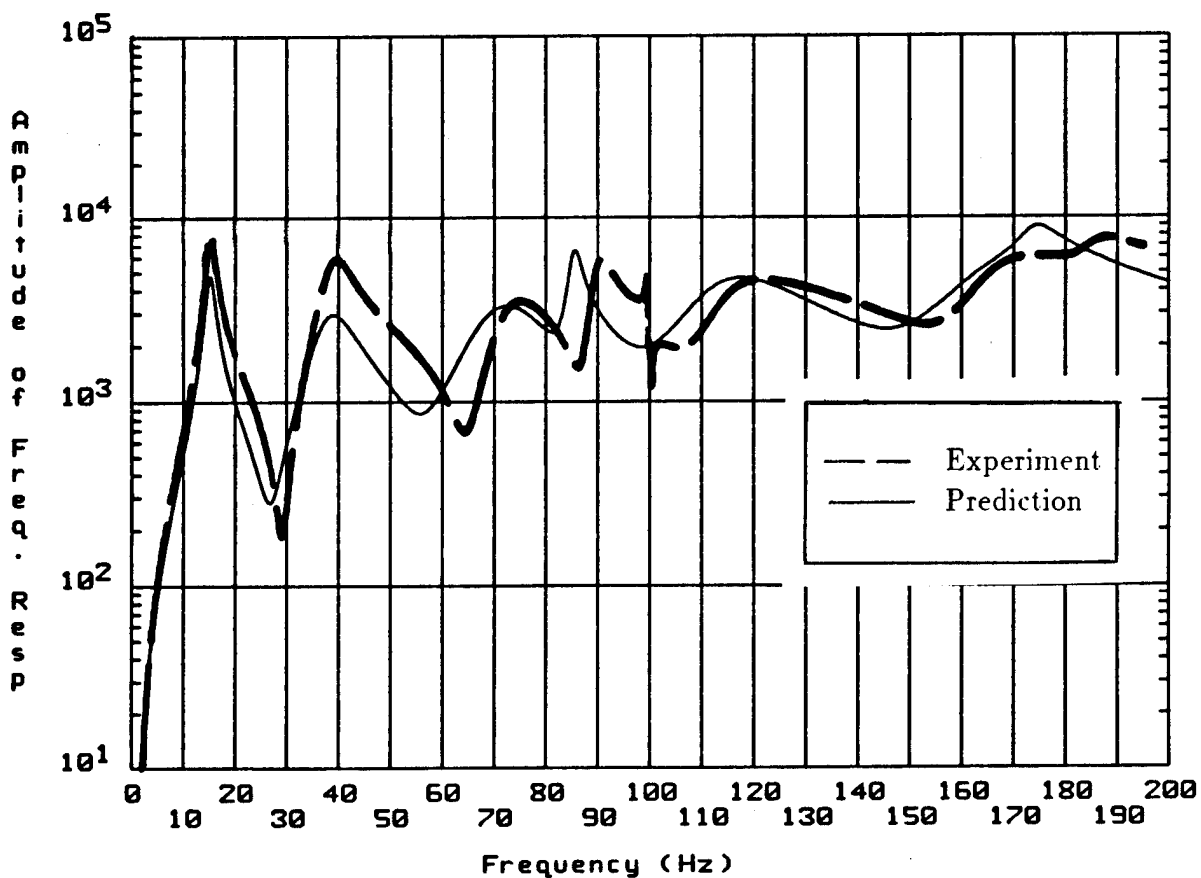


Figure 4.3. Overlay of the experimental and analytic frequency response functions for the damped beam. The dashed curve is the experimental data.

	AFWL Measured	Sandia Predicted	% Diff.
Mode	Frequency (Hz)	Frequency (Hz)	
1st Bending	13.38	13.75	2.7
2nd Bending	37.00	37.82	2.2
3rd Bending	72.12	74.01	2.6
1st Bending (in-plane)	99.77	100.70	0.9
1st Torsional	102.90	85.40	18.6
4th Bending	119.13	122.10	2.5
5th Bending	177.84	182.10	2.4
2nd Torsional	190.58	173.10	9.6

Table 4.2. Comparison of Undamped Beam Results

	AFWL Measured	Sandia Predicted	% Diff.			
Mode	Freq. (Hz)	Damp. (% Cr.)	Freq. (Hz)	Damp. (% Cr.)	Freq. (Hz)	Damp. (% Cr.)
1st Bending	15.7	5.8	15.1	6.1	3.9	5.0
2nd Bending	39.8	8.1	38.0	11.3	4.6	33.0
3rd Bending	73.8	8.5	70.6	12.0	4.4	34.1
1st Torsional	91.8	2.4	87.2	1.7	5.1	34.1
1st Bending (in-plane)	102.0	0.2	102.6	0.07	0.6	96.3
4th Bending	116.5	8.4	113.4	10.2	2.7	19.4
5th Bending	169.6	7.1	166.8	9.2	1.7	25.8
2nd Torsional	190.0	—	177.5	2.6	6.8	—

Table 4.3. Comparison of Damped Beam Results

important to note that the experimentally measured result is highly suspect due to the difficulty in imposing a purely vertical impulse at the driving point.

A method known as Modal Assurance Criterion (MAC) was also used in comparing the analytic and experimental results. MAC is a least squares approach to determining the consistency of estimated modal vectors of a system. MAC is calculated using the equation:

$$\text{MAC}_{m,n} = |(x_c^m)^T (y_c^n)^*|^2 / [(x_c^m)^T (x_c^m)^* (y_c^n)^T (y_c^n)^*] \quad (4.1)$$

where x_c^m is an estimate (in this case numerical) for the m'th complex eigenmode and

y_c^n is an estimate (in this case experimental) for the n'th complex eigenmode. A little algebra will verify that

$$1 - \text{MAC}_{m,n} = \frac{1}{(x_c^m)^T(x_c^m)^*} \min_{\alpha} |x_c^m - \alpha y_c^n|^2 \quad (4.2)$$

MAC is a scalar constant between 0 and 1 relating the two modal vectors. (It may be thought of as the square of the cosine between those vectors.) A MAC value of one or nearly one will give confidence that the modal vectors represent the same modes. If the MAC value is near zero, there is no linear relationship between the two estimates, indicating two different modal vectors.

The eight experimental and eight analytic modal vectors were compared using the MAC procedure. The results of this comparison are shown in Figure 4.4. The blocked-in area of the chart indicates the results when the similar analytic and experimental vectors were compared. These results, particularly the out-of-plane bending modes, give confidence that these modal vectors describe the same mode, and are nearly identical.

EXPERIMENTAL								ANALYTIC							
1	2	3	4	5	6	7	8	1	2	3	4	5	6	7	8
1.0 0.00 0.05 0.00 0.00 0.02 0.03 0.00	0.98	0.00	0.08	0.00	0.00	0.00	0.00	0.09	0.00	1					
1.0 0.01 0.00 0.00 0.09 0.01 0.01 0.00	0.98	0.00	0.00	0.00	0.00	0.08	0.00	0.00	0.00	2	E	X	P	R	I
1.0 0.01 0.00 0.03 0.04 0.01 0.06 0.00	0.94	0.00	0.00	0.02	0.08	0.00	0.00	0.00	0.00	3	E	M	N	T	A
1.0 0.01 0.00 0.01 0.01 0.00 0.00 0.00	0.78	0.01	0.00	0.00	0.00	0.00	0.00	0.00	0.00	4					
1.0 0.00 0.00 0.14 0.00 0.00 0.00 0.00	0.77	0.00	0.00	0.00	0.00	0.00	0.00	0.00	0.00	5					
1.0 0.03 0.01 0.02 0.10 0.01 0.00 0.00	0.91	0.04	0.00	0.00	0.00	0.00	0.00	0.00	0.00	6	A	N	L		
1.0 0.01 0.04 0.01 0.06 0.00 0.00 0.00	0.93	0.01	0.00	0.00	0.00	0.00	0.00	0.00	0.00	7					
1.0 0.00 0.01 0.00 0.00 0.22 0.00 0.00	0.65	0.00	0.00	0.00	0.00	0.00	0.00	0.00	0.00	8					
1.0 0.00 0.11 0.00 0.00 0.00 0.11 0.00	0.00	0.00	0.00	0.00	0.00	0.00	0.00	0.00	0.00	1					
1.0 0.00 0.00 0.00 0.00 0.12 0.00 0.00	0.00	0.00	0.00	0.00	0.00	0.00	0.00	0.00	0.00	2					
1.0 0.00 0.00 0.00 0.00 0.12 0.00 0.00	0.00	0.00	0.00	0.00	0.00	0.00	0.00	0.00	0.00	3	A	N	A		
1.0 0.00 0.00 0.00 0.00 0.00 0.00 0.00	0.00	0.00	0.00	0.00	0.00	0.00	0.00	0.00	0.00	4	L	Y			
1.0 0.00 0.00 0.00 0.00 0.00 0.00 0.00	0.00	0.00	0.00	0.00	0.00	0.00	0.00	0.00	0.00	5	T	I			
1.0 0.00 0.00 0.00 0.00 0.00 0.00 0.00	0.00	0.00	0.00	0.00	0.00	0.00	0.00	0.00	0.00	6	C				
1.0 0.00 0.00 0.00 0.00 0.00 0.00 0.00	0.00	0.00	0.00	0.00	0.00	0.00	0.00	0.00	0.00	7					
1.0 0.00 0.00 0.00 0.00 0.00 0.00 0.00	0.00	0.00	0.00	0.00	0.00	0.00	0.00	0.00	0.00	8					

Mode Number	Mode Description
1	1st Bending
2	2nd Bending
3	3rd Bending
4	1st Torsional
5	1st Bending (in-plane)
6	4th Bending
7	5th Bending
8	2nd Torsional

Figure 4.4. MAC parameters of experimental and analytic modal vectors for first eight complex modes.

5. Conclusions

Though the structure employed in this study was very simple, this study does demonstrate the predictive capability of the computational method of reference [4]. Though the structure had sufficient symmetries to preclude the existence of true complex modes, it did have sufficient character in its frequency response functions and damping parameters to permit some comparison of the desired sort.

Particularly encouraging was that the predicted and measured damping values for the beam agree to within the uncertainty of the viscoelastic properties of the damping polymer.

The study served its purpose in providing sufficient confidence in both the numerical and experimental methods to facilitate future studies involving more sophisticated structures.

Some further comments about the computational process are appropriate:

- Though the numerical implementation of the derivations of the second chapter of this report did require writing much original computer code, the onerous work of involving mesh generation, finite element eigen- and static analysis was done with the aid of the commercial codes PATRAN and MSC-NASTRAN.
- With the exception of the finite element analysis, the calculations can be performed with reasonably small matrices. This is achieved by using the elastic modes as generalized coordinates and restricting attention to the frequency range of interest.
- The complex modes can be assembled in a systematic manner from the mass, damping, and stiffness matrices using the formalism of Newland [6]. The complex modes can then be used, in the manner shown here, to calculate transient response (Equation 2.31) and frequency response (Equation 2.38).

References

- [1] D. Ross, E. E. Ungar, and E. M. Kerwin, "Damping of plate flexural vibrations by means of viscoelastic laminae", *Structural Damping*, ASME, New York, pp. 49-87.
- [2] C. D. Johnson and David Kienholz, "Finite element prediction of damping in structures with constrained viscoelastic layers", *AIAA Journal*, Vol 20, September 1982, pp. 1284-1290.
- [3] C. D. Johnson, D. A. Kienholz, and L. C. Rogers, "Finite element prediction of damping in beams with constrained viscoelastic layers", *Shock Vib. Bull.*, Vol. 51, Pt. 1, May 1981, pp. 71-81.
- [4] D. J. Segalman, "Calculation of damping matrices for linearly viscoelastic structures", *Journal of Applied Mechanics*, Vol. 109, September 1987, pp. 585-588.
- [5] J. D. Ferry, *Viscoelastic Properties of Polymers*, (Third Edition) John Wiley and Sons, New York, 1980, p. 68, Equations 39 and 40.
- [6] D. E. Newland, "On modal analysis of non-conservative linear systems", *Journal of Sound and Vibration*, Vol. 112, 1987, pp. 69-96.
- [7] *MSC/NASTRAN Users' Manual: MSC/NASTRAN Version 64*, MacNeal-Schwendler Corporation, Los Angeles, May 1976.
- [8] W. H. Vandevender, "The Slatec mathematical subprogram library version 2.0", SAND84-281, April 1984.
- [9] *PATRAN Plus Users Manual*, PDA Engineering, Costa Mesa, CA., 1987, Chapter 27, p. 130.
- [10] Kevin Smith, CSA Engineering Report No. 87-04-02, "Damping of a selected structure", April 1987.

A NEW APPROACH TO MODEL DETERMINATION OF LARGE FLEXIBLE SPACE SYSTEMS

F.Y. Hadaegh, D.S. Bayard, Y. Yam and E. Mettler

**Jet Propulsion Laboratory
California Institute of Technology
4800 Oak Grove Drive
Pasadena, California 91109**

ABSTRACT

The product moment matrix (PMM) is used for the estimation of linear model order for flexible space structures from the input-output data. A new automated frequency domain identification methodology is presented and experimentally verified for on-orbit determination of transfer functions. The identification process is initiated by applying stochastic inputs to the system giving rise to a nonparametric spectral estimate of the structural parameters. The PMM algorithm obtains an initial estimate of the model order and together with the initial parameter estimates, they provide an initializing transfer function. The system transfer function is then obtained by curve fitting the spectral estimates to a rational transfer function. This approach makes efficient use of the actuators and sensors already available on the system for control applications and also demonstrates that on-orbit identification capability is a realistic objective for the future space systems.

1. Introduction

The mathematical modeling and identification of large flexible space systems have been challenging tasks for several decades. The models for such systems should predict the behavior of the actual system under restricted experimental conditions. Furthermore, when correlated and tested against the actual data, they should explain the observed behavior of the system through post-mission data analysis. In practice, the identification problem is often separated into two parts: a) determination of the order for a linear model and b) estimation of the parameter values of the resulting model. Clearly, in a linear system the model structure is determined by the choice of the order. Hence, an incorrect structural assumption may manifest itself in biased parameter estimates or may even lead to erroneous conclusions on the results of the identification process (e.g., a large model order leads to over parameterizations and identifiability problems; whereas a small order may result in a large bias in parameter estimates). This is of particular interest in the case of on-orbit identification where model parameters have physical significance and the accuracy of the parameter estimate is the primary objective of the system identification experiment. On-orbit system identification enables on-line design of robust, high performance control systems. This capability has the potential to improve the performance robustness and control accuracy under operational constraints and environmental uncertainties far beyond that attainable by using nominal system descriptions obtained from ground testing and analysis alone.

This paper presents a new frequency domain system identification architecture designed to operate with a high degree of autonomy and to restrict the "human in the loop" requirements. This includes an automated estimation of model order in the presence of measurement noise; the main subject for discussion in this paper. Major theoretical and experimental developments associated with this approach are discussed in [10]. Different techniques for model order determination have been studied [1-9]. They include fit-error statistics [1], Akaike's criterion [2], Kalman filtering [3], likelihood ratio test [4], methods based on pole-zero cancellation [7], statistical F-test [8], and Parzen's criteria [9]. These methods are often estimation based oriented and utilize statistical methods for extracting information about a system model from the observed data. They often require normality assumption on the measurement noise and furthermore, they involve processing of large volumes of data. Here, the product moment matrix [5] approach is chosen for a variety of reasons and in each case it proves advantageous over alternate methods. For example, the PMM requires no a priori assumption on the model parameterization and form and it requires no knowledge of density or distribution functions of unknown parameters or data. This technique is applicable to both deterministic and stochastic systems. Finally, the PMM algorithm is robust with respect to uncertainties and it produces meaningful results even in the presence of significant additive measurement noise. A brief discussion of the PMM algorithm follows.

2. The Product Moment Matrix

The idea behind the PMM approach is to analyze the correlation function of the input-output variables for a linear model of changing structure. This will subsequently lead to a pronounced dynamic behavior around the "true" order of the system. This behavior may be observed through the determinants or eigenvalues of the product moment matrix with elements constructed as follows.

Let $\{u_k\}$ and $\{y_k\}$ be a set of observations of input and output respectively (data) which are contaminated by measurement noise. Let us also assume that the input signal is sufficiently rich such that it persistently excites all system modes of interest. A linear system of order n has a system function which is given by

$$H(z) = \frac{Y(z)}{U(z)} = \frac{\sum_{i=1}^n \theta_{2i-1} z^{-i}}{1 - \sum_{i=1}^n \theta_{2i} z^{-i}} \quad (1)$$

letting

$$\theta^T(n) = [\theta_1, \dots, \theta_{2n}] \quad (2)$$

and

$$\Lambda^T(k, n) = [u_{k-1}, y_{k-1}, u_{k-2}, y_{k-2}, \dots, u_{k-n}, y_{k-n}] \quad (3)$$

Then in time-domain, the measured system response is given by

$$y_k = \theta^T(n) \Lambda^T(k, n) \quad (4)$$

For N measurements, the "generalized Hankel matrix" $H(N)$ is as follows.

$$H(N) = \begin{pmatrix} y_0 & y_1 & \dots & y_{N-1} \\ y_1 & y_2 & \dots & y_N \\ \vdots & \vdots & & \\ y_{N-1} & y_N & & y_{2N-2} \end{pmatrix} \stackrel{\Delta}{=} y_{i+j-2} \quad i, j > 0 \quad (5)$$

Similarly, the generalized Hankel matrix for the $N \times N$ block matrices formed out of the shifted sequence $y_{k+\ell}$ will be

$$H(N) = [y_{i+j+\ell-2}]$$

If a finite-dimensional realization for the system exists, denoting n^* as the rank of its minimal realization, then [21]

$$n^* = \text{Rank } H(N) \quad (6)$$

Since n^* is the dimension of a **minimal** realization of the system which is unknown, it will subsequently be referred to as the "true" order of the system. Note also that the ordering of components in the vectors $\Lambda^T(k, n)$ and $\theta^T(n)$ are such that for a higher-order model, additional components are simply added to the end of these vectors. The product moment matrix of the system is defined by:

$$Q[n, N] \equiv Q_n \stackrel{\Delta}{=} \frac{1}{N} \sum_{k=1}^N \Lambda^T(k, n) \Lambda^T(k, n)^T$$

$$= \frac{1}{N} \begin{pmatrix} \sum_{k=1}^N u_{k-1}^2 & \sum_{k=1}^N u_{k-1} y_{k-1} & \cdots & \sum_{k=1}^N u_{k-1} y_{k-n} \\ \sum_{k=1}^N y_{k-1} u_{k-1} & \sum_{k=1}^N y_{k-1}^2 & \cdots & \sum_{k=1}^N y_{k-1} y_{k-n} \\ \vdots & & & \vdots \\ \sum_{k=1}^N y_{k-n} u_{k-1} & \sum_{k=1}^N y_{k-n} y_{k-1} & \cdots & \sum_{k=1}^N y_{k-n}^2 \end{pmatrix} \quad (7)$$

where n is an assumed order for the system and N is the number of data points. If the data is noise free, then Q_n will become singular for all $n > n^*$ [6], and

$$\text{Rank}[Q_n] = \left\{ \begin{array}{ll} = & 2n \\ = & n + n^* \end{array} \right\} \text{ for } n \left\{ \begin{array}{l} \leq \\ > \end{array} \right\} n^* \quad (8)$$

Hence, Q_n has the following properties:

$$\det[Q_n] = \left\{ \begin{array}{ll} \neq & 0 \\ = & 0 \end{array} \right\} \text{ for } n \left\{ \begin{array}{l} \leq \\ > \end{array} \right\} n^* \quad (9)$$

For an arbitrary value of N and an assumed value of n , the ratio

$$D_n = \frac{\det[Q_n]}{\det[Q_{n+1}]} \quad (10)$$

is calculated for succeeding model orders $n+1, \dots, n^*, \dots, n_{\max}$. If the value of D_n exhibits a distinct increase compared to D_{n-1} , then n corresponds approximately to n^* . In the presence of noise however, the $\text{Det}[Q_n]$ is usually non-zero for $n > n^*$.

In practice, where the measurement noise is nonwhite, the enhanced PMM given by

$$\check{Q}_n = Q_n - \sum_n \quad (11)$$

is used. An estimate of \sum_n , the measurement noise contributions to the PMM, is obtained by first collecting measurements from the system when the input to the system is identically zero. Denoting the input measurement noise by n_u and the output measurement noise by n_y , then \sum_n is computed as

$$\sum_n = Q_n | y = n_y, u = n_u$$

The \check{Q} product moment matrix henceforth referred to as enhanced product moment matrix (EPMM) will reduce to the formulations (7) depending upon the nature of noise in the data. The EPMM, although computationally less efficient, gives a better estimate of the system order in the presence of measurement noise.

An alternative representation of PMM is given as follows:

$$Q_n = E[a_n a_n^T] \quad (12)$$

where

$$a_n^T = [u_0 \ y_0 \ u_1 \ y_1 \dots u_{n-1} \ y_{n-1}]$$

and E is the statistical expectation operation. We will refer to Equation (12) as the stochastic representation of PMM and the Equations (7) and (11) as the deterministic representations of PMM.

When the underlying dynamical process is stationary, the correlations have the form:

$$\begin{aligned} E[u_i y_j] &= R_{uy}(j-i) \\ E[u_i u_j] &= R_{uu}(j-i) = R_{uu}(i-j) \\ E[y_i y_j] &= R_{yy}(j-i) = R_{yy}(i-j) \end{aligned} \quad (13)$$

Then by assuming that the process is ergodic, temporal averages are equivalent to ensemble averages, and the product moment matrix given in (7) has the simple analytical form:

$$\lim_{N \rightarrow \infty} Q(N, n) = Q_*(n) \quad (14)$$

$$Q_*(n) = \begin{bmatrix} Q_*^{(1,1)} & \dots & Q_*^{(1,n)} \\ \vdots & & \vdots \\ Q_*^{(n,1)} & \dots & Q_*^{(n,n)} \end{bmatrix} \quad (15)$$

$$Q_*^{(i,j)} = \begin{bmatrix} R_{uu}(j-i) & R_{yu}(j-i) \\ R_{uy}(j-i) & R_{yy}(j-i) \end{bmatrix} \quad (16)$$

This explicitly gives the product moment matrix without requiring any additional processing of the input and output data. Thus when correlations are available under these circumstances, the product moment matrix can be constructed with considerably fewer arithmetic operations than those required by the deterministic algorithms. The key practical issues are the validity of the assumptions regarding stationarity and ergodicity of the signals and the means for calculating the correlation functions based on finite-time data lengths. A brief description of modeling and identification algorithm architecture and methodology follows.

3. Functional Architecture, Modeling and Identification Description

The functional architecture is outlined schematically in Fig. 1. The flow of the various processes is automated and controlled from a single human operator as described below.

- a) The plant $p(e^{j\omega T})$ is excited by one of a variety of possible input excitations $u(kT)$ of both stochastic (i.e., wideband or narrowband) or deterministic (i.e., sine-dwell) types giving rise to plant output $y(kT)$.

The wideband input is simply a random number generator which produces independent uniformly distributed variates. The narrowband input is produced by digitally filtering the wideband input according to desired spectral characteristics. The capability for on-line digital filter design is provided as part of the system software. The sine-dwell inputs are piecewise constant approximations to true sinusoids, consistent with the sample-and-hold discretization.

Wideband signals are also constructed artificially using a technique which we call data composition. This is done by designing a bank of bandpass filters to cover a wideband portion of the frequency axis, and then running a separate experiment for each bandpass process. The input and output sequences from all bandpass experiments are then composed (i.e., added together respectively) to give data for what is effectively a single wideband experiment. The realization of such a wideband excitation in a single experiment would otherwise be impossible due to actuator power constraints.

- b) The plant transfer function is identified nonparametrically by spectral estimation (in the case of stochastic inputs) and by gain and phase estimation in the case of sine-dwell inputs.

For experiments using stochastic input excitation, spectral estimation is invoked to compute the correlations R_{uu} , R_{yy} , R_{uy} and spectral estimates P_{uu} , P_{yy} , P_{uy} from the input and output data, as well as the plant transfer function estimate from the cross-spectral estimate $h = P_{uy}/P_{uu}$.

For experiments using sine-dwell input excitation, the gain, phase, real and imaginary parts of $p(e^{j\omega T})$ at sine-dwell frequencies are determined in real-time using a recursive least squares estimator with exponential forgetting factor. This approach is particularly well suited to provide accurate estimation using sampled-data sinusoidal responses and to operate in the presence of low frequency resonances. The time constant for the forgetting factor is typically chosen to be several cycles of the sine-dwell response. The sine-dwell estimates of plant gain, phase and real and imaginary parts of $p(e^{j\omega T})$ over several frequencies can be stored for later use by the transfer function curve fitting routine.

- c) Anticipating parametric curve fitting to follow, the model order is estimated using a product moment matrix (PMM) test.

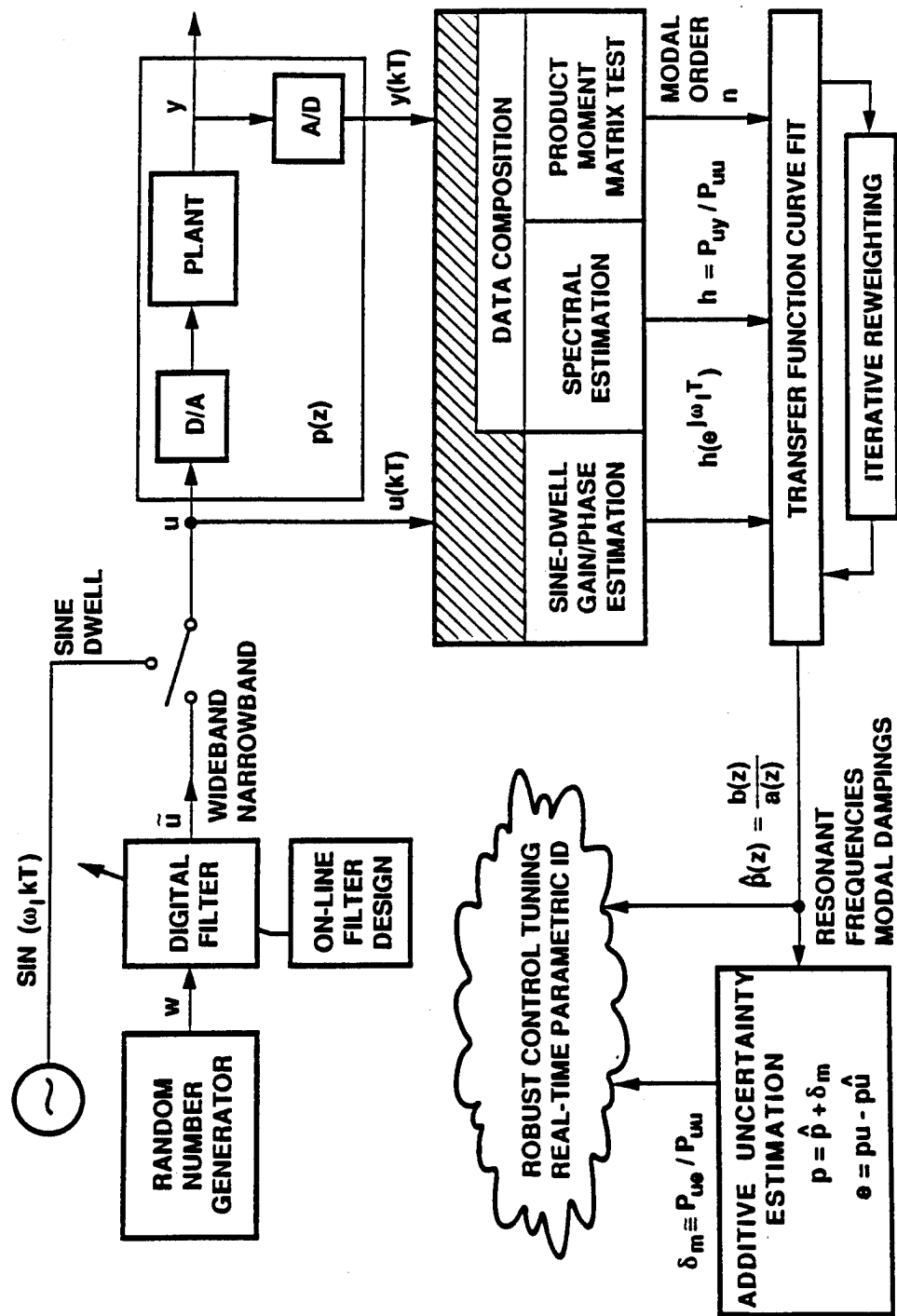


Figure 1. Functional Architecture of System ID Experiment.

To overcome much of the guessing and "human in the loop" efforts typically associated with model order determination task, an initial estimate of the model order is obtained by PMM test, and then followed by a search for the optimal order in the vicinity of this estimate by a sequence of curve fits with varying orders. The quality of each fit is judged by the output error profile.

The PMMD operates on raw data, and generates the PMM directly from the plant input and output. The PMMS assumes statistical stationarity for the underlying process and generates the PMM from the smoothed estimates of the auto and cross covariances produced from the spectral estimation software.

- d) **The plant is identified parametrically by fitting transfer function coefficients to the nonparametric data. Model order is determined by a sequential search starting at the PMM estimate.**

A parametric transfer function estimate \hat{p} is determined by curve fitting the coefficients of a rational transfer function to the nonparametric frequency domain data. The data in this case is specified to be the spectral estimate $h = P_{uy}/P_{uu}$ and/or sine-dwell estimates. The model order is determined by successively increasing the number of modes in the curve fit, starting at the PMM estimate, until an adequate output error profile is observed. The curve fit involves the use of a least squares algorithm with a special iterative reweighting technique which removes high frequency emphasis (typically associated with equation error methods), and assures minimum variance estimation of the transfer function coefficients. Resonant frequencies and damping estimates are automatically found by robustly factorizing the plant denominator polynomial with a special purpose routine.

- e) **The output error is determined to characterize the quality of the parametric transfer function estimate, and for later use in robust control analysis and design.**

The output error $e = pu - \hat{p}u$ is computed by subtracting the predicted output $\hat{y} = \hat{p}u$ from the measured data $y = pu$ and then the additive uncertainty $\delta_m = p - \hat{p}$ is estimated by the cross-spectral estimate $\Delta = P_{ue}/P_{uu}$. The nominal plant transfer function estimate \hat{p} and the estimate Δ of the additive uncertainty δ_m can then be used directly for robust control analysis and design. The motivation and usefulness of using the output error characterization of additive uncertainty, and its role in robust control design is discussed in [10].

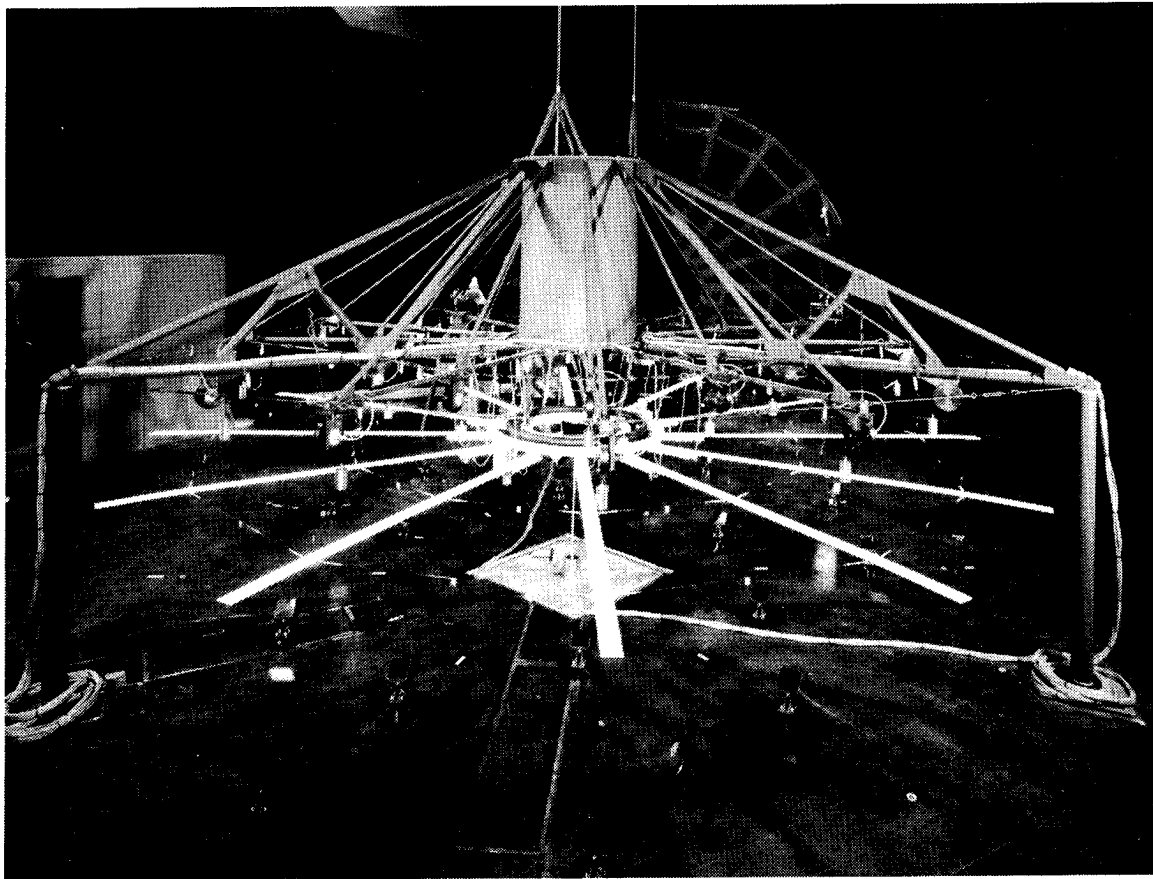
4. Testbed Description

Experimental demonstration and verification of modeling and identification software performance was conducted on the JPL/AFAL Flexible Structure Testbed. The design of this 3-D antenna-like structure was adopted as it exhibits many characteristics of a typical large space structure. These include many low frequency modes, densely packed modes, low structural damping, and three-dimensional structural interaction among components.

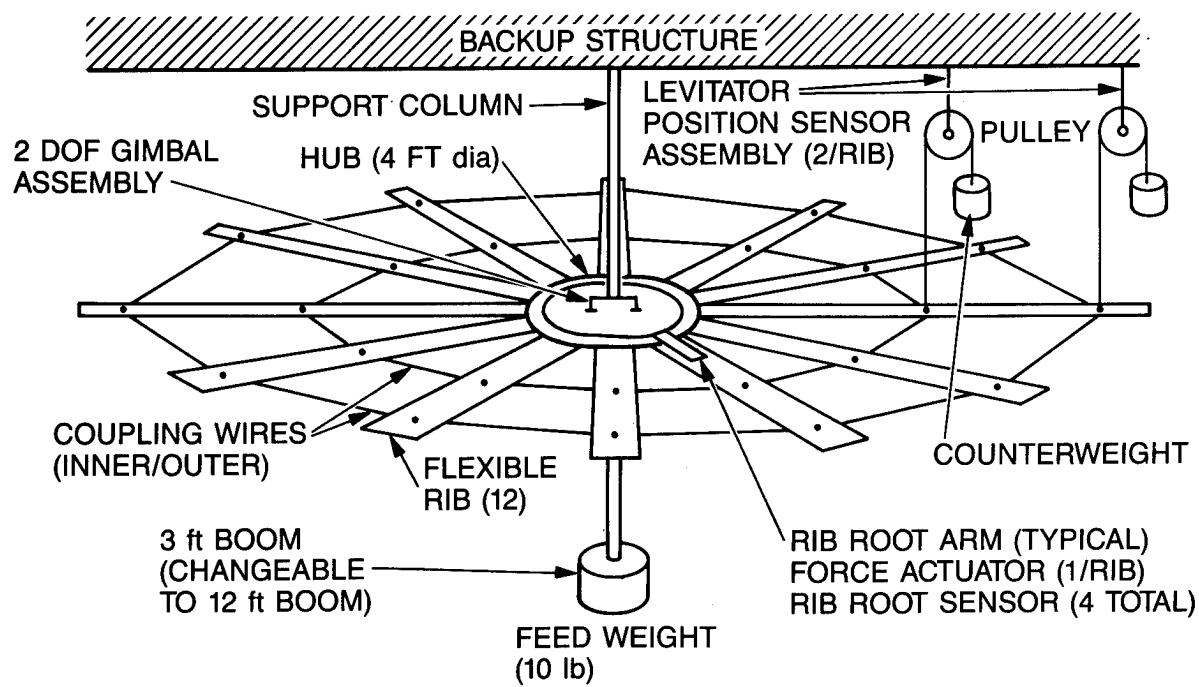
In this section, a brief description of the testbed facility is given. Detail description can be found in [10]. The main component of the testbed facility is shown in Figure 2. It consists of a central rigid hub to which are attached 12 ribs. The ribs are coupled together by two rings of pretensioned wires.

Functionally, the wires are intended to simulate the coupling effects of a reflective mesh installed over the rib frame in an actual antenna. The ribs are 2.25 m in length. The hub is of radius 0.6 m, making the dish structure 5.7 m in diameter. The tensioning wires are installed in two rings at approximate diameters of 3 m and 4.8 m. As intended to achieve low modal frequencies, the ribs are very flexible. Stand alone, they are unable to support their own weight without excessive droop. To prevent structural collapse due to gravity, each rib is supported at two locations along its free length by levitators. Each levitator is constituted by a counterweight attached to the rib with a wire which passes over a low-friction pulley. The support locations were calculated to minimize the rms shape deviation along the rib from the root to tip. The calculations led to supporting the rib at the 40% and 80% points which are 0.9 m and 1.8 m from the rib root, the same locations for coupling wire attachments. A flexible boom is attached to the central axis of the hub and has a mass at its lower end to simulate the feed horn of an antenna of the secondary mirror assembly or an optical system. The original boom length was 3.6 m, but for the convenience of conducting experiment at ground level, a second, 1 m long boom is being used for most of the experiments. The feed mass is 4.5 kg. The hub is mounted to a backup structure via a two-axis gimbal which allows rotational freedom about two perpendicular axes in the horizontal plane. The gimbal bearings support roughly one quarter the weight of the ribs, the entire weight of the hub, boom, and feed, and their respective sensing and actuation devices. Each of the ribs can be excited dynamically by a single rib-root actuator with a lever arm of about 0.3 m from the hub attachment point. Each rib-root actuator consists of a speaker-coil type device which reacts against a mount rigidly attached to the hub. In addition, two speaker-coil type actuators are mounted on the hub to provide controlled torquing about the two gimbal axes. These hub torquers apply linear forces to the hub at its outer circumference to yield the required torques about the axis of rotation. Together, these 14 actuators are capable of controlling all flexible modes of the structure. Each of the 24 levitators is equipped with an incremental optical encoder which measures the relative angular rotation of the levitator pulley. These angular measurements are then translated into the vertical motion of the ribs at the levitator/rib attachment points, relative to the backup structure. Additional linear variable differential transformers (LVDT) sensors are provided to determine the rib displacement measurements at four evenly space rib root actuator locations. Hub angular rotations about the two axes are measured by two rotary variable differential transformers (RVDT) mounted directly at the gimbal bearings.

Figure 2. JPL/AFAL Flexible Structure Testbed.



PHOTOGRAPH



SCHEMATIC

5. Case Study with Experimental Data

Results of a wideband excitation experiment are shown in Figures 3-A to H. The experiment was performed on one of the two hub axes of the JPL/AFAL Flexible Structure Testbed utilizing a collocated hub torquer and an RVDT angular sensor for instrumentation. The sampling frequency was 20 Hz. The experiment run time was 1638.4 sec. Figure A shows the white noise input excitation u uniformly distributed between the range ± 1.5 nt-m. The output response y is shown in figure B. Figure C shows the PMM test determinant values as a function of the assumed model order. The test yielded a model order estimate of 4 for the system. This estimate is based on a threshold used for singularity of PMM. The particular threshold value used in this experiment was found to consistently under estimate the final curve fit model order which in this case is 6. Figure D presents the transfer function spectral estimate $h = u_y / P_{uu}$. Transfer function curve fitting on h was performed giving rise to the identified parametric model of Figure E. The identified frequencies and damping coefficients are 0.114 Hz, 0.637 Hz, and 2.75 Hz, and 0.4, 0.0364, and 0.00604, respectively. The frequency values agree well with those of the finite element model of the structure for two axis of rotation as shown in figure 4. Figure F shows the computed output \hat{y} of the identified parametric model subjected to the same excitation input u . Figure G shows the output error $e = y - \hat{y}$, which has a maximum of 2.6 mrad as compared to 10 mrad for y . Finally, the additive uncertainty spectral estimate $\Delta = P_{ue} / P_{uu}$ is shown in figure H. It has a maximum gain value of 11.38 db. Compared with figure D, the value of Δ is 10 db less for the more heavily damped lowest mode, and 29 db less for the two lightly damped higher modes. This indicates that identification of their modal dynamics to within 30% and 10%, respectively, was obtained. Interestingly, there are two modes, apparent in figure D, that were not fitted. Figure H shows that error resulted from omitting those modes is even smaller than the fitting error of the identified modes. This indicates that the curve fitting algorithm has properly determined their omission and produced a reduced-order plant model which minimizes the additive uncertainty. The transfer estimate \hat{h} in figure E, and the additive uncertainty Δ in figure H are now directly usable for robust control design.

6. Conclusions

An automated model order determination and frequency domain identification methodology was presented for the identification and control of large flexible space structures. The product moment matrix approach was used for the estimation of a linear model order to avoid statistical methods which are estimation based, often require processing of large volumes of data, and require major assumptions on the nature of measurement noise. The identification methodology was designed to operate with a high degree of autonomy in an on-orbit environment, and was experimentally verified on a facility designed for emulation of on-orbit testing and control scenarios. The experimental results indicated a close agreement with those of the finite element model of the structure. Furthermore, it demonstrated that the identification algorithm developed produces reduced-order models which minimize a uniform bound on the additive uncertainty. Although the present investigation considered identification of single-input single-output transfer functions, multi-input

Figure 3. Experimental Results using the Autonomous Frequency Domain System Identification Methodology.

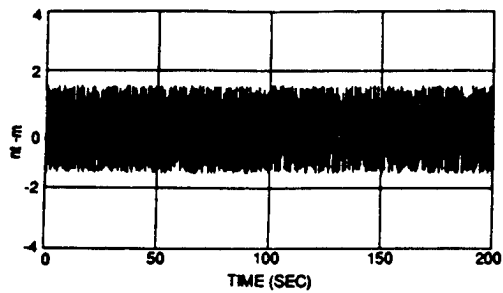


Figure A. Wideband Excitation Input u

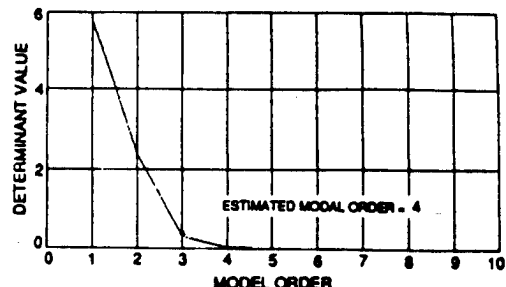


Figure C. PMM Test Determinant Plot

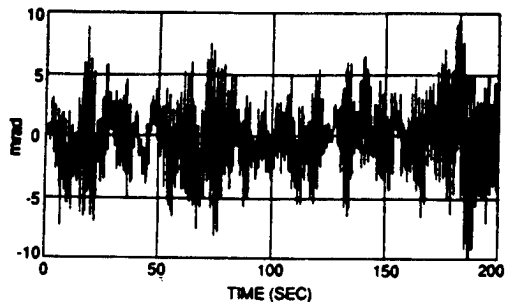


Figure B. Output Response y at Collocated Hub Sensor

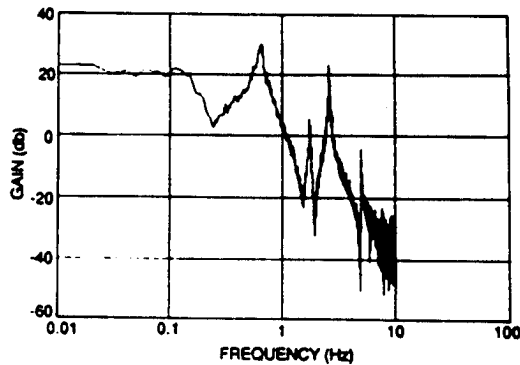


Figure D. Gain Plot of Transfer Function Spectral Estimate h

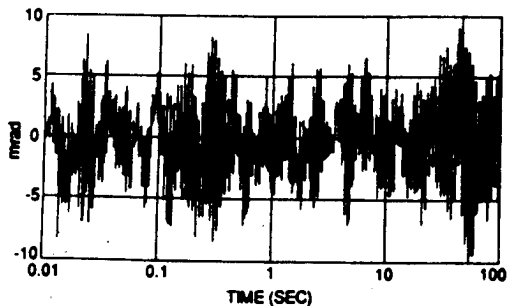


Figure F. Identified Parametric Model Response \hat{y} to Actual Input Excitation

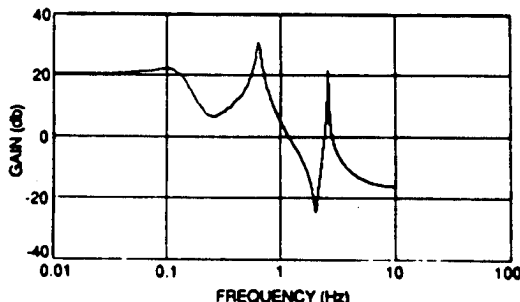


Figure E. Gain Plot of Identified Parametric Model Transfer Function \hat{h}

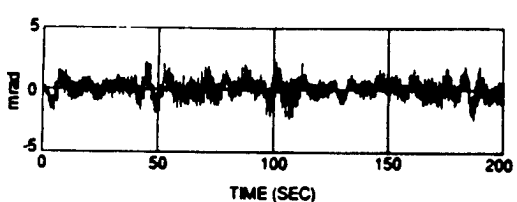


Figure G. Output Error $e = y - \hat{y}$

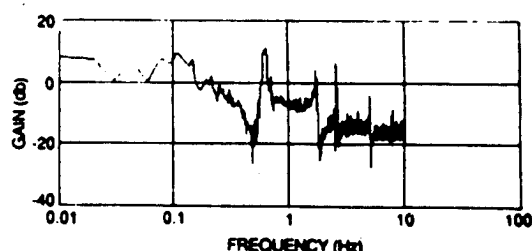


Figure H. Gain Plot of Additive Uncertainty Spectral Estimate A

Figure 4. Comparison of Finite Element Modeling (FEM) and Experiment Results for Boom-Dish Modal Frequencies.

Axis 1		Axis 2	
FEM Result	Experiment Result	FEM Result	Experiment Result
0.091	0.126	0.091	0.114
0.628	0.666	0.616	0.637
2.682	2.68	2.577	2.57

multi- output system identification would also be accommodated with the present scheme by processing each input-output pair separately.

Acknowledgements

The research described in this paper was performed at the Jet Propulsion Laboratory, California Institute of Technology, under contract with the National Aeronautics and Space Administration.

7. References

1. Soderstrom, T., "On Model Structure Testing in System Identification," Int. J. Control, Vol. 26, No. 1, 1977.
2. Akaike, H., "A New Look at the Statistical Model Identification," IEEE Trans. on Automatic Control, Vol AC-19, No. 6, 1974.
3. Ho, L.R., and Kalman, R.E., "Effective Construction of Linear State-Variable Models from Input-Output Functions," Regelungstechnik 12, 1965.
4. Akaike, H., "Likelihood of a Model and Information Criteria," Journal of Econometrics, Special Issue, 1981.
5. Woodside, C.M., "Estimation of the Order of LInear Systems," Automatica, Vol. 7, 1971.
6. Lee, R.C.K., "Optimal Estimation, Identification and Control," MIT Press, Cambridge, MA, 1964.
7. Soderstrom, T. "Test of Pole-Zero Cancelation in Estimated Models," Automatica, Vol. 11, 1975.
8. Astrom, K.J., "System Identification," Proc. 2nd IFAC Symposium on Identification and Parameter Estimation, 1970.
9. Parzen, E., "A New Look at the Statistical Model Identification," IEEE Trans. on Automatic Control, AC-19, 1974.
10. Yam, Y., et al, "Autonomous Frequency Domain Identification: Theory and Experiment," Jet Propulsion Laboratory, EM 343-1112-89.

PERTURBATIONS ON NATURAL MODES
DUE TO NONPROPORTIONALITY OF VISCOUS DAMPING

Benito M. PACHECO
Assistant Professor

Yozo FUJINO
Associate Professor

Department of Civil Engineering, University of Tokyo
7-3-1 Hongo, Bunkyo-ku, Tokyo 113, Japan
Tel. (03)812-2111 ext. 6096

The complex eigenvectors and eigenvalues of multi-degree-of-freedom system with moderately nonproportional viscous damping are approximated by a second-order perturbation method, in terms of the natural frequencies and mode shapes of the counterpart undamped system and the actual nonproportional damping matrix. Only the nonproportionality, not the overall level of damping itself, is assumed to be either moderate or weak. This new method can be particularly advantageous when designing, or when identifying, the system damping. Either task requires reanalysis of an eigenproblem of nonproportionally damped system each time that a different damping matrix is considered. The proposed technique requires only the smaller eigenproblem of counterpart undamped system to be analyzed directly, and only once. All the necessary explicit formulas are listed.

1. PROPORTIONAL VS. NONPROPORTIONAL DAMPING

Representing the mass of the discretized system by matrix \mathbf{M} , the stiffness by \mathbf{K} , and the damping by \mathbf{C} , all of size $n \times n$ when there are n degrees of freedom, the equation of non-gyroscopic motion subject to external forces represented by vector \mathbf{f} , may be set up as in Eq. 1 below.

$$\mathbf{M} \ddot{\mathbf{x}} + \mathbf{C} \dot{\mathbf{x}} + \mathbf{K} \mathbf{x} = \mathbf{f} \quad (1)$$

It is assumed that the coordinates \mathbf{x} have been so selected that the matrices \mathbf{M} and \mathbf{K} are positive definite. Being considered are cases where \mathbf{C} is positive definite and the overall damping level may be high but still

subcritical. The latter condition may be checked a priori, for instance, by the criterion of Inman and Andry [1].

Counterpart Undamped System Were the system undamped and freely vibrating (Eq. 2), the natural frequencies ω_{0j} and mode shapes \mathbf{y}_{0j} ($j=1, 2, \dots, n$) could be identified as in Eq. 3. Note that $i = \sqrt{-1}$.

$$\ddot{\mathbf{M}}\mathbf{x} + \ddot{\mathbf{K}}\mathbf{x} = \mathbf{0} \quad (2)$$

$$\mathbf{x}_j = \mathbf{y}_{0j} \exp(i \omega_{0j} t) \quad (3)$$

Consideration of Eq. 3 in Eq. 2 leads to the eigenvalue problem, or eigenproblem, described by Eq. 4. In the latter context, ω_{0j} are eigenvalues and \mathbf{y}_{0j} are eigenvectors.

$$(-\omega_{0j}^2 \mathbf{M} + \mathbf{K}) \mathbf{y}_{0j} = \mathbf{0}, \quad j = 1, 2, \dots, r, \dots, n \quad (4)$$

$$\mathbf{y}_{0k}^T \mathbf{M} \mathbf{y}_{0j} = \delta_{jk} \quad (5)$$

$$\mathbf{y}_{0k}^T \mathbf{K} \mathbf{y}_{0j} = \omega_{0j}^2 \delta_{jk} \quad (6)$$

It is assumed herein that the eigenvectors \mathbf{y}_{0j} are normalized such that the orthogonality properties are expressible as Eqs. 5-6. δ_{jk} is Kronecker delta. Eq. 5 is a very common and convenient choice of normalization in computer implementation of classical modal analysis.

Counterpart Proportionally Damped System Were the system damped such that \mathbf{C} is of a form \mathbf{C}_p that satisfies Eq. 7, which is Caughey and O'Kelly's proportionality criterion [2], the free damped vibration and associated eigenproblem would be described by Eqs. 8-12:

$$\mathbf{C}_p \mathbf{M}^{-1} \mathbf{K} = \mathbf{K} \mathbf{M}^{-1} \mathbf{C}_p \quad (7)$$

$$\ddot{\mathbf{M}}\mathbf{x} + \mathbf{C}_p \dot{\mathbf{x}} + \mathbf{K}\mathbf{x} = \mathbf{0} \quad (8)$$

$$\mathbf{x}_j = \mathbf{y}_{0j} \exp(\lambda_{0j} t) \quad (9)$$

$$(\lambda_{0j}^2 \mathbf{M} + \lambda_{0j} \mathbf{C}_p + \mathbf{K}) \mathbf{y}_{0j} = \mathbf{0}, \quad j = 1, 2, \dots, r, \dots, n, \dots, 2n \quad (10)$$

$$\lambda_{0j} = -\omega_{0j} \xi_{0j} + i \omega_{0j} \sqrt{1 - \xi_{0j}^2}, \quad j = 1, 2, \dots, r, \dots, n \quad (11)$$

$$\xi_{0j} = \mathbf{y}_{0j}^T \mathbf{C}_p \mathbf{y}_{0j} / 2 \omega_{0j} \quad (12)$$

ω_{0j} in Eqs. 11-12 are the natural frequencies of the counterpart undamped system (Eq. 4). With \mathbf{M} , \mathbf{K} and \mathbf{C}_p as specified after Eq. 1, each eigenvalue λ_0 is complex with negative real part; i.e., both natural

frequency ω_0 and damping ratio ξ_0 are positive. An ordering is assumed here such that the $(n+r)$ -th eigenvalue is conjugate of the r -th.

The essence of damping proportionality is that the mode shapes \mathbf{y}_{0j} of the counterpart undamped system (Eq. 4) are preserved as eigenvectors even of the damped system (Eq. 10). \mathbf{y}_{0j+n} and \mathbf{y}_{0j} are identical, as a consequence of the ordering of their respective λ_{0j} .

Complications due to Damping Nonproportionality From the above introduction, it is apparent why the hypothesis of proportional damping is convenient. Conceptually, it has the advantage that the real eigenvectors have the familiar interpretation as mode shapes. Computationally, iterative numerical algorithm to solve the quadratic eigenproblem of Eq. 10 is unnecessary; the eigenvalues and eigenvectors are directly expressible in terms of ω_{0j} , \mathbf{y}_{0j} and \mathbf{C}_p , as pointed out in the preceding two paragraphs.

Much as the proportionality hypothesis is convenient, however, it has to be abandoned in certain cases. For example, confidence in both modelling and testing of structural elements or substructures in some applications has grown to a level where the assembled or complete structure, materially nonhomogenous as it is, cannot but be modelled with nonproportional damping, unless \mathbf{C} turns out to be actually proportional. Also, when experimentally identifying the damping of existing structure, it is more general and hence arguably better to hypothesize that \mathbf{C} may be nonproportional. Thirdly, when designing damping into the structure, the optimally efficient distribution may correspond to a nonproportional \mathbf{C} .

Foss [3] more than 30 years ago pointed out that a generalized modal analysis can be applied to nonproportionally damped systems. The idea is summarized below.

Were the nonproportionally damped system freely vibrating, the free damped vibration and associated quadratic eigenproblem would be described by Eqs. 13-15 below. Note the formal analogies between (9) and (14), and between (10) and (15).

$$\ddot{\mathbf{M}}\dot{\mathbf{x}} + \mathbf{C}\dot{\mathbf{x}} + \mathbf{K}\mathbf{x} = \mathbf{0} \quad (13)$$

$$\mathbf{x}_j = \mathbf{y}_j \exp(\lambda_j t) \quad (14)$$

$$(\lambda_j^2 \mathbf{M} + \lambda_j \mathbf{C} + \mathbf{K}) \mathbf{y}_j = \mathbf{0}, \quad j = 1, 2, \dots, r, \dots, n, \dots, 2n \quad (15)$$

Like Eq. 10, Eq. 15 has $2n$ pairs of complex eigenvalue λ and eigenvector \mathbf{y} . The same ordering is assumed here for both eigenproblems. λ_j may also be expressed in form analogous to Eq. 11:

$$\lambda_j = -\omega_j \xi_j + i \omega_j \sqrt{1 - \xi_j^2} \quad (16)$$

By this analogy, ω_j may be called pseudo natural frequency, and ξ_j , pseudo damping ratio of mode j . Unlike Eq. 10, however, the eigenvectors of Eq. 15 are complex and cannot be as readily interpreted as physical shapes.

Computationally, the eigenproblem of Eq. 15 is much more demanding than Eq. 10 [3]. Nevertheless, the complex eigenvectors provide a set of base vectors through which a coordinate transformation enables the uncoupling of the second-order differential equations implied in Eq. 1, into first-order differential equations. As pointed out by Foss, the dynamic response $\mathbf{x}(t)$ may be obtained by a generalized modal superposition:

$$\begin{aligned} \mathbf{x}(t) &= 2 \operatorname{Re} \sum_{j=1}^n P_j(t) \mathbf{y}_j \\ &= \sum_{j=1}^n (2 \operatorname{Re} P_j)(\operatorname{Re} \mathbf{y}_j) - (2 \operatorname{Im} P_j)(\operatorname{Im} \mathbf{y}_j) \end{aligned} \quad (17)$$

where Re and Im stand for "real part of" and "imaginary part of", respectively. The scalar function P_j , which might be called modal complex coordinate or modal participation function, is:

$$P_j = \mathbf{y}_j^T \exp(\lambda_j t) [\int_0^t f(\tau) \exp(-\lambda_j \tau) d\tau + \lambda_j \mathbf{Mx}_0 + \mathbf{Cx}_0 + \dot{\mathbf{Mx}}_0] / [\mathbf{y}_j^T (2\lambda_j \mathbf{M} + \mathbf{C}) \mathbf{y}_j] \quad (18)$$

where effects of initial displacement \mathbf{x}_0 and velocity $\dot{\mathbf{x}}_0$ have been included. Modal uncoupling is demonstrated by Eq. 18, whereby the complex participation functions are obtained independently for each mode.

The generalized modal analysis method of Eq. 17, although mathematically well established, did not find early extensive application in structural engineering practice. Both computationally and conceptually, it is more complicated than the classical modal analysis of proportionally damped systems.

Many studies have since been published that assume the complex eigenvectors and eigenvalues to be known and concentrate the efforts on efficiently and accurately calculating the equivalent of P_j of Eq. 18. That is not to forget, however, that the computational effort required in solving Eq. 15 itself, can be much more than the requirement of the eigenproblem of the counterpart undamped system (Eq. 4), and certainly more than that of the counterpart proportionally damped system (Eq. 10). While each of \mathbf{M} , \mathbf{C} and \mathbf{K} is of size $n \times n$, numerical algorithms to solve

Eq. 15 actually solve the eigenproblem of a $2n \times 2n$ matrix. Techniques of reducing both storage and computing time should be much welcome, particularly when designing or when identifying the system damping. Either task requires reanalysis of a quadratic eigenproblem each time that a different damping matrix is considered.

Some perturbation techniques have been proposed for lightly damped systems [4-6] that may avoid increasing the eigenproblem size from $n \times n$ to $2n \times 2n$. Chung and Lee [7], applying the technique of Meirovitch and Ryland [6], proposed to use a counterpart proportionally damped system as the unperturbed system in obtaining the eigenproperties. The present authors recently proposed [8-10] a general second-order perturbation technique assuming that the nonproportionality is moderate, and derived explicit approximate formulas for the perturbations on frequencies, modal damping ratios, and nonproportionally damped "modes". The approach is equivalent in order, but different in formulation from Chung and Lee's.

Details of the method are presented below and in the cited references. Computational and conceptual advantages over "exact" solution of Eq. 15 are pointed out where most relevant.

2. MODERATE NONPROPORTIONALITY AS PERTURBATION

The eigenvalues ω_{0j} and mode shapes \mathbf{y}_{0j} of the counterpart undamped system (Eqs. 4-6) are assumed to be known. Modal matrix \mathbf{Y}_0 is defined such that its j -th column is \mathbf{y}_{0j} . Transforming the damping matrix \mathbf{C} using the modal matrix \mathbf{Y}_0 as in Eq. 19 below, and separating the diagonal and off-diagonal elements, it is possible to uniquely identify the counterpart proportional damping matrix \mathbf{C}_p (Eq. 20) and damping nonproportionality matrix \mathbf{C}_n (Eq. 21):

$$\mathbf{Y}_0^T \mathbf{C} \mathbf{Y}_0 = \text{diag} [2 \omega_{0j} \xi_{0j}] + \text{offdiag} \tilde{\mathbf{C}} \quad (19)$$

$$\mathbf{C}_p = \mathbf{Y}_0 \mathbf{M} \text{diag} [2 \omega_{0j} \xi_{0j}] \mathbf{M} \mathbf{Y}_0^T \quad (20)$$

$$\mathbf{C}_n = \mathbf{Y}_0 \mathbf{M} \text{offdiag} \tilde{\mathbf{C}} \mathbf{M} \mathbf{Y}_0^T \quad (21)$$

When the nonproportionality is moderate, as being considered here, the norm of \mathbf{C}_n is one order smaller than the corresponding norm of \mathbf{C}_p . The quadratic eigenproblem of Eq. 15 may now be rewritten as:

$$(\lambda_j^2 \mathbf{M} + \lambda_j (\mathbf{C}_p + \mathbf{C}_n) + \mathbf{K}) \mathbf{y}_j = \mathbf{0} \quad (22)$$

where \mathbf{C}_n is a perturbation due to damping nonproportionality.

The Unperturbed System From Eq. 22, neglecting C_n , the unperturbed (or zero-order perturbed) eigenproblem of Eq. 23 below is obtained, which is identical to Eq. 10:

$$(\lambda_j^2 M + \lambda_j C_p + K) y_j = 0 \quad (23)$$

with solutions known from Eqs. 4, 5, 11, 12, 24 and 25.

$$\lambda_j = \lambda_{0j} \quad (24)$$

$$y_j = y_{0j} \quad (25)$$

C_p in Eq. 12 need not be set up explicitly; it is replaced by C in actual calculation of (unperturbed) ξ_{0j} . Note that the eigenvectors (Eq. 25) are real, while the eigenvalues (Eq. 24) are complex. λ_{j+n} and λ_j are conjugates; y_{0j+n} and y_{0j} are identical.

Second-order Perturbations When the eigenproblem is perturbed by C_n , the eigenvalues and eigenvectors are assumed to be perturbed in the following forms:

$$\lambda_j = \lambda_{0j} + \lambda_{1j} + \lambda_{2j} \quad (26)$$

$$y_j = y_{0j} + y_{1j} + y_{2j} \quad (27)$$

$$y_{1j} = \sum_{k=1}^n a_{jk}(1 - \delta_{jk}) y_{0k} \quad (28)$$

$$y_{2j} = \sum_{k=1}^n b_{jk}(1 - \delta_{jk}) y_{0k} \quad (29)$$

where the first of two subscripts in Eqs. 26-27 indicates the order of perturbation. In Eqs. 28-29 for y_{1j} and y_{2j} , it is not necessary to include $k=j$, i.e. y_{0j} . The vector set $y_{01}, y_{02}, \dots, y_{0n}$ constitutes a complete vector space, in terms of which the expansion of y_j can be written; however y_{0j} is already included in the expansion (Eq. 23) as the first term.

The perturbations λ_{1j} and λ_{2j} , and perturbation coefficients a_{jk} and b_{jk} are obtainable by: substitution of Eqs. 26-27 into Eq. 22; grouping of terms of the same order of magnitude to yield three separate matrix equations, namely zero-order (Eq. 30), first order (Eq. 31) and second-order (Eq. 32); and application of ortho-normalization properties of Eqs. 5-6 and expansions Eq. 28-29.

$$(\lambda_{0j}^2 M + \lambda_{0j} C_p + K) y_{0j} = 0 \quad (30)$$

$$(\lambda_{0j}^2 M + \lambda_{0j} C_p + K) y_{1j} = - (2 \lambda_{0j} \lambda_{1j} M + \lambda_{1j} C_p + \lambda_{0j} C_n) y_{0j} \quad (31)$$

$$\begin{aligned}
(\lambda_0^2 \mathbf{M} + \lambda_{0j} \mathbf{C}_p + \mathbf{K}) \mathbf{y}_{2j} = & - (2 \lambda_{0j} \lambda_{1j} \mathbf{M} + \lambda_{1j} \mathbf{C}_p + \lambda_{0j} \mathbf{C}_n) \mathbf{y}_{1j} - \\
& ((2 \lambda_{0j} \lambda_{2j} + \lambda_{1j}^2) \mathbf{M} + \lambda_{2j} \mathbf{C}_p + \lambda_{1j} \mathbf{C}_n) \mathbf{y}_{0j}
\end{aligned} \tag{32}$$

Eq. 30 is identical to Eq. 10. As for Eq. 31, after some tedious but straightforward matrix algebra, it can be reduced to formulas for λ_{1j} and a_{jk} ; likewise Eq. 32 yields formulas for λ_{2j} and b_{jk} . Denoting the elements of \mathbf{C} as c_{jk} , the complex perturbations may be expressed as:

$$\tilde{c}_{jk} = \mathbf{y}_{0k}^T \mathbf{C} \mathbf{y}_{0j} \tag{33}$$

$$\lambda_{1j} = 0 \tag{34}$$

$$\lambda_{2j} = - \lambda_{0j} \sum_{k=1}^n a_{jk} (1 - \delta_{jk}) \tilde{c}_{jk} / 2 (\lambda_{0j} + \omega_{0j} \xi_{0j}) \tag{35}$$

$$a_{jk} = \lambda_{0j} \tilde{c}_{jk} / (\lambda_{0k} - \lambda_{0j}) (\lambda_{0k} + 2 \omega_{0k} \xi_{0k} + \lambda_{0j}) \tag{36}$$

$$b_{jk} = \lambda_{0j} \sum_{l=1}^n a_{jl} (1 - \delta_{jl}) \tilde{c}_{kl} / (\lambda_{0k} - \lambda_{0j}) (\lambda_{0k} + 2 \omega_{0k} \xi_{0k} + \lambda_{0j}) \tag{37}$$

The denominators of Eqs. 36 and 37 indicate that eigenvector perturbations are particularly large when both $\omega_{0j} \approx \omega_{0k}$ and $\xi_{0j} \approx \xi_{0k}$.

The approximated (perturbed) complex eigenvalues and eigenvectors may be rewritten explicitly in terms of their respective real and imaginary parts. The forms in Eqs. 38-40 below are so chosen that the real-valued perturbations may take on some physical interpretation. For example, α may be identified as nonproportionality-induced perturbation of natural frequency.

$$\omega_j = \omega_{0j} \sqrt{1 + \alpha_j} \tag{38}$$

$$\xi_j = \xi_{0j} \sqrt{1 + \beta_j} \tag{39}$$

$$\mathbf{y}_j = \mathbf{y}_{0j} + \sum_{k=1}^n \zeta_{jk} \mathbf{y}_{0k} + i \sum_{k=1}^n \eta_{jk} \mathbf{y}_{0k} \tag{40}$$

$$\text{Re } \mathbf{y}_j = \mathbf{y}_{0j} + \sum_{k=1}^n \zeta_{jk} \mathbf{y}_{0k} \tag{40a}$$

$$\text{Im } \mathbf{y}_j = \sum_{k=1}^n \eta_{jk} \mathbf{y}_{0k} \tag{40b}$$

α_j and β_j are nonproportionality-induced perturbations of natural frequency and modal damping, respectively. As for the eigenvector, Eq. 40 states that an eigenvector being complex is equivalent to damping-induced "coupling" of natural modes. As the perturbations ξ_{jk} and η_{jk} are generally not the same for all pairs of j and k , the relative values of these perturbations indicate which natural modes of the counterpart undamped system are significantly coupled due to damping nonproportionality. This can be a useful new way of understanding the complex eigenvectors.

The formulas for α_j , β_j , ξ_{jk} and η_{jk} are summarized below. For compactness of expressions, Eqs. 41-45 are introduced as definitions.

$$\sigma_{0j} = \omega_{0j} \xi_{0j} \quad (41)$$

$$\phi_{0j} = \omega_{0j} \sqrt{1 - \xi_{0j}^2} \quad (42)$$

$$R_{jk} = [\{ (\sigma_{0k} - \sigma_{0j})^2 + (\phi_{0k}^2 - \phi_{0j}^2) \} \phi_{0j} - \{ 2(\phi_{0k} - \phi_{0j}) \phi_{0j} \} \phi_{0j}] / D_{jk} \quad (43)$$

$$I_{jk} = -[\{ (\sigma_{0k} - \sigma_{0j})^2 + (\phi_{0k}^2 - \phi_{0j}^2) \} \phi_{0j} + \{ 2(\phi_{0k} - \phi_{0j}) \phi_{0j} \} \phi_{0j}] / D_{jk} \quad (44)$$

$$D_{jk} = \{ (\sigma_{0k} - \sigma_{0j})^2 + (\phi_{0k}^2 - \phi_{0j}^2) \}^2 + \{ 2(\sigma_{0k} - \sigma_{0j}) \phi_{0j} \}^2 \quad (45)$$

$$\gamma_j = \sum_{k=1}^n (R_{jk} - I_{jk} \sigma_{0j} / \phi_{0j}) \tilde{c}_{jk}^2 / 2\sigma_{0j} \quad (46)$$

$$\kappa_j = - \sum_{k=1}^n (R_{jk} \sigma_{0j} / \phi_{0j} + I_{jk}) \tilde{c}_{jk}^2 / 2\phi_{0j} \quad (47)$$

$$\alpha_j = \xi_{0j}^2 [(1 + \gamma_j)^2 - (1 + \kappa_j)^2] + (2\kappa_j + \kappa_j^2) \quad (48)$$

$$\beta_j = (\gamma_j^2 + 2\gamma_j - \alpha_j) / (1 + \alpha_j) \quad (49)$$

$$\xi_{jk} = R_{jk} \tilde{c}_{jk} + \sum_{l=1}^n (R_{jk} R_{jl} - I_{jk} I_{jl}) \tilde{c}_{jl} \tilde{c}_{kl} \quad (50)$$

$$\eta_{jk} = I_{jk} \tilde{c}_{jk} + \sum_{l=1}^n (R_{jk} I_{jl} + I_{jk} R_{jl}) \tilde{c}_{jl} \tilde{c}_{kl} \quad (51)$$

3. FURTHER DISCUSSIONS

With Eqs. 4-5, 11-12 (using C in place of C), 26-29, and 33-37, the complex eigenvectors and eigenvalues of Eq. 15 have been expressed in terms of the real eigenvectors, or mode shapes, and real eigenvalues, or natural frequencies, of Eq. 4. Eqs. 38-51 give the explicit approximate

formulas for the perturbations on natural frequencies, damping ratios, and mode shapes.

The latter equations may appear cumbersome; but they are in fact explicit formulas ready for computer coding. These may be added easily to standard subroutines that are originally intended for the eigenvalue problem of Eq. 4 subject to eigenvector normalization of Eq. 5. Unlike in numerical algorithms to solve Eq. 15, no iterations are required except in the solution of Eq. 4 itself. This can mean a big reduction in the required numerical calculations, especially when several eigenproblems have to be analyzed with the same \mathbf{M} and \mathbf{K} , but different \mathbf{C} 's.

For two-degree-of-freedom (2DOF) and three-degree-of-freedom (3DOF) systems, even the solution of the counterpart undamped eigenproblem (Eq. 4) can be obtained in closed form, allowing completely explicit approximate formulas for the pseudo natural frequencies, pseudo modal damping ratios, and complex modes. Such explicit approximate formulas for close-coupled 2DOF system have been reported by the authors [10].

Numerical examples and parametric studies are found in References [8], [9], and [10], with discussions of the accuracy of the present method. It has been shown through examples that the absolute values of the perturbations α_j , β_j , ξ_{jk} and η_{jk} indirectly serve as indicator of potential error due to the approximation inherent in the method.

It has also been shown through simple examples [8] that while the nonproportionality being considered by the method is moderate at most, the response error due to disregard of such moderate nonproportionality can be very significant.

ACKNOWLEDGMENTS

The authors are deeply grateful to Prof. M. ITO of University of Tokyo for his continued encouragement, and to Mr. Heeduck KIM, formerly graduate student at University of Tokyo, for his great help in the detailed derivations and calculations.

REFERENCES

- 1) Inman, D. J. and Andry, A. N. (1980): Some Results on the Nature of Eigenvalues of Discrete Damped Linear Systems, ASME J. App. Mech., 47, 927-930
- 2) Caughey, T. K. and O'Kelly, M. E. J. (1965), Classical Normal Modes in Damped Linear Dynamic Systems, ASME J. App. Mech., 32, 583-588

- 3) Foss, K. A. (1958), Coordinates which Uncouple the Equations of Motion of Damped Linear Dynamic Systems, ASME J. App. Mech., 25, 361-364
- 4) Lancaster, P. (1960), Free Vibrations of Lightly Damped Systems by Perturbation Methods, Quart. J. Mech. App. Math., 13(2), 138-155
- 5) Caughey, T. K. and O'Kelly, M. E. J. (1961), Effect of Damping on the Natural Frequencies of Linear Dynamic Systems, J. Acoustical Soc. of America, 33(11), 1458-1461
- 6) Mierovitch, L. and Ryland, G. (1979), Response of Slightly Damped Gyroscopic Systems, J. Sound Vib., 67(1), 1-19
- 7) Chung, K. R. and Lee, C. W. (1986), Dynamic Reanalysis of Weakly Nonproportionally Damped Systems, J. Sound Vib., 111(1), 37-50
- 8) Pacheco, B. M., Kim, H.-D., Fujino, Y. and Ito, M. (1989), Perturbation Technique for Modal Dynamic Analysis of Nonproportionally Damped Systems, J. Struct. Eng., 35A (in Japanese)
- 9) Pacheco, B. M. and Fujino, Y. (1989), Perturbation Technique to Approximate the Effect of Damping Nonproportionality in Modal Dynamic Analysis, JSCE J. Struct. Eng./Earthq. Eng., 6(1)
- 10) Pacheco, B. M. and Fujino, Y. (1989), Approximate Explicit Formulas for Complex Modes of Two-Degree-of-Freedom (2DOF) System, JSCE J. Struct. Eng./Earthq. Eng., 6(1)

LIST OF SYMBOLS

Matrices

$\underline{\mathbf{C}}$ = damping matrix
 \mathbf{C} = offdiagonal matrix from transformation of $\underline{\mathbf{C}}$ by \mathbf{Y}_0
 \mathbf{C}_n = nonproportional part of \mathbf{C}
 \mathbf{C}^p = proportional part of \mathbf{C}
 \mathbf{K}^p = stiffness matrix
 \mathbf{M} = mass or inertia matrix
 \mathbf{Y}_0 = modal matrix where column j is mode shape \mathbf{y}_{0j}

Vectors

$\mathbf{f}(t)$ = external force
 \mathbf{x}_0 = initial displacement
 $\dot{\mathbf{x}}_0$ = initial velocity
 $\mathbf{x}(t)$ = displacement
 $\dot{\mathbf{x}}(t)$ = velocity
 $\ddot{\mathbf{x}}(t)$ = acceleration
 \mathbf{y}_j = complex j -th eigenvector
 \mathbf{y}_{0j} = j -th mode, mode shape, or real eigenvector
 \mathbf{y}_{1j} = complex first-order perturbation on j -th mode
 \mathbf{y}_{2j} = complex second-order perturbation on j -th mode

Common scalars

i = unit imaginary number
 t = time

Scalars pertaining to mode j

$P_j(t)$ = complex coordinate or participation function
 α_j = perturbation on natural frequency
 β_j = perturbation on damping ratio
 γ_j = perturbation paired with κ_j (Eq. 46)
 κ_j = perturbation paired with γ_j (Eq. 47)
 λ_j = complex perturbed eigenvalue
 λ_{0j} = complex unperturbed eigenvalue
 λ_{1j} = complex first-order perturbation on eigenvalue
 λ_{2j} = complex second-order perturbation on eigenvalue
 ξ_{0j} = damping ratio when proportionally damped
 ξ_j = pseudo damping ratio
 σ_{0j} = absolute value of real part of λ_{0j} (Eq. 41)
 ϕ_{0j} = imaginary part of λ_{0j} (Eq. 42)
 w_{0j} = natural frequency
 w_j = pseudo natural frequency

Scalars relating modes j and k

D_{jk} = (Eq. 45)
 I_{jk} = (Eq. 44)
 R_{jk} = (Eq. 43)
 a_{jk} = complex coefficient of first-order perturbation on j-th mode
 b_{jk} = complex coefficient of second-order perturbation on j-th mode
 c_{jk} = element of C (Eq. 33)
 δ_{jk} = Kronecker delta
 ζ_{jk} = perturbation coefficient on real part of j-th mode
 η_{jk} = perturbation coefficient on imaginary part of j-th mode

MEASURED VIBRATION MODES OF CONSTRAINED LAYER DAMPING USING TIME AVERAGED HOLOGRAPHIC INTERFEROMETRY

**Paul R. Bernier
Slawomir T. Fryska
Christopher T. Griffen
Ann Marie Revello
General Motors Corporation
Chevrolet-Pontiac-Canada Group Engineering Center
Test Technology & Operations - Central Laboratory
30003 Van Dyke
Warren, Michigan 48090-9060
(313) 575-3774**

ABSTRACT

The dynamic response and vibration transmission characteristics of structures are determined by three inherent properties; mass, stiffness and damping. Of these, damping is least understood and most difficult to model, measure, and modify. Currently, the Complex Modulus test method is the most widely used to predict the relative effectiveness of a particular material. The one disadvantage of the method is that it cannot predict how the material will actually perform for a given application. In an effort to analyze the performance of constrained layer damping on a particular component, time averaged holographic interferometry was employed. Interferometry allowed imaging of the displacement amplitude field distribution of the component resonant modes. The test method also established a correlation between the interferometric modeshape results and animated modal analysis. The following paper discusses the interaction of these methodologies.

TEST TECHNOLOGY AND OPERATIONS OVERVIEW

This project which began mid-year 1988 was conducted by the Test Technology & Operations group at the GM - C•P•C Engineering Center as part of an effort to address noise, vibration and durability goals of design and development powertrain programs. Noise and vibration personnel utilize an extensive amount of sophisticated engineering tools to reach these targets. These tools provide the data acquisition and processing capability to understand system dynamic characteristics as they relate to steady state response, free vibration, onset and decay of transients, and mode instability/self-excited vibration. Damping plays a significant role in addressing component fatigue life, airborne and structural borne noise, as well as overall

increased system impedance to provide greater vibration isolation. The most important responsibility of the group is to develop appropriate state of the art techniques to improve overall vehicle characteristics related to powertrain performance design criteria.

THE INTERACTION OF VIBRATION AND DAMPING

A vibrating structure at any point in the vibration cycle contains kinetic and potential (strain) energy associated with modal mass and stiffness values. Realistic behavior involves energy dissipation as well. The non-conservative nature of mechanical energy conversion by definition is "damping".

Unlike mass and stiffness, damping does not manifest itself as a single phenomena. The mechanisms may include interface friction, fluid viscosity, turbulence, acoustic radiation, eddy currents, magnetic hysteresis, and mechanical hysteresis (material damping).

The primary effects of increased panel damping are reduction of vibration amplitude at the system resonance, more rapid decay at onset of free vibration, decreased spatial conduction of vibration (increased system impedance), and increased isolation during steady state response.

Because damping incorporates several mechanisms to manage the transport of energy many methods of measurement are available including loss factor, damping capacity, reverberation time, decay rate, logarithmic decrement, and spatial decay rate. All of these interrelated methods quantify the damping estimate with the degree of correlation and accuracy dependent on the testing method employed, test specimen, experimental control tolerance (i.e. frequency, temperature, and vacuum), and the engineering interpretation of data.

If damping measurements are carried out on a component interacting with a larger structure, the parameter measured is the "effective damping" accounting for the total system effect. The more complex the modeshape, as well as effectively controlling several modes with a single damping design, presents a difficult optimization challenge because of the need for intelligent and compromising selection of attachment and coverage areas.

The loss factor associated with damping (the most commonly used damping parameter) of most metals and structural materials is usually quite low and relatively independent of amplitude, temperature, and frequency provided stress levels are under the fatigue limit, temperatures well below the melting point, and excitation frequencies are low.

In contrast to this linear and stationary behavior, viscoelastic compounds have elastic moduli and loss factors strongly related to frequency, temperature, and amplitude. These materials are characterized by three regions illustrated in Figure 1 found on the following page.

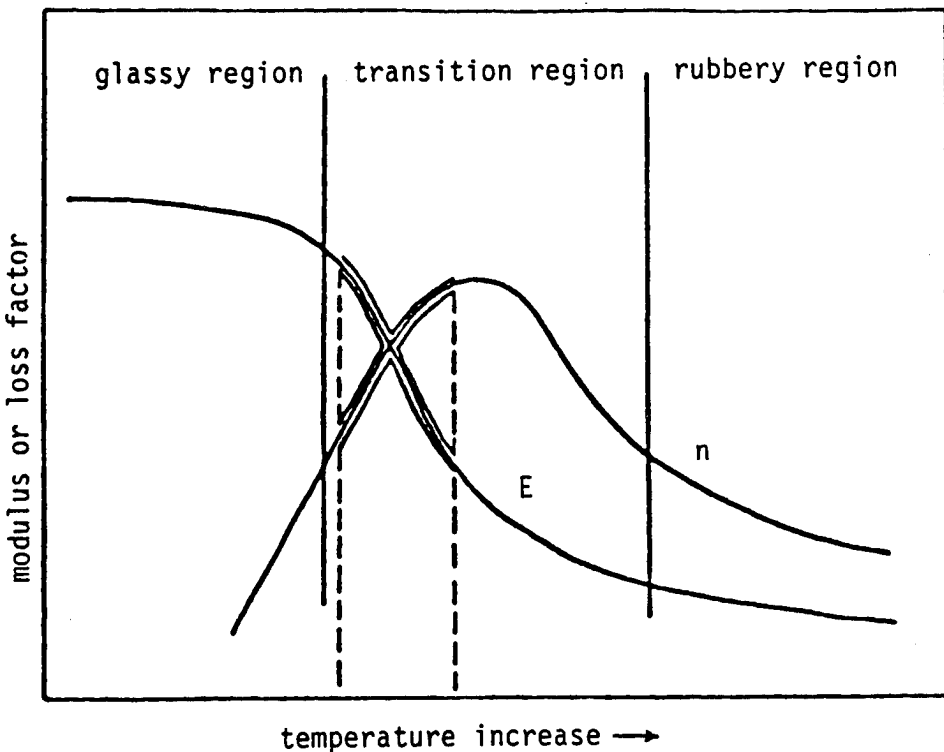


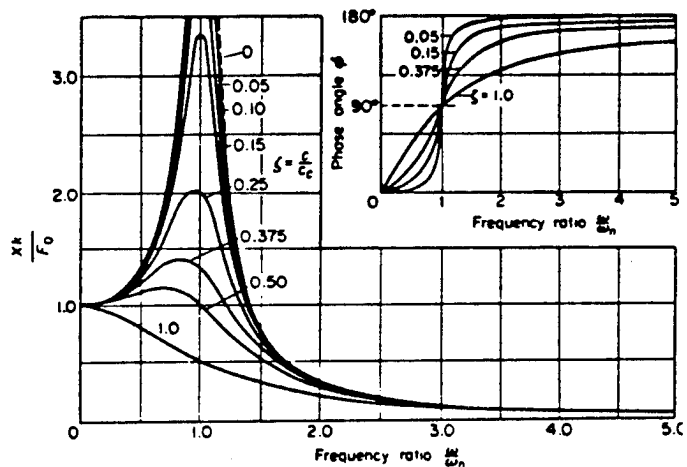
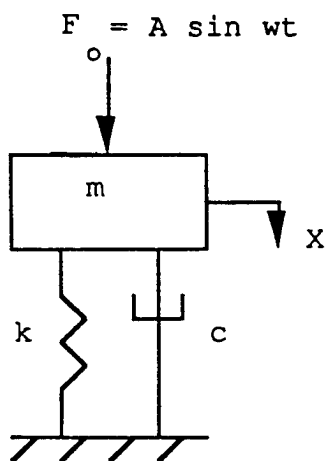
Figure 1: Loss factor and elastic moduli characteristics of damping materials.

The rubbery region offers little reaction force in generating any hysteretic loss to applied loads and no dissipation. In the glassy range the material behaves according to linear elastic theory with complete energy conservation. In the transition range maximum gains of damping occur with non-recoverable energy loss. This behavior is typical of most polymers and elastomer materials. The elastic modulus and loss factor can vary significantly depending on bond site inhibiting plasticizers and bond initiating fillers. The resulting change in dynamic properties of two nominally identical samples from different suppliers or different batches from the same source can result in dramatically different damping effectiveness.

Bending of a panel, which has a number of layers of damping materials, generally causes each layer to bend, extend, and deform in shear. With each type of deformation in each layer there is some storage of strain energy associated with it as well as energy dissipation. It is important to realize that when designing the matched performance of a damping material, the effectiveness of the material is dependent on the product choice, modeshape characteristics, bond integrity, and the forcing function excitation frequency in the operating environment. The

material should undergo the same flexural strains as the panel surface when fixed directly to the structure. The method of bonding will affect the composite damping performance, since any deformation/displacement taking place within the adhesive layer will reduce the strain and dissipation energy in the damping sheet.

Modal analysis of discrete and continuous systems depends on solution of the characteristic equation of the eigenvalue problem. The necessary assumption for solution is no damping. By incorporating the approximation of mass and/or stiffness linear proportionality to damping or a lightly damped system (matrix cross terms are zero by Basile's theorem) the damped response solution can be obtained. The concept and convenience of damping expressed by vibration theory is explained by Figure 2.



EQUATIONS:

$$(1) \quad F \sin \omega t = mx + cx + kx$$

$$(2) \quad e^{i\omega t} = \cos \omega t + i \sin \omega t$$

$$(3) \quad x = \frac{F/k}{\sqrt{[1 - (\omega/\omega_n)^2]^2 + [2\zeta(\omega/\omega_n)]^2}}$$

$$(4) \quad \tan \phi = \frac{2\zeta(\omega/\omega_n)}{1 - (\omega/\omega_n)^2}$$

Legend: ζ = damping factor = c/c_c

ϕ = phase angle

Figure 2: Single degree of freedom oscillator theoretical model and governing equations.

The classical single degree of freedom oscillator with damping has an equation of motion under steady state harmonic forces described by equation 1. The response solution must take a form of equation 2. If terms involving the sine and cosine coefficients are equated after substitution of equation 2 into equation 1 the amplitude and phase relationship can be described by equations 3 and 4. The response is characterized by a ratio of the excitation force ratio to a combined stiffness involving the physical spring element and damping term. At relatively low excitation frequencies (relative to natural frequency) the displacement depends only on the force oscillatory amplitude and the spring constant. At high excitation frequencies the response is determined by the force amplitude discrete mass value and the excitation frequency squared. The system response is then bounded by the physical elements of the mass and spring. At or near resonance the loss factor plays a significant role. As the frequency of excitation approaches the natural frequency with no damping present the denominator approaches zero with theoretically infinite response. With damping or the loss factor present, the system "Q" application is not infinite with the degree of response inversely proportional to magnitude of damping. It is important that the loss factor is also varying with the excitation frequency. The overall damping design sensitivity is highly dependent on the ratio of the excitation frequency to the natural frequency.

An alternative way of expressing classical vibration modeling is by the use of complex stiffness notation. Most techniques for measuring complex stiffness use a material sample as a spring. The most widely used test method is the frequency response method or the Complex Modulus test method (American Standard Test Method E756-83). In this method, a variable frequency sinusoidal force is applied to the test sample and the amplitude of vibration is plotted as a function of frequency as shown in Figure 3 on the following page. The test method is versatile in that it enables damping measurements to be made over a range of frequencies as well as temperatures. The actual test method can differ among suppliers because of their different substrate bar size which produces different results for a particular damping material. Figure 4 on page 7 shows a schematic diagram of the Complex Modulus test apparatus. The test procedure is relatively simple. First, the damping material is bonded to the Oberst bar in a manner suitable for the material. The bar is then mounted into the test jig. The clamping force around the root of the bar simulates a fixed boundary condition. The transducers are positioned approximately 1mm away from the sample bar. Either a sinusoidal (sweep) or random (bandwidth) signal can be applied to the excitation transducer by means of a power amplifier/signal generator.

The frequency response of the bar is measured by the displacement, velocity, or acceleration transducer and recorded as a function of frequency and amplitude for a given temperature. The "effective damping" is obtained by applying

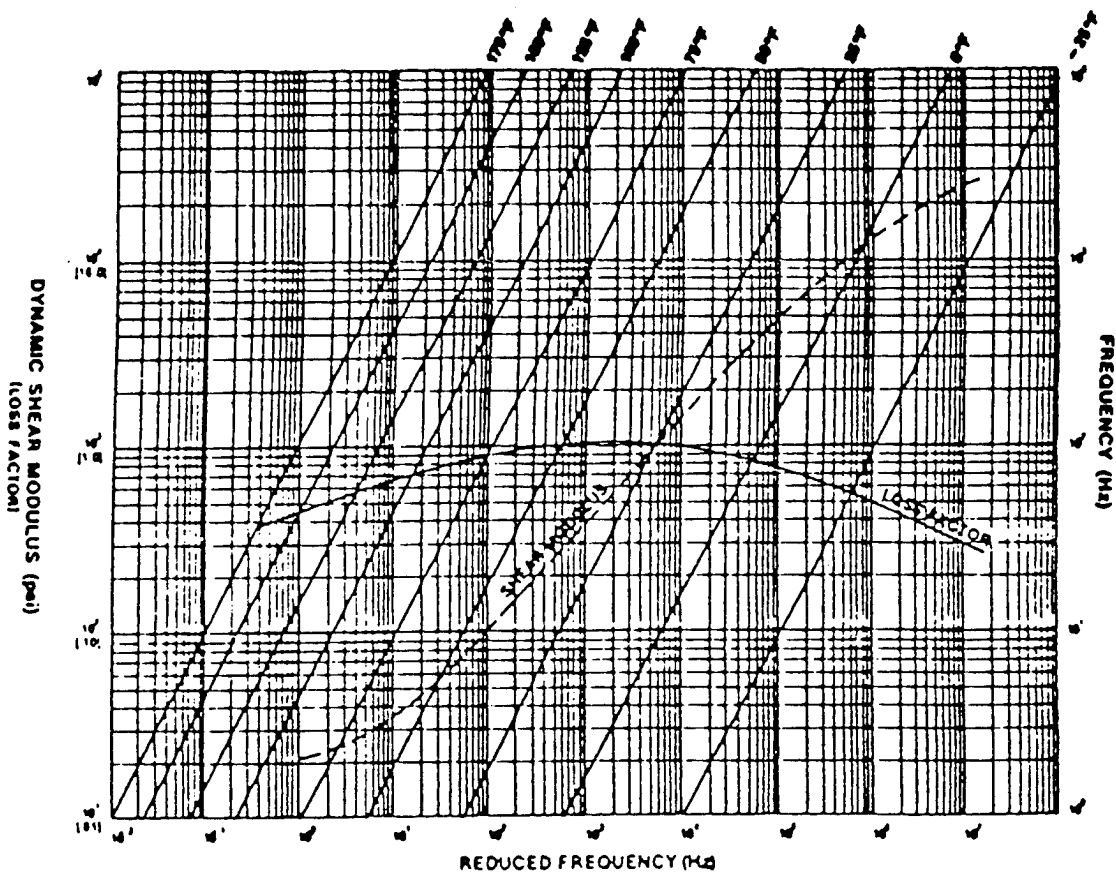


Figure 3: Example of data generated from Complex Modulus Test (Reduced Frequency Nomogram).

the half power bandwidth (3 dB down) at each resonant mode and taking the ratio of the frequency band defined by the half power points to the center resonant frequency to define the loss factor value. The test method assumes linearity, however high levels of excitation can generate nonlinearities in the response leading to unreliable data. The amplitude of the force signal applied to the specimen is kept constant as a function of excitation frequency. The loss factor of the base metal is assumed to be zero (0.001) since it is at least a magnitude less than the composite bar. The material loss factor is then calculated from the composite measurement compensated by the Oberst bar damping value.

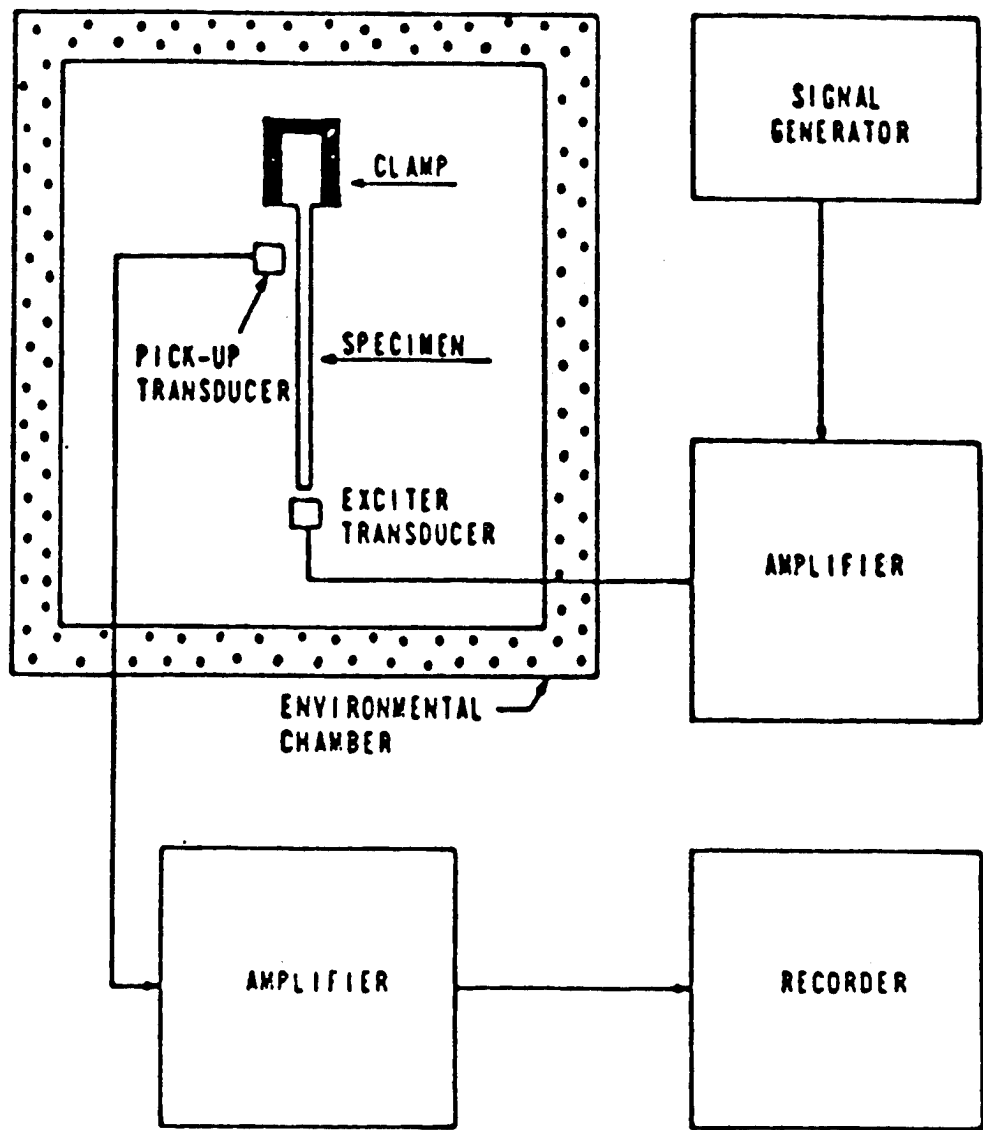


Figure 4: Schematic of Complex Modulus test apparatus.

DAMPING OPTIMIZATION AND TEST PROCEDURE

Base structure - The general flow and approach to damping optimization is shown in Figure 5 on the following page.

The base component chosen is predicated on prior testing of the overall system with results that suggest high sensitivity of the component to damping modifications and

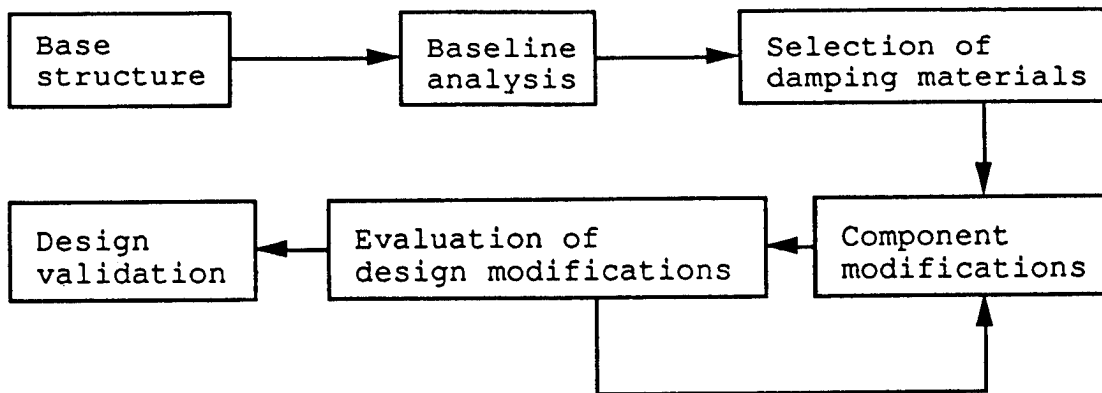


Figure 5: Flowchart of damping design optimization.

potential improvement of the dynamic response characteristics. For example, the transmission oil pan (Figure 6) indicated a high degree of noise contribution during various operating speeds based on sound intensity measurements and sound power rankings of the overall powertrain system.

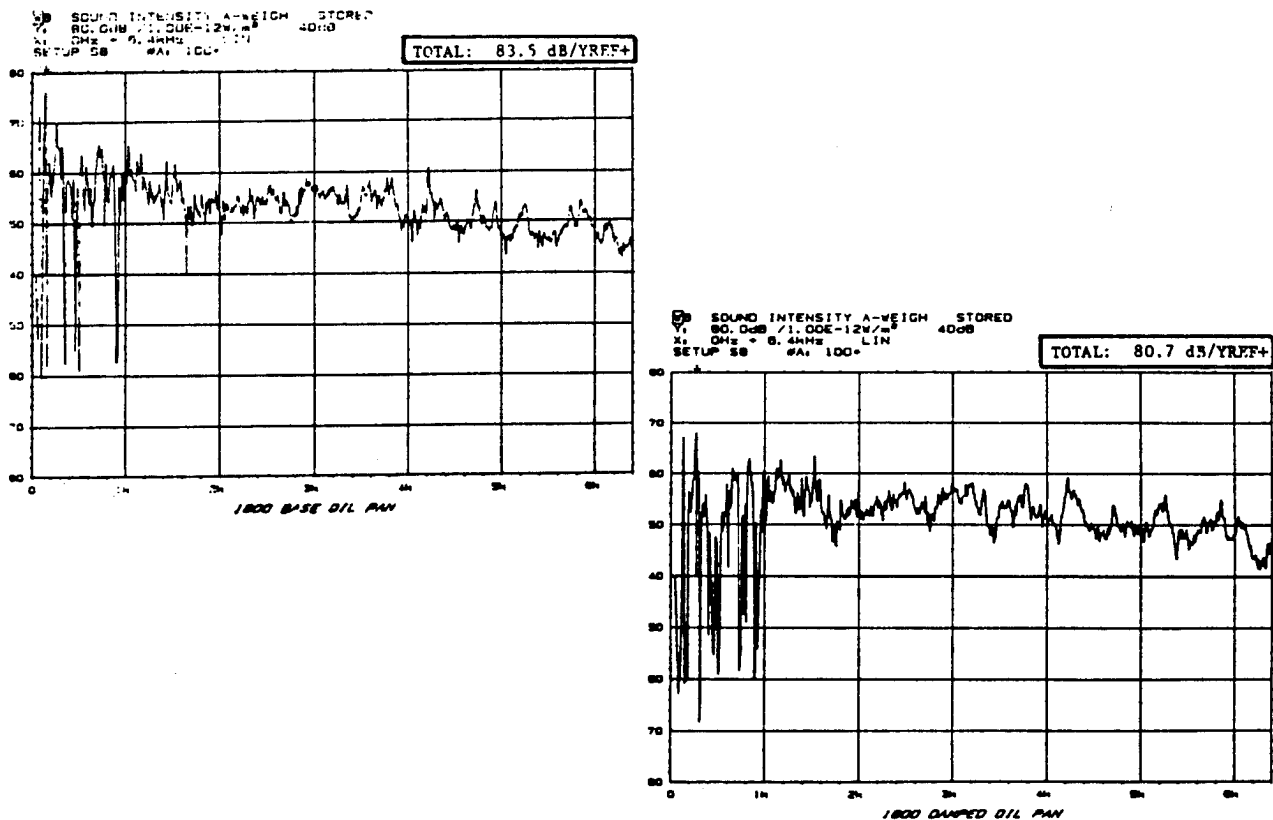


Figure 6: Data from semi-anechoic noise source testing.

Baseline Analysis - Upon completion of the powertrain baseline system testing at the GM - C•P•C semi-anechoic facility, experimental modal analysis and holographic interferometry methods were applied at the GM - C•P•C Optical Test laboratory (Figure 7).

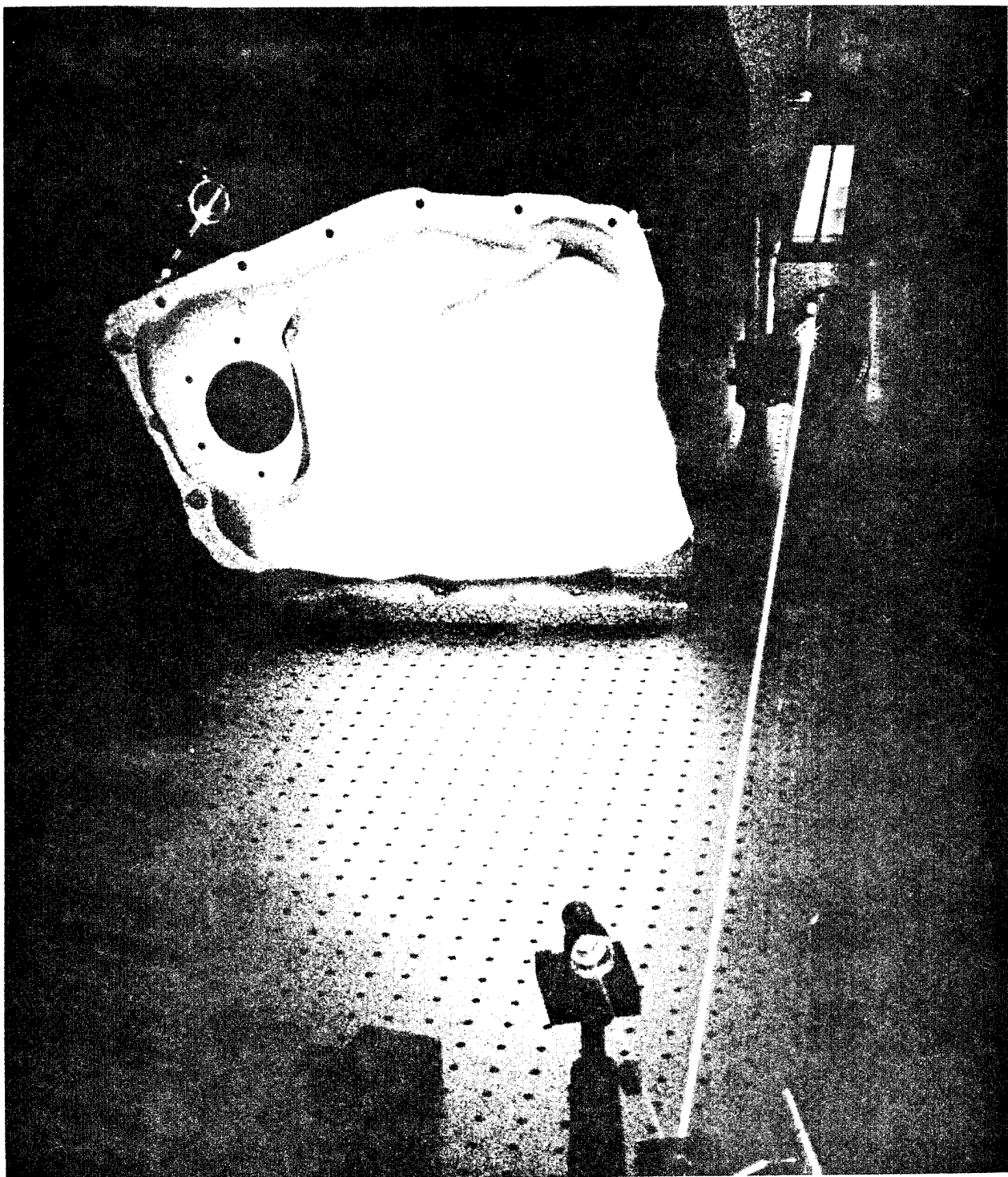


Figure 7: Holographic setup in the Optical Test laboratory.

No finite element analysis methods were used on this project application due to the hardware component availability. The modal analysis performed on the baseline pan identified resonant frequencies of the oil pan and corresponding modeshapes associated with excitation speeds identified by the signature analysis. The amount of baseline "effective damping" was also calculated using the half power bandwidth method on each resonant frequency.

The driving point frequency response function from the modal analysis provided the necessary resonant frequency information (Figure 8) to perform time averaged holographic interferometry and image the modeshape amplitudes already animated by modal analysis (Figures 9,10,11 on the following pages).

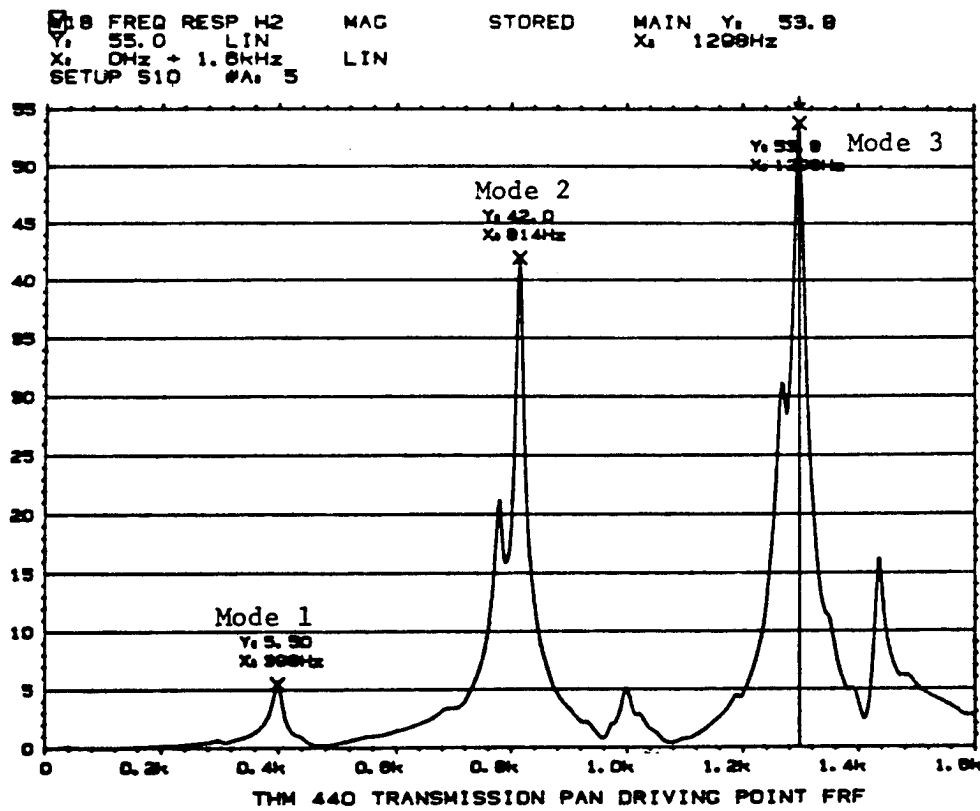


Figure 8: Driving point frequency response function of the baseline transmission oil pan.

Trace A : 01(398.893 Hz)
Mode #: 1
Frequency : 398.89 Hz
Damping : 1.55 %

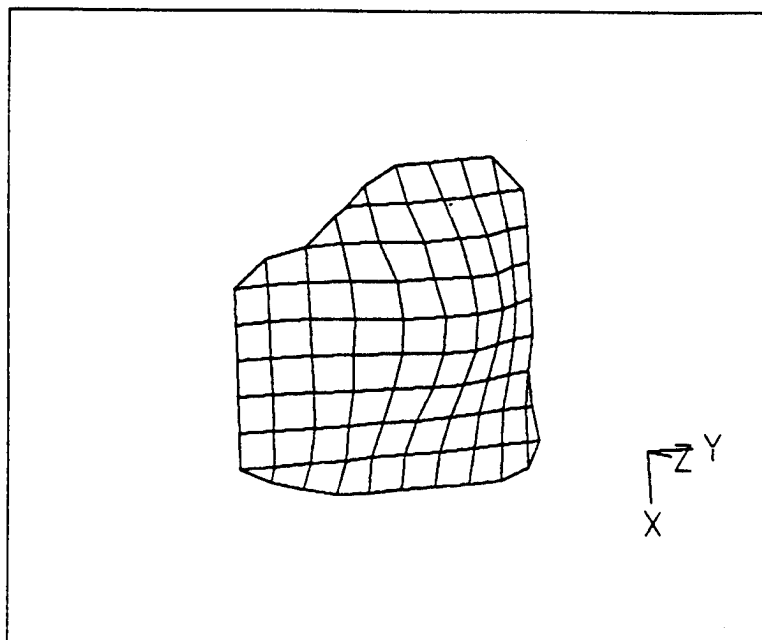


Figure 9 - Mode 1

Trace A : 04(814.934 Hz)
Mode #: 2
Frequency : 814.94 Hz
Damping : 638.55e %

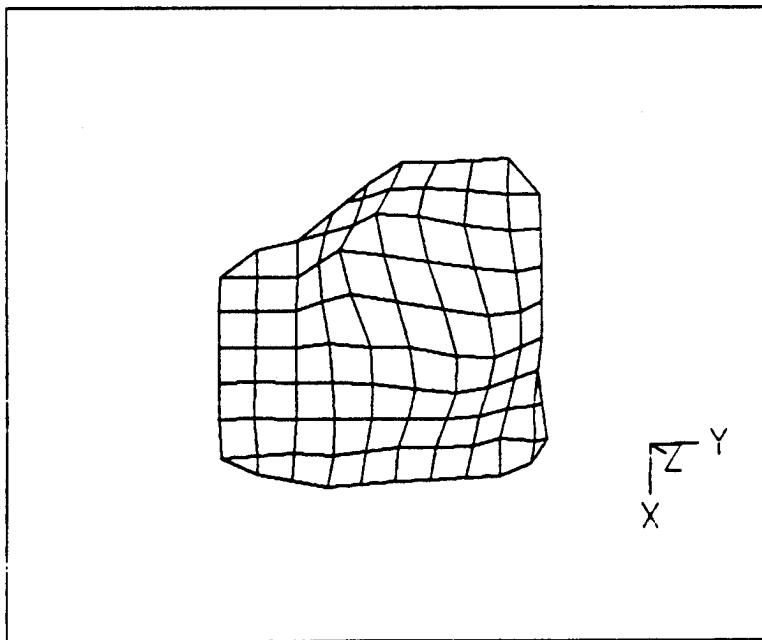


Figure 10 - Mode 2

Trace A : 811(1.297 Hz)
Mode # : 3
Frequency : 1.30K Hz
Damping : 659.23% X

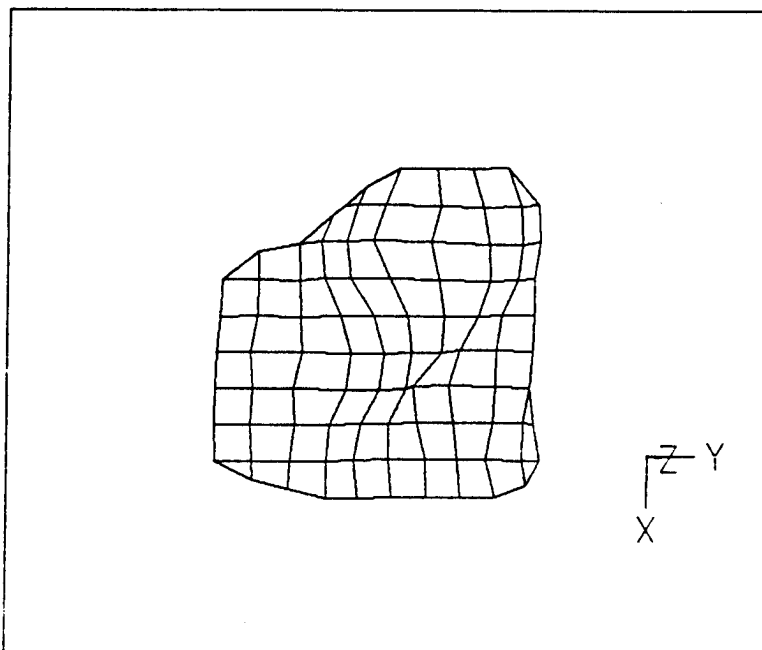


Figure 11 - Mode 3

Figures 9, 10, 11: Animated modal analysis modeshape images of baseline transmission oil pan.

An in depth review of interferometric techniques will not be discussed (reference 1), however a brief discussion is essential to appreciate the value of this supplemental method. The component to be imaged is placed on an isolation table and fixtured with an excitation device (an electromagnetic shaker placed normal to the pan surface) that is decoupled (isolated) from the optical elements on the table. The component is illuminated with a laser source (20mW 632.8nm HE-NE) with the reflected object light recorded on a high resolution photographic plate. Approximately 10% of the illumination beam is split to a second optical reference path that simultaneously exposes the plate. The plate is then developed by standard photographic techniques. Alternative recording media may be used such as thermoplastic cameras (used during this project). The choice is one of pure convenience. The recording process requires a second reconstruction or readout procedure to view and utilize the holographic image. This is achieved by illuminating the developed transparency plate with the original reference beam while viewing the plate. The hologram imaged will be the exact duplicate of the original component in three dimensions. The basic steps in forming the hologram can be used to record the time averaged (averaging of the maximum

and minimum displacement over time) dynamic response of the object with the difference being the harmonic excitation of the component at it's resonant frequency during exposure. The reconstructed hologram will then contain both the original three dimensional image as well as displacement contours of the component response corresponding to bright and dark interference bands superimposed on the image. It is this information that is interpreted in conjunction with modal analysis. Time averaged interferometry images are shown for three modes in Figures 12,13 and 14.

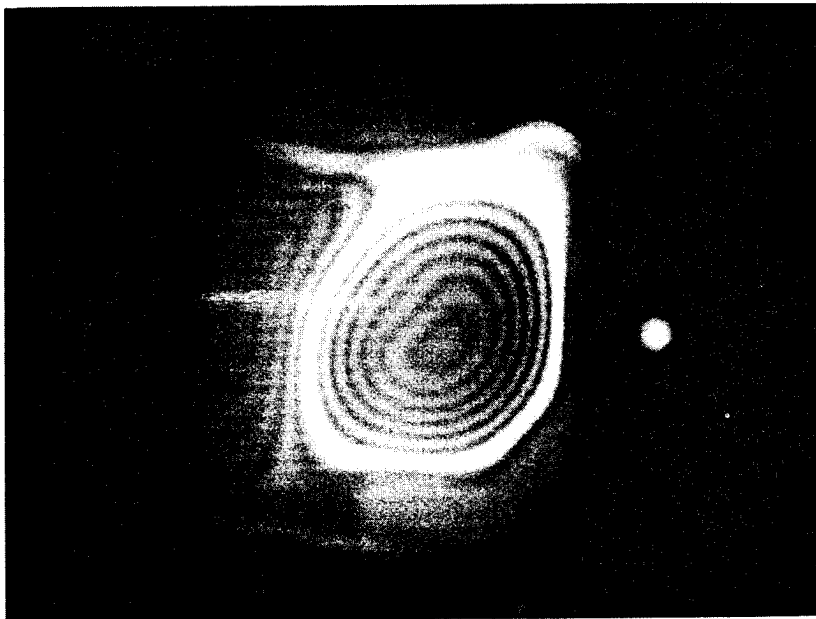


Figure 12 - Mode 1

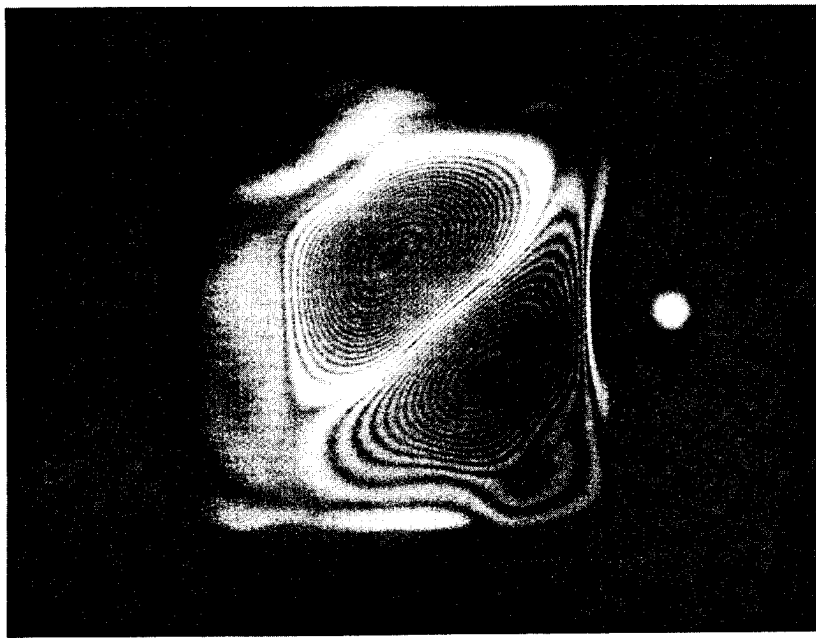


Figure 13 - Mode 2

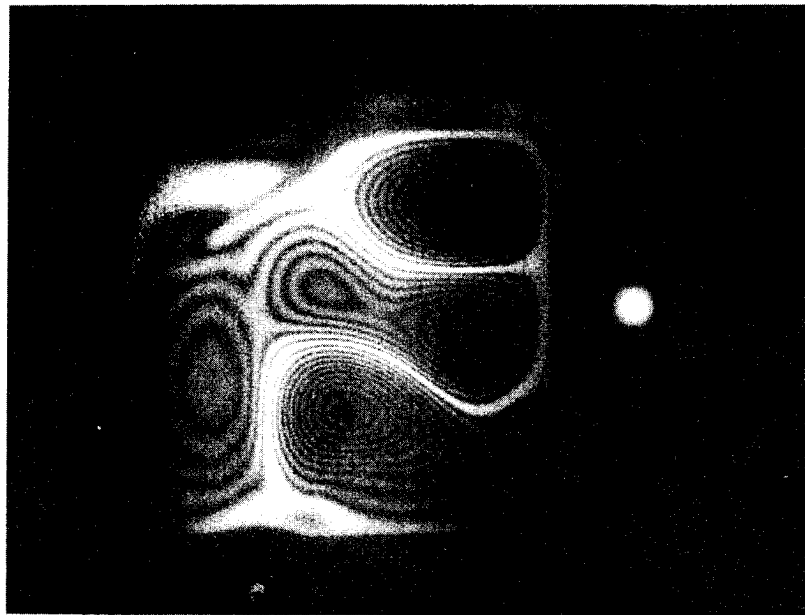


Figure 14 - Mode 3

Figures 12, 13, 14: Holographic interferometry modeshape images of baseline transmission oil pan.

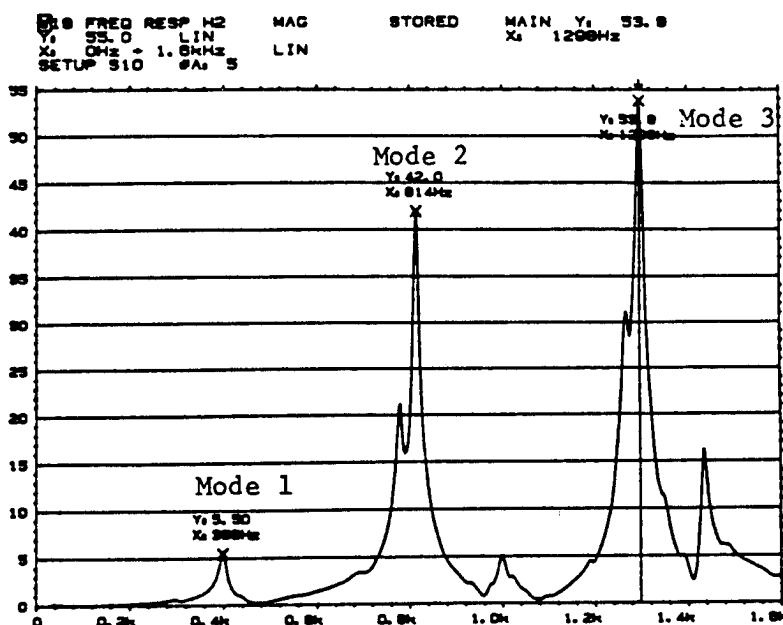
Selection of Damping Materials - After the resonant mode frequencies have identified along with environmental temperatures, appropriate damping materials and associated loss factors can be chosen from reduced frequency nomograms established by the damping supplier. A major caution at this stage of the development program is that the supplier test specimen construction and geometry, along with the particular specimen testing method, will generate nomogram data based on resonant modes and test specimen dynamic characteristics unrelated to the product design. This deficiency can be partially offset in the development cycle time by accurate placement of the damping layer, optimized boundary constraints, and secure bonding to the component.

Component Modifications - The animated modeshapes of the baseline transmission oil pan described the relative amplitude and phase as well as an estimate of nodal locations. The greatest shortcoming of this is the degree of resolution that is defined by a discrete measurement technique. The resolving capability is determined by the number of frequency response function measurements on the component surface. As the natural frequency/modeshape complexity increases so does the requirement for more data.

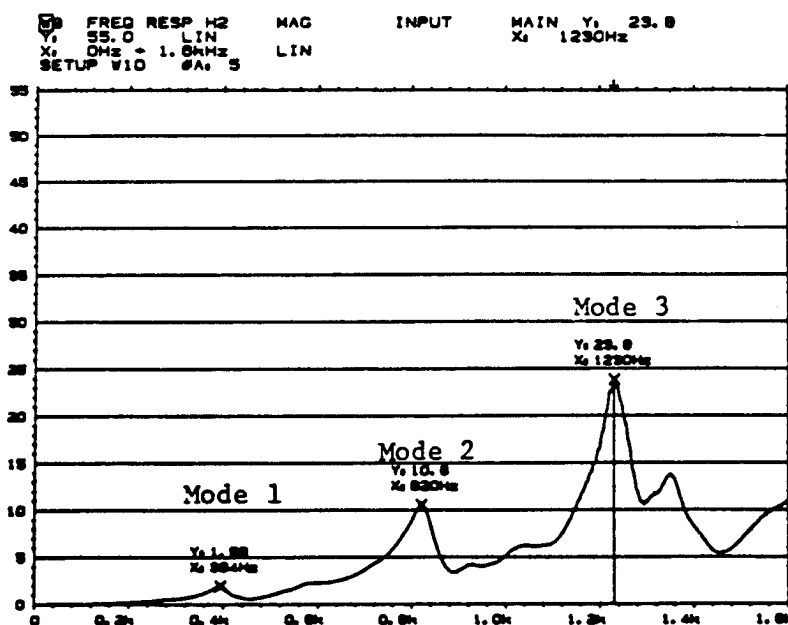
The interferometry method overcomes this limitation by the inherent full field imaging characteristics. The overall amplitude distribution, maximum displacement, and nodal boundaries are completely described. The first step in determining the component area to be treated is locating the nodal boundary for the modeshape of interest. For a combination of modeshapes the compromise involves their superposition as well as effectively controlling the maximum contribution mode. This can be done by careful analysis of sound intensity data. Once the application boundary is established the damping material and constraining layer can be applied.

Evaluation of the Design Modification - The modified component requires only a new driving point frequency response function to calculate the increase in damping and the changes in resonant frequencies associated with the addition of mass, damping, and residual stiffness from the constraining layer. Modal analysis is not required since the remaining information is obtained by re-imaging the new modeshapes with interferometry. Reductions in amplitude can be verified by decreased fringe density. Any disbonding between the damping material and structure will be evident by abrupt discontinuities in contour shape between successive fringes. A simple comparative fringe analysis can be performed with the assumption of a unity sensitivity vector (summation of the observation and illumination vector plane directions) and all displacements normal to the component surface. The fringe patterns are assigned and counted with the 0th order fringe defined as the brightest fringe located on the image. This is referred to as the first root of the 0th order Bessel function and is the optical analog of vibration nodes. Each successive dark to light fringe is assigned an increasing root number. The displacement at any point on the surface is then the root number \times laser source wavelength/2. For a component location of the 9th root fringe at a wavelength of 632.8nm, the out of surface plane displacement is 2,847.8EXP(-9) meters.

Design Validation - Design/release depends solely on validation of the component. Assurance of meeting/exceeding design and development targets can include noise and vibration criteria, fatigue and durability goals, corrosion, and other requirements of the system that maybe influenced by the damping design. Regardless of the degree of design optimization the final measure of success relies on the integrated performance of the total system and the realistic gains achieved. Very rarely does this approach theoretical predictions and initial expectations. The final project results comparing the baseline and modified oil pan are summarized in Figures 15 thru 19, on the following pages, showing the difference in driving point frequency response functions, increase in damping, and decreased dynamic response of the resonant modes.



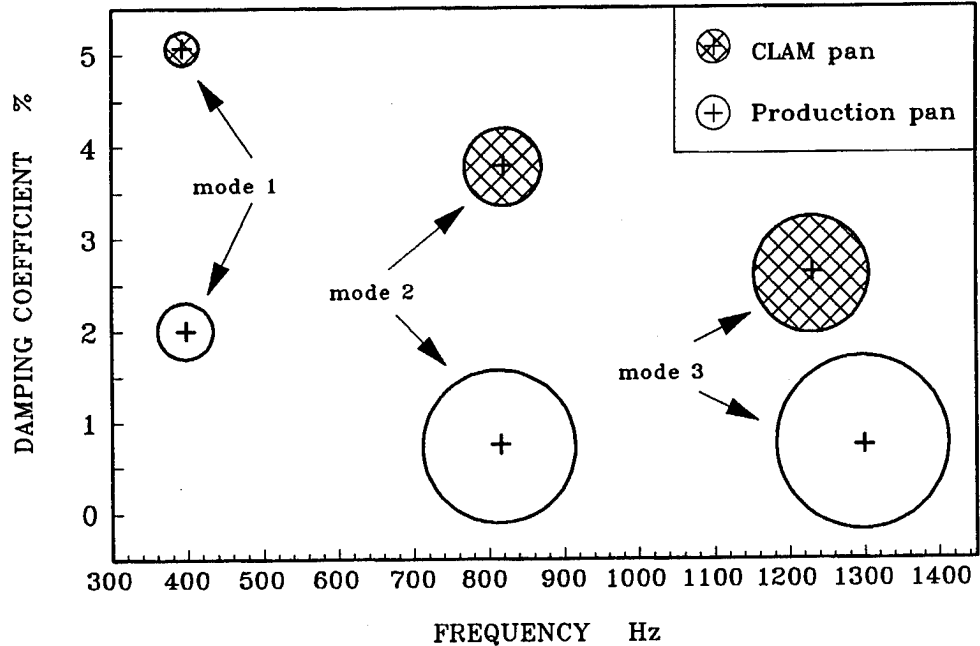
THM 440 Transmission Pan Baseline



THM 440 Transmission Pan Constrained Layer

Figure 15: Comparative frequency response functions between baseline and modified transmission oil pan.

PRODUCTION vs. CLAM TRANSMISSION PAN
 Comparison of resonance frequency, damping,
 and frequency response function amplitude



NOTE: circle diameter is proportional to the amplitude of the Frequency Response Function at a resonance frequency

Figure 16: Comparison of damping coefficient (loss factor) between baseline and modified transmission oil pan.

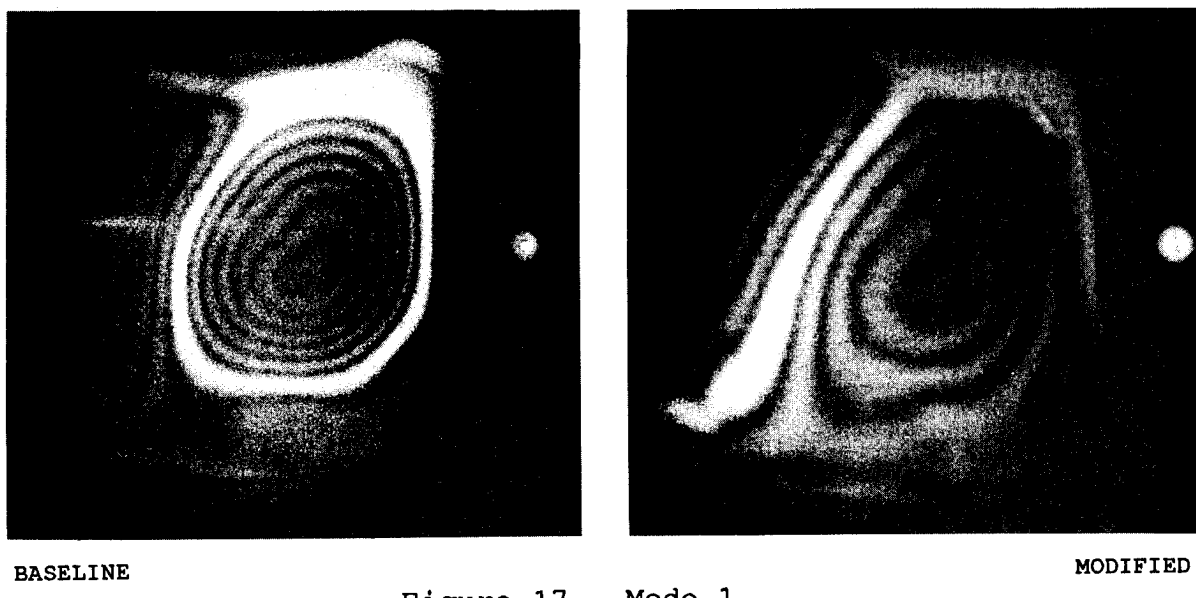
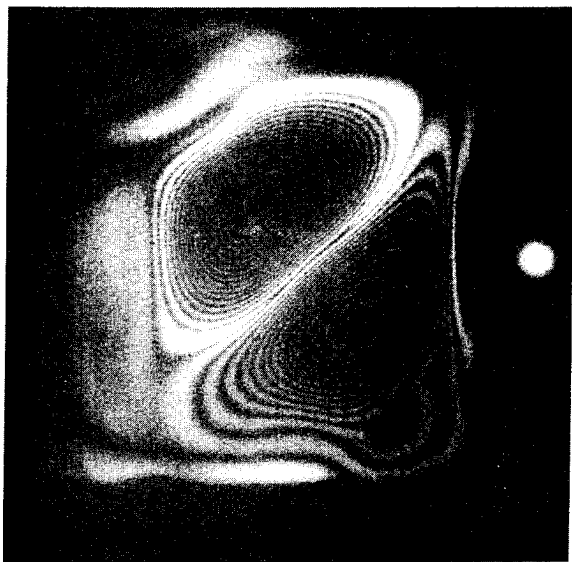


Figure 17 - Mode 1

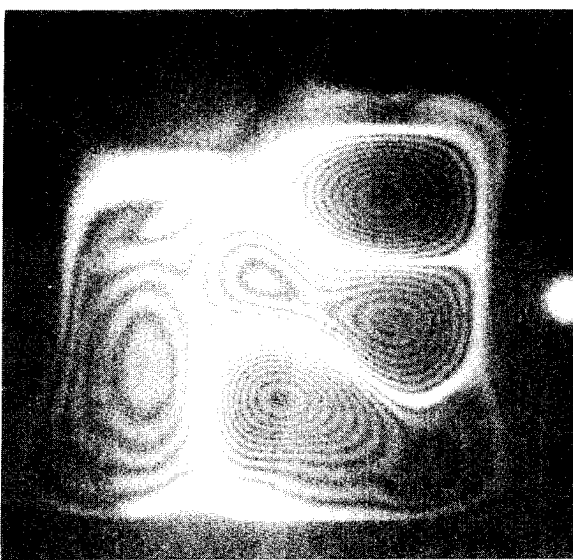


BASELINE

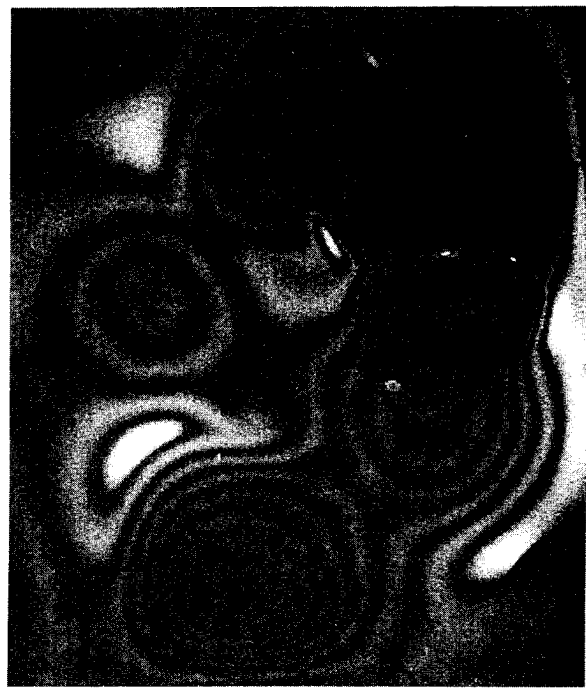


MODIFIED

Figure 18 - Mode 2



BASELINE



MODIFIED

Figure 19 - Mode 3

Figure 17, 18, 19: Interferometric image comparison between baseline and modified transmission oil pan.

SUMMARY OF FIGURES

Figure 1 - Loss factor and elastic moduli characteristics of damping materials.

Figure 2 - Single degree of freedom oscillator theoretical model and governing equations.

Figure 3 - Example of data generated from Complex Modulus Test (Reduced Frequency Nomogram).

Figure 4 - Schematic of Complex Modulus test apparatus.

Figure 5 - Flowchart of damping design optimization.

Figure 6 - Data from semi-anechoic noise source testing.

Figure 7 - Holographic setup in the Optical Test lab.

Figure 8 - Driving point frequency response function of the baseline transmission oil pan.

Figure 9,10,11 - Animated modal analysis modeshape images of baseline transmission oil pan.

Figure 12,13,14 - Holographic interferometry modeshape images of baseline transmission oil pan.

Figure 15 - Comparative frequency response functions between baseline and modified transmission oil pan.

Figure 16 - Comparison of loss factor between baseline and modified transmission oil pan.

Figure 17,18,19 - Interferometric image comparison between baseline and modified transmission oil pan.

REFERENCES

- (1) C.T. Griffen - Applications of Holographic Interferometry in Automotive Component Testing, SAE paper no.870883.
- (2) A.M. Revello - Standardization of Vibration Damping Materials Performance Parameters, Chevrolet-Pontiac GM of Canada Group Headquarters and GMI Engineering & Management Institute, May 13, 1988.
- (3) University of Dayton - Vibration Damping Short Course.
- (4) L. Meirovitch - Analytical Methods in Vibration.

ACKNOWLEDGEMENTS

A special thanks to the following individuals for their support, contributions, and expertise in making this test procedure an exciting part of optical testing at General Motors.

N. J. Egan
D. Hall (Defiance)
J. N. Lighthall
D. T. Moore of Moore Plastics
M. Moore of Moore Plastics

Damping Associated with Incipient Melting in Aluminum-Indium Alloys.

O. Diehm, C.R. Wong*, and D.C. Van Aken

Department of Materials Science & Engineering
University of Michigan
Ann Arbor, MI 48109-2136

*David Taylor Research Center
Physical Metallurgy Branch
Code 2812
Annapolis, MD 21402-5067

Abstract

The strain amplitude dependent damping of binary aluminum-indium alloys containing nominally 0.6 to 17.3 weight percent indium was studied. A DuPont Dynamic Mechanical Analyzer model 983 was used to measure the damping capacity of these materials. Pure aluminum (99.99%) exhibited strain dependent damping at strain values as low as $70 \mu\epsilon$. The addition of 0.6 weight percent indium reduced the strain independent damping by a factor of 2, but the strain dependent damping was equivalent to that of the pure aluminum. Binary aluminum-indium alloys containing 4, 8, 12, and 16 weight percent indium exhibited a general increase in loss factor with increasing indium content; however, the strain dependent damping was no greater than that of the pure aluminum sample. No significant increase in damping was observed when the binary alloys were tested at temperatures above the melting point of indium. Two damping peaks were observed near the eutectic melting point when tested at 10 Hz and differential scanning calorimetry verified both of these peaks as due to the melting of the indium inclusions. It was concluded that the higher temperature damping peak was associated with smaller indium inclusions and that the damping peaks were related to the solute segregation associated with the binary eutectic reaction.

Introduction

The typical structural aluminum (Al) has a high stiffness, but a low specific damping capacity. The typical loss factor for a precipitation hardened Al-based alloy is between 10^{-3} and 10^{-4} . Metal matrix composites have shown increased damping [1] but these materials can not be considered high damping because they have loss factors less than 10^{-2} [2]. An alternate approach to the development of a high damping composite would be by the incorporation of a viscoelastic fiber in addition to the stiff fibers used for reinforcement. Thus, the matrix would provide the structural stiffness and the various fibers would provide the desired damping capacity and the added stiffness. Although the composite material would show a lower stiffness than the stiff metal matrix composite, the increase in damping capacity may be of greater importance.

Indium (In) is a viscoelastic metal with an ultimate tensile strength of 3.1 MPa (450 psi) at room temperature. The loss factor of In has been reported to vary from 0.06 at room temperature to 0.2 at 100°C [3]. The melting point of pure indium is 156 °C and when combined with Al forms an immiscible alloy system, as shown in the phase diagram in Fig. 1. An alloy of 17.3 weight percent In will solidify by a monotectic reaction ($L \rightarrow Al + L_2$) which produces a continuous Al-matrix with an In-rich (L_2) entrapped liquid. At 156 °C, the In-rich liquid will solidify by the eutectic reaction $L_2 \rightarrow Al + In$. This final eutectic reaction will normally produce inclusions which are single-phase, i.e. pure indium. The small weight fraction of Al produced during the eutectic reaction is "divorced" to the pre-existing Al-matrix. The resulting microstructure will consist of an Al-matrix with a dispersion of In inclusions.

It is the purpose of this paper to examine the effect of a viscoelastic inclusion, such as In, on the damping capacity of Al. It is expected that the composite microstructure will demonstrate strain dependent damping as a result of micro-plasticity (dislocation motion) within the inclusion. In addition, high temperature loss factor measurements will be used to determine the damping associated with liquid inclusions. It is also expected that the first order transformation (the eutectic reaction) at 156 °C will produce both an anomalous modulus effect and a frequency dependent loss peak. The following formula from Nowick and Berry[4] describes the relaxation time, τ , as a function of the radius, r , of the second phase particle for a two phase material during a first order transformation.

$$\tau = r^2 / 3 D Vf \quad (1)$$

Where D is the diffusivity and Vf is the volume fraction of the second phase particle. It should be noted that the relaxation time will be strongly dependent upon the size of the second phase such that smaller particles would exhibit a shorter relaxation time.

Experimental Procedure

Binary Al-In alloys, with nominal compositions 0.6, 4, 6, 8, 12, and 16 weight percent In, were arc-melted in an argon gas atmosphere. These alloys were prepared from In, and Al, metals which each had a metallic purity better than 99.99%. The total weight of each arc-melted button was below 10 g to assure a homogeneous melt. The Al-17.3% In alloy was produced by induction melting in an argon gas atmosphere and was solidified at a slow rate using a ceramic insulator to produce a coarse distribution of In particles. Each sample was then cold-rolled 30%, annealed at a temperature of 532°C, and then cold-rolled and annealed again to produce a nominal sample thickness of 1mm. Rectangular-beam coupons

were cut from the rolled slab, using a diamond saw, to produce a sample shape with nominal dimensions 40 mm x 10 mm x 1 mm.

A DuPont Dynamic Mechanical Analyzer (DMA) model 983 was used to measure the damping response of the test coupons. At room temperature, and a fixed frequency of 0.1 Hz, the maximum strain amplitude was varied from 20 to 300 $\mu\epsilon$ by changing the oscillation amplitude and clamping distance between the pivot arms, see Fig.2. The driver arm produces a sinusoidal displacement inducing both a shear and bending stress. The damping capacity was measured as the loss factor which is equal to the tangent of the phase angle, $\tan \delta$, between the stress and the strain. Elevated temperature tests from 100 - 200°C were conducted at a strain amplitude of 70 $\mu\epsilon$ at both 1 Hz and 10 Hz. A heating ramp of 1 °C per minute and a helium gas atmosphere were used to minimize the temperature lag of the sample with respect to the furnace-controlling thermal couple. The eutectic melting temperature of the binary alloys was established using a Perkin-Elmer differential scanning calorimeter model 7.

Metallographic samples were prepared by mechanical polishing and etching in a hot aqueous solution of NaOH. Cross-sectional samples were cut to view the long transverse microstructures of the binary alloys. Electron microscopy studies were performed at The University of Michigan Electron Microbeam Analysis Laboratory. Thin foils for transmission electron microscopy were prepared by twin jet electropolishing in a solution of 20% nitric acid (by volume) and methanol.

Results

The room temperature damping results for the pure-Al and binary Al-In alloys are shown in Figs. 3 and 4. Each alloy exhibits a transition to a strain amplitude dependent damping at approximately 70 $\mu\epsilon$. A comparison between the Al and the binary Al-0.6In alloy (all compositions are in weight percent) is shown in Fig.3. The addition of 0.6 In reduced the strain independent damping by a factor of 2, but the strain dependent damping was equivalent to that of the pure Al. The strain independent damping of the pure Al was also greater than the binary Al-In alloys, with the exception of the two highest In concentrations, i.e. Al-12In and Al-16In. In general, the damping capacity of the Al-In alloys increased with increasing In content, see Fig. 4. The microstructures exhibit elongated stringers of indium aligned parallel with the rolling direction as shown in Fig. 5.

The results of a typical 1 Hz temperature scan are shown in Fig. 6 for an Al-6In alloy. A first order transformation was observed between 160 and 170°C. The change in the storage modulus with respect to temperature shows an anomalous behavior in this temperature range. The eutectic melting temperature of 156 °C was verified by differential scanning calorimetry (DSC). However, the DSC results also revealed a second melting peak at 160 °C as shown in Fig. 7. Fig. 8 shows that both melting peaks were observed with the DMA during a 10 Hz temperature scan. The loss factor associated with this transformation did not vary significantly with respect to increasing the weight percentage of In as shown in Fig. 9. Although the total damping appears to increase with In content, the difference between the peak height and the background is nearly constant.

At the eutectic melting temperature, the binary alloys exhibit strain dependent damping as demonstrated by the Al-17.3In alloy in Fig. 10. This particular alloy had a coarse distribution on In particles due to its slow cooling rate from the melt. The temperature scan in Fig. 11 shows a large damping peak to background ratio at lower frequencies for the Al-17.3In alloy. When measuring the loss factor at the eutectic temperature for various

oscillation frequencies, the relative height of the peak was observed to increase from values of 0.002 at 1 Hz to 0.014 at low frequencies of 0.1 Hz.

Discussion

The strain dependent damping of the Al-In alloys appears to be associated with dislocation motion in both the Al-matrix and the In-particles. Thus, the damping of the Al-In alloys increases with increasing In content, but the total damping is less than that of the pure Al. This may indicate that the damping contribution from the matrix decreases with increasing In content. This effect may be explained if we associate the magnitude of the matrix damping with a mean-free-path of dislocation motion. Upon the addition of second phase particles, the mean-free-path of the dislocations will decrease in two ways: the In-particles will inhibit the grain size during annealing and the In-particles will act as dislocation traps. Both of these effects are a function of the volume fraction of the second phase. Therefore, the damping contribution from the matrix would be expected to decrease as the volume fraction of second phase is increased. A minimum would then be expected for the Al-In alloys since the damping contribution from the In-particles would increase with increasing volume fraction. This minimum is approximately at the Al-4In composition.

The addition of In also affects the strain independent damping of the Al-matrix, as shown in Fig. 3. Indeed, the addition of a very small amount of In (0.6%) reduces the loss factor to one-half that measured for pure Al, but this effect appears to be related to processing history. Electron microscopy studies have just begun to examine the differences in structure which results from the addition of In and the subsequent processing. For example, a second Al-0.6In alloy was processed without annealing and the microstructure is shown in Fig. 12. The microstructure shows a fine subgrain structure with In particles on the subgrain boundary. However, this particular alloy shows a much higher loss factor. In fact, the loss factor measured for this sample was constant, with $\tan \delta = 0.016$, up to a strain amplitude of $150 \mu\epsilon$. Thus, further microstructural work is required before any conclusions can be made with regard to the strain independent regime.

The damping peak observed between 160 and 170°C is believed to be related to the eutectic melting temperature observed at 156°C by the differential scanning calorimeter. The difference in temperature is a reflection in the thermal lag associated with the DuPont DMA. The pivot arms are made of stainless steel and are in direct contact with the sample. Thus, the pivot arms act as a thermal reservoir with respect to the sample. This effect was minimized by flowing helium gas through the furnace as the temperature was ramped. The thermal lag for the Al-In samples varied between 4 and 10 °C.

Equation 1 provides a means to calculate the test frequency at which peak damping would be observed for a 2-phase microstructure going through a first order transformation. In the present case, the reaction is a eutectic where the In alloys with the surrounding Al-matrix to form a liquid. Self-diffusion of In in the liquid and in the solid state near the melting point is approximately $10^{-5} \text{ cm}^2/\text{s}$ and $10^{-9} \text{ cm}^2/\text{s}$, respectively [5]. If the typical diameter of the In inclusion is taken as $2 \mu\text{m}$, and a volume fraction of 0.02 is assumed, relaxation times of 170 and 0.017 seconds are expected using the self-diffusion rates for In in the solid and liquid states, respectively. This would correspond to test frequencies of approximately 0.01 Hz and 60 Hz for the solid and liquid states, respectively. Resolution of the damping peak was obtained at a test frequency of 0.1Hz, which would indicate an intermediate diffusivity. The diffusion rate of Al in In would be expected to be higher than the self-diffusion of In in the solid state since the atomic radius of Al is smaller than that of

In. Thus, a diffusivity between 10^{-7} and 10^{-8} cm²/s may be reasonable. In terms of order-of-magnitude calculations, this would produce a relaxation time on the order of 10 seconds, or a test frequency of 0.1 Hz. The peak observed at the higher test frequencies may then be related to a smaller indium particle. It should be noted that the melting temperature of In is size dependent [6]. This effect is easily demonstrated by differential scanning calorimetry of an arc-melted Al-12In alloy, see Fig. 13. The moderate solidification rate will produce a fine structure of In particles which melt at a higher temperature. Upon cold-working, and subsequent annealing, the number of high melting In particles is reduced, as observed in the DSC results reported in Fig. 7.

Conclusions

The addition of In to Al exhibited a general increase in loss factor with increasing In content; however, the strain dependent damping was no greater than that of the pure Al sample. A precipitation hardening alloy would be more appropriate for evaluating the damping contribution resulting from the addition of a viscoelastic inclusion. No significant increase in damping was associated with liquid metal inclusions, but a large damping peak was observed which was associated with the eutectic transformation and the diffusion of Al solute in the In inclusions.

Acknowledgements

This work was sponsored by the Office of Naval Research and the Office of Naval Technology under contract 87-K-0452. The technical monitor was Dr. D.E. Polk. The authors are grateful for the assistance of Mr. Steve Miller in performing the differential scanning calorimetry.

References

1. A.K. Ray, V.K. Kinra, S.P. Rawal, and M.S. Misra, Role of Interfaces on Material Damping, eds. B.B. Rath and M.S. Misra, ASM International, (1985) p. 95.
2. D. Birchon, "Hidamets: Metals to Reduce Noise and Vibration", The Engineer, 22, 207 (1966).
3. C.R. Wong, D.C. Van Aken, and O. Diehm, paper JDB of these proceedings.
4. A.S. Nowick and B.S. Berry, Anelastic Relaxation in Crystalline Solids, Academic Press, 1972, p. 485.
5. G.H. Geiger and D.R. Poirier, Transport Phenomena in Metallurgy, Addison-Wesley, 1980, p.458.
6. H. Saka, Y. Nishikawa, and T. Imura, "Melting temperature of In particles embedded in an Al matrix", Phil. Mag. A, 57, 895 (1988).

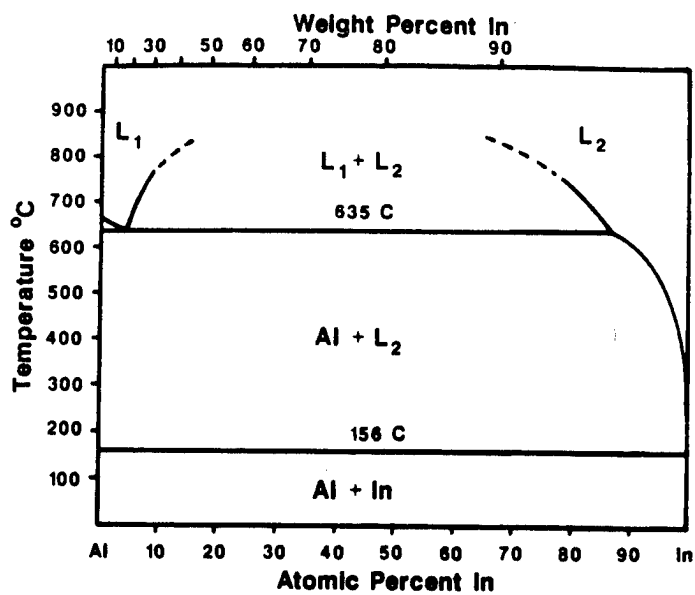


Fig. 1: Phase diagram of the Al-In binary system showing a liquid immiscibility gap.

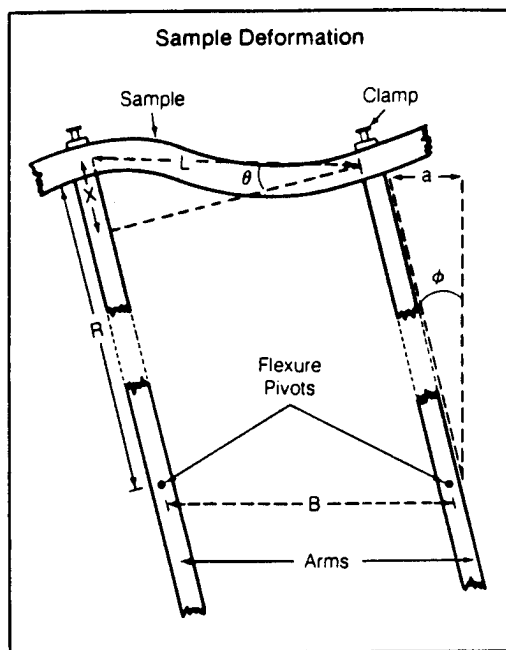


Fig. 2: Schematic representation of the pivot arm system for the DuPont DMA 983

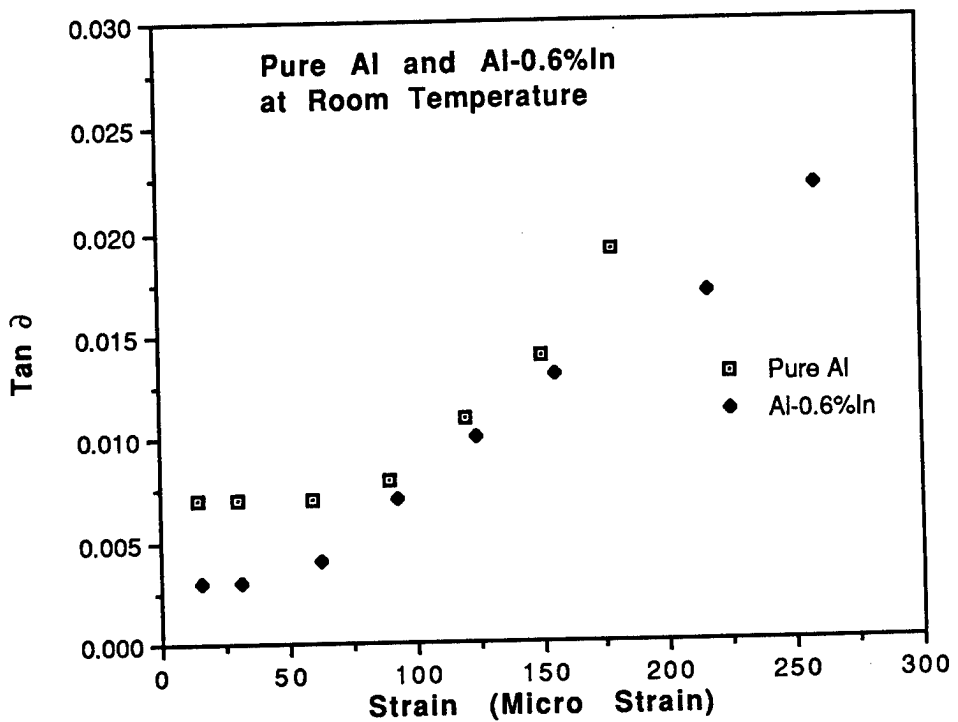


Fig. 3: Room temperature damping results of Pure Aluminum (99.99%) and Al-0.6In for various strain amplitudes.

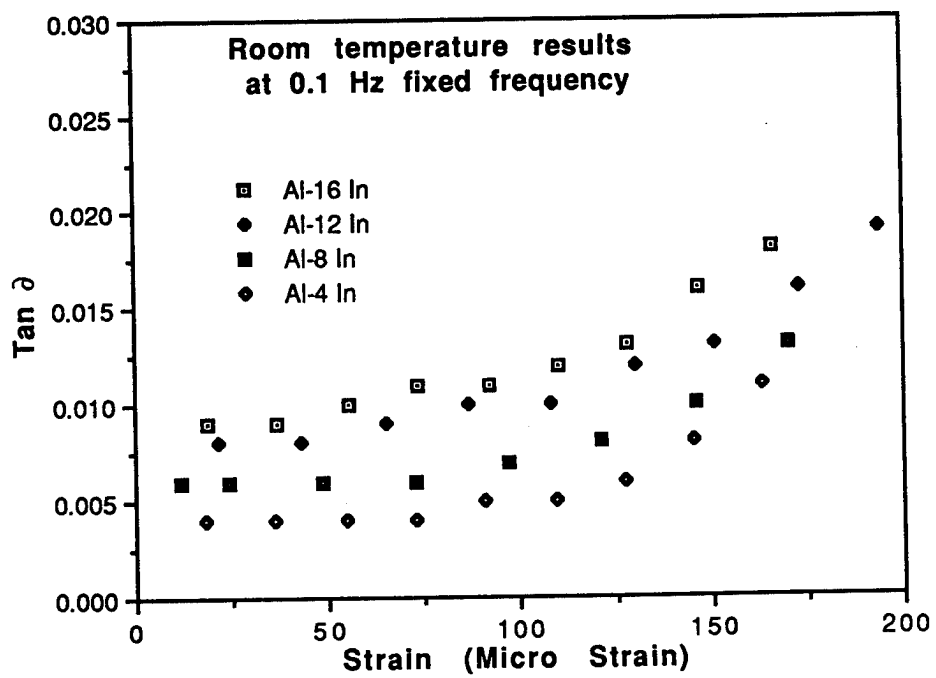


Fig. 4: Room temperature damping results of Al-4In, Al-8In, Al-12In, and Al-16In for several strain amplitudes.

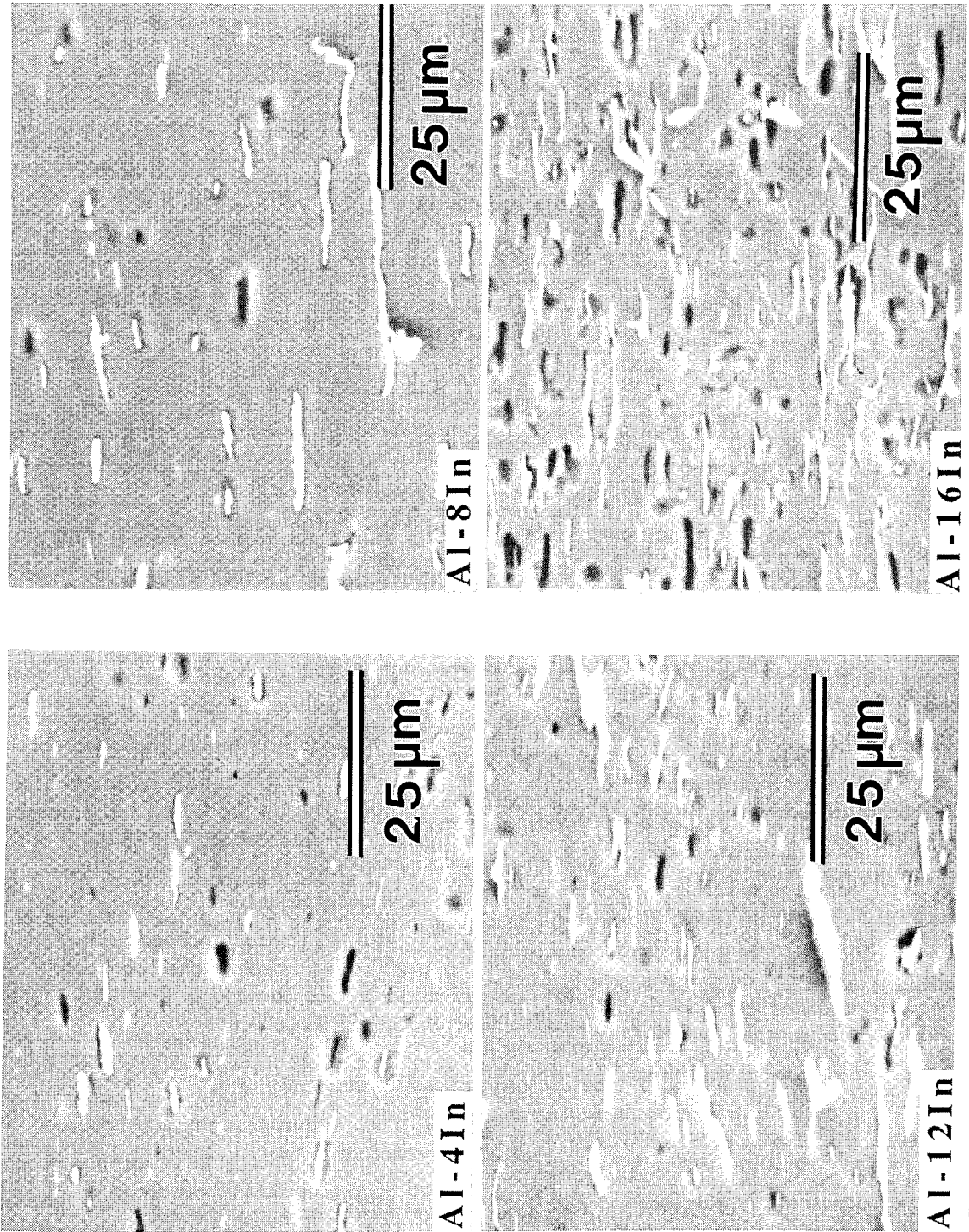


Fig. 5: Scanning electron micrographs of the Al-4In, Al-8In, Al-12In, and Al-16In alloys showing elongated indium stringers parallel to the rolling direction. The samples were polished and then etched in a warm aqueous solution of NaOH.

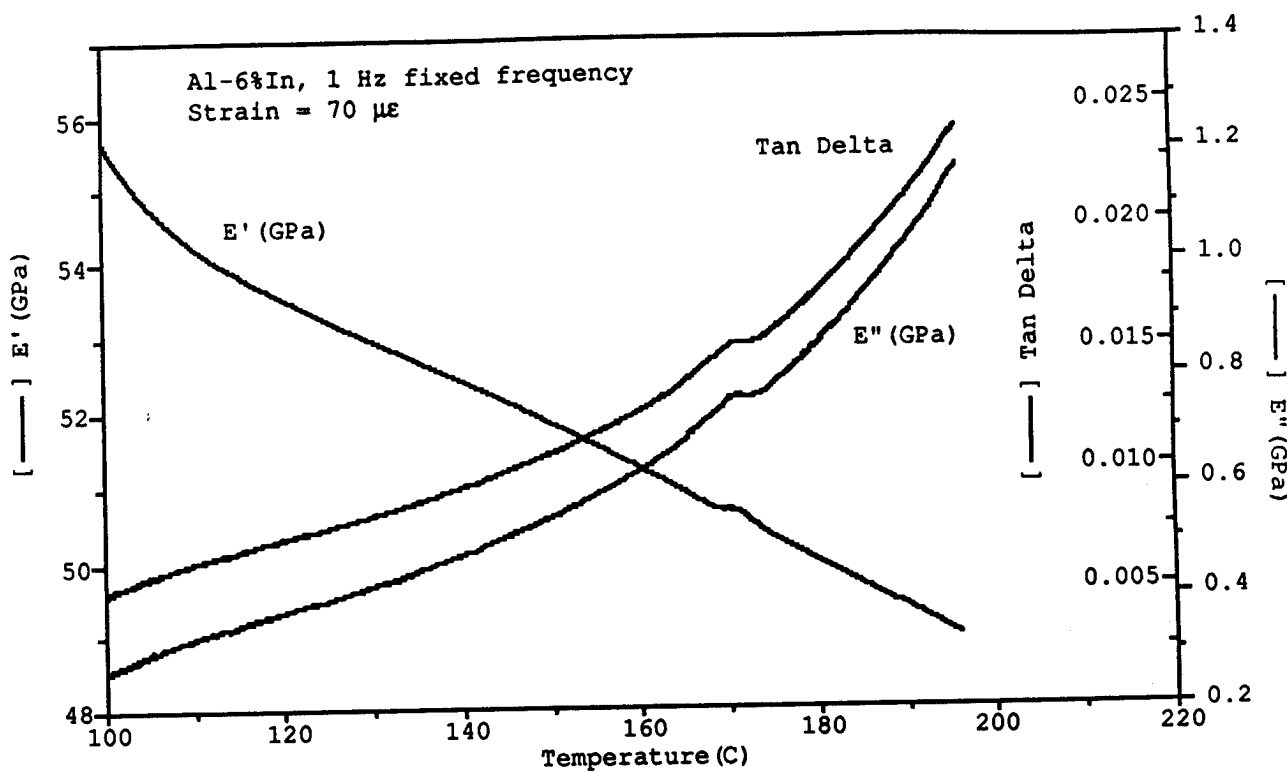


Fig. 6: Damping results from 100-200°C for the Al-6In alloy using a fixed frequency of 1 Hz and a strain amplitude of 70 $\mu\epsilon$.

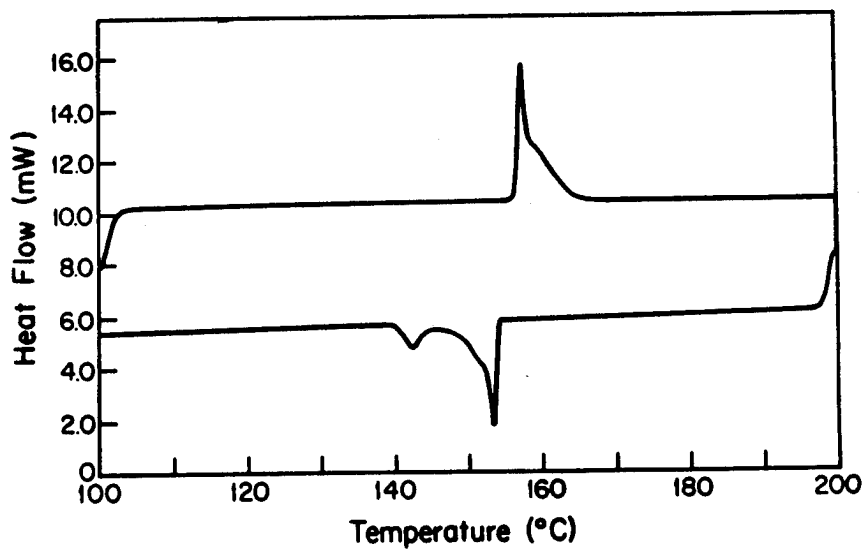


Fig. 7: Differential Scanning Calorimetry results from the Al-17.3In alloy exhibiting two melting peaks upon heating (top line) and three solidification peaks upon cooling (bottom line). The smallest peak (140°C) is associated with solid nucleation of the finest indium particles.

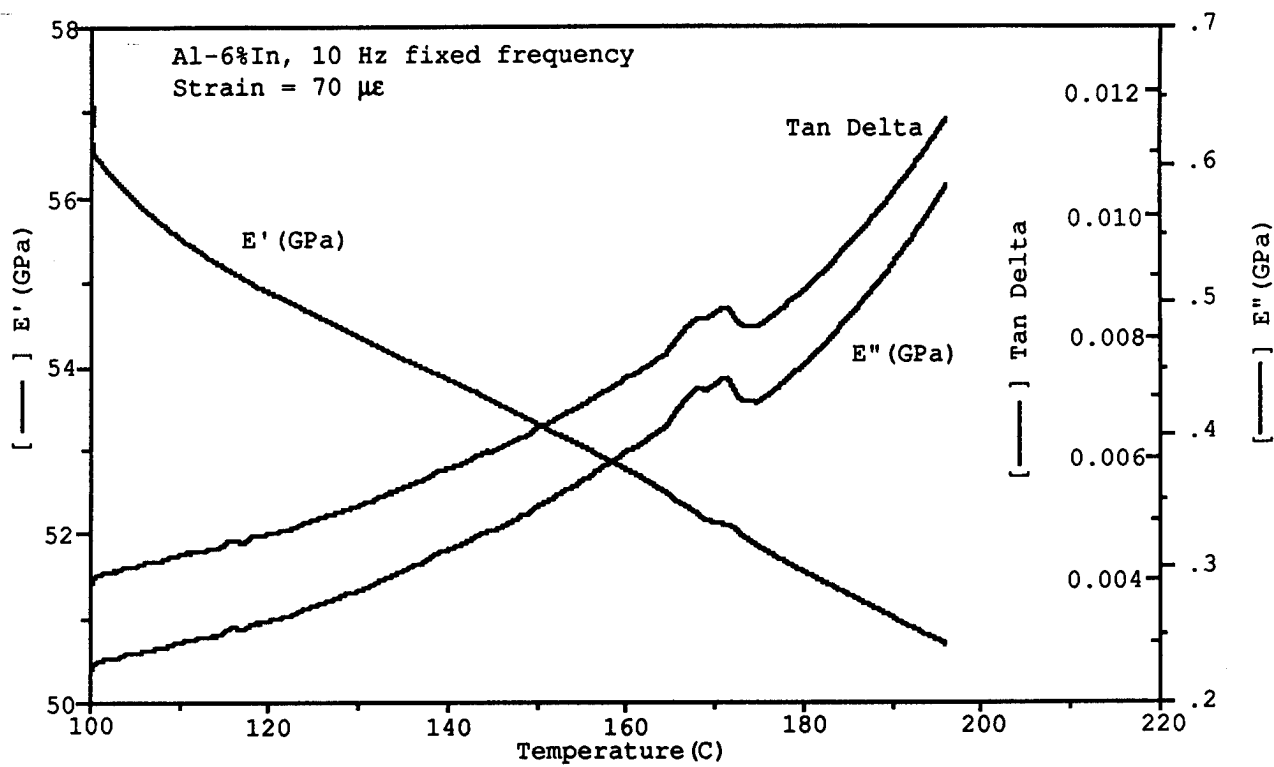


Fig. 8: Damping results for the Al-6In alloy at 10 Hz fixed frequency and strain amplitude of $70 \mu\epsilon$ showing two distinct damping peaks.

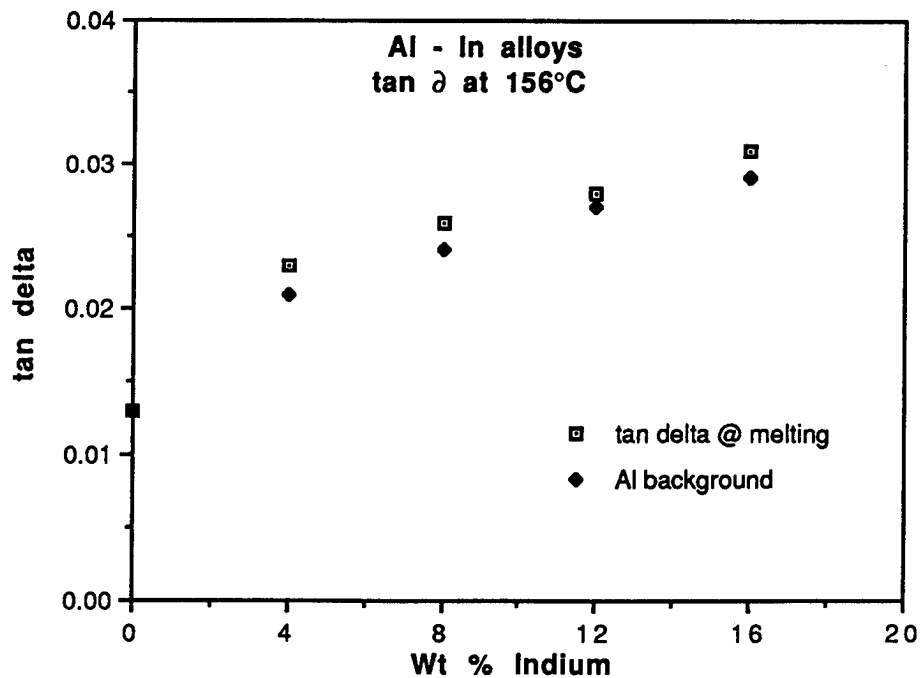


Fig. 9: DMA results indicating a slight increase of damping capacity at 156°C with increasing indium content and also showing damping contribution from the Al-matrix.

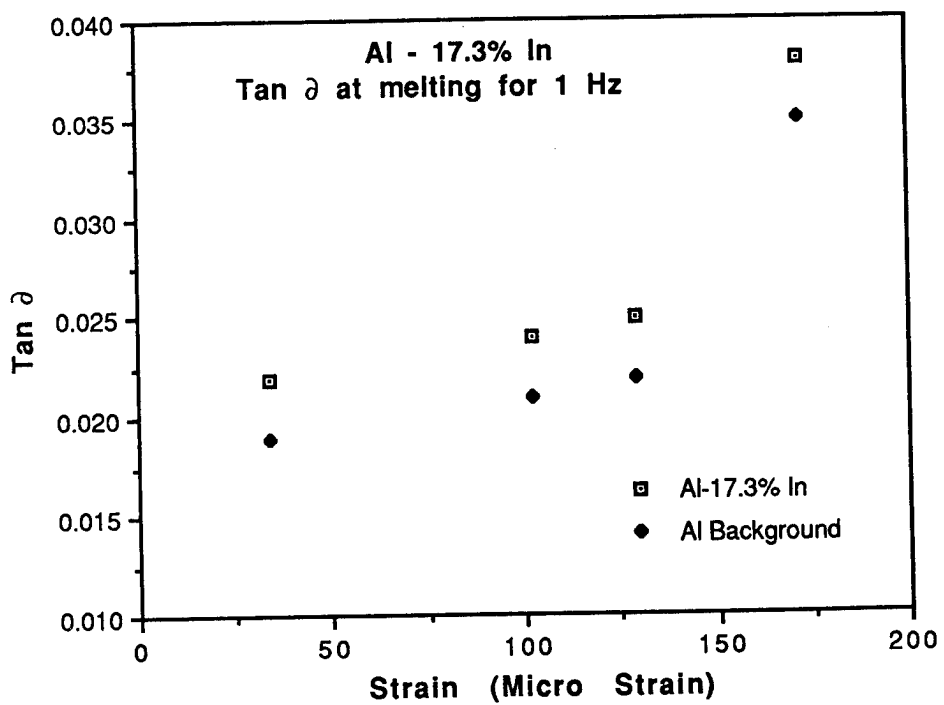


Fig. 10: Damping capacity results for the Al-17.3In alloy at 156°C at different strain amplitudes.

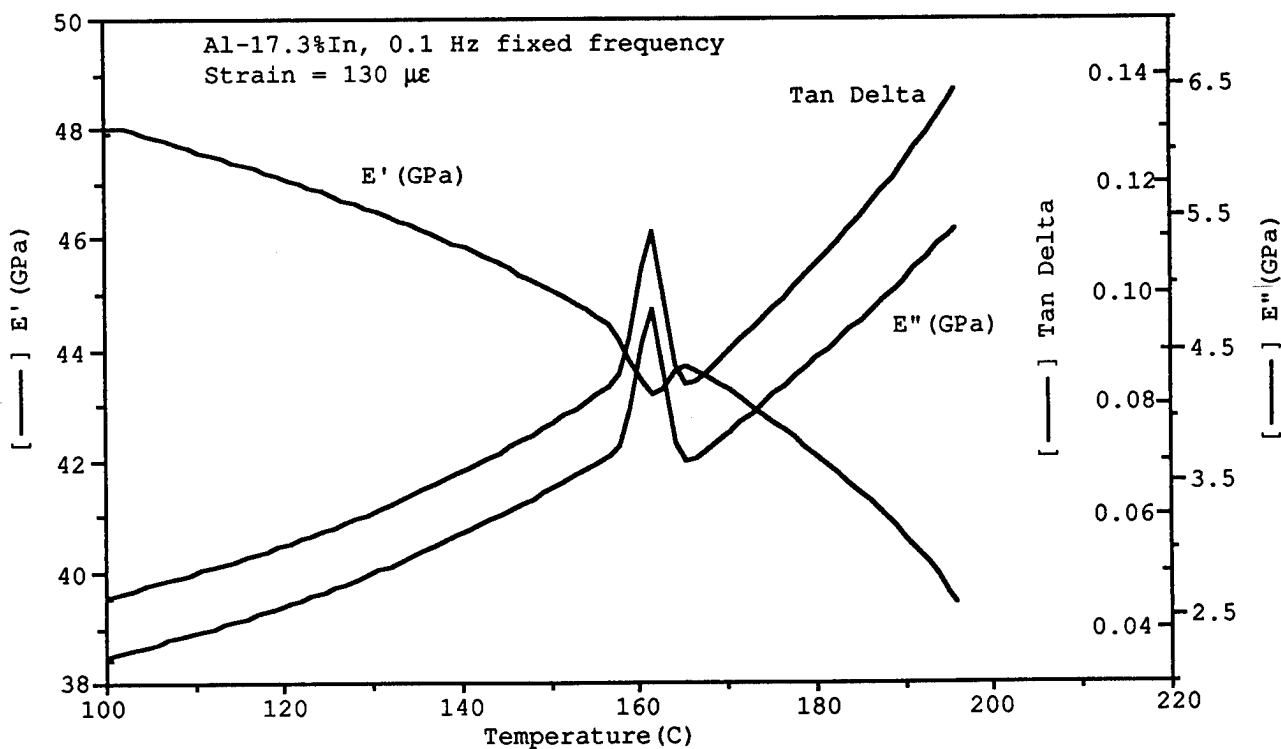


Fig. 11: DMA results for the Al-17.3In alloy at a frequency of 0.1 Hz demonstrating a larger damping peak to background ratio at lower frequencies.

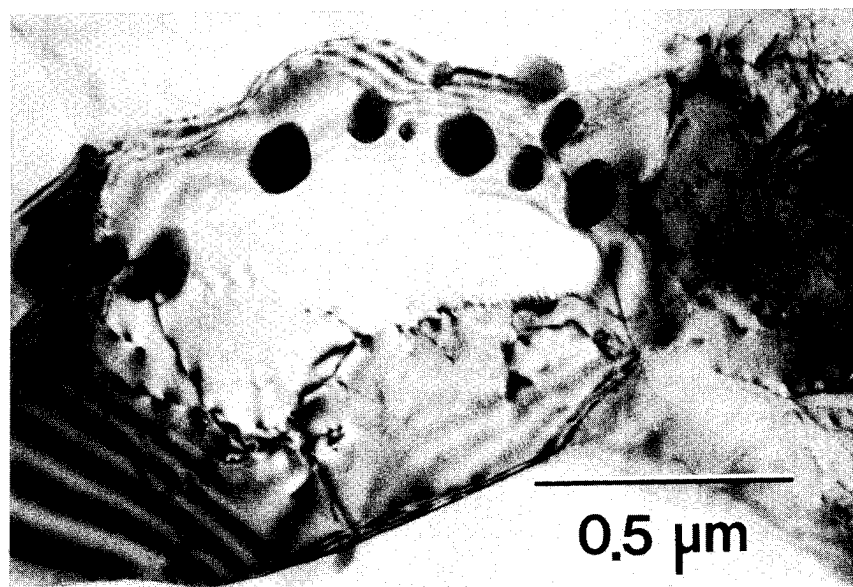


Fig. 12: Bright field transmission electron micrograph of the Al-0.6In alloy showing indium particles on a subgrain boundary.

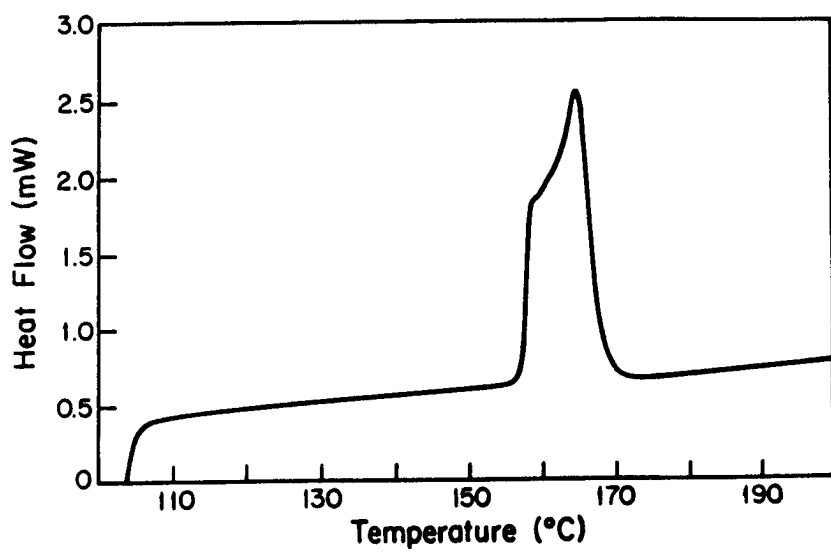


Fig. 13: DSC results for the Al-12In alloy indicating a second melting peak due to a fine structure of indium particles which melt at a higher temperature.

DAMPING CAPACITY OF ALUMINUM 6061-INDIUM ALLOYS.

C.R. Wong, D.C. Van Aken*, and O. Diehm*

David Taylor Research Center
Physical Metallurgy Branch
Code 2812
Annapolis, MD 21402-5067

*Dept. Materials Science and Engineering
University of Michigan
Ann Arbor, MI 48109-2136

ABSTRACT

Type 6061 aluminum alloys containing between 0 and 5.2 volume percent indium and pure indium samples were fabricated. Each sample was characterized by metallographic and analytical electron microscopy and the damping capacity and storage modulus was measured. The model proposed by L.G. Nielsen was used to calculate the damping capacity and storage modulus of the alloys using the damping capacity and storage modulus of the constituents. The damping capacity of the Al-6061-In-T6 alloys were higher than the Al-6061-T6 alloy and increased with increasing indium content. The Nielsen model gave a good first approximation of the damping capacity and storage modulus of the alloys.

DAMPING CAPACITY OF ALUMINUM 6061-INDIUM ALLOYS.

C.R. Wong, D.C. Van Aken*, and O. Diehm*

David Taylor Research Center
Physical Metallurgy Branch
Code 2812
Annapolis, MD 21402-5067

*Dept. Materials Science and Engineering
University of Michigan
Ann Arbor, MI 48109-2136

ABSTRACT

Type 6061 aluminum alloys containing between 0 and 5.2 volume percent indium and pure indium samples were fabricated. Each sample was characterized by metallographic and analytical electron microscopy and the damping capacity and storage modulus was measured. The model proposed by L.G. Nielsen was used to calculate the damping capacity and storage modulus of the alloys using the damping capacity and storage modulus of the constituents. The damping capacity of the Al-6061-In-T6 alloys were higher than the Al-6061-T6 alloy and increased with increasing indium content. The Nielsen model gave a good first approximation of the damping capacity and storage modulus of the alloys.

INTRODUCTION

An important characteristic of a structural material is it's damping capacity. While metallic materials exhibit adequate stiffness for structural use, the damping capacity may be quite low, having a typical loss factor on the order of 10^{-4} . In contrast, polymeric materials will exhibit very high damping, with loss factors on the order of one, but rather low stiffness. Their stiffness can be increased with the use of fillers and fibers but the resultant resin matrix composites exhibit lower damping properties, with loss factors on the order of 10^{-2} . Attempts made to improve the damping response of the resin matrix composite by adding rubber did not result in significant improvements [1]. It was shown that synergistic effects from interactions between the rubber and the resin were responsible for the lower than expected damping behavior.

In the case of metal matrix composites, work by Ray, Kinra, Rawal and Misra has shown that the damping of aluminum alloy 6061 is increased by the addition of graphite fibers [2]. However, the increase in damping was low considering the high volume fraction (0.34) of graphite. Recent work by Diehm, Wong and Van Aken has shown that the addition of a viscoelastic inclusion (indium) to pure aluminum will produce high damping materials [3], but it was uncertain whether the principal damping resulted from the matrix or the inclusion since both have high damping capacities.

In the present paper the addition of indium to an age-hardening alloy, such as 6061 aluminum, was examined in order to discriminate between inclusion and matrix damping. The dynamic properties of pure (99.99%) indium and 6061-T6 aluminum alloy were determined. The dynamic properties of the composite were calculated by using the values of the monolithic material in the composite model proposed by L.G. Nielsen [4,5] and directly compared with the experimental results.

NIELSEN MODEL

The model developed by Nielsen [4] predicts the complex modulus of isotropic two phase materials with arbitrary phase geometry. It is based on a continuum mechanics composite sphere assemblage model but is semi-empirical. The model assumes that the alloy is isotropic, strained only in the elastic range, and is phase symmetric, that is both the matrix and second phase geometries are identical at equal respective volume concentrations. Equations 1-4 below, from Nielsen's model [5], calculate Young's modulus of the alloy, E_y , using the Young's moduli of the matrix, E_y^s , and second phase, E_y^i , and the volume concentration, c . The volume concentration = $\frac{V^i}{(V^s + V^i)}$ where V^i and V^s are the volumes of the second phase and matrix respectively.

$$E_y = e E_y^s \quad \text{eq.1}$$

where e is the relative Young's modulus of the alloy.

$$e = \frac{n + \gamma + \gamma c(n - 1)}{n + \gamma - c(n - 1)} \quad \text{eq.2}$$

where n is the relative stiffness and γ is the shape function.

$$n = \frac{E_y^i}{E_y^s} \quad \text{eq.3}$$

$$\gamma = \frac{1}{2} \left\{ \rho [1 - c(1 - n)] + \sqrt{\rho^2 [1 - c(1 - n)]^2 + 4n(1 - \rho)} \right\} \quad \text{eq.4}$$

and ρ is the shape factor which is dependent on the morphology of the composite.

The complex modulus of the matrix, E^s , and second phase, E^i , is defined as follows.

$$E^s = a^s + i b^s \quad \text{and} \quad E^i = a^i + i b^i \quad \text{eq.5}$$

where a and b are the storage and loss modulus respectively and the superscripts s and i refer to the matrix and second phase respectively. The conversion from Young's modulus equations to complex modulus equations is accomplished with the use of the correspondence principle. The complex moduli from equation 5 are substituted for the Young's moduli in equations 1 and 3 and the real and imaginary parts are separated. Starting with equation 3 we have

$$n = \frac{E^i}{E^s} = \frac{a^i + i b^i}{a^s + i b^s} = \frac{(a^i + i b^i)(a^s - i b^s)}{(a^s + i b^s)(a^s - i b^s)} = \frac{a^i a^s + b^i b^s}{(a^s)^2 + (b^s)^2} + \frac{i(a^s b^i - a^i b^s)}{(a^s)^2 + (b^s)^2}$$

$$\text{Let } n = A + Bi \quad \text{where } A = \frac{a^i a^s + b^i b^s}{(a^s)^2 + (b^s)^2} \quad B = \frac{a^s b^i - a^i b^s}{(a^s)^2 + (b^s)^2} \quad \text{eq.6}$$

Now recalling equation 4

$$\gamma = \frac{1}{2} \left\{ \rho [1 - c(1 - n)] + \sqrt{\rho^2 [1 - c(1 - n)]^2 + 4n(1 - \rho)} \right\}$$

Upon substituting equation 6 the first part of equation 4 becomes

$$\rho[1 - c(1 - n)] = \rho - \rho c + \rho cn = \rho - \rho c + \rho cA + \rho cBi \quad \text{eq.7}$$

The second part of equation 4 is $\sqrt{\rho^2[1 - c(1 - n)]^2 + 4n(1 - \rho)}$

$$\begin{aligned} [1 - c(1 - n)]^2 &= 1 - 2c(1 - n) + c^2(1 - n)^2 \\ &= 1 - 2c + 22n + c^2 - 2c^2n + c^2n^2 \\ &= 1 - 2c + c^2 + (2c - 2c^2)n + c^2n^2 \end{aligned}$$

$$\text{since } n^2 = (A + iB)(A + iB) = A^2 - B^2 + 2ABi$$

$$\text{then } [1 - c(1 - n)]^2 = (1 - 2c + c^2) + (2c - 2c^2)A + c^2(A^2 - B^2) + i[(2c - 2c^2)B + 2c^2AB]$$

$$\text{therfore } \sqrt{\rho^2[1 - c(1 - n)]^2 + 4n(1 - \rho)}$$

$$\begin{aligned} &= \left\{ \rho^2[1 - 2c + c^2 + (2c - 2c^2)A + c^2(A^2 - B^2)] \right. \\ &\quad \left. + i\rho^2[(2c - 2c^2)B + 2c^2AB] + 4A(1 - \rho) + i4B(1 - \rho) \right\}^{\frac{1}{2}} \\ &= \left\{ \rho^2[1 - 2c + c^2 + 2c(1 - c)A + c^2(A^2 - B^2)] \right. \\ &\quad \left. + 4A(1 - \rho) + i[\rho^22c(1 - c)B + 2c^2AB\rho^2 + 4B(1 - \rho)] \right\}^{\frac{1}{2}} \end{aligned}$$

$$\text{Let } \sqrt{\rho^2[1 - c(1 - n)]^2 + 4n(1 - \rho)} = [\alpha + i\beta]^{\frac{1}{2}} \quad \text{eq.8}$$

$$\text{where } \alpha = \rho^2[(c - 1)^2 - 2c(c - 1)A + c^2(A^2 - B^2)] + 4A(1 - \rho) \quad \text{eq.9}$$

$$\text{and } \beta = \rho^22c(1 - c)B + 2c^2AB\rho^2 + 4B(1 - \rho) \quad \text{eq.10}$$

In order to find the square root we change coordinates.

$$r = (\alpha^2 + \beta^2)^{\frac{1}{2}} \quad \text{eq.11}$$

$$\theta = \arctan \left(\sqrt{\frac{\beta}{\alpha}} \right) \quad \text{eq.12}$$

substituting equations 11 and 12 into equation 8 we have

$$\sqrt{\rho^2[1 - c(1 - n)]^2 + 4n(1 - \rho)} = r^{1/2}[\cos(\theta/2) + i\sin(\theta/2)] = r^{1/2}e^{i\theta/2} \quad \text{eq.13}$$

Combining equations 7 and 13 gives the complex shape function, γ^* .

$$\gamma^* = \frac{1}{2} \left\{ \rho[1 - c(1 - A)] + \rho c Bi + r^{1/2}e^{i\theta/2} \right\} \quad \text{eq.14}$$

Substituting the complex values of γ from equation 14 and the complex values of n from equation 6 into equation 2 gives the complex relative modulus, e^* .

$$\begin{aligned} e^* &= \frac{n + \gamma^* + \gamma^*c(n - 1)}{n + \gamma^* - c(n - 1)} = \frac{n + \gamma^* + cn\gamma^* - \gamma^*c}{n + \gamma^* - cn + c} \\ &= \frac{A + \operatorname{Re}(\gamma^*) - c\operatorname{Re}(\gamma^*) + c[A\operatorname{Re}(\gamma^*) - B\operatorname{Im}(\gamma^*)]}{(A + \operatorname{Re}(\gamma^*) - cA + c) + i(B + \operatorname{Im}(\gamma^*) - cB)} \\ &\quad + \frac{i \left\{ B + \operatorname{Im}(\gamma^*) - c\operatorname{Im}(\gamma^*) + c[A\operatorname{Im}(\gamma^*) + B\operatorname{Re}(\gamma^*)] \right\}}{(A + \operatorname{Re}(\gamma^*) - cA + c) + i(B + \operatorname{Im}(\gamma^*) - cB)} \end{aligned} \quad \text{eq.15}$$

$$\text{Let } \xi = A + \operatorname{Re}(\gamma^*) - c\operatorname{Re}(\gamma^*) + c[A\operatorname{Re}(\gamma^*) - B\operatorname{Im}(\gamma^*)] \quad \text{eq.16}$$

$$\text{and } \eta = B + \operatorname{Im}(\gamma^*) - c\operatorname{Im}(\gamma^*) + c[A\operatorname{Im}(\gamma^*) + B\operatorname{Re}(\gamma^*)] \quad \text{eq.17}$$

and substitute into equation 15.

$$\begin{aligned} e^* &= \frac{\xi + \eta i}{(A + \operatorname{Re}(\gamma^*) - cA + c) + i(B + \operatorname{Im}(\gamma^*) - cB)} \\ &= \frac{(\xi + i\eta)[(A + \operatorname{Re}(\gamma^*) - cA + c) - i(B + \operatorname{Im}(\gamma^*) - cB)]}{(A + \operatorname{Re}(\gamma^*) - cA + c)^2 + (B + \operatorname{Im}(\gamma^*) - cB)^2} \\ &= \frac{\xi(A + \operatorname{Re}(\gamma^*) - cA + c) + \eta(B + \operatorname{Im}(\gamma^*) - cB)}{(A + \operatorname{Re}(\gamma^*) - cA - c)^2 + (B + \operatorname{Im}(\gamma^*) - cB)^2} \\ &\quad + \frac{i\eta(A + \operatorname{Re}(\gamma^*) - cA + c) - \xi(B + \operatorname{Im}(\gamma^*) - cB)}{(A + \operatorname{Re}(\gamma^*) - cA - c)^2 + (B + \operatorname{Im}(\gamma^*) - cB)^2} \end{aligned} \quad \text{eq.18}$$

Finally the complex modulus of the alloy is found by combining equations 1, 5 and 18.

$$\begin{aligned} E^i &= e^*E^s = \operatorname{Re}(e^*)a^s - \operatorname{Im}(e^*) + i[\operatorname{Im}(e^*) + \operatorname{Re}(e^*)b^s] \\ &= \frac{a^s[\xi(A + \operatorname{Re}(\gamma^*) - cA + c) + \eta(B + \operatorname{Im}(\gamma^*) - cB)]}{(A + \operatorname{Re}(\gamma^*) - cA - c)^2 + (B + \operatorname{Im}(\gamma^*) - cB)^2} \\ &\quad - \frac{b^s[\eta(A + \operatorname{Re}(\gamma^*) - cA + c) - \xi(B + \operatorname{Im}(\gamma^*) - cB)]}{(A + \operatorname{Re}(\gamma^*) - cA - c)^2 + (B + \operatorname{Im}(\gamma^*) - cB)^2} \\ &\quad + i \left\{ \frac{a^s[\eta(A + \operatorname{Re}(\gamma^*) - cA + c) - \xi(B + \operatorname{Im}(\gamma^*) - cB)]}{(A + \operatorname{Re}(\gamma^*) - cA - c)^2 + (B + \operatorname{Im}(\gamma^*) - cB)^2} \right. \\ &\quad \left. + \frac{b^s[\xi(A + \operatorname{Re}(\gamma^*) - cA + c) + \eta(B + \operatorname{Im}(\gamma^*) - cB)]}{(A + \operatorname{Re}(\gamma^*) - cA - c)^2 + (B + \operatorname{Im}(\gamma^*) - cB)^2} \right\} \end{aligned} \quad \text{eq.19}$$

Where the real of equation 19 is the storage modulus of the composite and the imaginary part of equation 19 is the loss modulus.

EXPERIMENTAL PROCEDURE

Aluminum 6061 alloys with additions of 0 to 12 weight percent indium were prepared by plasma arc-melting. The starting alloys were pure indium (99.99%) and 6061 alloy. The chemical composition of the alloys were determined by wet-chemistry. The volume fraction of indium was calculated using the weight fraction and density of each alloy by assuming complete immiscibility between aluminum and indium. The arc-melted ingot was then reduced 60 to 80% in thickness, by repeatedly cold-working 20 to 30% and annealing, to produce a flat sample with a nominal thickness of 1.5 mm. The alloys were given a T6 temper consisting of solution treatment at 532 °C (990 °F) and aging 193 °C (380 °F) for 7 hours. Samples of pure indium were likewise plasma arc-melted and rolled.

Each sample was characterized by metallographic and analytical electron microscopy. Electron microscopy studies were performed at the University of Michigan Electron Microbeam Analysis Laboratory. Thin foils for transmission electron microscopy were prepared by twin jet electropolishing in a solution of 20% nitric acid (by volume) and methanol.

The damping capacity and modulus of the samples were measured with a Polymer Laboratories Dynamic Mechanical Thermal Analyzer (DMTA) located at the Naval Research Laboratory. The DMTA uses a fixed-guided cantilever arrangement where the left clamp holds the sample to a stationary frame while the right clamp attaches the sample to the drive shaft. A small sinusoidal mechanical stress is applied to a cantilevered sample and the resulting sinusoidal strain is transduced. Comparison of the amplitude of the stress, σ , and strain, ϵ , signals yields the storage modulus, a , and the phase lag of strain behind the stress gives the phase angle, δ . The complex modulus, E , and loss modulus b are calculated using the following equation:

$$a(1 + i \tan \delta) = E = a + ib \quad \text{eq. 20}$$

where $\tan \delta$ is the loss factor. The frequency of the vibrations was cycled between .1, 1 and 10 Hz while the temperature was increased one degree C per minute from 20 °C (68 °F) to 100 °C (212 °F). Each sample was measured at least twice to check the consistency of the measurements.

RESULTS

The measured chemical composition and the calculated volume fraction of indium are presented in table 1. The volume percent varied from 0 to 5.2. The microstructures of the indium containing alloys are shown in Fig. 1. A uniform dispersion of indium particles was found in all the samples with the individual areas of indium increasing in size and number with the increase in volume percent. The micrographs show the indium phase to be roughly spherical. Examination of the age-hardened matrix using transmission electron microscopy revealed that the age-hardening process was affected by the addition of indium. A typical 6061 T6 microstructure consists of a uniform distribution of Guinier-Preston zones (GPZ) and β' (rod shaped Mg_2Si) precipitates in the aluminum matrix as shown in Fig. 2a. The diffraction conditions are optimized in Figs. 2a and 2b to show the β'

precipitates. The aged microstructures of the alloys, containing 1.4, 1.7, and 5.2 volume percent indium are shown in Figs. 2b to 2d. It is apparent that the aging kinetics have been affected by the additions of indium. The general trend is that the precipitation of β' is inhibited and the volume fraction of second phase is reduced. Only the GPZ's are observed in the 1.7 and 5.2% alloys.

The results of the DMTA testing are shown as plots of loss modulus, ($\tan \delta$), versus the storage modulus on logarithmic axis in order to eliminate temperature and frequency measurement error from the data. As the temperature was increased from 20 °C to 100 °C the loss factor increased as the storage modulus decreased. The measurements of pure indium and the 6061 T6 alloy are shown in Fig. 3. For the temperature range tested, the storage modulus of the 6061 T6 alloy did not vary significantly from 71 GPa while the storage modulus of the indium varied from 2 GPa at room temperature to 0.9 GPa at 100 °C. The loss factor of the 6061 T6 alloy was approximately 0.002 which is typical of precipitation hardened aluminum alloys. In contrast the pure indium alloy exhibited high damping with the loss factor ranging from 0.06 to 0.2 at 100 °C. It was generally observed that the storage modulus decreased and the loss factor increased with increasing addition of indium as shown in Fig. 4. The storage modulus of the sample containing 5.2 volume percent indium exhibited a more dramatic change than alloys containing less than 3.2 volume percent indium, as illustrated in Fig. 4. The loss factor of the 5.2 volume percent indium alloy at room temperature was measured to be 0.01. This was likely due to increased continuity of the indium phase.

The storage modulus and loss factor were calculated with the Nielsen model using the data from the monolithic material in equations 19 and 20 and a shape factor of one. A shape factor of one describes round second phase areas completely surrounded by the matrix. The results of these calculations are presented in Fig. 5. The calculated and measured values of the 0 volume percent indium alloy are constrained to be equal. Comparing the calculated values to the measured values as in Fig. 6 and 7 it is obvious that although the calculated values show the same trends as the measured values, they consistently overestimate both the measured storage modulus and the loss factor of the alloys. For the alloys containing less than 3.2 volume percent the storage modulus is only overestimated by 2% and the loss factor is overestimated by 30%. However, in the case of the 5.2 volume percent indium alloy the storage modulus was overestimated by more than 100% while the loss factor was overestimated by 60%. These results may indicate a synergistic effect such as the partitioning of alloying elements present in the 6061 material to the indium.

DISCUSSION

High damping aluminum alloys may be obtained by the addition of a viscoelastic inclusion. In the present case a volume fraction of at least 0.05 is required to produce an alloy with a loss factor greater than 0.01. However, there is a significant loss of stiffness associated with the addition of the indium and there appears to be a synergistic effect between the matrix and the inclusion. The aged 6061-T6 microstructure shows a decreasing precipitate density with increasing indium content and the measured loss factors are much less than the

calculated values based on the damping capacities of the monolithic samples. It is tempting to speculate that these observations are related. Indeed, the solubility of magnesium in indium is greater than 30 atomic percent at the T6 aging temperature used in this experiment [6]. Thus the low volume fraction of precipitates may be related to the partitioning of magnesium to the indium inclusions. Furthermore, the indium-magnesium inclusions may have a lower damping capacity than the pure indium. If indeed the damping of the indium inclusion is a strain dependent mechanism, such as dislocation motion, the addition of solute atoms will result in a lower loss factor for a comparable cyclic strain.

The Nielsen model failed to predict the dynamic properties of indium containing 6061-T6 alloys, but did provide a good first approximation. Future modeling of this system will use the dynamic properties measured from monolithic indium-magnesium alloys to compensate for the synergistic effects encountered and the shape factor will be varied in an attempt to compensate for non-spherical inclusions.

CONCLUSIONS

Additions of indium, a viscoelastic second phase particle, to 6061-T6 aluminum, a stiff matrix, have resulted in an increased damping capacity while still maintaining most of the stiffness of the matrix. The measured and calculated values agree that damping capacity increases and the storage modulus decreases with increasing indium content. The Nielsen model is a good first approximation for both the prediction of the maximum damping capacity and stiffness of a particular alloy system and the tailoring of alloys to obtain the damping capacity and stiffness required by a given application.

ACKNOWLEDGMENTS

The assistance of Dr. M.A. Imam and Mr. K. Robinson of the Naval Research Laboratory with the operation of the DMTA and Mr. J. Newton of the University of Missouri Dept. of Physics with the complex algebra is greatly appreciated.

REFERENCES

1. G. Rohrauer, S.V. Hoa and D. Feldman, 5th Inter. Conf. Composite Materials, Eds. Harrigan, Strife, and Dhingra, The Minerals, Metals & Materials Society, (1986) p. 1683.
2. A.K. Ray, V.K. Kinra, S.P. Rawal, and M.S. Misra, Role of Interfaces on Material Damping, Eds. B.B. Rath and M.S. Misra, ASM International, (1985) p. 95.
3. O. Diehm, C.R. Wong, and D.C. Van Aken, this conference proceedings, JDAL.
4. Nielsen, L.G. "Elastic Properties of Two-phase Materials", Materials Science and Engineering, Vol. 52 (1982) p. 39.
5. Nielsen, L.G. "Elasticity and Damping of Porous Materials and Impregnated Materials", J. Amer. Ceramic Soc., Vol. 67 No. 2, (1984) p. 93.
6. A.A. Nayeb-Hashemi and J.B. Clark, Bull. Alloy Phase Diagrams, Vol. 6, (1985) p. 2

Table 1. Chemical Compositions of 6061-T6 Aluminum Alloys

Calculated Volume Percent	Measured Weight Percent						
	Indium	Magnesium	Chromium	Silicon	Copper	Iron	Aluminum
0.00	0.00	0.77	0.048	0.71	0.26	0.23	98 97
0.78	2.08	0.74	0.047	0.83	0.27	0.25	95.78
1.43	3.77	0.70	0.046	0.76	0.26	0.24	94.22
1.67	4.37	0.67	0.045	0.73	0.25	0.22	93.72
2.16	5.63	0.70	0.044	0.75	0.26	0.22	92.40
2.66	6.87	0.73	0.045	0.71	0.25	0.21	91.19
3.20	8.20	0.73	0.041	0.70	0.28	0.22	89.83
5.16	12.80	0.70	0.042	0.64	0.23	0.20	85.39

FIG. 1 MICROSTRUCTURES OF 6061-T6 ALUMINUM WITH 1.4 - 5.2 VOLUME PERCENT INDIUM

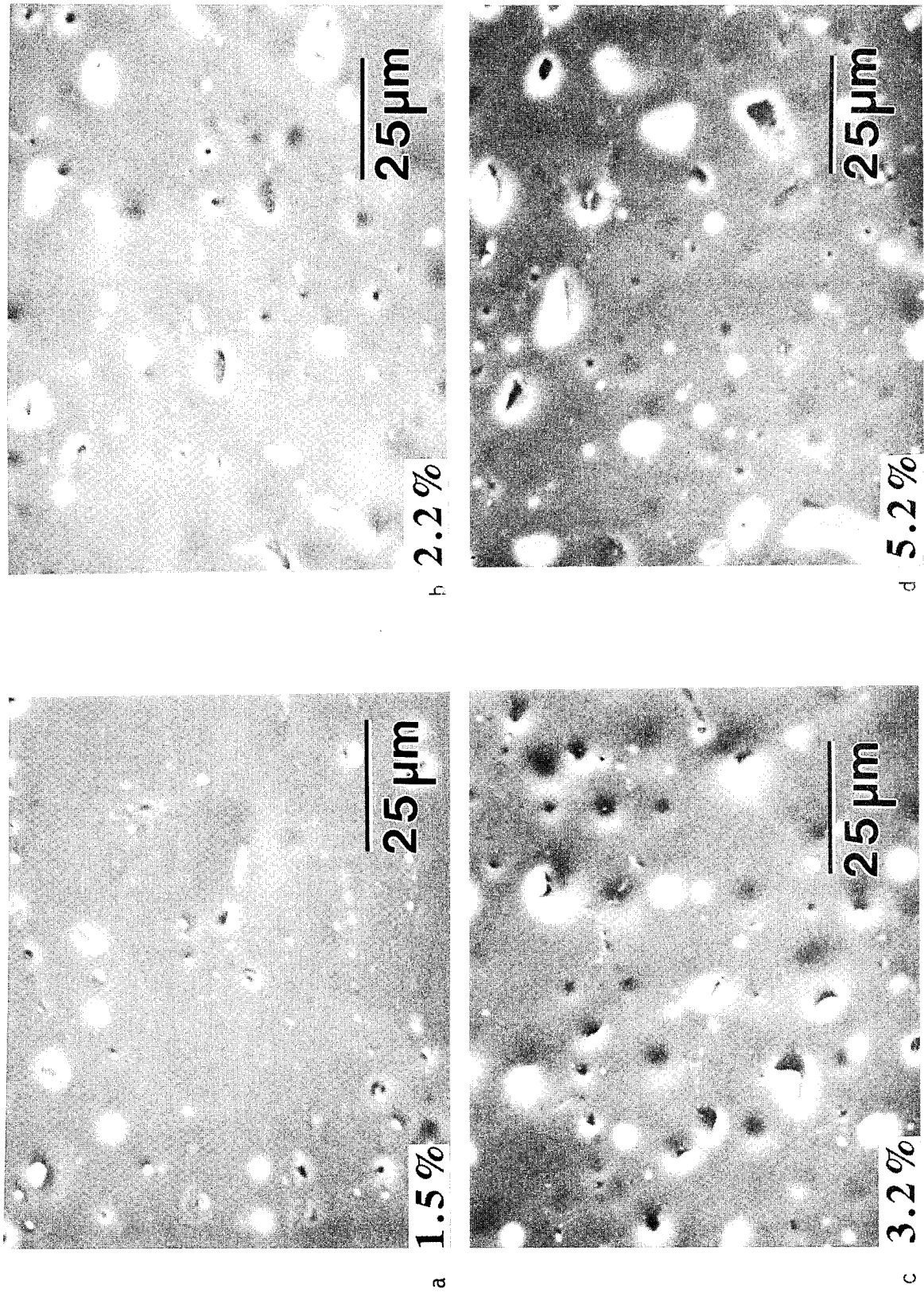
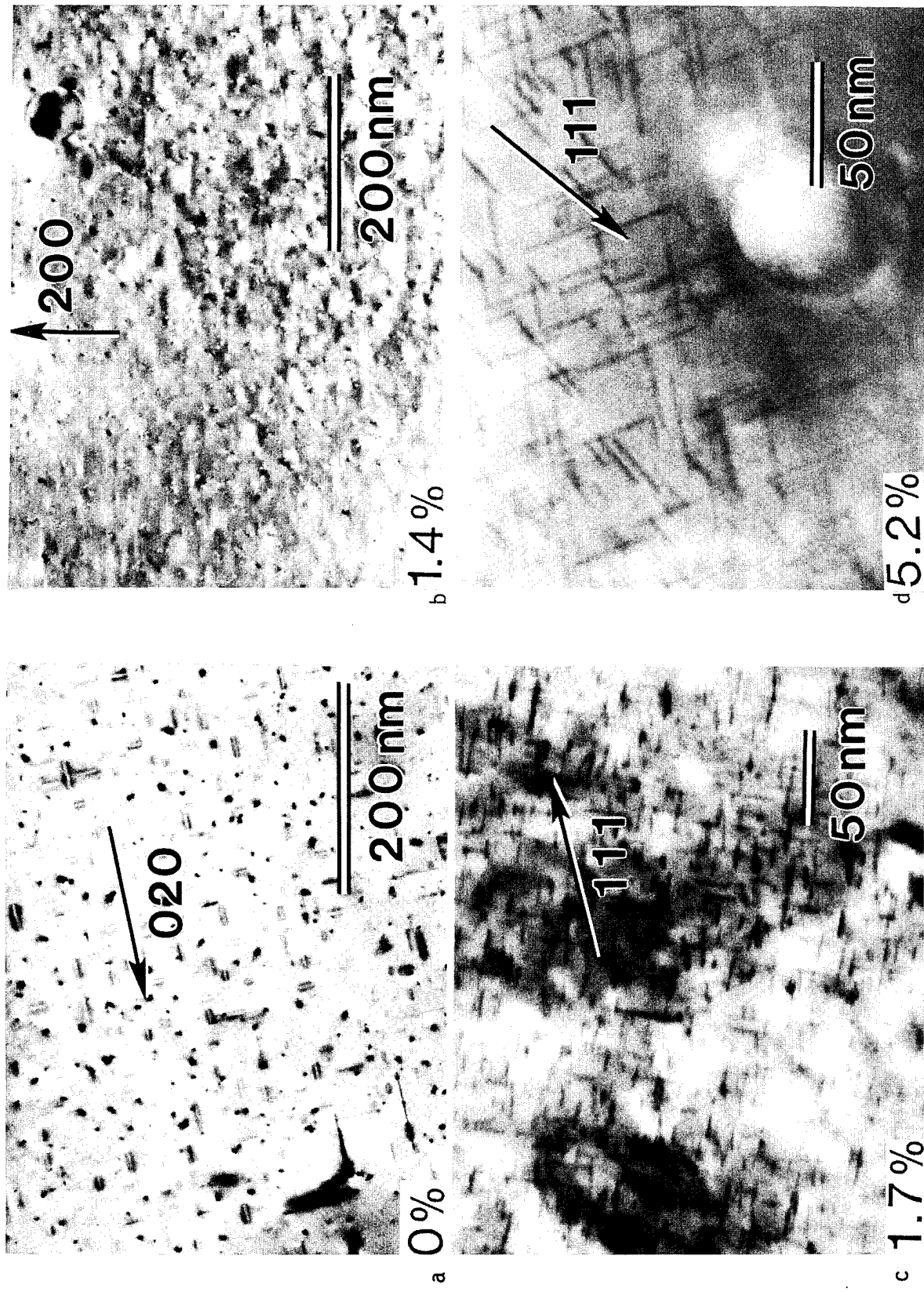


FIG. 2 PRECIPITATES IN 6061-T6 ALUMINUM WITH 0 - 5.2 VOLUME PERCENT INDIUM



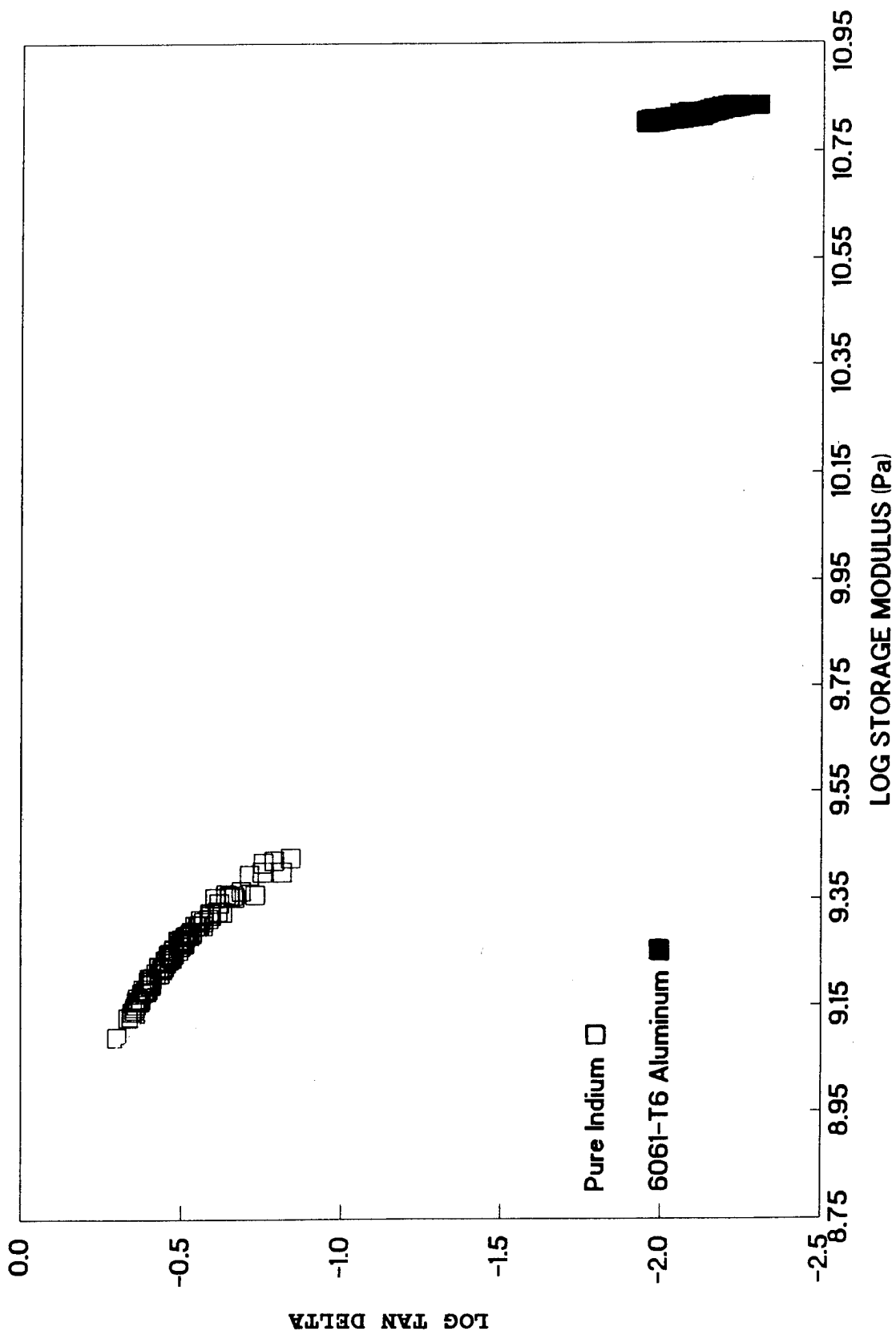


Fig. 3. Measured Values of the Loss Factor and Storage Modulus of the Monolithic Materials.

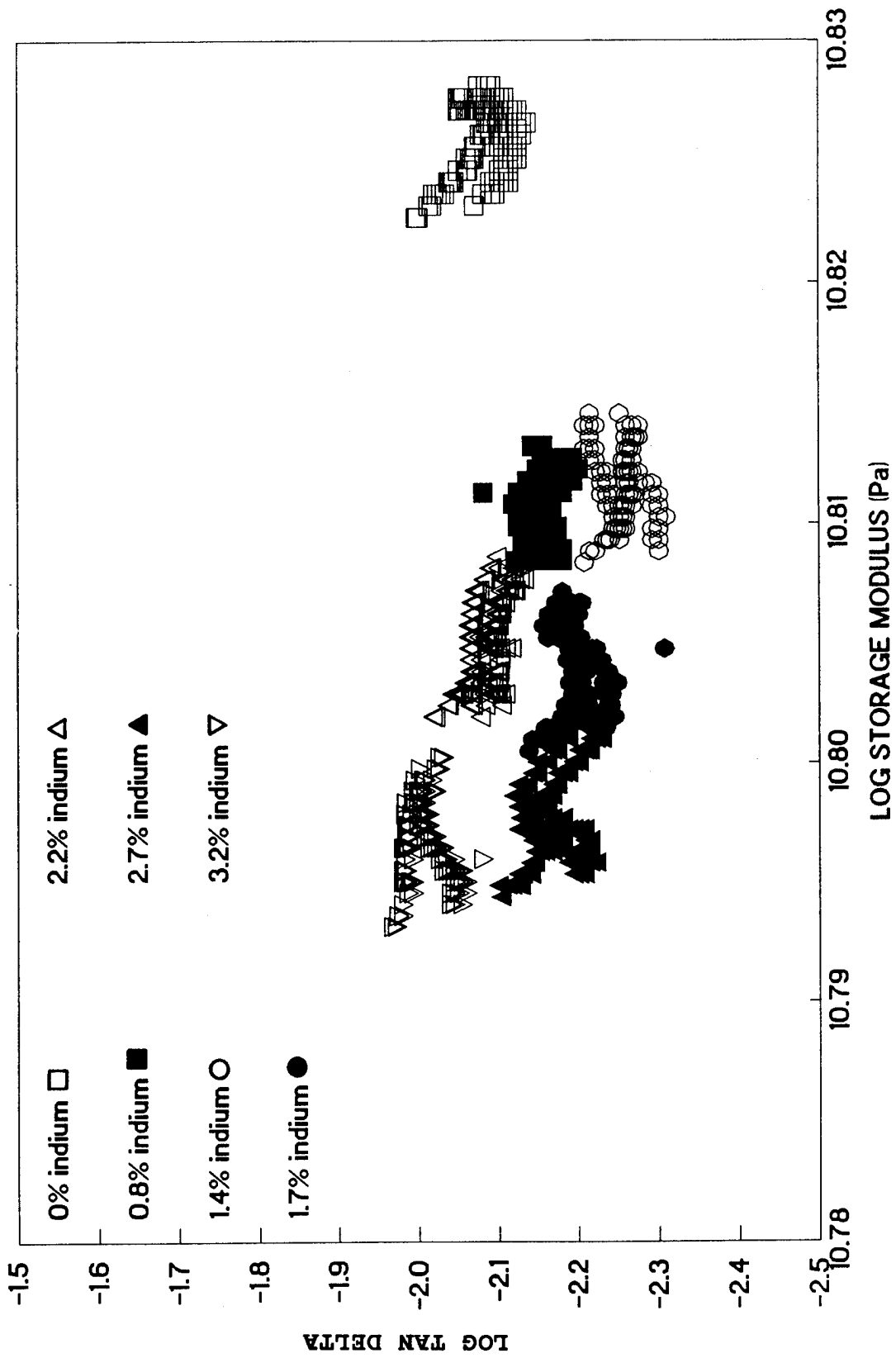


Fig. 4. Measured Values of the Loss Factor and Storage Modulus of 6061 Aluminum with 0 to 3.2 Volume Percent Indium.

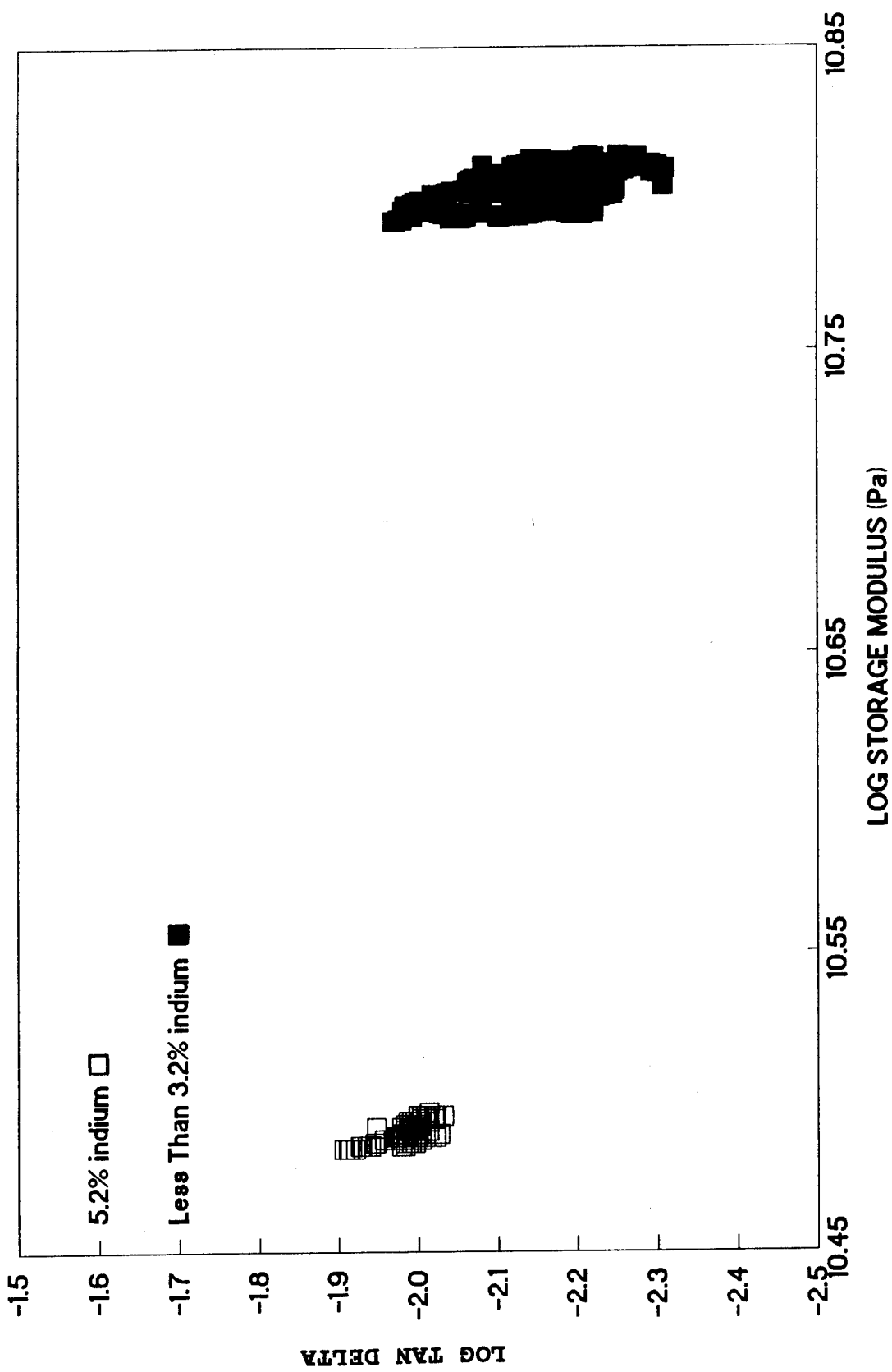


Fig. 5. Measured Values of the Loss Factor and Storage Modulus of 6061 Aluminum with 0 to 5.2 Volume Percent Indium.

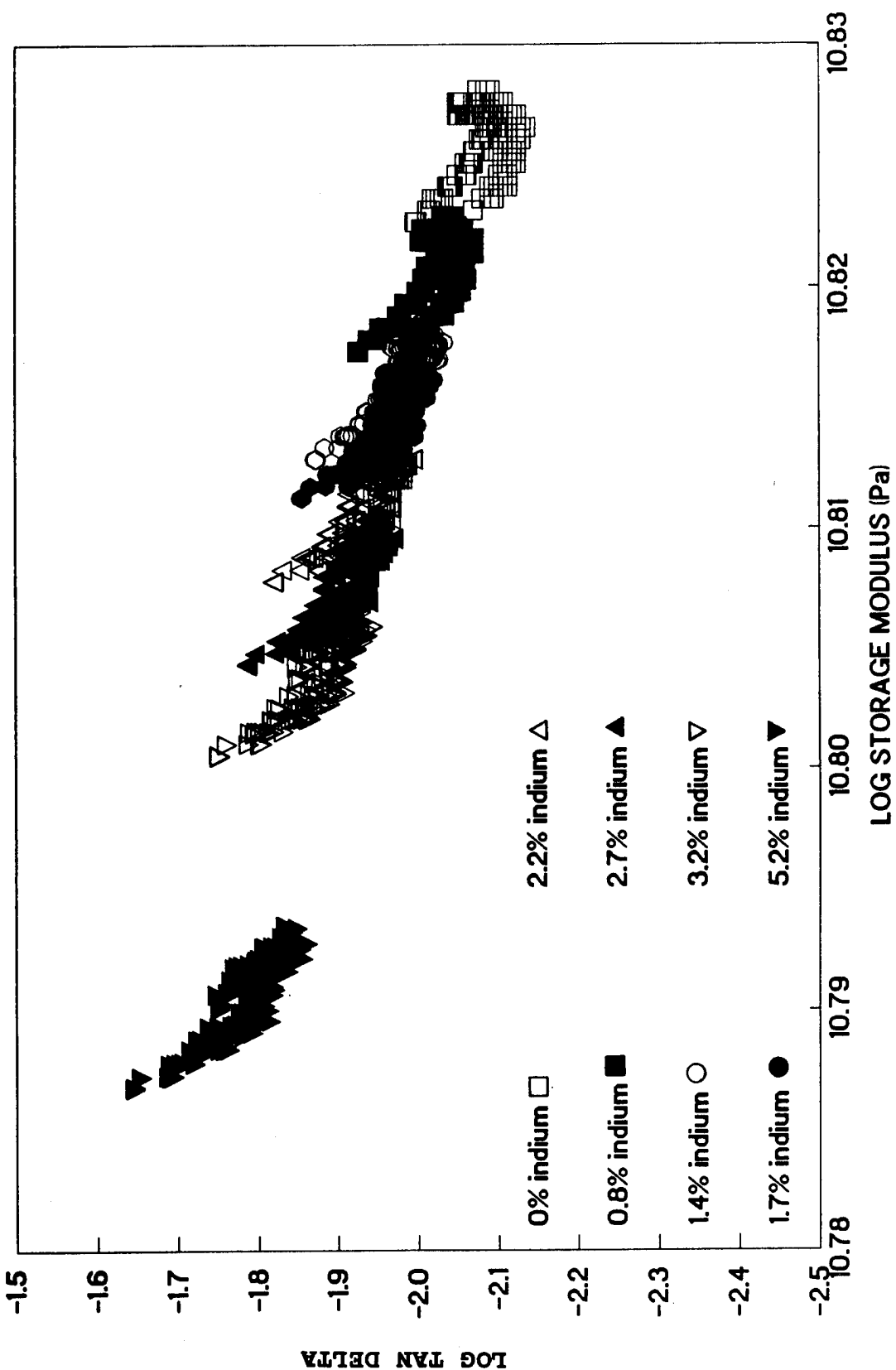


Fig. 6. Calculated Values of the Loss Factor and Storage Modulus of 6061 Aluminum with 0 to 3.2 Volume Percent Indium.

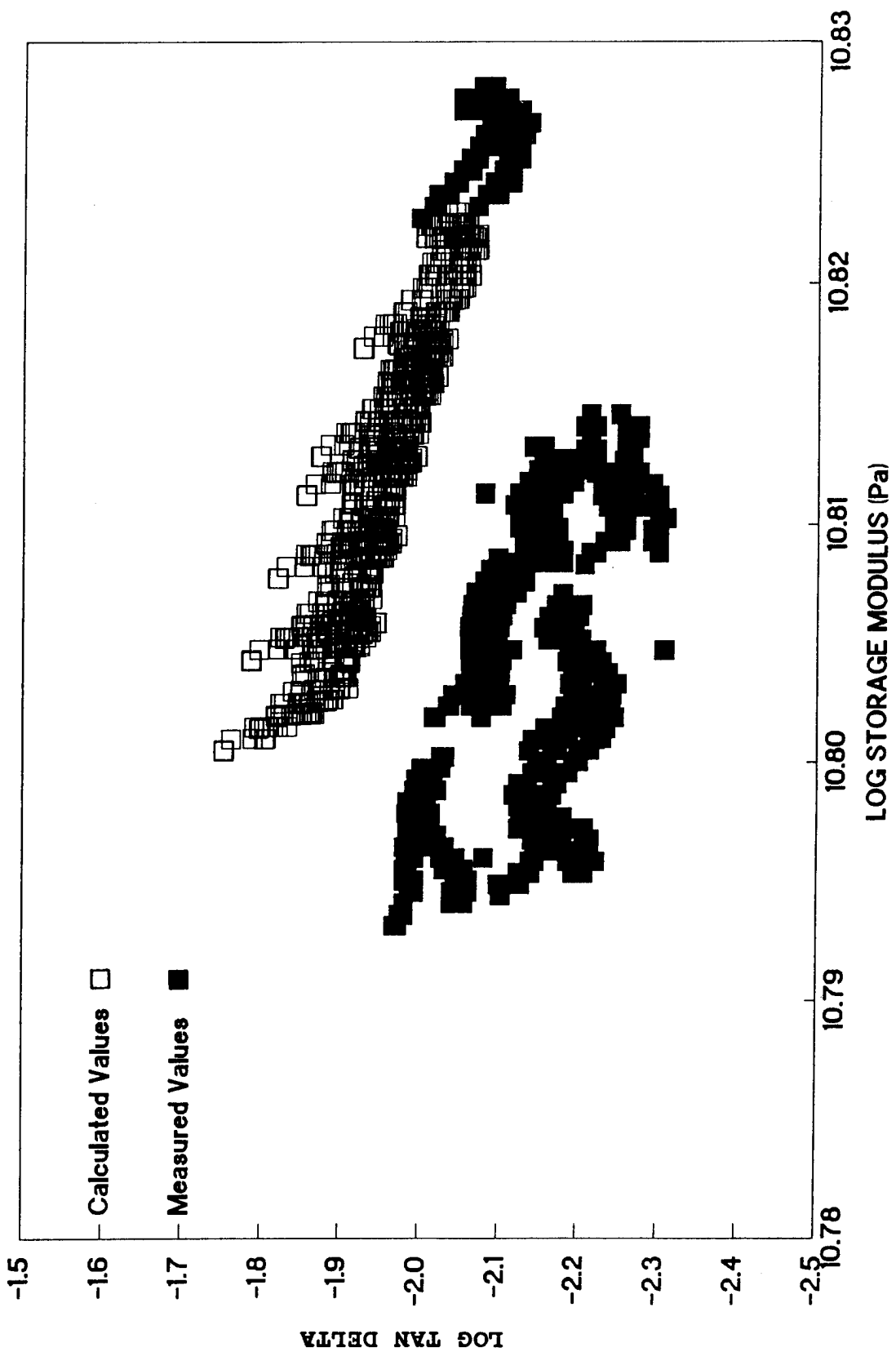


Fig. 7. Comparison of Measured and Calculated Values of the Loss Factor and Storage Modulus of 6061 Aluminum with 0 to 3.2 Volume Percent Indium.

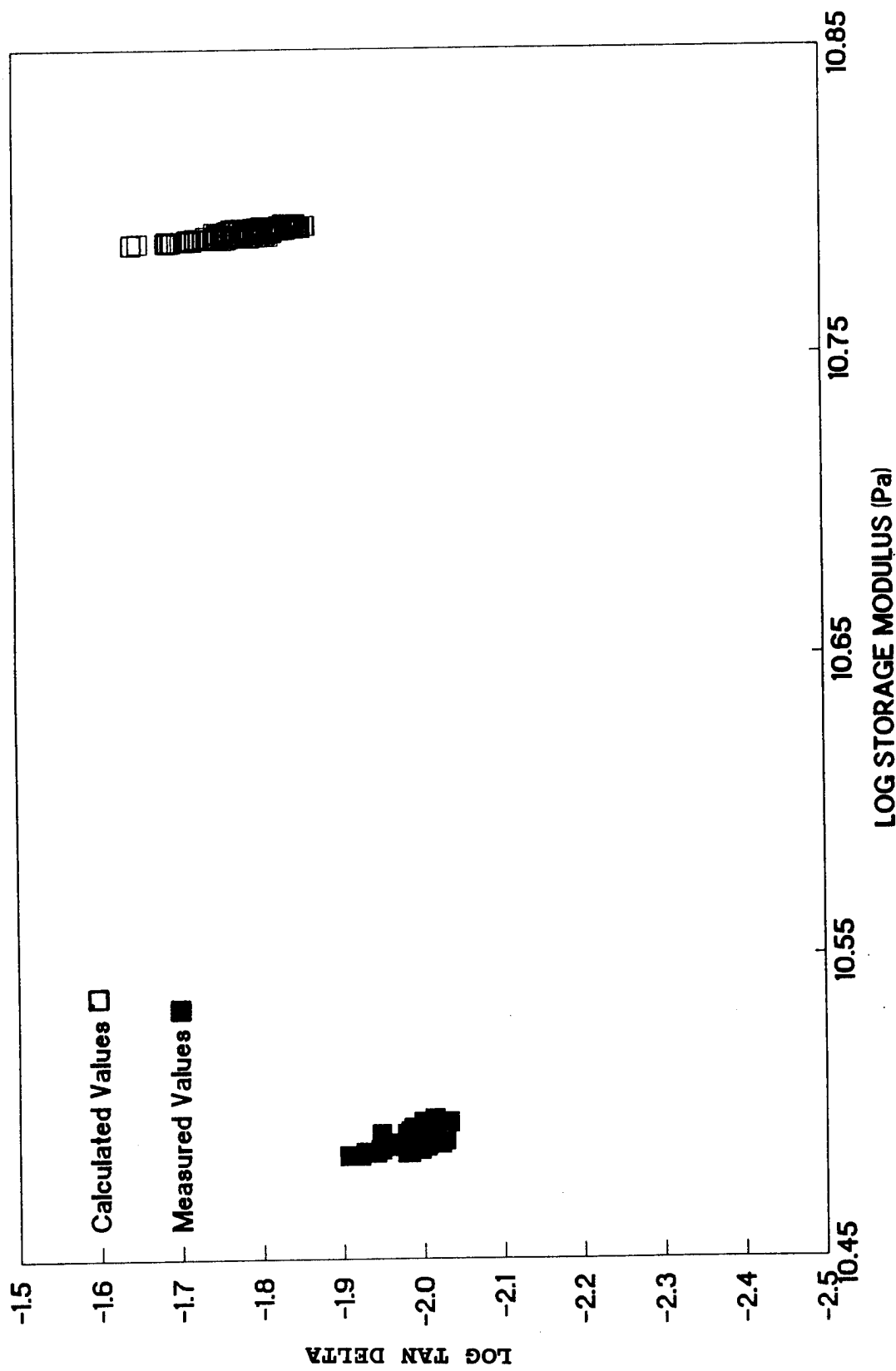


Fig. 8. Comparison of Measured and Calculated Values of the Loss Factor and Storage Modulus of 6061 Aluminum with 5.2 Volume Percent Indium.

INTERLABORATORY STUDY OF DAMPING CAPACITY IN LEADED BRASS AND LEAD-FREE BRASS

A. Wolfenden, T.G. Aldridge, Jr., and E.W. Davis, Jr.

*Mechanical Engineering Department
Texas A&M University
College Station, TX 77843 USA
(Tel: 409-845-4835)*

*V.K. Kinra and G. G. Wren
Aerospace Engineering Department
Texas A&M University
College Station, TX, 77843 USA
(Tel: 409-845-1667)*

*J.M. Wolla
Composites and Ceramics Branch (Code 6372)
Naval Research Laboratory
Washington, DC 20375 USA
(Tel: 202-767-3433)*

ABSTRACT

By pooling the resources of three laboratories, the damping in leaded brass and lead-free brass has been explored over a wide range of variables, including frequency (0.03 Hz to 80 kHz), strain amplitude (10^{-7} to 7×10^{-4}), temperature (25 to 400°C), and vibrational modes (longitudinal and flexure). For investigations at frequencies less than 50 Hz, cantilevered beams were tested, at frequencies in the range 0.03 to 200 Hz, fixed guided beams (Dynamic Mechanical Thermal Analyzer, DMTA) were used, while the high frequency (80 kHz) studies were performed with the PUCOT (Piezoelectric Ultrasonic Composite Oscillator Technique). The results from the DMTA experiments yielded an effective activation energy of about 1.67 eV/atom for the initiation of rapid increases in damping as a function of temperature. This value is close to the value of 1.7 eV/atom found by Youssef for the short-range ordering process of Zn and Cu atoms these type of alloys. The PUCOT results for the leaded brass revealed a strong damping peak near 327°C, the melting point of the lead inclusions. This peak is denoted as transient liquid phase (TLP) damping. The amplitude dependence data on leaded brass showed that the break away effect, where the amplitude independent damping changed to amplitude dependent damping, was temperature dependent, with a maximum break away stress of over 2 MPa near 270°C. This temperature was close to the 280°C value observed by Youssef for short-range ordering of Cu-Zn alloys. The PUCOT data agreed well with the earlier results of Wolfenden and Robinson on similar alloys. On the other hand, no damping peaks near 327°C were found for the lead-free brass. The results of this study confirmed that TLP damping is a mechanism that offers possibilities of enhancing the level of damping in alloys containing low melting point inclusions. Taking into consideration the thermoelastic (Zener) effects for flexural damping, the damping data from the three laboratories were compared to see if consistent and reliable results could be obtained.

INTRODUCTION

The search for materials with high stiffness and high intrinsic damping continues, driven by the needs of the aerospace and space industries, and by developments within the US Department of Defense. In this study, the intrinsic damping of materials is approached from a fundamental point of view. There is no standard technique for the measurement of damping and, as a result, several instruments that measure damping for different vibration modes over different ranges of temperature, strain amplitude, and frequency have been developed. To assess the accuracy, repeatability, and reliability of the experimental methods, specimens from the same stock have been tested and the corresponding data compared. This research focussed on the following areas: thermoelastic (Zener) damping, transient liquid phase (TLP) damping, dislocation break away phenomena, and short-range ordering effects. The basic aim of the present research was to measure and analyze the damping in brass as a function of temperature, frequency, strain amplitude, lead content, and vibration mode.

MATERIALS

For this study, two types if brass alloys were used: 1) lead-free brass and 2) leaded (free-machining) brass. The lead-free bar stock came in two compositions and thicknesses. Thick samples (3.18 mm original thickness) had a composition by weight of 59.1% Cu, 38.1% Zn, and less than 0.05% Pb. The thin bar stock (1.59 mm original thickness) had a composition of 68.8% Cu, 29.0% Zn, and less than 0.05% Pb. The composition by weight of the leaded brass was 61.4% Cu, 35.4% Zn, with 2.65% Pb. Specimen sizes were tailored for the three instruments used for the damping measurements.

INSTRUMENTATION

The three instruments used for the damping measurements were the Cantilevered Beam (CB), the Dynamic Mechanical Thermal Analyzer (DMTA), and the Piezoelectric Ultrasonic Composite Oscillator Technique (PUCOT). Details of these techniques have been reported elsewhere [1-5]. The typical sizes of the specimens used in the three instruments were 250 x 12 x 2.1 mm, 34 x 6 x 1 mm, and 50 x 2 x 1.6 mm, respectively. The CB technique performed damping measurements in the frequency range of 15 to 50 Hz, in a vacuum environment, and at room temperature. The DMTA was used for measurements at frequencies in the range of 0.03 to 200 Hz, at temperatures in the 25°C to 340°C range, and in an air environment. The PUCOT operated at 80 kHz, covering the temperature range of 25°C to 400°C, with the specimens in an air environment. The strain amplitudes for the three techniques were 5×10^{-5} , 5×10^{-4} to 8×10^{-4} , and 10^{-7} to 10^{-4} , respectively. The CB and DMTA instruments used the flexural vibration mode, while the PUCOT used the longitudinal vibration mode.

RESULTS AND DISCUSSION

1. CB Technique

Figures 1-6 show the damping as a function of applied frequency for leaded and lead-free brass. There are numerous definitions for damping in current use. For the CB technique, the applicable definition is:

$$\Psi = \Delta W/W, \quad (1)$$

where ΔW is the energy dissipated during one cycle and W is the maximum stored energy. Furthermore, the three definitions used in this interlaboratory work are related by:

$$\Psi = \Delta W/W = 2\pi \tan \delta = 2\pi Q^{-1}, \quad (2)$$

with $\tan \delta$ (δ is the loss angle) measured by the DMTA and Q^{-1} , the internal friction, measured by the PUCOT. The continuous curves in Figs. 1-6 is the thermoelastic damping due to the Zener effect [6,7] that is given by:

$$\Psi/\Psi_0 = (\omega\tau) / (1 + \omega^2\tau^2), \quad (3)$$

$$\Psi_0 = (2\pi\alpha^2 ET) / (\rho C_p), \quad (4)$$

$$\tau = (h^2\rho C_p) / (\pi^2 k), \quad (5)$$

where Ψ_0 is a characteristic damping, τ is a characteristic time of the problem, ω is the circular frequency, α is the coefficient of thermal expansion, T is the absolute temperature, ρ is the mass density, C_p is the thermal capacity (at constant pressure) per unit mass, and k is the thermal conductivity. These physical properties for the two types of brass used in this study are listed in Table I. The total damping measured by the CB technique is thermoelastic damping plus the intrinsic damping due to all other sources. Therefore, it is reassuring to note that the thermoelastic damping serves as a lower bound for all measurements. The difference between the measured values and the Zener curve is attributed to dislocation damping. In Figs. 5 and 6, the damping data are plotted in accordance with the universal damping curve for brass (Eq. 3).

Table I - Physical properties of two types of brass at room temperature (21°C).

	Lead-free	Leaded
Coefficient of thermal expansion (K ⁻¹)	18.9 x 10 ⁻⁶	18.9 x 10 ⁻⁶
Young's Modulus (GPa)	103	103
Mass Density (g/cm ³)	8.44	8.49
Specific heat (J kg ⁻¹ K ⁻¹)	385	385
Thermal conductivity (W m ⁻¹ K ⁻¹)	144.1	144.1

2. DMTA Technique

Figures 7 and 8 show representative plots of damping ($\tan \delta$) as a function of temperature for lead-free and leaded brass, respectively, at several frequencies. Figure 7 indicates that the damping

is low and essentially constant up to temperatures near 200°C, where the damping levels begin to rise. The temperature at which the damping begins to rise, called the activation temperature, increases as the frequency increases. Similar trends are observed in Fig. 8 for leaded brass. The curve for the test at 200 Hz seems to give anomalous behavior which is believed to be due to improper equipment functioning at this frequency. Using temperature estimates from Figs. 7 and 8, plus data from other DMTA tests on the same material, the frequency dependence of the activation temperature (T_a) for these alloys was examined. It should be noted that there was no significant difference in activation temperatures between the leaded and lead-free brass. Figure 9 shows the plot of the natural logarithm of the frequency versus the reciprocal of the activation temperature. The data are approximately linear, suggesting that the frequency and temperature can be related by an equation of the form:

$$f = f_0 \exp(-H/RT_a), \text{ or} \quad (6)$$

$$\ln(f) = \ln(f_0) - (H/R)(1/T_a), \quad (7)$$

where H is an effective activation energy for the increase in damping with temperature, R is the gas constant, and f_0 is a constant parameter. The slope of the plot yields an effective activation energy of 1.67 eV/atom or 38.3 kcal/mole. This value is close to the value of 1.7 eV/atom found by Youssef [8] for the short-range ordering process in Cu-Zn alloys, being equal to the activation energy for Zn diffusion in coarse-grained Cu. These results suggest that a diffusion damping mechanism causes the rise in damping in the frequency range covered by the DMTA.

Figure 10 shows the damping as a function of frequency for the leaded brass at 30°C. The data indicate the trend typical of thermoelastic damping with a peak between 3 and 10 Hz. This result is similar to those from the CB experiments, but the strain amplitudes used were an order of magnitude higher with the DMTA. Thus, one would expect there to be increased dislocation damping in specimens tested in the DMTA. This is the case for the data from this study (note that values for CB need to be divided by 2π for direct comparison), as, for example, the peak value from the DMTA is 2.5 times larger than the peak value from CB measurements. This difference is greater than expected and indicates possible problems with the accuracy of the damping measurements by the DMTA under the current testing procedures.

3. PUCOT

An Arrhenius plot of the damping data for leaded brass and lead-free brass is shown in Fig. 11. Clearly, there are significant differences in the damping curves for the two types of brass. The lead-free brass shows smoothly increasing damping as temperature increases, with no sign of damping peaks. On the other hand, the curves for the leaded brass show small peaks in damping near 280°C and near 327°C. These results have been discussed earlier [4] in terms of the melting of lead inclusions at and near the grain boundaries in the leaded brass. The strain amplitude dependence of damping for leaded brass at several temperatures is given in Fig. 12. The curves show the classical strain amplitude independent damping at low strains, and the amplitude dependent damping at higher strains. This behavior, in terms of the Granato Lücke (GL) dislocation damping theory [9], represents the break away of dislocations from their minor pinning points, resulting in increases in damping. The break away stress needed to free dislocations from their anchor points can be calculated from plots such as those in Fig. 12 by determining the break away strain and converting it to a stress via the Young's modulus of the materials. Figure 13 shows a plot of the break away stress as a function of temperature for leaded brass with some earlier data by Wolfenden and Robinson [4] on a similar material included. There is a pronounced peak in stress at 270°C, which is near to the temperature of 280°C observed by Youssef [8] as the short range order-disorder temperature in Cu-Zn alloys of similar composition to those used in this

work. Thus, it appears that the details of the disordering process affect the ease with which dislocations can break away from their pinning points under the application of a vibratory stress.

4. Comparison of Data

Figure 14 shows the damping data obtained from room temperature tests on the lead-free brass and leaded brass. It is emphasized that the damping data from the CB have been corrected to extract out the portion ($\approx 2/3$) of the damping arising from thermoelastic (Zener) effects. For the lead-free brass, the data from the CB and PUCOT techniques agree with each other to within a factor of 1.3, while the results for leaded brass agree within a factor of two. These levels of agreement are good, especially when considering the low damping levels present. The DMTA results, not shown in Fig. 14, were considerably higher than those from the CB and PUCOT. It is felt that DMTA technique has not been sufficiently optimized to provide accurate measurements of the damping levels when the damping is low, as is the case for these alloys at room temperature. However, the activation temperature results from the DMTA testing, where the ability to detect changes in damping as a function of temperature, are promising and further optimization of the technique is in progress.

SUMMARY

From this interlaboratory study of the damping in lead-free and leaded brass the following summary statements and conclusions can be listed:

1. The measurements of damping over the wide range of experimental variables used in this study require the use of more than one instrument.
2. A comparison of the damping data from the three instruments (CB, PUCOT, and DMTA) for the two types of brass measured at room temperature revealed that the CB and PUCOT techniques gave essentially identical measurements of damping (when allowances were made for thermoelastic damping), whereas the DMTA measured higher damping, possibly due to a systematic error.
3. The results from the DMTA instrument yielded an effective activation energy of 1.67 eV/atom for the rapid increase in damping as a function of temperature for temperatures below 300°C. This activation was close to that found by Youssef for the short-range disordering process of Zn and Cu atoms in similar alloys.
4. The PUCOT results for the leaded brass revealed a strong damping peak (TLP camping) near 327°C, the melting point of lead.
5. The amplitude dependence study of damping with the PUCOT indicated that the break away effect for dislocations was temperature dependent with a maximum break away stress of over 2 MPa near 270°C. This temperature was close to that observed by Youssef for the short-range ordering of Cu-Zn alloys.

REFERENCES

1. G.G. Wren and V.K. Kinra, J. Testing and Eval. 16, 77-85 (1988).
2. G.G. Wren and V.K. Kinra, "On the Effect of an End-Mass on Beam Damping," Exp. Mech. (in press).
3. W.H. Robinson and A. Edgar, IEEE Trans. Sonics and Ultrasonics SU-21, 98 (1974).
4. A. Wolfenden and W.H. Robinson, Acta Met. 25, 823-826 (1977).

5. R.A. Wetton, M.R. Morton, and A.M. Rowe, American Laboratory (January 1986).
6. C. Zener, Elasticity and Anelasticity of Metals, Univ. of Chicago Press, Chicago (1948).
7. C. Zener, Phys. Rev. 52, 230-235 (1937).
8. T.H. Youssef, Zeit. f. Naturf. 27a, 1232 (1972).
9. A.V. Granato and K. Lücke, J. Appl. Phys. 27, 583 and 789 (1956).

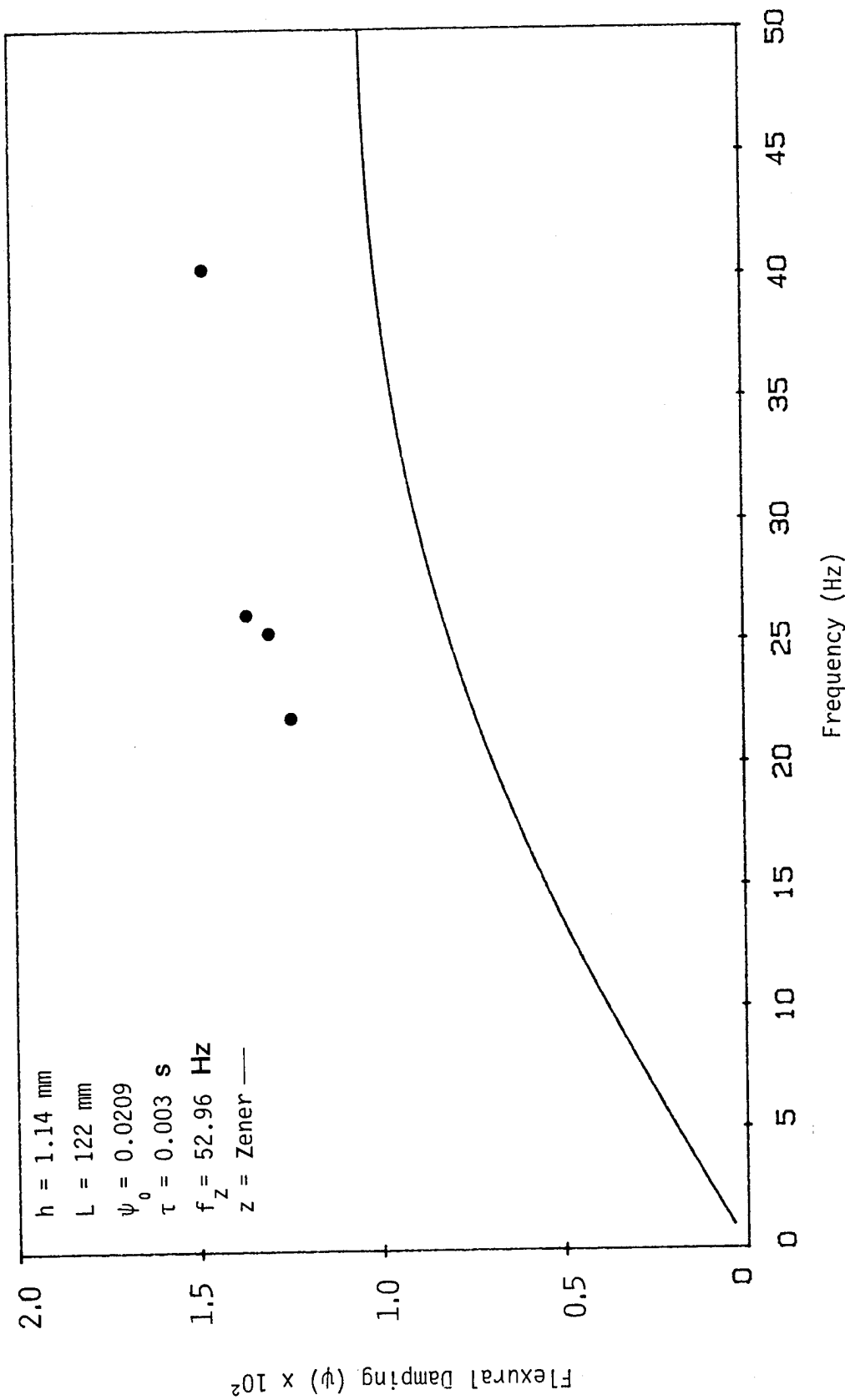


Fig. 1 - Flexural damping versus frequency for brass/2.65% lead as measured by the CB technique.

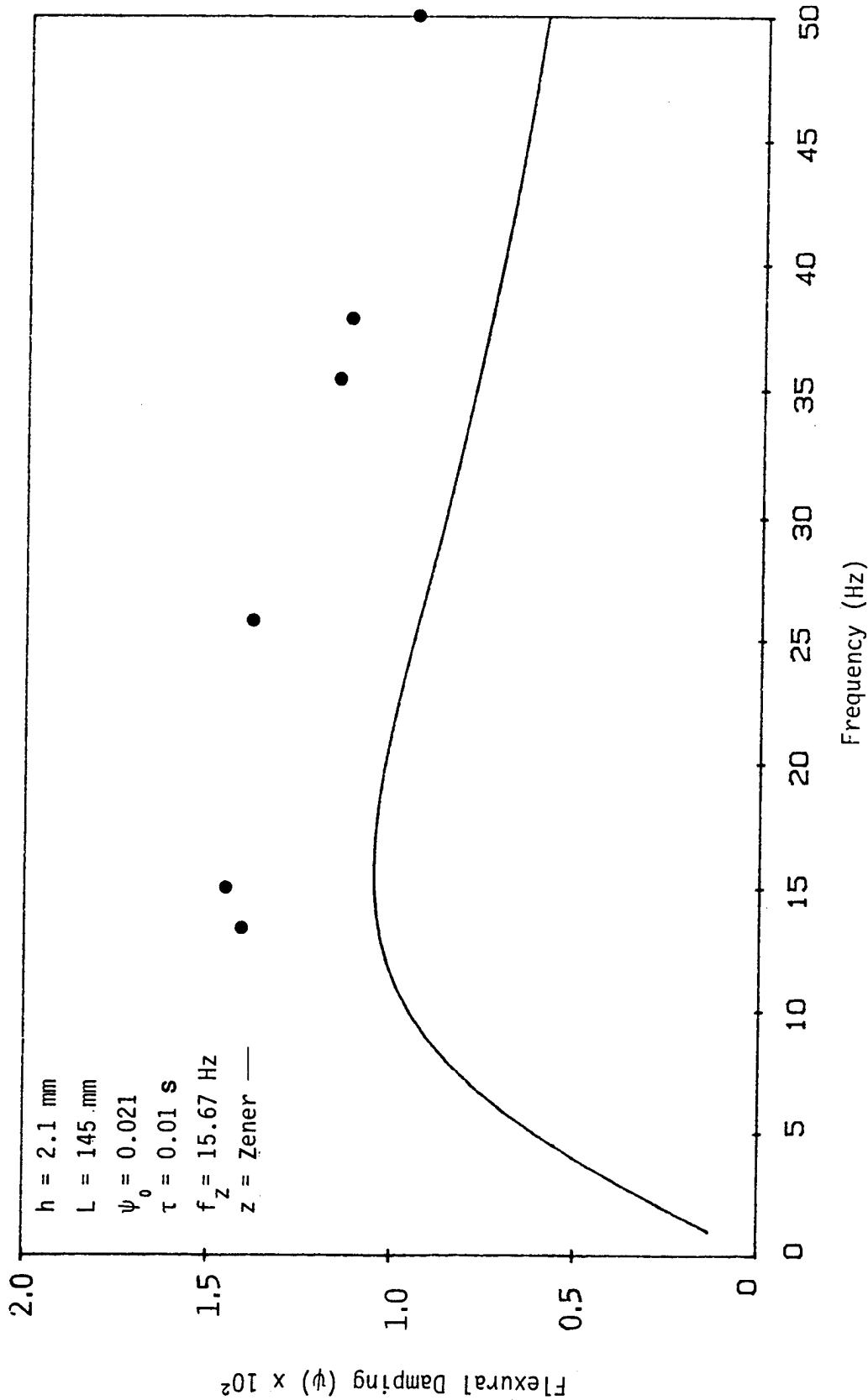


Fig. 2 - Flexural damping versus frequency for lead-free brass as measured by the CB technique.

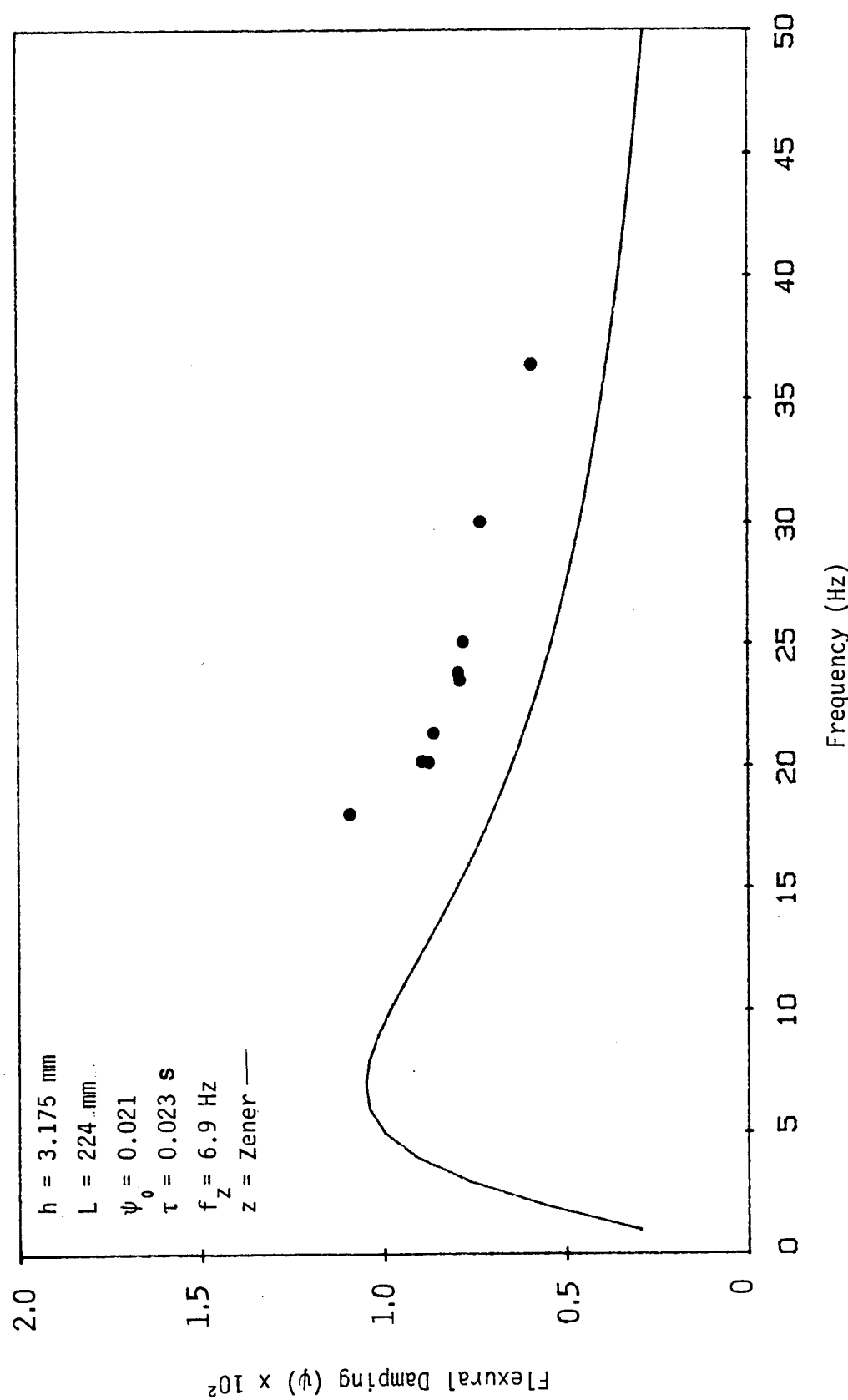


Fig. 3 - Flexural damping versus frequency for lead-free brass as measured by the CB technique.

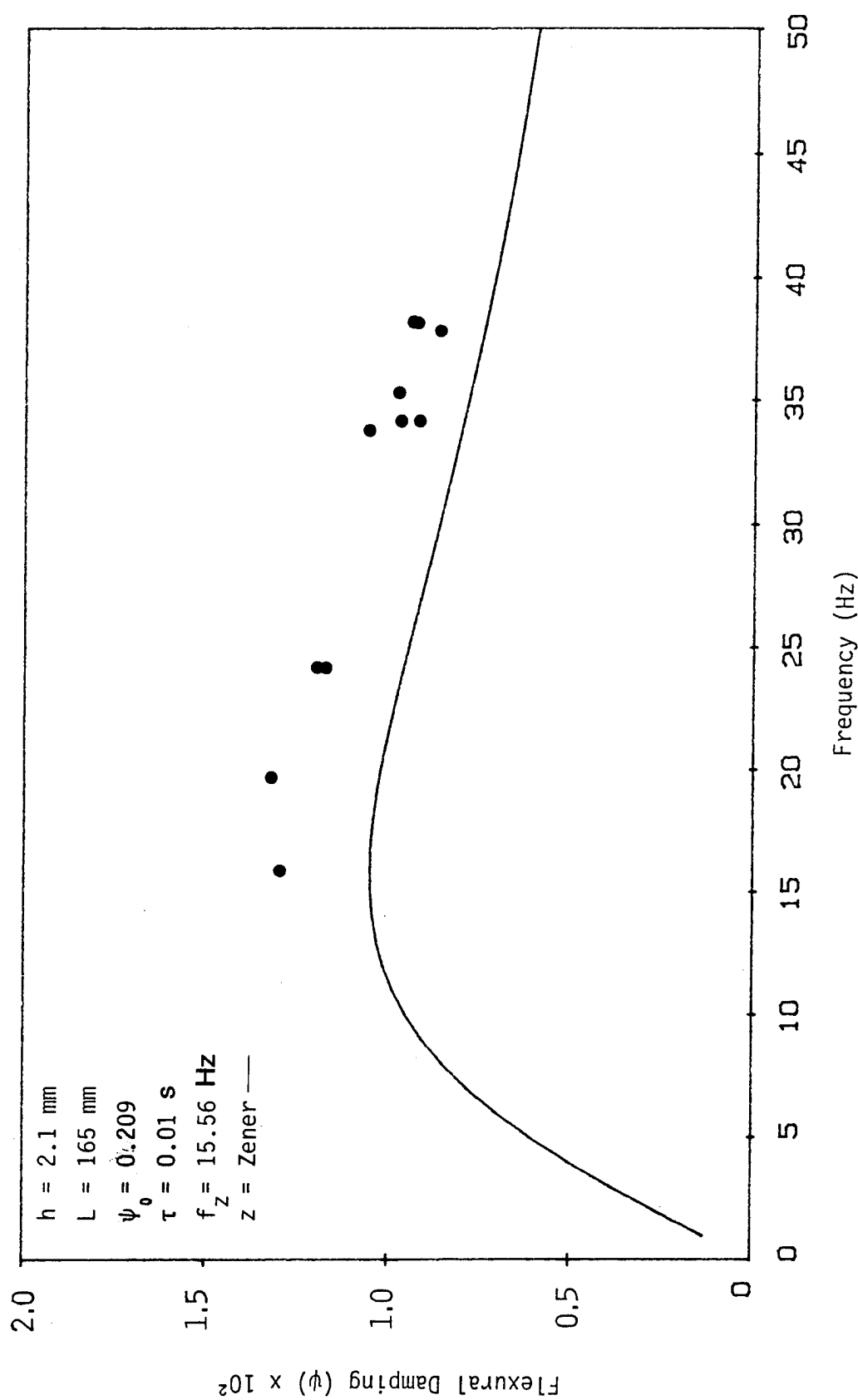


Fig. 4 - Flexural damping versus frequency for brass/2.65% lead as measured by the CB technique.

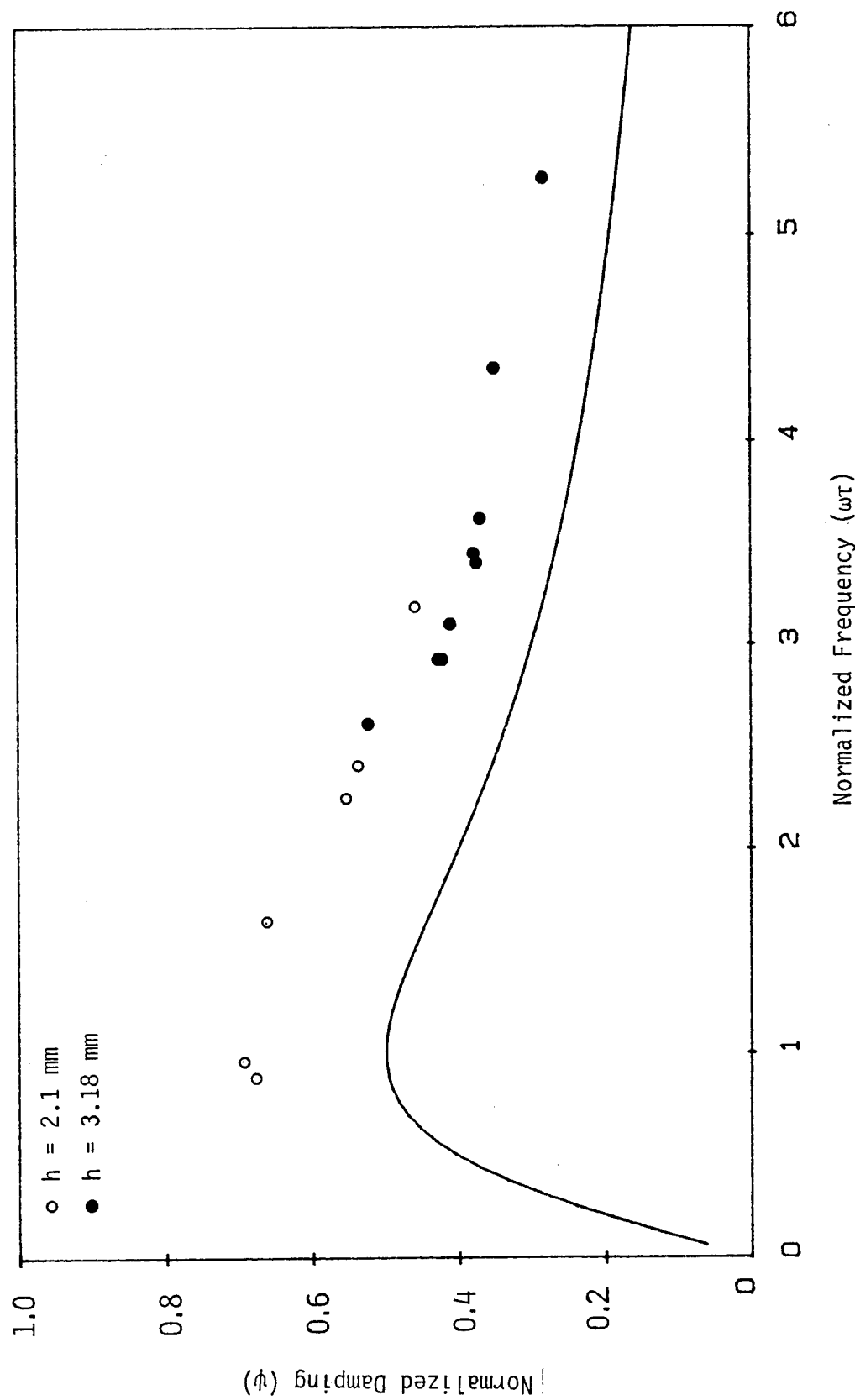


Fig. 5 - Normalized flexural damping versus normalized frequency for lead-free brass as measured by the CB technique.

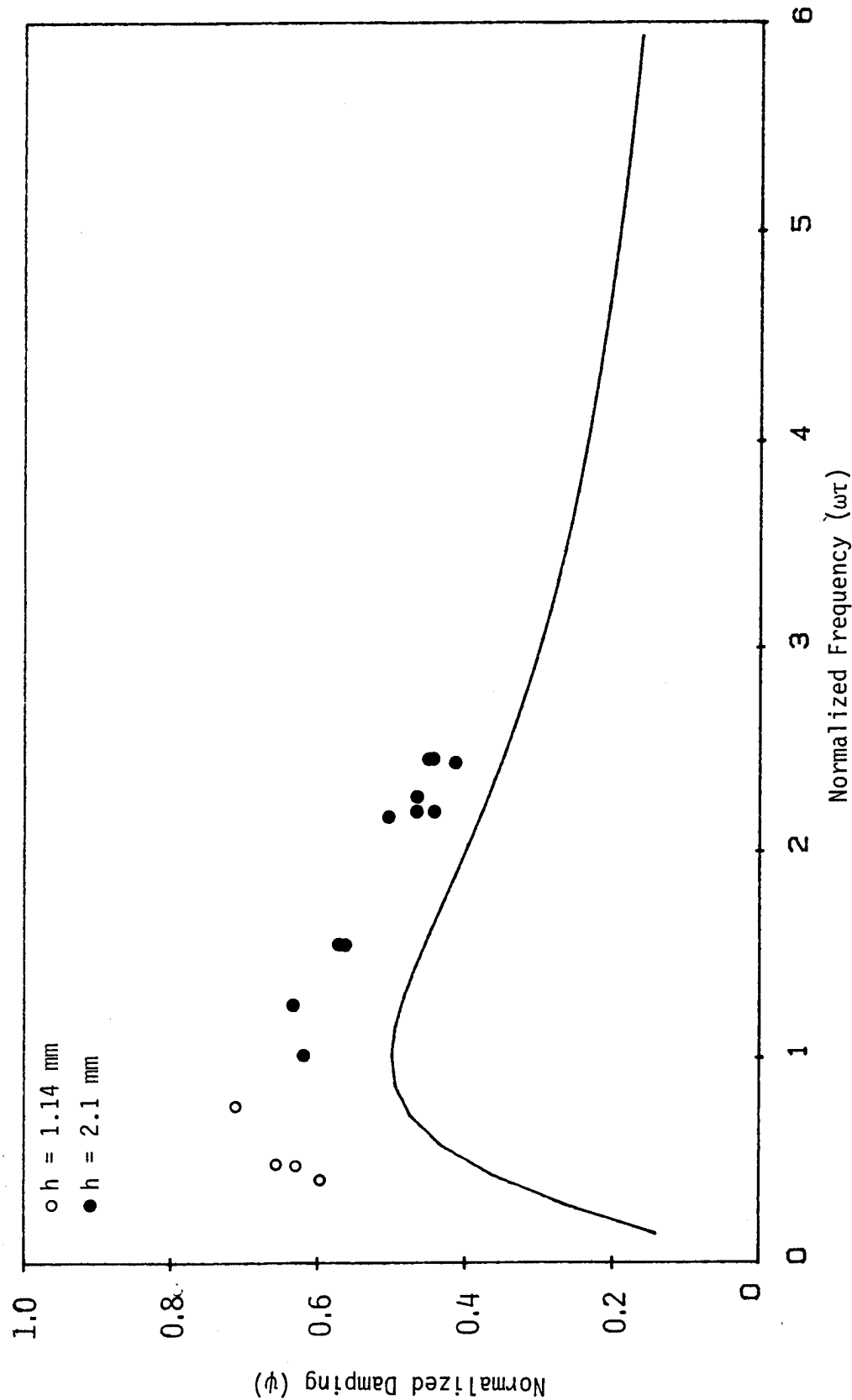


Fig. 6 - Normalized flexural damping versus normalized frequency for brass/2.65% lead as measured by the CB technique.

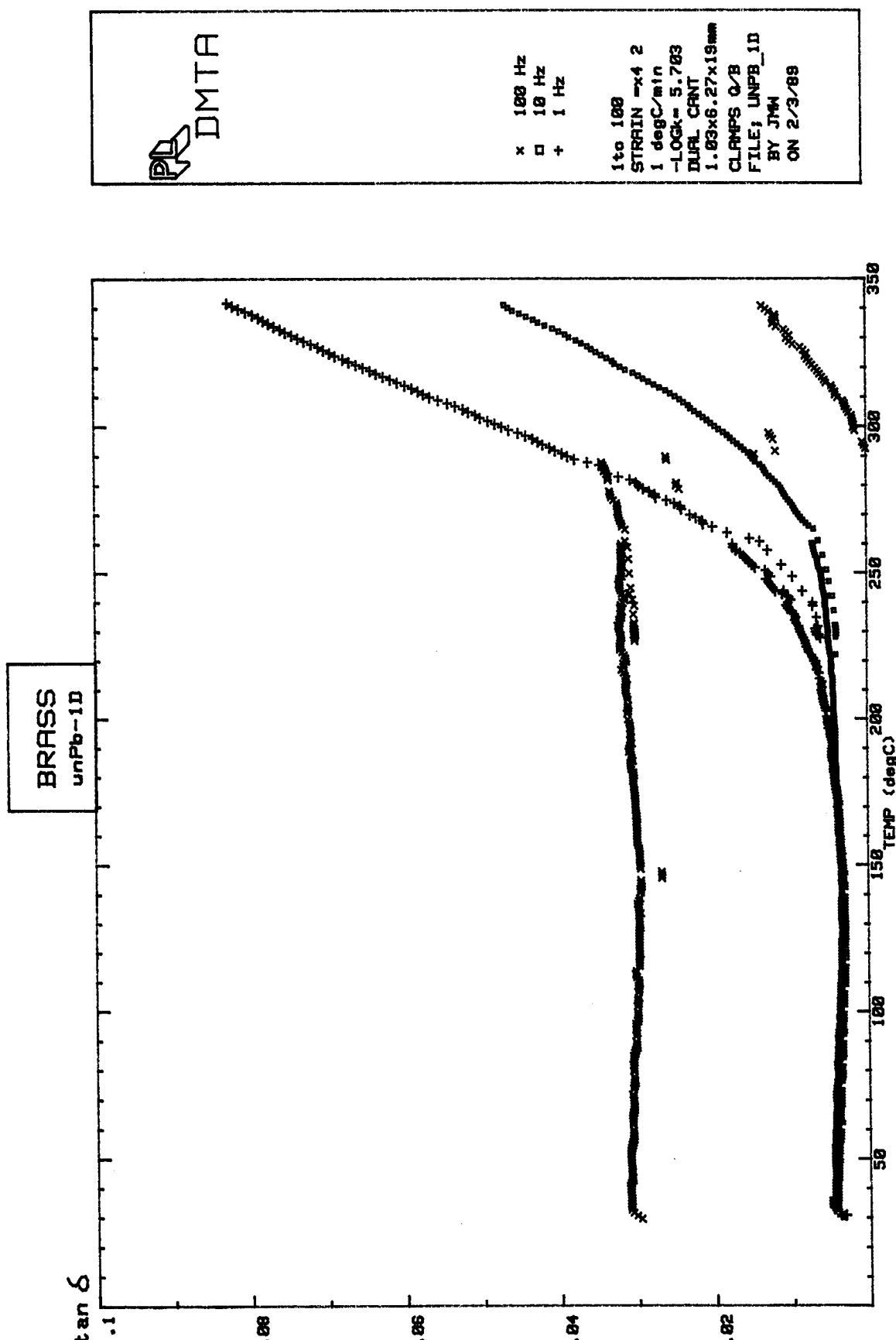


Fig. 7 - Damping as a function of temperature for lead-free brass as measured by the DMTA. The different curves are for different frequencies.

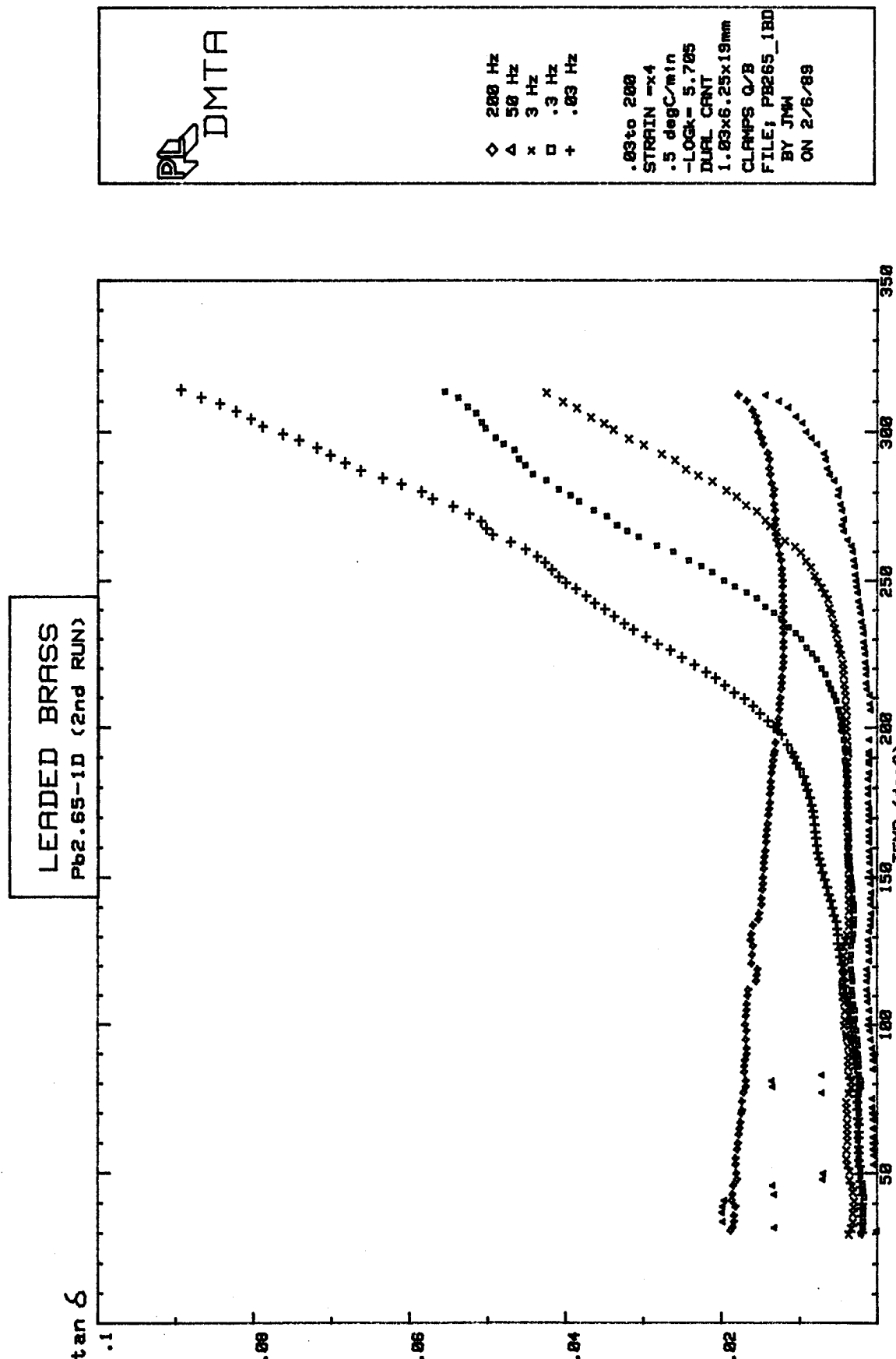


Fig. 8 - Damping as a function of temperature for leaded brass as measured by the DMTA. The different curves are for different frequencies.

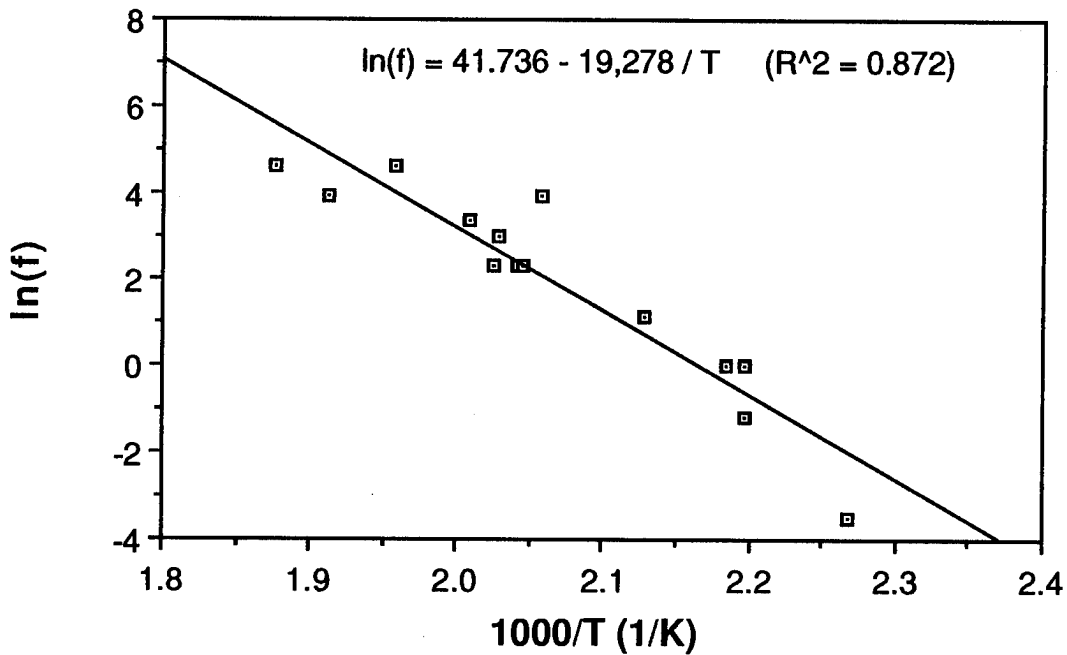


Fig. 9 - Arrhenius plot of the logarithm of the test frequency versus reciprocal temperature for lead-free brass and leaded brass as measured by the DMTA. The data points correspond to the activation temperatures where there was a rise in damping as shown in Figs. 7 and 8.

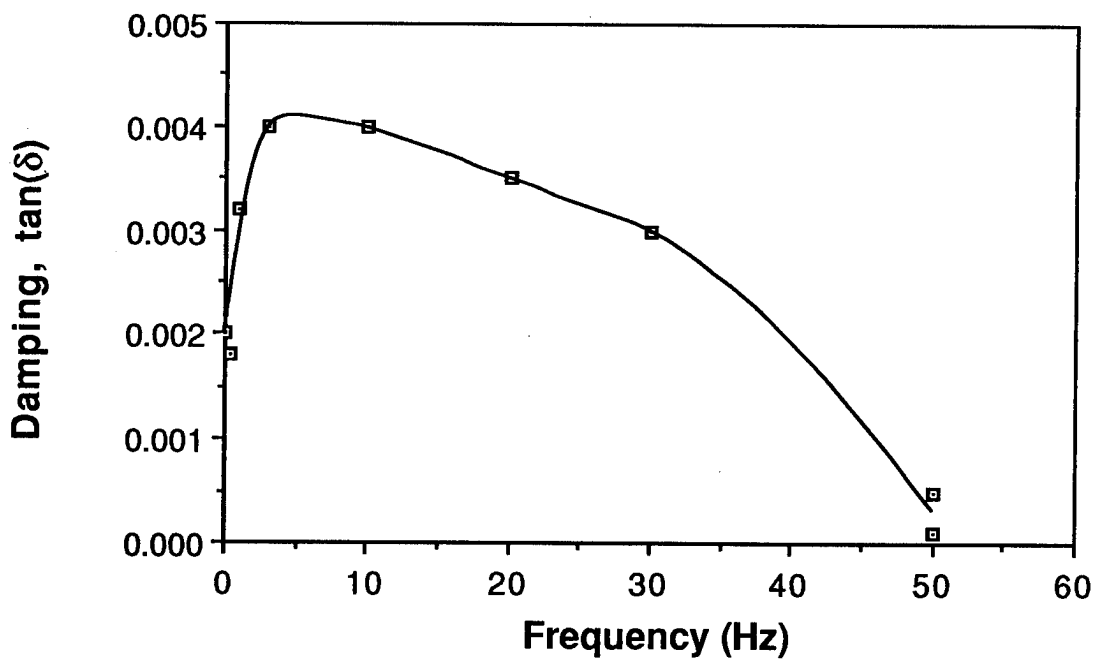


Fig. 10 - Damping as a function of frequency for leaded brass at 30°C as measured by the DMTA.

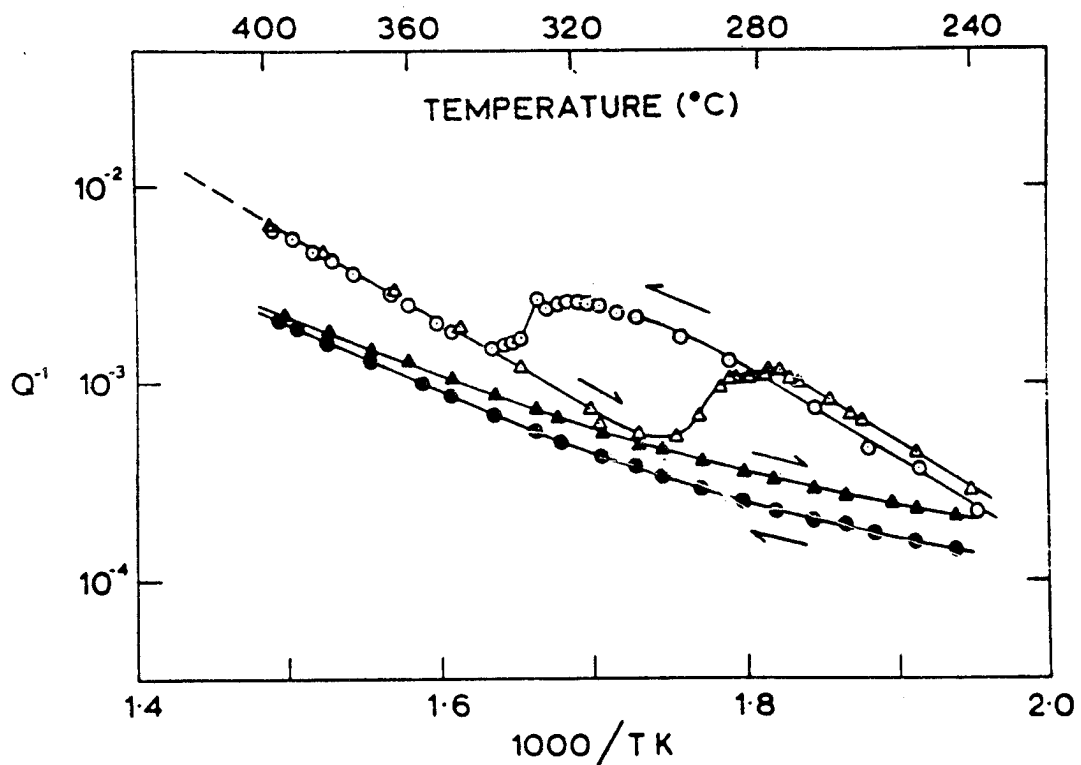


Fig. 11 - An Arrhenius plot of the mechanical damping of leaded (open data points) and lead-free (filled data points) brass as measured by the PUCOT at 40 kHz and at a maximum strain amplitude of 10^{-7} . (From [4].)

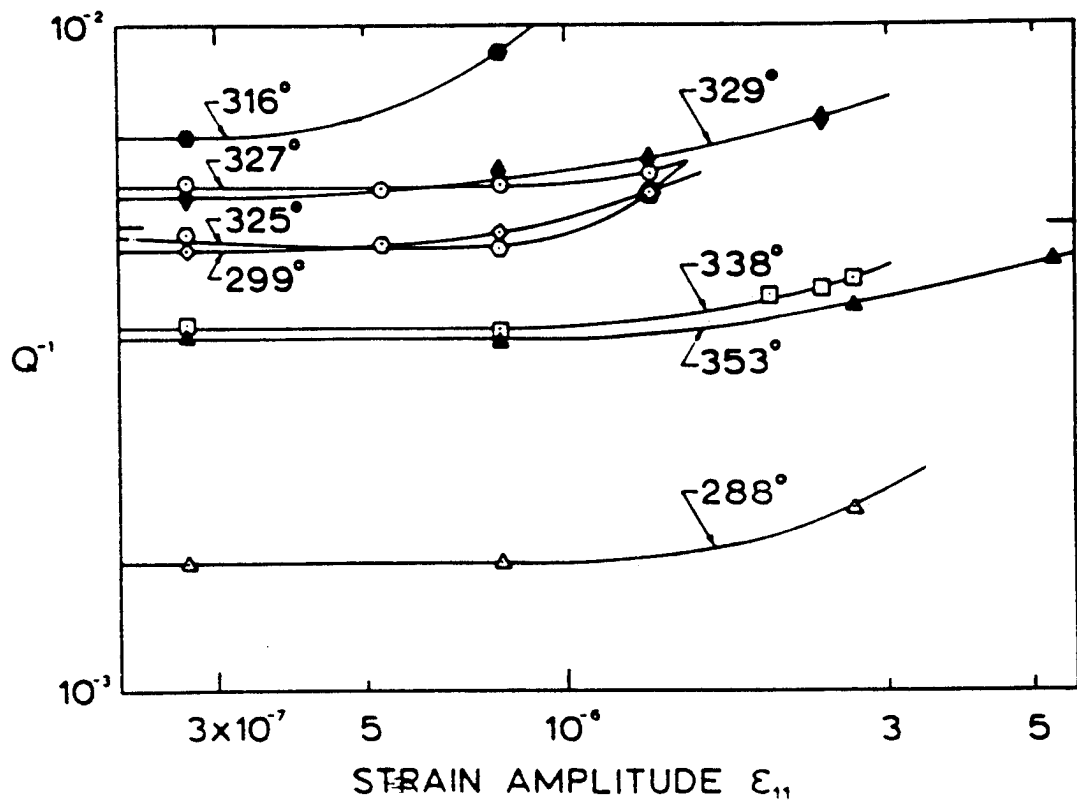


Fig. 12 - Amplitude dependence of the mechanical damping of leaded brass at various temperatures as measured by the PUCOT at 40 kHz. (From [4].)

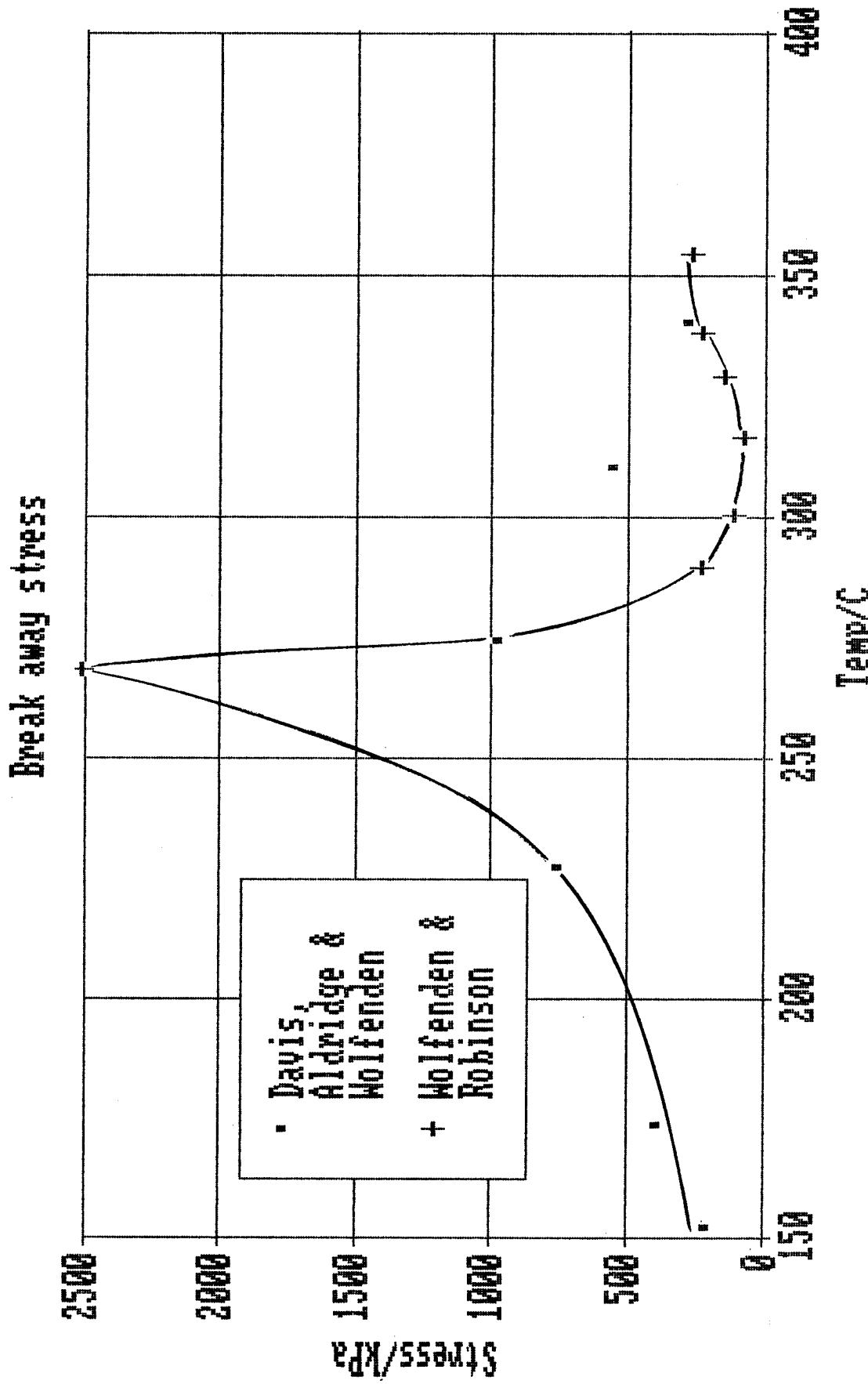


Fig. 13 - Stress required to cause break away of dislocation lines from pinning points as a function of temperature for leaded brass.
Earlier data from Wolfenden and Robinson [4] are also shown.

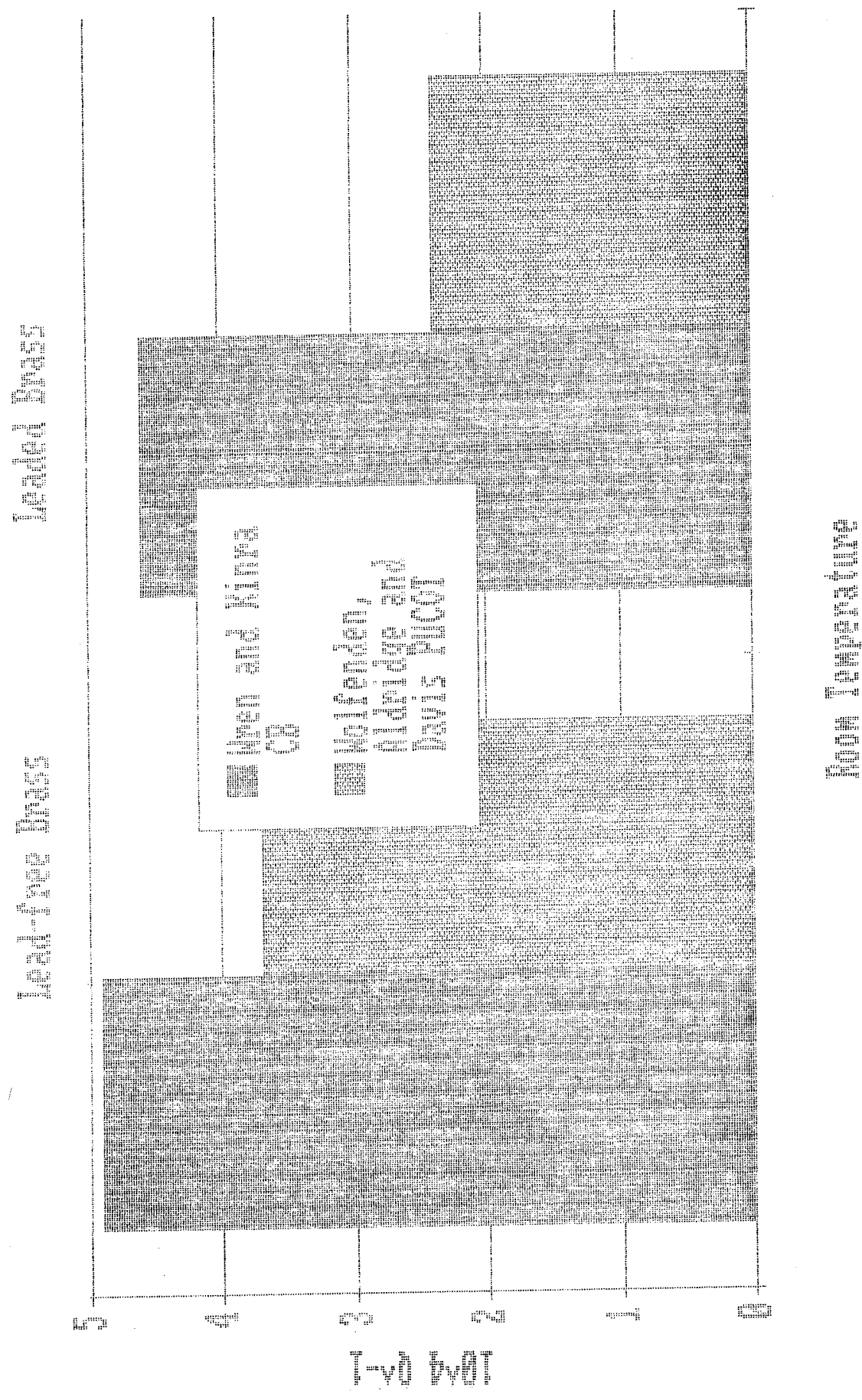


Fig. 14 - A comparison of the damping data as measured by the CB and PUCOT for lead-free and leaded brass tested at room temperature.

Investigation of Structural Damping Combining Linear and Non-linear Constrained Viscoelastic Mechanisms

Joseph M Ting
Massachusetts Institute of Technology
37-384
77 Massachusetts Ave.
Cambridge, MA 02139
(617) 253-7010

Connie K. Kim
Rocketdyne
Mail Code LB25
6633 Canoga Ave.
Canoga Park, CA 91303
(818) 700-4106

Prof. E.F. Crawley
Massachusetts Institute of Technology
37-341
77 Massachusetts Ave.
Cambridge, MA 02139
(617) 253-7510

Abstract

A damping scheme combining the linear effects of a viscoelastic material and the non-linear effects of an array of constraining plates was investigated. The damping material, Poron, was applied to the surface of an aluminum beam and constrained by a layer of thin aluminum segments. The segments were spaced so that their edges would come into contact as the beam deflected. At deflections smaller than those which cause segment contact, the linear viscoelastic damping of the Poron was observed. At larger amplitudes, additional dissipation was expected due to the impact of the segments. Several configurations of the beams were tested in free fall in the ASTROVAC, a vacuum facility devoted to the testing of space structures. Compared to theory, the results of the linearly damped beams showed good correlation. The beams with contacting segments showed only a small amount of additional dissipation

1. Introduction

There are many ways that damping can be added to a structure. The method that will be discussed in this paper involves the use of a passive damping layer applied to the surface of a structure. Unconstrained viscoelastic damping materials usually produce small increases in linear damping. One way to increase damping is to add a layer of stiffer material to constrain the viscoelastic layer (Ungar , 1966, Kerwin, 1959). The constraining layer causes the viscoelastic material to shear, introducing additional energy loss. Because most of the shearing occurs at the ends of a constrained viscoelastic layer, damping can be increased by segmenting the constraining layer up so that there is more shear. In fact, the length of the constraints can be optimized (Plunkett and Lee, 1970).

Further increases of damping might be achieved by exploiting non-linear effects. In this project, an attempt was made to introduce non-linearities using the segmented constraint layer of an existing damping scheme. A viscoelastic layer was applied to the surface of several beams. This layer was then covered with a layer of constraining plates. The plates were spaced so that when the beam vibration exceeded a certain amplitude, the constraints would

impact. The objective was to give large, non-linear damping at high amplitudes and smaller linear decay at low amplitudes.

2. Theoretical Background

The damping of a free viscoelastic layer applied to a beam in bending is due to losses through the stretching and bending of the layer (see Fig. 2.1). The associated loss factor (equal to twice the damping ratio ζ for light damping) for a beam treated on one side is given by,

$$\eta = \frac{\beta_2}{1 + \frac{k^2(1 + \beta_2^2) + (r_1/H_{12})^2[(1 + k)^2 + (\beta_2 k)^2]}{k[1 + (r_2/H_{12})^2[(1 + k)^2 + (\beta_2 k)^2]]}} \quad (1)$$

where,

β_2 =Loss factor of viscoelastic layer

$k=E_1 H_1 / E_2 H_2$ =Ratio of extensional stiffnesses

$r_1=H_1/\sqrt{12}$ =Radius of gyration of the beam

$r_2=H_2/\sqrt{12}$ =Radius of gyration of the viscoelastic layer

$H_{12}=(H_1+H_2)/2$ =Distance between neutral planes of the two layers

E_i =Modulus of elasticity of the i th layer

H_i =Thickness of i th layer

assuming a loss-less beam (Ungar, 1966). This loss factor is clearly related to the material and geometrical properties of the beam and viscoelastic layer. Adding this prediction to the material damping of the beam, due for example to transverse thermal currents, gives a prediction for the system damping ratio.

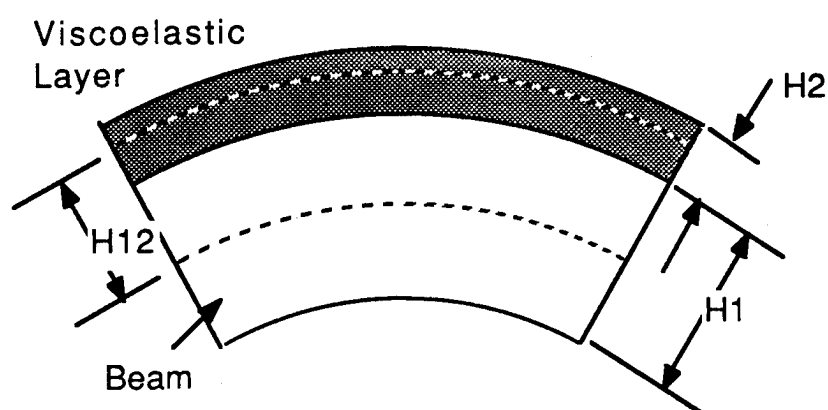


Figure 1
Structure with free viscoelastic layer

When a constraining layer is added, shear effects must be included in the model (see Fig. 2.2). These effects depend on the curvature of the structure which can be seen in the governing equation (Kerwin, 1959),

$$\eta_1 = \eta' \frac{3E_3 t_3}{\pi E_1 t_1} \frac{\int_a^{a+L} \left[\frac{d^2 y}{dx^2} \right]^2 dx}{\int_0^L \left[\frac{d^2 y}{dx^2} \right]^2 dx} \quad (2)$$

where η_1 is the modified loss coefficient of a system, E_3 is the modulus of elasticity of the constraining layer, H_3 is the thickness of the layer, and η' is defined as the unmodified loss coefficient of a constrained structure given by,

$$\eta' = 4\pi \frac{1}{w} \left[\frac{\sinh(A)\sin(\theta/2) - \sin(B)\cos(\theta/2)}{\cosh(A) + \cos(B)} \right] \quad (3)$$

where,

$$\tan^{-1}\theta = \beta_2$$

$$A = w \cos(\beta_2/2)$$

$$B = w \sin(\beta_2/2)$$

$$w = L_1/B_0$$

$$B_0 = (t_2 t_3 E_3 / G_2)^{1/2}$$

G_1 =Shear modulus of viscoelastic material

t_i =Thickness of ith layer

Equations 2 and 3 show the dependence of the damping on the shearing of the viscoelastic layer, the bending of the base structure, and the length of the constraining layer.

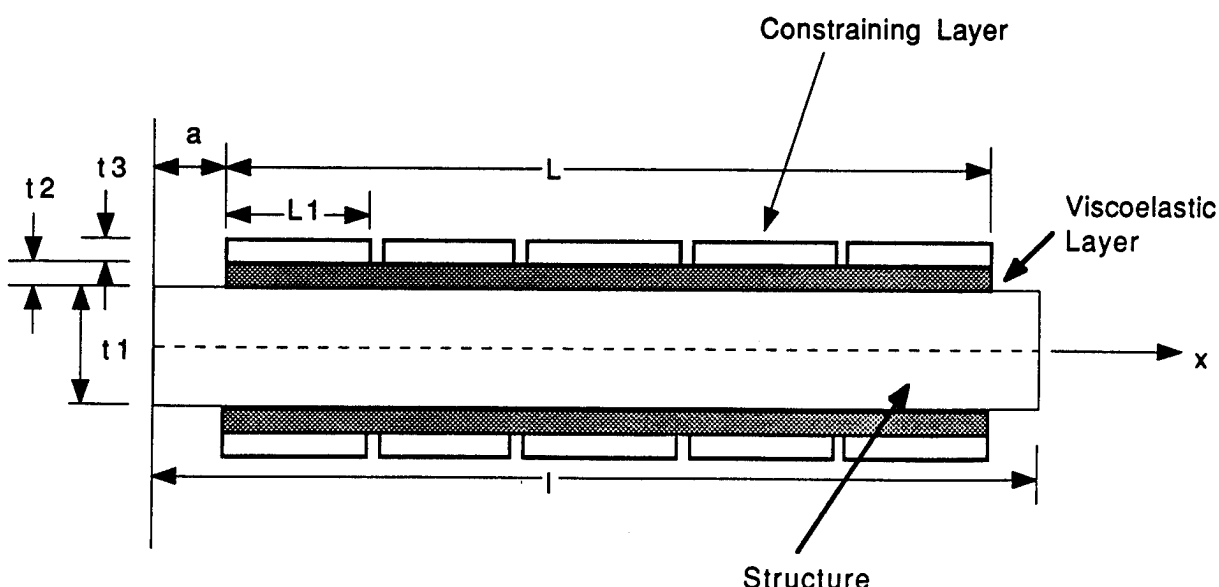


Figure 2
Segmented Constrained Beam

The relationship between the damping and the length of the constraining layer can be exploited to increase the loss factor. Most of the shearing of the viscoelastic layer occurs at the edges of the constraining layer. This effect can be seen in Figure 3. As a result, the number and length of the segments of the top layer can be optimized (Plunkett and Lee, 1970). One can further increase the loss of energy of a structure by extending the concept of viscoelastic damping by using multiple layers. There is another way to increase the damping however, by introducing non-linear damping.

Given the structure of a constrained viscoelastic damping layer, there are several ways one can introduce non-linear phenomena. One of these ways is to cause the segments of the constraining layer to impact (see Fig. 2.3). The impact would effectively add another energy dissipation mechanism. The only requirement is the careful spacing of the segments so they will touch. One drawback of this scheme is the difficulty of modeling the phenomena of impact damping.

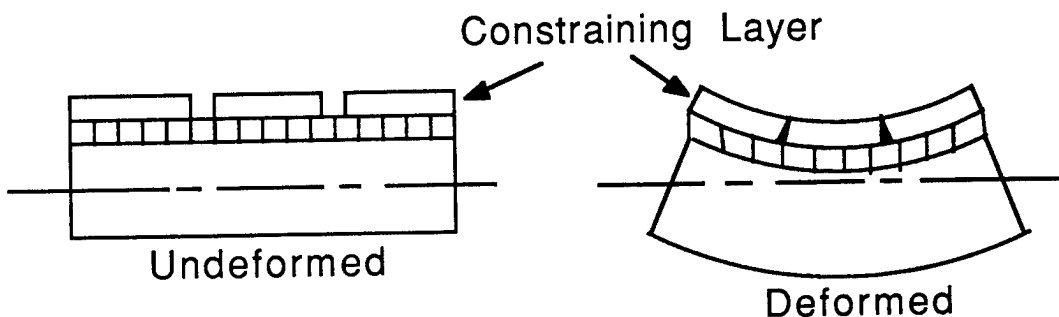


Figure 3
Non-linear damping mechanism

3 Experimental Apparatus

A set of experimental specimens was built to explore the possibility of added impact damping. Six test specimens were constructed, each a beam ($27'' \times 1'' \times 1/8''$) of 6061-T6 aluminum. Each beam was modified with a different damping mechanism, allowing the effect of each different layer to be observed separately. The first was a beam to determine the material damping without any damping treatment. Then a beam with a $1/16''$ thick free layer of Poron damping material on both faces was tested. An untreated area was left in the center for strain gauges. A third beam with a "continuous" constraining layer of $1/32''$ sheet aluminum was tested and compared to the unconstrained beam. In fact, the constraining layer was broken in the middle so that there were two segments. The length of the constraint segments was very close to the optimal length. Two beams tested were treated with segmented constraining layers which consisted of 10 $2.625''$ segments on each side (see Fig. 4). One specimen had the segments separated by a small gap set by using a feeler gauge. This gap ($.002''$) was chosen so that the segments would touch when the tip deflections of the free-free beam reached $1/2''$. The other beam had a gap of $.01''$ - enough to guarantee separation. Finally, a beam with the same size segments bonded to the surface without a viscoelastic layer was tested. The segments were spaced so that they would touch when the tip deflection exceeded $1/2''$.

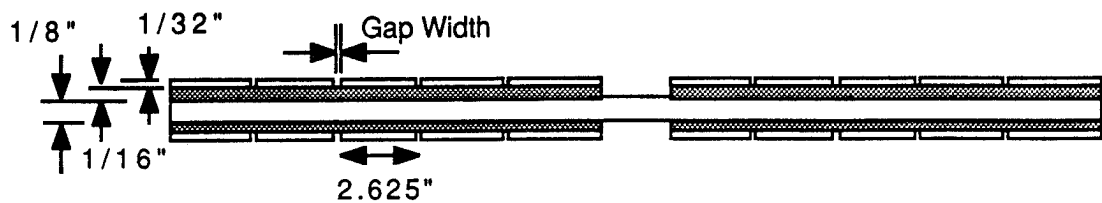


Figure 4
Test Specimen With Segmented Constrained Damping Layer

4. Experimental Procedure

Tests were performed in the ASTROVAC Space Simulation Facility at M.I.T. The ASTROVAC consists of a vacuum chamber (14' tall, 10' diameter), launcher, data acquisition system, and shaker system adapted for use in vacuum (see Fig. 5).

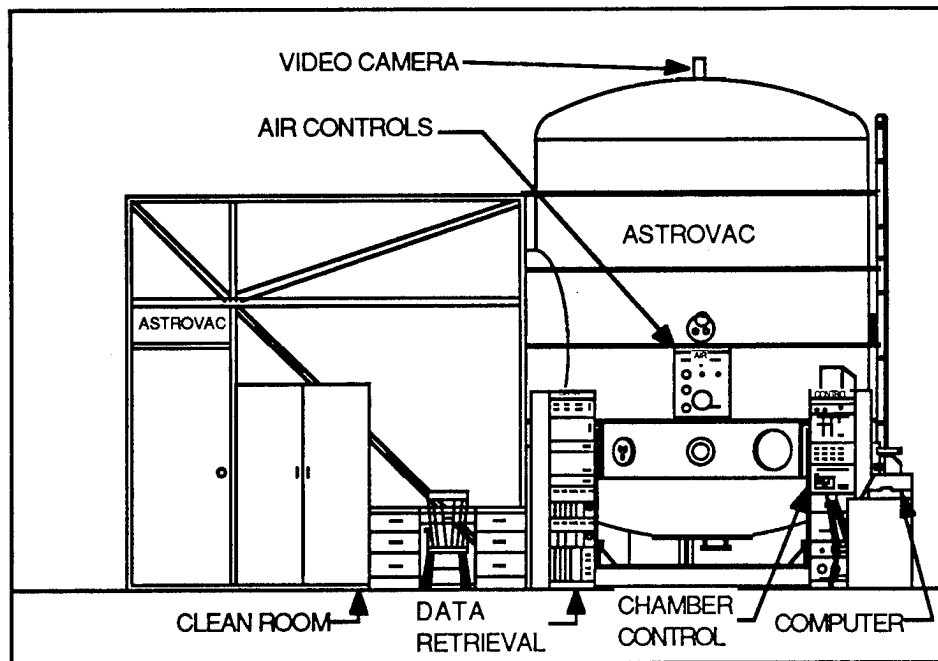


Figure 5
ASTROVAC Space Simulation Facility

Each test involved lofting a specimen in the ASTROVAC using the launcher (see Fig. 6). First, the specimen was set on the launch bed. Then the strain gauge wires were plugged into the follower which kept the short, light, leak wires slack during the test. Next, the vacuum chamber was evacuated to a pressure of 10^{-2} Torr and the beams were launched. While a beam was vibrating in free fall, the data from the strain gauges was sent to a CAMAC Crate for storage. Then the data was sent to an IBM XT for post-processing (Crawley, 1985).

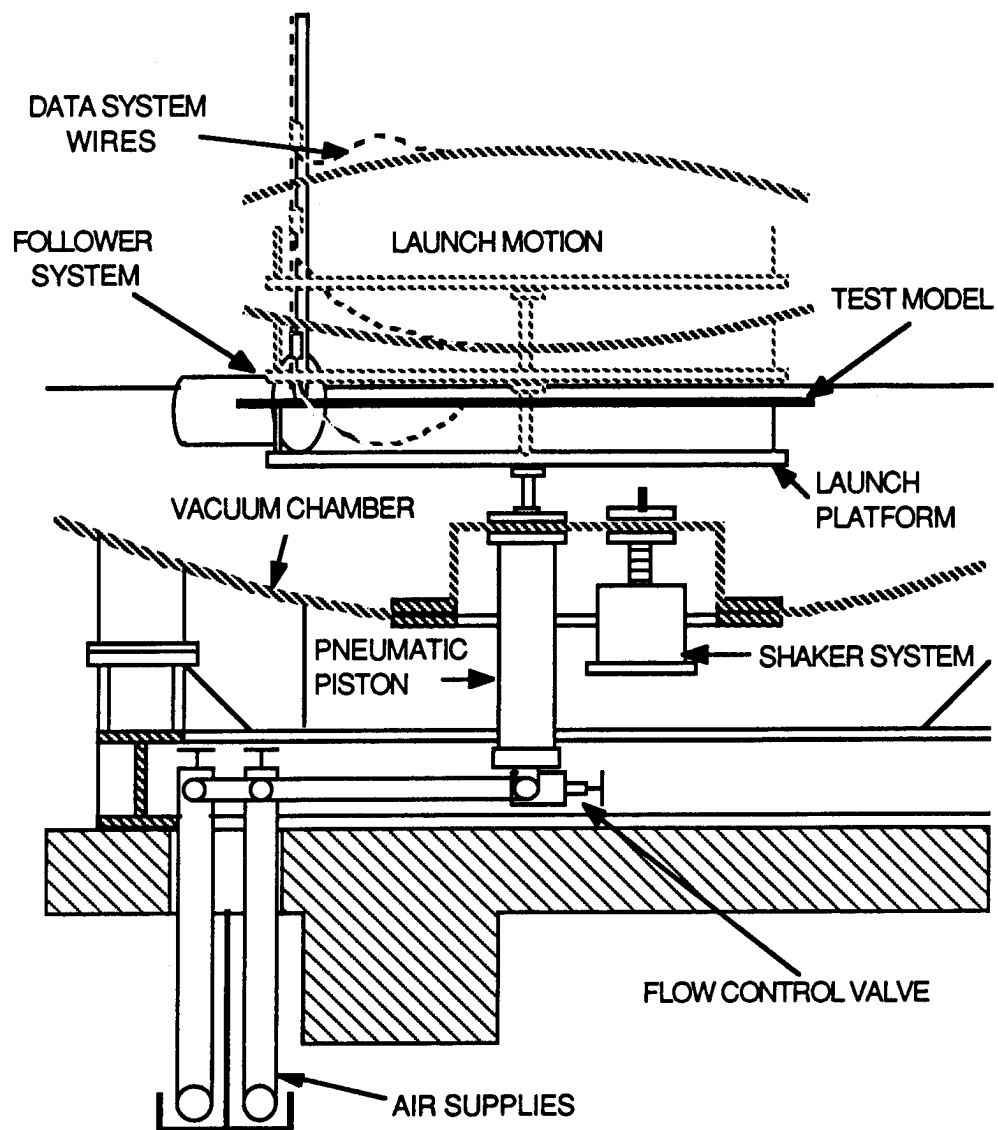


Figure 6
Launch of test specimen

5. Results

The strain data from each launch was plotted vs time (see Fig. 7). Damping ratios were obtained from plots using a log-decrement method.

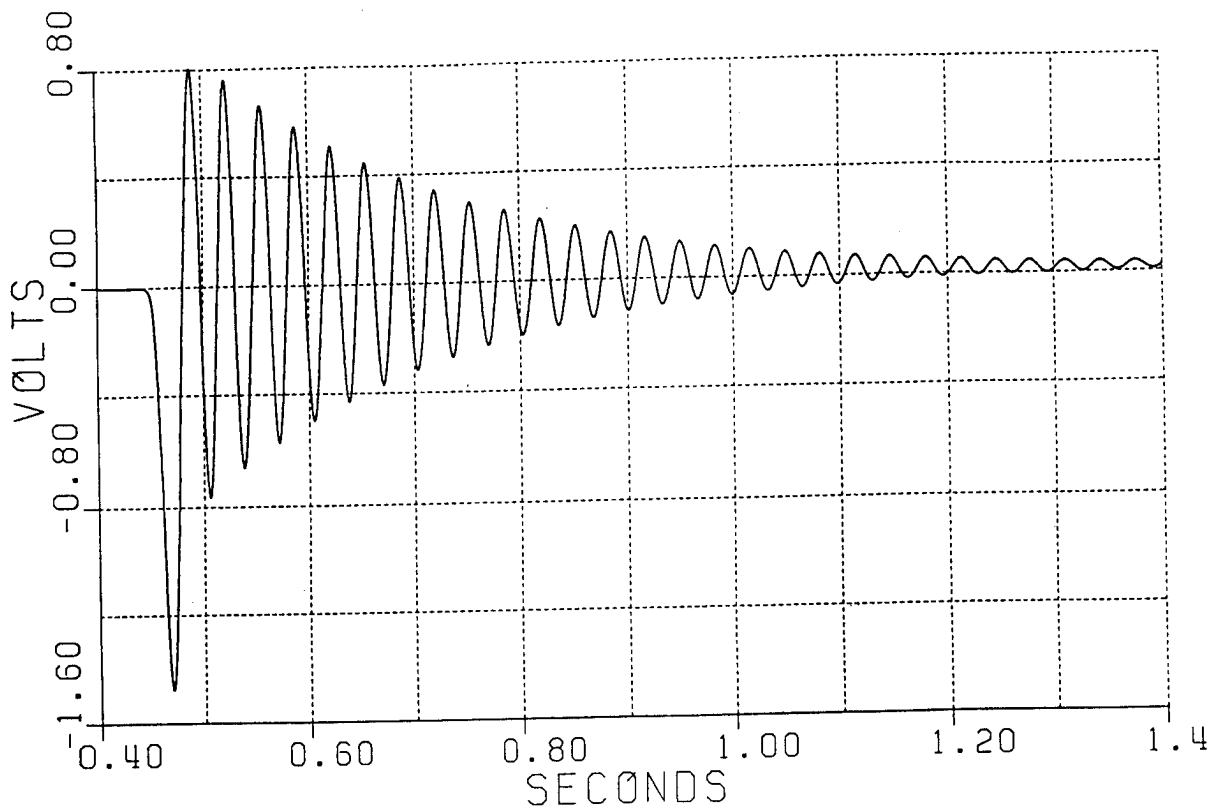


Figure 7
Sample plot of strain (volts) vs. time (seconds)

The damping ratios for each of the specimens is shown in Table 1 for an average of 6 launches. The beam with no damping layer showed the lowest damping while the beam with the segments of optimal length showed the largest damping increase. Comparing the results of the segmented constrained layer with linear and non-linear spacing, there was only a slight increase in damping. However, this increase was within the range of the scatter of the data. In addition, the damping ratio of the non-linear specimen showed little variation with amplitude.

Specimen	Damping Ratio, ζ (%)
Aluminum Beam	.08
Free damping layer	.10
2 segment constraining layer	3.99
10 segment constraining layer	1.97
.002" gap width	
10 segment constraining layer	2.15
.01" gap width	
10 segment bonded layer	.46

6. Conclusions

The comparison of experimental vs. theoretical results showed good correlation with theory (see Fig. 8). Damping ratio increase for the constrained segmented specimens, represented by CC and SCL (two element constraining layer, and 10 element constraining layer respectively) followed the pattern predicted by theory. The non-linear specimens represented by SCN and NNN (constrained damping layer and bonded layer with non-linear spacing

respectively) showed little damping increase compared to their linear counterparts. This smaller than expected increase was probably due to several factors, the principle being manufacturing problems which made it difficult to accurately control the gap between the segments. Another possibility was that the plates did touch and the impact was too small to be significant.

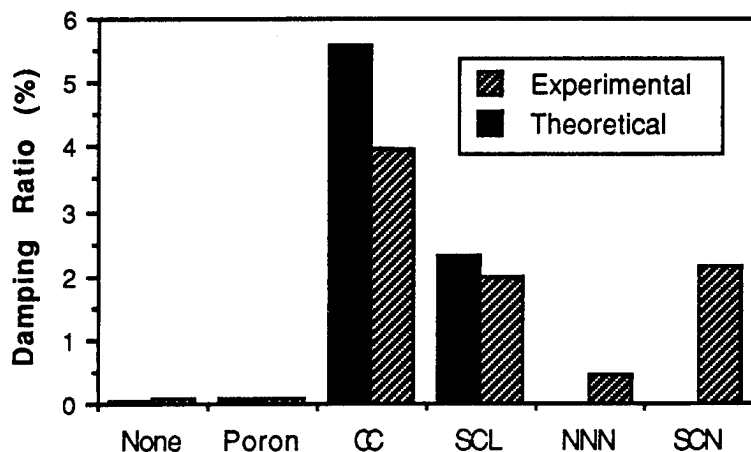


Figure 8
Experimental vs. theoretical damping ratios

References:

Kerwin, Edward M., 1959, "Damping of Flexural Waves by a Constrained Viscoelastic Layer," *The Journal of the Acoustical Society of America*, Vol. 31.

Crawley, E.F. and Mohr, D.G., 1985, "Experimental Measurements of Material Damping in Free Fall With Tunable Excitation," *AIAA Journal*, Vol. 23, No. 1, January 1985, pp. 125-131.

Plunkett, R. and Lee, C.T., 1970, "Length Optimization for Constrained Viscoelastic Layer Damping," *The Journal of the Acoustical Society of America*, Vol. 48.

Ungar, E.E., 1966, "Damping of Panels," *Noise and Vibration Control*, McGraw-Hill.

Vibration Reduction via Constrain Layer Damping Techniques

Mr. John F. Schultze and Dr. John B. Kosmatka

Department of Mechanical Engineering
Virginia Polytechnic Institute and State University
Blacksburg, Virginia

Abstract

Experimental methods to extract loss factors in constrain layer damped beams are compared. Comparison of integral and additive damping treatments are considered. Investigation of partial coverage treatment relation between application length and effective damping ratio for isotropic beams is performed. Results indicate that optimum length exist for cantilever first mode, while the other modes of investigation, clamped/clamped first and second and cantilever second, show consistent increase in effective damping with increase in application length. Integrally damped composite beams show significant increase in damping ratio without reduction in bending stiffness. Log decrement appears to be the best method for measuring damping values for cantilever first mode. Real and Imaginary components extract data that agree well with each other, while forming an upper bound for the log decrement method.

Introduction

Structural vibration is a recurring problem in such diverse fields from machinery silencing in mining equipment to response attenuation in composite aerospace structures. In current aerospace design, use of composite materials allows the engineer to tailor a material to meet application requirements of mass and stiffness. Vibrations, which cause cyclic loading of a structure, considerably reduce fatigue life thereby increasing failure rate. The use of viscoelastic materials to attenuate response of structures through increasing the composite damping has gained popularity in recent years. Discussions on the use of viscoelastics are presented by Mar¹.

The evaluation of one damping technique is often done through experimentation. A comparison of several techniques will be presented. Evaluation of partial coverage and integrally damped structures will also be pursued.

Passive damping seems the most effective technique for structures that have limited number of modes of concern. One major technique is Constrain Layer Damping (CLD). This method involves sandwiching a viscoelastic medium between two stiff outer layers. The viscoelastic, a rubber-like compound, dissipates energy via shear deformation. The two outer layers undergo the significant bending and extensional loads while the central withstands the shear forces. The incorporation of viscoelastic materials into existing structures (via CLD) has been thoroughly investigated by numerous researchers²⁻¹⁵.

Viscoelastic damping is incorporated in one of two ways; 1.) additive damping tape or 2.) integrally incorporated damping central layer. The additive damping tapes have been used in an ad-hoc method to solve existing vibration problems. Partial coverage with damping tapes allows the treatment to be applied in the area and amount to effect the desired result for some applications. Integrally damped structures are a relatively new phenomena. The damping layer is often sandwiched between two symmetric constraining layers. Two sets of boundary conditions, cantilever and clamped/clamped, are investigated for the partial coverage treatment on an isotropic beam. The integrally damped beams are subjected to cantilever investigation only.

The rationale behind investigating partial coverage treatments is twofold; first, determine level of damping treatment will meet design criteria, and second, investigate possibility of an optimum length of treatment for a given mode and structure. The driving force behind investigation of integrally damped beams is; to determine effect of damping incorporated within design of beam and located in center of symmetric beam. It is obvious that integrally damped beams involve additional steps in manufacture and design. In the beams investigated here, the two additional steps of; 1.) special lay-up with pre-cured graphite/epoxy composite and 2.) pressure bonding of the damping material to the composite, were required. Another design consideration in the incorporation of additive damping is weight, compared with graphite epoxy the density is about equal, with the damping tape on isotropic aluminum beam the density is also about the same (the backing is the significant factor). Experimental method comparisons are neces-

sary because it is not always feasible to run the best suited test. Citing this, it must be known how test results correlate with actual values.

The principle objectives of this paper are to investigate different experimental methods to extract damping values for beams with simple boundary conditions and to evaluate partial coverage and integrally damped beams. This survey will be useful to designers and analysts of advanced aerospace structures where fatigue is a significant problem. The two boundary conditions considered are a fixed/fixed (spar-like) beam and a cantilever member (similar to wings and other rotary wing structures) (refer Figure 1.a.,b). The research is conducted using experimental results which can later be compared with analytical and finite element models.

Experimental Methods and Formulations

The two basic frameworks that most structural dynamics experimentation are performed in are; 1.) time domain and 2.) frequency domain. Frequency domain techniques such as a Fast Fourier Transform (FFT) to develop a Frequency Response Function (FRF) are often used. This function, FRF, then is used to extract modal information of natural frequency, modes shapes, damping and other frequency dependent structural properties. This technique assumes linear damping. The primary technique in the time domain is the Log Decrement Time History (LDTH). This model does not assume linear damping but can not give mode shape information readily.

Frequency Response Methods

Three basic FRF methods used in this investigation are; 1.) Real component of the FRF ($\text{Re}(\text{FRF})$), 2.) Imaginary component of the FRF ($\text{Im}(\text{FRF})$), and 3.) Circle Fit of Nyquist plot data. Looking at the imaginary part of the acceleration FRF (ref Figure 2.a), for a single degree of freedom system (SDOF),

$$\text{Im}(\text{FRF}) = \frac{2\zeta \frac{\omega_n}{\omega}}{\left(1 - \left(\frac{\omega_n}{\omega}\right)^2\right)^2 + \left(2\zeta \frac{\omega_n}{\omega}\right)^2} \quad (1)$$

where $\omega_n = \sqrt{\frac{k}{m}}$, ω is the driving frequency and ζ is the damping ratio. It can be shown that the maximum response, or resonance, is near the natural frequency (within 1-3 %) for moderate damping ($\zeta < .05$), and has a magnitude of,

$$\text{Im}(\text{FRF})_r \approx \frac{1}{2\zeta} = m \frac{\ddot{X}}{F} \quad (2)$$

where \ddot{X} , F , and m are the acceleration, magnitude of the driving force and effective mass. By looking at a point, b , near resonance a relation for relative magnitudes can be developed;

$$Im(FRF)_b = \frac{2\zeta \frac{\omega_n}{\omega_b}}{\left(1 - \left(\frac{\omega_n}{\omega_b}\right)^2\right)^2 + \left(2\zeta \frac{\omega_n}{\omega_b}\right)^2} \approx \frac{\ddot{X}_b}{\ddot{X}_r} \frac{1}{2\zeta}. \quad (3.)$$

Let

$$\frac{\omega_n}{\omega_b} = D; \quad \frac{\ddot{X}_b}{\ddot{X}_r} = R. \quad (4.a,b)$$

By incorporating equations 4.a and 4.b into equation 3. and restructuring the result, it can be seen;

$$\zeta \approx \frac{|1 - D^2|}{2\sqrt{D\left(\frac{1}{R} - D\right)}}. \quad (5.)$$

Looking at the real part of the acceleration FRF (ref Figure 2.b), SDOF,

$$Re(FRF) = \frac{1 - \left(\frac{\omega_n}{\omega}\right)^2}{\left(1 - \left(\frac{\omega_n}{\omega}\right)^2\right)^2 + \left(2\zeta \frac{\omega_n}{\omega}\right)^2}, \quad (6.)$$

where ω_n , ω and ζ are defined as before. The point at which this function crosses the zero axis is the natural frequency ω_n . It can also be shown that

$$\left(\frac{\omega_n}{\omega_{\min}}\right)^2 = 1 \pm 2\zeta, \quad \left(\frac{\omega_n}{\omega_{\max}}\right)^2 = 1 \pm 2\zeta, \quad (7.a,b)$$

where ω_{\min} and ω_{\max} are the frequencies of maximum and minimum values of response. While one will occur one each side of the crossing frequency, which will have a higher frequency is dependent of the mode shape of response. From this it is obvious that;

$$\zeta = \frac{1 \mp \left(\frac{\omega_n}{\omega_{\max}}\right)^2}{2}, \quad \frac{1 \mp \left(\frac{\omega_n}{\omega_{\min}}\right)^2}{2}. \quad (8.a,b)$$

Circle fit theory is of a much more complicated nature and can be referenced in Ewins¹⁶ and Luk and Mitchell¹⁷. Basically it involves constructing a plot of the real versus imaginary components of the FRF into a Nyquist plot. It can then be shown that the developed circle has a diameter inversely proportional to the damping constant, ζ . This plot is only truly a circle for the mobility FRF for viscous damping and the dynamic compliance FRF for structural damping. In the case if light damping, less than 1 percent most models work well. Two other frequently used methods are the magnitude of the total FRF and the phase angle of the FRF (refer Figure 3.a.,b).

Log Decrement Method

The log decrement method entails exciting a structure and measuring the decay of the cyclic vibration when the exciter is removed. From the relative amplitude of successive cycles of vibration and period of damped vibration, τ_d , the damped natural frequency, ω_d , damping ratio, and natural frequency, ω_n , can be extracted. The log of relative amplitudes of successive cycles is called the log decrement, δ and is defined as;

$$\delta = \ln \frac{x_i}{x_{i+1}} = \frac{1}{n} \ln \frac{x_i}{x_{i+n}} \quad (9.)$$

where, x_i , x_{i+1} , and x_{i+n} are amplitude of response at those points in time. From this, for light damping ($\zeta < .03$), it can be shown;

$$\zeta = \frac{\delta}{2\pi} \quad , \quad \omega_d = \frac{2\pi}{\tau_d} \quad (10.a,b)$$

Through plotting, log decrement results, on semi-log paper one can determine easily (often visually) if the damping is indeed linear or of another relation.

Experimental Results

Looking first at the results of the partial coverage experimentation, (refer Figure 4.a.,b and 5.a.,b), the structure tested here was a isotropic beam of Aluminum 6061-T6 with damping treatment of ISD-112 (from 3M), a viscoelastic material. The physical dimensions were; for the base beam 9.00 (l) by .875 (w) by .125 (t), the damping treatment was .875 (w) by .005 (t) for the viscoelastic and .010 (t) for the aluminum backing material (all dimensions inches). The application length, A, of the treatment was varied in 25 percent increments of total length, L, ($A/L = 0.25, 0.50, 0.75, 1.00\%$).

The cantilever first mode shows good agreement between real and imaginary FRF techniques. The log decrement graph reports lower damping values and an earlier peak than the FRF methods. The circle fit data, though in a loosely related pattern, doesn't provide useful information about this mode. It appears that the FRF methods bound the log decrement methods from above. Both show a peak in the neighborhood of 50 % (A/L). This is in agreement with previous authors work. The circle fit data discrepancy is due in part to the moderate damping values, decision to use viscous damping model, and the use of acceleration FRF.

The cantilever second mode shows good agreement between real, imaginary, and circle fit methods up to 75 % (A/L). This graph also shows that there is a continual gain in damping with increasing application length.

The fixed/fixed first mode shows less than ten percent deviation for the entire test between all methods used. It also shows that the damping ratio increases consistently with increasing treatment in an almost linear fashion.

The fixed/fixed second mode shows significant deviation in the methods. This difference reaches a maximum of 40 % at an application length of 50 % between the Re(FRF) and circle fit methods. The complement of the test has more reasonable 20 % or less deviations. The main cause in this error is attributable to the low resolution of this high frequency mode.

The time domain approach, as previously mentioned, compared well with the frequency response methods for the cantilever first mode. For the integrally damped beams the effects are not as readily apparent. The first beam was a 3-ply graphite-epoxy laminate [90/0/90] (refer Figure 6.a). This beam was used as a building block for the successive beams. By extracting the damping of this structure, future beams could be thought of a three layer beams with this as one of the layers. The second beam was constructed of two of these laminates surrounding a 10 mil layer of polypropylene (refer Figure 6.b). This increased the bending moment of inertia thereby increasing the relative bending stiffness. The next beam replaced the polypropylene with damping material (ISD-112 from 3M) of equal thickness (refer Figure 7.a). This was designed to increase damping while not effecting stiffness significantly. The final beam was constructed two of the laminates, similar to the third beam, subsisted of sandwiching a 10 mil thick layer of polypropylene (refer Figure 7.b).

The first beam had a damping constant of 1.2%. The second beam reported a value of .4% damping, this is in part due to the increased moment and the slight stiffening the polypropylene gives the beam. The third beam reports a value of 11% damping, demonstrating the significant effect integral damping can achieve. Note also that the natural frequency did not change greatly, indicating that the bending stiffness was not adversely effected. The last beam reports the same value for damping as the third. The natural frequency of the forth beam is much less than the third which may show that the central layers are not adding much stiffness mainly weight. The plot of integrally damped beam response on semi-log format shows a nearly linear relation, indicating close to linear damping, (refer Figures 8.a.,b).

Conclusions

The partial treatment shows an optimum for the first mode cantilever in there neighborhood of 50 % (A/L) application length. The second modes of clamped/clamped and cantilever in addition to first mode clamped/clamped show consistently increasing damping with increasing application length.

The incorporation of damping material in the central part of the structure appears to be the most efficient method to increase damping.

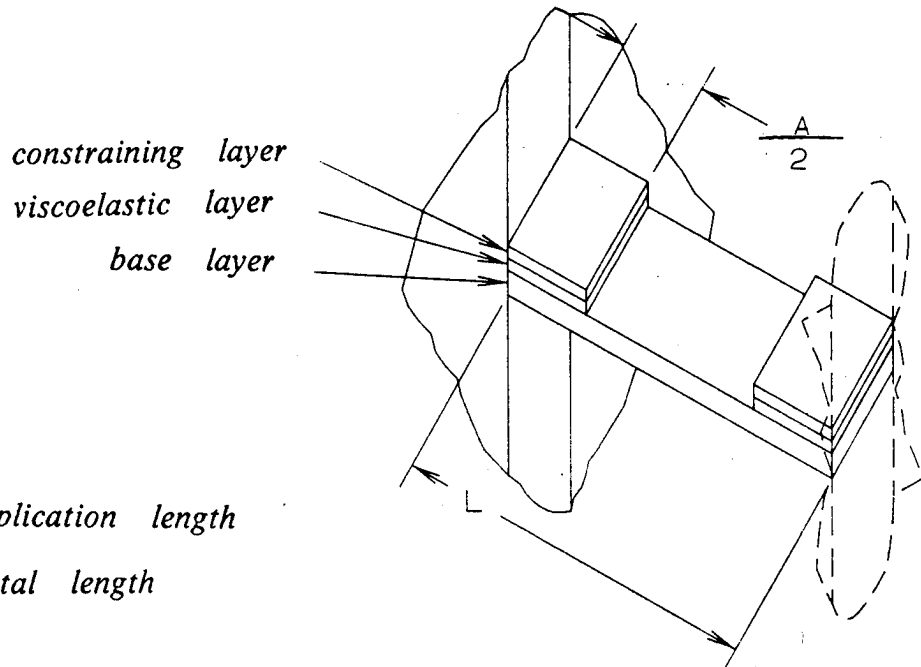
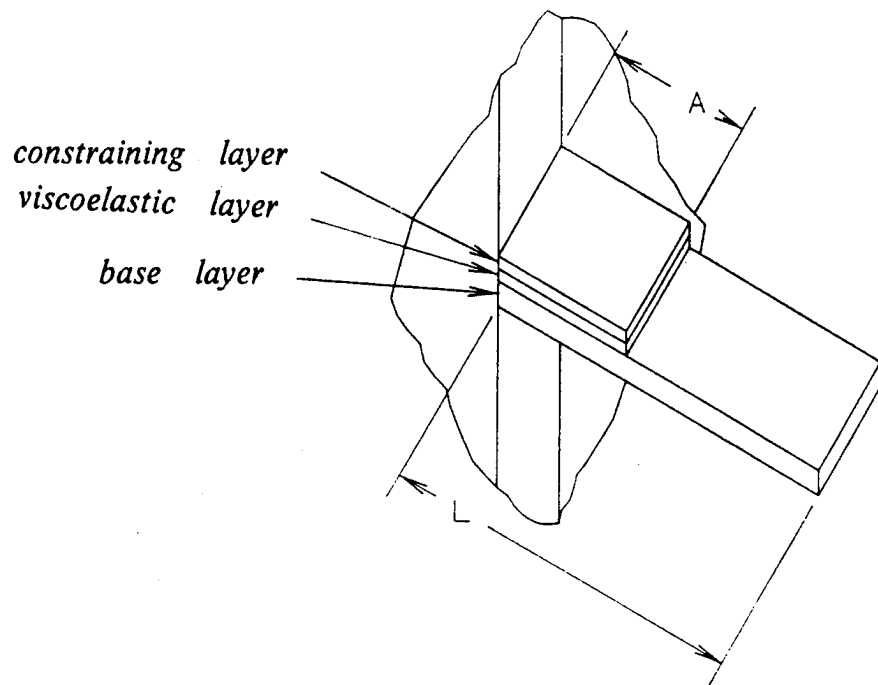
The frequency domain techniques of the Real and Imaginary components of the FRF agree reasonably well with each other for the light damping investigated here, but care must be taken to assure sufficient spectral resolution of test. They also appear to be an upper bound for the log decrement method. The circle fit data must be re-evaluated using a mobility FRF model.

The log decrement tests show that damping is fairly linear for all the beams tested. Also the test showed peaks in the expected region for the case of cantilever first mode.

REFERENCES

1. Mar, J. W.; "Some Musings on How to Make Damping a Creative Force in Design" Vibration Damping 1984 Workshop Proceedings, Wright-Patterson Air Force Base, November, 1984.
2. Oberst, H. "ueber die Dampfung der Biegeschwingungen dunner Bleche durrch fest haftende Belage," Acustica, Vol.2, Akustische Beihefte No.4, 1952, pp.181-194. (Translation by H.L. Blackford, Inc., 24 Commerce St., Newark, N.J.)
3. Ross, D., Ungar, E.E., and Kerwin, Jr., E.M., "Damping of Flexural Vibrations by Means of Viscoelastic Laminae," Section III *Structural Damping*, ASME, New York, NY, 1959.
4. DiTaranto, R. A.; "Effect of End Constraints on the Damping of Laminated Beams" *The Journal of the Acoustical Society of America*, Vol. 39, No. 2, 1966, pp. 405-407.
5. DiTaranto, R. A. and W. Blasingame; "Effect of End Constraints on the Damping of Laminated Beams" *The Journal of the Acoustical Society of America*, Vol. 39, No. 2, 1966, pp. 405-407.
6. DiTaranto, R. A. and W. Blasingame; "Composite Damping of Sandwich Beams" *Journal of Engineering for Industry*, November, 1967, pp. 633-638.
7. Mead, D.J., and Markus, S., "The Forced Vibration of Three-Layer, Damped Sandwich Beams with Arbitrary Boundary Conditions," *Journal of Sound and Vibration*, Vol. 10, No. 2, 1969, pp. 163-175.
8. Mead, D.J., and Markus, S., "Loss Factors and Resonant Frequencies of Encastre' Damped Sandwich Beams," *Journal of Sound and Vibration*, Vol. 12, No. 1, 1970, pp. 99-112.

9. Mead, D.J., "Governing Equations for Vibrating Constrained-Layer Damping Plates and Beams," *Journal of Applied Mechanics*, June, 1973, pp. 639-640.
10. Kerwin, E. M. Jr., , "Damping of Flexural Waves by a Constrain Viscoelastic Layer," *The Journal of the Acoustical Society of America*, Vol. 31, ,No. 7, 1959, pp. 952-962.
11. Rao, D. K., "Frequency and Loss Factors of Sandwich Beams Under Various Boundary Conditions," *Journal of Mechanical Engineering Science*, Vol. 20, ,No. 5, 1978, pp. 271-282.
12. Drake, M. L., "A different Approach to 'Designed In' Passive Damping" *Shock and Vibration Bulletin* No. 55, June, 1985, pp. 109-117
13. Carne, T.; "Constrained Layer Damping Examined By Finite Element Analysis"; Society of Engineering Science 12th Annual Meeting, Austin, Texas, 20-22 October 1975, Proceedings of the University of Texas, 1975, pp. 567-576.
14. Liguore, S. L.; "Evaluation of Analytical Methods to Predict Constrain-Layer Damping Behavior" Virginia Polytechnic Institute and State University, **Master's Thesis**, May, 1988.
15. Liguore, S. L. and J. B. Kosmatka ; "Evaluation of Analytical Methods to Predict Constrain-Layer Damping Behavior" Proceedings of the Sixth International Modal Conference, February, 1988. pp 421-427.
16. Ewins, D. J.*Modal Testing: Theory and Practice* Research Studies Press LTD, Letchworth Hertfordshire, England, 1986. pp 153-170.
17. Luk, Y. W. and L. D. Mitchell; "System Identification of Via Modal Analysis" *Modal Testing and Refinement*, , AMD-59, Ed: D. F. H. Chu, ASME, Nov. 13-18, 1983, pp. 31-49.



A = application length

L = total length

Figure 1.a.,b Partial Coverage Treatment of Isotropic Beams -
Cantilever and Fixed/Fixed

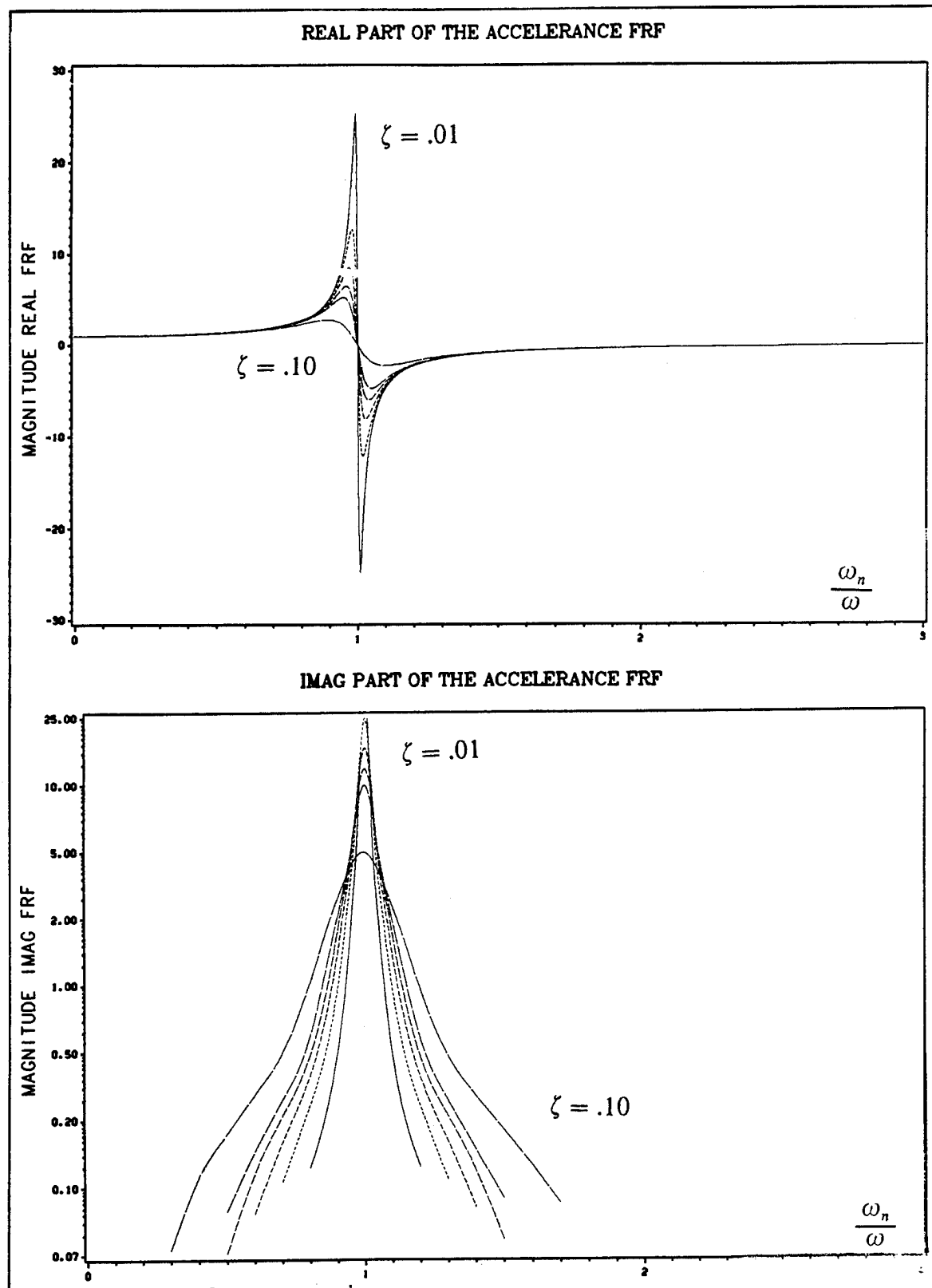


Figure 2.a,b Imaginary and Real Components of FRF - ζ from .01 to .10

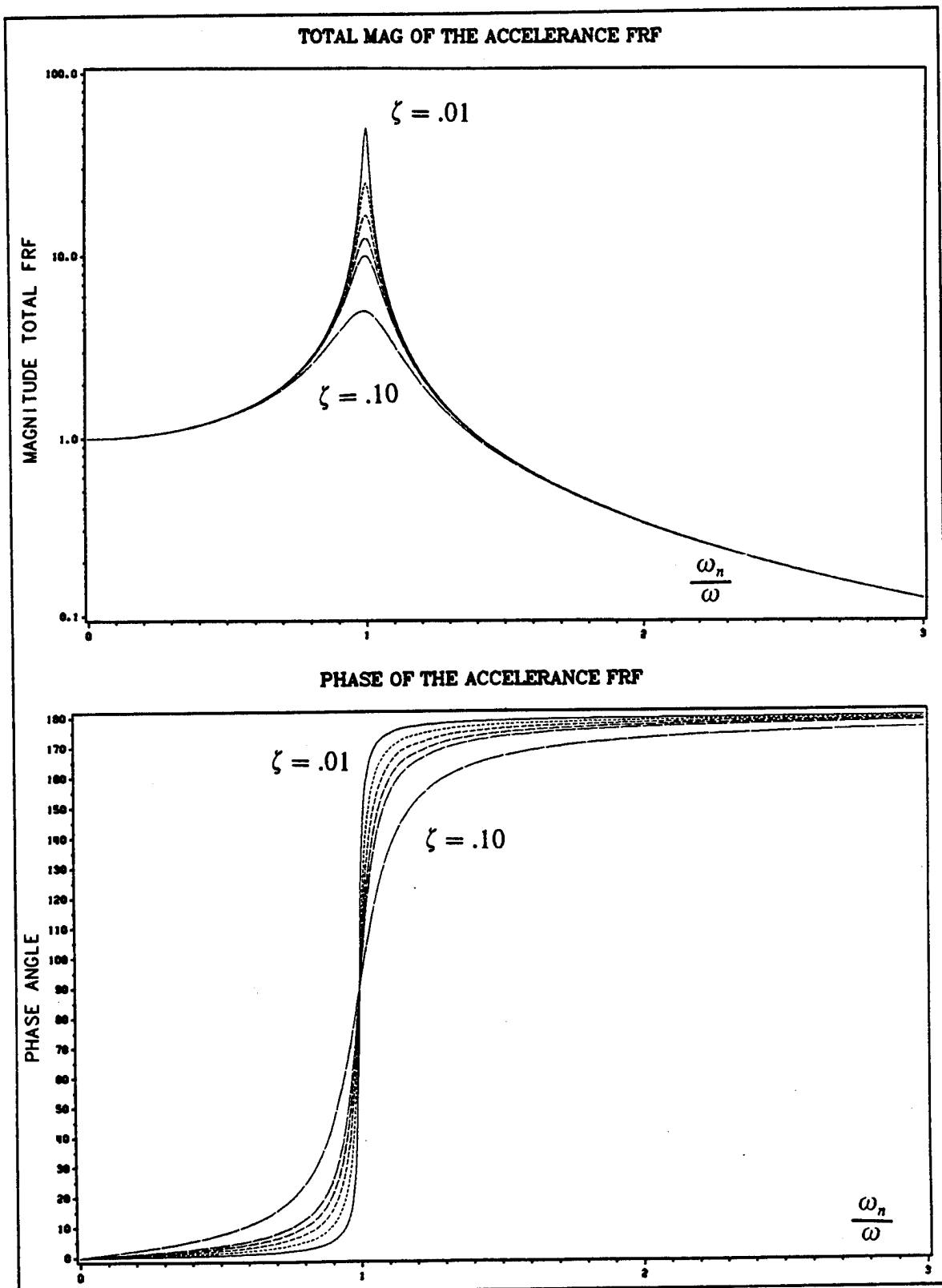
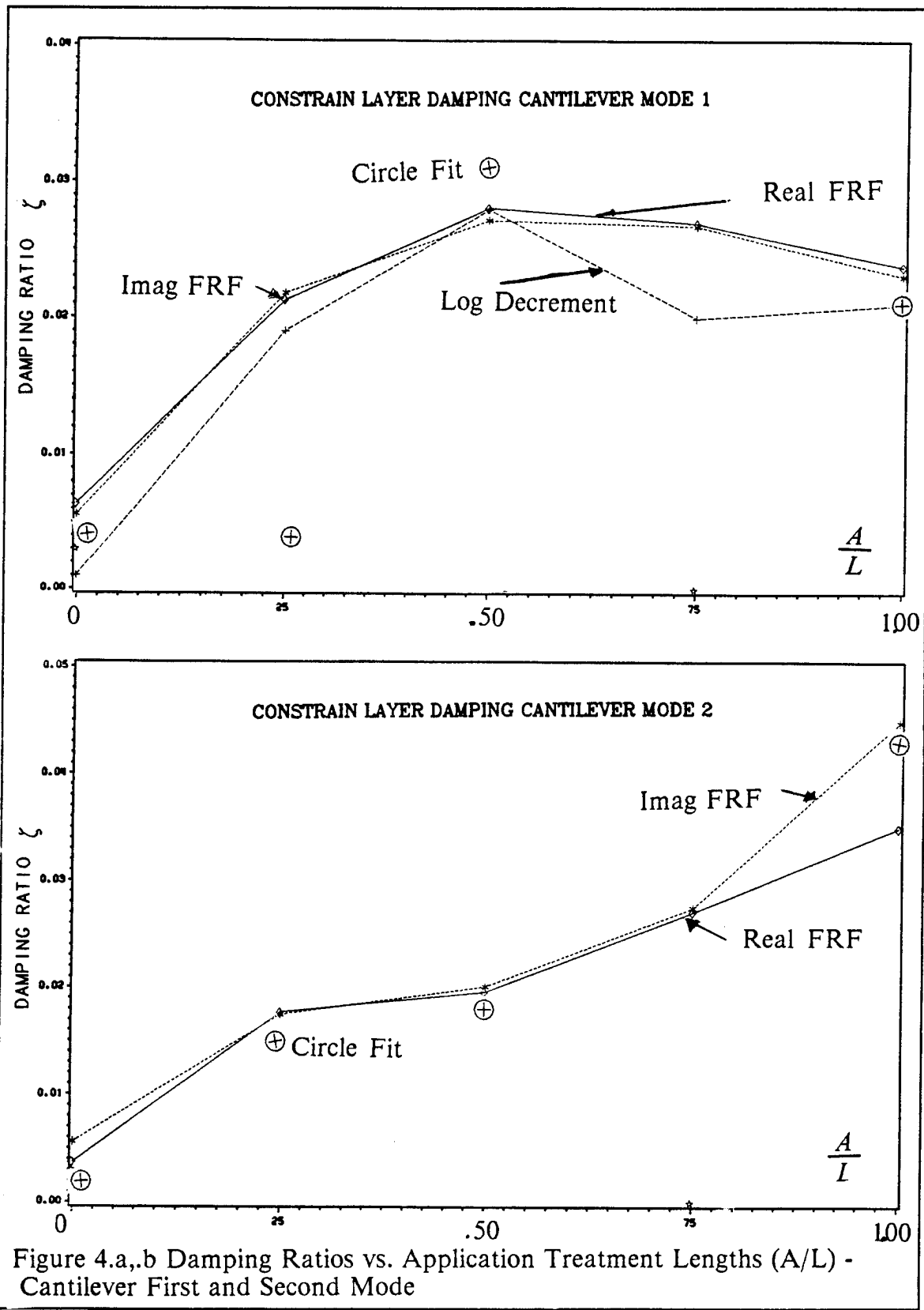
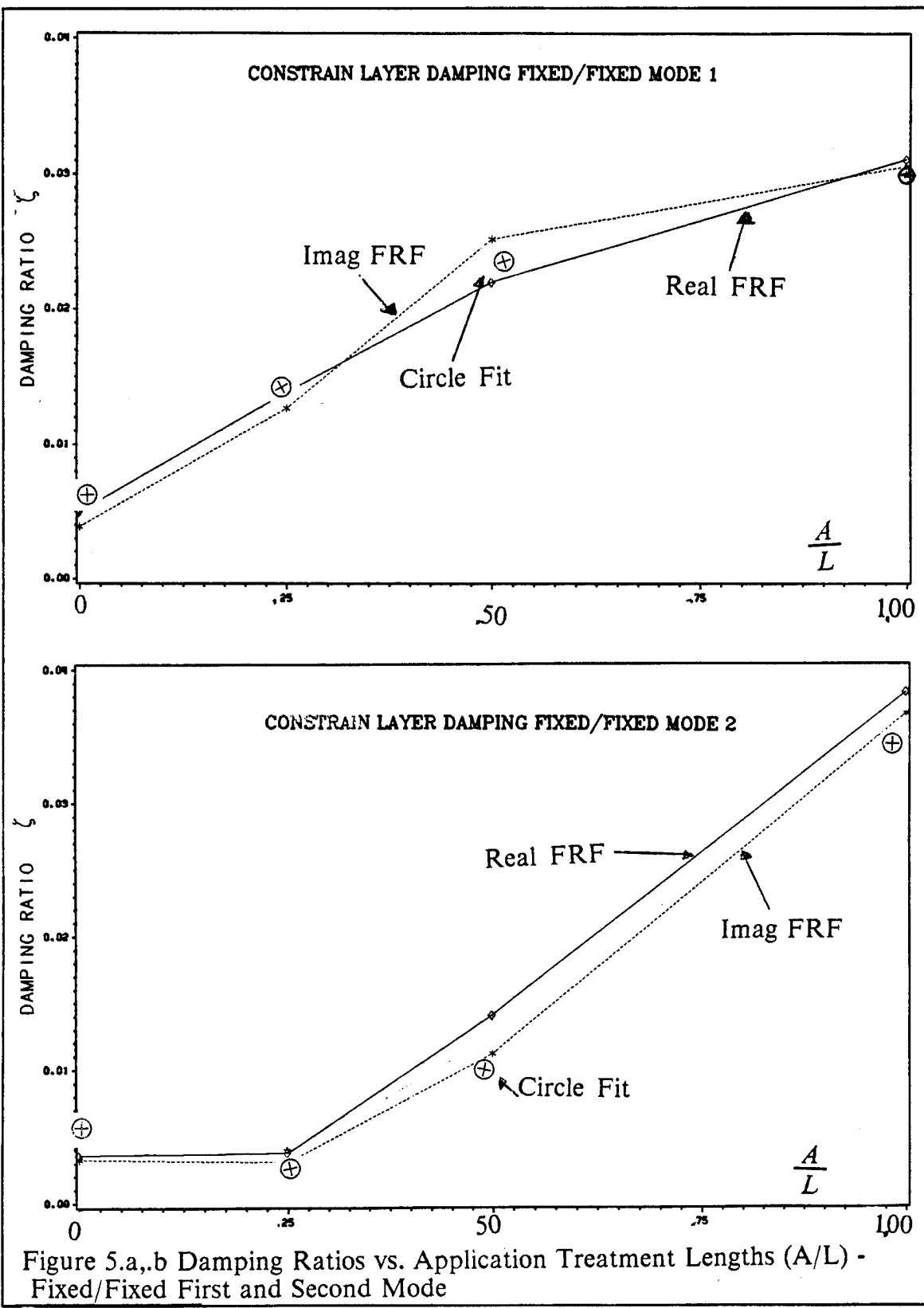
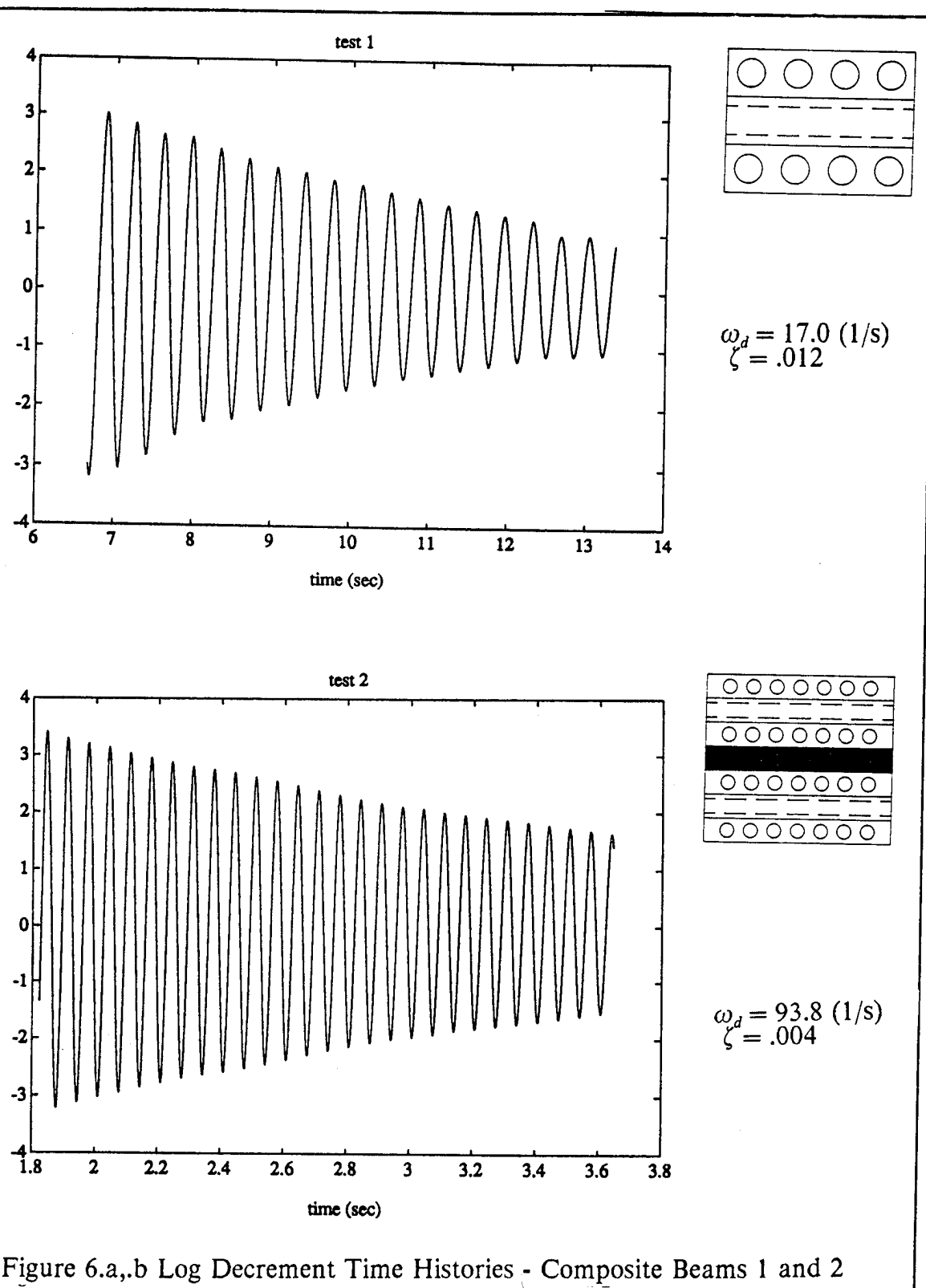
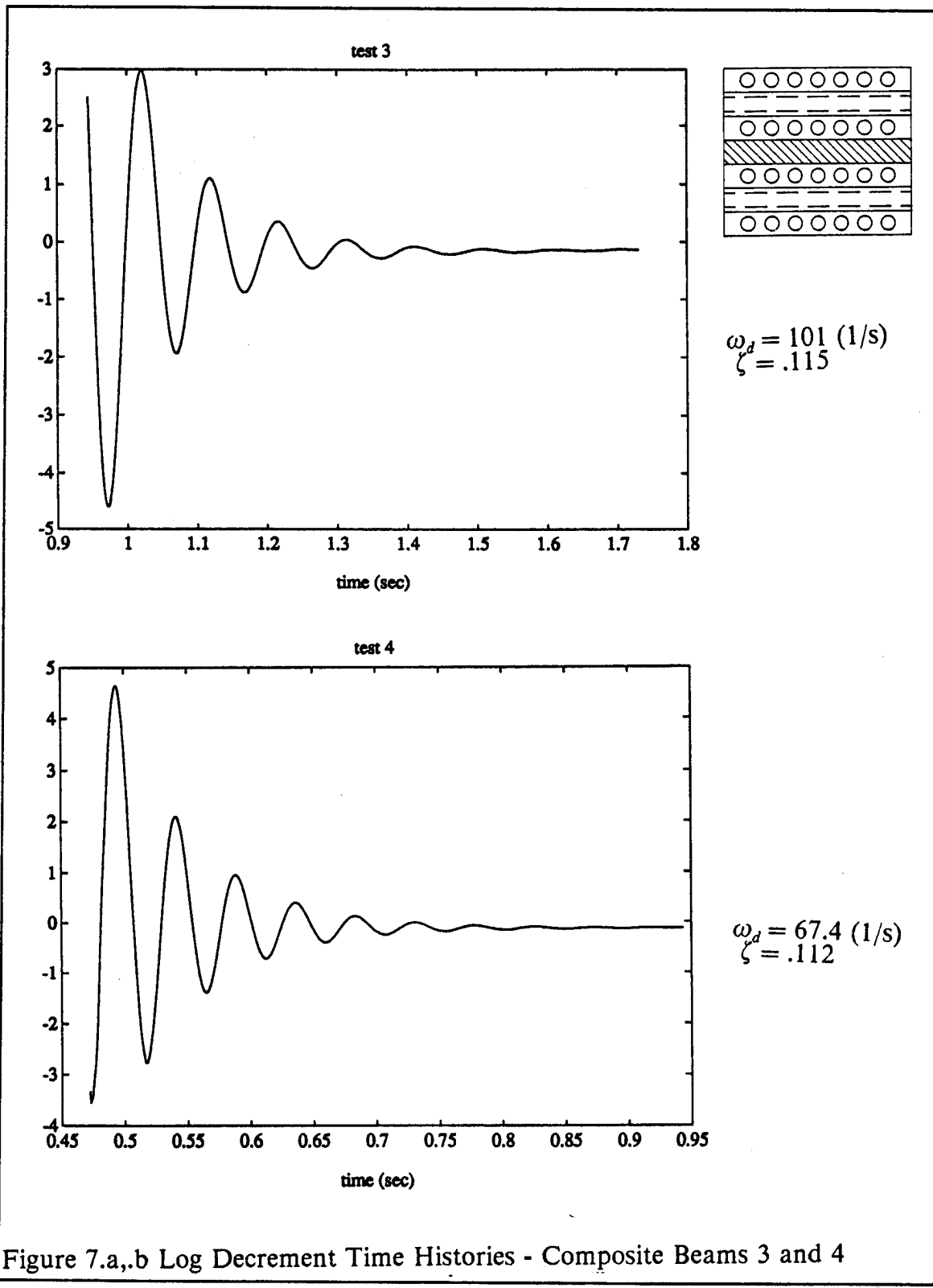


Figure 3.a,b Magnitude and Phase of Total FRF - ζ from .01 to .10









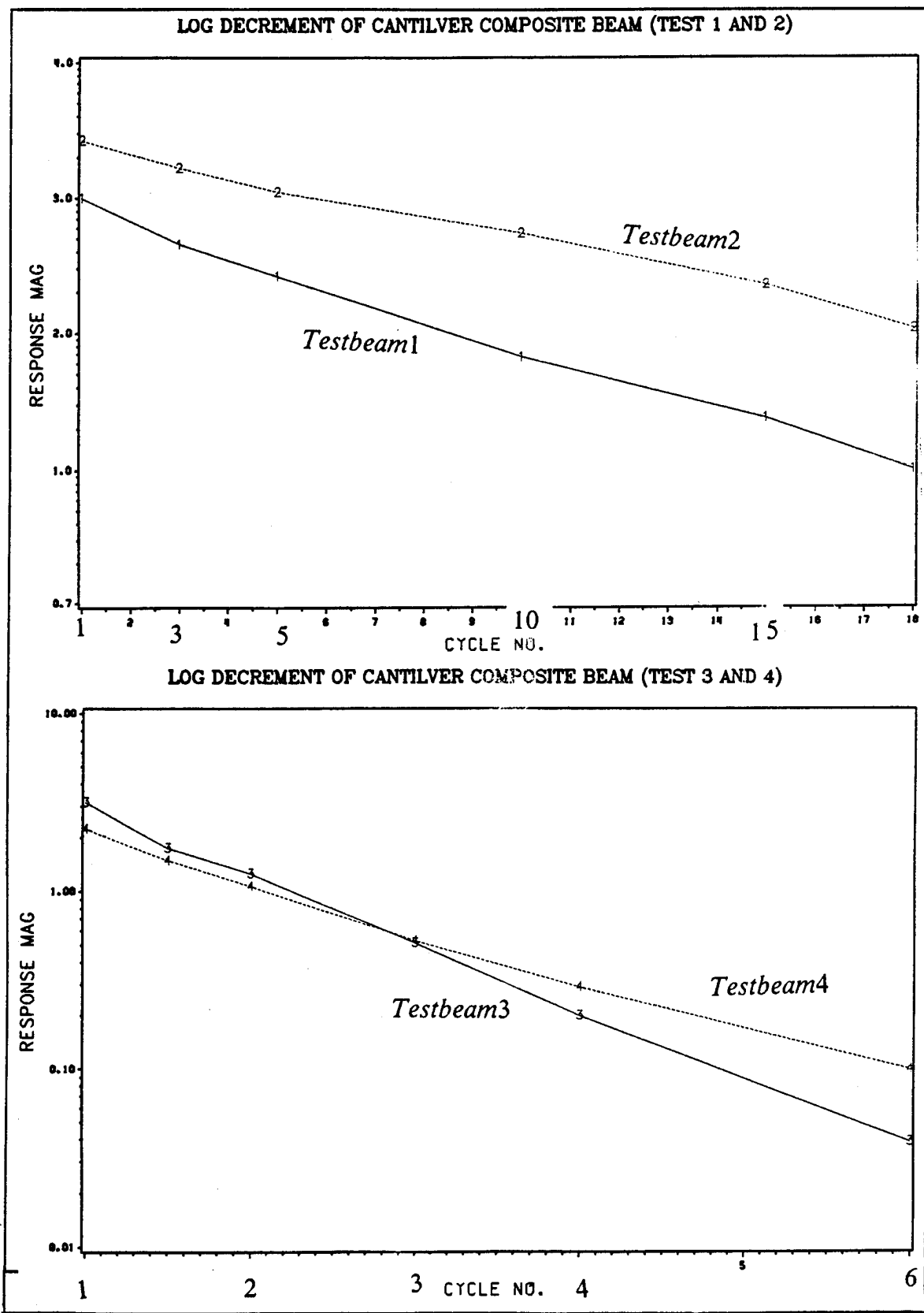


Figure 8.a,b Log Decrement Time Histories -
All Composite Beams (semi-log)

DAMPING BEHAVIOUR OF FLEXIBLE LAMINATES

by

V.A. Coveney, A.H. Muhr & A.G. Thomas

Malaysian Rubber Producers' Research Association
Tun Abdul Razak Laboratory
Brickendonbury,
Hertford SG13 8NL
England

ABSTRACT

Formulae for the mechanics of flexing of laminates of a viscoelastic material, such as an elastomer, and an inextensible material, such as steel, have been derived and compared to experiment. In particular, equations for the profile, stiffness and partition of energy between elastomer and metal are given.

The effect of an axial load on the lateral stiffness of laminar struts is investigated both theoretically and in experiments on free oscillation. As the axial load approaches the buckling load, the apparent damping level to lateral oscillations becomes very large. Conversely for an axial tension the lateral stiffness is enhanced and the damping to lateral oscillations is diminished. Other examples of this phenomenon, which is not peculiar to the laminates, are given.

1. INTRODUCTION

A characteristic of rubber springs is that they have relatively high damping, and within limits the rubber compound can be chosen to give the required level of damping. Each type of conventional rubber spring has a characteristic force-deformation behaviour which may be convenient for a particular application. In this work the properties of an unconventional rubber spring will be described, which lends itself to control of the damping level, and may have other advantages for some applications. The spring consists of a sandwich structure of metal and rubber (Figure 1). Attention will be concentrated on the flexing mode of deformation (analogous to that of a leaf spring).

The mathematical expressions for the mechanical properties of the laminate are relatively simple, so the properties can be readily calculated. While this is a desirable state of affairs for an engineering component, it also means that physical insight is not obscured by mathematical complexity. For example, not only is the effect of an axial load on the stability and apparent damping level (to lateral oscillations) easy to investigate for the laminates, but the effect also helps provide insight into a general phenomenon.

2. MECHANICS OF FLEXING OF RUBBER-STEEL LAMINATES

It is assumed that:

- (i) there is no strain normal to the plane of flexure (so all forces etc. will be taken per unit breadth of laminate)
- (ii) the rubber is incompressible.

Thin, inextensible metal layers

Then, if the further assumption is made that the metal layers are inextensible and much thinner than the rubber layers ($t \ll h$), it follows that the state of deformation of the rubber is simple shear and the metal layers deform to have a common centre of curvature. This is demonstrated in Figure 2, from which it may be readily concluded that the volume of the element PQRS is constant provided:

$$\delta v = h \delta \theta \quad (1)$$

which is the condition of inextensibility.

Since the element PQRS is not necessarily initially in a state of zero shear, δv may be identified with the increase in shear movement of one metal layer relative to the other. Thus the angle of shear γ is related to the slope θ of the laminate by:

$$d(\tan \gamma)/d\theta = 1 \quad (2)$$

Equation (2) may be integrated and for the case that the deflection y of the laminate is small so that all the angles are small, simplified to give:

$$\tan \gamma = \theta + \text{constant} = dy/dx + \text{constant} \quad (3)$$

where the co-ordinates (x, y) are defined in Figure 2. Throughout the rest of this paper the choice of co-ordinates allows the constant term in (3) to be dropped, since it can in each case be seen that $\tan \gamma = 0$ when $dy/dx = 0$. Only in relating θ to dy/dx has the assumption of small angles (and hence large radius of curvature of the laminate and small strain in the rubber) been made, equations (1) and (2) being of more general validity.

The shear in an element of rubber imposes an increment δF in compressive force per unit breadth on one metal layer and a corresponding increment in tensile force on the other layer:

$$\delta F = G \delta x \cdot \tan \gamma \quad (4)$$

where G is the shear modulus of the rubber. Integration of equation (4), using appropriate boundary conditions, yields the compressive (or tensile) force F as a function of x .

The differential equation describing the profile of the flexed laminate can be derived by consideration of the forces on an element, as depicted in Figure 3. The total shear force S per unit breadth borne by the laminate is distributed between the shear force S_R borne by the rubber layer and the shear forces S_1 and S_2 borne by the metal layers.

$$S = S_1 + S_2 + S_R \quad (5)$$

Relating S_R to the shear in the rubber and S_1 and S_2 to the curvature gradient in the metal ($S_1 = -dM_1/dx$, $S_2 = -dM_2/dx$, where M_1 and M_2 are the bending moments in the metal layers), equation (5) can be written as

$$\begin{aligned} S &= Ght \tan \gamma - d(M_1 + M_2)/dx \\ &= Ght \tan \gamma - K(d^3 y/dx^3) \end{aligned} \quad (6)$$

where it has been assumed that the radius of curvature is large compared to the laminate thickness and K is given by

$$K = k_1 + k_2 = (E_1 t_1^3 + E_2 t_2^3)/12 \quad (7)$$

where k_1 , k_2 are the bending stiffnesses of the metal layers, E_1 , E_2 are their Young's moduli and t_1 , t_2 are their thicknesses (in the rest of this paper $E_1 = E_2$, $t_1 = t_2$ so that the subscripts will be dropped). Inserting (3) into (6) gives

$$S = Gh(dy/dx) - K(d^3 y/dx^3) \quad (8)$$

which is applicable for the case that $t \ll h$ and the metal layers are inextensible.

The local strain energy density in the rubber is just $0.5G(\tan\gamma)^2$ so that the total strain energy (per unit width) U_R stored in the rubber is

$$U_R = 0.5Gh \int (\frac{dy}{dx})^2 dx \quad (9)$$

where use has been made of equation (3).

The energy stored in the metal layers can similarly be calculated as

$$U_M = 0.5K \int (\frac{d^2y}{dx^2})^2 dx \quad (10)$$

The total energy stored is $U_R + U_M$

Geometric effect of thick metal layers

If the metal layers have an appreciable thickness the assumption that $t \ll h$ must be relaxed. However, to a small angle approximation assumptions (i) and (ii) are satisfied if the deformation is such that the central lines of the metal layers have a common centre of curvature. The rubber is not then just deformed in simple shear but suffers some compression and extension on the surfaces bonded to the metal in regions of curvature. However, the effect is still an increment δv to the shear movement, given this time by:

$$\delta v = (h + (t_1 + t_2)/2)\delta\theta \quad (11)$$

Thus equation (3) becomes:

$$\tan\gamma = \frac{2h+t_1+t_2}{2h} (\frac{dy}{dx})$$

A further modification required for thick metal layers is that the shear stress in the laminate falls from $G\tan\gamma$ in the rubber to zero across the thickness of the metal layers, so that the shear term S_R in equation (5) becomes:

$$S_R = G\tan\gamma(h + (t_1 + t_2)/2)$$

Thus equation (8) becomes:

$$S = G \frac{(2h+t_1+t_2)^2}{4h} \frac{dy}{dx} - K \frac{d^3y}{dx^3} \quad (12)$$

Equation (12) has the same form as equation (8) but the geometric effect of the thick metal layers enhances the magnitude of the shear term from the rubber core. Hence in most of the work below the results are derived from (8), but the results are valid for thicker metal layers provided Gh is replaced by $G(2h+t_1+t_2)^2/4h$.

Effect of extension of the metal layers

Under the actions of the forces given by equation (4) the metal layers will suffer some longitudinal extension. The neutral axes will no longer coincide with the centre lines, and equations (1) and (11) will not be accurate. Mead and Markus¹ have allowed for this effect by means of an additional term involving the longitudinal extensions. This leads to an additional differential equation to their analogue of equation (8) or (12). Elimination of the longitudinal extensions from the pair of differential equations yeilds a fifth order differential equation analogous to (8) or (12).

This complication is not addressed in our work. As a consequence, the limits as $h \rightarrow 0$ (but G is kept fixed) correspond to metal layers which are allowed to slip at the interface, instead of metal layers which are bonded at the interface (which then becomes the common neutral axis). Thus there is an implicit assumption that as h is reduced to zero, so G is reduced to zero. A criterion for the validity of our equations is derived below.

3. THREE-POINT BEND GEOMETRY

Profile

The three point bend geometry, shown in Figure 4, is a convenient deformation for experimental measurement of the dynamic properties of the laminate on a servohydraulic test machine. It is necessary to treat the laminate in two parts, $0 < x < l$ which covers the central region, and $-a < x < 0$ which covers the overhanging region. It can be shown that in the two extreme cases of $G=0$ and of $K=0$ that the overhanging region does not influence the force-deflection behaviour, but it does have to be considered in the general case.

The profile will be symmetrical about $x=l$, so it is only necessary to solve the problem for $x < l$.

Considering first the portion of the laminate for $0 < x < l$, the bending moment B exerted on a portion of laminate to the left of the point (x, y) is given by

$$B = -Wx \quad (13)$$

B is related to the shear force S in the beam by

$$S = -dB/dx \quad (14)$$

inserting (14) into equation (8), and making use of (13) gives

$$W = Gh(dy/dx) - K(d^3y/dx^3) \quad (15)$$

The differential equation describing the profile in the region $-a < x < 0$ is the same as (15) but with W set to zero.

These differential equations are required to be solved subject to the boundary conditions

(i) at $x = -a$, $d^2y/dx^2 = 0$ since the bending moment in the metal here must be zero as it is a free end

(ii) at $x = 0$, $y = 0$ while dy/dx and d^2y/dx^2 must be the same for both equations

(iii) at $x = \lambda$, $dy/dx = 0$ as required by symmetry.

The solutions are

$$\text{for } -a < x < 0, y = A_2(e^{\alpha x} - 1) + B_2(e^{-\alpha x} - 1)$$

$$\text{for } 0 < x < \lambda, y = A_1(e^{\alpha x} - 1) + B_1(e^{-\alpha x} - 1) + Wx/Gh$$

$$\text{where } \alpha^2 = Gh/K$$

$$A_1 = (W/\alpha Gh) \frac{q^2 - 1 - 2pq^2}{2(1+p^2q^2)} \quad (16)$$

$$A_2 = A_1 + (W/2\alpha Gh)$$

$$B_1 = p(A_1 p + W/\alpha Gh)$$

$$B_2 = -A_2/q^2$$

$$p = e^{\alpha \lambda}, \quad q = e^{\alpha a}$$

It has been reported previously² that equation (16) is in good agreement with experimental observation of the profile. The deflection Y at $x = \lambda$ can be found from (16) and this leads to an expression for the stiffness of the laminate in the 3-point bend geometry:

$$(2W/Y)(\lambda/2Gh) = \frac{2\alpha\lambda(1+p^2q^2)}{2\alpha\lambda(1+p^2q^2)+(1-p)(3-q^2-p+3pq^2)} \quad (17)$$

The quantity $\lambda/2Gh$ represents the compliance in the limit of $\alpha\lambda \rightarrow \infty$, and is equal to that of a rubber spring undergoing simple shear. The quantity $\alpha\lambda$ is a non-dimensional measure of the relative importance of rubber and metal, and it is convenient to express all the results as functions of $\alpha\lambda$ (as in equation (17)).

Stored energy in 3-point bend

Inserting equation (16) into the integral expression (9) the energy stored in the rubber is given by

$$U_{R1} \text{ overhang} = \frac{Gh}{2} \int_{-a}^0 (dy/dx)^2 dx$$

$$= \frac{Gh\alpha}{4} \{ A_2^2 (1 - 1/q^2) - B_2^2 (1 - q^2) - 4\alpha a A_2 B_2 \} \quad (18)$$

$$U_{R2} \text{ central section} = \frac{Gh}{2} \int_0^{\lambda} (dy/dx)^2 dx$$

$$= \frac{Gh\alpha}{4} \{ A_1^2 (p^2 - 1) - B_1^2 (1/p^2 - 1) - 4\alpha \lambda A_1 B_1 \}$$

$$+ 2(W/Gh)^2 \lambda / \alpha + (4W/\alpha Gh) \{ A_1 p + B_1 / p - A_1 - B_1 \} \quad (19)$$

Since the energy loss associated with deforming rubber (per unit of stored energy) greatly exceeds that of metals (for strains below the yield point) the energy loss associated with deforming the laminate will be proportional to $U_R = U_{R1} + U_{R2}$. A plot of $U_R/(U_R + U_M)$ versus $\alpha \lambda$ is given in Figure 5 with values of a/λ as a parameter. It is apparent that the overhang region ($-a < x < 0$) only makes an appreciable difference for values of $\alpha \lambda$ such that the total energy is fairly evenly partitioned between rubber and metal. This effect is investigated further in Figure 6 where $U_{R1}/(U_R + U_M)$ is plotted against $\alpha \lambda$ with a/λ as a parameter. At small values of $\alpha \lambda$ the simple theory predicts a significant fraction of the deformation energy to be stored in the rubber in the overhang region. This is a manifestation of the effect of a constrained layer on the damping of panels since it suggests that a constrained layer covering a large region of a panel will have a useful damping effect on a local deformation.

Forces in the metal layers

It follows from equations (4) and (11), and from the fact that the axial force in the metal layer at $x = -a$ is zero, that the compressive force per unit width in the top metal layer is

$$F = G \frac{2h+t_1+t_2}{2h} (y - Y_a) \quad (20)$$

where $Y_a = y(x = -a)$.

It is apparent from (20) that F rises to a maximum value of $F=G(Y+Y_a)$ at $x=\ell$. If this maximum value is sufficiently large the metal layer can buckle in a manner similar to an Eulerian strut, (although the constraint of bonding to the rubber must be taken into account). This has the effect of limiting the permissible deflection Y .

The force in the bottom metal layer will, according to the boundary condition, be equal and opposite to that in the top layer. A further significance of these forces is that the resultant strain in the metal layers may lead to a departure from the assumption of inextensibility which was used to derive equation (1).

The condition of inextensibility of the metal layers may be expressed as

$$\int \epsilon dx \ll 0.5 v_{\max} = 0.5(h+(t_1+t_2)/2)(dy/dx)_{\max} \quad (21)$$

where the left hand side is the change in length of one metal layer due to its axial strain and the right hand side is the shear displacement predicted by equation (11) (reduced by a factor of one half since it is 'shared' between the metal layers). The axial strain ϵ is just F/Et , which using (20) gives

$$\epsilon = \frac{G}{Et} \frac{(2h+t_1+t_2)}{2h} (Y-Y_a) \quad (22)$$

For the extreme case of large $\alpha\ell$, $y=(x/\ell)Y$ (with $y=0$ in the overhang) so that (21) becomes

$$G/E \ll ht/\ell^2 \quad (23)$$

while for the extreme case that $\alpha\ell$ is small, $y=(W/2K)(\ell^2 x - x^3/3)$ (with dy/dx constant in the overhang) so that (21) can be recast as

$$G/E \ll ht/(a^2 + 2\ell a + 5\ell^2/6) \quad (24)$$

For rubber $G \sim 1\text{ MPa}$ while for steel $E = 210\text{ GPa}$, so the left hand side of (23) or (24) is about 5×10^{-7} . This means that provided the length to thickness ratio of the laminate is less than 100, a ratio of up to 100 between t and h is allowable. Thus for the system studied here equations (8) or (12) have a very broad range of validity. They may also be applicable to many cases of composite beams with a core layer of viscoelastic material other than rubber.

4. LAMINAR STRUTS SUBJECTED TO AN AXIAL FORCE

Profile

Interconnecting the metal layers of the laminate depicted in Figure 7 leads to the following boundary conditions:

$$\begin{aligned} \text{at } x=0 & \quad y=0 \\ \text{at } x=0, \ell & \quad dy/dx=0 \end{aligned} \quad \} \quad (25)$$

where the second condition expresses the fact that the radius of curvature of the metal layer is finite.

The total bending moment B applied by the laminate on the right hand side of position x to the laminate on the left hand side is

$$B = M + W(\ell - x) + P(Y - y) \quad (26)$$

where Y is the deflection at $y = \ell$.

Proceeding as for the three-point bend geometry then leads to

$$W = (Gh - P)dy/dx - K(d^3y/dx^3) \quad (27)$$

Integrating the equation once gives

$$d^2y/dx^2 - \alpha^2y = -Wx/K + C \quad (28)$$

where $\alpha^2 = (Gh - P)/K$

Since α is imaginary for $P > Gh$ it is convenient to express the solution of (28) in hyperbolic functions rather than exponentials:

$$y = A \sinh \alpha x + B \cosh \alpha x - \frac{Wx}{K\alpha^2} + \frac{C}{\alpha^2} \quad (29)$$

Using the boundary conditions (25) to find values for the integration constants A , B and C gives

$$\begin{aligned} y &= W/K\alpha^3 [p \cosh \alpha x - \sinh \alpha x + \alpha x - p] && \} \\ \text{where } \alpha^2 &= (Gh - P)/K && \} \quad (30) \\ p &= \tanh(\alpha\ell/2) && \} \end{aligned}$$

Stiffness

The stiffness W/Y may be found from (30) by setting $x = \ell$. Algebraic simplification then leads to

$$\frac{W}{Y} = \frac{Gh}{\ell} \left(1 - \frac{P}{Gh}\right) \left(\frac{\alpha\ell}{\alpha\ell - 2p}\right) \quad (31)$$

The quantity Gh/ℓ has been isolated in equation (31) because it is the value that W/Y takes for zero P and infinite $\alpha\ell$, and is equivalent to a rubber simple shear spring. A plot of $(W/Y)(\ell/Gh)$ for $P=0$ versus $\alpha_0\ell$ (where $\alpha_0^2 = Gh/K$) is given in Figure 8.

The effect of P on the stiffness is of interest. When $P > Gh$, equation (31) becomes

$$\frac{W}{Y} = \frac{Gh}{\lambda} \left(\frac{P}{Gh} - 1 \right) \left(\frac{\beta\lambda}{2q - \beta\lambda} \right) \quad (32)$$

where $\beta^2 = (P - Gh)/K$
 $q = \tan(\beta\lambda/2)$

Using equation (31) when $P < Gh$ and equation (32) when $P > Gh$, the non-dimensional stiffness $(W/Y)(\lambda/Gh)$ can be plotted against the non-dimensional normal load P/Gh . The results are given in Figure 9, with $\alpha_0 \lambda$ as a parameter.

Stability

As $\beta\lambda \rightarrow \pi$, $q \rightarrow \infty$ so that, from equation (32), the stiffness falls to zero. This is the point of instability, and the stability criterion may be expressed as

$$\Rightarrow \frac{\beta^* \lambda}{P} = \frac{\pi}{Gh(1 + (\pi/\alpha_0 \lambda)^2)} \quad (33)$$

For $Gh = 0$, this reduces to the usual Eulerian buckling relation.

Elastic energy stored in the flexed laminate

Equation (30) may be used to evaluate dy/dx and hence U_R , using equation (9). This gives

$$U_R = (Gh^2/2K\alpha^5) \{3\alpha\lambda/2 - 3p - p^2\alpha\lambda/2\} \quad (34)$$

Substituting for W^2 using equation (31) gives

$$U_R/Y^2 = \frac{1}{2} \left(\frac{Gh}{\lambda} \right) \cdot \frac{1}{\alpha\lambda} \cdot \{3\alpha\lambda/2 - 3p - p^2\alpha\lambda/2\} \left(\frac{\alpha\lambda}{\alpha\lambda - 2p} \right)^2 \quad (35)$$

In the case the $P > Gh$, (35) becomes

$$U_R/Y^2 = \frac{1}{2} \left(\frac{Gh}{\lambda} \right) \frac{1}{\beta\lambda} \{3\beta\lambda/2 - 3q + q^2\beta\lambda/2\} \left(\frac{\beta\lambda}{\beta\lambda - 2q} \right)^2 \quad (36)$$

The term $0.5(Gh/\lambda)$ may be identified as the energy stored in a rubber simple shear spring at unit deflection (ie. the limit as $\alpha_0 \lambda \rightarrow \infty$). A plot of the non-dimensional energy $U_R/(Y^2 Gh/2\lambda)$ versus P/Gh is given in Figure 10 with $\alpha_0 \lambda$ as a parameter. For $P/Gh=1$ the profile will be independent of $\alpha_0 \lambda$, thus explaining why all the plots in the Figure coincide at that point, since the energy in the rubber (U_R) depends on the profile. In all cases U_R exceeds the value for rubber in uniform simple shear ($GhY^2/2\lambda$). This is because the profile departs from a straight line configuration, for which the shear energy in the rubber is a minimum, when K is non zero.

It is also of interest to consider the ratio E_R of the energy stored in the rubber to the work done by the lateral force in deflecting the strut:

$$E_R = U_R / 0.5WY$$

A plot of E_R versus P/Gh is given in Figure 11 with α_L as a parameter. The magnitude of E_R determines the degree of damping experienced by lateral oscillations, as discussed below.

Forces in the metal layers

There are three contributions to the axial loading F in the metal - the imposed axial load P , the imposed moment M and the contributions δF from the shear in the rubber (equation (4)). This makes the domain of validity of the equations less broad than implied by equations (23) or (24). However, the values of P and M applied in the experiments were so modest as to not greatly affect the earlier conclusions regarding validity.

5. EXPERIMENTAL

Experimental checks of some aspects of the theory have been reported previously^{2,3} and where appropriate these results have been entered as points on the diagrams, thus allowing comparison with the theory.

Of particular interest here are the experimental measurements of the fraction of energy stored in the rubber, $U_R/(U_R + U_M)$ (Figure 5). The dynamic behaviour of the laminates was measured using a servohydraulic test machine. There were initial problems regarding the method of support of the laminate in three point bend configuration, since the metal layer tended to slide over the supports as the laminate was bent, causing frictional energy loss. This was overcome by bonding to the supports small resilient rubber pads which could deform very easily in shear, but themselves dissipate very little energy. In this manner a reliable measurement of the loss angle δ_L of the laminate could be made. The fraction of deformation energy of the laminate stored in the rubber can be found from δ_L and an independent measurement of the loss angle δ_r of the rubber:

$$U_R/(U_R + U_M) = \sin\delta_L / \sin\delta_r \quad (37)$$

where it has been assumed that the loss in the metal is negligible.

Further experimental work has now been undertaken to check the theory for the effect of axial load on the stiffness and damping of struts consisting of laminates with the metal layers interconnected at each end. These laminates were constructed by bonding (during vulcanization) nominal 0.25mm spring steel strips to each side of an unfilled natural

rubber compound. The spring steel layers were separated at each end by mild steel blocks, through which bolts passed which served as both a means of attaching the struts and to prevent relative shear displacements (at the ends of the strut) between the metal layers. The shear modulus of the rubber was measured using a separate testpiece (double shear) on a servohydraulic machine, giving a value of $G = 0.52 \text{ MPa}$. The logarithmic decrement of the rubber was determined from free torsional oscillation of the double shear testpiece at 9.3Hz. This gave a value of 0.0729, and there was very little frequency dependence. The pertinent laminate dimensions were $\ell = 257\text{mm}$ (measured from the inside edges of the mild steel end blocks), width of rubber = 44mm, width of spring steel = 57mm, $K = 0.74 \text{ Nm}$ (calculated from the measured thickness of steel, 0.27mm, and adjusted according to the excess width of steel).

The axial load was applied by means of weights as depicted in Figure 12. The stiffness W/Y and damping of the combined laminates were calculated from the frequency f and logarithmic decrement Λ of the natural oscillations of the structure according to

$$W/Y = M(2\pi f)^2 \quad (38)$$

$$\Lambda = \frac{\ln(A_n/A_m)}{n-m} \quad (39)$$

where A_n is the amplitude of the n th cycle. M is taken as the mass of the weights plus that of half of the total (unladen) structure, since the structure was symmetrical about the mid point of the laminates. For tensile axial loads the structure was hung from the top board and weights were placed on the lower board.

On the assumption that only the rubber is responsible for energy dissipation, Λ may be related to U_R by

$$\Lambda = \pi \tan \delta (U_R / 0.5 Y W) \quad (40)$$

since the fraction of energy lost on a full cycle (positive and negative shear strains) is $2\pi \tan \delta$ for low to moderate values of the loss angle δ .

The results are compared to the predictions of the theory in Figures 13 and 14.

6. DISCUSSION

It has been shown here that provided $\alpha \ell$ is sufficiently large then most of the deformation energy is stored in the rubber. It has been shown elsewhere⁴ that provided $\alpha \ell$ is neither large nor too small the springs can undergo larger deflections than conventional metal leaf springs of the same length, a compromise value of $\alpha \ell$ being around 10. It thus appears that the laminated springs have useful characteristics and are, in essence, rubber springs. The sole function of the metal layers is to constrain the deformation of the rubber to be simple shear.

An additional feature of the spring is that by using a multilayer construction, rubbers of different levels of damping can be used together in a parallel deformation. This may allow layers of very high damping elastomer to be used, as analogues to oil-filled dampers, in combination with a layer of highly elastic rubber. Elastomers with very high damping are seldom used in conventional rubber springs because, on their own, they generally suffer from unacceptably high creep. Most conventional rubber springs do not lend themselves to parallel deformation of two separate elastomers.

The effect of axial load on lateral stiffness, stability and damping of the laminar struts is close to that predicted. Considering that there are no fitting parameters available (all parameters having been determined by independent experiments) the agreement may be taken as satisfactory.

Figure 14 suggests that in fact the predicted load for instability is slightly in error, which may be due, for example, to some uncertainty in the rubber modulus. The deviation of the experimental results below the theoretical values for tensile P may arise from imperfections in the clamping at the ends of the struts, which might progressively come to resemble pin joints as the tension increases. This would act to reduce the lateral stiffness towards P/λ . The theoretical result in Figure 14 can, in fact, be interpreted as the provision by the flexing stiffness of the strut of an almost constant extra lateral stiffness, of magnitude Gh/λ , over and above the axial force term (for a pin-jointed rod) of P/λ .

As the axial load approaches the buckling load the apparent level of damping to horizontal vibrations increases asymptotically. The explanation of this phenomenon is that the apparent damping is determined by the ratio of the energy dissipated in a lateral deflection (of the given magnitude) to the energy required to achieve the deflection. The dissipated energy depends primarily on the deflection and is comparatively insensitive to the axial load (see Figure 10). In particular, the dissipated energy remains finite at the buckling load. However, the energy required to deflect the strut laterally falls towards zero as instability is approached, so that the ratio rises asymptotically.

This phenomenon is quite general, and has been reported previously for conventional laminated rubber bearings.^{5,6} Such bearings are used as building mounts to achieve isolation from seismic accelerations. Substantial damping is an essential requirement for base isolation mounts, because some excitation of the natural frequency of the building on the mounts invariably occurs. It appears that enhancement of damping could usefully be contrived by designing the system such that some of the bearings are loaded close to their point of instability. These bearings will make little contribution to the lateral restoring force, but will make a useful contribution to damping.

The sensitivity of the lateral stiffness and the damping to the axial load also has significance for the measurement of material properties. For example, the apparent damping level of a taut strip of rubber undergoing lateral vibrations is much lower than the true level of damping of the material. This phenomenon is exploited to good effect in stringed musical instruments, but may cause some test methods to give misleading results for material properties (Thomas, work to be published).

REFERENCES

1. Mead, D. J. and Markus, S., 1969, J. Sound Vib. 10(2), 163-175
2. Muhr, A. H. & Thomas, A. G., paper No.77, Rubber Division meeting of the ACS, Cincinnati, October.
3. Thomas, A.G., 1985, Proc. Int. Rubber Conf., Kuala Lumpur, Malaysia, pages 97-100.
4. Brimblecombe F.A., Muhr, A.H. & Thomas, A.G. 1987, Rubber & Plastics News, August 10th.
5. Thomas, A.G. 1982, Proc. Int. Conf. on Natural Rubber for Earthquake Protection of Buildings and Vibration Isolation, Kuala Lumpur, Malaysia (published MRRDB) pages 1-14.
6. Chan, G.K. & Kelly, J.M., 1987, Report No. UCB/EERC-86/12, Earthquake Engineering Research Center, University of California.
7. Pond, T.J. & Thomas, A.G. 1989, to be published in Journal of Natural Rubber Research.

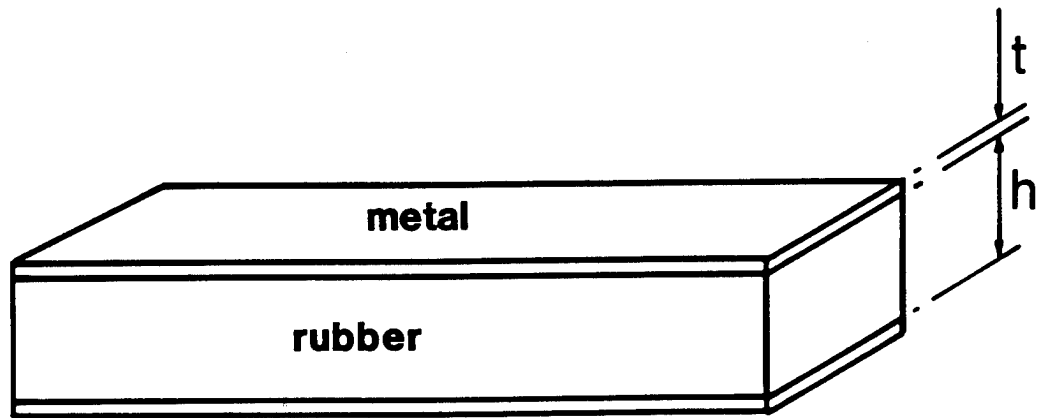


Figure 1

Structure of the laminates

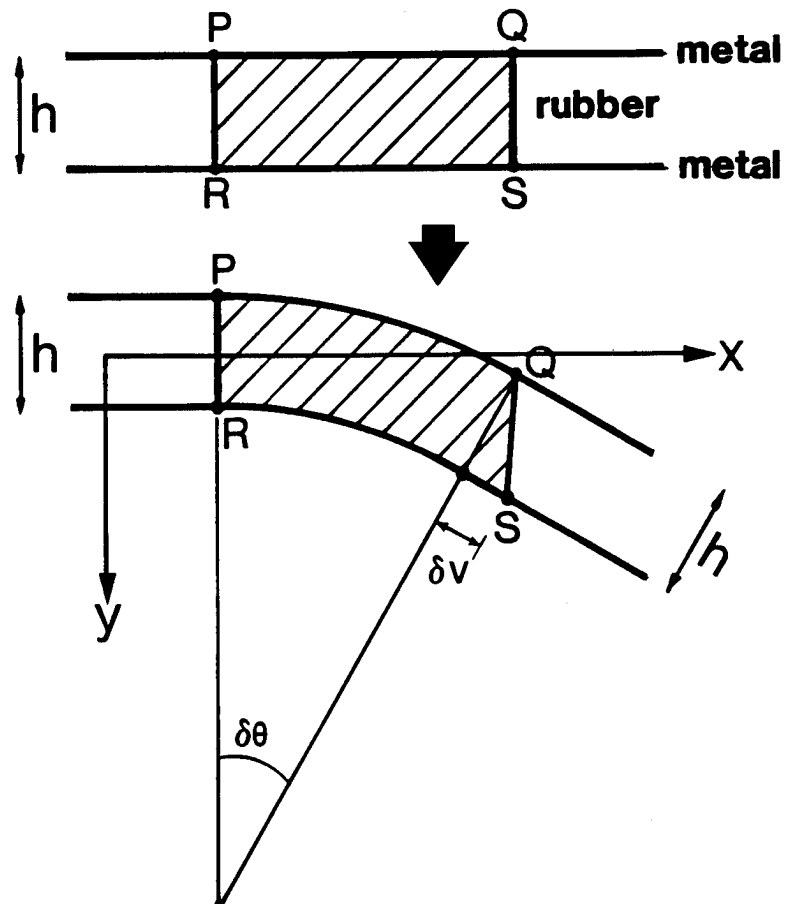


Figure 2

Deformation of an element of rubber between thin, inextensible layers of metal

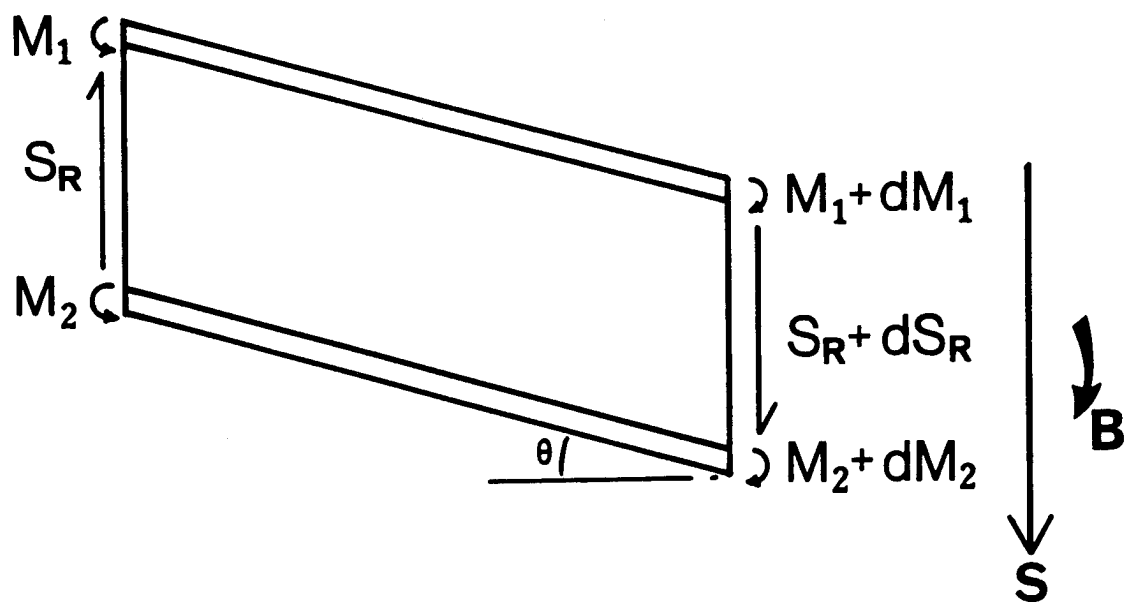


Figure 3

System of forces applied to an element of the laminate.

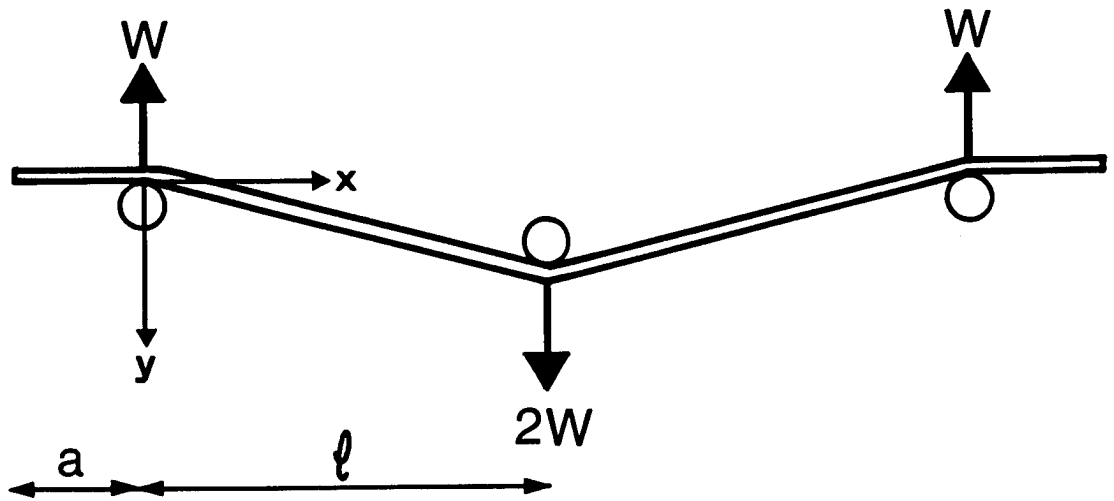


Figure 4

Three point bend geometry.

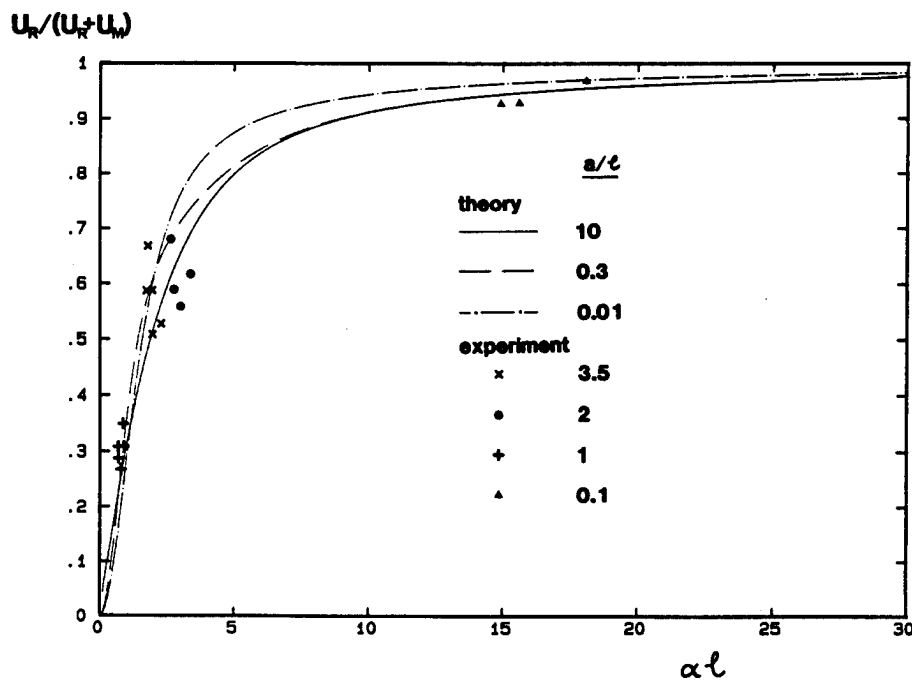


Figure 5

Fraction of energy ($U_R/(U_R+U_M)$) stored in the rubber in three point bend deformation as a function of the non-dimensional parameter $\alpha l = \sqrt{Gh/R}$

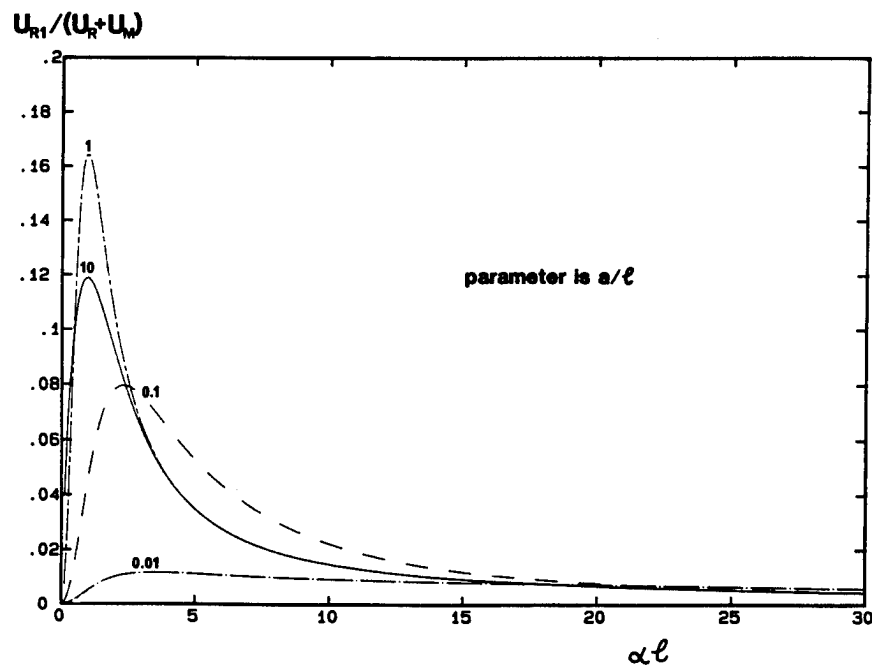


Figure 6

Fraction of energy ($U_{R1}/(U_R+U_M)$) stored in the rubber in the overhang for the three point bend deformation

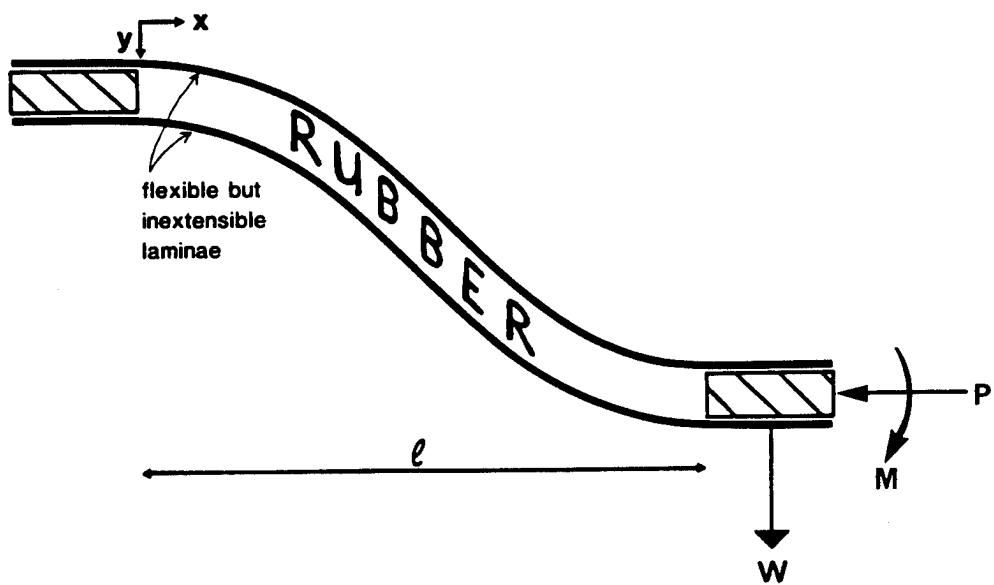


Figure 7

Laminar strut geometry (note that the metal layers are interconnected at the ends).

$(W/Y)(\ell/Gh)$

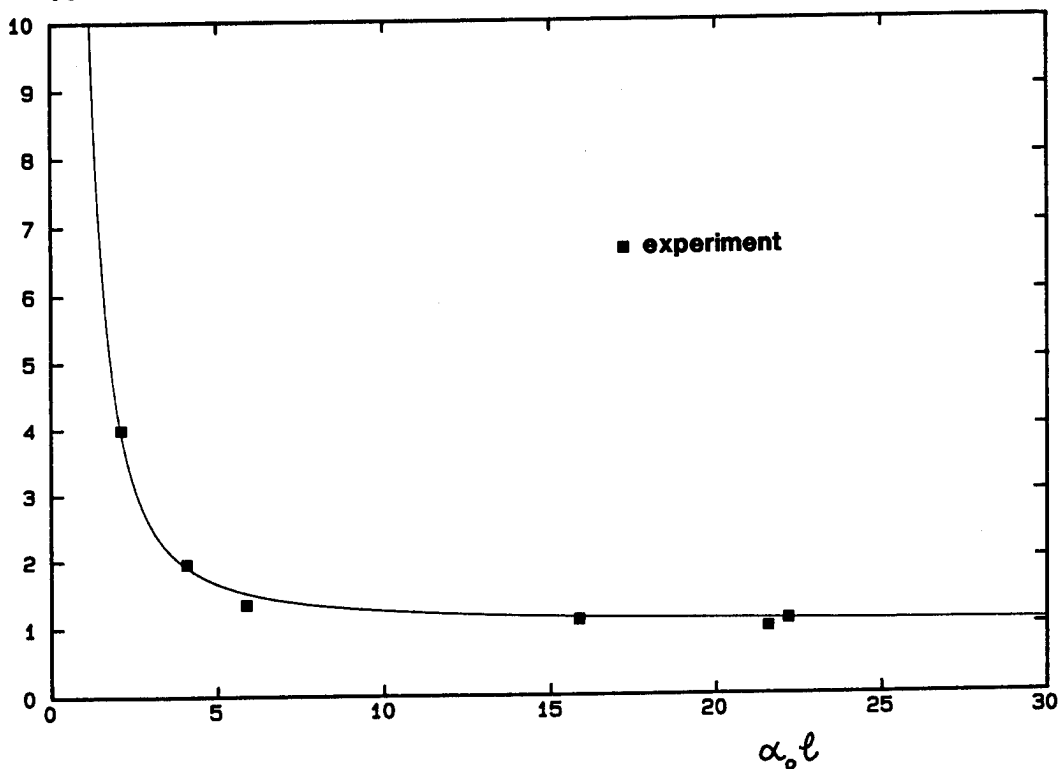


Figure 8

Lateral stiffness of laminar strut (with zero axial load) versus the non-dimensional parameter $\alpha_0 \ell$ (equal to $\sqrt{Gh/K\ell}$)

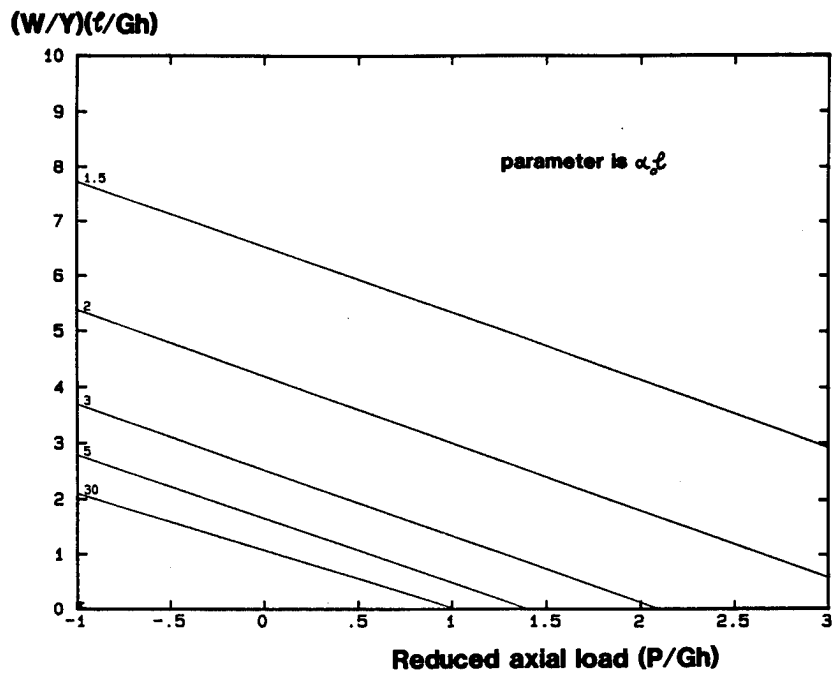


Figure 9

Effect of axial load P on the lateral stiffness of laminar struts

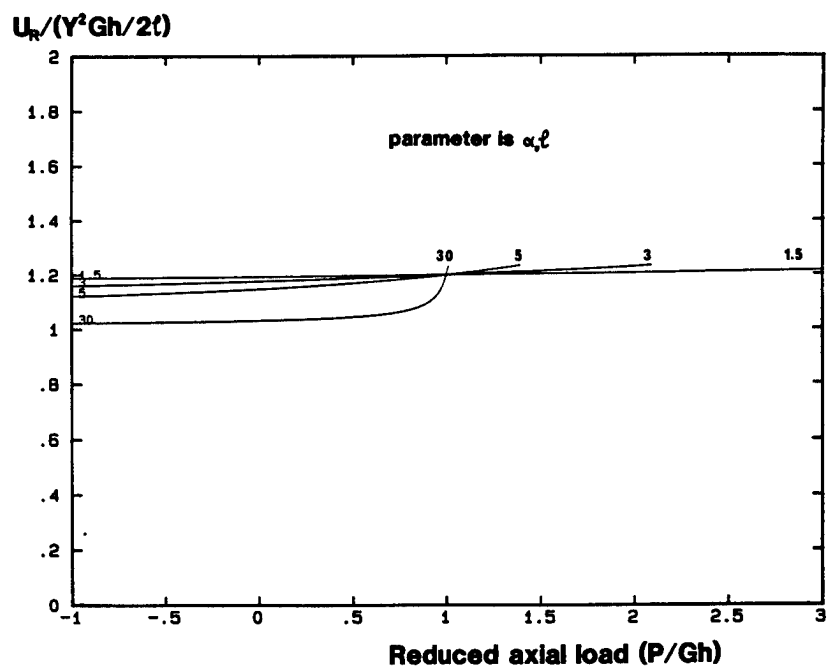


Figure 10

Effect of axial load P on the energy stored in the rubber for a laminar strut (at unit lateral deflection)

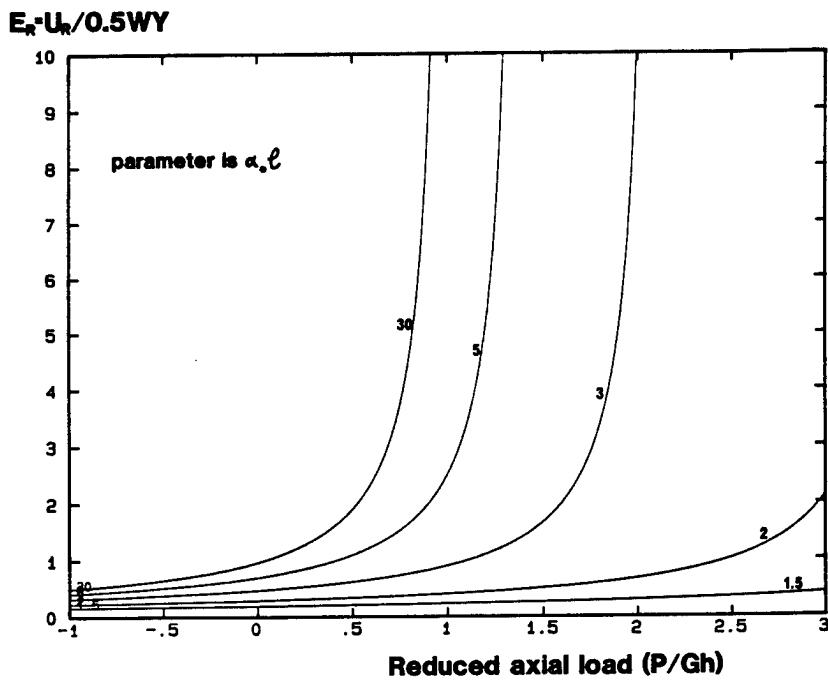


Figure 11

Effect of axial load P on the damping of lateral oscillations of laminar struts

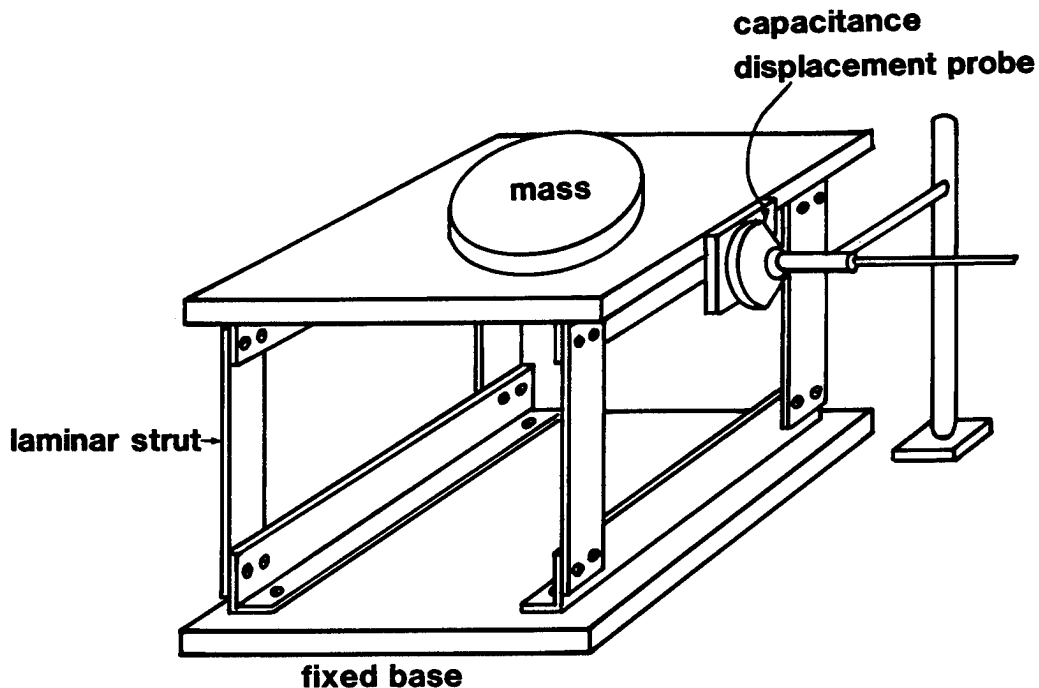


Figure 12

Arrangement for measuring the effect of axial load on the lateral stiffness and damping of laminar struts

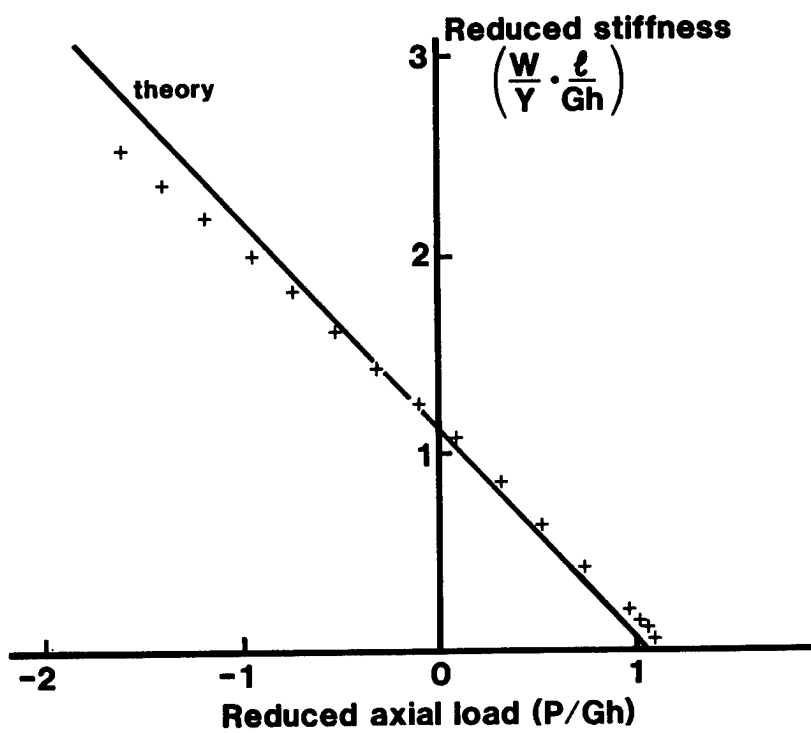


Figure 13

Experimental check of the effect of axial load (P) on the stiffness of laminar struts

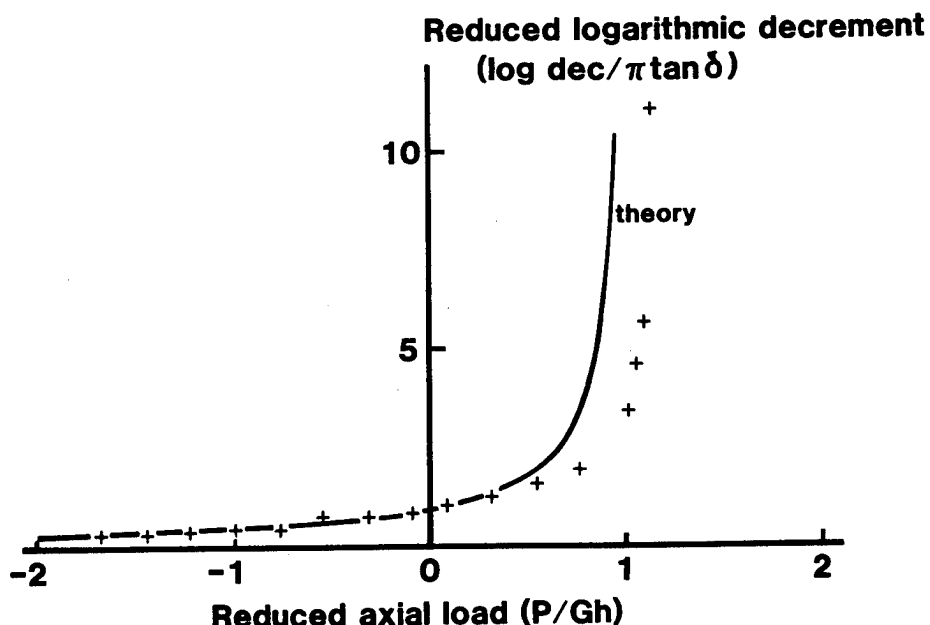


Figure 14

Experimental check of the effect of axial load (P) on the logarithmic decrement of lateral oscillations of laminar struts

APPLICATION OF THE COMPONENT ELEMENT METHOD TO THE IMPACT
DAMPED SIMPLE HARMONIC OSCILLATION

C.M. North
Rose-Hulman Institute of Technology
Box 145
5500 Wabash Avenue
Terre Haute, Indiana 47803
812-877-8216

and

R. E. Jones
Graduate Student
Texas A & M University
1917 Vinewood Drive
Bryan, Texas 77802
409-845-9599

ABSTRACT

Time histories of the impact damped simple harmonic oscillator in free decay are studied. The numerical technique of finite differences with central difference approximations is used to integrate the equations of motion. The impact process is modeled during finite time by an equivalent linear spring and viscous damper representing, respectively, material deformation and energy loss during primary and secondary mass impact. This work corroborates, by an independent method, the results of G.V. Brown and C.M. North¹ who used closed form solutions and modeled impact, in infinitesimal time, by a restitution model.

DEFINITION OF SYMBOLS

ENGLISH SYMBOLS

A = Dimensional primary mass wall thickness.

C = Dimensional viscous damping coefficient.

C_c = Dimensional critical damping coefficient.

C_M = Dimensional equivalent primary mass damping coefficient.

d = Dimensional secondary mass width.

D = Dimensional cavity width.

e = Coefficient of restitution.

E = Dimensionless total system energy at any time t.

E_0 = Dimensionless initial total system energy.

F(T) = Dimensional forcing function.

F_o = Dimensional forcing function amplitude constant.

f_o = $F_o/K\epsilon$ = Dimensionless forcing function amplitude constant.

K = Dimensional external elastic spring coefficient.

k = K_M/K = Dimensionless equivalent primary mass spring coefficient.

K_M = Dimensional equivalent primary mass spring coefficient.

M = Dimensional primary mass.

m = Dimensional secondary mass.

T = Current dimensional time.

t = $\Omega_n T$ = Current dimensionless time.

X = Dimensional primary mass displacement.

dX/dT = Dimensional primary mass velocity.

d^2X/dT^2 = Dimensional primary mass acceleration.

x = X/ϵ = Dimensionless primary mass displacement.

x_0 = Dimensionless primary mass initial displacement at t = 0.

$dx/dt = (dX/dT)/\epsilon\Omega_n$ = Dimensionless primary mass velocity.

$d^2x/dt^2 = (d^2X/dT^2)/\epsilon(\Omega_n)^2$ = Dimensionless primary mass acceleration.

dx_0/dt = Dimensionless primary mass initial velocity at time $t = 0$.

Y = Dimensional secondary mass relative displacement.

dY/dT = Dimensional secondary mass relative velocity.

d^2Y/dT^2 = Dimensional secondary mass relative acceleration.

$y = Y/\epsilon$ = Dimensionless secondary mass relative displacement.

$dy/dt = (dY/dT)/\epsilon\Omega_n$ = Dimensionless secondary mass relative velocity.

dy'/dt = Dimensionless secondary mass relative velocity immediately following impact in the restitution equation.

$d^2y/dt^2 = (d^2X/dT^2)/\epsilon(\Omega_n)^2$ = Dimensionless secondary mass relative acceleration.

dy_0/dt = Dimensionless secondary mass initial relative velocity at time $t = 0$.

Z = Dimensional secondary mass absolute displacement.

dZ/dT = Dimensional secondary mass absolute velocity.

d^2Z/dT^2 = Dimensional secondary mass absolute acceleration.

$z = Z/\epsilon$ = Dimensionless secondary mass absolute displacement.

$dz/dt = (dZ/dT)/\epsilon\Omega_n$ = Dimensionless secondary mass absolute velocity.

$d^2z/dt^2 = (d^2Z/dT^2)/\epsilon(\Omega_n)^2$ = Dimensionless secondary mass absolute acceleration.

GREEK SYMBOLS

δ = Logarithmic decrement.

ϵ = D - d = Dimensional maximum secondary mass undeformed cavity travel.

η = Loss factor.

ν = m/M = Mass ratio.

Ω_f = Dimensional sinusoidal forcing function natural frequency.

Ω_m = $(K_M/M)^{0.5}$ = Dimensional primary mass material natural circular frequency.

Ω_n = $(K/M)^{0.5}$ = Dimensional system natural circular frequency.

Ω_s = $[K/(M+m)]^{0.5}$ = Dimensional stuck system natural circular frequency.

ω_f = Ω_f/Ω_n = Dimensionless sinusoidal forcing function natural circular frequency.

ω_m = Ω_m/Ω_n = $(k/\nu)^{0.5}$ = Dimensionless natural circular frequency or the primary mass material.

ω_n = Ω_n/Ω_n = 1 = Dimensionless harmonic oscillator natural circular frequency.

ω_s = Ω_s/Ω_n = $[1/(1+\nu)]^{0.5}$ = Dimensionless natural circular frequency of the stuck primary and secondary masses.

ζ = C/C_c = Damping ratio.

ζ_m = C_M/C_c = Hysteretic damping ratio.

ζ_s = C/C_c = Dimensionless stuck damping ratio.

1. INTRODUCTION

DESCRIPTION OF THE IMPACT DAMPER

The impact damper, known also as an acceleration damper or rattle damper, is a passive type mechanical damper. It consists of an oscillator containing a secondary mass which is able to travel freely between two stops either mounted directly to the oscillator (primary mass) or between opposite walls inside a hollow cavity within the primary mass.

The system is excited either by a forcing function or a nonzero set of initial conditions (displacement and velocity). Vibratory motion of the system causes the secondary mass to strike the stops or cavity walls of the primary mass introducing energy dissipation in the form of elastic waves, heat and noise.

Practical use of impact damping includes any application where its simplicity and reliability are required. One example is space station vibrations. Impact damping is unaffected by the cold vacuum of space and would require little maintenance. A second possible application is in turbomachinery. Implementation of impact damping in turbine blades and for rotor torsional vibration would not require external structural modification.

HISTORICAL DEVELOPMENT OF IMPACT DAMPING

Publications as early as 1833 exist in the literature. The first comprehensive analysis seems to have been reported in 1945 by P. Lieber and D.P. Jensen (see P.J. Soller's² chronology) using a forced plastic impact model without external damping. Various studies were performed until S.F. Masri in 1969 demonstrated both analytically and experimentally that two equally spaced impacts per cycle did exist (see P.J. Soller²). After this, analysis of the single degree of freedom system declined because coverage of this system was thought to be adequate.

In 1982 C.M. North, while working as a Summer Faculty Fellow at NASA Lewis Research Center, initiated the study of the transient motion of the impact damped simple harmonic oscillator. In a later study he added Coulomb friction between the primary and secondary masses. Under the direction of C.M. North, S.E. Pyle⁴ in 1983 modeled the transient motion of a simple harmonic oscillator containing a viscous fluid as well as a secondary mass inside the cavity. These studies showed that the energy removed from the system by friction or by the presence of a viscous fluid was insignificant compared to that removed by impact damping.

Under the direction of C.M. North, P.J. Soller² in 1985 did a transient analysis of the externally forced and viscously damped harmonic oscillator with a single impact damper. His work checked the results of previous studies and reported the effect of mass ratio and coefficient of restitution on amplitude of vibration and duration of transient response.

In 1987, G.V. Brown and C.M. North¹ reported the results of a transient free decay time history solution of the impact damped simple harmonic oscillator. Their work showed that all the important characteristics of impact damping could be determined from a single transient free decay, precluding the need of a long term forced motion study. They reported three behavior ranges:

- 1.) a low amplitude range with less than one impact per cycle resulting in very low impact damping;
- 2.) a useful middle amplitude range with a finite number of impacts per cycle;
- 3.) a high amplitude range with an infinite number of impacts per cycle and progressively decreasing impact damping with increase in amplitude.

P.J. Torvik and W. Gibson³, in 1987, parametrically investigated the impact damper analytically and experimentally. Their work compared analytical predictions to experimental results.

In 1988, under the direction of C.M. North, T.A. Nale⁵ reported the study of the transient free decay motion of the impact damped cantilever beam. This model explored the influence of cavity location, secondary mass travel, and the higher modes on the effects of impact damping. The results revealed that cavity location and secondary mass travel can be used to optimize the damper effects on vibration amplitude. Of significance was the fact that the first mode proved to be predominant in influencing the vibratory motion of the beam, and consequently, higher modes are not required to produce an accurate assessment of the effects of the impact damper.

OBJECTIVE OF THIS STUDY

The primary objective of this study is to evaluate the effectiveness of the Component Element Method⁶ in modeling the transient free decay response of the viscously damped, simple harmonic oscillator. The method models material deformation during finite time of impact with the internal impact damper. The evaluation is made by comparison of results obtained with the previous work of G.V. Brown and C.M. North¹.

COMPONENT ELEMENT METHOD DESCRIPTION

Springs, masses and dampers comprise an assemblage of elementary components. The Component Element Method⁶ uses a finite difference step-by-step process of integrating the equations of motion of the assemblage. Because of this feature, system complexity is not limited by the ability to find closed form solutions as it is when using purely analytical methods.

The method chosen here for approximating derivatives by finite differences is the central difference approximation. As long as the time interval chosen is kept within $2(\pi)/\omega_n$, where ω_n is the highest natural frequency (rad/sec) in the system, the solutions will be accurate and converge to the exact solution (see Levy et al.⁶).

2. SYSTEM MATHEMATICAL MODEL

PHYSICAL SYSTEM

The modeled system is a simple harmonic oscillator with one internal impact damper with optional viscous damping and an optional sinusoidal forcing

forcing function. The sliding contact surfaces between the primary and secondary masses are assumed to be frictionless. The configuration shown in Fig. A is the dimensional representation of the system. The absolute displacement of the primary mass M is X . The relative and absolute displacements of the secondary mass m are Y and Z , respectively. The corresponding external spring and viscous damping coefficients are K and C , respectively. The sinusoidal force $F(T)$ is a function of real time T . The primary mass cavity wall thickness is A . The cavity width is D and d is the width of the secondary mass.

The free decay motion in this study begins at dimensionless time zero. The primary mass is released from rest with an initial dimensionless displacement of 6.0. All other initial values of relative displacement and velocity are 0.0. The primary mass equivalent material components, K_M and C_M represent, respectively, the material deformation and structural damping of the primary mass as it undergoes impact with the secondary mass (see L. Meirovitch⁷ and G.K. Hobbs⁸). Although the secondary mass also deforms and registers energy loss due to hysteresis damping, these losses are lumped into the equivalent spring and viscous damper shown schematically in Fig. A as a part of the primary mass cavity wall.

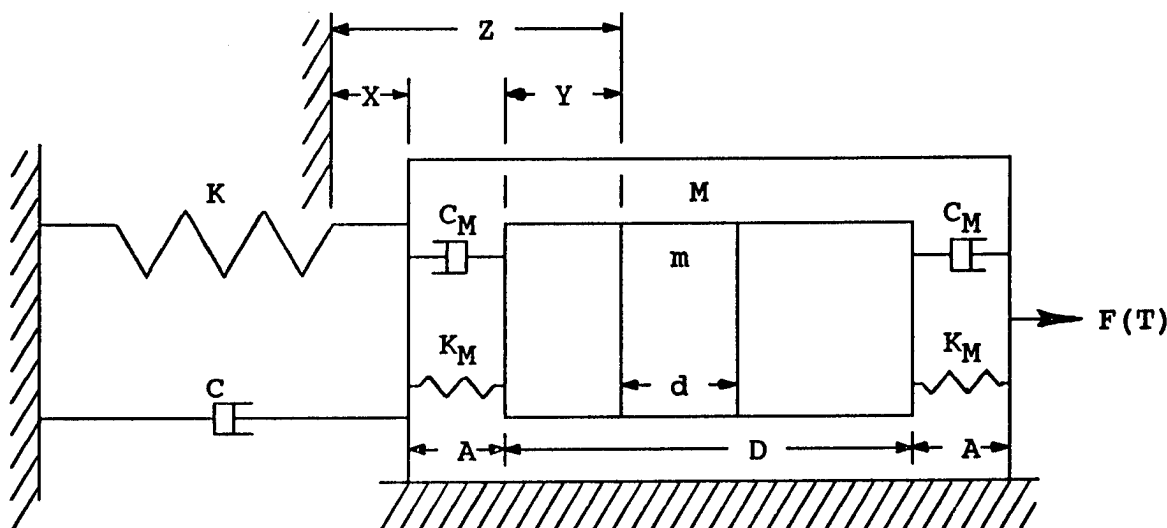


Figure A System Configuration in Free Motion

PRESENT MODEL DESCRIPTION

The model developed here uses the numerical method of finite difference with central difference approximations to integrate, with respect to time, the equations of motion of the primary and secondary masses.

Free motion is the condition where the two masses are experiencing frictionless sliding contact, but without contact between the secondary mass and the cavity wall of the primary mass.

The impact model at the cavity walls accounts for the deformation, energy, displacement, velocity, and acceleration changes that occur during a finite time of impact.

The elastic deformation of the primary mass during impact with the

secondary mass is modeled by an equivalent linear spring whose material elastic modulus is K_M . Assumptions are:

- 1.) the material is linearly elastic;
- 2.) no permanent deformation occurs;
- 3.) the secondary mass is small compared to the primary mass;
- 4.) the deformations of the primary mass cavity walls due to impact with the secondary mass are small compared to the secondary mass travel ϵ within the cavity.

Resultant hysteretic damping due to impact with the secondary mass is modeled as an equivalent linear viscous damper whose damping coefficient is C_M and whose damping ratio, ζ_m , is determined iteratively by a subroutine contained in a FORTRAN computer model. This subroutine models the deformation and energy loss from a collision between the motionless primary mass and the secondary mass by simulating the impact between a secondary mass m of unit velocity and a spring damper pair like the one shown in Fig. B. The spring is the equivalent linear spring whose elastic modulus is K_M and the damper is the equivalent linear viscous damper whose damping coefficient is C_M .

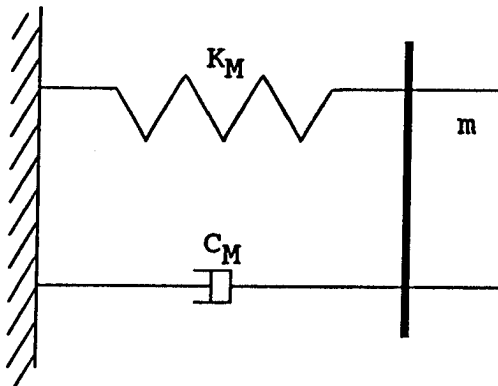


Figure B Iterative Impact Model

The subroutine uses the known values of the dimensionless spring elastic modulus, k , coefficient of restitution, e , and initial unit impact velocity of the mass m . Closed form solutions are used to step through the impact process beginning with a small assumed value of the structural damping ratio ζ_m . A minimum of one hundred steps is used to assure accuracy of ζ_m within an error of 10^{-8} . At the conclusion of impact the secondary mass m has returned to the impact starting position and its relative velocity is checked against the relative velocity provided by the restitution model. If the velocities do not agree within the error of 10^{-8} , ζ_m is changed iteratively until the restitution model is satisfied to within the required tolerance.

A phenomenon called "bounce-down" appears in a time study of a sufficiently excited impact damped system. Bounce-down commences when the secondary mass fails to acquire the velocity necessary to reach the opposite cavity wall before colliding again with the previously impacted cavity wall.

In free decay bounce-down will always terminate in the stuck regime (definition to follow).

Bounce-down impact frequency rapidly increases while relative displacement amplitude decreases. This motion continues until separation of the two masses ceases to occur. Their motion, however, continues as minute deformation induced oscillations without physical separation until hysteretic damping dissipates the deformation induced oscillatory motion. This is analogous to dropping a ball on a sidewalk and letting it bounce to a stop.

Bounce-down ends and the "stuck" condition begins when the secondary mass relative velocity and relative acceleration become zero. The secondary mass adheres to and moves with the primary mass until primary mass acceleration changes sign reducing the normal reaction between the masses to zero. At that point the secondary mass no longer adheres to the primary mass, but is "slung" free, initiating a free motion regime.

In free decay when the primary mass dimensionless amplitude diminishes from its initial value of 6.0 to an approximate value of 5.0, bounce-down and the associated stuck condition cease to occur. Subsequently, the number of impacts per half cycle decreases with decreasing dimensionless primary mass peak amplitude until less than one impact per half cycle is recorded. This point in the time history is called "Impact Failure" and designates the loss of damping effectiveness of the impact damper.

DIMENSIONLESS EQUATIONS OF MOTION

To obtain results in a general form with the widest applicability the equations of motion are made dimensionless as shown below. (See R.E. Jones⁹ for the complete derivation.)

Time is made dimensionless with respect to the reciprocal of the primary mass undamped natural circular frequency (which is the period of the undamped primary mass motion). The circular frequency $\Omega_n = (K/M)^{0.5}$. The corresponding dimensionless time is

$$t = \Omega_n T. \quad (1)$$

Displacements are made dimensionless with respect to the secondary mass free travel $\epsilon = D - d$ within the cavity. The dimensionless displacements x , y , z are: $x = X/\epsilon$, $y = Y/\epsilon$, $z = Z/\epsilon$. By letting $\omega_f = \Omega_f/\Omega_n$ and $f_o = F_o/(K\epsilon)$ the Sinusoidal forcing function can be written in the dimensionless form

$$F(T)/(K\epsilon) = f_o \sin(\omega_f t). \quad (2)$$

FREE MOTION MODEL

Free motion is the resulting motion of the primary and secondary masses when they are not impacting. The equations of free motion for the primary and secondary masses are well known (see R.K. Vierck¹⁰, or S.S. Rao¹¹). The dimensionless equations of free motion for the primary and secondary masses are,

$$\frac{d^2x}{dt^2} + 2\omega_n \zeta \left(\frac{dx}{dt} \right) + (\omega_n)^2 x = f_o \sin(\omega_f t) \quad (3)$$

$$\frac{d^2y}{dt^2} = -d^2x/dt^2 \quad (4)$$

IMPACT MODEL

The primary mass experiences deformation of the cavity wall due to secondary mass impact. The normal force between the two masses is non-zero. The dimensionless equations of motion for impact at the left cavity wall are:

$$\begin{aligned} \frac{d^2x}{dt^2} + 2\omega_n\zeta(dx/dt) + (\omega_n)^2x = \\ \nu[2\omega_m\zeta_m(dy/dt) + (\omega_m)^2y] + f_o \sin(\omega_f t) \end{aligned} \quad (5)$$

$$\frac{d^2y}{dt^2} + 2\omega_m\zeta_m(dy/dt) + (\omega_m)^2y = -d^2x/dt^2 \quad (6)$$

The dimensionless equations of motion for impact at the right cavity wall are:

$$\begin{aligned} \frac{d^2x}{dt^2} + 2\omega_n\zeta(dx/dt) + (\omega_n)^2x = \\ \nu[2\omega_m\zeta_m(dy/dt) + (\omega_m)^2(y - 1)] + f_o \sin(\omega_f t) \end{aligned} \quad (7)$$

$$\frac{d^2y}{dt^2} + 2\omega_m\zeta_m(dy/dt) + (\omega_m)^2(y - 1) = -d^2x/dt^2 \quad (8)$$

STUCK MODEL

In the stuck regime the two masses are in contact but the normal force between them is not zero. This condition results in the same equation of motion when the secondary mass is stuck at either cavity wall. The equations of motion for the stuck regime are:

$$\frac{d^2x}{dt^2} + 2\omega_s\zeta_s(dx/dt) + (\omega_s)^2x = f_o \sin(\omega_f t) \quad (9)$$

$$\frac{d^2y}{dt^2} = -d^2x/dt^2. \quad (10)$$

SYSTEM ENERGY ANALYSIS

The total dimensionless energy of the system at any time is the sum of the dimensionless kinetic and potential energy in the system.

$$E = 0.5\{(dx/dt)^2 + \nu[(dx/dt)^2 + (dy/dt)^2] + x^2\}$$

The ongoing percent of system energy at any time is determined by dividing the current system energy by the initial system energy,

$$E_0 = 0.5\{(dx_0/dt)^2 + \nu[(dx_0/dt)^2 + (dy_0/dt)^2] + (x_0)^2\}.$$

3. ANALYSIS OF COMPUTER RESULTS

GENERAL COMMENTS

This work used the numerical technique of finite differences to integrate the equations of motion (3) - (10) in a FORTRAN 77 computer program to generate the transient time history of the viscously damped simple harmonic oscillator with impact damping.

When the dimensionless primary mass displacement is greater than approximately 5.0 (mass ratio $\nu = 0.02$, coefficient of restitution $e = 0.6$, and viscous damping ratio $\zeta = 0.0$) the secondary mass experiences the

bounce-down phenomenon that in free decay always terminates in the stuck condition. The greater the dimensionless primary mass peak amplitude the shorter the time duration that the secondary mass spends in the bounce-down condition and the greater the time duration it is stuck to a cavity wall of the primary mass. To prevent a lengthy stay in the bounce-down and stuck conditions (which occurred in G.V. Brown and C.M. North¹ where the initial dimensionless primary mass displacement was 10.0) the initial dimensionless primary mass displacement was set here at 6.0. At the end of bounce-down and the stuck regime, the number of impacts per half cycle that the secondary mass experiences on one cavity wall before gaining sufficient relative velocity to impact with the opposite cavity wall decreases with diminishing dimensionless amplitude. This decline in number of impacts per half cycle continues until impact failure ensues when less than one impact per half cycle occurs at an approximate dimensionless amplitude between 0.1 and 0.05. The range of greatest damping effectiveness for the impact damper lies between bounce-down termination and impact failure. It is in this regime of primary mass amplitude that the secondary mass acquires its greatest relative velocity due to impacts on the advancing cavity wall. Structural damping is represented here by an equivalent viscous damper. Therefore, damping is a function of the relative velocity between the primary and secondary masses. As the absolute value of the dimensionless primary mass peak amplitude decreases, dimensionless secondary mass relative velocity increases faster than the dimensionless primary mass velocity decreases, resulting in an increase in the relative velocity between the two masses. Thus the high relative velocity between the two masses due to impacts on approaching cavity walls is responsible for the high rate of impact damping effectiveness.

All the results discussed here were generated from the output files of a computer program whose source code and executable file are stored on the accompanying diskette of R.E. Jones⁹. Figures 1 - 6 were made directly from these computer output files where the mass ratio $\nu = 0.02$, the coefficient of restitution $e = 0.6$ and viscous damping ratio $\zeta = 0.0$. All "Dimensionless Amplitude" data plotted on the ordinate of Fig. 7 and the abscissas of Figures 8 - 14 were generated from the absolute values of the dimensionless peak primary mass displacement at each half cycle of the primary mass motion. In Fig. 15 the "Dimensionless Amplitude" is the peak primary mass dimensionless amplitude that occurs during the half cycle in which an impact or impacts may also occur. Therefore one value of dimensionless amplitude may apply to several impacts. This is not to be confused with the dimensionless amplitude of the primary mass at the time of the impact.

SYSTEM MOTION

The secondary mass experiences several types of motion from bounce-down to impact failure. Three of these motion geometries (relative to the cavity walls) are shown in Figures 1 - 3 which occur at approximate primary mass dimensionless amplitudes of 5.6, 2.6, 0.6, respectively. Fig. 1 illustrates the bounce-down condition followed by the stuck regime. Later on, after bounce-down ceases, the secondary mass in Fig. 2 is impacting a cavity wall three times before gaining sufficient relative velocity to cross the cavity travel width to the opposite cavity wall. Even later in the time history, in Fig. 3, the secondary mass impacts a cavity wall twice before alternating with a single impact on the opposite cavity wall.

In Figures 4 - 6 the approximate primary mass dimensionless amplitudes are 0.4, 0.2, 0.05, respectively. The dimensionless secondary mass absolute displacement is represented by a dashed line and the absolute displacement of the two cavity walls is represented by two solid lines. Two unequally spaced impacts per cycle are shown in Fig 4. Later in the free decay, two equally spaced impacts per cycle are shown in Fig. 5. Fig. 6 clearly exhibits the point where the impact damper loses its effectiveness when impact failure begins.

LOSS FACTOR

The loss factor is a measure of damping effectiveness, where the greater the loss factor, the more effective the damper is at reducing the primary mass vibratory motion. The loss factor is defined as the change in primary mass energy that occurs between the two extreme absolute dimensionless primary mass displacement peaks of a cycle divided by the primary mass energy at the absolute dimensionless primary mass half cycle peak that lies midway between the two full cycle peaks; i.e., the loss factor is

$$\eta = \Delta E/E,$$

where E is the total system energy. When the simple harmonic oscillator is at a peak amplitude, the kinetic energy vanishes and the total energy is:

$$E = kx^2/2$$

Since $\Delta E = kx\Delta x$ then the loss factor per cycle is:

$$\eta = 2\Delta x/x$$

AVERAGED LOSS FACTOR

To generate the "Averaged Loss Factor" each point of the data shown in Figures 8 - 14 is the result of a least squares parabolic fit applied to the absolute values of primary mass peak amplitudes for ten successive half cycles (eleven data points). These data are used to determine the averaged loss factor. This smoothing or averaging is necessary because of the variations in peak amplitudes. Some data required the application of the least squares fit to as many as 18 half cycles in order to present the data in acceptably smooth form. The averaging process has the effect of broadening and reducing the loss factor peaks.

In Figures 8 - 15 the primary mass dimensionless displacement amplitudes are decreasing as the free decay time history progresses.

AMPLITUDE DECAY

Fig. 7 displays the decay curves of the absolute value of the dimensionless peak half cycle amplitudes versus the time of the amplitude occurrence. For this figure the external damping ratio $\zeta = 0.0$, and mass ratio is $\nu = 1, 2, 4$ percent, while all other parameters are held constant. The efficiency of impact damping for a given set of parameters corresponds to the slope of the curve. Clearly illustrated is the increase in loss factor

with decrease in amplitude until impact failure commences at a dimensionless amplitude of between approximately 0.05 - 0.1. Impact failure is easily recognized here by the curve tails close to the horizontal axis. The bounce-down and stuck regime is in the dimensionless primary mass amplitude range above approximately 5.0.

EFFECTS OF THE MASS RATIO

In Fig. 8 the coefficient of restitution, $e = 0.6$, external damping ratio $\zeta = 0.0$, and three values of mass ratio, $\nu = 1, 2, 4$ percent are used to demonstrate the increase in loss factor with a decrease in amplitude. Comparing Fig. 8 with Figures 4 and 5 indicates that maximum damping efficiency due to impact damping occurs when the secondary mass experiences one impact per half cycle. The similarity between the curves depicted in Fig. 8 suggests a factor may exist, when applied to each curve, that would cause the three to converge on one common curve. The curves in Fig. 8 are reduced nearly to a single curve as shown in Fig. 9 by dividing the averaged loss factor by the mass ratio (also called the "Specific Total Loss Factor"). The specific total loss factor is a constant at any given amplitude for mass ratios up to 4 percent. This demonstrates that the loss factor and the dissipated energy due to impact (Fig. 8) are approximately proportional to the mass ratio.

EFFECTS OF VISCOUS DAMPING

Fig. 10, with a single value of the coefficient of restitution $e = 0.6$ and mass ratio of $\nu = 2$ percent, compares the loss factors resulting from viscous damping ratios of 0.0, 0.2, 0.4, 0.8 percent.

The "Specific Secondary Mass Loss Factor" is obtained when the damping contribution made by twice the viscous damping ratio 2ζ is subtracted from the averaged loss factor in Fig. 10, and the result is divided by the mass ratio. This contribution of viscous damping 2ζ is obtained from the logarithmic decrement, δ , which is a measure of the rate of decay between any two successive cycles (for detailed derivation, see R.E. Jones⁹).

The simple additive nature of viscous and impact damping is illustrated in Fig. 11. The nearly identical overlapping curves show that viscous damping on the primary mass and impact damping are additive for very small viscous damping ratios. This near coincidence of the curves provides a single curve that closely describes the specific secondary mass loss factor as a function of dimensionless amplitude. However, this curve is unique for the value of the coefficient of restitution $e = 0.6$. Different curves can be generated for other values of the coefficient of restitution. Over most of the length of the curve, the specific secondary mass loss factor increases as the dimensionless amplitude decreases.

Fig. 12 illustrates to what extent the apparent approximate correspondence between amplitude and the specific secondary mass loss factor exists in Fig. 11. To show this the specific secondary mass loss factor from Fig. 11 is multiplied by the dimensionless amplitude. The resulting overlapping of the curves justify the correspondence. In the dimensionless amplitude range from 0.1 - 6.0 the curve has variations within ± 31 percent of the average ordinate value 0.339. The approximate constant value of the ordinate provides an easy estimate of impact damping over a wide amplitude

range.

EFFECTS OF THE COEFFICIENT OF RESTITUTION

The general effect of changing the coefficient of restitution e is shown in Fig. 13. The dimensionless amplitude multiplied by the specific secondary mass loss factor is represented for values of $e = 0.4, 0.6, 0.8$ and mass ratio $\nu = 2$ percent, and viscous damping ratio $\zeta = 0.0$. The lower value of $e = 0.4$ results in increased loss factor in the middle dimensionless amplitude range of 0.1 to bounce-down termination. Bounce-down ends at approximately 2.0 and 5.0 for coefficients of restitution $e = 0.4$ and 0.6, respectively. For coefficient of restitution $e = 0.8$ bounce-down ends at an amplitude beyond the scope of this study (greater than 6.0). For coefficients of restitution values of $e = 0.4, 0.6, 0.8$, impact failure begins at approximately 0.15, 0.1 and 0.01, respectively. To summarize, for lower values of the coefficient of restitution, e , bounce-down ends at lower dimensionless amplitudes and impact failure begins at higher values of the dimensionless amplitude. Higher values of the coefficient of restitution e have just the opposite effect.

Fig. 14 is obtained from Fig. 13 by dividing the ordinate values in Fig. 13 by $(1 - e)$. The merging of the curves demonstrates that within impact damping active range (implied by Fig. 13), the damping is approximately proportional to $(1 - e)$.

IMPACT PHASE ANGLE

Fig. 15 is a phase plot (without viscous damping) of the secondary mass impacts that occur during a half cycle where the dimensionless primary mass amplitude is the absolute value of the dimensionless primary mass peak amplitude in a half cycle. The coefficient of restitution $e = 0.6$ and the mass ratio $\nu = 0.02$. The phase angle in degrees is determined from the secondary mass cavity wall impact point between primary mass crossings of the zero dimensionless displacement axis. A half cycle of 180 degrees is defined between the dimensionless primary mass displacement amplitude zero crossings. The secondary mass impact phase in degrees is defined by the point in time at which the impact of the secondary mass occurs during the dimensionless primary mass displacement half cycle. This point is established when the dimensionless secondary mass relative displacement is zero (impact at the left cavity wall) or one (impact with the right cavity wall). The relationship is

$$\text{Phase} = \frac{\text{Time from last zero crossing to impact}}{\text{Time between zero crossings}} \times 180^\circ.$$

The initial time for the data shown in Fig. 15 corresponds to the initial dimensionless amplitude of 6.0 and the time history progresses as amplitude decreases. Impact points are shown in the figure as small squares. The darkened area in the upper right corner of the figure represents the stuck regime where the secondary mass moves in temporary contact with the primary mass until the dimensionless primary mass acceleration changes sign. The area beneath the stuck region all the way down to the horizontal axis is the realm of bounce-down. Notice that in the bounce-down region the impact phase (at a given dimensionless amplitude) increases as the stuck regime is approached

vertically from the horizontal axis until bounce-down terminates in the stuck regime. At an approximate dimensionless amplitude of 5.0 bounce-down and the stuck regime cease. At that point, as the dimensionless amplitude diminishes, the number of impacts per half cycle also diminishes. Note that at progressively decreasing amplitudes of approximately 4.4, 4.0, 3.3, 2.5, 1.3, 0.2 in Fig. 15, clear patterns of six, five, four, three, two, and one impacts per half cycle, respectively, are indicated. The plot clearly shows that regular impact regions per half cycle alternate with regions of chaotic impact. Comparing Fig. 15 with the slopes of the curves in Fig. 7, impact damping is seen to be most efficient (for coefficient of restitution $e = 0.6$ and mass ratio $\nu = 0.02$) in the region of single impacts per half cycle. This corresponds to a dimensionless amplitude range from approximately 0.2 to impact failure, which ensues at approximate dimensionless amplitudes of 0.05 - 0.1.

4. COMPARISON OF RESULTS TO THOSE OF G.V. BROWN AND C.M. NORTH¹ SIMILARITIES AND DIFFERENCES

In comparing these results with those of the previous work of G.V. Brown and C.M. North¹, the observable differences can be attributed to:

1. the inherent difference between the two models;
2. initial conditions;
3. a variation in the least squares method used for loss factor averaging.

Although all the results compare well, close scrutiny shows a very small difference in data point to data point comparison. During one comparative run of identical parameters the dimensionless time required for reducing vibratory motion from initial primary mass displacement to impact failure was approximately 5 - 10 percent less here than in G.V. Brown and C.M. North¹. However, more study should be performed to verify this observation. Also the chaotic regions appear to be less chaotic in Fig. 15 than in G.V. Brown and C.M. North¹.

G.V. Brown and C.M. North¹ began the free decay time history at a dimensionless primary mass displacement amplitude of 10.0. The present study initiated free decay with a dimensionless primary mass displacement amplitude of 6.0. The larger of these two amplitudes causes the primary and secondary masses to remain in the bounce-down and stuck regime for a longer length of time for all of the results presented. As a consequence, their time histories will always require longer dimensionless times to reach impact failure since more time was spent in the bounce-down and stuck regimes where small damping occurs.

In each of the loss factor curves (Figures 8 - 12) a maximum value peak in the region of impact failure is lower and broader here than in G.V. Brown and C.M. North¹. The peak in question is located at a dimensionless amplitude of approximately 0.1 in Figures 8 - 12. In Figures 13 and 14 the peak corresponding to each of the three curves in each figure occurs at dimensionless amplitude of approximately 0.08, 0.1, 0.12. G.V. Brown and C.M. North¹ used a variation of the loss factor averaging scheme in the vicinity of

this peak causing the difference in appearance of the curve in the two works. It is noted however, that the region of impact failure appears to contain little meaningful information.

SUMMARY

The overall results given here are qualitatively identical to G.V. Brown and C.M. North¹. This similarity of results from the two studies supports the assumptions of G.V. Brown and C.M. North¹ while lending credibility to the model in the present work. The present work uses finite differences with central difference approximations to integrate the equations of motion. The actual impact process is modeled using discrete time intervals during impact between the primary and secondary mass. The deformation and energy losses of the impacting masses are assumed to be equivalent to a linear spring and viscous damper, respectively, for the small deformations involved. G.V. Brown and C.M. North¹ used closed form solutions and initiated free decay with a dimensionless primary mass initial displacement of 10.0. The coefficient of restitution was used to model across impact by assuming the time duration of impact to be infinitesimally small compared to the time required for the secondary mass to travel between impacts. The differences between these basic models accounts for all of the deviations between the results obtained from the two studies.

5. CONCLUSIONS

The accuracy of the numerical method is dependent directly on the size of the time step used. The smaller the time step, the more accurate the results. The spring and damper components used are all assumed to be linear and subject to linear restrictions (e.g., small deformations). The equivalent linear damper used to simulate structural damping is viscous and it is therefore velocity dependent. Structural damping is typically nonlinear and dependent upon the magnitude of deformation. For small secondary mass to primary mass ratios, the justification for using the more convenient viscous damping for a structural damping model comes from assuming small structural deformations resulting from impacts between the primary and secondary masses.

The component element method with its utilization of the numerical finite difference technique is shown to be a useful analysis tool for investigating the impact damped simple harmonic oscillator in freely decaying motion. The impact process is modeled as if the deformation and energy losses from the impacting primary and secondary masses were replaced by an equivalent linear spring and viscous damper. The results obtained have been shown to compare favorably, for small mass ratios, to G.V. Brown and C.M. North¹ who used closed form solutions to model the motion and a restitution model across impact. The accuracy of the results make the component element method worth consideration for future investigations of more complex systems of multiple components and impact dampers where closed form solutions may prove difficult or impossible to obtain. Although not utilized here, the component element method has the flexibility of incorporating nonlinear expressions or even data bases to represent component moduli.

The present computer model confirmed the following results obtained earlier by G.V. Brown and C.M. North¹:

- (1) A low amplitude and corresponding low effective impact damping range occurs for impact damping for coefficients of restitution $e = 0.4, 0.6, 0.8$. Impact failure is dominant for the diminishing dimensionless amplitudes starting at 0.15, 0.1, 0.01, respectively, where less than one impact per half cycle occurs.
- (2) Between bounce-down and the stuck regime to the beginning of impact failure a middle dimensionless amplitude range of useful impact damping exists. The number of impacts per half cycle in this range depends on the dimensionless primary mass amplitude (i.e., the greater the amplitude the more impacts per half cycle).
- (3) In the bounce-down and stuck regime impact damping is decreasingly effective. Dimensionless primary mass amplitudes are above approximately 2.0 and 5.0 for coefficients of restitutions $e = 0.4, 0.6$ respectively. The number of impacts per half cycle is large and can increase without bound as the coefficient of restitution approaches one.

For additional light viscous damping the impact damping in the middle dimensionless amplitude range from the bounce-down and stuck regime to impact failure is shown to be:

- (1) represented by one curve for a given coefficient of restitution implying that impact damping is proportional to the mass ratio;
- (2) additive to proportional viscous damping;
- (3) a unique function of vibration amplitude where the loss factor increases as the dimensionless primary mass amplitude decreases;
- (4) proportional to $(1 - e)$, where e is the coefficient of restitution.

For a coefficient of restitution $e = 0.6$ and mass ratio $\nu = 0.02$ impact damping is most effective when the dimensionless amplitude is about 10 percent of the secondary mass cavity travel (dimensionless value of one). The loss factor has a maximum value of nearly 0.1 and over a wide range of dimensionless amplitudes the loss factor is 0.01. Impact damping is a strong function of amplitude and produces substantial damping for small mass ratios. Because of this, several impact dampers may be combined with different secondary mass travel gaps to provide damping over wide ranges of amplitude.

6. REFERENCES

- [1] Brown, G.V., C.M. North. "The Impact Damped Harmonic Oscillator in Free Decay," The Role of Damping in Vibration and Noise Control, ASME Publication, DE-Vol. 5, 1987, pp. 53-64.
- [2] Soller, P.J. "The Development of a Computer Model as an Aid to the Solution of the Problem of Impact Damping," Masters Thesis, Rose-Hulman Institute of Technology, Terre Haute, IN, 1985.
- [3] Torvik, P.J., W. Gibson. "The Design and Effectiveness of Impact Dampers for Space Applications." The Role of Damping in Vibration and Noise Control, ASME Publication, DE-Vol. 5, 1987, pp. 53-64
- [4] Pyle, S.E. "Computer Simulation of Internal Viscous Damping." Masters Thesis, Rose-Hulman Institute of Technology, Terre Haute, IN, 1983.
- [5] Nale, T.A. "Time History Study of a Classical Cantilever Beam Damped by Internal Mechanical Means," Masters Thesis, Rose-Hulman Institute of Technology, Terre Haute, IN, 1988.
- [6] Levy, S., J.P.D. Wilkinson. The Component Element Method In Dynamics, (New York, N.Y.: McGraw-Hill, 1976).
- [7] Meirovitch, Leonard. Analytical Methods in Vibrations, (New York, N.Y.: Macmillan, 1967).
- [8] Hobbs, G.K.. "Methods of Treating Damping in Structures," AIAA/ASME 12th Structures, Structural Dynamics and Materials Conference, ASME Publication, AIAA Paper No.71-347, 1971.
- [9] Jones, R.E. "Application of the Component Element Method to the Impact Damped Simple Harmonic Oscillator," Masters Thesis, Rose-Hulman Institute of Technology, Terre Haute, IN, 1988.
- [10] Vierck, R.K.. Vibration Analysis, Second Edition. (New York, N.Y.: Harper & Row, 1979).
- [11] Rao, S.S.. Mechanical Vibrations, (Reading, MA: Addison-Wesley, 1986).

7. FIGURES

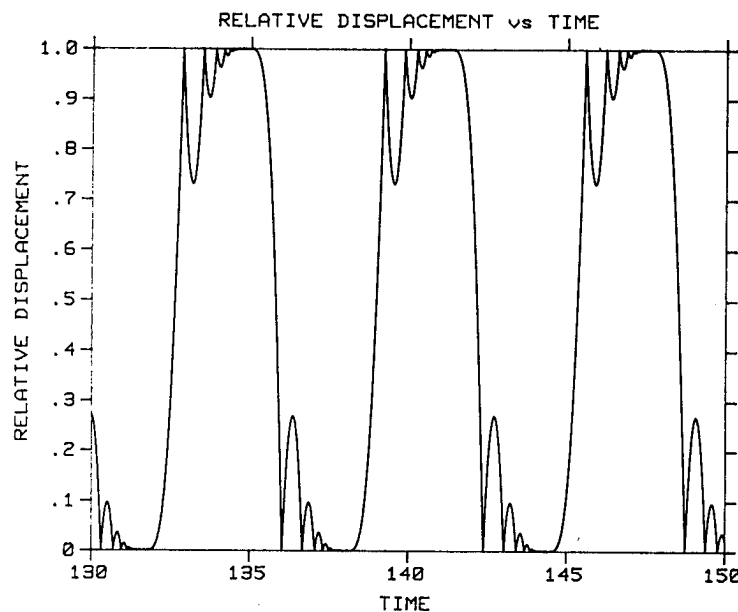


Figure 1 Large Number of Impacts in Each Half Cycle.

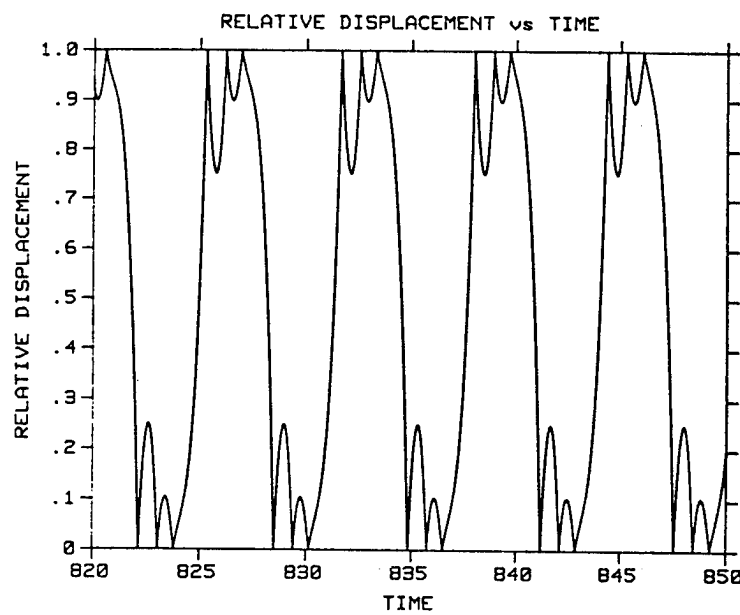


Figure 2 Three Impacts in Each half Cycle.

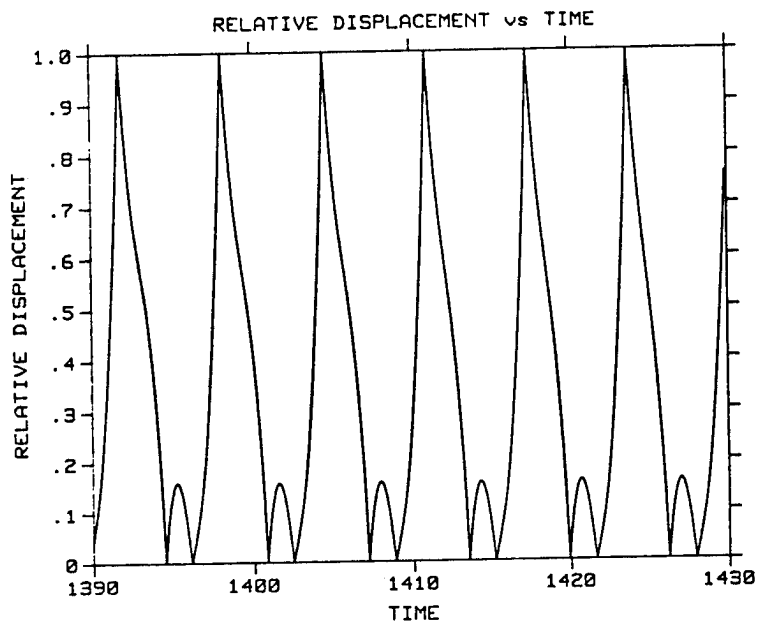


Figure 3 One Impact in Each Half Cycle Alternating with Two.

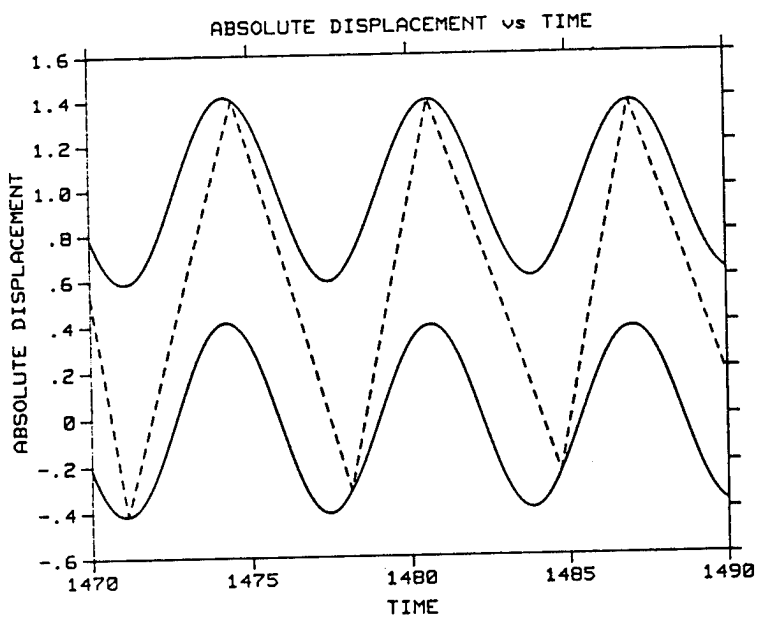


Figure 4 Two Unequally Spaced Impacts in Each Cycle.

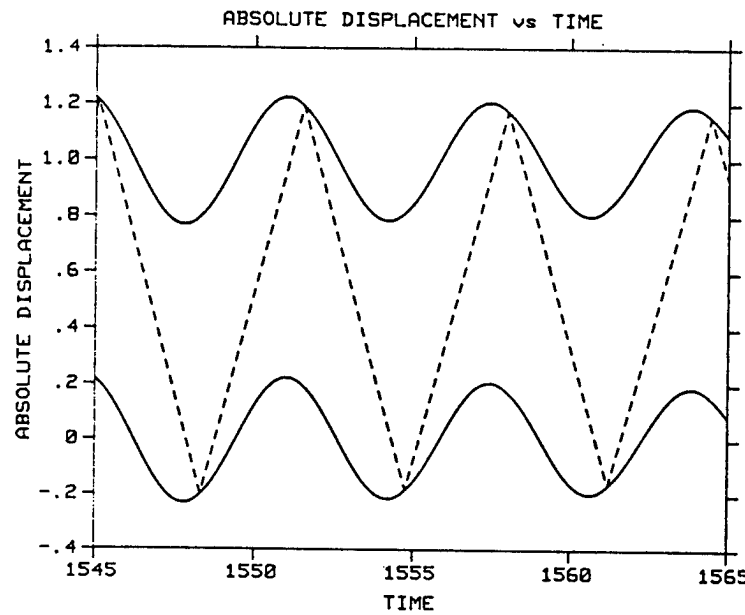


Figure 5 Two Equally Spaced Impacts in Each Cycle.

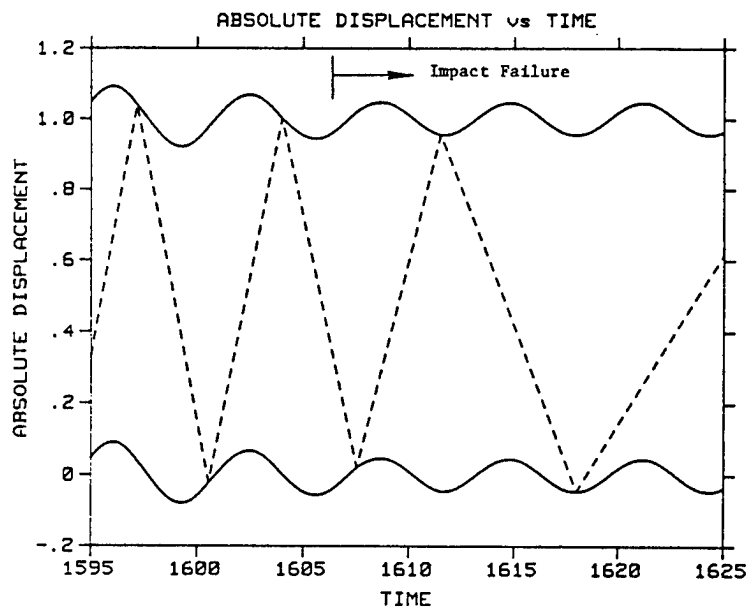


Figure 6 Beginning of Impact Failure.

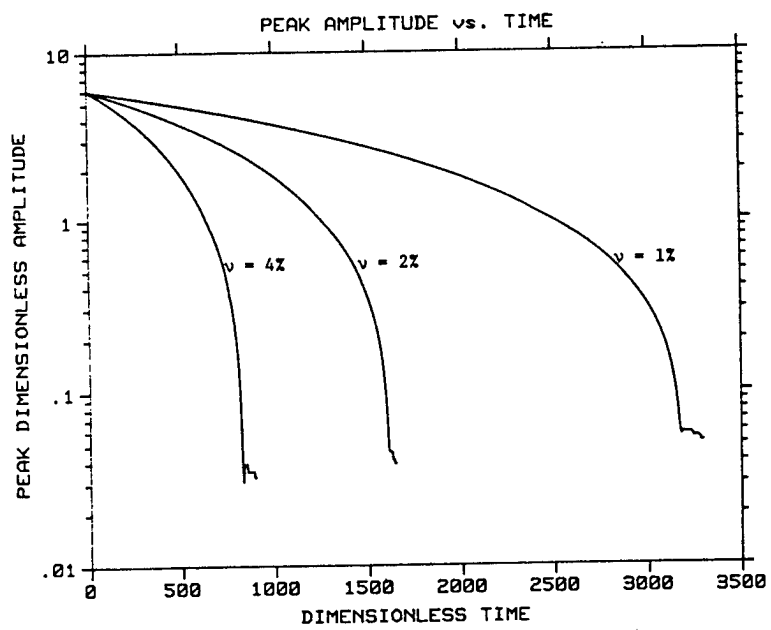


Figure 7 Amplitude Decay Curves. $e = 0.6$

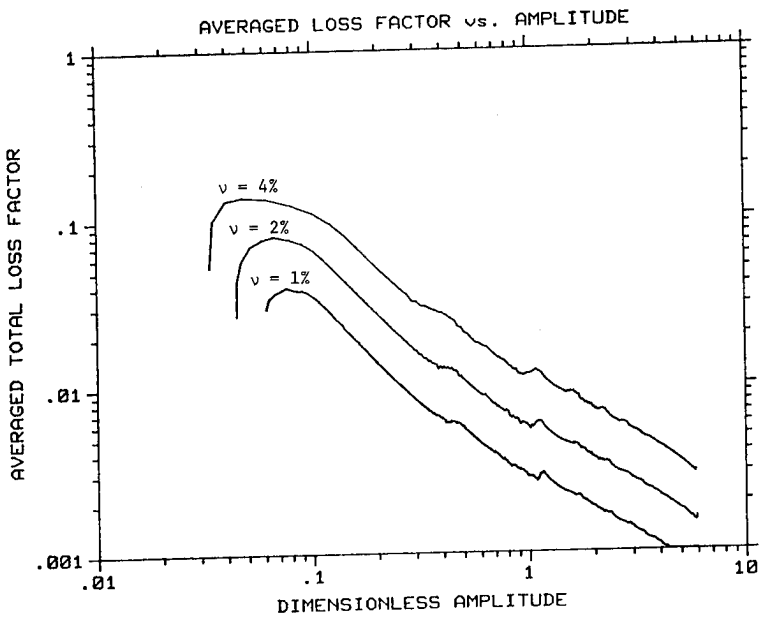


Figure 8 Averaged Total Loss Factor as a Function of Amplitude for Three Values of the Impactor Mass Ratio. $e = 0.6$; $\nu = 1, 2, 4$ percent.

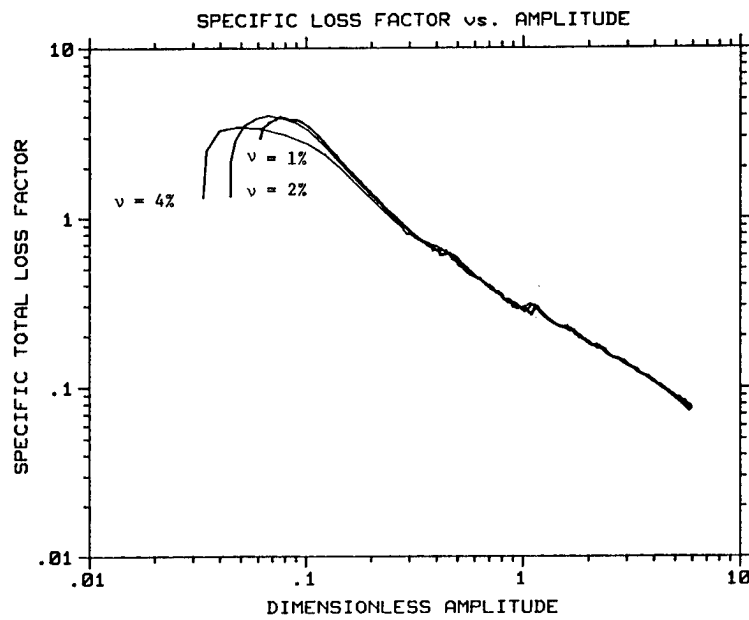


Figure 9 Specific Total Loss Factor as a Function of Amplitude for Three Values of the Impactor Mass Ratio $e = 0.6$; $\nu = 1, 2, 4$ percent.

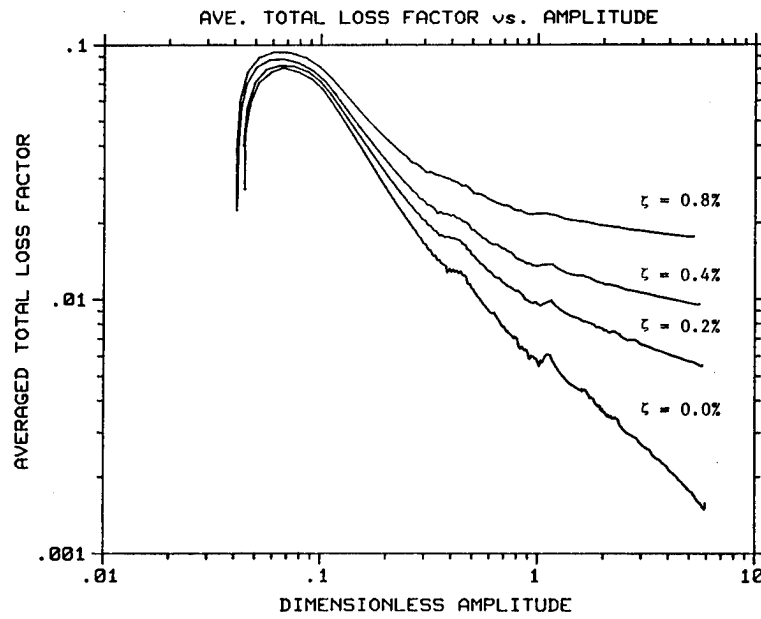


Figure 10 Averaged Total Loss Factor as a Function of Amplitude for Four Values of Viscous Damping Ratios. $\nu = 0.02$; $e = 0.6$; $\zeta = 0.0, 0.2, 0.4, 0.8$ percent.

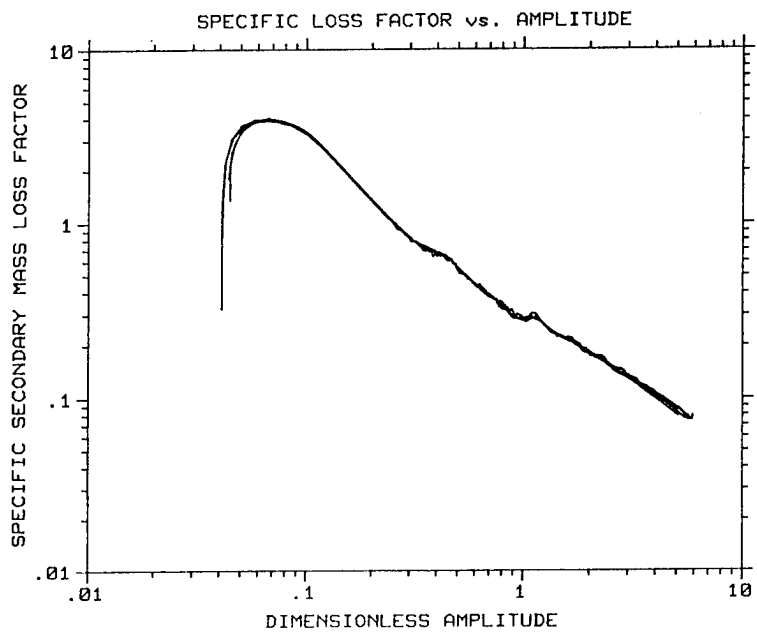


Figure 11 Specific Secondary Mass Loss Factor as a Function of Amplitude for Four Values of Viscous Damping Ratios. $\nu = 0.02$; $e = 0.6$; $\zeta = 0.0, 0.2, 0.4, 0.8$ percent.

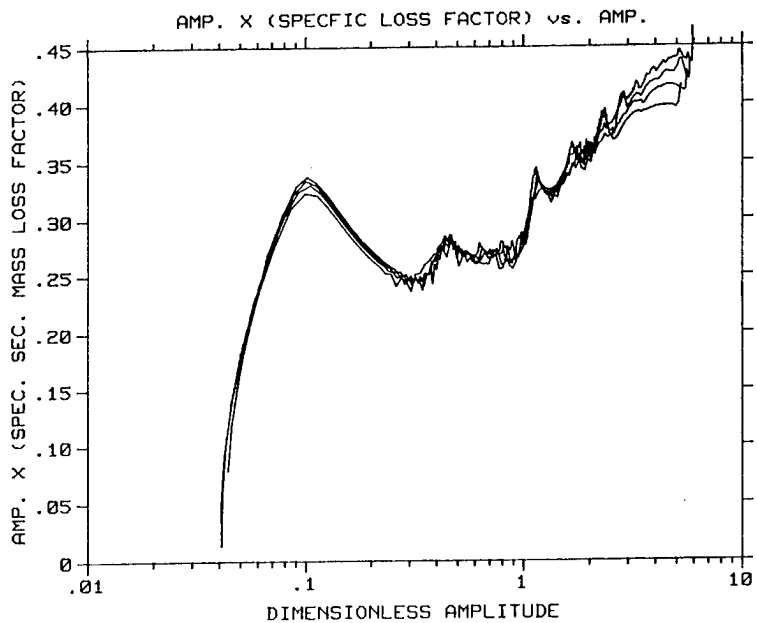


Figure 12 Amplitude Multiplied by the Specific Secondary Mass Loss Factor as a Function of Amplitude for Four Values of Viscous Damping Ratios. $\nu = 0.02$; $e = 0.6$; $\zeta = 0.0, 0.2, 0.4, 0.8$ percent.

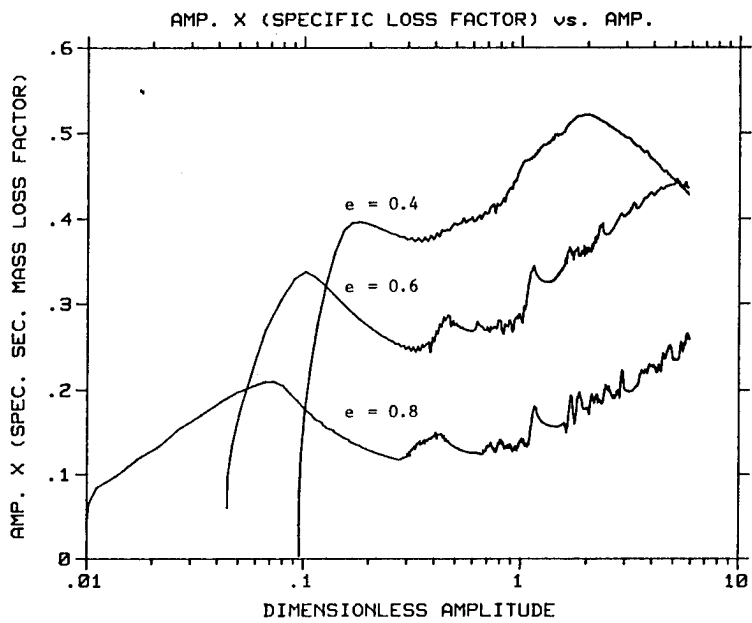


Figure 13 Amplitude Multiplied by Specific Secondary Mass Loss Factor for Three Values of the Coefficient of Restitution.
 $\nu = 0.02$; $e = 0.4, 0.6, 0.$

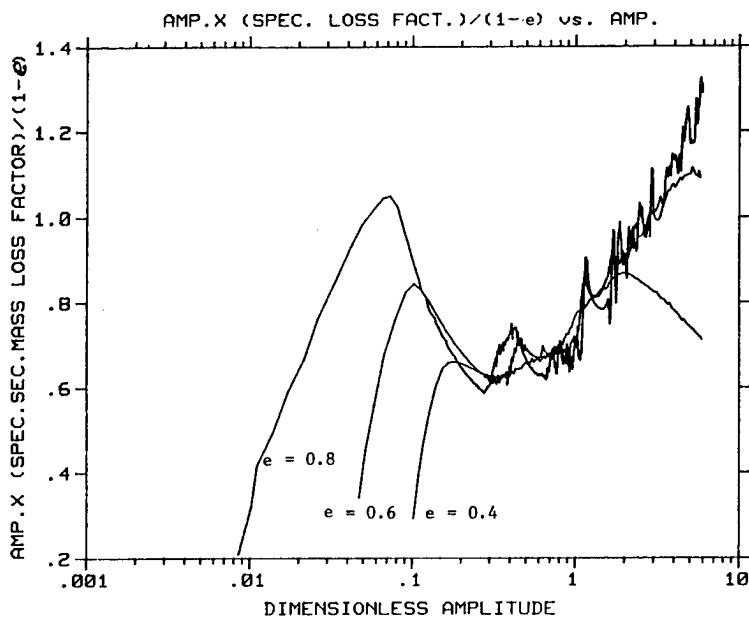


Figure 14 Amplitude Multiplied by the Specific Secondary Mass Loss Factor Divided by $(1 - e)$ for Three Values of the Coefficient of Restitution. $\nu = 0.02$; $e = 0.4, 0.6, 0.8$

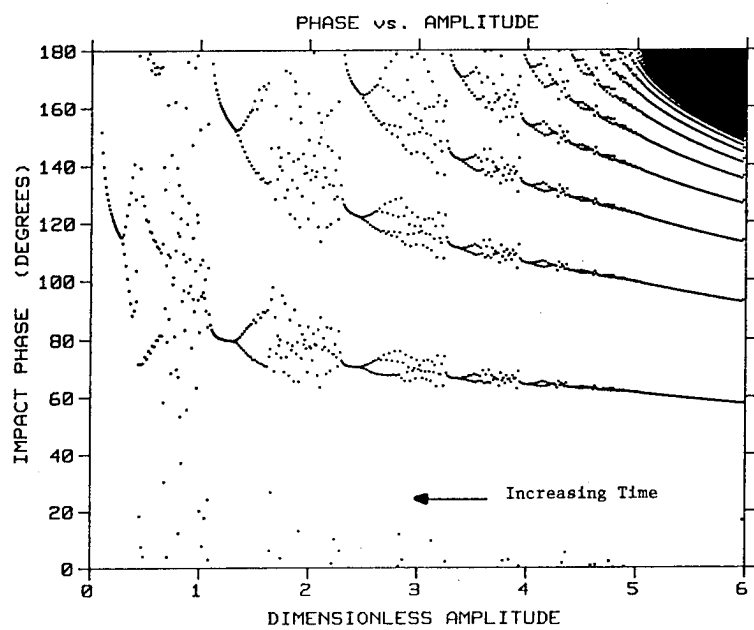


Figure 15 Impact Phase as a Function of Amplitude. $\nu = 0.02$; $e = 0.6$

TIME HISTORY STUDY OF A CLASSICAL CANTILEVER BEAM
DAMPED BY INTERNAL MECHANICAL MEANS

C. M. North
Rose-Hulman Institute of Technology
Terre Haute, Indiana USA

and

T. A. Nale
General Motors Corporation
Allison Gas Turbine Division
Indianapolis, Indiana USA

ABSTRACT

The impact damped classical elastic cantilever beam in free decay is studied in its many states of vibration by means of time history studies. The effective damping is correlated with the impact mass behavior. The three major behavior regimes studied are: (1) a high amplitude range with an infinite number of impacts per half cycle resulting in decreased damping effectiveness, (2) a moderate amplitude range with a highly useful finite number of impacts per half cycle resulting in the most effective damping, and (3) a low amplitude range with less than one impact per half cycle yielding very low damping. The relative effects on energy dissipation produced in the beam by variations in the number of natural modes used during calculation, impactor/beam mass ratio, and impactor/beam coefficient of restitution are studied. These parametric studies have shown that the impactor reduces the amplitude of beam vibration in the same fashion regardless of the number of natural modes used during calculation. Furthermore it is shown that the most effective damping occurs when the dimensionless amplitude of transverse beam vibration at the longitudinal cavity coordinate is less than 1.0 independent of all other parameters.

NOMENCLATURE

A	Beam Height
B	Beam Width
C	Cavity Depth
D	Impactor Height
e	Coefficient of Restitution
E	Linear Spring Potential Energy
ΔE	Change in Linear Spring Potential Energy
EI	Beam Flexural Rigidity
E_x	Cavity Width
E_y	Total Cavity Length
e_x	E_x/L - Dimensionless Cavity Width
F_o	Magnitude of Sine Input
f_o	$F_o/\rho V^2$ - Dimensionless Magnitude of Sine Input
$F(X)$	Initial Beam Displacement
$f(x)$	$F(X)/L$ - Dimensionless Initial Beam Displacement
$G(X)$	Initial Beam Velocity
$g(x)$	$G(X)/L$ - Dimensionless Initial Beam Velocity
H	$E_y - D$ - Cavity Length (Gap)
h	H/L - Dimensionless Cavity Length (Gap)
L	Beam Length
M	Impactor Mass
m	Dimensionless Impactor to Beam Mass Ratio
P_i	Magnitude of Impulse During Impact at $T = T_i$
p_i	$P_i/\rho LV$ - Dimensionless Impulse During Impact
T	Real Time
T_c	Beam Characteristic Wave Time
t	T/T_c - Dimensionless Time
t_i	Dimensionless Time of Impact with Cavity Wall
T_n	Average Period of Oscillation Across Five Cycles
$U(T)$	Relative Displacement of Impactor
$u(t)$	$U(T)/H$ - Dimensionless Impactor Relative Displacement
$W(T)$	$Y(X_o + 0.5E_x, T)$ - Cavity Deflection
$w(t)$	$W(T)/L$ - Dimensionless Cavity Deflection
X	Beam Longitudinal Coordinate
x	X/L - Dimensionless Beam Longitudinal Coordinate
X_f	Longitudinal Coordinate of Sine Force $X_f = X_o + (0.5)E_x$
x_f	X_f/L - Dimensionless Location of Sine Force
X_o	Longitudinal Coordinate of Cavity Left Wall $0 < X_o < X_o + E_x < L$
x_o	X_o/L - Dimensionless Location of Cavity
y	Linear Spring Deflection
Δy	Change in Linear Spring Deflection
$Y(X, T)$	Transverse Beam Deflection (Neutral Axis)
$y(x, t)$	$Y(X, T)/L$ - Dimensionless Transverse Beam Deflection
$l(T)$	Heaviside Unit Step Function
$\delta(T)$	Dirac Impulse Function
η	Loss Factor for One Half Cycle
ρ	Beam Mass per unit Length
ϕ_i	Phase angle at Impact t_i
Ω	Angular Frequency of Sine Input
ω_f	ΩT_c - Dimensionless Angular Frequency of Sine Input
ω_k	Beam Natural Modal Frequencies

INTRODUCTION

Impact damping dissipates vibrational energy by internal mechanical means. The primary model of the mechanism by which energy is removed from the system is the coefficient of restitution. A simple but effective illustration of how the coefficient of restitution is used to model energy loss during impact is a bouncing ball in a uniform gravitational field. During the bouncing process the maximum height reached during each successive cycle is smaller than that of the previous cycle. For this to be true the energy of the ball, which is the sum of the kinetic and potential energies at any point in time, has decreased by some finite amount. This decrease in the total energy is a function of the decrease in the ball's maximum height between two successive cycles. For the case of a ball bouncing on a hard floor in a constant gravitational field in the absence of air resistance the "coefficient of restitution is simply the square root of the ratio of the maximum height after impact to the maximum height before impact"¹. It can be easily shown that the ball's rebound height becomes successively smaller while approaching zero. Although the ball will theoretically go through an infinite number of bounces, this occurs in a finite period of time. For practical purposes the ball is said to be resting on the floor at the end of this finite time. This phenomenon is referred to herein as "bounce-down". It will be shown later that the damping effectiveness of an impact damped system depends heavily upon the amplitude of oscillation at the cavity.

The history of impact damping can be traced to 1833 in published literature. Although this subject has a long history it appears that the majority of recently published work has been done by Masri², Bapat and Popplewell³. Past work done in the area of impact damping has concentrated on the analysis of steady-state forced oscillators. In doing this the authors have assumed a steady-state solution, generally two impacts per half cycle. These assumed solutions limit the impactor analysis to a narrow range of cavity amplitudes. The use of these limited solutions does give the reader an indication of the effectiveness of impact dampers but is inadequate for determining the optimum damper effectiveness.

In 1982, under sponsorship of NASA Lewis Research Center, Brown and North⁴ initiated the study of the transient response of the simple harmonic oscillator with a single internal impact damper. These studies began with the development of an analytical and a digital computer model of an undamped, freely vibrating simple harmonic oscillator having a single cavity containing a single frictionless impact damper. A second model that was developed by North (unpublished) included the effects of Coulomb friction between the impactor and the primary mass. In 1986 the authors began to develop a digital model of the free and forced vibration of a classical elastic cantilever beam damped by a single internal frictionless impact damper. The results obtained from the beam model are the subject of this document.

The study of a continuous beam subject to impact damping in free decay may appear to be unimportant compared to the study of impact damping of the forced beam. This is not necessarily so. Analysis of the transient free decay of the impact damped beam provides a great deal of valuable information which can be applied to the forced vibrating beam with impact damping.

First, there exist several characteristics of transient free decay which also apply to forced response. It is later shown that impact damping is

frequency independent. This leads to the conclusion that impact damping effectiveness is independent of a forcing function's frequency. Impact damping is found to be most heavily dependent upon the amplitude of vibration experienced by the beam cavity. Free decay initial cavity amplitudes are used to span a wide range of forcing functions magnitudes. This allows free decay analysis to be applied to forced motion response of various transient and steady state cavity amplitudes.

Secondly, the simplicity of free motion makes it more advantageous to study than forced motion response. The absence of large transient conditions during free decay make it possible to observe the several impactor behavioral characteristics within shorter time intervals than would be required for transient forced motion. Free decay characterizes impact damping across a wide range of beam cavity vibrational amplitudes using a single time-history profile with appropriately chosen initial conditions. The patterned behavior which characterizes impactor motion is more easily discerned with the use of free decay time histories. The presence of a forcing function can eliminate a significant portion of the impactor's patterned spectrum.

Finally, the study of transient free decay can be made to simulate the recovery from the occurrence of a transient disturbance to a steady state beam⁴. All of these reasons make the use of transient free decay time-history studies useful.

The application of impact damping would provide a means of significantly decreasing the amplitude of vibration without altering the external configuration of the system. The use of impact dampers also could reduce the fatigue effects of vibration experienced by aerospace parts. This would allow the stringency of design criteria for such parts to be relaxed. The reduced effects of fatigue would allow lighter weight parts with a longer working lifetime to be produced.

This study was initiated to determine the characteristics and effectiveness of impact damping applied to a continuous elastic cantilever beam. The overall motivating factor for these studies is a desire to investigate the concept of adding very light damping to aerospace systems which exhibit self-excited vibration or forced vibration near a natural frequency. This research was performed with the following objectives in hand:

- 1.) Compare the effects of impact damping applied to continuous elastic cantilever beams with that of simple harmonic oscillators. Determine the similarities and differences in the behavior of the two applications.
- 2.) Determine the effects of higher modal frequencies on the characteristic behavior of the impactor and the ability of impact damping to effectively reduce continuous elastic cantilever beam vibration amplitude.
- 3.) Evaluate the ability of impact dampers to inhibit vibration. This decrease in vibration amplitude is quantified by means of loss factor evaluation.
- 4.) Determine impactor behavior and damping effectiveness as the cavity vibrational amplitude decays.

- 5.) Measure the change in effective damping with respect to variations in the impactor/beam mass ratio.
- 6.) Evaluate the effects of the coefficient of restitution on the characteristic behavior and damping effectiveness of the impactor.

IMPACTOR BEHAVIOR AND DECAY STUDY

A FORTRAN digital model of the impact damped classical elastic cantilever beam, Figures 1 and 2, was developed for the purpose of performing parametric studies of beam impactor performance. The longitudinal position of the beam cavity, x_0 , is set at 0.684 units. This cavity location was determined by use of beam mode shape displacement analysis. This cavity position is used to maximize the vibrational activity of the beam at the location of the impactor⁵. During this study the initial conditions of the beam were such that the first mode was excited with an initial generalized displacement of 0.05 and no initial generalized velocity. The magnitude of the resulting initial dimensionless displacement of the cavity was 6.0 units. The effects of varying the initial conditions are not explored in this study. Mass ratios of 1.0, 2.0, and 3.0 percent and coefficients of restitution of 0.5, 0.6, 0.7, and 0.8 were used to generate the time histories. The geometrical configuration of the beam is kept unchanged for the time history studies discussed in this report. The magnitudes of the dimensionless physical beam dimensions were determined by a comparative analysis with the data used by Brown and North⁴. A cavity width, e_x , of 0.04 units and a cavity length, h , of 0.01 units are used, Figures 1 and 2. The beam is unforced with no initial relative displacement or relative velocity of the impactor. Another parameter that is varied in this study is the number of mode shapes used during computation. Time histories were made with 1, 2, 5, and 10 mode shapes for the varying mass ratios with a constant coefficient of restitution of 0.6. From this comparative analysis it was found that the higher modal frequencies are of little significance when determining the damping effectiveness of the impactor.

The impactor relative displacement and absolute displacement curves presented in the Appendix, Figures 3 thru 7, show how the impactor behaves as the cavity amplitude of vibration decays. Note that in Figures 6 and 7 the solid lines represent the top and bottom cavity walls with the dashed line representing the impactor. At first, during high amplitude motion, Figure 3, the impactor experiences an infinite number of impacts per half cycle. This occurs because the cavity wall is moving in the same direction as the impactor with a velocity of greater magnitude than that of the impactor. This type of impactor behavior is referred to as bounce-down and is followed immediately by stuck impactor failure. During bounce-down and stuck impactor failure the impactor exhibits a low level of damping effectiveness. This type of high cavity amplitude impactor behavior ceases at moderate amplitudes and is immediately followed by a range during which a finite number of impacts per half cycle occur. This can be observed in two predominate patterns, the first being an equal number of impacts on each side of the cavity for successive half cycles with the second type of motion being an alternating pattern of even to odd numbers of impacts on opposite cavity walls for successive half cycles. The effectiveness of impact damping steadily increases during this behavior to a maximum damping effectiveness when one impact per half cycle is the pattern of motion, Figures 5 and 6. The damping effectiveness of this

motion is attributed to the fact that the impactor is striking an advancing cavity wall resulting in the most effective reduction of beam velocity experienced as a result of impact damping. When one impact per half cycle is occurring impact damper failure soon follows. When the cyclic motion of the impactor degenerates to occasional random impacts along the cavity wall with less than one impact per half cycle for successive periods, Figure 7, impact damping is no longer effective. Once this occurs the damping of the impactor quickly diminishes.

The presence of higher modes does not alter the basic types of behavior the impactor experiences. However, higher modal frequencies do cause the presence of bounce-down and stuck impactor failure to be less predominate at high amplitudes. As a result the impactor experiences a finite number of impacts per half cycle over a wider cavity amplitude range.

The amplitude decay for the impact damped classical elastic cantilever beam is a simple and quick indicator of the damping occurring as a result of the impactor. The amplitude decay is determined by plotting the amplitude of beam cavity vibration for each half cycle versus the corresponding dimensionless time at which the amplitude occurs (see Figures 8 thru 10).

The effects of the higher mode shapes on the amplitude decay curves are minimal. It is demonstrated in Figure 8 that the amplitude decay for 1, 2, 5, and 10 modes all follow the same general trend with a small increase in the range of time during which low damping effectiveness occurs. This extension of the upper portion of the curve results in the effective regime of behavior to be shifted to a later period in time. Another effect of the higher modes is to cause impact failure to occur at a slightly higher amplitude. Although the point at which impact failure occurs is very important when designing an impact damped system, the higher mode shapes do not significantly change the results from those observed in the single mode case.

The amplitude decay curves for mass ratios of 1, 2, and 3 percent are presented collectively in Figure 9. From this figure the observation can be made that increasing the mass ratio decreases the period of time during which damping of low effectiveness occurs.

The amplitude decay curves for varying values of the coefficient of restitution ranging from 0.5 to 0.8 are shown in Figure 10. From this graph it can be seen that lower values of the coefficient of restitution reduce the time required for equivalent damping. It can also be seen that the decrease in the time required for equivalent damping is not linearly related to the decrease in the coefficient of restitution. As the coefficient of restitution becomes smaller (less than 0.6) the decrease in the time required for equivalent damping becomes significantly less.

LOSS FACTOR RESULTS

The loss factor is defined as the change in beam energy with respect to initial beam energy over a cycle of beam vibration. It can be shown that the loss factor is simply a function of the change in beam cavity amplitude over a cycle of beam vibration with respect to the initial amplitude of the cycle. Applying this fact the calculation of the loss factor was performed using a least squares parabolic fit. This fit is performed to smooth the loss factor

curve and calculate an averaged loss factor, which will be referred to as the loss factor (see Appendix B). The loss factor is plotted with reference to the cavity amplitude. By observing the amplitude decay curve, Figure 8, one would expect the loss factor to increase as the amplitude decreases to the point of impact damper failure. Figure 12 does indeed show this to be the case with impact failure occurring in an amplitude range of 0.3 to 0.07. From this figure it is also observed that the most effective damping which the beam experiences occurs in a cavity amplitude range less than unity. From phase plot Figure 17 whose construction is detailed later, it is illustrated that chaotic and one impact per half cycle behavior of the impactor occurs at amplitudes less than and equal to unity while two impacts per half cycle are experienced by the impactor at an amplitude slightly greater than unity. From this it is concluded that the most effective damping correlates to impactor behavior beginning at the transition from two to one impacts per half cycle.

As previously discussed the influence of higher modes does not play a major factor in changing the behavior of the impact damped classical elastic cantilever beam. This fact is again illustrated by observing the loss factor curves for 1, 2, 5, and 10 modes with all other variables held constant. Figure 11 shows that the presence of higher mode frequencies does not significantly alter the loss factor curve with respect to the cavity amplitude. The presence of higher modal frequencies does tend to band the loss factor about those results obtained for the single mode case. The center of this band width occurs about the first mode. It is therefore concluded that the effects of other parameters on the loss factor can be based upon a first mode comparative analysis.

The impactor to beam mass ratio plays a significant role in determining the value of the loss factor for any given cavity amplitude. More specifically, as seen in Figure 12, increasing the mass ratio results in an increase in the loss factor for all amplitudes prior to impact failure. It is also observed that this increase is a constant value change which can be directly expressed as a function of the reciprocal of the mass ratio. To illustrate this fact the loss factor is divided by the mass ratio to obtain the specific total loss factor. Figure 13 shows that the specific total loss factor reduces all mass dependent loss factors to one common curve as a function of cavity amplitude. The specific total loss factor begins with a magnitude of 0.09 at a cavity amplitude of 6.0 while undergoing stuck impactor behavior and reaches a peak value of 9.0 prior to impact damper failure. From the Mass Normalized Loss Factor plot, Figure 13, it is observed that the specific total loss factor behaves as a linear function of the cavity amplitude with a slope of approximately negative one. To show the extent to which this is true the product of the specific total loss factor and cavity amplitude is illustrated in Figure 14. When observing this result it can be inferred that this product behaves on the average as a constant of magnitude approximately 0.4 for all cavity amplitudes. This constant value interpretation is valid within an error range of ± 25 percent prior to impact damper failure. A significant point of interest is that the simple harmonic oscillator was found to behave in a very similar manner with reference to the loss factor's dependence upon the mass ratio and cavity amplitude⁴.

A third parameter which plays a major role in the evaluation of impact damper performance is the coefficient of restitution denoted by e. It is observed that any increase in the coefficient of restitution results in a

decrease in the effectiveness of the impact damper. Another conclusion that can be made is that this decrease in the loss factor is not linearly related to the coefficient of restitution. To effectively amplify changes in the loss factor curve for varying values of the coefficient of restitution the product of the specific total loss factor and cavity amplitude is used to generate the Amplitude Specific Loss Factor curve, Figure 15. From these results it can be more clearly observed that the loss factor is not linearly related to the coefficient of restitution for all cavity amplitudes. Applying a relationship developed by Brown and North⁴ the quotient of the amplitude specific loss factor and (1-e) results in Figure 16. This result is valid only within the range of motion for which a finite number of impacts occurs during each half cycle. As with the amplitude specific loss factor this curve can be reasonably approximated as a constant of value 1.0 to within an error of ± 30 percent. This illustrates that the loss factor for the classical elastic cantilever beam and simple harmonic oscillator investigated by Brown and North⁴ behave in a similar manner with regard to variations in the coefficient of restitution.

IMPACT PHASE

From the beam's initial amplitude of vibratory motion to the point at which impact damper failure occurs there exist several time spans of distinct motion which the impactor experiences. These types of behavior can be observed by calculating the phase angle for each impact across a half cycle of vibration (see Appendix C). Plotting this phase angle in the range from 0° to 180° as a function of the cavity amplitude of vibration yields distinct and well defined patterns and trends for the impactor. These patterns for the one mode case are illustrated in Figure 17. Each impact is denoted by a point marker on these figures. Phase plots are read from bottom to top while progressing from right to left as time increases and amplitude decreases. By reading this graph the number of impacts per half cycle can be determined for any given amplitude. For the case of higher amplitudes the phase plot depicts an infinite number of impacts for a given amplitude. This fact can be observed by noticing that the point markers, representative of each impact, meld into a solid line. When amplitudes diminish below the bounce-down and stuck impactor failure range it is clear that well defined periodic motion of the impactor is occurring. This periodic motion takes one of two forms. The first is a pattern exhibiting an even number of impacts per half cycle while the second contains an odd number of impacts. From this well defined periodic motion the impactor motion degenerates into what is referred to as chaotic motion. This is a type of motion during which no discernible pattern can be extracted. Each zone of chaotic motion then flows into two clear paths known as period doubling. These two paths soon merge into one solid line during which well defined periodic motion of one less order occurs. The combined use of phase plot Figure 17 and loss factor Figure 12 leads to the conclusion that the effectiveness of the impactor increases as the number of impacts per half cycle decreases prior to impact damper failure.

In the case of the phase plot, Figures 18 and 19, the higher mode shapes do play a significant factor in the analysis of impactor behavior. The presence of higher modal frequency vibration disrupts the well ordered motion that is observed in the simple harmonic oscillator and one mode classical elastic cantilever beam case; Figure 17. The presence of higher frequencies

also disrupts the phenomenon of stuck impactor failure. In place of stuck impactor failure the impactor experiences low relative displacement impacting or high intensity bounce-down. In the event the impactor does become stuck it is quickly slung free by the presence of high frequency vibration. While the higher mode frequencies do disrupt the ordered behavior of the impactor it can be seen that significantly fewer impacts per half cycle occur at lower cavity amplitudes.

This study, like that of Brown and North⁴, found that variations in the mass ratio affected the phase plots only by increasing and decreasing the number of impacts that occur in a set time frame for the case of one mode. It is observed that smaller mass ratios yield more dense plots because of the increased number of impacts which occur during a incremental decrease in beam cavity amplitude. From this it is concluded that a decrease in the impactor to beam mass ratio increases the number of impacts required to lower the beam cavity vibrational amplitude by a constant value. This implies that the individual effectiveness of each impact is reduced as the mass ratio is lowered. Another point of significance is that variations in the mass ratio do not affect the amplitudes or phase angles for which each distinct pattern of motion occurs. In the presence of higher mode frequencies the phase plots differ as a result of varying the mass ratio but in no discernible pattern.

Unlike the mass ratio, variations in the coefficient of restitution, e , do have a major affect on the phase plot. This analysis shows that while lower values of the coefficient of restitution result in higher loss factors, Figure 15, lower coefficients of restitution also cause bounce-down and stuck impactor failure to occur at much lower amplitudes; Figures 20 and 21. An example of this is a value of the coefficient of restitution equal to 0.5 for which stuck impactor failure occurs at an amplitude as low as 3.0. In comparison a value for the coefficient of restitution of 0.6 results in the termination of stuck impactor failure at an amplitude of 5.0. As previously discussed lowering the value of the coefficient of restitution becomes less effective in decreasing the time required to damp the continuous elastic cantilever beam vibration oscillation to a given amplitude when the coefficient of restitution is less than 0.5. The use of phase plot Figure 20 may help to explain this phenomenon by noting that lowering the value of the coefficient of restitution decreases the amplitude at which stuck impactor failure ceases. This in turn narrows the amplitude range during which efficient damping occurs. This results in a trade off between the energy dissipative properties of the coefficient of restitution and the lower efficiency damping of bounce-down and stuck impactor failure.

CONCLUSIONS

1. The impactor behavior for an impact damped continuous elastic cantilever beam is characteristically the same as that of an impact damped simple harmonic oscillator.
2. The magnitude of the damping effectiveness for an impact damped continuous elastic cantilever beam behaves similarly to the damping effectiveness of a simple harmonic oscillator.
3. The most effective damping of the continuous elastic cantilever beam and simple harmonic oscillator occurs when the cavity vibrational amplitude is less than unity. With the use of phase plots it is shown that this corresponds to impactor motion of less than 2 impacts per half cycle.
4. The presence of higher mode frequencies does not change the damping effectiveness of the impactor. This leads to the conclusion that the first modal frequency predominates impactor damping effectiveness.
5. The loss factor is directly related to the mass ratio. A specific loss factor can be determined by dividing the loss factor by the mass ratio. This results in a single specific loss factor curve with respect to the cavity vibrational amplitude.
6. The loss factor is a function of $1/(1-e)$ during periodic motion with a finite number of impacts occurring per half cycle. Dividing the specific loss factor by $(1-e)$ yields a single curve with respect to the cavity amplitude with the exception of the bounce-down followed by stuck impactor failure and total impact damper failure.
7. The loss factor can be expressed as a constant of magnitude 1.0. It is shown that the product of the loss factor and cavity amplitude divided by the product of the mass ratio and $(1-e)$ is reasonably constant.
8. For the case of one mode clear patterns of impactor motion can be observed from the phase plot. This motion begins with bounce-down followed by stuck impactor failure at high cavity amplitudes. This degenerates to periodic motion with a distinct finite number of impacts per half cycle at moderate cavity amplitudes. This periodic motion is characterized by chaotic motion and period doubling. Impactor motion of one impact per half cycle is soon followed by impact damper failure. This occurs at low cavity amplitudes when the impactor experiences less than one impact per half cycle.
9. The presence of higher modal frequencies disrupts the regularity of impactor motion.
10. The time scale of the amplitude decay curve is directly related to the mass ratio. Cavity amplitude plotted with respect to the product of the mass ratio and dimensionless time results in a single curve.
11. While the impact damper does not require frequency tuning it does require amplitude tuning. This is the result of the fact that impact damping effectiveness is a function of the cavity's vibrational amplitude.

REFERENCES

- [1] Soller, Peter J., "The Development of a Computer Model as an Aid to the Solution of the Problem of Impact Damping", M.S. Thesis, Rose Hulman Institute of Technology, Terre Haute, IN, 1985.
- [2] Masri, S.F., "Analytical and experimental Studies of Impact Dampers", Ph.D. Thesis, California Institute of Technology, Pasadena, CA, (CIT Dynamics Laboratory Report), 1965.
- [3] Bapat, C.N., N. Popplewell, and K. McLachlan, "Stable Periodic Motions of an Impact-Pair", Journal of Sound and Vibration, 1983, Volume 87, Number 1.
- [4] Brown, Gerald V. and C. Mallory North, "The Impact Damped Harmonic Oscillator in Free Decay", NASA Technical Memorandum 89897, Lewis Research Center, 1987.
- [5] Nale, Timothy A., "Time History Study of a Classical Cantilever Beam Damped by Internal Mechanical Means", M.S. Thesis, Rose Hulman Institute of Technology, Terre Haute, IN, 1988.

APPENDIX A - SYSTEM MATHEMATICAL MODEL

A continuous beam with frictionless impact damping is represented by Figures 1 and 2. A detailed derivation of the equations of motion which model this system are presented by Nale⁵. Figures 1 and 2 are representative of the physical system in dimensional variable form. For this study and the benefit of future studies the system is made dimensionless in the following manner. The beam length, L, is the unit of length with the exception of the impactor relative displacement. The cavity length, H = E_y-D, is used as the unit of length for the dimensionless analysis of the relative displacement. The unit of time is the beam characteristic wave time, T_c. The beam mass is used as the unit mass. The equation of motion of the beam is

$$EI \frac{\partial^4 Y}{\partial X^4} + \frac{\partial^2 Y}{\partial T^2} = F_0 \exp(i\Omega T) l(T) \delta(X-X_f) + \frac{1}{E_x} \left[l(X-X_o) - l(X-X_o-E_x) \right] \sum_{i=1}^n p_i \delta(T-T_i) \quad (A.1)$$

with boundary conditions given by

$$Y(0, T) = \frac{\partial Y}{\partial X}(0, T) = \frac{\partial^2 Y}{\partial X^2}(L, T) = \frac{\partial^3 Y}{\partial X^3}(L, T) = 0 \quad T > 0$$

and initial conditions given by:

$$Y(X, 0) = F(X) \quad \text{and} \quad \frac{\partial Y}{\partial T}(X, 0) = G(X) \quad 0 \leq X \leq L$$

The equation of motion (A.1) which models the physical system shown in Figures 1 and 2 is made dimensionless with respect to the appropriate unit variables in equation (A.2). Dimensionless variables in (A.2) are denoted by lower case letters corresponding to upper case dimensional variables in (A.1).

$$\frac{\partial^4 y}{\partial x^4} + \frac{\partial^2 y}{\partial t^2} = f_0 \exp(i\omega_f t) l(t) \delta(x-x_f) + g_0(x) \sum_{i=1}^n p_i \delta(t-t_i) \quad (A.2)$$

where: $g_0(x) = \frac{1}{e_x} \left[l(x-x_o) - l(x-x_o-e_x) \right]$

Boundary conditions:

$$y(0, t) = y'(0, t) = y''(1, t) = y'''(1, t) \quad t > 0$$

Initial conditions:

$$y(x, 0) = f(x) \quad \text{and} \quad \dot{y}(x, 0) = g(x) \quad 0 \leq x \leq 1$$

The impactor motion of the impact damped classical elastic cantilever beam is characterized by four distinct types of behavior. Each of these types of motion are individually modeled by an appropriate set of equations. Once the type of behavior that is occurring is determined the correct model is used to calculate the position, velocity, and acceleration of the impactor and beam at the next point in time.

The simplest case of impactor behavior is impactor free motion (impactor not at the cavity wall). During this period of motion the beam and impactor are totally independent of one another. The beam is modeled as a simple classical elastic cantilever beam having a single sinusoidal point load located anywhere along the beam length with the exception of the center of the beam cavity. The equation of motion for the beam is solved using the method of generalized displacements (see Nale⁵). The generalized displacements, velocities, and accelerations are determined using the method of LaPlace transforms. The resulting Fourier solutions for beam displacements, velocities, and accelerations are valid until the next impact is experienced.

The impactor in free motion is modeled as a free particle in rectilinear motion. The constant velocity with which the impactor travels is determined at the time of the most recent previous contact with the beam cavity wall.

When the position of the impactor coincides with that of the beam cavity wall an impact or collision of the beam cavity wall and impactor occurs. The impact is modeled by applying the coefficient of restitution theory. The relative velocity \dot{u}_i between the impactor and the beam immediately prior to impact is related to that immediately after impact \dot{u}_i' by:

$$\dot{u}_i' = -e\dot{u}_i \quad (\text{A.3})$$

The time at which impact occurs is determined when the absolute displacement of the beam cavity wall is equal to that of the impactor. While this time of impact is modeled as instantaneous, the resulting impulse applied to the beam occurs across a finite nonzero cavity width.

A more difficult type of motion to model is that of bounce-down. Motion of this nature is experienced by the system when consecutive impacts on the same cavity wall occur with consistently shorter time intervals between impact. This results in smaller maximum relative displacements between the impactor and cavity wall for consecutive impacts. While experiencing this type of motion an infinite number of impacts occur during a finite period of time. The finite time during which bounce-down occurs is readily determined by means of a convergent geometric series expansion (see Nale⁵). Bounce-down terminates with the impactor resting at the cavity wall for until the acceleration of the cavity wall reverses direction. This occurrence is referred to as "stuck impactor failure".

The impactor is said to be stuck at the cavity wall when the following three conditions occur simultaneously. First, the impactor must be located at the cavity wall. Second, the velocity of the impactor relative to the beam must be zero. Finally, the beam must be accelerating toward the impactor.

During stuck impactor failure the total energy of the freely vibrating impact damped classical elastic cantilever beam system remains constant. At the same time energy is being exchanged between the impactor and beam. This energy transfer process from the beam to the impactor during stuck impactor failure explains why minimal damping occurs even when the impactor is stuck at the beam cavity wall.

While the impactor is stuck there exists a normal reaction between the impactor and the cavity wall. This normal reaction is a direct function of the cavity acceleration. The impactor is slung free of the beam cavity wall and set back in free motion when the normal reaction vanishes. The normal reaction between the impactor and cavity wall is eliminated only when the beam cavity acceleration changes direction.

These four states of impactor activity are used to determine the appropriate set of equations to be used in calculating the position, velocity, and acceleration of the impactor and beam for each progressive point in time. Free motion and simple impact are modeled with relative ease. Bounce-down and stuck impactor failure are more difficult, but not intractable (see Nale⁵).

APPENDIX B - LOSS FACTOR

The loss factor is first illustrated for the simple harmonic oscillator. The results are later applied to the beam model. The loss factor is defined as the change in potential energy E with respect to itself. This relationship is expressed in its most general form as shown in Equation (B.1):

$$\eta = \frac{\Delta E}{E} \quad (B.1)$$

For the case of the simple harmonic oscillator the potential energy, $E = ky^2/2$, is simply the potential energy of the linear spring. The derivative of the spring energy with respect to the spring deflection, y , is used to approximate the change in energy, $\Delta E = ky\Delta y$. Using the expressions for E and ΔE for the simple harmonic oscillator in the general expression (B.1) the loss factor is expressed simply as a function of spring amplitude of vibration:

$$\eta = 2\Delta y/y \quad \text{per cycle} \quad (B.2)$$

The loss factor is in practice calculated using an averaging process by means of a least squares parabolic fit about five full cycles of motion. The change in amplitude, Δy , is expressed as a function of the time rate of change of the amplitude and the average period of oscillation. For this study the loss factor is expressed in dimensionless form. This is done by dividing the loss factor per cycle by 2π resulting in a loss factor per radian. Substitution of the change in amplitude results in Equation (B.3).

$$\eta = \frac{1}{\pi} \frac{\dot{y}(t_n)}{y(t_n)} \bar{T}_n \quad \text{per radian} \quad (B.3)$$

The loss factor for the impact damped classical elastic cantilever beam is determined in a similar manner from (B.3) by using the beam cavity amplitude of vibration in place of the spring deflection y used for the simple harmonic oscillator. This substitution results in a loss factor for the impact damped cantilever beam at the center of the cavity longitudinal coordinate.

APPENDIX C - PHASE ANGLE CALCULATION

The phase angle is used to determine where the impactor collides with the sinusoidal oscillating cavity wall. This measure is made in degrees across each half cycle from 0° to 180° . The phase angle ϕ_i for the impact which occurs at time t_i is easily calculated using Equation (C.1).

$$\phi_i = 180^\circ (t_i - t_n) / (t_{n+1} - t_n) \quad (\text{C.1})$$

The times, t_n and t_{n+1} , are representative of when the acceleration of the cavity wall changes direction sign.

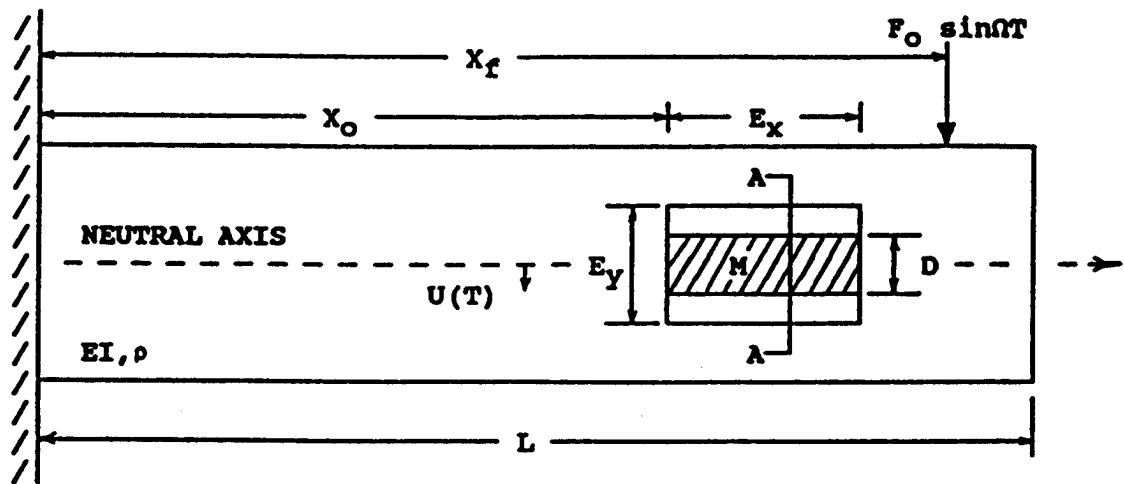


FIGURE 1 - SIDE VIEW SCHEMATIC OF IMPACT DAMPED CLASSICAL ELASTIC CANTILEVER BEAM.

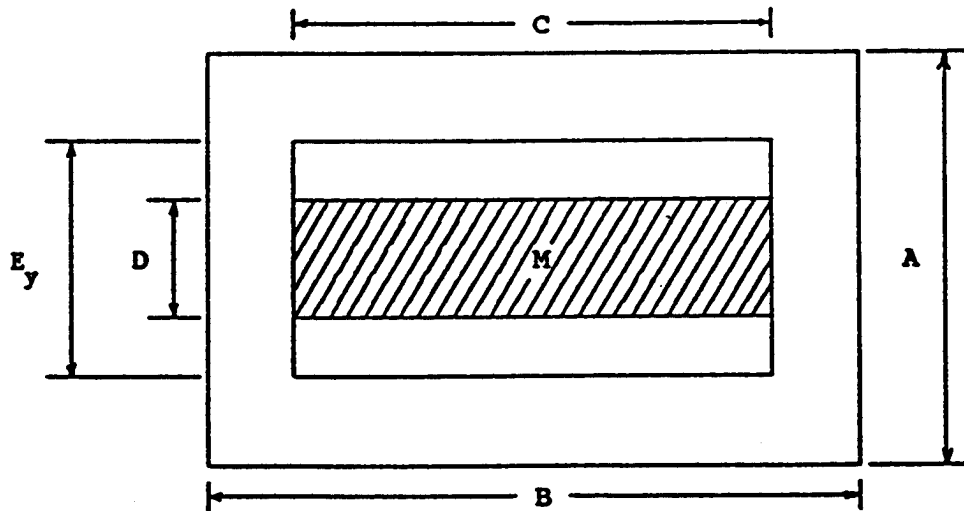


FIGURE 2 - CROSS SECTION A-A OF THE IMPACT DAMPED CLASSICAL ELASTIC CANTILEVER BEAM.

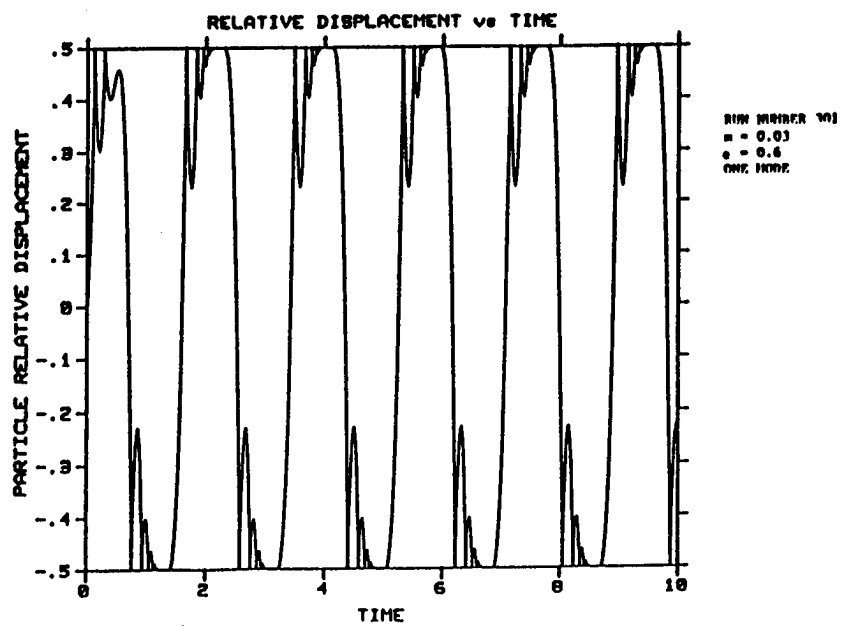


FIGURE 3 - RELATIVE IMPACTOR DISPLACEMENT OF AN INFINITE NUMBER OF IMPACTS EACH HALF CYCLE; $m = 0.03$; $e = 0.6$; ONE MODE.

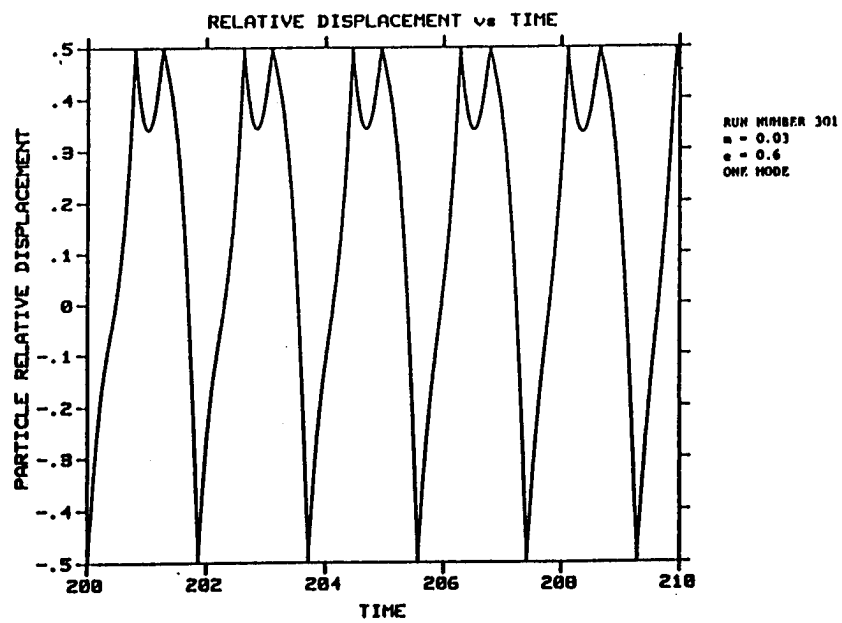


FIGURE 4 - RELATIVE IMPACTOR DISPLACEMENT OF ONE IMPACT PER HALF CYCLE ALTERNATING WITH TWO; $m = 0.03$; $e = 0.6$; ONE MODE.

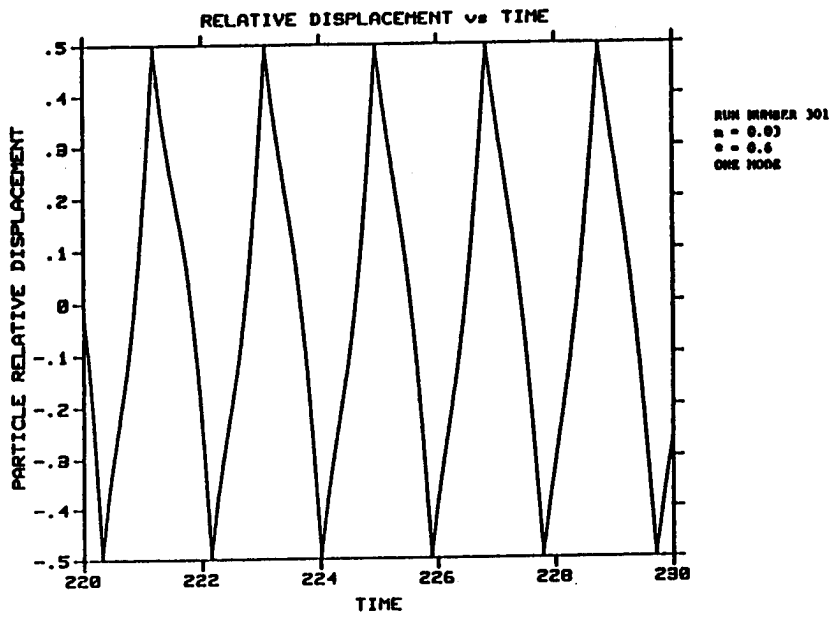


FIGURE 5 - RELATIVE IMPACTOR DISPLACEMENT OF ONE IMPACT EACH HALF CYCLE: $m = 0.03$; $e = 0.6$; ONE MODE.

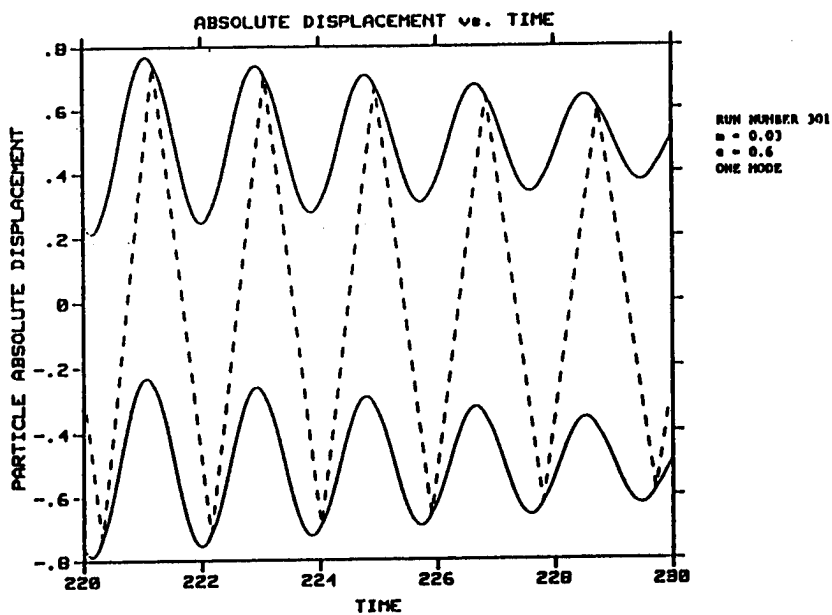


FIGURE 6 - ABSOLUTE IMPACTOR AND CAVITY DISPLACEMENT OF ONE IMPACT EACH HALF CYCLE; $m = 0.03$; $e = 0.6$; ONE MODE.

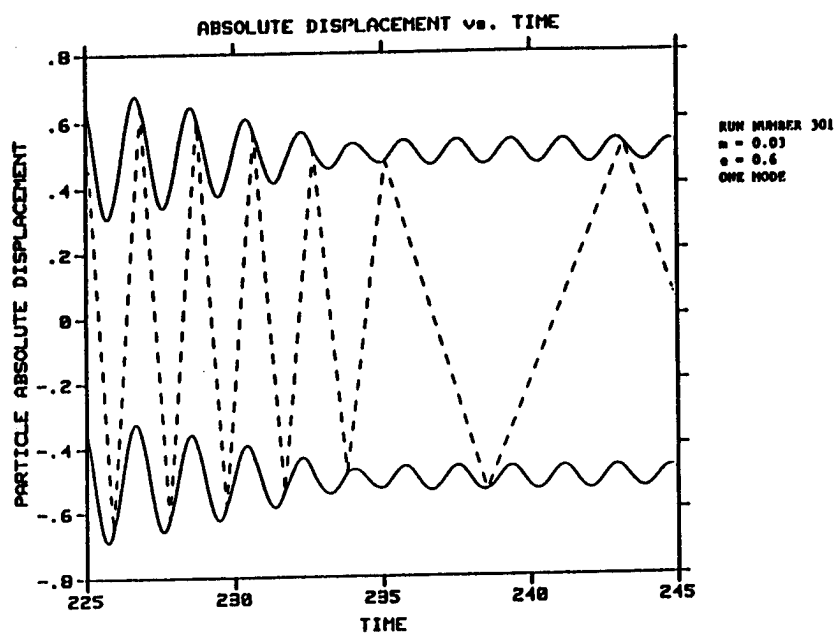


FIGURE 7 - ABSOLUTE IMPACTOR DISPLACEMENT AT THE BEGINNING OF "IMPACT DAMPER FAILURE"; $m = 0.03$; $e = 0.6$; ONE MODE.

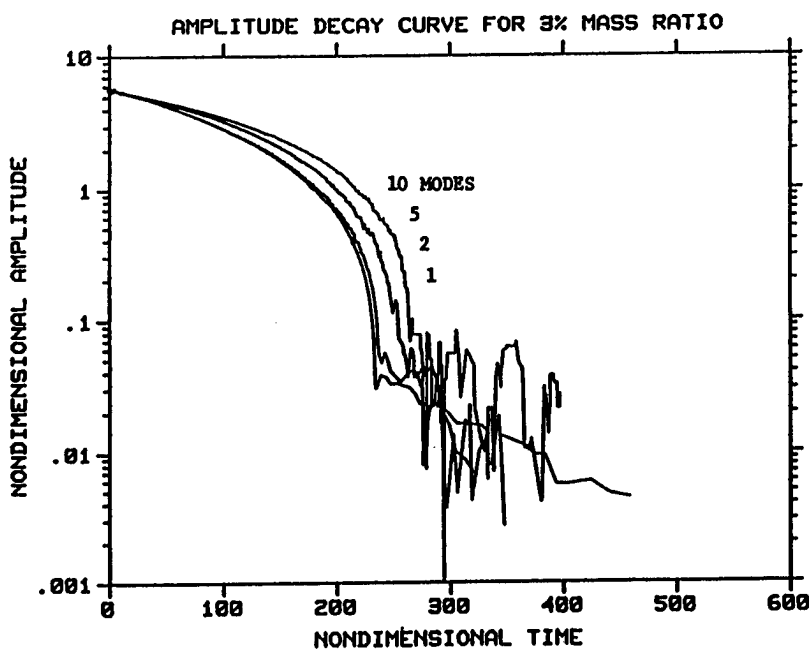


FIGURE 8 - AMPLITUDE DECAY; $m = 0.03$; $e = 0.6$; 10, 5, 2, AND 1 MODE.

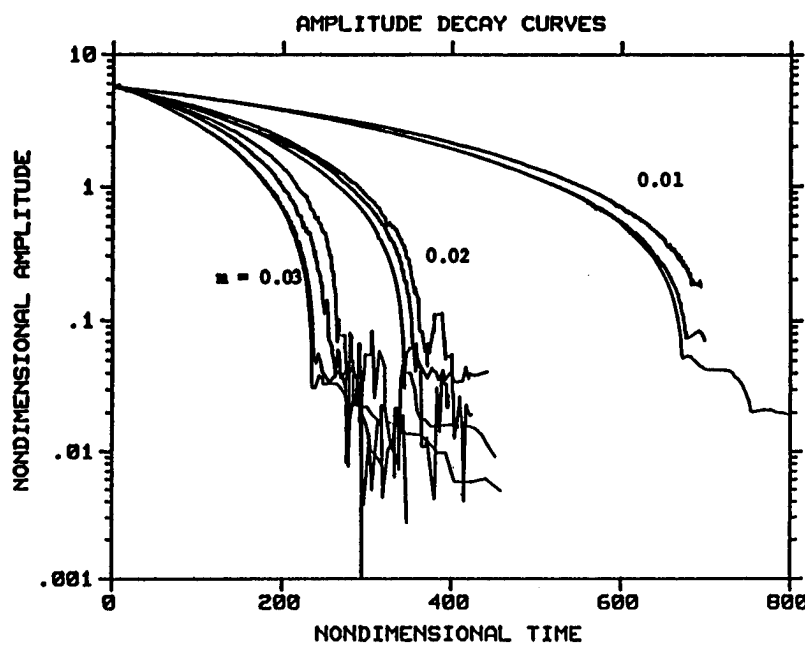


FIGURE 9 - AMPLITUDE DECAY; $m = 0.03, 0.02, 0.01$; $e = 0.6$; 10, 5, 2, AND 1 MODE.

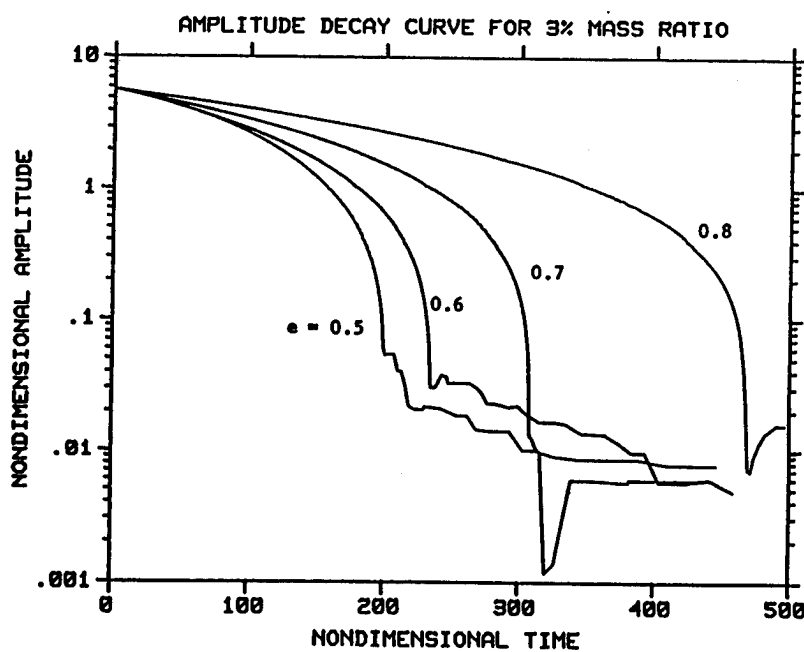


FIGURE 10 - AMPLITUDE DECAY; $m = 0.03$; $e = 0.5, 0.6, 0.7, 0.8$; ONE MODE.

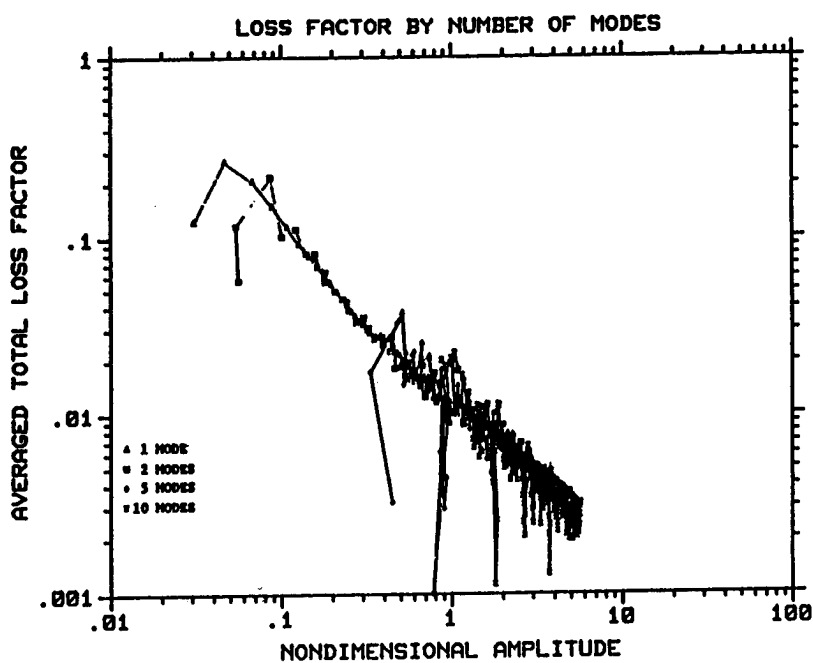


FIGURE 11 - AVERAGE TOTAL LOSS FACTOR; $m = 0.03$; $e = 0.6$; 10,5,2,1 MODE.

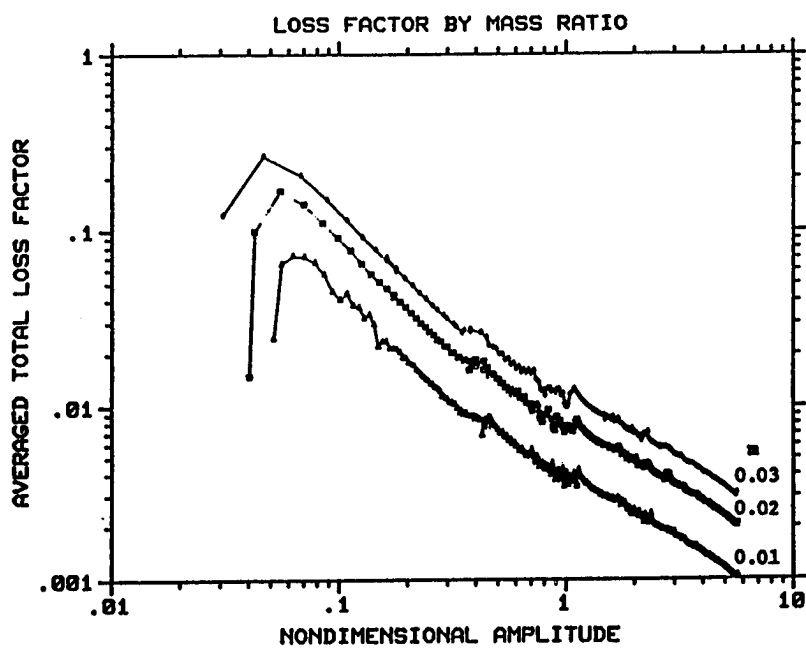


FIGURE 12 - AVERAGE TOTAL LOSS FACTOR; $m = 0.03, 0.02, 0.01$; $e = 0.6$; ONE MODE.

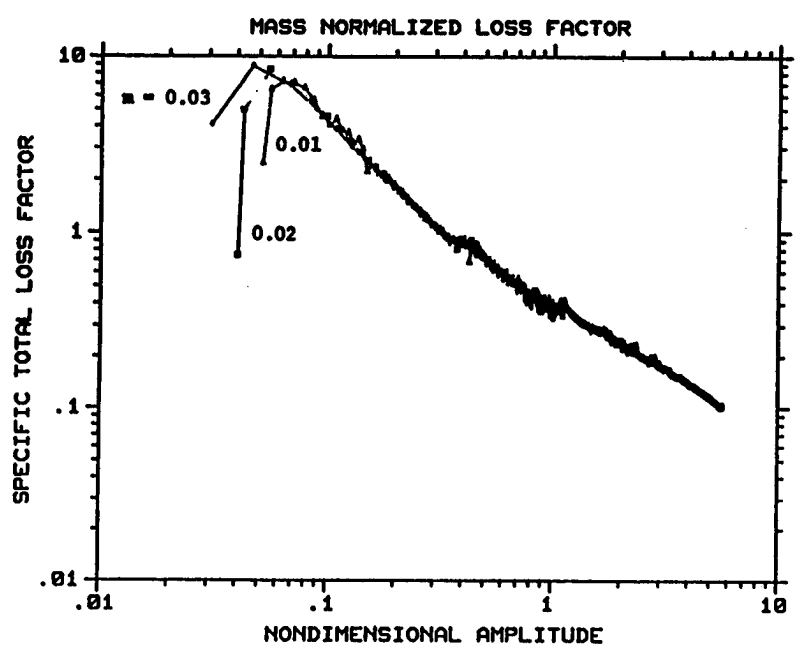


FIGURE 13 - SPECIFIC TOTAL LOSS FACTOR; $m = 0.03, 0.02, 0.01$; $\epsilon = 0.6$; ONE MODE.

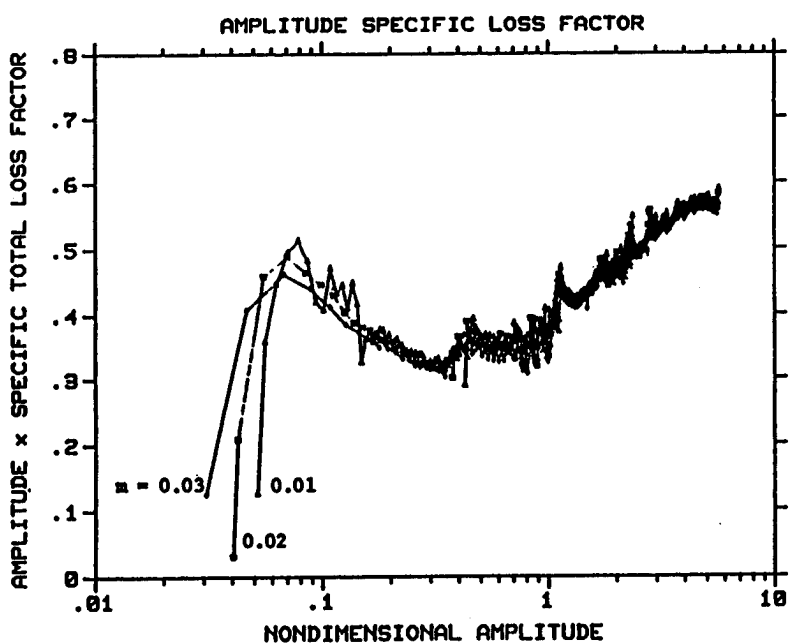


FIGURE 14 - AMPLITUDE AND SPECIFIC IMPACTOR LOSS FACTOR PRODUCT; $m = 0.03, 0.02, 0.01$; $\epsilon = 0.6$; ONE MODE.

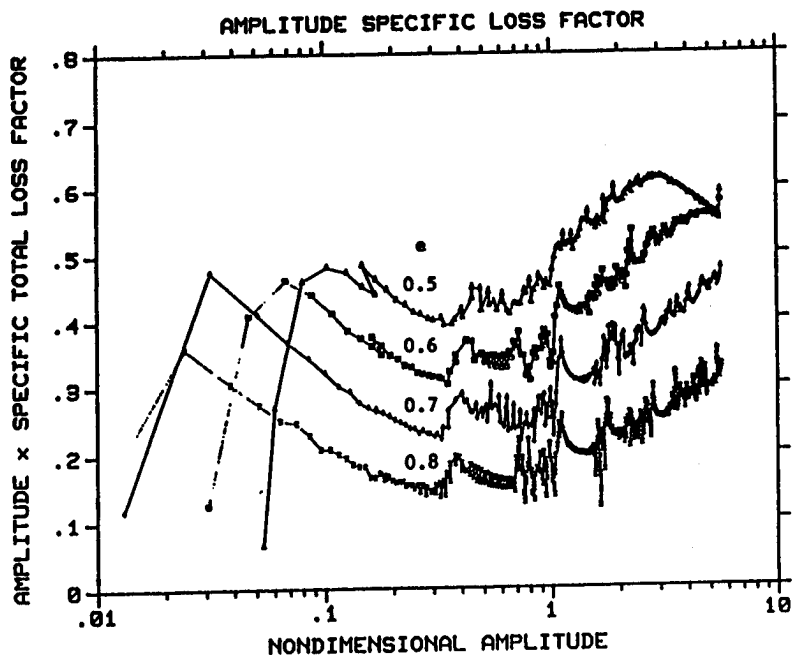


FIGURE 15 - AMPLITUDE AND SPECIFIC IMPACTOR LOSS FACTOR PRODUCT;
 $m = 0.03$; $e = 0.5, 0.6, 0.7, 0.8$; ONE MODE.

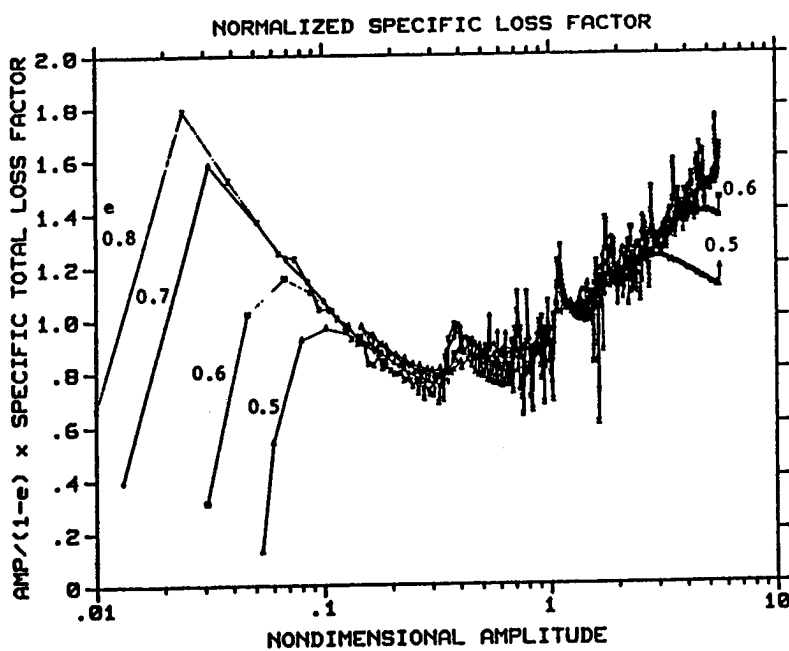


FIGURE 16 - NORMALIZED AMPLITUDE SPECIFIC LOSS FACTOR; $m = 0.03$;
 $e = 0.5, 0.6, 0.7, 0.8$; ONE MODE.

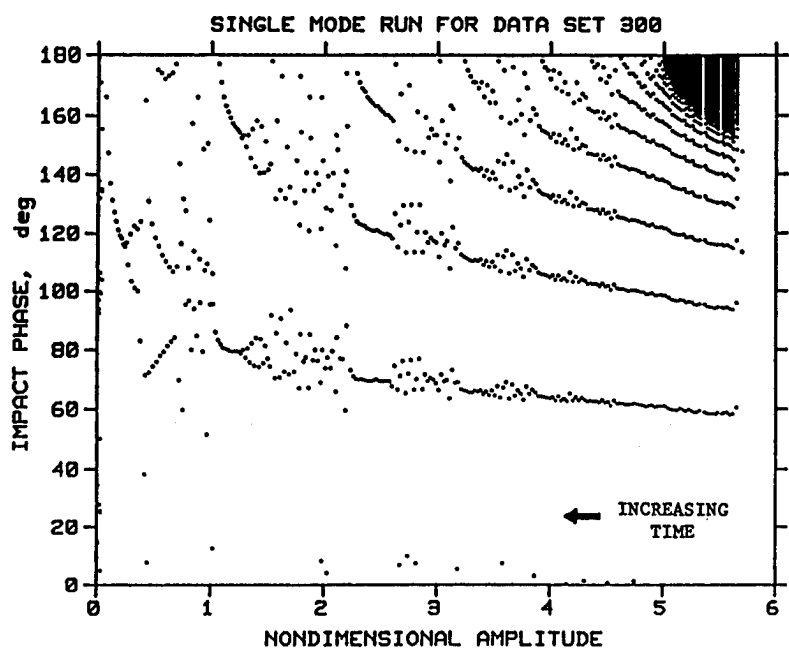


FIGURE 17 - IMPACTOR PHASE MEASURED FROM ZERO CROSSING; $m = 0.03$; $e = 0.6$; ONE MODE.

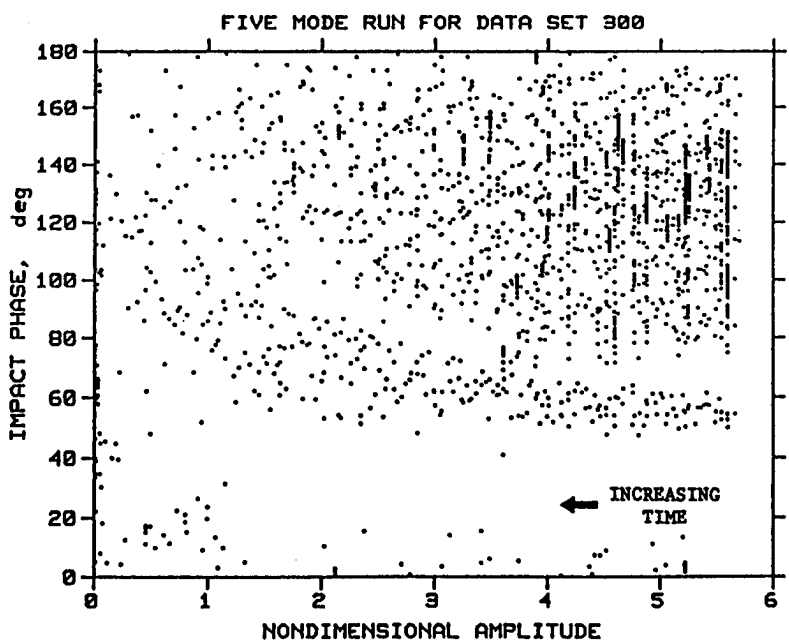


FIGURE 18 - IMPACTOR PHASE MEASURED FROM ZERO CROSSING; $m = 0.03$; $e = 0.6$; FIVE MODES.

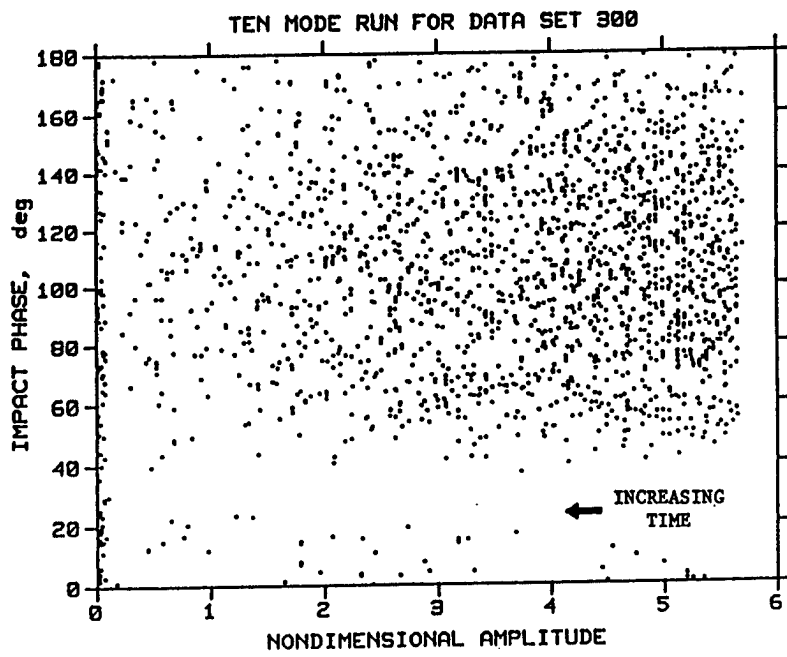


FIGURE 19 - IMPACTOR PHASE MEASURED FROM ZERO CROSSING; $m = 0.03$; $e = 0.6$; TEN MODES.

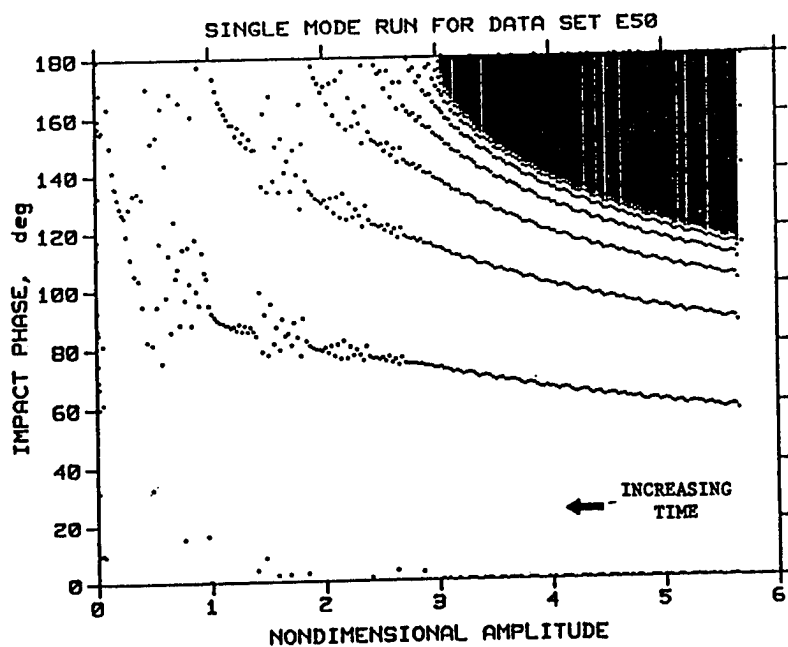


FIGURE 20 - IMPACTOR PHASE; $m = 0.03$; $e = 0.5$; ONE MODE.

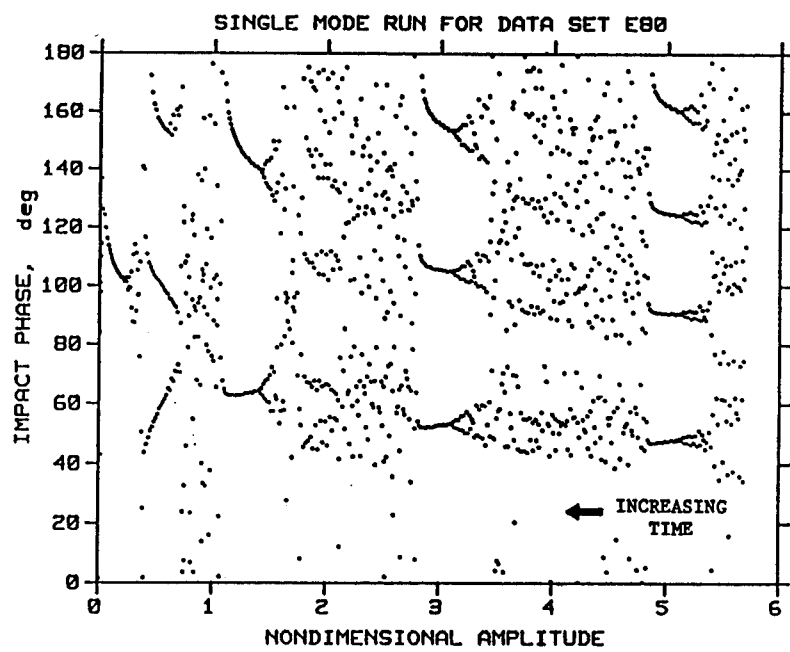


FIGURE 21 - IMPACTOR PHASE; $m = 0.03$, $e = 0.8$; ONE MODE.

NONOBSTRUCTIVE IMPACT DAMPING APPLICATIONS FOR
CRYOGENIC ENVIRONMENTS

H. V. Panossian

Rockwell International/Rocketdyne Division
Canoga Park, California

Abstract

Viscoelastic materials cannot be utilized for vibration damping applications in cryogenic and severe pressure and flow environments. Such environments exist in many rocket engines; it is a challenging task to design for optimal structural damping in such systems. Impact damping techniques essentially work on the basis of momentum exchange via the energy dissipated by collisions of the impacting material with the vibrating mechanical structural. This method can be effectively utilized in rocket engines when used in such a way that it does not obstruct this flow.

Extensive impact damping experimentation was carried out in Rocketdyne's Engineering Development Laboratory on the Space Shuttle Main Engine (SSME) liquid oxygen (LOX) inlet splitter vanes. These splitter vanes often experience very high amplitude and high frequency (around 4000 Hz) vibrations, and during some post-hot-fire test inspections, cracks have been identified on their vane/shell interface, internally. In an effort to reduce the overall mentioned vibration levels of these vanes, holes were made through one of the abovementioned vanes and were filled with different metallic and nonmetallic materials at different levels; vibrations were induced by an impact hammer and a high frequency/high amplitude electromechanical shaker and responses were measured under different fill levels and with different materials filling the holes. The overall grms vibration levels were reduced drastically with the holes filled at 3/4 level. This paper will report on the findings of these experiments, will analyze the results, and will make recommendations for the application of such unobstructive methods for damping structures in harsh environments.

Work reported herein was sponsored by NASA/Marshall Space Flight Center under Contract NAS8-40000.

Introduction

In cryogenic and severe pressure and flow environments, and even in high temperatures, vibration damping¹ is a challenging problem, to say the least. Viscoelastic materials have found widespread applications in moderate to normal environments under ambient temperatures and pressures. However, very little (if anything) has been done in the areas of cryogenic damping.

The abovementioned harsh environment exists in many parts of rocket engines, and this is often coupled with high-amplitude vibrations that can potentially be catastrophic. Thus, it is desirable to design some form of structural damping into such systems in order to be able to damp out the anomalous vibrations. Design changes are often effective;¹ however, sometimes simpler solutions can be more appropriate since it is not always possible to implement design modification without resorting to drastic measures.

The effectiveness of damping treatments is related to the extent of vibration energy being converted into some other form of energy. In the case of viscoelastic materials, some of the vibration energy is dissipated in the form of heat, while in impact damping applications, this energy is transformed into kinetic energy via the motion of the impacting particles, and eventually into heat through friction.² The main reason for damping treatments is to reduce vibration amplitudes and thus avoid structural failures. There are normally two main sources of structural vibration failures: fatigue failure that is related to stress level when parts fail due to increased dynamic stress,³ and displacement of the structural parts that fail when it exceeds a particular threshold.⁴

In an effort to find an alternate option (alternate to the now implemented and successful vane modification--see Ref. 1) to fix the anomalous vibrations of the liquid oxygen (LOX) inlet splitter vanes of the Space Shuttle Main Engine (SSME), a study was initiated that was directed toward utilizing the impact damping methodology with a new approach. The idea was to make holes through the length of the vanes (from top to bottom) and fill these holes with different materials and study their effects on the vibration of the vanes. The vibrations were induced by a high-frequency/high-amplitude electromechanical exciter (Wilcoxon D125L) and an impact hammer for low-frequency response. Measurements of acceleration were recorded from five accelerometers equidistantly located along the midspan of the right vane (right as one looks down through the LOX inlet right-side-up) and at the driving point (Fig. 1). Moreover, mode shapes were derived from a 25-point grid of accelerometers located equally spaced on the surface of the vanes (5 x 5). The damping ratios for each mode were generated and compared with the damping ratios under each material damping. A band-limited flat random excitation between 3000 and 6000 Hz was used to excite the tee at the bottom of the vanes, on the shell between the two leading edges of the vanes.

Description of Tests

The vibration and modal tests of the baseline tee were carried out first, and data was recorded and processed in the form of frequency response functions (FRFs), power spectral densities (PSDs), mode shapes, and damping ratios. Then, four 1-mm-diameter holes were made by EDM through the vanes (Fig. 1). These holes were first filled and tested with 7-, 11-, and 23-mil steel balls at 1/2-, 3/4-, and 7/8-full levels. It was determined that the 3/4-full level was the best among the three levels tested. Then zirconium oxide (ceramics) balls of 10-mil diameter were introduced in the holes and tested for vibration levels with virtually the same amplitude and vibration conditions applied. Similar tests were carried out with nickel powder and tungsten powder.

All the tests were performed according to the rules of modal/vibration testing. Namely, the tee was suspended by flexible rubber bands to simulate a free-free condition and the shaker was bolted on a fixture with the moving tip (with a load cell (PCB) attached to it) glued on the bottom of the tee (Fig. 2). The driving point response was kept at 13.7 grms, and the vane responses at different locations along the midspan ranged from 20 grms all the way to 154.6 grms at the leading edge midpoint of the right vane.

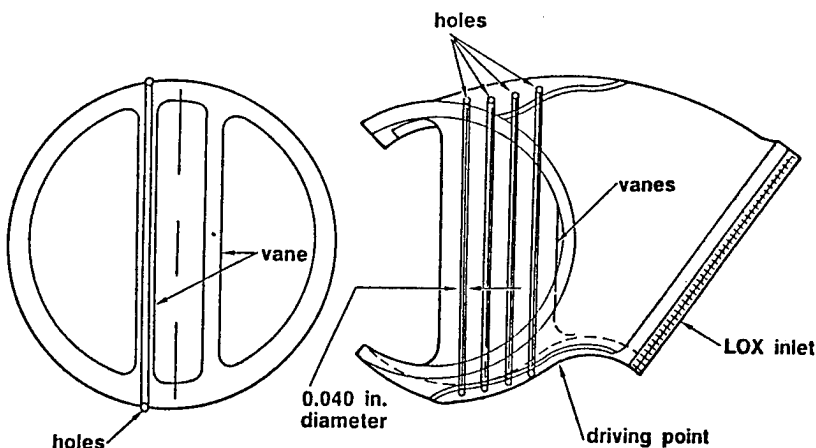


Fig. 1. LOX Inlet Tee

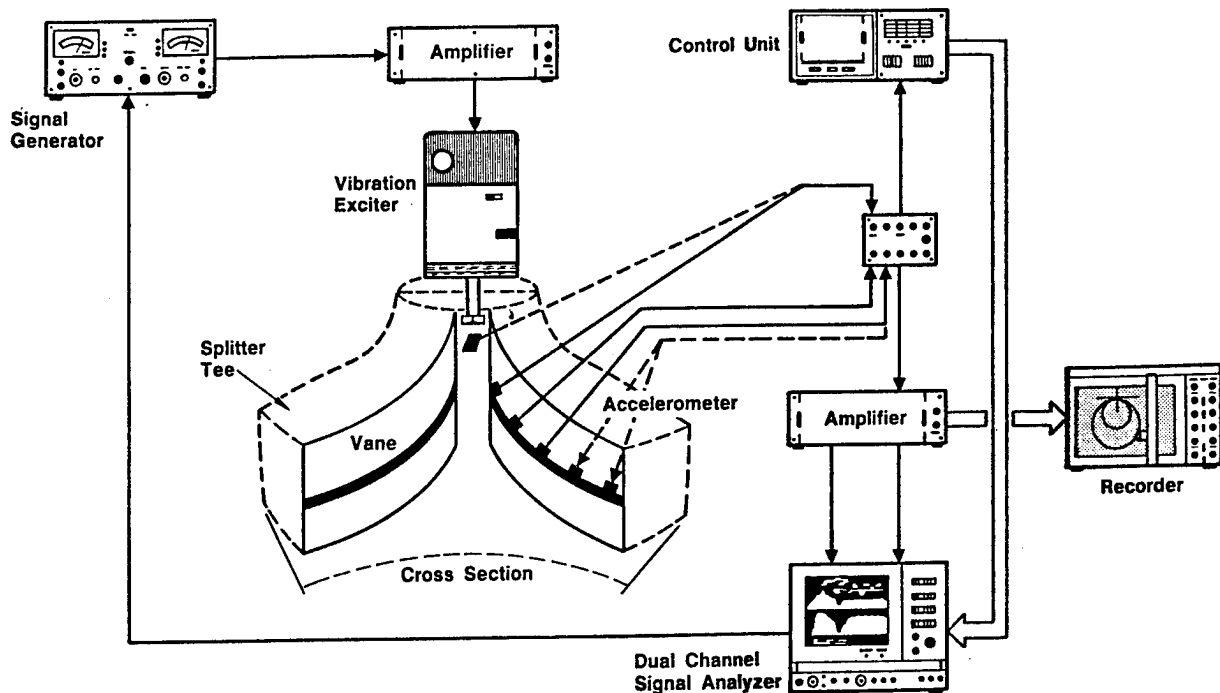


Fig. 2. Measurements of Modal/Vibration Tests

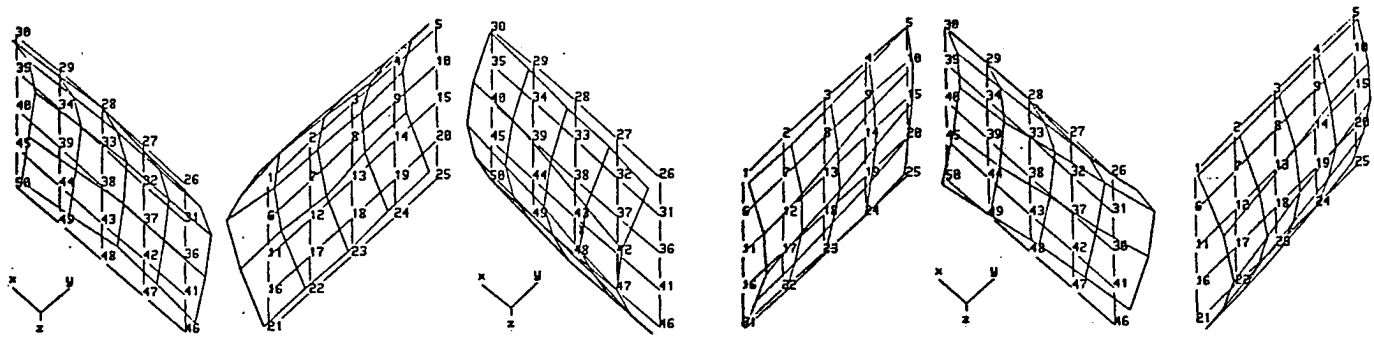
Test Results

Two main types of data were generated in the present tests. Namely, modal data: mode shapes and damping ratios at various frequencies and vibration (acceleration) levels of various modes at different material conditions.

Vane Mode Shapes and Damping Ratios (Baseline)

The vibration mode shapes of the vanes were generated from a 25-point grid acceleration measurements on each vane. These mode shapes are plotted on separate plots (Fig. 3). As the summed FRF indicates (Fig. 4), there are about 10 modes between 3000 and 6000 Hz. Moreover, there are only a couple of modes below 3000 Hz. The dominant modes are above 4200 Hz and are torsional modes, especially the dominant modes at 4740 Hz (the probable 4-kHz mode under LOX loading--see Ref. 1) is the strongest. The less dominant modes below 4200 are bending modes (Fig. 3).

The damping ratios of these modes were quite low (Table 1). They ranged from 0.076% for a strong symmetrical torsional mode at 4748 Hz to 0.20% for a mode at 5239 Hz.

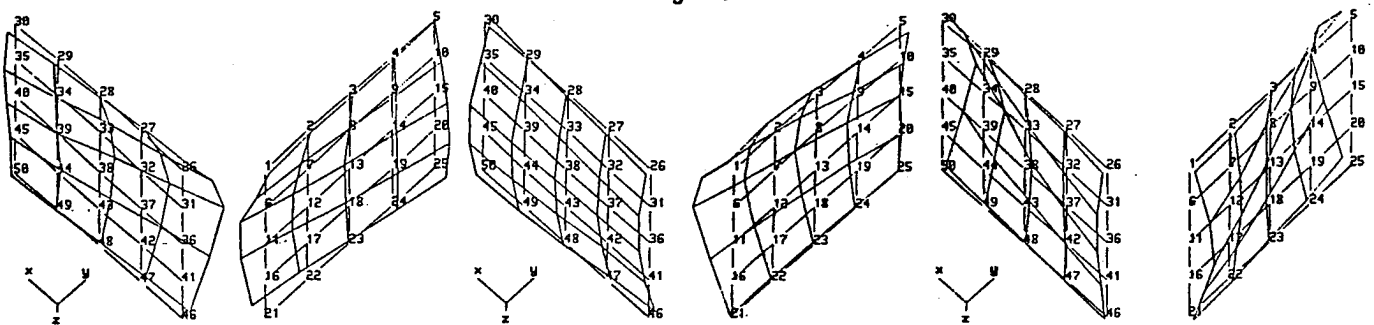


SYMM. BENDING, F = 3533 Hz

SYMM. BENDING, F = 3810 Hz

OPPOSITE BENDING, F = 4065 Hz

Fig. 3

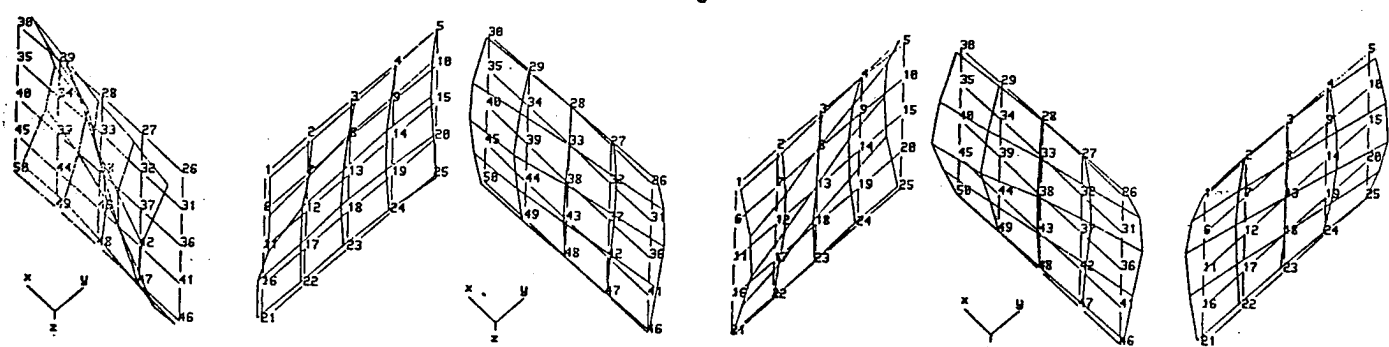


SYMM. BENDING, F = 4265 Hz

RIGHT TWISTING, F = 4320 Hz

SYMM. TWISTING, F = 4736 Hz

Fig. 3

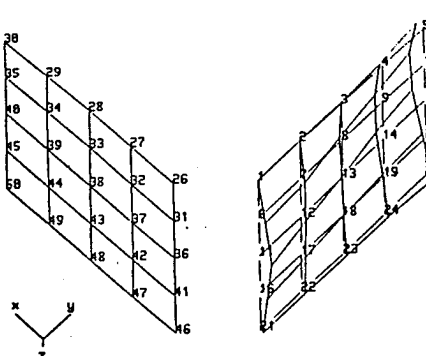


LEFT TWISTING, F = 4763 Hz

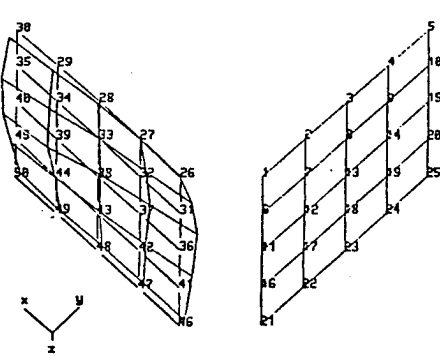
OPPOSITE TWISTING, F = 5011 Hz

SYMM. TWISTING, F = 5224 Hz

Fig. 3



RIGHT TWISTING, F = 5595 Hz



LEFT TWISTING, F = 5605 Hz

Fig. 3. Vane Mode Shapes

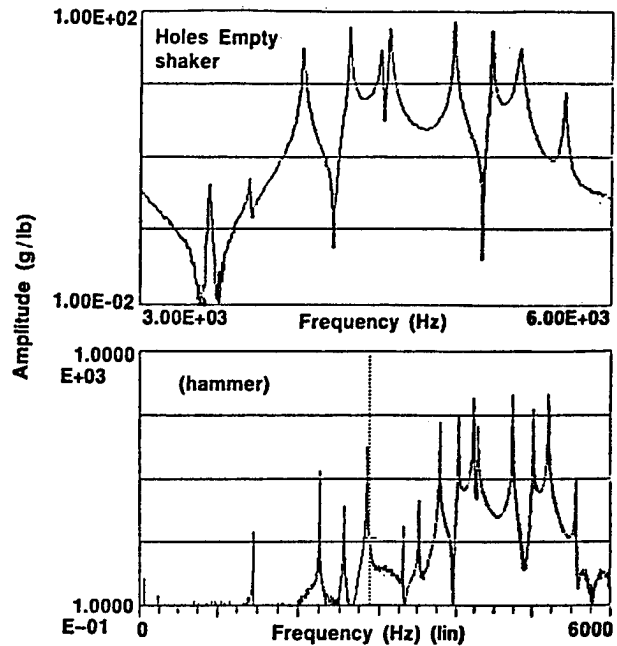


Fig. 4. Vane FRF

Vibration (Acceleration) Amplitudes Under Different Materials

Eight of the 10 modes above 3000 Hz were isolated and the acceleration amplitudes and damping ratios for each material fill (at 3/4-full level) were recorded (Table 1). The results of damping performance with such a little amount of mass added (the mass of steel taken out was about 1 gram and the amount of the heaviest material (tungsten) added was also 1 gram) is really surprising. The amplitude reduction with tungsten seemed to be the greatest in general. Thus, for the torsional mode at 5021 Hz, the damping ratio was 0.0006 and the amplitude was 52.8 g/lb when empty, and it changed to 0.0035 and 9.5 g/lb (Fig. 5), respectively, a factor of greater than 5. See Table 1 for details. A sample of three modes is presented in Fig. 5 through 7.

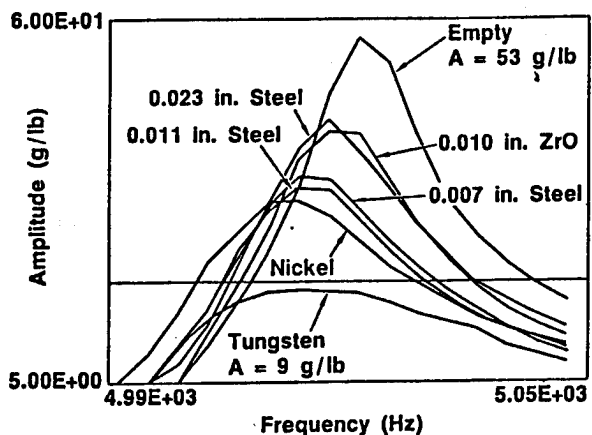


Fig. 5. Accelerance Amplitudes of a Torsional Mode at 5021 Hz Under Various Materials

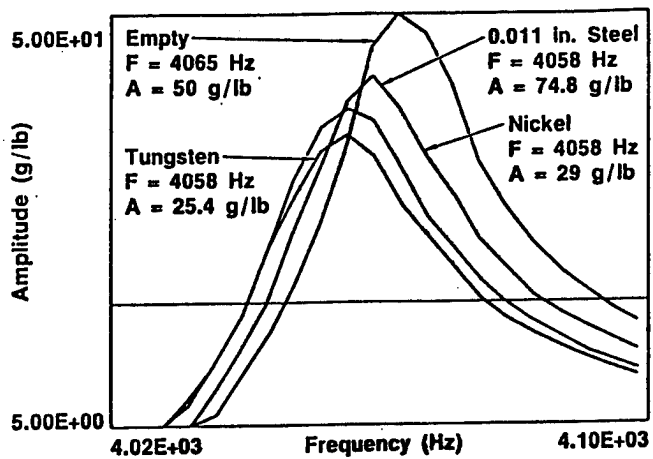


Fig. 6. Accelerance Plots to Show Damping Effects of Various Materials for a Bending Mode of the LOX Splitter Vanes

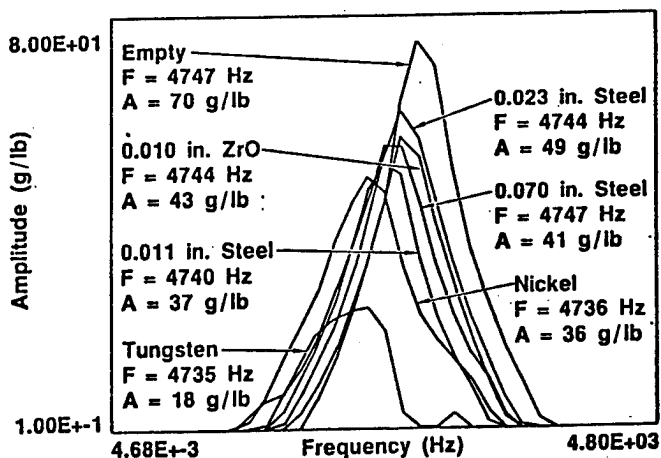


Fig. 7. Accelerance Plots to Show Damping with Various Materials for a Torsional Mode of the LOX Inlet Splitter Vane

**Table 1. Amplitudes and Damping Ratios of LOX Inlet Tee
Splitter Vanes Under Various Material Damping**

MODE		HOLES FILLED WITH DIFFERENT MATERIALS - 3/4 FULL						
FREQ., AMPLI., DAMPING REDUCTION FACTOR		EMPTY	STEEL 23	ZIRCON OX.	STEEL 7	STEEL 11	NICKEL PDR.	TUNGSTEN PDR.
Frequency-Hz	B	3807	3805	3805	3807	3805	3807	3804
Amplitude g/lb		30.2	30.5	26.3	24.5	27.0	29.3	27.5
Damping Ratio		0.0009	0.0009	0.0009	0.001	0.0009	0.001	0.0011
Vibration Reduction Factor		-	1	1	1.2	1	1.2	1.25
								1
Frequency-Hz	B	4064	4063	4061	4061	4060	4057	4056
Amplitude g/lb		57.5	43.4	39.8	37.3	34.9	29.0	25.2
Damping Ratio		0.0009	0.0011	0.0012	0.0013	0.0014	0.0017	0.0016
Reduction Factor		-	1.2	1.3	1.4	1.6	1.9	1.8
								2
Frequency-Hz	T	4257	4258	4256	4259	4257	4257	4258
Amplitude g/lb		27.6	32.6	27.1	30	30.5	20.4	25.5
Damping Ratio		0.0015	0.0011	0.0015	0.0012	0.0012	0.0013	0.0013
Reduction Factor		-	-1.2	1	-1.1	-1.1	1.4	1.1
								3
Frequency-Hz	T	4309	4308	4308	4308	4306	4306	4306
Amplitude g/lb		55.5	48.5	40.5	52.8	38.4	46.4	41.5
Damping Ratio		0.0012	0.0013	0.0013	0.0013	0.0014	0.0016	0.0015
Reduction Factor		-	1.14	1.4	1.06	1.45	1.2	1.34
								4
Frequency-Hz	T	4748	4744	4743	4741	4740	4737	4734
Amplitude g/lb		70.1	49.0	42.7	41.1	37.0	35.0	18.2
Damping Ratio		0.0008	0.001	0.0009	0.001	0.0013	0.0017	0.0028
Reduction Factor		-	1.4	1.64	1.7	1.9	2	3.9
								5
Frequency-Hz	T	5021	5017	5018	5015	5014	5010	5010
Amplitude g/lb		52.8	30.1	27.6	20.4	18.9	17.1	9.4
Damping Ratio		0.0006	0.0009	0.001	0.0012	0.0015	0.0017	0.0035
Reduction Factor		-	1.76	1.9	2.6	2.8	3.1	5.6
								6
Frequency-Hz	T	5239	5233	5234	5235	5232	5232	5234
Amplitude g/lb		29.5	26.4	26.3	20.5	22.6	32.7	30.9
Damping Ratio		0.002	0.0028	0.0025	0.0034	0.0025	0.0016	0.0017
Reduction Factor		-	1.12	1.12	1.44	1.31	-1.11	-1.05
								6
Frequency-Hz	T	5606	5604	5603	5605	5603	5593	5593
Amplitude g/lb		7.9	7.0	7.0	6.0	7.0	6.9	6.4
Damping Ratio		0.001	0.0011	0.0011	0.0012	0.0011	0.001	0.001
Reduction Factor		-	1.13	1.13	1.32	1.13	1.15	1.2
								8

NOTE: B = Bending mode T = Torsional mode Reduction Factor = Amplitude empty ÷ Amplitude filled

Conclusions and Recommendations

The modal and vibration tests reported herein add significantly to the knowledge base on damping characteristics of structures. The methodology presented, commonly called impact damping technology in the industry, has been used extensively in many applications. But the approach taken in these experiments--with tiny amounts of various materials added to such a small volume and producing such a tremendous effect--is novel. The potential application of such an approach to rocket engine components (like turbine blades) to laser systems, etc., is promising. Further experimentation is necessary to fully understand the mechanisms involved, the optimal fill levels necessary, and the best dimensions of holes for specific applications.

References

1. O'Connor, G. M. and J. Jones, "Flow-Induced Vibrations of the SSME LOX Inlet Tee Vanes," presented at the AIAA 24th Joint Propulsion Conference, Boston, MA, July 1988.
2. Semercigil, S. E., Popplewell, N., and Tyc, R., "Impact Damping of Random Vibrations," Journal of Sound and Vibration, Vol. 121, pp. 178-184, 1988.
3. Newland, D. E., An Introduction to Random Vibrations and Spectral Analysis, (2nd ed.) Longman, New York, 1984.
4. Aoki, S. and K. Suzuki, "Reduction of First Excursion Probability of Mechanical Systems under Earthquake Excitation by Inelastic Restoring Force-Deformation Relation," Bulletin of the Japanese Society of Mechanical Engineers, Vol. 28, No. 240, pp. 1226-1232, 1985.

DAMPING TREATMENT FOR JITTER REDUCTION ON A HIGH POWER OPTICAL BENCH

Paul H. Chen
TRW Space and Technology Group
Redondo Beach, California

Eric M. Austin
CSA Engineering, Inc.
Palo Alto, California

ABSTRACT

As part of a High Energy Laser program, a large optical laser system is required to meet a stringent RMS specification for residual jitter. Using MSC/NASTRAN, the optical jitter due to ground and coolant-flow excitations was predicted as a combination of the dynamic motions of several optics. The modal strain energy method was used both in identifying the best candidate locations for damping treatments as well as predicting damping levels. The final solution incorporated constrained layer damping treatments on an interface component between the mirrors and their mounts and link dampers between selected locations on the optical bench.

1. Introduction and Objectives

A proposed high power laser system modification requires an optical bench and associated optics and their mounts. Some of these optics require coolant flows to maintain proper mirror figure. The coolant flowing through the high power mirrors generates substantial optical jitter. This jitter degrades the quality of the propagated laser beam. One of the primary priorities of the optical bench design was to minimize optical jitter.

Jitter reduction techniques applied to this high power optical bench (HPOB) can be summarized in three categories: 1) reduce the disturbance energy input from the coolant flow and the surrounding excitation environment, 2) improve the structural design to enhance its rigidity, and 3) provide a good passive damping treatment design to minimize mirror vibration response. This paper presents the technique, approach, and results of the passive damping treatment on the HPOB.

Six optics are in the primary beam path of the HPOB. Three of these are cooled mirrors. All mirrors are kinematically mounted on three-tab tangent flanges. The tangent flange, in turn, is mounted on a relatively rigid and heavy ball-mount. All mounting connections are jointed by spherical washers and bolts. The ball-mounts are bolted on their respective supporting plates, which are 3/4-inch-thick steel plates, welded to the bench members. The HPOB is designed as a three-dimensional space frame structure. Its overall dimensions are 44 inches wide, 180 inches long, and 81 inches high. The main frame members are 6x6x1/2 inch rectangular steel tubes. The bench's diagonal bracings are W6x25 steel I-beams.

2. Damping Design Analysis

This project was split into several phases of work: Phase I was a study of the feasibility of reducing residual beam jitter by adding passive damping to the HPOB, and Phases II and III were concerned with the design of the passive damping treatments. The residual jitter is calculated as a function of the angular displacements (rotations) of the mirrors on the bench. NASTRAN was used to predict these rotations and evaluate the optical (ray-tracing) equations under random excitations applied at both the base of the bench and at the cooled mirrors. The residual jitter is given as a displacement power spectral density function (PSD). The overall goal of the program was to reduce the residual jitter to a normalized RMS jitter of 1.0 unit. The sources of disturbances for the optical bench were excitations from equipment and seismic effects and the coolant flowing through the cooled mirrors.

2.1 Phase I Analysis

The Phase I analysis was performed using a crude finite element model. The optical bench is modeled with BAR elements, typically one element per span of the structure. The model is crude because the optics are represented only by lumped masses and stiff bars. There are six optical components represented in the model. Figure 1 shows the Phase I finite element model and the locations of these optical components.

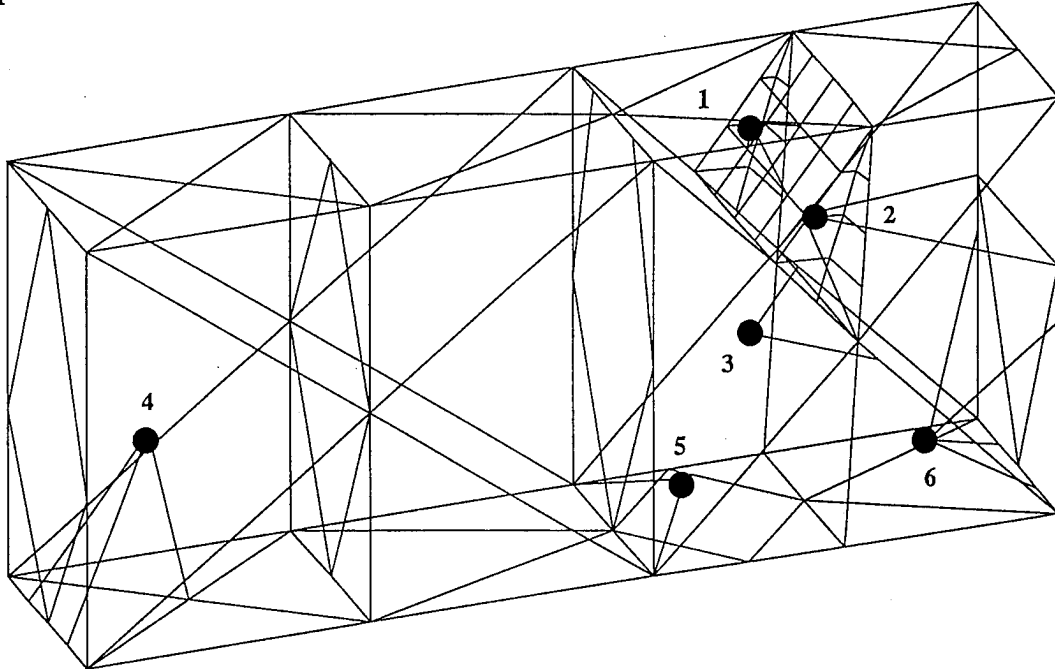


Figure 1. Baseline Phase I finite element model

A random response analysis was performed using the Phase I finite element model with the given excitations and the residual jitter predicted. Approximately 91% of the total residual jitter was due to only four modes between 87 and 245 Hz. The suppression of these modes was the criteria for the effectiveness of the Phase I damping study.

Three different approaches to damping were considered: constrained layer damping, damped links, and tuned-mass dampers. All three have certain types of situations in which they work best.

Constrained layer treatments work by placing a viscoelastic material (VEM) layer between the structure and a constraining layer. As the structure is deformed, the constraining layer opposes the motion and causes shear in the VEM. Strain in the VEM is the mechanism for energy dissipation. The treatments are mode shape dependent and work best for frequencies that were targeted by the design, but their effectiveness may spill over to all modes in which the particular member

participates. Several diagonal I-beams were chosen to receive a constrained layer treatment. These I-beams were modeled in detail in order to predict the strain energy in the viscoelastic material accurately. A 0.050-inch-thick layer of Sound-coat's DYAD 606 was chosen as the VEM, with a 0.50-inch-thick steel constraining layer. The predicted RMS of the residual jitter was reduced by 56% using this treatment.

Damped links dissipate energy by connecting pairs of points on the structure that have high relative displacements with a viscoelastic spring. These dampers, like constrained layer treatments, are not explicitly frequency dependent. They will work to some degree for any mode that has relative displacements between the endpoints. Four damped links were incorporated into the Phase I model and shown to be effective in reducing the jitter.

Tuned-mass dampers (TMD's) are a way of damping a single mode only. They work by attaching a damped spring-mass device to the structure at a location of high displacement. TMD's are inherently frequency dependent. They need to be tuned, usually by varying the mass, to a specific frequency just below the target frequency. The potential for damping is very high, but the tuning must be precise. By combining damping links and TMD's, a 64% reduction of residual jitter was predicted.

It was shown during the Phase I analysis that, using either the constrained layer treatments or a combination of link dampers and TMD's, the predicted RMS residual jitter could be reduced by over 50%. The Phase I analysis showed that by successfully identifying the modes causing jitter, passive damping treatments on a relatively small portion of the structure could be used to reduce the residual jitter on a relatively heavy and stiff steel bench.

The Phase I model was used to ascertain if passive damping was a viable method of reducing the jitter. However, the detail of this model was insufficient to actually design the passive damping treatments. Also, the relatively flexible optical components were not modeled. With the incorporation of these optical components, it was known that the problem modes could be altered and the overall jitter could be expected to increase substantially.

2.2 Phase II Analysis

The finite element model used for the Phase II analysis (see Figure 2) contained more detailed models of some of the optical components and their support structures, but was otherwise similar in resolution to the Phase I model. The actual mirrors were still modeled as concentrated masses attached to the outer housing through a tangent flange. The finite element model of the Phase II mirror tangent flange is shown in Figure 3.

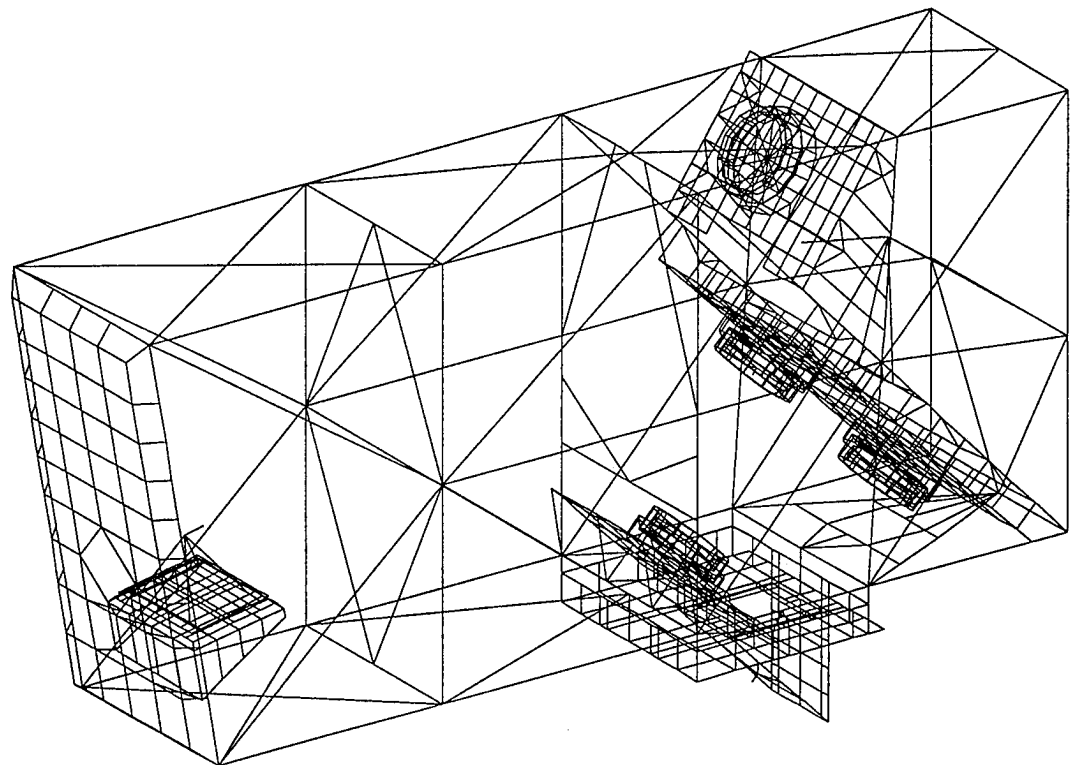


Figure 2. Baseline Phase II finite element model

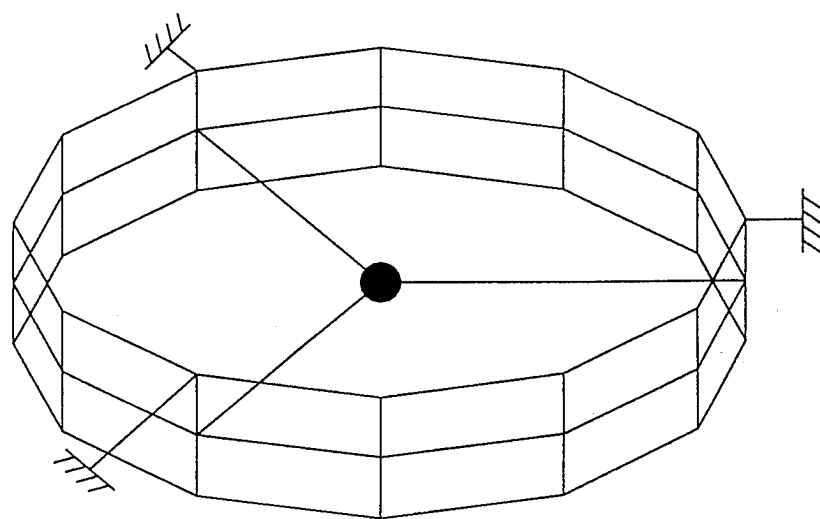


Figure 3. Phase II finite element model of mirror tangent flange

The Phase II baseline analysis showed that the highest jitter-contributing modes were now in the optical components rather than the bench. Based on the modal strain energy (MSE) distribution shown in Table 1, the best areas for damping treatments are, in order, the tangent flanges, the mirror support structures, and the frame elements. Damping on the tangent flanges was judged to be the most effective.

	% of Total Jitter from this Mode	Percent of modal strain energy		
		Tangent Flanges	Mirror Support	Frame Members
Mode 11	59%	74%	17%	4%
Mode 13	7%	89%	5%	1.6%
Mode 22	15%	8%	59%	24%
Mode 33	7%	6%	72%	13%

Table 1. Critical modes predicted by the Phase II model with their contributions to the total residual jitter

The frame members themselves do not contribute much of the MSE to any of the troublesome jitter modes. However, the motion of the frame cannot be neglected if the final jitter goal is to be met. The Phase I analysis produced two possible approaches to damp frame modes: constrained layer damping and link dampers. Considering all factors, the link dampers were selected for the frame damping treatment.

The modal strain energy distribution in the modes of interest showed strain energies in many of the bench members. From a large number of candidate pairs of end points, eight locations were chosen. The endpoints were chosen based on the highest relative displacements along the lines between them.

The link dampers were designed so that they could be fabricated from commercially available materials. The damped link is essentially a pipe that spans between two points on the structure and contains a viscoelastic joint inserted along its length. Figure 4 shows a schematic drawing of the link along with the end fittings.

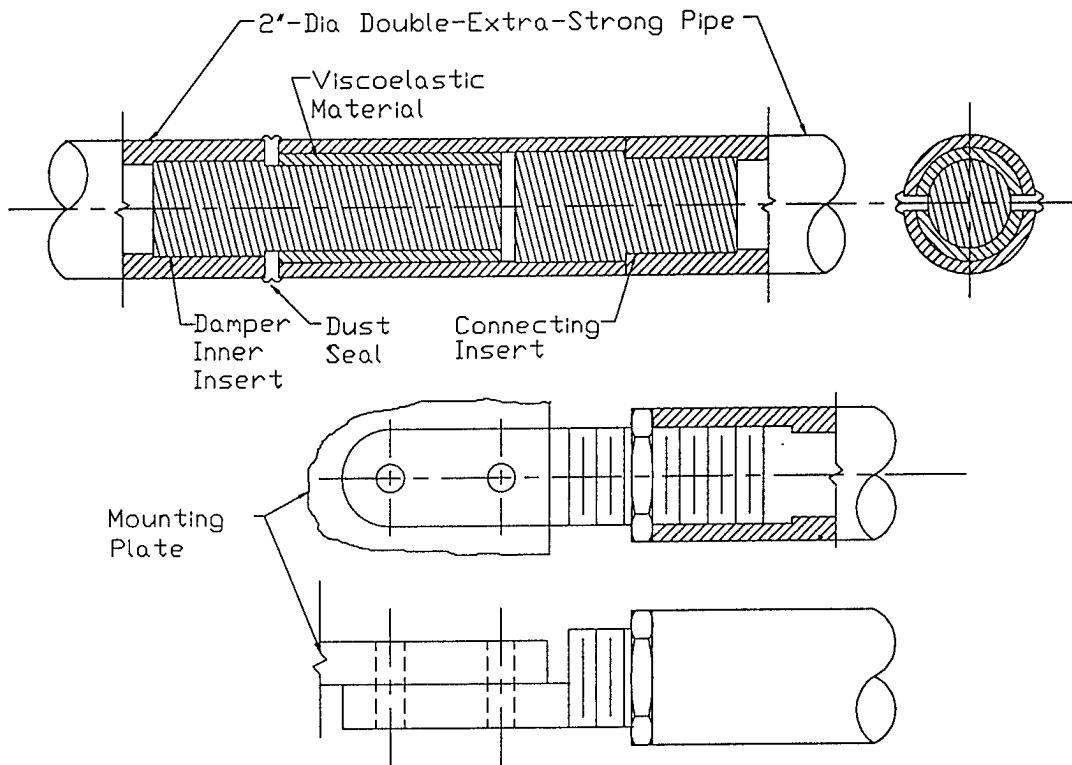


Figure 4. Schematic drawing of the damped link and its end fittings

2.3 Phase III Analysis

The finite element model of the tangent flange used in Phases I and II was coarse and neglected some structural details that turned out to be important, most notably the rim used for attachment to the ball-mount and the three "tabs" used to attach the mirror to the tangent flange. The goal of Phase III was to verify the damping design and analysis of this most critical jitter component. A detailed finite element model of the mirror and tangent flange was created and the frequencies and mode shapes were verified using results from a modal test. The model was then used in designing an optimal damping treatment under the known restrictions. Figure 5 depicts the updated tangent flange finite element model.

The verified and tuned finite element models of the mirror assemblies were then integrated into the Phase III system model together with several other structural updates, such as increasing the thickness of the ball-mount supporting plates and adjusting the supporting brackets. Figure 6 presents the Phase III system finite element model of the High Power Optical Bench.

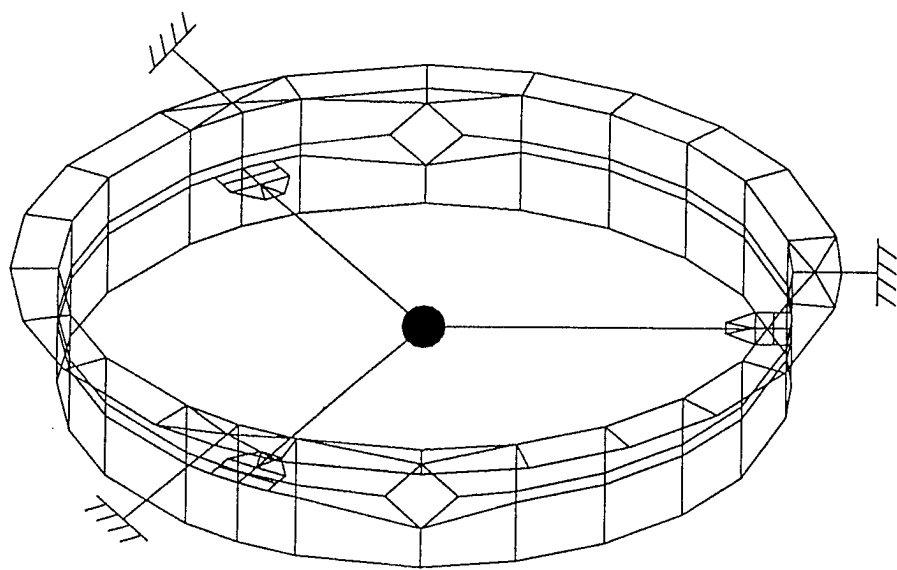


Figure 5. Phase III finite element model of mirror tangent flange

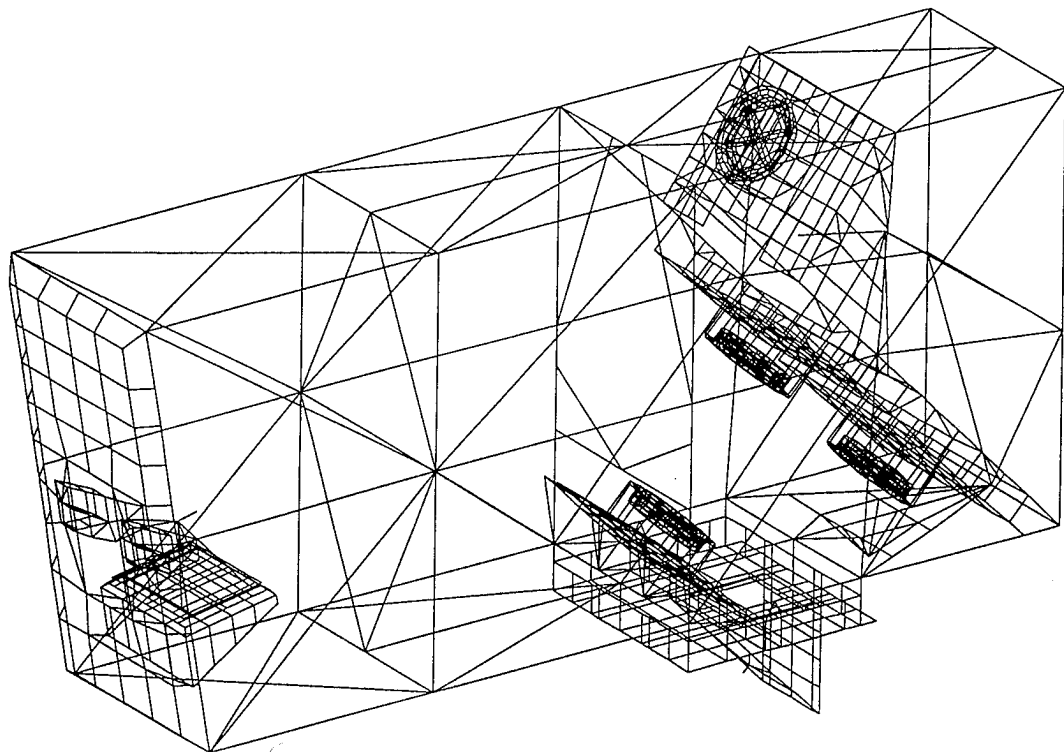


Figure 6. Baseline Phase III finite element model

2.3.1 Residual Jitter of the Baseline System

Dynamic analysis of the complete Phase III model was executed, the system modal strain energy distributions were recalculated, and residual jitter for the undamped baseline structure was determined. An inherent damping level of 0.4% structural ($Q=250$) was assumed for the "undamped" analysis and was also added to the predicted damping for the damped analysis. Table 2 gives the approximate percentage contributions of the major jitter modes. Additionally, the percentage of the modal strain energy for each mode is given for the tangent flanges as a group, the support plates as a group, and the space frame. The last row of the table gives a weighted average of the contributions of the three groups. This average is the sum of the percentage of the MSE for each group multiplied by the percentage RMS contributions for each mode. It is only a rough indicator of the relative contribution of each group to the overall residual jitter.

This table shows that four modes contribute over seventy percent of the RMS jitter. The tangent flange components are still the top area requiring vibration suppression. The supporting structures rank second, and the space frame contributes less than 20 % to the RMS jitter.

Modes 16, 17, and 19 contribute over sixty percent of the total RMS jitter. These fall in the frequency range of the primary modes of the tangent flanges. However, in contrast to the Phase II analyses, only between one-half and two-thirds of the modal strain energy of these modes is attributable to the tangent flanges: the rest is divided between the support plates and the frame elements. The conclusion from these results is that the tangent flanges as a group still contribute more to the residual jitter than any other areas of the structure, but not by as much as previously predicted. This does not eliminate the need to damp the tangent flanges, but it does de-emphasize it slightly. It is likely that any additional significant increases in damping will have to come from damping treatments for the mirror support structures and the space frame.

The support plates contribute the next largest amount to the residual jitter. The percentages listed in the Table give the total modal strain energy in all of the parts of the support plates, i.e., base plate, grout plate, grout, stiffeners, etc.

The modal strain energy in the frame is the sum of the main frame members. It gives a rough idea of the potential for damping through link dampers and constrained layer treatments on frame members. The latter concept was investigated during Phase I, but found to be too inefficient to justify the cost in design and application.

	% of total jitter from this Mode	Percent of modal strain energy		
		Tangent Flanges	Mirror Supports	Frame Members
Mode 16 134 Hz	47.4%	42.1%	27.6%	19.5%
Mode 17 137 Hz	4.3%	36.6%	7.3%	40.9%
Mode 19 142 Hz	10.5%	49.6%	16.3%	16.8%
Mode 22 148 Hz	2.5%	43.3%	7.9%	39.3%
Mode 36 199 Hz	5.1%	25.7%	43.9%	16.7%
Mode 39 224 Hz	7.6%	23.3%	58.7%	9.7 %
Mode 47 280 Hz	3.0%	35.5%	30.8%	22.3 %
Weighted Contribution		33.5%	26.8%	17.2%

Table 2. Major modes for residual jitter in the undamped Phase III baseline model along with their contribution and composition

2.4 Residual Jitter of the Damped System

During Phase II, link dampers were found to be an effective way of introducing damping into frame-dominated modes. As a result of damping design analysis performed during Phase III, three additional links were proposed for the frame. The locations of the damped links are shown in Figure 7.

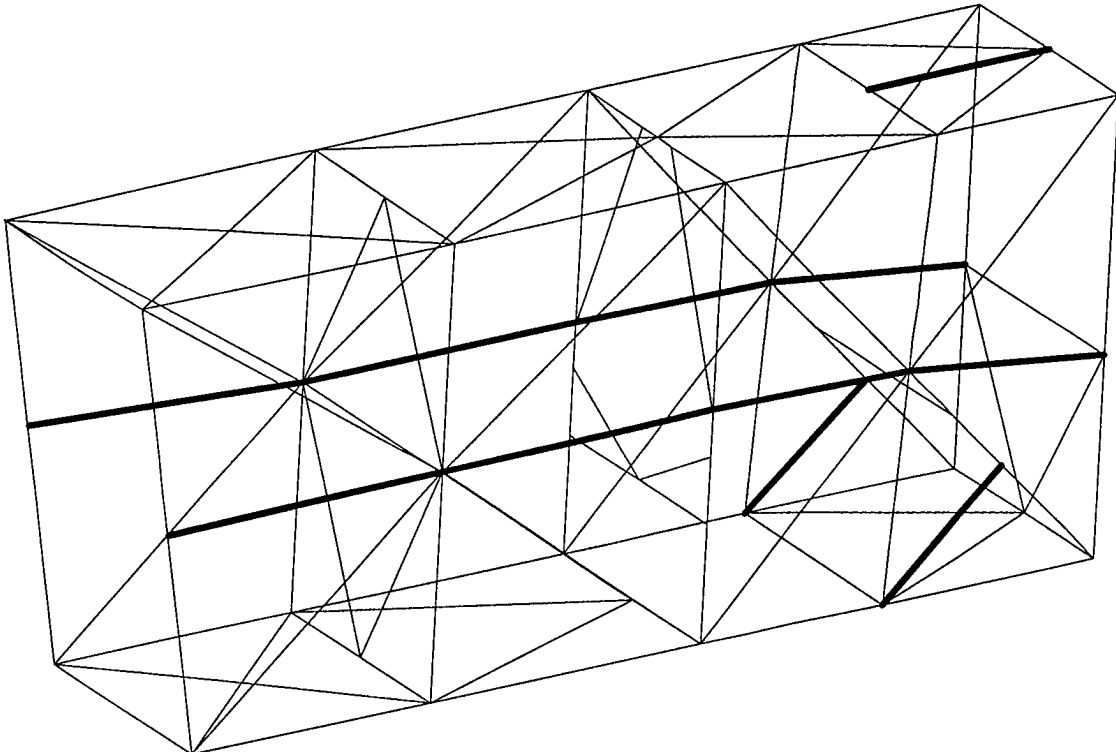


Figure 7. Proposed locations of link dampers for the HPOB

Due to design constraints, the Phase II damping concept for the tangent flanges was determined to be the best type of treatment. The optimal treatment uses a constraining layer separated into two pieces. The treatment consists of a two-piece, 40-mil-thick stainless steel constraining layer with 5 mils of ISD 110 VEM.

Before the residual jitter of the damped system was calculated, the stiffness due to the link and tangent flange damping treatments was added to the model. The models of the tangent flanges were tuned so that their frequencies matched closely those of the damped tangent flange model. The damped links were included using ROD elements.

The damping was predicted by the modal strain energy (MSE) method using the strain energies predicted by the model of the damped system. The MSE method states that the damping is the product of the VEM's modal strain energy and loss factor. However, the sheer size of the system model and detail needed to model

the VEM meant that the amount of VEM strain energy had to be inferred from the isolated detailed model of the damped tangent flange. The damped links were included in the model as rod elements whose properties give it an axial stiffness equivalent to that of the actual damping link. The modal strain energy of each group (tangent flanges and links) was multiplied by the loss factor of the VEM and again by a *participation* factor. This participation factor is an estimate of the percentage of the strain energy that the VEM would see if it were in the model. For example, the participation factor for the damped links is 0.9 since calculations show that 90% of the links' strain energy will go into the VEM. However, only about 5% of the system strain energy in the tangent flanges can be considered to be VEM strain energy.

After all of the updates to the system finite element model, a random response analysis was performed. Figure 8 shows the damped residual jitter and RMS plotted over the undamped baseline. Most of the modes have shifted upwards in frequency due to the stiffness added to the system by the damping treatments.

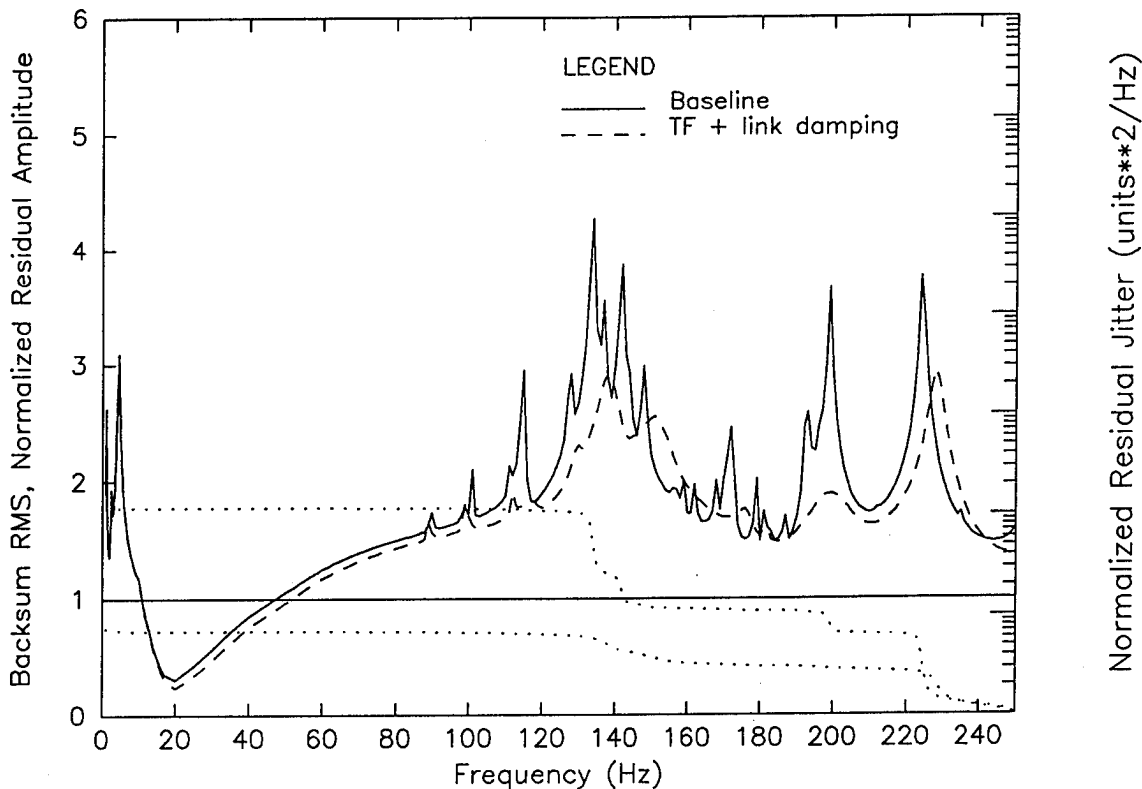


Figure 8. Residual jitter for the HPOB with link and tangent flange damping treatments

There are only three distinct jumps in the RMS curve. The modes causing these jumps and their approximate composition are listed in Table 3. The tangent flanges are still the largest contributors to the jitter, but either the frame or mirror support plates also participate strongly in each of the modes. Constraints on the tangent flange damping treatments make the prospects for greatly improved damping of the tangent flanges poor. The likely place to concentrate efforts for additional damping would be either the frame elements or the mirror support structures.

	% of total RMS from this Mode	Percent of modal strain energy		
		Tangent Flanges	Mirror Supports	Frame Members
Mode 16 138 Hz	27.5%	37.9%	27.0%	24.1%
Mode 21 151 Hz	6.1%	39.5%	8.9%	41.8%
Mode 39 228 Hz	13.2 %	24.8%	58.0%	9.2 %

Table 3. Major modes for residual jitter in the damped system along with their contribution and composition

3. Summary

The final RMS value for the residual jitter of the damped system is 0.73 units, which meets the residual jitter goal of 1.0 units. Table 4 presents in summary form the reduction of jitter predicted during each of the three Phases. The passive damping treatments on the HPOB reduced the residual jitter by 60 percent. The most effective concept for the optics' damping is a constrained layer treatment on the mirror mount tangent flange. The promising damping concept for the heavy steel optical bench is link dampers at selected bench locations.

Phase		Damping Treatment	% Jitter Reduction
I	IA	0.05" DYAD 606 VEM, 0.5" Steel Plate on 8 Diagonal Members	56
	IB	4 Link Dampers + 2 Tuned-Mass Dampers	64
II	II	5 Mils 3M ISD 110 VEM with 40-Mil Stainless Steel Plates on Tangent Flanges, 8 Link Dampers on the Bench	67
III	III	Same as Phase II, 13 Link Dampers Used	59

Table 4. Summary of residual jitter reduction

ANALYSIS AND TESTING OF A DAMPING TREATMENT FOR A MULTI-COMPONENT SPACE STRUCTURE

Eric M. Austin and Conor D. Johnson
CSA Engineering, Inc.
Palo Alto, California

Laurence S. Gittleson
Lockheed Missiles and Space Company, Inc.
Sunnyvale, California

ABSTRACT

A large space structure required at least 1% viscous damping for each of its four lowest global modes to reduce vibration response. Due to the complexity of the problem, two of the three components in the system were represented only by stiffness and mass matrices at a reduced set of points. The third component was represented by a finite element model. Damping designs were produced and their performance predicted by computing system-level modal strain energy using both the finite element model and the condensed stiffness matrices. The chosen design produced the required damping with less than 0.2% added weight.

1. Problem Description

This paper summarizes joint work between Lockheed Missiles and Space Company, Inc. (LMSC), and CSA Engineering to design, implement, and test a space-qualified add-on damping treatment for a multi-component space structure. The damping treatment was designed for a cylindrical, barrel-like portion of a structure that is connected to two other larger, more complex structural components. Due to modeling and other interface considerations, only a finite element model (MSC/NASTRAN) of the main section was available for analysis. The remaining subcomponents of the structure were provided in the form of mass and stiffness matrices represented at a reduced set of points in the condensed structures.

The modes of interest for the structure were the first four; the first two being the most critical. These modes occurred in two pairs: the first pair at approximately 16 Hz and the second at 23 Hz. The goal was to increase the system-level viscous damping in both pairs of modes to at least one percent. There was a severe restriction on added weight for the structure, and the main section had many areas which were inaccessible due to proximity of surrounding structure.

2. Analysis Techniques

The system analyses were performed by integrating the main structure and two substructures into a full system model. The three components of the system model are shown schematically in Figure 1. The process of integrating the condensed matrices with those of the finite element model was as follows. All of the operations were done within MSC/NASTRAN using Direct Matrix Abstract Programing (DMAP). Substructure 1 was condensed down to 44 points scattered throughout the structure. There were a total of 129 nonconstrained degrees of freedom (DOF's) among these points, and there were six attachment points between the main finite element model and the first substructure. Given the relationship between the DOF's in the matrices and the attachment points to the finite element model, the inclusion process started by defining GRID points for each of the 38 internal points in the condensed structure. The remaining six points correspond to the attachment points, and were already included as GRID points in the finite element model. A partition vector was then created for the substructure based on sets defined in the MSC/NASTRAN input whose members were the connection and "dummy" GRID points. The partition vector was used to insert the outside mass and stiffness values into the global mass and stiffness matrices. Finally, a MERGE command was done to integrate these matrices in to the system matrices. A similar procedure was followed for the Substructure 2.

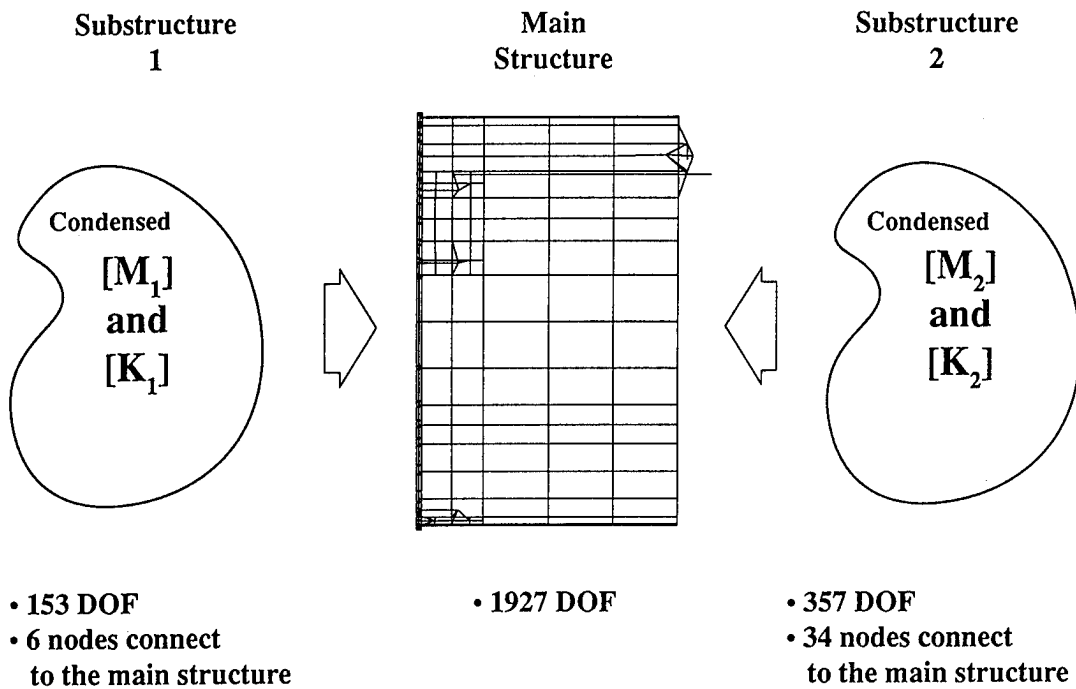


Figure 1. Schematic view of system finite element model

To make predictions of the system-level damping, it was necessary to have knowledge of the system-level strain energy for the modes of interest. NASTRAN will calculate the strain energy for any or all of the model's structural elements. However, the substructures' matrices contain no structural elements *per se*. A method of correctly extracting the strain energy from the missing parts of the structure was therefore required. The strain energy was obtained by performing the following triple-product of the stiffness matrix and partitioned eigenvector for the two condensed portions of the system model.

$$(Strain Energy)_i = \frac{1}{2} \{\phi_i\}^T [K] \{\phi_i\} \quad (1)$$

where

$\{\phi_i\}$ = component eigenvector of mode "i" partitioned out of the system eigenvector

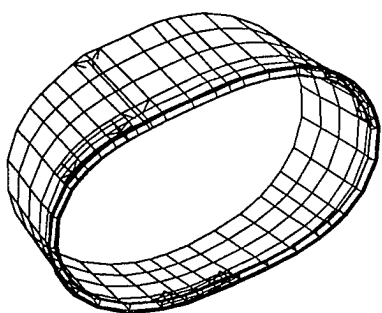
$[K]$ = component stiffness matrix

Mode	Substructure		
	1	2	Main
1	2.2%	25.1%	72.7%
2	2.4%	26.2%	71.4%
3	21.1%	59.0%	20.0%
4	22.8%	58.0%	19.2%

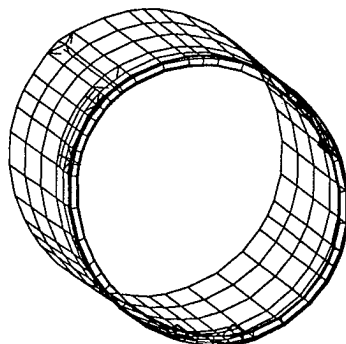
Table 1. Distribution of modal strain energy in the system for the first four modes

The modal strain energy (MSE) was printed out for each of the substructures in the form of vectors with lengths equal to the number of eigenvectors extracted in the analysis. The system-level MSE was found by simply adding the absolute strain energies of the three components. From this, the percentage of MSE in any particular set of elements could be found. This technique was checked for accuracy on a test model.

Table 1 gives the percentage of strain energy predicted for the three components of the undamped system model. The task of obtaining 1% viscous damping (2% structural) in Modes 3 and 4 is formidable since the structure on which a damping treatment can be applied only has 20% of the system-level modal strain energy for these modes. The predicted mode shapes of the modes of interest are shown in Figure 2. Since the mode shapes are predominantly global, the modal strain energy is predictably well distributed.



First mode pair
~ 16 Hz



Second mode pair
~ 23 Hz

Figure 2. Lowest two mode pairs predicted by the baseline finite element model

3. Candidate Damping Designs

Past experience with similar cylindrical structures has shown that high damping levels, on the order of 10% viscous, could be achieved if the main structure were integrally damped, i.e., the panel sections were made of sandwiched viscoelastic material construction. However, since the structure already existed, this strategy could not be implemented. An add-on treatment of this type was also out of the question due to the large amount of added weight that would have resulted.

The weight-efficient alternative to a full-coverage constrained-layer treatment is to apply damping treatments selectively to structural members containing high MSE in the modes of interest. Analysis showed that the stiffening rings were good candidates. Of these rings, Ring 1 was chosen for detailed study; it had the best combination of accessibility and modal strain energy. Figure 3 shows the undeformed finite element model of the main structure. Ring 1 has been refined to allow for modeling of candidate damping treatments. Even though this ring was accessible, there were some tight space limitations on the inner and outer surfaces. Figure 4 shows the cross section of the ring and the envelope for the damping treatment.

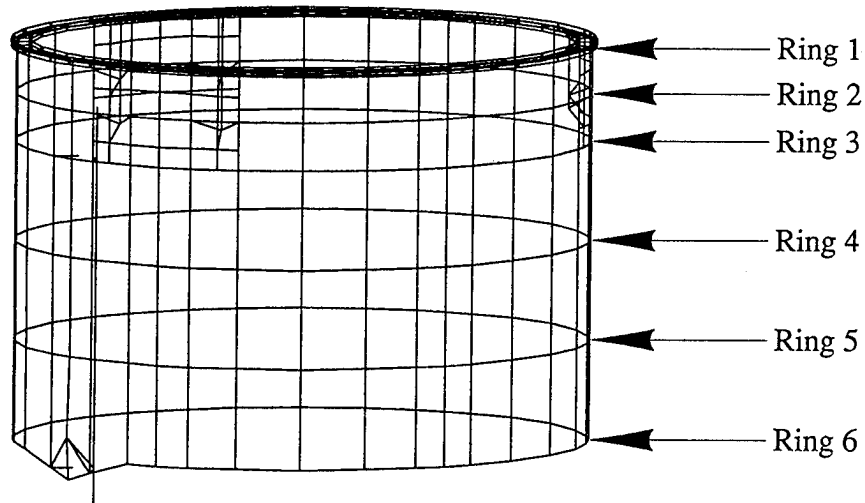
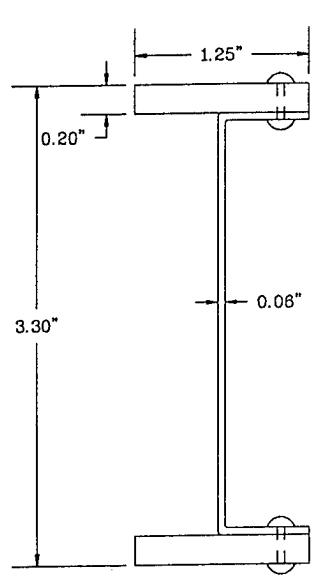


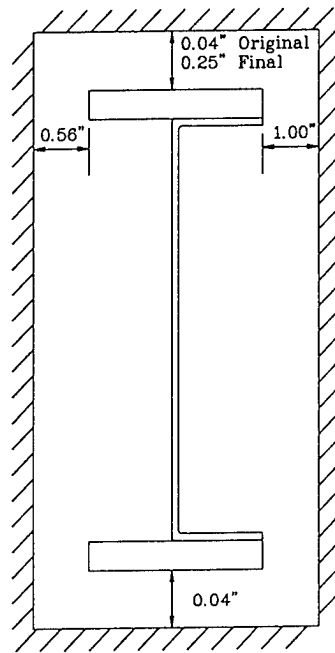
Figure 3. Undeformed finite element model of the main structure

Throughout the iterative design processes, the designs were also driven by factors other than maximum damping. Ease of application was one, since disassembly of the actual article was not possible. Another factor, as shown in Figure 4, was that the outer flanges of Ring 1 were riveted to an inner C-section every few inches. The height of the rivet heads was roughly 0.050 inches.



Nominal Dimensions

R
↑



Envelope Allowed for
Damping Treatment

Figure 4. Cross section of Ring 1 with the original space restrictions

Three types of add-on passive damping treatments were investigated: tuned-mass dampers, damped links, and constrained-layer damping. Tuned-mass dampers were ruled out mainly because of the practical problems of tuning and maintaining the devices for a space application. Also, the nature of the mode shapes and the fact that there were two pairs of closely spaced modes meant that tuned-mass dampers were not a good candidate solution for this problem. Link dampers were not a viable solution since there are not any accessible locations of the structure having large relative motions. The remaining choice was some type of constrained-layer treatment.

Many types of constrained-layer treatments were evaluated. Since the target modes shapes were simple, all of the preliminary designs were evaluated on a model of one quarter of Ring 1 with symmetric boundary conditions. All of the early treatments sought to use the relatively large clearances, 0.56 and 1.0 inches, on the front and back sides of the ring, as shown in Figure 4. Some candidate solutions are shown in Figure 5. Within the original space restrictions, none of the candidate solutions was found to produce the required damping, but the treatments with the constrained-layer treatment on the outer rim of the ring were the most promising.

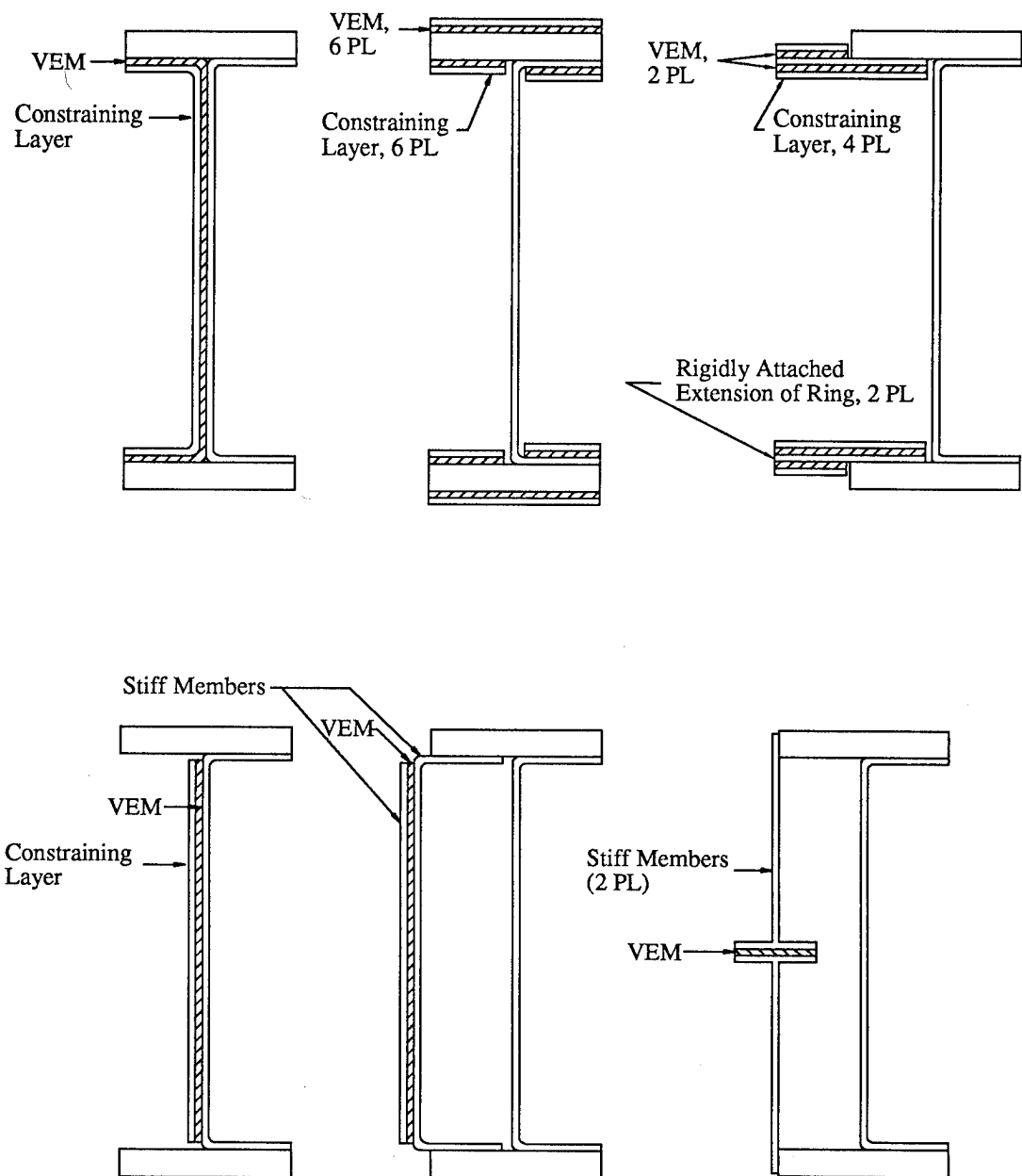


Figure 5. Candidate add-on damping treatments for Ring 1

At this point, these preliminary results were presented for review. The original clearance envelope was based on worst-case assumptions of adjoining structures moving out of phase with respect to each other. After reanalysis of these conservative restrictions, Lockheed decided to increase the allowable space on the outer surface of the ring from 0.040 to 0.25 inches. This allowed for a much stiffer constraining layer on the outer surface of the ring. The eventual recommended treatment consisted of 0.060 inches of 3M's ISD 110 and a stiff, 0.19-inch-thick graphite-epoxy constraining layer. Analysis showed that a three-piece constraining layer could be used.

ISD 110 was chosen because its shear modulus, 900 psi, was near optimum for this application and its loss factor, 1.4, was outstanding. A simple free-free beam was fabricated to verify the VEM properties at the frequency and temperature (room temperature) of the application.* Since ISD 110 is not self-adhesive at room temperature, 3M recommends either an epoxy or heat treating to adhere the VEM to the base structure. Beams using both methods were built. From a modal test of the beam, the shear modulus and loss factor were inferred using 6th-order theory.** The shear modulus was close to the expected value, but the loss factor was roughly 60% low.

Faced with lowering the system damping predictions by 60%, an alternate viscoelastic material had to be sought. The revised design called for 0.090 inches of 3M's Y4945 acrylic foam tape. This material had a shear modulus lower than the optimum, but its loss factor was an excellent 1.1. The free-free beam tests were repeated, and the material properties were confirmed. Additional qualification tests were performed by the manufacturers of the structure. These tests, tailored to this specific mission, included outgassing, life, humidity, and flammability. The VEM was judged satisfactory in all respects except outgassing. The exposed edges of the material were subsequently coated to prevent any possible harmful effects from outgassing.

The choice of Y4945 had two notable side benefits: 1) it is self-adhesive and 2) two 0.045-inch-thick layers would easily clear the rivet heads. During application, the first 0.045-inch layer was applied over the rivet heads, leaving a visible bump. A tool best described as a "cookie cutter" was then used to remove the VEM in the local area of the rivets. After the second layer of VEM was applied, no discernable bump existed over the rivet heads.

*This work pre-dates use of the direct complex modulus testing now in use at CSA.

**Rao, D.K., "Frequency and Loss Factors of Sandwich Beams Under Various Boundary Conditions," Journal of Mechanical Engineering Science, No. 20, Vol. 8, 1978.

4. Test Confirmation

A modal test was instituted to verify the effectiveness of the damping treatment. The treatment applied to the test article differed from the recommendation only in that the constraining layer was 0.25-inch-thick steel instead of 0.19-inch-thick graphite-epoxy. This variation was due to the tight test schedule. The system was tested in both damped and undamped configurations. Table 2 shows a comparison of the frequencies predicted with the undamped NASTRAN model versus the measured frequencies. Note that the damping values were obtained for this "undamped" configuration. These figures represent the inherent damping that exists in spacecraft structures assembled from many components. Damping of this type is not predictable and can only be determined through testing.

	Mode 1	Mode 2	Mode 3	Mode 4
Analysis (% viscous)	16.44 Hz (—)	16.57 Hz (—)	22.10 Hz (—)	23.47 Hz (—)
Test (% viscous)	15.55 Hz (0.32)	16.28 Hz (0.38)	23.31 Hz (0.85)	23.66 Hz (0.60)

Table 2. Predicted and measured frequencies of the untreated structure

The frequencies predicted using the NASTRAN model of the damped system are given in Table 3 along with the test results. The predicted frequencies agreed fairly well with the measured values, generally within 5%. The NASTRAN-predicted damping values shown in Table 3 have been obtained by adding the inherent damping given in Table 2 to the damping prediction from the finite element analysis. It is not clear if this approach is correct since it is not known how the inherent damping is effected by the add-on damping treatment; somewhere between none and all of the damping measured in the "undamped" structure should be added to the analytical predictions.

There are several possible reasons for the over prediction of the damping values, but most would be sources of only small inaccuracies. The most likely candidate is the quality of the system-level mode shapes and, consequently, the distribution of the system-level modal strain energy. Also, it was known that the finite element model was not entirely representative of the actual structure in its test configuration. One major difference was a mass hung on the test structure that participated heavily in the third and fourth modes. This could help explain why the correlation for these modes was not as good as for the first two.

	Mode 1	Mode 2	Mode 3	Mode 4
Analysis (% viscous)	16.64 Hz (2.0)	16.79 Hz (2.2)	22.14 Hz (1.1)	23.48 Hz (0.8)
Test (% viscous)	16.11 Hz (1.9)	17.04 Hz (2.2)	23.37 Hz (1.0)	23.53 Hz (1.0)
Analysis plus inherent damping	(2.3)	(2.6)	(1.9)	(1.4)

Table 3. Predicted and measured frequencies of the damped test structure

5. Conclusion

A lightweight damping treatment was designed successfully for a large, multi-component structure. The modal strain energy was applied to predict system-level damping, even though much of the structure was represented by condensed mass and stiffness matrices. Good agreement was achieved between results of a modal test and the analysis. Faced with obstacles like weight, size, and outgassing, a treatment was designed that met all of the goals at a weight increase of roughly 0.2%. The validation of this damping solution has allowed LMSC to consider integrally designed damping treatments in possible critical situations to minimize the number and magnitude of late-emerging problems.

Modal Survey of the PACOSS DTA

Russell N Gehling

Martin Marietta Space Systems
Denver, Colorado

Abstract

Many future space systems will be constructed of large, flexible structures and will possess high modal density at low frequencies. Some missions envisioned for these large space systems (LSS) require rapid retargeting and precision pointing which lead to control bandwidths overlapping several structural modes. Therefore, some form of structural control will be necessary to avoid excessive excitation of the flexible modes. The purpose of passive/active damping is to allow the system to efficiently meet its performance goals.

The Passive and Active Control of Space Structures (PACOSS) program investigated the accuracy and practicality of designing and implementing passive damping in structures typical of many LSS configurations. This involved design and fabrication of a passively damped Dynamic Test Article (DTA) possessing high modal density at low frequencies. Also, an active modal damping system was designed and implemented. In order to verify the design methodology and effectiveness, a comprehensive modal survey was conducted on the DTA to identify flexible modes in the 1 to 10 Hz range. This paper discusses the modal survey, modal parameter identification, and comparison of measured and analytic results.

Modal parameter identification proved to be difficult for several DTA modes in the frequency range of interest. While the identified natural frequencies were quite repeatable, damping ratios and mode shapes tended to exhibit scatter on the order of 20% about the average, depending on the particular measurement and curve fit parameters. The difficulties were traced to both the highly damped, closely spaced nature of the modes and, to some extent, the data quality. Although parameter identification was inconsistent in some instances, the overall correlation between the test results and analytic predictions was quite good. Tests with the active modal damping system turned on (closed loop) were also conducted. Measured results were compared with corresponding analytic predictions of the control system performance and the system functioned as predicted, working in concert with the passive damping design.

Important conclusions may be drawn from the results of the DTA modal survey. Of most significance is the fact that predictable levels of passive damping can be designed into complex LSS-type structures. Also, the achievable damping levels significantly improve performance such as LOS settling time. Testing of the DTA revealed the need for study and application of more robust parameter identification algorithms to systems possessing highly damped, closely spaced modes.

INTRODUCTION

The ultimate goal of the PACOSS program was to demonstrate the synergistic benefit of passive damping working in concert with active vibration damping as applied to large space systems. Demonstration and verification of the technology required development of the Dynamic Test Article (DTA) pictured in Figure 1. The DTA is dynamically traceable to future large space systems through the Representative System Article (RSA) described in Reference 1, and depicted in Figure 2. A methodology for passive/active control design and its application to the RSA is presented in Reference 2. Details of the design and analysis of the several DTA substructures are given in Reference 3. Following fabrication, fixed interface modal surveys were conducted on each substructure. Results from these tests are discussed in Reference 4. An important aspect of system traceability is the presence of high modal density. In order to verify the high modal density of the DTA, and measure the accuracy and effectiveness of the damping design methodology, a modal survey was conducted on the DTA. This paper presents the results of the DTA modal survey and analytic modal analysis.

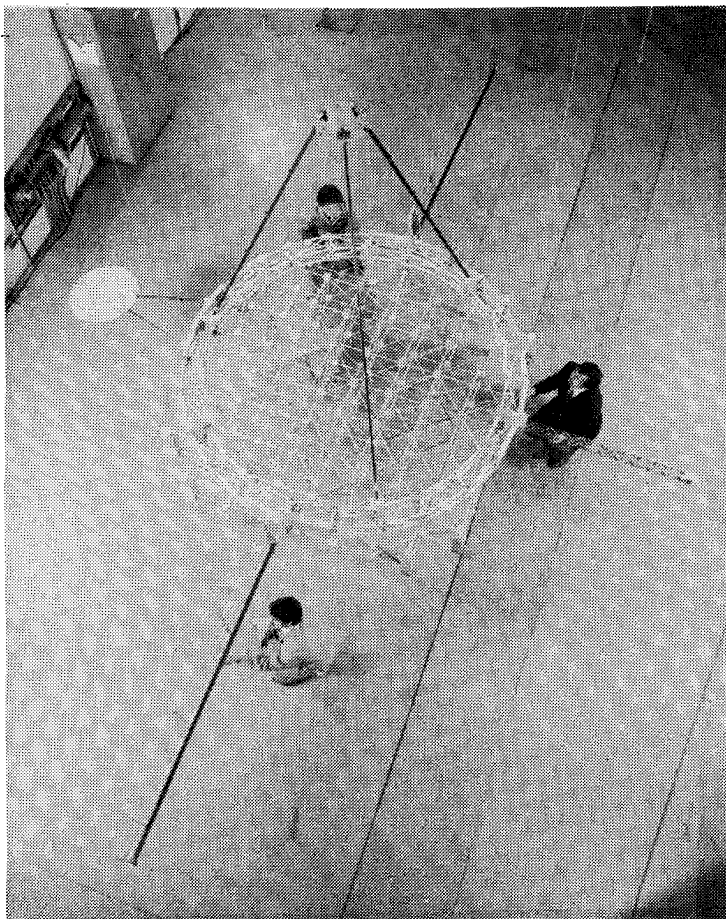


Figure 1 PACOSS Dynamic Test Article (DTA)

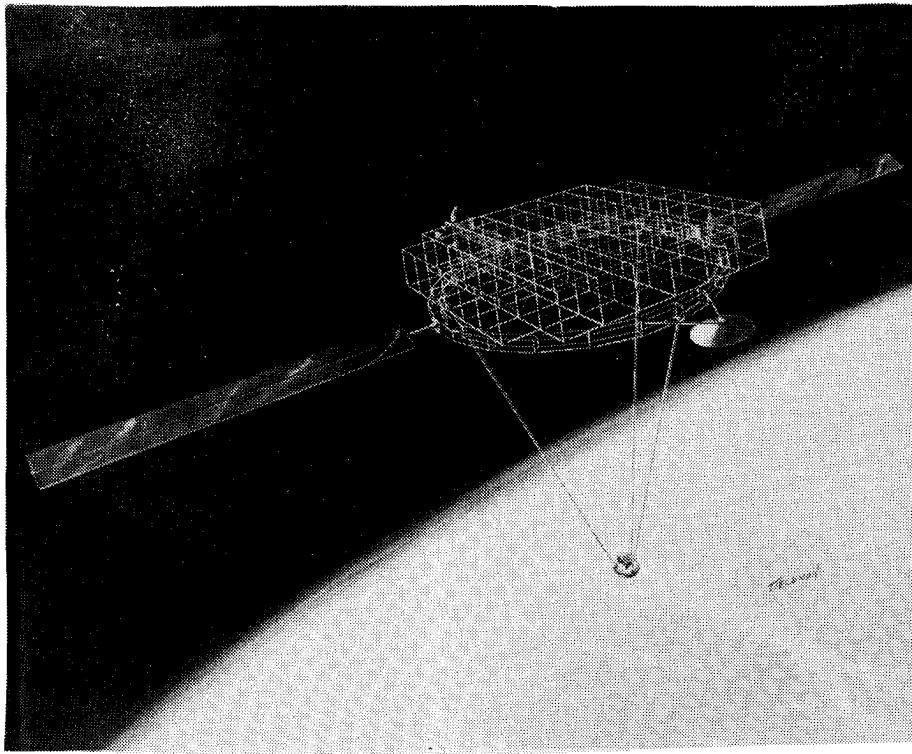


Figure 2 PACOSS Representative System Article (RSA)

TEST SETUP

The modal survey of the DTA generally followed the initial test plan. However, preliminary investigations, test modifications, and additional shaker configurations were included as the testing progressed. These efforts were undertaken in an effort to assure that the best possible data, within equipment and time constraints, were acquired. The following paragraphs present a brief overview of the DTA modal survey setup and testing.

Setup for the DTA testing involved assembly of a temperature control chamber, erection of a support fixture, and assembly of the DTA. The overall test setup is diagramed in Figure 3. The temperature control chamber performed quite well throughout the DTA testing, although wide fluctuations of the temperature outside the chamber (65.F to 90.F) required that the air conditioner be on continuously. The air flow from the air conditioner was directed upwards and did not measurably disturb the DTA.

The primary goal of the DTA modal survey was accurate determination of the modal parameters (frequency, damping ratios, shapes) for flexible modes below 10 Hz. Also, the performance and effectiveness of the active damping system was to be accessed through measurement of the increase in damping it provided to selected DTA modes. The modal parameters were to be determined through curve fitting of frequency response functions generated by measuring an external force and the resulting accelerations at selected points on the structure.

Figure 4 shows the measurement point locations on the DTA. The large number of measurements were required in order to obtain a valid reduction of the analytic mass matrix for use in orthogonality products between the measured and predicted mode shapes. Also, measurements were included across component interface points to allow troubleshooting of interface stiffness if the need arose.

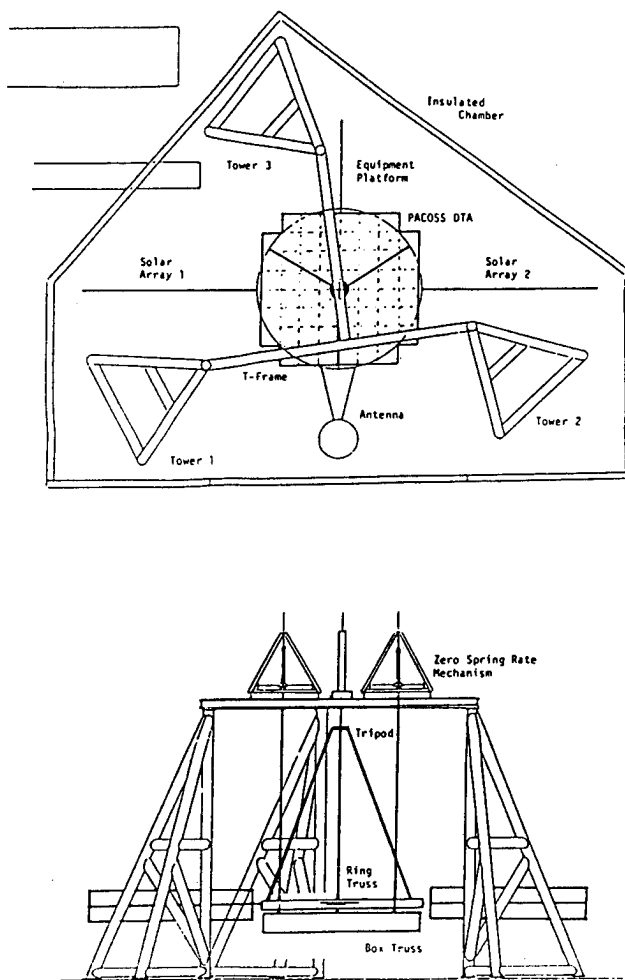


Figure 3 Modal Survey Setup

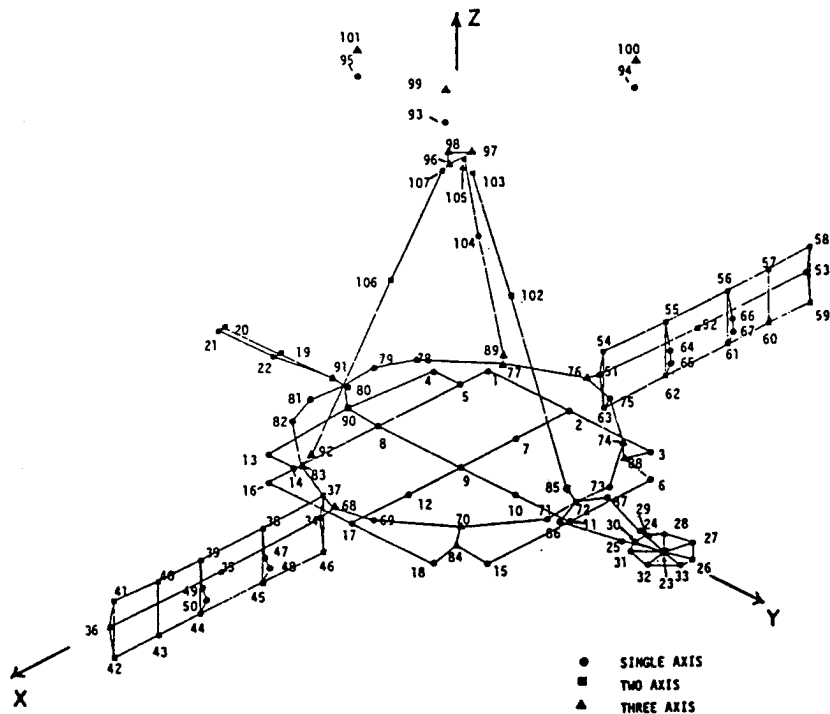


Figure 4 DTA Measurement Point Diagram

The relatively low frequency range of interest and the light weight of some DTA components required that shakers fixed to ground be used to excite the DTA. Suspending the shakers invariably resulted in coupling of the shaker suspension dynamics to the dynamics of the structure through rotational and lateral stiffness of the stinger in the 1 to 3 Hz range. However, in some instances, achieving a stiff shaker fixture with frequencies above 15 Hz was not possible. Also, the bending stiffness of the stinger can change the test article's behavior when attached to a fixed shaker. Therefore, swivel stingers with ball joints on each end were used to eliminate dynamic coupling of the shaker and DTA through rotational and lateral stinger stiffness. The platform which supported the shaker for excitation of the tripod top plate was a case where stinger stiffness allowed coupling of the platform dynamics to the DTA. Figure 5 dramatically demonstrates the effect on the drive point FRF of using a relatively stiff nylon stinger compared to the swivel stinger. The significant differences between the FRFs in the 3 to 6 Hz range are probably due to large rotational deflection of the tripod top plate for DTA modes in that frequency range. The same measurement was acquired using an impact hammer (no stinger involved) which, although noisy, verified the FRF acquired using the swivel stinger.

Figure 6 is a photo of the overall DTA test setup inside the thermal control chamber. Note the previously mentioned shaker support platform constructed around the tripod top plate visible at the top center of the photo. Previous testing of the components demonstrated that the many accelerometers cables hanging from the structure have no measurable effect of the DTA dynamics.

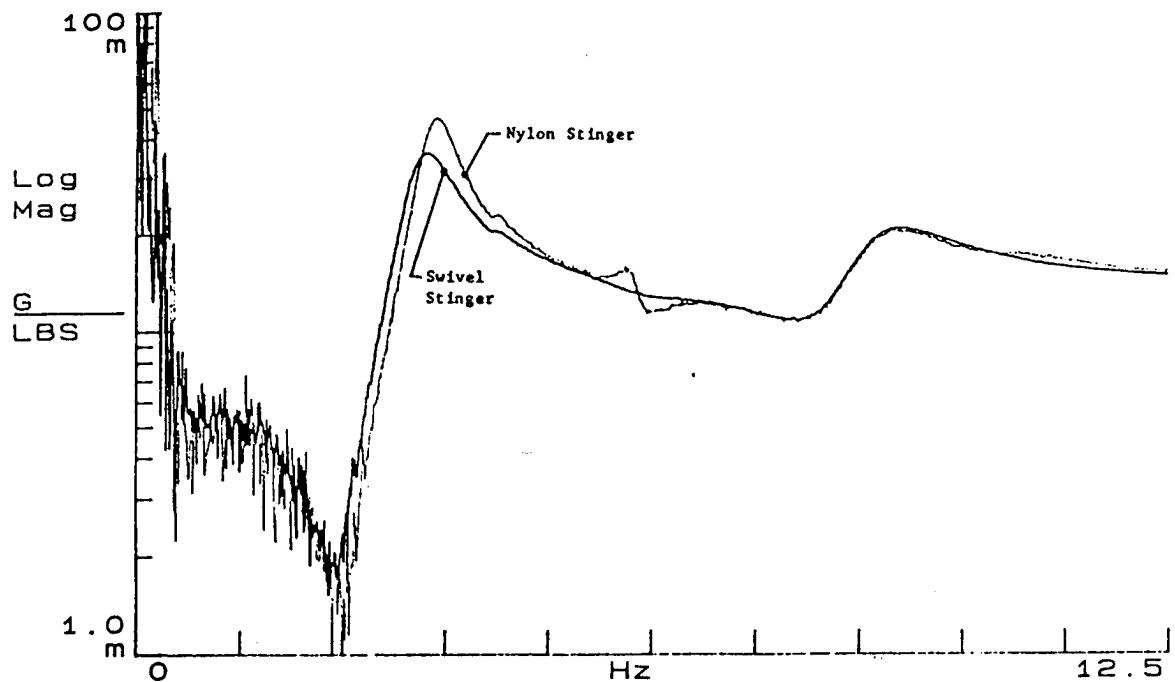


Figure 5 Nylon versus Swivel Stinger FRF



Figure 6 DTA Test Setup

Before acquisition of full 188 measurement data sets, several excitation methods were attempted at a few drive points to determine appropriate force levels and to identify the method which gave the highest quality data. Also, the necessary frequency resolution was determined by comparing curve fit results (multi-degree of freedom polynomial) from data collected for several values of resolution. The results indicated that a frequency resolution of 0.03125 Hz was adequate for acquiring the frequency response function (FRF) measurements in that fitting of data acquired at higher resolution produced virtually the same modal parameters as that acquired at 0.03125 Hz. Burst random excitation for 80% of the acquisition time period (32 seconds using 401 spectral lines and a 12.5 Hz bandwidth) with no windowing produced slightly better quality data than straight random excitation and Hanning windowing. Swept sine testing generated far better quality data but had little effect on curve fit results at points of relatively high response. To avoid conflicts in facility scheduling, multipoint random excitation and measurement techniques were selected for acquisition of the FRFs from which modal parameters would be extracted.

A Hewlett-Packard 3565 Modal System running Structural Measurement Systems (SMS) multi-input, multi-output software was used to acquire and process the measurements. This system, as configured for the DTA test, allows acquisition of up to 55 response points from up to four uncorrelated inputs. Thus, 220 FRF measurements may be acquired simultaneously. Using the acquisition parameters mentioned above, and taking ten averages, measurement of 55 response points takes only 5 minutes and 20 seconds. Including processing time, storage, and setup recall, a full set of 752 (188 x 4) FRF measurements took about 1.5 hours. This rapid data acquisition combined with the test chamber temperature stability allowed data to be acquired for the full DTA at a virtually constant temperature.

DATA ASSESSMENT AND ANALYSIS

Assessment and analysis of the measured data were conducted as the data sets were acquired. The FRF measurements were qualitatively reviewed immediately, and preliminary parameter identification was performed before the test configuration was changed. This process allowed discovery of several instrumentation problems and measurement anomalies which were investigated and corrected without repeating a configuration setup. Limitations of the available instrumentation resulted in poor measurements at points of low response, (typically on the order of 0.005 g's or less). This complicated the identification and separation of several closely spaced modes, particularly those involving coupled horizontal bending of the solar array masts and blankets. However, many modes were consistently identified and thus are likely to be very accurate. The following paragraphs discuss the FRFs and the process of parameter identification performed on the measurements.

Generally, the quality of the measurements was quite good at the drive points and at points of high response level. Figures 7(a) and 7(b) show typical drive point FRFs as examples of the data quality. The coherence for most of these measurements was excellent throughout the acquisition bandwidth. An anomaly seen in some of the data was high level noise in horizontal solar array blanket FRFs acquired using multipoint random excitation. Specifically, the response on the blanket due to excitation at points far removed from the solar array, such as the equipment platform, was very noisy as shown by Figure 8. This figure compares FRFs 20x/21x and 39y/21x. The level of 39y/21x is well above the noise floor of the PCB-302 accelerometers, and other data indicated that the level should have been much lower. Also, measurement 39y/42y, which was acquired simultaneously is much cleaner as shown by Figure 9.

The poor quality and high level of 39y/21x was probably caused by nonlinear behavior of the TMDs which contaminated the separation of responses performed by the multipoint random excitation algorithm which assumes a linear system. The TMD nonlinearity arises from the geometric lateral stiffening effect and plastic behavior of the TMD beams. In general, tests where the solar arrays were excited directly tended to produce somewhat more noisy measurements than when the arrays were not being driven directly, again probably due to nonlinear response of the TMDs.

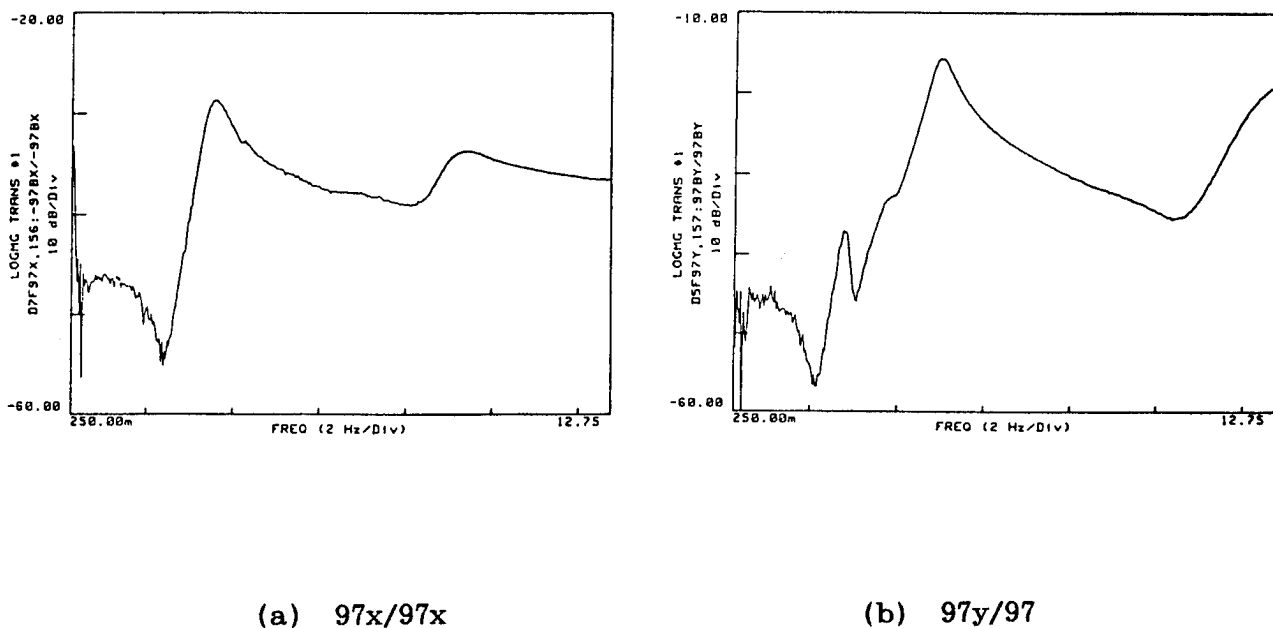


Figure 7 Typical Drive Point FRFs

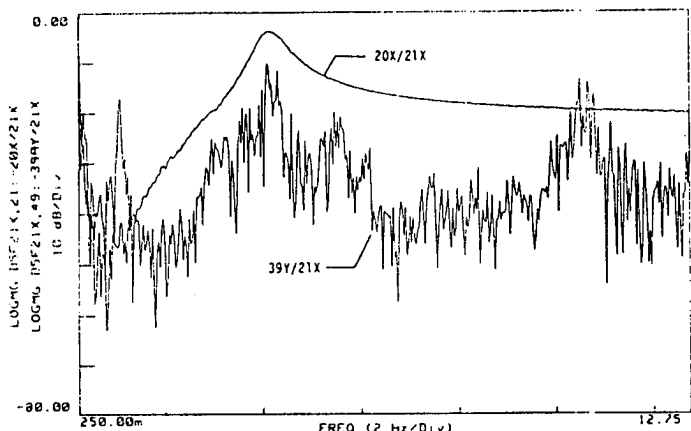


Figure 8 Measured FRFs:
39y/21x and 20x/21x

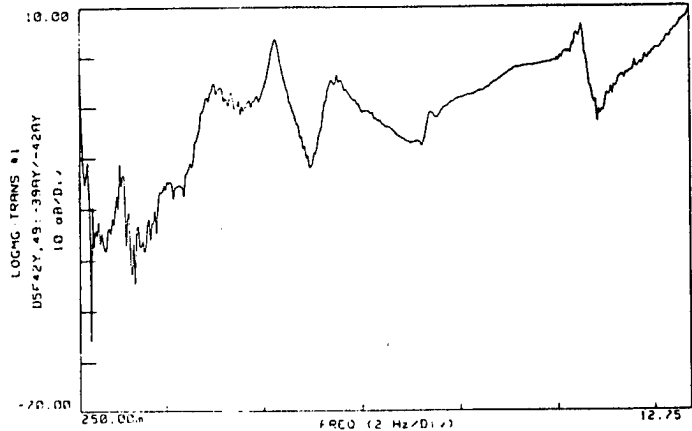


Figure 9 Measured FRF:
39y/42y

Parameter Identification

Identifying the number of modes and their parameters in the 1 to 10 Hz range of interest proved to be a challenging task. While several modes were easily and consistently fit, many closely spaced modes could not be adequately separated by local, multi-degree of freedom rational fraction polynomial (RFP) curve fitting techniques (Ref. 5). The combined effects of high modal density and high damping tended to mask distinct modes in the FRFs, thereby resulting in two or more modes being fit as a single mode. An example of this is seen by considering a portion of the measured FRF: 42y/42y.

As shown in Figure 10(a), a curve fit of the three modes apparent in the FRF from 2.44 to 6.47 Hz appears satisfactory and gives the modal parameters shown in the figure. However, when the three poles identified from 42y/42y are used to fit the measurement: 20x/42y, the extremely poor fit shown by Figure 10(b) results. This occurs because there are actually six modes present in the response at 42y. Note that 20x is on the axis of symmetry and thus should only show antisymmetric modes (refer to Figure 4). If 20x/42y is refit to determine the additional three modes as shown in Figure 10(c), and then all six of the identified poles are used to determine the modal residues for each FRF, satisfactory results are achieved for both measurements as shown by Figure 11. Attempting to determine all six poles from either measurement gives results like that shown in Figure 12 where the algorithm uses the additional modes to match

noise in the data. Essentially, the features in the FRF caused by the several modes are not as strong as noise in the measurement, even though the measurement is of acceptable quality. However, if the poles present in the FRF are known (and accurate), using the RFP method to find the residues results in a very good fit. This effect was seen even when working with extremely clean data.

Thus, the important task is to identify and estimate all the poles present in a given set of FRFs. Polyreference techniques were developed for just this purpose. The polyreference method tried on the DTA data was a time domain technique which tends to be sensitive to noise and did not work well on the highly damped DTA modes. Frequency domain polyreference techniques may work better on the DTA data, but this has not been investigated or demonstrated under the PACOSS program.

The aforementioned effects limited the accuracy of estimated modal damping ratios even when using the best measurements for determining a selected pole. While estimates of natural frequencies were consistent from one measurement to another, modal damping estimates varied by up to 20 percent for closely spaced, highly damped modes.

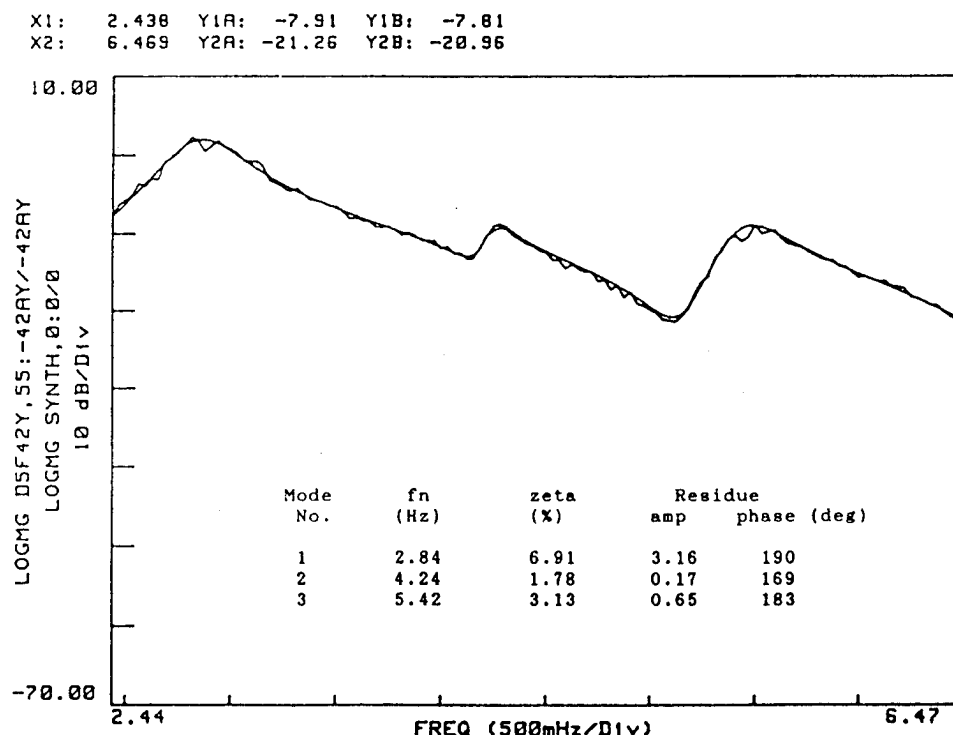


Figure 10(a) 3 Mode Fit of 42y/42y

X1: 2.438 Y1A: -30.43 Y1B: -28.87
 X2: 6.469 Y2A: -52.45 Y2B: -37.06

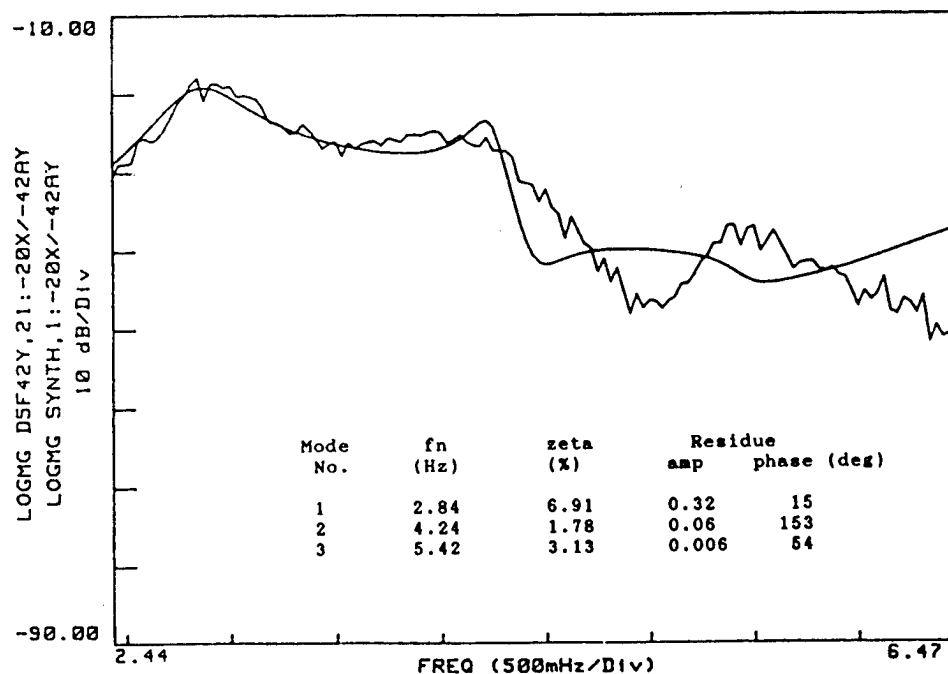


Figure 10(b) 3 Mode Fit of 20x/42y

X1: 2.438 Y1A: -30.43 Y1B: -29.83
 X2: 6.469 Y2A: -52.45 Y2B: -50.52

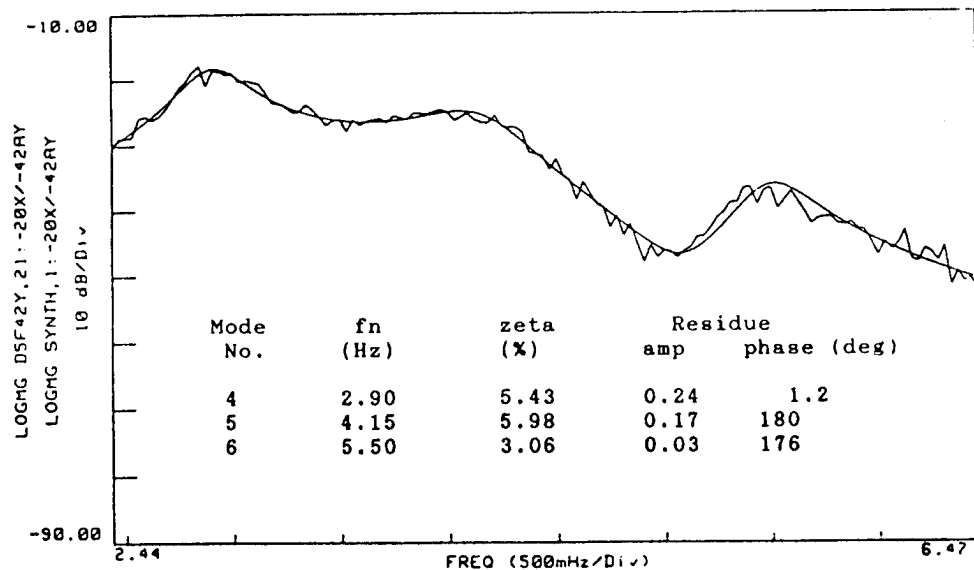


Figure 10(c) Second 3 Mode Fit of 20x/42y

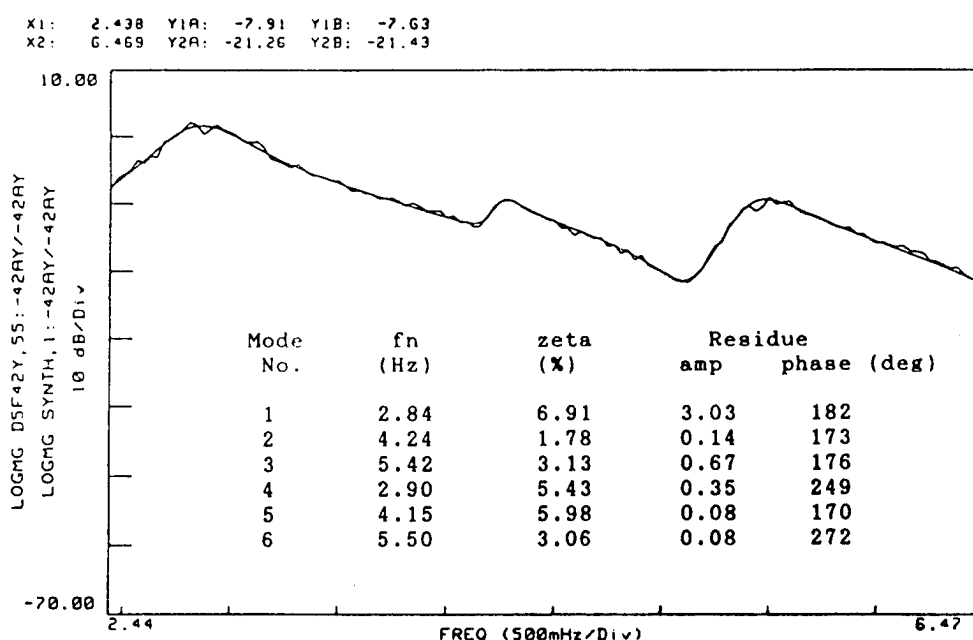


Figure 11 6 Mode Fit of 42y/42y

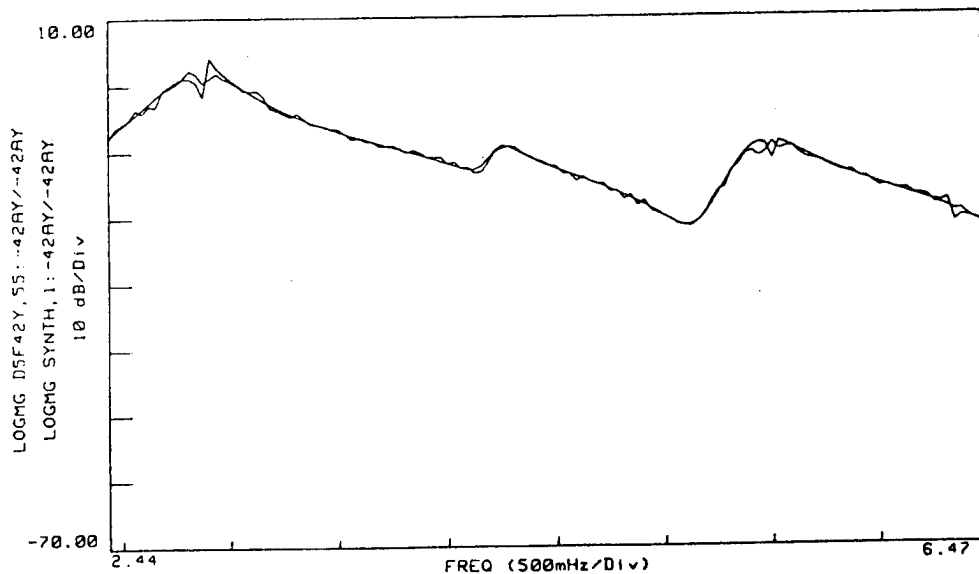


Figure 12 Local 6 Mode Fit of 42y/42y

A total of 22 unique modes were identified from the DTA testing. The identified modes are listed in Table 1 with the observed ranges listed for the modal frequencies and damping ratios. The quantity listed as weighted phase error in the table is defined by the following equation:

$$\bar{\theta} = \frac{\sum_{i=1}^{n \text{ dof}} |\Delta\theta_i \phi_i|}{\sum_{i=1}^{n \text{ dof}} |\phi_i|}$$

where:

$\bar{\theta}$ = weighted phase error

$\Delta\theta_i$ = phase difference (-90° to $+90^\circ$)
between dof i and dof of greatest magnitude

ϕ_i = modal magnitude at dof i

Weighted phase error is an indication of the quality of the synthesized mode shape. Generally, the smaller the weighted phase error, the more accurate the estimate of the mode shape. Note that in Table 1, relatively high phase error generally corresponds to modes exhibiting greater scatter in their frequency and damping estimates. The high phase error is attributable to a failure of the curve fitting technique to fully separate closely spaced, highly damped modes. This occurs when the response components present in an FRF due to individual modes (complex residues) are not correctly determined by the particular parameter identification technique applied to the data.

The procedure used in determining estimates of the mode shapes was to obtain the best estimates of the poles in a given data set and frequency range. The poles were obtained using the RFP multi-degree of freedom method. Once a satisfactory and complete set of poles was obtained, the mode shapes were found by holding the poles constant while determining the residues for each measurement. Based on the consistency of results, and on orthogonality products discussed below, a set of orthogonal modes was selected as the "best" measured modes for use in correlation with the analytic model.

Table 1 Summary of Identified Modes

Measured Mode No.	Description	Range of f_n (Hz)	Range of ζ (%)	Range of Weighted Phase Error (Degrees)	Fit Confidence*
1	1st Blanket Bending, Solar Array 1	1.02 - 1.04	3.0 - 4.1	19.9 - 33.6	M
2	1st Blanket Bending, Solar Array 2	1.10 - 1.11	4.8 - 6.0	20.7 - 24.7	M
3	1st Symmetric Ring Truss Bending	2.59 - 2.61	2.4 - 4.7	8.1 - 15.2	H
4	Symmetric Horizontal Solar Array Mast Bending	2.80 - 2.85	3.4 - 7.0	16.9 - 42.4	L
5	Anti-Symmetric Horizontal Solar Array Mast Bending	2.87 - 2.94	4.4 - 9.6	28.3 - 41.0	L
6	Anti-Symmetric Solar Array Vertical Bending w/Box Truss Rocking	3.25 - 3.30	4.9 - 6.3	19.4 - 30.9	H
7	Anti-Symmetric Solar Array Vertical Bending w/Tripod	3.53 - 3.66	5.9 - 8.8	15.1 - 26.9	H/M
8	Equip Platform Vertical Bending w/Tripod & Solar Array Symmetric Bending	3.72 - 3.88	4.3 - 5.7	11.2 - 30.3	H
9	Equip Platform Horizontal Bending	4.10 - 4.13	7.1 - 7.2	19.4 - 20.0	H
10	1st Blanket Torsion, Solar Array 1	4.10 - 4.30	1.6 - 2.2	9.0 - 16.0	H
11	1st Blanket Torsion, Solar Array 2	4.18 - 4.33	1.1 - 2.6	8.0 - 26.2	H
12	Symmetric Antenna Bending w/Tripod Bending	4.83 - 4.96	4.5 - 5.8	5.6 - 21.3	H/M
13	Tripod Torsion	4.95 - 4.98	5.5 - 6.0	13.9 - 20.8	H/M/L
14	Symmetric Antenna Dish, Equipment Platform, Tripod	5.04 - 5.45	4.6 - 13.4	19.0 - 42.6	
15	2nd Blanket Bending, Solar Array 2	5.41 - 5.47	2.9 - 3.8	6.4 - 18.9	H
16	2nd Blanket Bending, Solar Array 1	5.34 - 5.48	2.5 - 3.0	10.0 - 23.7	H
17	Anti-Symmetric Tripod Bending w/Box Rocking & Solar Array Vertical Bending	6.37 - 6.48	7.8 - 12.7	20.5 - 43.0	L M
18	2nd Blanket Torsion, Solar Array 1	8.89	5.5	21.1	
19	Anti-Symmetric Tripod Bending	8.77 - 9.04	3.5 - 7.0	17.6 - 28.3	L
20	Symmetric Tripod Bending w/Antenna & Ring Bending	9.10 - 9.26	6.9 - 8.6	24.6 - 29.6	L
21	2nd Blanket Torsion, Solar Array 2	9.32	4.5	16.5	M
22	Symmetric Antenna Dish Bending	9.17 - 9.47	5.4 - 10.3	13.5 - 27.7	M

* L = Low
M = Moderate
H = High

ANALYTIC MODEL CORRELATION

The measured results agreed fairly well with the pretest analytic model. This indicated that data from a sufficient number of excitation points had been acquired to allow identification of all major flexible modes below 10 Hz. The following paragraphs discuss the post-test tuning of the DTA finite element model and present the final comparison of predicted and measured modal parameters.

A comparison of the predicted and measured natural frequencies and mode shapes indicated that the dynamic coupling of the solar arrays to the rest of the DTA was different from that predicted by analysis. Final correlation and tuning of the solar array substructure model with the results from substructure testing had not been completed before the full DTA test. Therefore, modification of the DTA solar array models involved completing the substructure tuning.

Results from the solar array substructure modal surveys indicated that the initial modeling of the root assembly was too stiff. This was due to the physical nature of the actual root assembly which consists of a solid aluminum insert bonded inside the solar array mast. In order to more accurately characterize the stiffness of the bonded root assembly, a model including the inner member, the mast tubing, and the bonding material was constructed for comparison with the properties of the original model. The inner member was modeled using solid elements, as was the bonding material, and the mast tubing was modeled using plate elements. In the analyses, the stiffnesses of the various members alone were adjusted to have equivalent stiffnesses to beams. For example, unit loads were applied to the insert model alone and the material properties adjusted so that the resulting deflections and rotations were the same as those of a beam with a solid section of the same size.

The stiffness of the bonded assembly model was 62% that of an equivalent beam. It was noted, however, that the model might be in error due to the use of solid elements. To determine the accuracy of the model, the bonding material was replaced with aluminum and the resulting stiffness was again compared with an equivalent beam. This analysis showed that the model using aluminum properties for the bonding material was 80% as stiff as an equivalent beam. Therefore, the final stiffness of the assembly was adjusted to be 0.62/0.8 or 78% that of a uniform aluminum beam.

The pretest DTA model also did not include the deformed geometry of the solar arrays. The tip of the solar array mast deflected more than 5 inches under gravity over a mast length of 8 feet. This geometry was included in the final DTA analysis.

The only other significant change in the DTA modeling was the addition of differential stiffness in the tripod analysis to account for compression in the tripod legs. A minor correction made to the modeling was the deletion of some accelerometer masses that had remained in the substructure models from correlation with substructure modal survey results. These small masses were not deleted from the pretest DTA model in the interest of expediency in completing the pretest analysis. Note that no arbitrary changes such as stiffness or mass adjustments were made in order to obtain better agreement between the analysis and test results. This philosophy, followed throughout the development of the substructure models, has resulted in a DTA model which is based solely on standard and measured physical properties. In fact, the final DTA model could be considered a rigorous pretest model.

In order to more accurately represent the frequency dependency of VEM material properties, the component models were run with both 4 Hz and 9 Hz VEM stiffness. Modes below 6.5 Hz were taken from the 4 Hz run, and those above from the 9 Hz run. VEM loss factors at specific modal frequencies were used in the damping calculations.

Results Comparison

Analysis of the tuned DTA model was performed using direct stiffness coupling of the reduced substructure models. Analytic modal damping ratios were determined via the modal strain energy (MSE) method using the appropriate loss factors (Ref 6).

For discussion of the experimentally identified modes, the analytic modes may be grouped into four categories based on the modal strain energy distributions. The four categories and number of flexible modes in each category are:

- 10 Global modes
- 10 Nearly repeated solar array blanket modes
(symmetric/antisymmetric pairs)
- 7 Local appendage modes
- 12 Tuned mass damper (TMD) modes

Global modes are defined as modes in which no one component possesses more than 90 percent of the modal strain energy. These modes are typically of greatest interest to the analyst because of their importance to system performance. They are the modes most easily disturbed by spacecraft maneuvers and, by their nature, affect the entire system. Therefore, accurate prediction of global modes and the associated damping design (passive or active) for those modes is critical to achieving system performance goals.

The five pairs of nearly repeated solar array blanket modes posed a problem in terms of correlation with experimental modes through a cross orthogonality product. Experimentally, the synthesized modes tended to result in either one blanket or the other possessing all the motion, i.e., they looked like a linear combination of the analytic pair. For repeated roots, any linear combination of the repeated mode shapes is itself a mode shape or, eigenvector. Thus, the analytic blanket mode pairs were added and subtracted to obtain modes for comparison with the measured modes. Two pairs of repeated modes are dominated by the TMDs. The high damping and somewhat local nature of these four modes precluded their identification.

The local appendage modes include a variety of modes where a single substructure possesses more than 90 percent of the modal strain energy. One of the predicted appendage modes was not identified because it involved only antenna dish bending which could not be adequately excited without driving the dish directly.

The 12 TMD modes are very local in nature. They are uncoupled from the rest of the DTA and may only be disturbed by directly exciting the TMDs. Since any attachment of a stinger to a TMD would drastically alter its behavior, no attempt was made to identify these modes.

The points discussed above led to a set of 22 target modes. During analysis of the test data, it became obvious that the nonlinear behavior of the TMDs, and the relatively high noise level of the TMD instrumentation had seriously degraded the measurements on the TMDs. This degradation was serious enough to introduce large errors into the synthesized TMD modal deflections. Therefore, orthogonality products were computed without the TMD measurements.

In order to perform the orthogonality checks without the TMD measurements, a mass matrix reduced to the measurements to be used in the orthogonality products had to be generated. A static reduction of the DTA mass and stiffness matrices without including the TMD measurements results in significant error in the solar array blanket modes. Therefore, this method could not be used to generate a reduced mass matrix. An alternate approach to generating a reduced mass matrix is to use the analytic modes calculated from a valid reduction. Briefly, the unmeasured degrees of freedom are deleted from the modal vectors and the resulting modes are then used to compute the test analysis matrix (TAM) using the pseudo-inverse:

$$TAM = (\phi^T)^{-\dagger} \cdot \phi^{-\dagger}$$

where

$$\phi^{-\dagger} \text{ is the pseudo-inverse: } (\phi^T \phi)^{-1} \phi^T$$

Conditioning problems will arise if the modal vectors are very similar (nearly linearly dependent). This can occur if the primary degrees of freedom involved in a mode are deleted but the mode is retained in generating the test analysis mass matrix. For the DTA, only the target modes were retained, and all TMD measurements were deleted.

As previously mentioned, measured modal damping ratios tended to exhibit some variation depending on the identification method. However, the modes selected for comparison with the analytic results were chosen on the basis of small weighted phase error and good orthogonality. Therefore, the damping ratios of the selected modes were assumed to be the best estimates of the true DTA behavior, and were the specific values used for comparison with the analytic results. The results are presented in Table 2 which lists the comparison of the measured and analytically predicted frequencies and damping ratios of the target modes. Also listed in the table are the diagonal terms of the unnormalized generalized mass and cross orthogonality products. These products were computed using the real measured modes defined as:

$$\phi_{i\text{real}} = \phi_i \cos \theta_i$$

where:

$\phi_{i\text{real}}$ = real modal amplitude at DOF i

ϕ_i = complex modal amplitude at DOF i

θ_i = phase angle between DOF i and DOF of greatest magnitude

The orthogonality products are defined as:

$$GM = \phi_{\text{real}}^T \cdot TAM \cdot \phi_{\text{real}}$$

where:

ϕ_{real} = the measured real mode shape as given above

TAM = is mass matrix as given in Section 4.3

Note that the modal synthesis technique used in computing the mode shapes should produce modes with unity generalized mass.

$$XORTH = \bar{\phi}_{\text{real}}^T TAM \phi_a$$

where:

$\bar{\phi}_{\text{real}}$ = ϕ_{real} normalized to TAM

ϕ_a = the analytic modes matrix used to generate TAM

The data presented in Table 2 show that all the target modes were identified and that most correlate very well with the analytic predictions. Correspondence of frequencies is excellent with the exception on modes 9 and 18. Mode 9 is a local equipment platform mode and mode 18 is a local antenna mode which is sensitive to the postbuckled state of the antenna dish. The postbuckled state and effects were noted during the antenna substructure modal survey, but could not be accurately modeled.

Damping estimates agree reasonably well with the predicted values. In fact, the analytic value is bracketed by the measured range in many cases (see Table 1). Excellent qualitative agreement of the modes is shown in Figures 13(a) and (b) which present plots of the corresponding measured and predicted shapes for two global modes.

While the diagonal cross-orthogonality terms listed in Table 2 and the mode shape plots indicate good correlation for most of the modes, the full orthogonality products exhibit significant off diagonal coupling. The self orthogonality normalized to unity generalized mass is given in Table 3, and the cross orthogonality with the analytic target modes is given in Table 4.

Table 2 Comparison of Identified and Predicted Modal Parameters

Target Mode No.	Analytic		Measured Mode No.	Measured Results *		Orthogonality Results	
	f_n (Hz)	ζ (%)		f_n (Hz)	ζ (%)	GM	X-Orth Diagonal Term
1	1.00	4.2	1	1.03	4.1	0.83	0.96
2	1.03	4.2	2	1.10	6.0	0.71	0.99
3	2.61	2.8	3	2.61	3.6	1.06	0.97
4	3.01	5.0	4	2.81	4.4	2.70	0.64
5	3.08	4.0	5	2.89	7.0	3.02	0.68
6	3.29	4.4	6	3.25	5.0	0.94	0.93
7	3.50	8.2	7	3.53	8.8	1.27	0.88
8	3.70	4.7	8	3.72	5.2	1.01	0.97
9	3.81	4.0	9	4.13	7.1	0.90	0.99
10	4.14	2.0	10	4.15	1.6	0.87	0.91
11	4.14	2.0	11	4.24	1.6	1.03	0.91
12	4.60	7.8	12	4.83	4.5	3.12	0.88
13	4.81	10.4	14	5.04	11.4	0.85	0.94
14	4.86	7.0	13	4.96	5.5	1.96	0.97
15	5.32	4.0	15	5.41	3.8	0.83	0.98
16	5.32	4.0	16	5.43	3.0	0.74	0.95
17	6.12	10.0	17	6.48	12.7	1.43	0.91
18	7.52	6.0	22	9.40	10.3	0.98	0.76
19	8.94	1.8	18	8.90	5.5	0.67	0.96
20	8.95	1.8	21	9.32	4.5	0.57	0.98
21	9.04	6.8	19	8.92	7.0	1.11	0.96
22	9.28	7.0	20	9.26	8.6	2.26	0.88

* See Table 1 for Variation in Results.

Table 3 Normalized Generalized Mass Matrix

NORMGM		1	2	3	4	5	6	7	8	9	10	11	12	13	14	15	16	17	18	19	20	21	22	
ROW		1	0.03	1.10	2.61	2.81	2.89	3.25	3.53	3.72	4.13	4.15	4.24	4.83	4.96	5.04	5.42	5.43	6.48	8.89	8.92	9.26	9.32	9.40
1	1.00	0.12	-0.11	0.57	-0.10	-0.12	-	-	-	-0.19	-	-	-	-	-	-	-	0.14	-	-	-	-	-	
2	0.12	1.00	-	0.52	0.65	-	-	-	-	-0.25	-	-	-	-	-	-	-	-	-	-	-	-	-	
3	-0.11	-	1.00	-0.31	-	-	-	0.12	-	-	-	-	-	-	-	-	-	-	-	-	-	-	-	
4	0.57	0.52	-0.31	1.00	0.26	-	-	-	-	-0.17	-0.20	-	-	-	-	-	0.10	-	-	-	-	-	-	
5	-0.10	0.65	-	0.26	1.00	-	-	-	-	-0.23	-	-	-	-	-	-	-	-	-	-	-	-	-	
6	-0.12	-	-	-	-	1.00	-	-	-	0.11	-	-	-	-	-	-	-	-	-	-	-	-	-	
7	-	-	-	-	-	-	1.00	-	-	-	-	-	-	-	-	-	-	-	-	-	-	-	-	
8	-	-	0.12	-	-	-	-	1.00	-	-	-	-	-	-	-	-	-	-	-	-	-	-	-	
9	-	-	-	-	-	-	-	-	1.00	-	-	-	-	-	-	-	-	-	-	-	-	-	-	
10	-0.19	-	-	-0.17	-	0.11	-	-	-	1.00	-	-	-	-	-	-	-	-	-	-	-	-	-	
11	-	-0.25	-	-0.20	-0.23	-	-	-	-	-	1.00	-	-	-	-	-	-	-	-	-	-	-	-	
12	-	-	-	-	-	-	-	-	-	-	-	1.00	-0.15	0.31	-	-	-0.15	-	-	-	-	-	0.36	
13	-	-	-	-	-	-	-	-	-	-	-	-0.15	1.00	0.11	-	-	0.14	-	0.15	0.22	-	-	-	
14	-	-	-	-	-	-	-	-	-	-	-	0.31	0.11	1.00	-	-0.15	-	-	0.31	-	0.35	-	-	
15	-	-	-	-	-	-	-	-	-	-	-	-	-0.15	-	1.00	-	-	-	-	-	-	-	-	
16	-	-	-	-	-	-	-	-	-	-	-	-	-	-0.15	-	1.00	-0.11	-	-	-	-	-	-	
17	-	-	-	-	-	-	-	-	-	-	-	-	-	-0.15	0.14	-	-0.11	1.00	-	0.45	-0.12	-	-0.11	
18	0.14	-	0.10	-	-	-	-	-	-	-	-	-	-	-	-	-	1.00	-	-	-	-	-	-	
19	-	-	-	-	0.23	-	-	-	-	-	-	0.15	-	-	-	0.45	-	1.00	-0.16	-	-	-	-	
20	-	-	-	-	-	-0.16	0.14	-	-	-	-	0.22	0.31	-	-	-0.12	-	-0.16	1.00	-	0.18	-	-	
21	-	-	-	-	-	-	-	-	-	-	-	-	-	-	-	-	-	-	1.00	-	0.18	-	-	
22	-	-	-	-	-	-	-	-	-	-	-	0.36	-	0.35	-	-	-0.11	-	-	0.18	-	1.00	-	-

Table 4 Cross-Orthogonality Product

"CROSS-ORTHOGONALITY CHECK (EXPERIMENTAL/ANALYTICAL)"										
f _n	1.00	1.03	2.61	3.01	3.08	3.29	3.50	3.70	3.81	4.14
f _n	ROW	1	2	3	4	5	6	7	8	9
1.03	1	0.96	0.21	-	-	-	-	-	0.11	-
1.10	2	-	0.99	-	-	-	-	-	-	-
2.61	3	-0.14	-	0.97	-	-	-	-	-	-
2.81	4	0.46	0.55	-0.14	0.64	-0.11	-	-	-0.16	-
2.89	5	-0.23	-0.63	-	0.13	0.68	-	-	0.10	-0.10
3.25	6	-0.11	-	-	-	0.93	0.39	-	-	-
3.53	7	-	-	-	-	-0.35	0.88	-	-	-
3.72	8	-0.10	-	-	-	-	-0.97	-	-	-
4.13	9	-	-	-	-	-	0.99	-	-	-
4.15	10	-0.30	-	0.15	-0.17	-	0.12	0.91	-	-
4.24	11	-	-0.32	-	-0.10	-	-	0.93	-	-
4.83	12	-	-	-	-	-	-	-0.88	0.37	-
4.96	13	-	-	-	-	-	-	0.14	-0.97	-
5.04	14	-	-	-	-	-	-	0.94	-0.10	-0.20
5.42	15	-	-	-	-	-	-	-	0.98	-
5.43	16	0.11	-	-	-	-0.10	-	-	0.95	-
6.48	17	-	-	-	-	-	0.15	-	-	0.91
8.89	18	0.13	-	-	-	-	-	-	-0.18	-
8.92	19	-	-	-	-	-	-	-	0.17	-
9.26	20	-	-	-	-	-0.10	-	-	0.30	-
9.32	21	-	-	-	-	-	-	-0.15	-	-
9.40	22	-	-	-	-	-	-0.49	0.36	-	0.76

-: Absolute Value Less Than 0.10

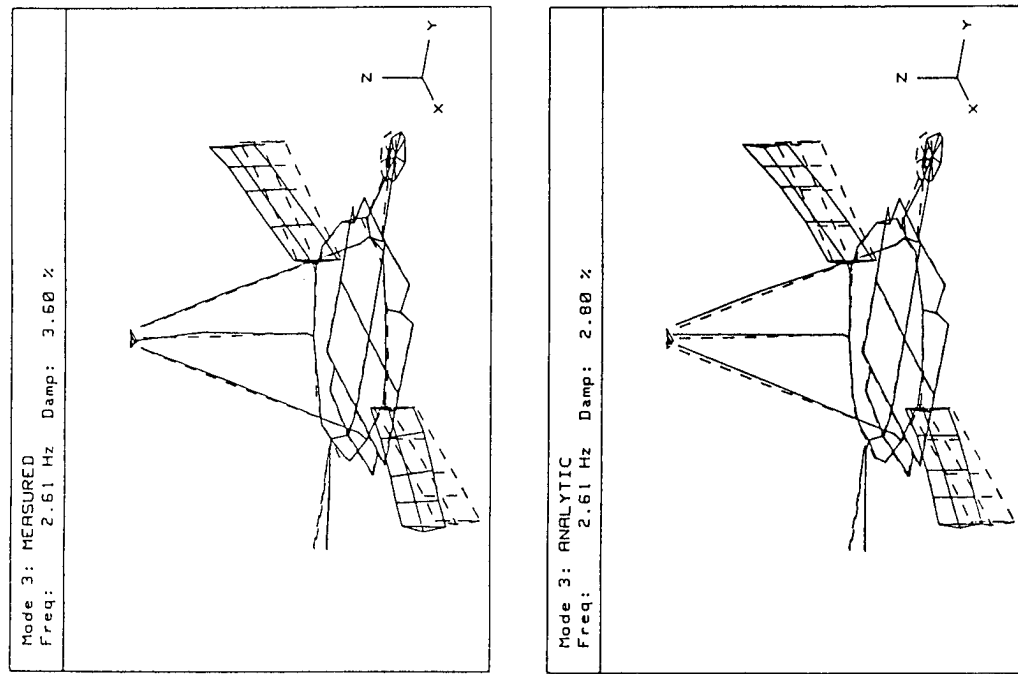


Figure 13(a) Measured Mode 3 and Analytic Mode 3

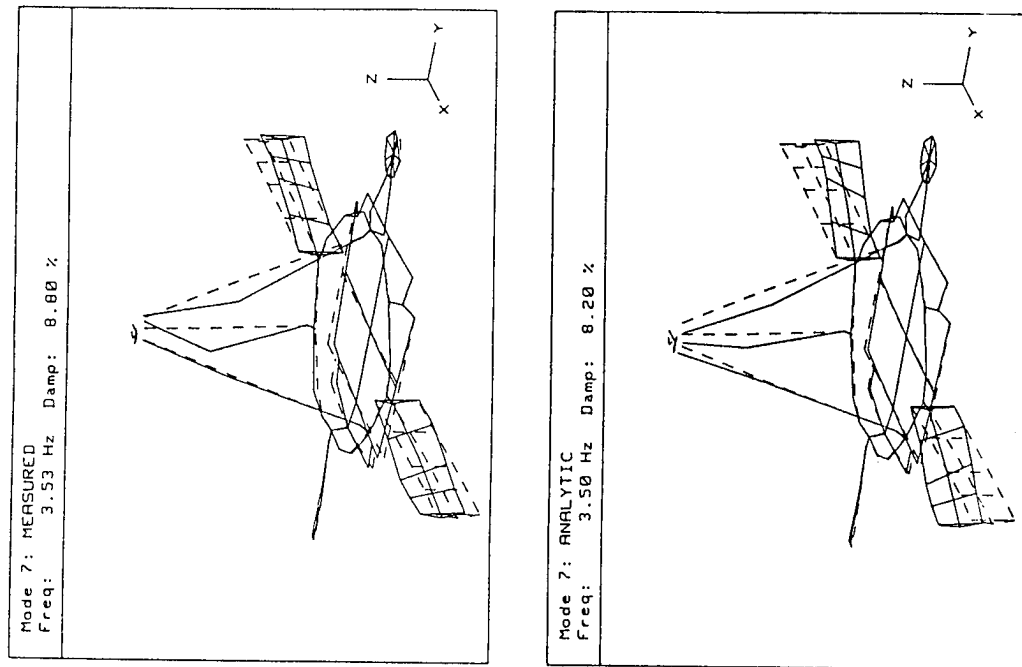


Figure 13(b) Measured Mode 7 and Analytic Mode 7

The correlation between the measured and analytically predicted modes is exceptional considering the dynamic complexity of the DTA. All global modes were predicted accurately in terms of frequency and damping. However, the orthogonality products show significant coupling between similar modes. Consideration of both the generalized mass and cross orthogonality products gives an indication of the source of error. Some experimentally synthesized modes appear to be quite accurate while others possess error due to the identification difficulties previously discussed.

For example, experimental modes 6 and 7 (see Table 2) exhibit little coupling in the self orthogonality product, (Table 3). However, there is significant coupling on the order of 30% with their analytic counterparts as shown by Table 4. Together, these observations indicate that these two particular experimental modes are accurate estimates of the true behavior of the DTA. Other factors such as repeatability and small phase error also indicate that the 3.25 Hz and 3.53 Hz modes were accurately identified. Thus, the coupling of terms corresponding to these modes in the cross orthogonality product is attributable to some physical difference between the actual DTA and the finite element model. Comparison of a measured FRF with the corresponding analytic prediction (Figure 14) confirms that the structure behaves somewhat differently in the 3 to 4 Hz range due to these modes. Note that modes 6 and 7 are both antisymmetric, global modes which are rather closely spaced in terms of frequency considering the damping present. Modes such as these can be quite sensitive to small variations in the structure and thus are difficult to precisely predict.

Examples of modes not accurately identified are measured modes 4 and 5. The presence of nearby, highly damped TMD / blanket modes, and noisy TMD measurements, made consistent parameter estimation of these modes impossible using the RFP technique previously mentioned. This is indicated by the variation shown in Table 1. Thus, the relatively poor orthogonality results for these two modes are primarily due to error in the measured mode shapes. However, as shown in Figure 15, comparison of analytic and measured FRFs indicates that while the behavior is similar, there is a definite frequency difference between the analytic model and actual DTA in the 2 to 3 Hz range. This must be due to a modeling error.

Overall, the agreement between measured and predicted DTA modal parameters is excellent. This is shown by agreement of modal frequencies and damping ratios, and demonstrated by comparison of measured and predicted FRFs. Coupling in the orthogonality products is primarily due to parameter identification difficulties traceable to the algorithms used on the measured data. Use of more sophisticated techniques may improve the synthesized mode shapes and thereby the orthogonality products.

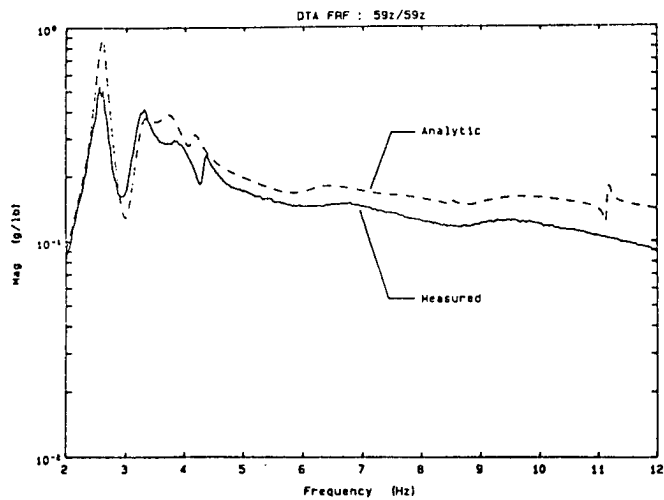


Figure 14 Measured and Analytic FRFs:
59z/59z

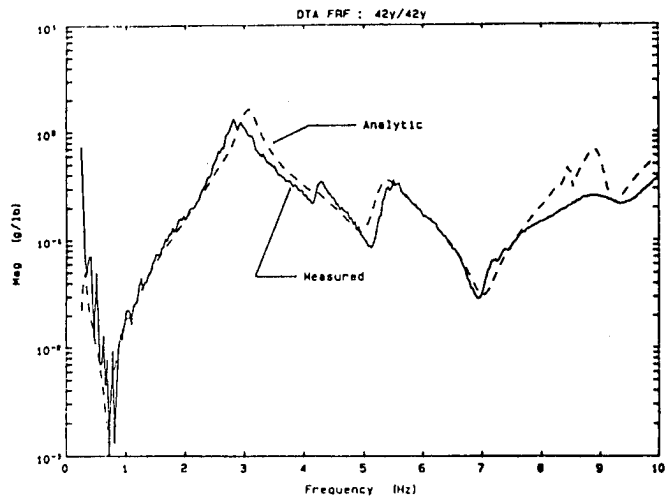


Figure 15 Measured and Analytic FRFs:
42z/42z

CONTROL SYSTEM PERFORMANCE

Investigation of the DTA active damping system performance was conducted by performing the same tests as in open-loop cases but with the control system on, and feedback gains set to design values. Analysis of the local velocity feedback system was accomplished by coupling the actuator dynamics and feedback gains to the DTA modal model. The active damping system consisted of six proof mass actuators mounted on the DTA ring truss at the locations shown in Figure 16. These locations were selected in order to actively damp the 2.6 Hz DTA mode. Figure 17 shows a photo of two actuators attached to the ring truss. The control law applied to the DTA was local direct velocity feedback where the inertial velocity at a control point is fed back to apply a proportional force opposite the velocity. Ideally, this force appears as a dashpot to ground on the structure. Feedback gain settings were selected such that the active control system would apply 5% modal damping to the 2.6 Hz mode (in addition to the passive damping present). Besides the inertial velocity feedback, relative velocity between the proof mass and housing was sensed and fed back in order to adjust the local damping of the actuator second order system.

Table 5 lists the actual feedback settings used in the closed-loop tests. Analysis predicted that the control system would apply significant damping to four modes in the 1 to 10 Hz range. Fitting of the data from the tests confirmed the increased damping in four modes with all other modes not significantly affected.

The design feedback levels and actuator dynamics were coupled to the tuned DTA modes in order to predict the closed-loop damping. Table 6 lists the predicted closed-loop damping ratios together with the corresponding range of measured values for the four actively controlled modes. Again, variation in the damping estimates was seen depending on fit method. The data demonstrate that the control system, while functioning as expected, had somewhat less authority in the 2.6 Hz mode than predicted. This was due to a somewhat smaller modal amplitude at the control points than predicted.

Comparison of predicted to measured FRFs at the control points showed good qualitative agreement and verified that the control system was behaving as predicted. Figure 18 presents the measured and predicted FRFs at control point 3. Note the very low levels of the transfer functions which, in the modal survey test, resulted in RMS accelerations on the order of 0.005 g's. Even with these low acceleration levels, the control system performed well, indicating that friction in the actuators was not a factor in the testing. At points of higher response such as the solar array tip, the desired effect of actively lowering the response of the 2.6 Hz mode was achieved. This is shown by Figures 19 and 20 which present the open- and closed-loop FRF and decay trace respectively, at the solar array tip.

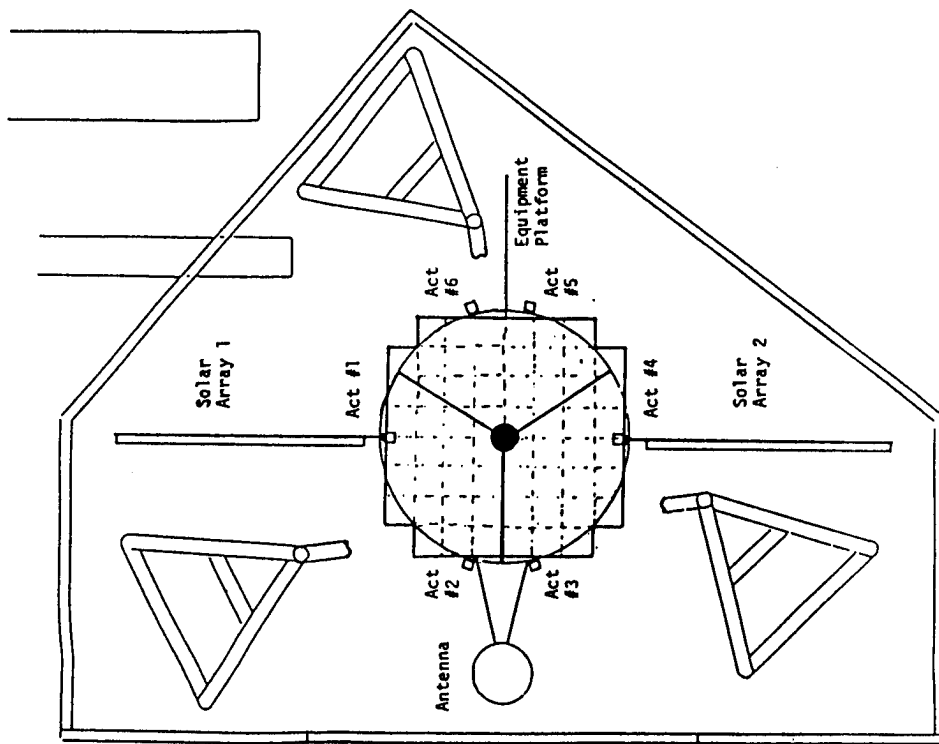


Figure 16 DTA Actuator Locations

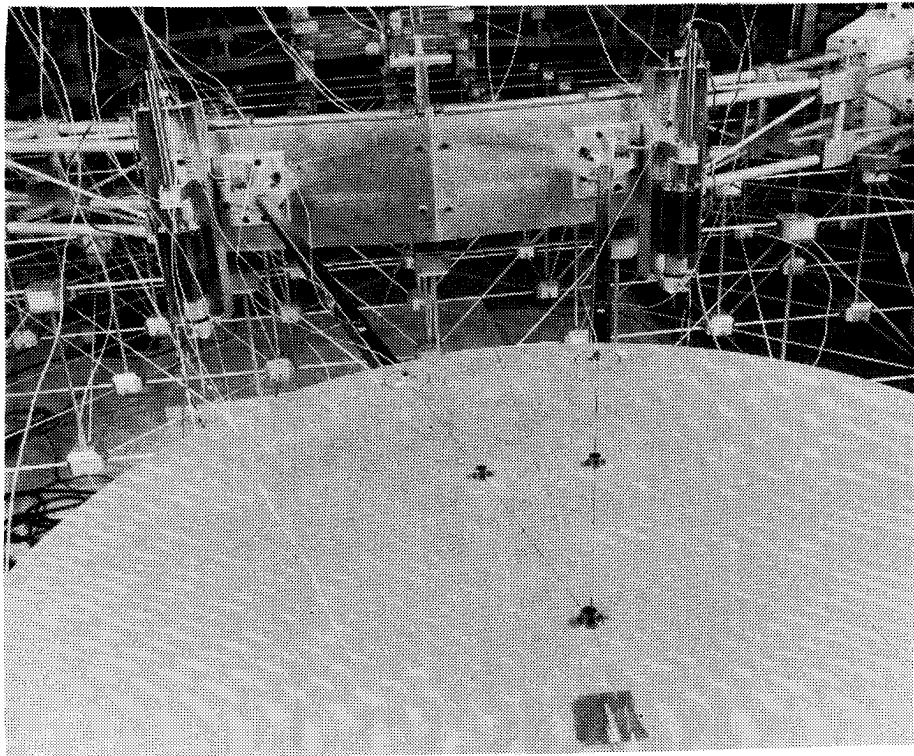


Figure 17 Actuators Mounted on DTA

Table 5 Feedback Gain Settings

RELATIVE VELOCITY FEEDBACK SETTINGS		INERTIAL VELOCITY FEEDBACK SETTINGS	
(%)	(ζ_a %)	(%)	(lb-sec/in.)
50	38	89	4.6
22	20	65	3.5
25	20	74	3.5
50	38	84	4.6
25	20	70	3.5
27	20	69	3.5

Table 6 Closed-Loop Results

TARGET MODE NO.	f_n (Hz)		ζ (%)	
	ANALYTIC	MEASURED RANGE	ANALYTIC	MEASURED RANGE
3	2.54	2.51 → 2.60	8.1	6.7 → 8.1
13	4.67	4.91 → 5.05	15.7	13.0 → 16.0
17	5.96	6.35 → 6.40	17.8	15.1 → 19.6
22	9.20	8.94 → 9.38	11.7	12.8 → 13.1

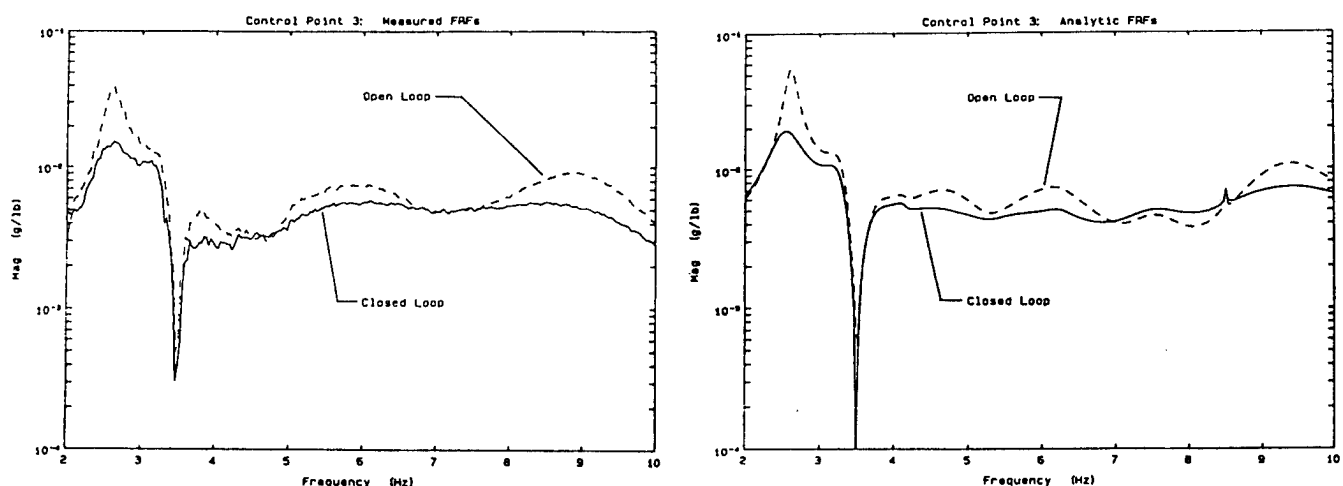


Figure 18 Open- and Closed-Loop FRFs at Control Point 3

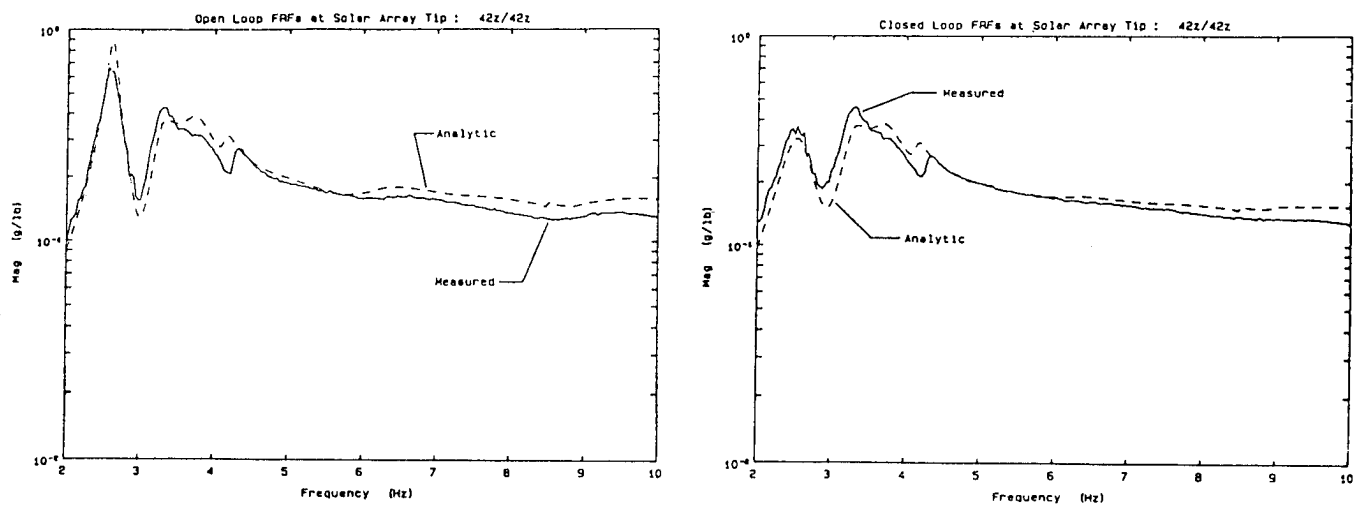


Figure 19 Open- and Closed-Loop FRFs at Solar Array Tip

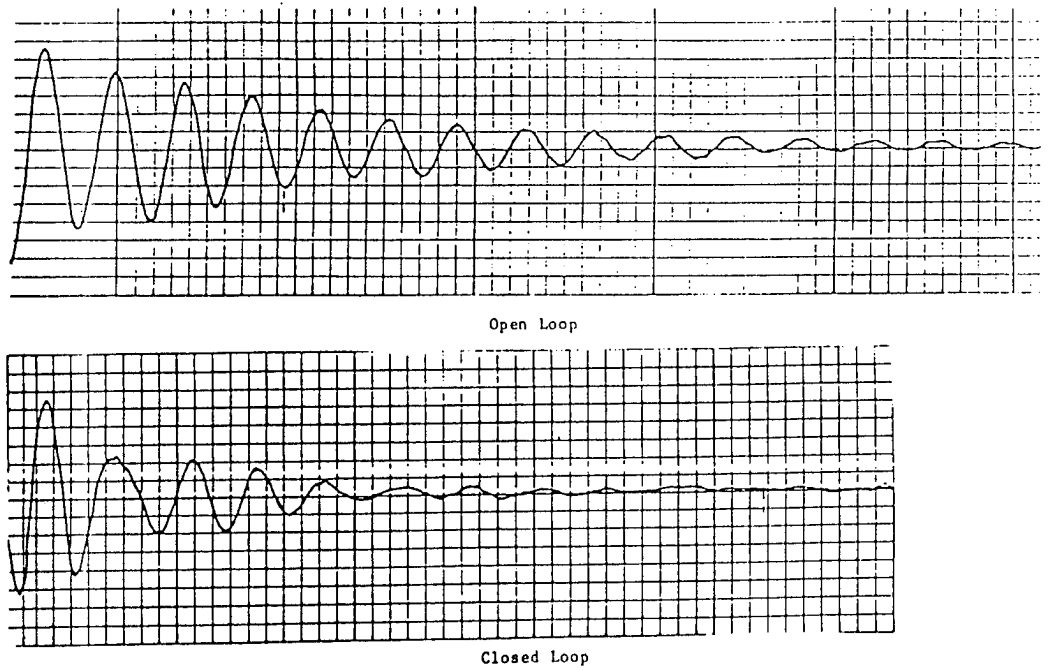


Figure 20 Open- and Closed- Loop Decay Traces

CONCLUSIONS

The modal survey of the Dynamic Test Article (DTA) achieved the goal of identifying all significant structural modes in the 1 to 10 Hz frequency range of interest. The test chamber, test setup, and data acquisition system allowed acquisition of a large volume of data at nearly constant temperature, thereby avoiding temperature dependent viscoelastic material property variations. Data quality was very good at excitation points and points of high response level. Also, measurements were repeatable and indicated nearly symmetric behavior of the DTA. During testing, excitation levels were such that many measurements were of too low a level to obtain quality data with the available instrumentation. However, the low response levels correspond to small modal amplitudes and thus are not very important in terms of synthesized mode shape accuracy. Nonetheless, future testing will be improved by using very low noise instrumentation which is good down to 1 Hz.

Parameter identification performed on the measured data was very successful in consistently estimating 11 of the 22 target modes, while achieving moderate accuracy for another 9 modes. However, because of the closely spaced, highly damped character of the DTA modes, significant variation of modal parameters, particularly damping and residues, was seen for several modes. Only two modes were relatively poorly identified. This experience points to the need for application of more sophisticated parameter identification techniques to the DTA data, and perhaps some theoretical development or tailoring of methods specifically for this type of problem. Also, the effect of real world concerns such as noise and nonlinearity in the data, and small phase errors due to instrumentation must be assessed and, if possible, accounted for.

Other issues of concern were control system performance and behavior of the TMDs on the solar arrays. The active control implementation functioned well in concert with the passive damping and produced the expected results. With regard to the TMDs, the particular tuned mass damper design used on the solar array blankets behaved nonlinearly and thereby degraded some measurements. However, the TMD design did successfully damp the blanket modes.

Overall, agreement between the measured and analytic modal parameters is exceptionally good. The DTA is the most dynamically complicated, damped structure to be rigorously modeled and tested, yet the correlation of results is better than achieved in most modal surveys. Perhaps more important than achieving precise agreement with the analysis is the fact that targeted damping levels can indeed be successfully designed into the fundamental modes of complex structures. This was accomplished using both discrete and distributed passive damping approaches.

On a system level, the DTA modal survey demonstrated that high levels of passive damping can be predictably designed into the dynamically complex structures characteristic of future large space systems. Further, passive damping will allow a relatively simple active control system to be focused on only a few modes while greatly improving performance. The demonstrated achievable damping levels will perform quite effectively in improving the dynamic performance of the structure in terms of settling and jitter response. This is shown by Figure 21 which compares open and closed loop line of sight (LOS) transfer functions to that predicted if the DTA possessed the nominal damping of 0.2% (a level typical of precision structures). Benefits to the overall system include reliable, robust performance with lower weight at possible lower cost compared to approaches not using passive damping.

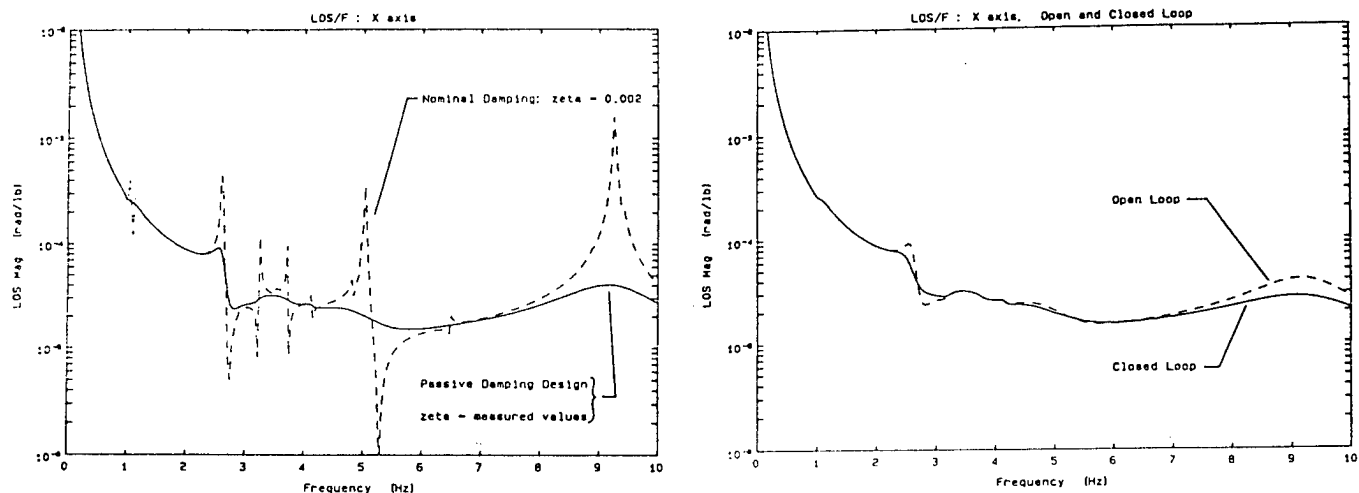


Figure 21 LOS Transfer Functions

ACKNOWLEDGMENT

This work was supported by the Air Force Wright Aeronautical Laboratories under the Passive and Active Control of Space Structures (PACOSS) program, Contract Number F33615-82-C-3222.

REFERENCES

1. Morgenthaler, D. R., and Gehling, R. N., "Design and Analysis of the PACOSS Representative System," Damping 1986 Proceedings, AFWAL-TR-86-3059, Las Vegas, Nevada, 5-7 March 1986.
2. Morgenthaler, D. R., "Passive and Active Damping Techniques Applied to the PACOSS Representative System," to be presented at Damping 1989 Conference, West Palm Beach, Florida, 8-10 February 1989.
3. Morgenthaler, D. R., "Design and Analysis of Passively Damped Large Space Structures," The Role of Damping in Vibration and Noise Control, 1987 ASME Conference on Mechanical Vibration and Noise, Boston, Massachusetts, 27-30 September 1987.
4. Gehling, R. N., "Large Space Structure Damping Treatment Performance," The Role of Damping in Vibration and Noise Control, 1987 ASME Conference on Mechanical Vibration and Noise, Boston, Massachusetts, 27-30 September 1987.
5. Richardson, M. H., and Formenti, D. L., "Parameter Estimation from Frequency Response Measurements Using Rational Fraction Polynomials," 1st International Modal Analysis Conference, Orlando, Florida, November 8-10, 1982.
6. Johnson, C. D., Kienholz, D. A., and Rogers, L. C., "Finite Element Prediction of Damping in Beams with Constrained Viscoelastic Layers," Shock and Vibration Bulletin, No. 50K, Part 1, May 1981.

APPLICATION OF PASSIVE AND ACTIVE DAMPING
TECHNIQUES TO THE PACOSS REPRESENTATIVE SYSTEM

Daniel R. Morgenthaler

Martin Marietta Astronautics Group
Denver, Colorado 80201

ABSTRACT

This paper presents the results of a study performed on the Passive and Active Control of Space Structures (PACOSS) Representative System Article (RSA). The RSA is a representative large space structure (LSS) with optical components inherent in its design. The study examines methods of achieving a performance goal for a slew maneuver of the RSA generated by an attitude control system. In order to achieve a prescribed goal for the slew, damping is added to the flexible structural modes. Two damping approaches are considered: active control alone, and the passive/active damping design approach utilized on the PACOSS program. Quantitative estimates of the properties of the damped systems generated using the two approaches are compared. The passive/active approach is seen to result in a much more efficient overall system design. Even using assumptions which favor the active control component, the passive/active design methodology resulted in nearly 25% less added weight due to active and/or passive control measures. Also, a 97% savings in active control energy, and a simpler and more reliable overall system were achieved.

INTRODUCTION

Future military and civilian space systems will typically be very large but lightweight. These characteristics lead to dense modal spectra at low frequencies which often will overlap attitude control bandwidths. The mission profiles of these systems also require low vibration levels of critical components in order to meet mission goals. The PACOSS RSA design (Figure 1) is based on a survey of planned and conceptual space systems required to meet specific mission objectives. This survey revealed extensive requirements for relatively large, lightweight structures possessing the ability for precise pointing and, in some instances, rapid retargeting. The survey included consideration of both military and civilian system concepts, and disturbances affecting such systems. Further details of the mission survey, RSA configuration, and system design are given in several publications (References 1,2,3).

The configuration of the RSA is not mission specific but a representation of several missions and requirements in one system. The RSA reflects the mission requirements of first generation LSS, and it is assumed that its mission would utilize the reflecting surfaces inherent in its design in an optical, infrared, or communication system. The analysis and design results, therefore, are representative of systems with similar reflecting components and other systems with requirements for vibration control.

There are essentially two design methodologies which can be used to reduce structural vibrations: active control and passive damping. This study examines the system properties following application of active damping to the RSA using velocity feedback and also following application of both passive and active damping in an integrated methodology. A summary of the methodology is given in Reference 4.

The RSA is a symmetric structure, facilitating uncoupled control systems for pitch and roll-yaw motions. This study considered only symmetric (pitch) dynamics, and damping design was only considered for modes which degrade slew

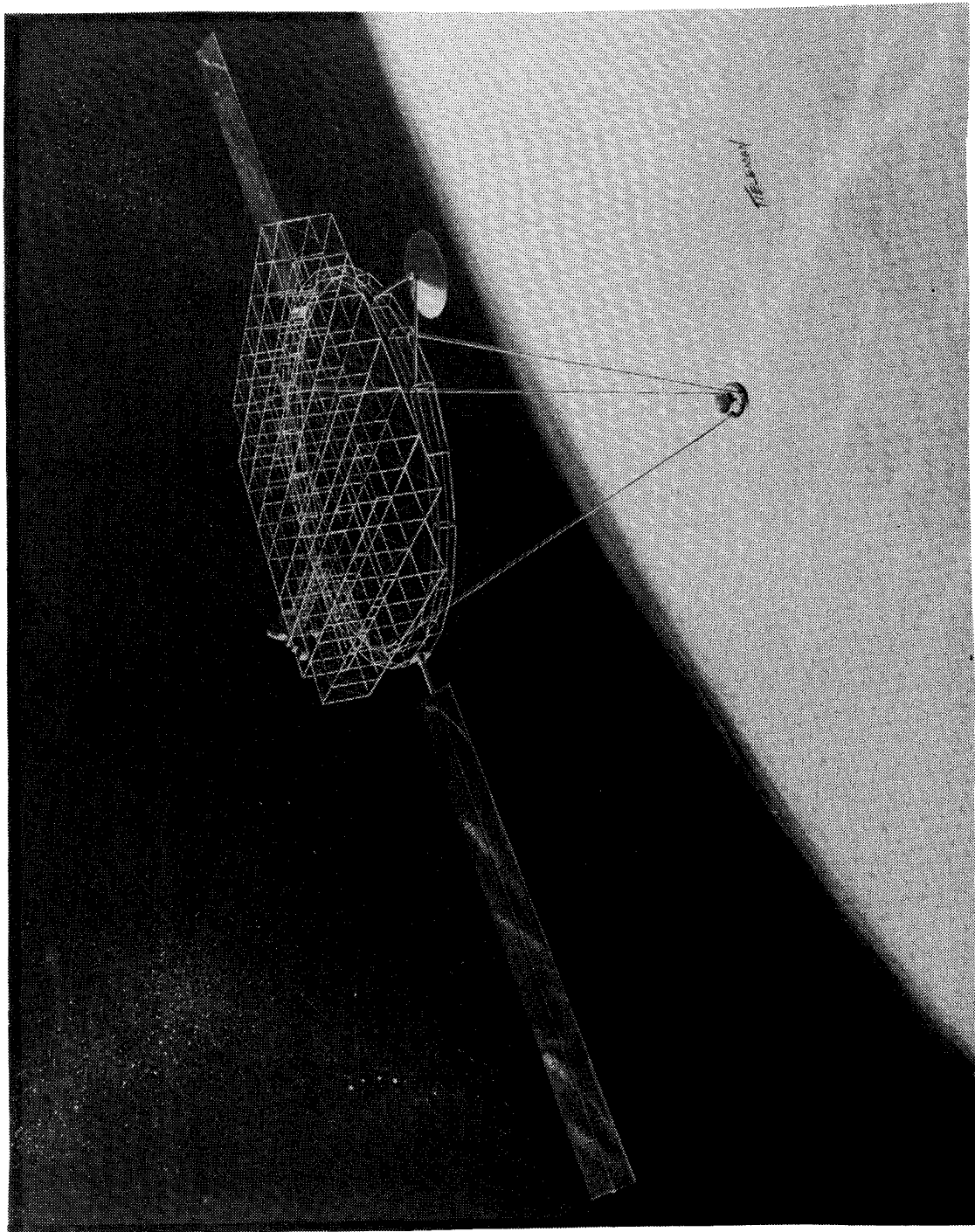


Figure 1 - PACOSS Representative System (RSA)

KCD-2

performance for this axis. The methodology and results would be similar if roll-yaw dynamics were considered.

RSA Configuration and Performance Measure

The RSA consists of seven substructures, each with a specific function to perform to meet mission goals. Table 1 contains a description of the various components and future systems to which these substructures are traceable. The sizes of components can be considered representative of a typical spacecraft. Weight and stress constraints were not considered, but strain energy distributions were adjusted to produce a reasonably weight efficient design while accommodating passive damping treatments.

Table 1 - RSA Component Overview

COMPONENT	DIMENSION (m)	MASS (kg)	FUNCTION	APPLICABLE SYSTEMS
1) Box Truss	20x20x2.5	2295	Primary reflecting surface support and/or spacecraft subsystem carrier	Space Based Radar Large Earth Observing System Mobile Communications Satellite Space Station
2) Ring Truss	Diameter: 22.4	1113	Central support hub: ties system component together	Generic Truss Structure
3) Tripod	Diameter of Base: 20 Height: 20	840	Secondary reflecting surface support	Space Based Laser Large Deployable Reflector
4) Equip. Platform	Length: 10	2634	Support/isolate sensitive equipment or experiments away from main structure	Space Station Strategic Defense Initiative (SDI)
5) Antenna	Diameter: 5	345	Earth communications: command and control	Space Base Radar Space Station Satellites
6, Solar 7) Arrays	Length: 20	786	Power generation, sized for 20 kW	Space Based Radar Space Station Satellites

A Cassegrain optical system is contained in the baseline RSA design, consisting of reflecting surfaces located on box truss and tripod structures. Of primary interest to the overall performance of this system is the instantaneous pointing angle of the optical system or line-of-sight (LOS). The mathematical definition of the LOS is given in Figure 2. The LOS is written relative to the rotation of a reference sensor in this definition.

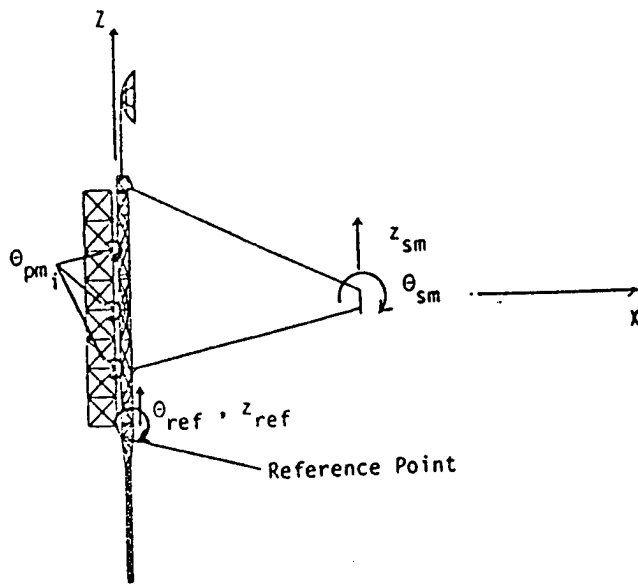
RSA Performance Goal and Attitude Control System

The major disturbance source for the RSA was assumed to be a maneuvering of the vehicle in order to repoint the optical system. The torques necessary to slew the spacecraft were generated by an attitude control system using four torque wheels mounted on the structure. The design of the attitude control was conceived to be simple but characteristic of those which will be used on first generation LSS. The attitude control system is discussed in detail in Reference 2. The disturbance source considered was a small angle slew (0.01 rad) generated by the attitude control.

The attitude control system uses angular rate and position feedback to eliminate pointing errors relative to a target angle. The control design consisted of selecting feedback gains and filter characteristics to achieve acceptable closed-loop slew performance which while minimizing structural vibration and remaining within slew acceleration limits. These parameters for the control system are included on Figure 3, along with the attitude control actuator locations and a block diagram. The resulting closed-loop rigid body frequency and damping were approximately 0.50 Hz and 0.707, respectively.

The baseline system also included an actuator to control the secondary mirror angle which was gimballed from its support structure on the tripod. Feedback gains were selected such that the closed-loop frequency and damping of the mode consisting of rotation of the secondary mirror on its support were 0.50 Hz and 0.707, respectively. These gains produced acceptable response of the mirror for slew maneuvering while uncoupling mirror rotation from higher frequency disturbances.

The figure of merit utilized for evaluation of the system's performance for the slew maneuver was settling time. This is a measure of the time required for the system to return to a state where it may operate satisfactorily following the transient disturbance. For spacecraft slew maneuvers, typically a maximum angular acceleration is available (or allowable) and fast settling time following conclusion of the maneuver is the goal. For the RSA, 0.1 rad/sec² was considered as the angular acceleration limit. The goal under for the slew maneuver was to settle within 1.0 second of maneuver completion to below a 50 micro-rad error to target. A summary of the slew maneuver and performance goals are included in Table 2.



$$LOS_y = \left(2 \frac{f_s}{f_p} - 1\right) \theta_{ref} + \frac{2}{13} \sum_{i=1}^{13} \theta_{pm_i} - 2 \frac{f_s}{f_p} \theta_{sm} - \frac{1}{f_p} (z_{ref} - z_{sm}) flex$$

Where,

f_s = Focal length of secondary mirror

f_p = Focal length of primary mirror

$(z_{ref} - z_{sm}) flex$ = Relative z deflection of secondary mirror to reference point due to structural deformation

NOTES:

Sum over θ_{pm_i} represents an average primary mirror deformation

LOS about z-axis has sign change on relative translation term;

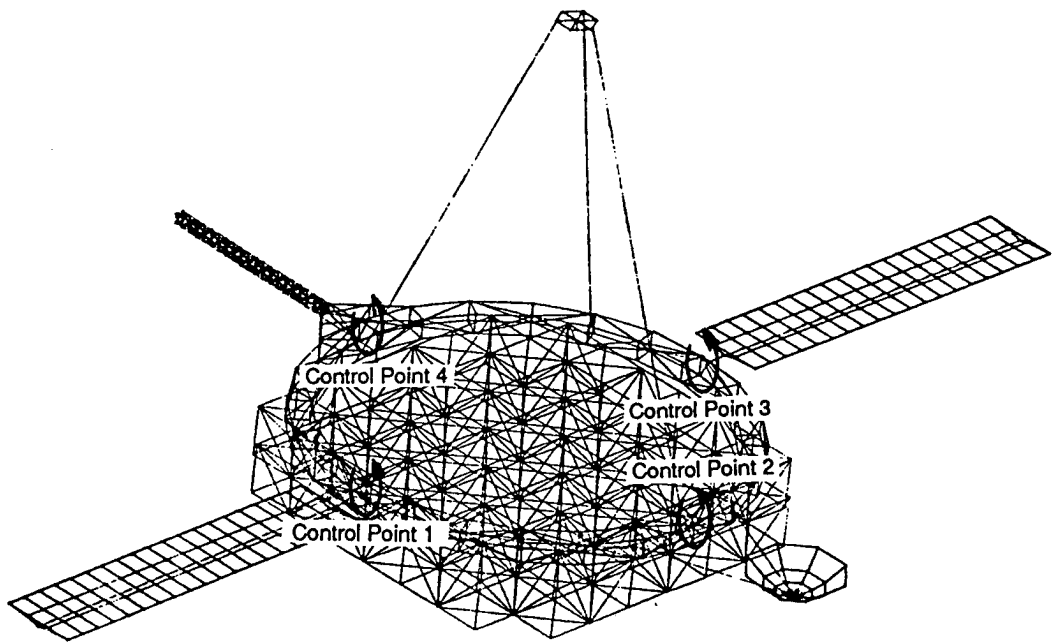
$$-\frac{1}{f_p} (z_{ref} - z_{sm}) flex \Rightarrow +\frac{1}{f_p} (y_{ref} - y_{sm}) flex$$

Relative LOS is defined as : Inertial LOS - Rigid Body Motion

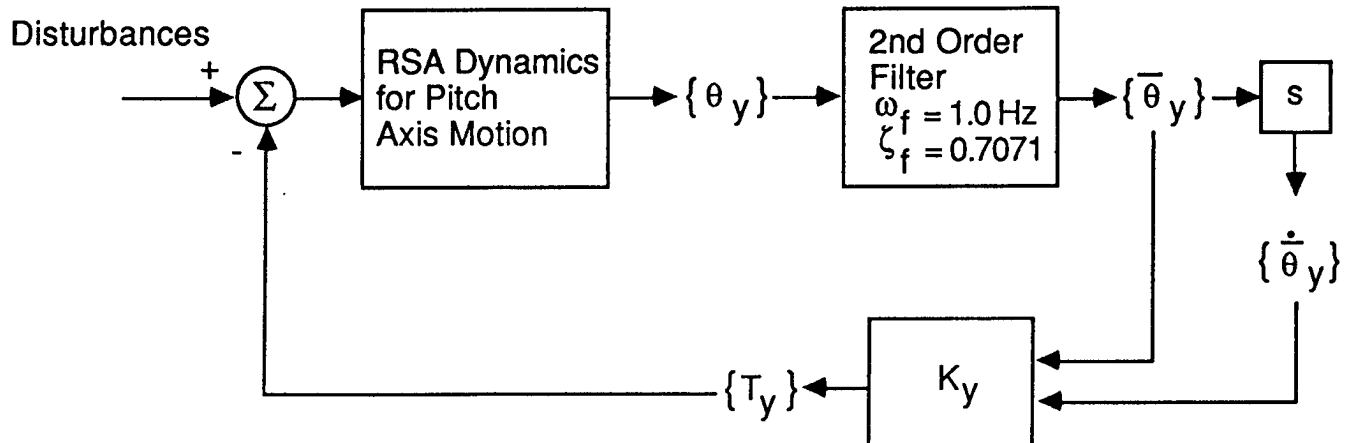
Figure 2 - LOS Mathematical Definition

Table 2 - RSA Performance Goals for Slew

DISTURBANCE	DISTURBANCE VALUES	GOAL FOR PERFORMANCE
Spacecraft slew maneuver	0.01 rad slew with 0.1 rad/sec ² maximum angular acceleration	Pointing error settle to within 50 μrad within 1 sec of slew completion



Note: Inertial reference sensor is located at Control Point 4



$$\{T_y\} = [2.12 \times 10^6 \quad 1.91 \times 10^6] \begin{Bmatrix} \bar{\theta}_y \\ \dot{\bar{\theta}}_y \end{Bmatrix}$$

where:

T_y = attitude control torque
(1/4 of this applied at each control point)

$\bar{\theta}_y$ = pitch target angle error at reference sensor

$\dot{\bar{\theta}}_y$ = filtered angle error signal

$\ddot{\bar{\theta}}_y$ = filtered angle error signal rate

Figure 3 Attitude Control System Block Diagram
and Torque Wheel Locations

RSA Baseline Model

Analysis of the RSA system required a model of the structure and associated hardware. Passive damping analysis required a relatively detailed finite element model to allow subsequent Modal Strain Energy (MSE) distribution calculations. The finite element modeling and analysis was performed using the MSC/NASTRAN program.

Component mode synthesis was used to compute the frequencies, mode shapes and strain energy distribution of the RSA model. A total of 210 system modes were found to be present in the frequency range of interest (0-10 Hz). Many of these modes involve local solar array motion at very low frequencies. System modes which are global in character are likely to be important in attitude control and performance evaluation. A relatively high number of RSA system modes are global; that is, several components possess significant kinetic and potential (strain) energy in a given system mode. This characteristic of the RSA, and future LSS, will complicate the control design process.

Candidate passive damping treatments and member sets to be damped were selected during the modeling process, and these are given in Table 3. The final member sizes are such that high strain energy is contained in the selected member sets for global system modes. From the strain energy distributions in these global modes it was apparent that modes with high box truss participation possessed a high percentage of strain energy in the diagonals. Similarly, modes with high tripod participation had high energy in the tripod legs. These distributions allowed for the efficient application of passive damping treatments to damp these important global modes.

Table 3 - Selected Component Damping Treatment Types

COMPONENT	POSSIBLE TREATMENTS
Box Truss	Extensional shear damper with static load capability (diagonals)
Ring Truss	None
Tripod	Constrained layer treatment (legs)
Equipment Platform	Extensional shear damper (diagonals)
Antenna	Constrained layer treatment (legs)
Solar Arrays	Constrained layer treatment (blanket hinge lines)

Baseline Structural Performance

In order to determine the performance of the baseline system and also modes requiring passive or active damping, a slew maneuver of the system was simulated. The modes which could couple significantly with the attitude control were selected for use in the analysis, as were flexible modes which were important for LOS analysis. The modal LOS was calculated using the definition of the LOS and the values of the translations and rotations of the appropriate points in the mode shapes.

Closed-loop poles for the flexible system coupled to the previously described control system were calculated assuming 0.2% modal viscous damping (a damping level characteristic of precision large space structures), and including 25 flexible modes. Table 4 lists the natural frequencies and damping ratios of the baseline closed-loop system including these modes. The effects of truncation were examined, and these modes were determined to be a sufficient set to characterize spillover and coupling between the attitude control system while providing accurate LOS simulation.

Because the closed loop system was unstable, the open-loop damping levels of those modes which were driven unstable (modes 129, 158, and 201) were increased to a level such that the closed loop damping of these modes was the nominal value of 0.2%. This system was used to compute the nominal performance. The slew response of the stabilized closed loop system for a pitch axis maneuver was generated and is given in Figure 4. Notice that the response involves several modes and has a lengthy settling time. The time to complete the slew maneuver if the RSA were a rigid body is approximately 3.25 seconds. After 1.0 seconds following the rigid body maneuver time, the baseline system "settles" to within an error of 4.5×10^{-4} radians as shown in the figure. This exceeds the goal level of 50 micro-radians by a factor of 10. The time required for this system to settle to the 50 micro-radian level is approximately 230 seconds.

Required Damping and Achievable Passive Damping Estimates

The damping levels required to meet the design goals for the slew maneuver may be selected in many different ways, which will in general result in damping the various modes to differing levels. For this study, damping levels based on modal settling times were used.

In order to calculate the required damping ratios for each mode, the LOS response of the system was decomposed into its various modal contributions. The settling time for the individual modes was taken to be the time required for the amplitude of the modal response to fall below the error bound of 50 micro-radians. As a preliminary step in determining the required damping levels, the attitude control torque as a function of time for a rigid RSA was generated and applied to the open loop RSA. Similarly, modal settling times were calculated for the nominal system with the attitude control loop closed. Table 5 contains a list of the modes with individual settling times greater than the settling time of 1.0 sec for these two cases.

Table 4 Natural Frequencies and Damping Values for
Nominal System With Attitude Control Loop Closed

SYSTEM MODE #	OPEN LOOP		CLOSED LOOP	
	f_n (Hz)	ζ (%)	f_n (Hz)	ζ (%)
Rigid Body	0	0	0.46	60.1
Filter	1.0	70.7	0.54	81.3
7	0.01	0.2	0.50	70.7
21	0.69		0.65	0.22
23	0.73		0.77	1.72
30	1.02		0.96	1.45
32	1.02		1.02	0.20
44	1.50		1.49	0.62
48	1.53		1.51	0.75
118	2.72		2.72	0.20
124	2.78		2.78	0.45
129	2.86		2.87	-0.15
158	4.03		4.04	-0.05
165	4.21		4.22	0.17
176	4.38		4.38	0.20
182	4.55		4.55	0.16
185	5.11		5.12	0.08
187	5.68		5.68	0.16
188	5.81		5.81	0.20
191	6.45		6.45	0.10
192	6.49		6.49	0.20
196	6.96		6.96	0.18
198	7.15		7.15	0.18
199	7.31		7.31	0.15
201	7.38		7.38	-0.10
206	8.77		8.77	0.02
209	9.53	0.2	9.53	0.02

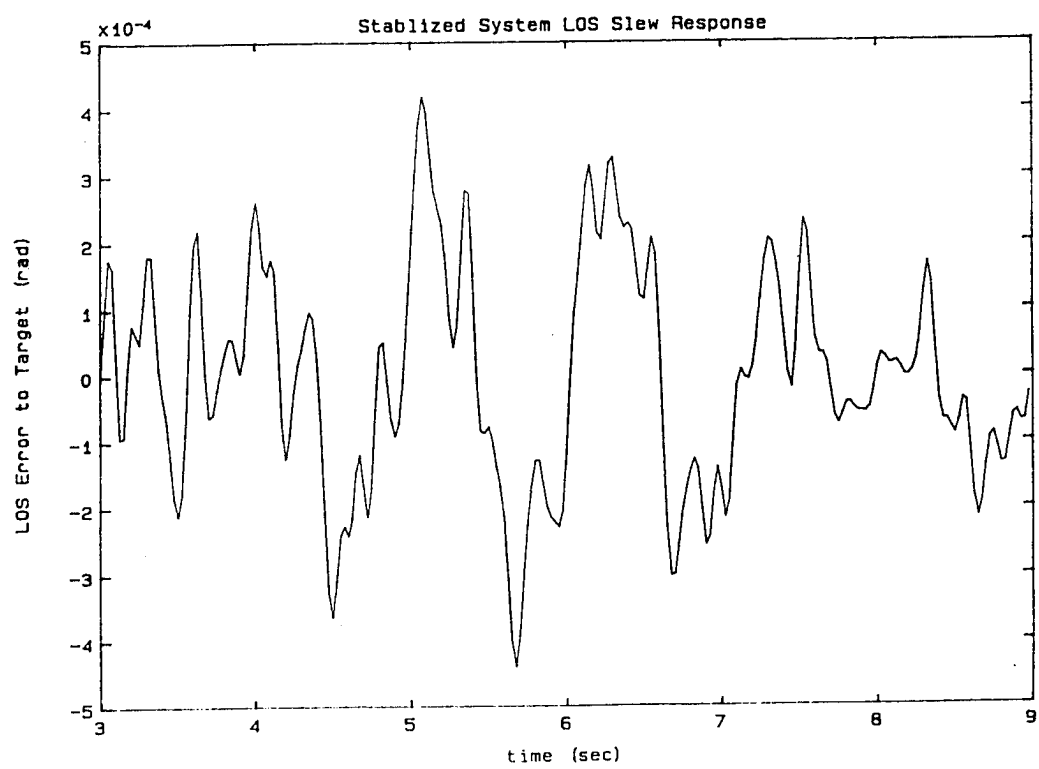
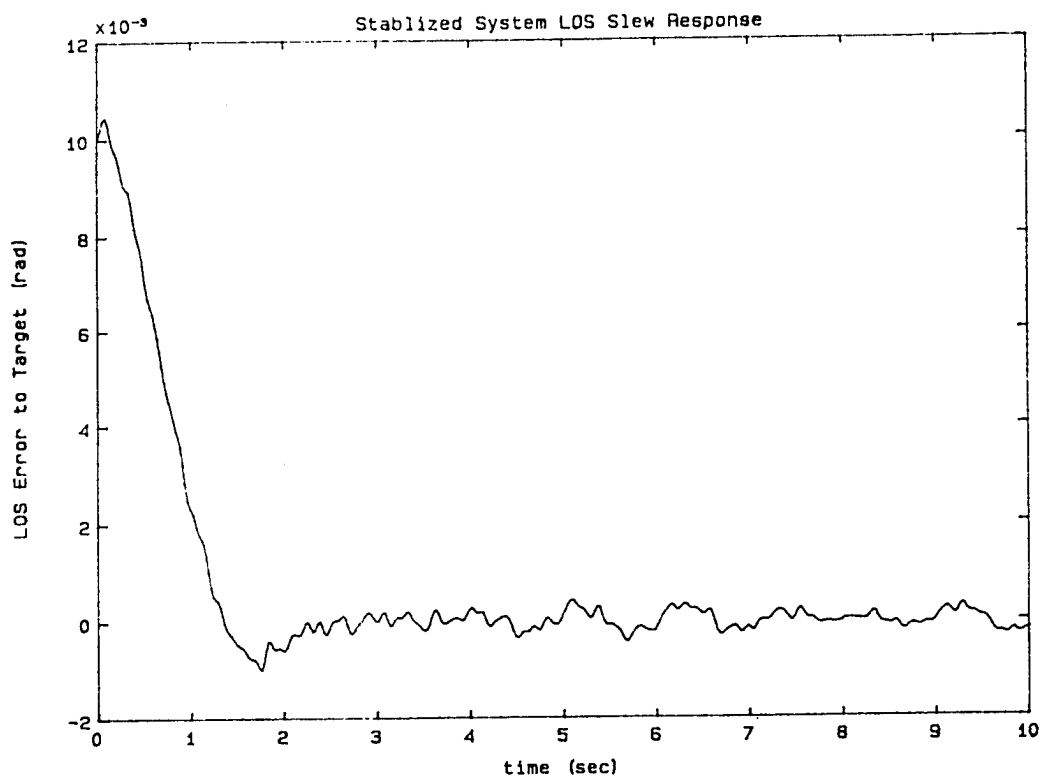


Figure 4 -- Baseline System LOS Slew Response

KCD~ 10

Table 5 - Modes with High Settling Time
for Baseline System

SYSTEM MODE NO.	SETTLING TIME FOR RIGID RSA TORQUE (sec)	SETTLING TIME FOR STABILIZED BASELINE CLOSED-LOOP SYSTEM (sec)
30	357	244
23	326	174
32	171	84
124	84	73
129	75	68
158	48	49
185	24	26
201	20	24
209	11	14
48	7	5
21	6	0
191	5	3
187	5	4
199	3	8
206	2	3

To find preliminary damping levels for each individual mode, the damping levels were determined so that each mode settle to within the 50 micro-radians minus a margin to allow for the addition of other modal responses at their corresponding phase angles. The modal damping values which caused the individual modes to meet the settling criterion value were calculated by iteration.

Because the responses of modes which are controllable and observable by the attitude control alter the control torque, the response of any mode was dependent on the damping of all other modes. To include these effects, the attitude control system was coupled to the flexible system using the damping levels selected as explained previously. The damping levels were then iteratively adjusted such that the closed-loop modal settling times were equal for all modes requiring damping augmentation, and the system response just met the performance goals.

The required damping levels for the targeted modes based on the above criterion are included in Table 6. Notice that there are two low frequency modes (modes 23 and 30) which are within the controller bandwidth that require high damping levels, and many modes which require low levels of damping augmentation. The modes which require high damping augmentation and have high modal settling times are the system target modes (modes 23, 30, 32, 124, 129, 158, 185, 201, and 209). These modes were specifically targeted for damping augmentation. Modes which require only low damping levels can be considered the observable modes. Most of these modes do not

Table 6 - Modal Damping Levels Selected for Modes
with High Settling Time

Mode No.	Freq. (Hz)	Req'd. (%)
23	0.73	11.0
30	1.02	12.0
32	1.03	3.0
48	1.53	1.0
124	2.8	4.0
129	2.9	4.0
158	4.0	2.5
165	4.2	1.0
182	4.5	1.0
185	5.1	2.0
187	5.7	1.0
191	6.5	1.0
196	7.0	1.0
198	7.1	0.5
199	7.3	0.5
201	7.4	1.5
206	8.8	1.0
209	9.4	1.5

have settling values above the goal, but their responses are large enough when undamped that they can add with the targets to produce a slew response which does not meet the goal. The damping levels given in Table 6 imply that passive damping could greatly benefit the system, as only low to moderate levels of damping are required for a majority of the system modes.

The passive damping which may be designed into the structure using the treatments on Table 3 can be found using the modal strain energy method. In order to facilitate estimates, the modal strain energy method was utilized in the form:

$$n_j = \sum_{i=1}^{nms} n_i * \%SE_{ij} * DEF_i$$

where:

- n_j = modal loss factor for jth mode
- $\%SE_{ij}$ = % strain energy in ith set of damped members in jth mode
- DEF_i = Assumed damping efficiency factor of ith set of damped members. Defined as the ratio of strain energy in viscoelastic used in treating the member to total member energy.
- nms = # of damped member sets

Representative damping efficiencies based on the treatment types, and experience using similar treatments on the PACOSS Dynamic Test Article (DTA) were used in the estimates (Reference 4). The DTA is a scale model of the RSA.

The calculated damping of the target modes based on assumed damping efficiencies and the modal strain energy distribution using these treatments was calculated assuming a viscoelastic loss factor of 0.7, which roughly corresponds to the value of the loss factor for acrylic foam tape at 1.0 Hz and 70 F. The damping attributable to treatment of the various components is given in Table 7, along with the maximum achievable damping using these treatments.

Notice that the required damping for all target modes may be obtained using the selected treatments except for system modes 23 and 30. This table shows that by applying treatments to damp the low frequency target modes, significant damping can be achieved in the higher frequency targets and observable modes. This "passive damping spillover" is an attractive benefit found in passive damping design.

Table 7 - Maximum Achievable Damping from Treatments by Component

Req'd. (%)	Mode No.	Freq. (Hz)	Achievable Modal Damping (%)					
			Box Diagonals	Truss Diagonals	Tripod Legs	Equipment Platform Diagonals	Antenna Legs	Solar Array Hinges
11.0	23	0.73	-	0.3	0.6	2.5	0.2	3.6
12.0	30	1.02	-	0.2	3.3	1.2	1.1	5.8
3.0	32	1.03	-	-	1.1	0.3	3.5	4.9
1.0	48	1.53	-	0.7	2.7	0.4	0.4	4.2
4.0	124	2.8	1.9	3.6	-	0.13	-	5.6
4.0	129	2.9	22.7	0.13	0.14	-	-	23.0
2.5	158	4.0	3.0	1.1	-	0.4	-	4.5
1.0	165	4.2	0.53	3.6	-	0.13	-	4.3
1.0	182	4.5	1.1	4.1	-	-	-	5.2
2.0	185	5.1	3.1	0.09	-	1.2	-	4.4
1.0	187	5.7	9.2	1.5	-	0.53	-	11.2
1.0	191	6.5	1.7	0.11	12.3	0.43	-	14.5
1.0	196	7.0	23.7	0.19	0.42	-	-	24.3
0.5	198	7.1	18.4	0.83	-	0.21	-	19.4
0.5	199	7.3	20.3	0.14	1.3	-	-	21.7
1.5	201	7.4	7.6	0.39	2.9	0.22	-	11.1
1.0	206	8.8	11.6	1.5	0.42	0.21	-	13.7
1.5	209	9.4	25.8	0.04	0.22	-	-	26.1

Control System Evaluation for Various Passive Levels

With the required modal damping levels known, a trade was examined between actively and passively achieving these levels. This trade allowed a reasonable selection of the mix of the two damping approaches based on the power requirements for the actuators and relative ease with which the required level of passive or active control could be incorporated.

In order to determine the effect of the passive and active damping levels on the system, an active control system was designed for various percentages of the maximum achievable passive damping levels given in Table 7. For example, a passive level of 50% achievable damping may be selected; this corresponds to using damping values of one-half those in the final column of Table 7. An active control system was then designed which augmented the target mode damping levels to the required levels. As the active and passive damping add approximately linearly for the levels of damping considered, the active damping was simply the difference between the required and passive damping levels. Eleven cases were considered, with percentages of achievable damping ranging from 0% to 100% by steps of 10%.

The active control algorithm implemented in each case was a form of modal space control using colocated sensors and actuators. The use of velocity feedback with colocated sensors and actuators gives an unconditionally stable system (assuming ideal sensors and actuators). However, observation and control spillover effects can seriously degrade closed-loop performance. In order to avoid spillover into the rigid body mode, the algorithm was cast such that only relative velocities were sensed and the sensor signal was the relative angular velocity between each vibration control sensor point and the reference attitude control sensor located on the ring truss. A torque was applied at the attitude control system reference point which exactly negated the torques applied at the vibration control points, so that zero net torque was applied to the system. The feedback gain matrix is thus given by:

$$K = -\phi_c^{-T} [2\zeta\omega_c] \phi_c^T$$

where ϕ_c is the relative open-loop modal matrix and $[2\zeta\omega_c]$ is the desired diagonal active modal damping matrix for the controlled modes. Note that there must be as many sensor/actuator pairs as controlled modes in this approach.

Efficient sensor/actuator pair locations were selected through consideration of over 300 candidate locations, and the points making the determinant of the ϕ_c matrix a maximum for the modes requiring damping were selected in each case.

The active control was then implemented through the following relation:

$$u_c = K y_{rel}$$

and the closed-loop system was generated using the state-space form of the flexible RSA.

For no passive damping augmentation, active control of the nine target modes was required. These modes were selected for active control since they require the highest damping, and when considered separately each had a LOS settling time which violated the performance goal. Actuator gains were determined, and the closed-loop system poles were calculated. Due to spillover the required damping was not achieved using the results of the first gain calculation, so the damping levels used in the gain calculations were iteratively adjusted to achieve closed-loop damping equal to the desired level in each controlled mode. The actuator locations selected to control these modes are identified in Figure 5. Actuators which are in symmetric pairs were considered a single actuator in the gain calculation, since only symmetric modes were considered in the analysis.

Table 8 contains the closed-loop frequencies and damping of the actively controlled system without passive damping augmentation. Notice that spillover effects due to those modes which were not considered in the gain calculation resulted in increased damping in those modes which were not targeted for active control.

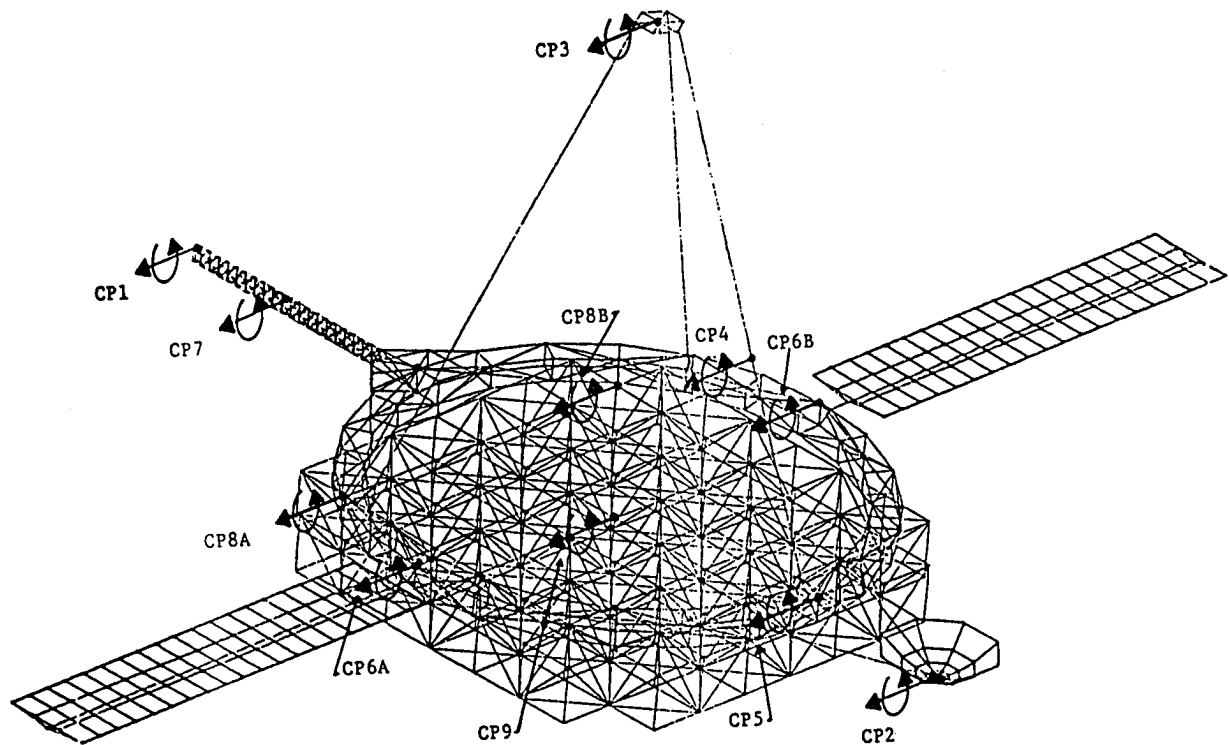


Figure 5 - Sensor/Actuator Locations for Modal Control

Table 8 - Closed-Loop Frequencies and Damping of Controlled System Without Passive Damping

SYSTEM MODE #	OPEN LOOP		CLOSED LOOP	
	f_n (Hz)	(%)	f_n (Hz)	(%)
Rigid Body	0	0	0.46	51.3
Filter	1.0	70.7	0.50	93.5
7	0.01	0.2	0.50	70.61
21	0.69		0.69	0.32
* 23	0.73		0.79	11.64
* 30	1.02		0.96	13.5
* 32	1.02		1.02	0.21
44	1.50		1.50	0.20
48	1.53		Overdamped	
118	2.72		2.72	0.23
*124	2.78		2.80	4.3
*129	2.86		2.85	4.0
*158	4.03		4.04	2.73
165	4.21		4.40	2.4
176	4.38		4.37	0.46
182	4.55		4.40	2.4
*185	5.11		5.09	2.0
187	5.68		5.8	3.0
188	5.81		5.81	0.25
191	6.45		Overdamped	
192	6.49		6.58	6.35
196	6.96		6.96	1.52
198	7.15		7.26	0.77
199	7.31		7.44	0.77
*201	7.38		7.36	1.6
206	8.77		Overdamped	
*209	9.53	0.2	9.53	1.63

*Denotes active control target mode

System mode 32, which is a mode involving torsion of the solar array blanket out of phase with motion of the main structure, requires damping but was nearly uncontrollable using reasonable actuator locations. Even though high damping levels were used for this mode in the gain calculation, the required closed-loop damping could not be achieved due to spillover. To actively damp this mode effectively would require actuators located on the flexible and lightweight solar array blankets. It was found that by using 6.0% active damping in the gain calculation for mode 32, the performance of this mode was equivalent to the 3.0% passively damped case due to coupling with other modes. Therefore, when active control of mode 32 was needed, 6.0%

damping was always used in the gain calculation. The closed-loop damping in all other modes was adjusted to be above the required level but not greater than 1.15 the required level. This factor resulted in a reasonable number of iterations to achieve the gains, while achieving active control damping levels which were at most slightly higher than necessary.

Increases in the passive damping allowed fewer modes to be actively controlled. The addition of passive damping also resulted in lower gains to control the modes which still required active damping. The active system used in each case was similar to the modal space control previously described, where the control gains were selected based on the modes still requiring active augmentation and the required active augmentation levels. The required number of actuators for each case are given in Table 9.

In order to compare the performance of the controlled systems, the LOS slew responses of the 11 cases were plotted on the same graph. This is given as Figure 6. Notice that equivalent closed-loop damping in the targeted modes results in nearly identical responses.

To allow comparison of the control effort, in each case the closed loop system was subjected to a slew maneuver of the spacecraft and the energy which would be required to drive electromechanical actuators was calculated. Figure 7 shows a graph of the energy required to drive the actuators versus the percentage of available passive damping in the system. Note that the energy requirements drop rapidly as the passive damping level increases from nominal, due to the fewer number sensors and actuators required.

Table 9 Required Number of Actuators for Percentages of Maximum Achievable Damping

PERCENT OF MAXIMUM ACHIEVABLE DAMPING	NUMBER OF ACTUATORS REQUIRED
0	9
10	9
20	6
30	6
40	5
50	5
60	4
70	3
80	2
90	2
100	2

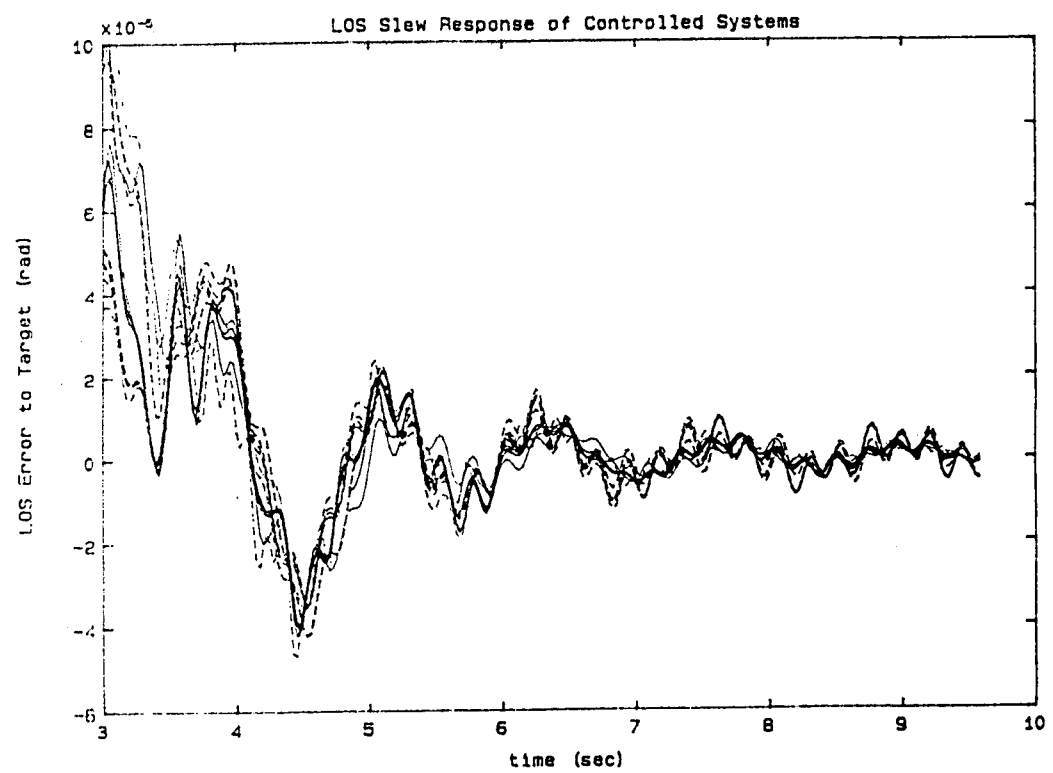
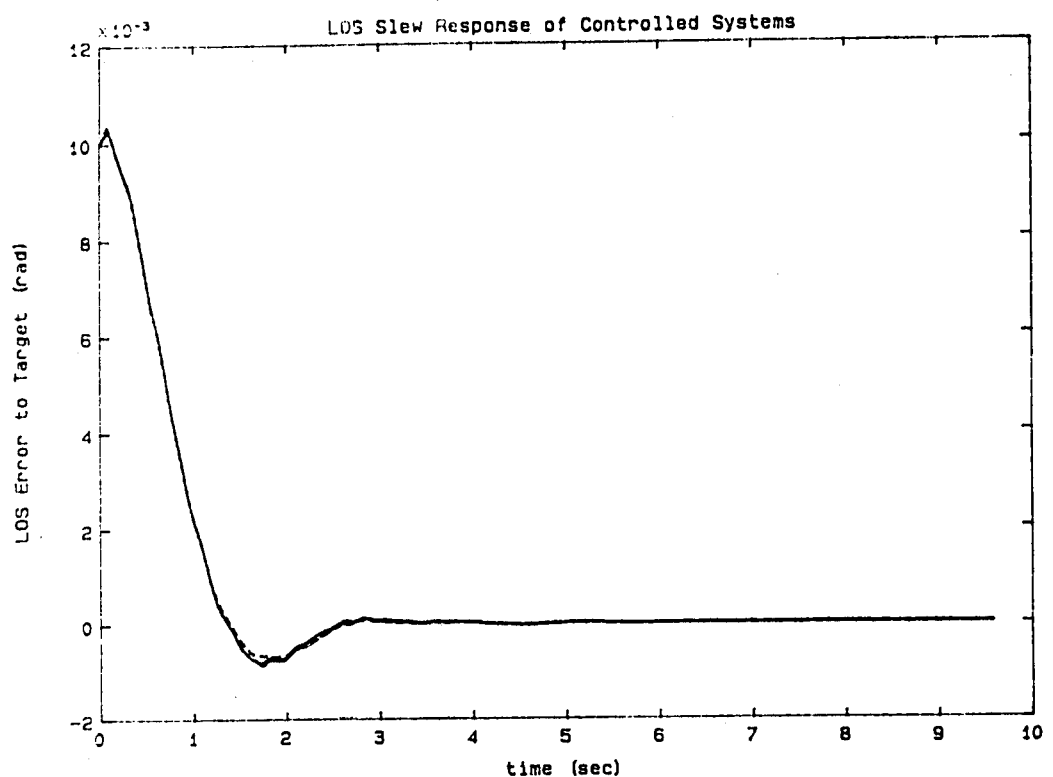


Figure 6 – LOS Slew Responses of Controlled Systems

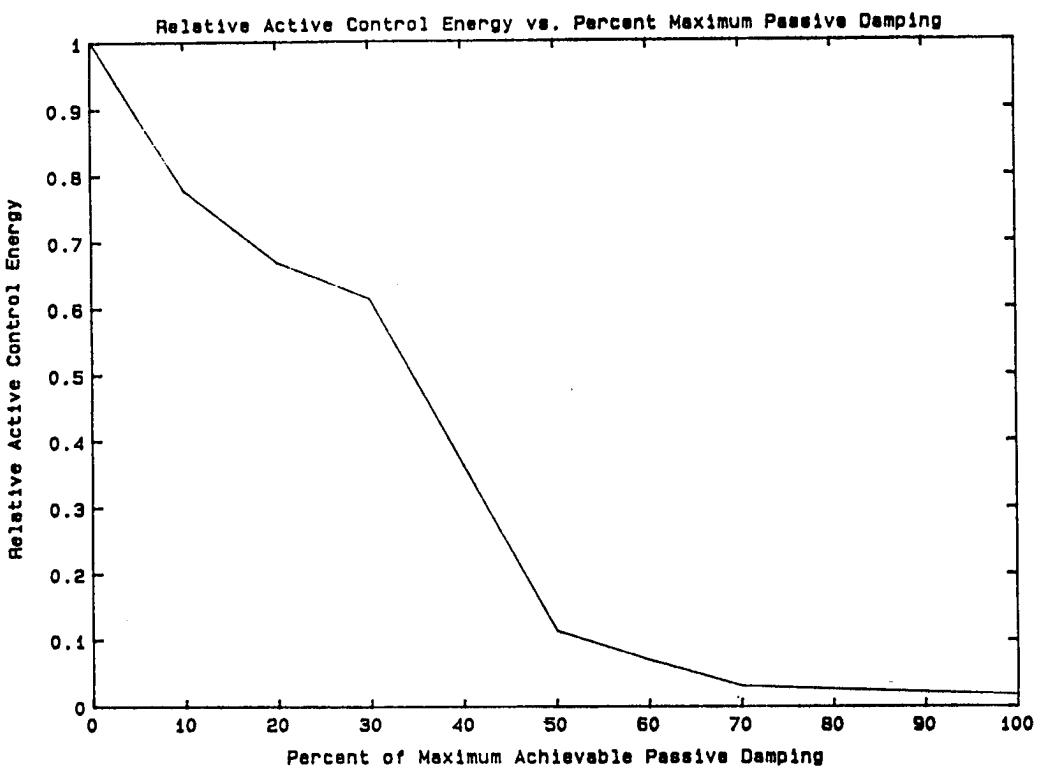


Figure 7 - Active Control Energy for Percentages of Achievable Passive Damping

As noted previously, spillover into modes not considered in the gain calculation affects the performance of the modal space control approach. This accounts for some of the higher energy requirements of the active system for low passive levels. For the control system for the undamped structure, three modes not intended to receive active damping augmentation were overdamped while several controlled modes did not have damping levels equal to the required values until the gains were adjusted iteratively. This can be interpreted as an inefficient use of control energy in that control effort is used to control modes of little importance to system performance. Use of a more sophisticated control algorithm and more sensors and actuators would reduce the spillover effects, but would be more sensitive to modeling errors and could lead to instabilities.

Selection of a Mix of Passive and Active Control

Using the results of the previous analyses, a mix of passive and active damping components was selected. A reasonable selection of the mix of the active and passive components was made on the basis of Figure 7 and Table 7.

Figure 7 shows a rapid decrease in the power required by the active control system as the percentage of available damping is increased from

nominal. At approximately 75% of the potential passive damping, the benefits of lower power requirements for the active system as passive level increases show diminishing returns. This can be seen by examining the maximum achievable damping on Table 7, and noting that at 75% of maximum all modes except 23 and 30 reach their design damping value. At this passive level, only the two sensor/actuator pairs were required, the control gains had acceptable values, and achieving the desired passive level would seem to be a relatively easy task. An important observation is that these damping levels correspond to achieving at least the target damping levels in all target modes except 23 and 30 and augmenting the damping of modes 23 and 30 actively.

Passive Damping Treatment Design

The passive damping analysis included design of the discrete damping devices to be used in the box truss and equipment platform structures; and the constrained layer treatments for the tripod legs, antenna support legs, and solar array hinges. The design process also included selection of the damping member locations for the box truss and equipment platform, and locations for the constrained layer treatments.

Table 7 shows that very high damping levels may be achieved in several modes with high box truss participation, damping levels which are not required for the system to meet the performance goals. The table also shows that the equipment platform dampers do not contribute damping levels sufficient to meet the performance goals for modes 23 and 30, but contribute more than enough damping to damp other modes to the required level. This implies that neither all the box truss or equipment platform diagonals need be damped. The number of diagonals selected in these two components were only those required to meet the design damping levels for the targets other than modes 23 and 30. Similarly, constrained layer treatments were applied only as required. The goal in subsequent damping design was therefore to achieve the design levels given in Table 6 for all target modes excluding modes 23 and 30 passively, and then to augment these two modes with an active system to their selected damping design values.

The designs of the discrete damping devices used on the RSA are very similar to the designs used for corresponding elements on the PACOSS DTA. The extensional shear damper design used for the DTA box truss includes a spring between two relatively stiff damper support rods, and a section of viscoelastic wrapped around each rod and connected in parallel with the spring through a stiff clamshell. The design process for members of this type is discussed in several Reference 4. This design process was used to achieve a damper design with a high damping efficiency factor. Damped member weight was then calculated based on the member dimensions and materials. The final damper design corresponds to an approximate mass of 0.94 kg versus the original RSA box truss diagonal mass of 0.11 kg. The design damping efficiency of the box truss damper was 85%.

The locations for the dampers were selected from the strain energy distributions of the target modes. The number of damping locations was

selected such that the damping goals in all the target modes with high box truss participation were achieved with a minimum number of devices. The number of dampers required for the box truss was 40 members, of a total of 248 diagonals. The total mass of the box truss component was previously 2295 kg. Damping treatments add to this by approximately 1.6%.

The design of the extensional shear dampers for the equipment platform was very similar to that used for the box truss. A single shear design was utilized which does not include the elastic center spring. This design allows for more weight efficient utilization of the damping material. The final equipment platform damper design has a mass of 0.079 kg as compared to the weight of the original diagonal member of 0.018 kg. The damping efficiency of these members was 90%. A total of 18 dampers were required in order to achieve the damping attributed to the equipment platform for the final design damping levels. This corresponds to a negligible increase in mass of the original equipment platform mass of 2634 kg.

Since the design of constrained layer treatments for the tripod and antenna legs would be performed using solid elements and plate elements in MSC/NASTRAN, the actual design and analysis of these treatments was not performed due to cost and schedule constraints. A refined approximation of the damping effect and additional weight of the components due to these treatments was calculated based on the damping efficiency and relative thicknesses of the viscoelastic materials and constraining layers applied to the DTA tripod legs.

The final dimensions and damping material for the treatment of the DTA tripod legs was a 0.050 in. thick acrylic core foam layer with a graphite epoxy constraining layer 0.050 in. thick applied to the legs which had a wall thickness of 0.065 in. This size relationship was used for the final estimates of all RSA constrained layer treatment performance. This treatment had a damping efficiency factor of approximately 17%. It should be noted that this design was in no way optimized on the DTA, so that the same damping efficiency may be achievable with lower relative VEM and constraining layer thicknesses.

Review of the strain energy distribution in the RSA tripod indicated that it was not necessary to damp the full length of the tripod legs. The major portion of the tripod leg strain energy was located toward the tripod apex in modes with significant tripod participation. This allowed only the upper three-fifths of the tripod legs to be treated in order to meet the target damping levels for these modes.

Similarly, the strain energy distribution in modes with antenna participation showed that only half of each antenna leg (half toward ring truss) required a constrained layer treatment. It was also determined that all the solar array hinges required treatment.

The final passive damping ratios of the RSA were calculated using the strain energy distribution for the treated elements in the final design (Table 10), the design damping efficiencies (Table 11), and the value for the loss

factor of acrylic core foam tape at 1.0 Hz and 70°F (0.73). This leads to final passive damping levels as given in Table 3-12.

To estimate the additional mass due to the constrained layer treatments, each treatment was considered to have the relationship that the constraining layer and viscoelastic material were each 77% as thick as the wall of the structural member to be treated, as in the DTA tripod design. Using this relationship and the densities of the structural and viscoelastic material, the added mass due to the constrained layer treatments was then calculated.

Table 13 contains a comparison of the system mass properties prior to the passive damping treatment application, and the estimated mass properties of the structure including damping treatments. Notice that the mass of the damping treatments is only a small percentage of the total system mass. A further benefit of the constrained layer damping treatments should be noted, however. Application of constrained layer treatments typically stiffens the structure, thereby increasing the system natural frequencies and lowering response levels. If identical natural frequencies were desireable, less added weight would be required for these treatments.

Table 10 - Strain Energy Percentages in Treated Elements for Final Design

Percent Strain Energy in Treatments						
Mode No.	Freq. (Hz)	40 Box Truss Diagonals	3/5 of Tripod Legs	18 Equip Plat Diagonals	1/2 Antenna Legs	All Solar Array Hinges
23	0.73	-	2.37	1.03	45.9	3.46
30	1.02	-	1.43	5.32	22.7	20.7
32	1.03	-	-	1.73	5.17	66.5
48	1.53	-	6.01	4.06	7.12	7.74
124	2.8	5.62	59.9	-	2.24	0.6
129	2.9	57.1	2.34	0.08	-	-
158	4.0	7.25	17.4	-	3.86	-
165	4.2	1.09	56.7	-	1.33	-
182	4.5	3.19	52.2	-	-	-
185	5.1	7.96	1.77	-	12.6	-
187	5.7	20.6	19.7	-	1.29	-
191	6.5	1.88	1.30	30.4	4.77	-
196	7.0	47.5	2.65	1.10	-	-
198	7.1	26.9	11.8	-	3.02	-
199	7.3	18.0	2.0	-	-	-
201	7.4	8.60	48.3	8.01	1.51	-
206	8.8	31.5	24.0	1.17	2.78	-
209	9.4	34.4	-	-	-	-

Table 11 - Damping Efficiencies for Final Passive Damping Calculations

BOX TRUSS DAMPERS	TREATED TRIPOD LEGS	EQUIPMENT PLATFORM DIAGONALS	TREATED ANTENNA LEGS	TREATED SOLAR ARRAY HINGES
0.85	0.17	0.90	0.17	0.15

Table 12 - Damping Attributable to Component Treatments in Final Design

Percent Modal Damping Attributable to Treatments								
Req'd. (%)	Mode No.	Freq. (Hz)	40 Box Diagonals	3/5 of Truss Legs	18 Equip Diagonals	1/2 Plat Legs	All Antenna Array Hinges	Total
11.0	23	0.73	-	0.15	0.34	2.85	0.19	3.5
12.0	30	1.02	-	0.09	1.75	1.41	1.13	4.4
3.0	32	1.03	-	-	0.57	0.32	3.64	4.5
1.0	48	1.53	-	0.37	1.33	0.44	0.42	2.6
4.0	124	2.8	1.74	3.72	-	0.14	0.13	5.7
4.0	129	2.9	17.7	0.15	0.03	-	-	17.9
2.5	158	4.0	2.25	1.08	-	0.24	-	3.6
1.0	165	4.2	1.28	3.52	-	0.08	-	4.9
1.0	182	4.5	0.99	3.24	-	-	-	4.2
2.0	185	5.1	2.47	0.11	-	0.78	-	3.4
1.0	187	5.7	6.39	1.22	-	0.08	-	7.7
1.0	191	6.5	0.58	0.08	9.99	0.30	-	11.0
1.0	196	7.0	14.7	0.16	0.36	-	-	15.2
0.5	198	7.1	8.35	0.73	-	0.19	-	9.3
0.5	199	7.3	5.58	0.12	-	-	-	5.7
1.5	201	7.4	2.67	3.00	2.63	0.09	-	8.4
1.0	206	8.8	9.77	1.49	0.38	0.17	-	11.8
1.5	209	9.4	10.7	-	-	-	-	10.7

Table 13 - Estimated Mass Change Due to Damping Treatments

SUBSTRUCTURE	ORIGINAL MASS (kg)	CHANGE DUE TO TREATMENT MASS (kg)	% COMPONENT MASS CHANGE
Box Truss	2295	35.9	1.56
Ring Truss	1113	-	-
Tripod	840	227	27.0
Equipment Platform	2634	1.10	0.0
Antenna	345	71	21.0
Solar Arrays	786	13.2	1.68
SYSTEM	8013	348	4.3

The active control algorithm was used to provide additional damping to modes 23 and 30 for the final passive design. The final open and closed loop frequencies and damping ratios for the passive/active RSA design are listed in Table 14. This table shows that although spillover effects were present for the passively damped system, they are far less severe than observed with only nominal passive damping. Notice that the required damping ratios with a 1.5 factor of safety have been achieved by passive damping in the modes which were the original targets; excluding modes 23 and 30 which have their target levels achieved through a combination of passive and active damping.

Table 15 contains a summary of the mass properties of several candidate actuators which could be used for the active control system. For the active-alone system, the maximum torques required from the actuators during the slew maneuver were calculated and are included in Table 16. Notice that high torques are required of several actuators. Selecting the actuators which can produce the required torques and have minimum mass, the additional system mass due to the actuators is given in Table 17. Actuators which are in symmetric pairs were given the mass properties of a single actuator, but the actual implementation is two actuators each producing one half the torque on Table 16. The inclusion of only one actuator mass assumes that there exists actuators of one half the mass of the Bendix MA 500 actuators which can produce one half the torque.

The actuator data indicates that in order to achieve the necessary active control authority for the active-alone system, two Sperry 600 actuators and seven Bendix MA 500 actuators were needed. The mass associated with this hardware has a total of 620 kg. The maximum torques required for the two actuators in the passive/active system were also calculated and are included in Table 18. The passive/active system would therefore require two Bendix MA 500 actuators along with the passive damping treatments.

Table 14 - Open and Closed-Loop Frequencies and
Damping for Final Passive/Active System

SYSTEM MODE #	OPEN LOOP		CLOSED LOOP	
	f_n (Hz)	ζ (%)	f_n (Hz)	ζ (%)
Rigid Body	0	0	0.45	59.7
Filter	1.0	70.7	0.55	82.7
7	0.01	0.2	0.50	70.63
21	0.69	0.2	0.69	0.33
* 23	0.73	3.5	0.80	11.63
* 30	1.02	4.4	0.96	13.70
32	1.02	4.5	1.02	4.52
44	1.50	0.2	1.50	0.53
48	1.53	2.6	1.56	14.29
118	2.72	0.2	2.72	0.21
124	2.78	5.7	2.78	6.57
129	2.86	17.9	2.88	18.45
158	4.03	3.6	4.05	4.71
165	4.21	4.9	4.21	5.40
176	4.38	0.2	4.38	0.21
182	4.55	4.2	4.55	4.26
185	5.11	3.4	5.13	7.30
187	5.68	7.7	5.67	8.41
188	5.81	0.2	5.81	0.23
191	6.45	11.0	6.11	81.41
192	6.49	0.2	6.45	4.30
196	6.96	15.2	6.95	15.14
198	7.15	9.3	7.14	9.56
199	7.31	5.7	7.28	6.00
201	7.38	8.4	7.32	8.14
206	8.77	11.8	8.75	12.46
209	9.53	10.7	9.53	10.71

*Denotes active control target mode

Table 15 - Control Moment Gyro Characteristics

Mfr	Model No.	Gimbal Type	Angular Momentum		Rate (r/min)	Torque		Weight (lb)	Envelope (in.)	Design Status	Applications
			N-m-s	ft-lb-s		(N·m)	(ft-lb)				
Bendix	MA 5-100-1	Double	6.78	5	8,000	135.6	100	38	10 dia X 10	Lab prototype	LAPSO pointer prototype
Bendix	MA 500 AC	Single	399-1,017	250-750	7,850	678	500	145	20 dia X 32	Experimental	
Bendix	MA 500 DC	Single	399-1,017	250-750	7,850	678	500	155	20 dia X 32		
Bendix	MA 1000	Double	1,356	1,000	11,400	237.3	175	230	39 dia sphr	Experimental	NASA - Langley
Bendix	MA 2300	Double	3,119	2,300	9,000	165.4	122	418	49 dia sphr		Skylab
Bendix	MA 2000	Double	1,356-4,068	1,000-3,000	4,000-12,000	237.3	175	558	44 dia sphr	Advanced development	
										Skylab unit	
Sperry	30	Double	40.7	30	4,750	6.8	5 (pk)	32	22 dia X 12	Prod	COMSAT/TRW
Sperry	75	Double	102	75	4,000	3.0	2.2 (pk)	48	20 dia X 10	Prod	COMSAT
Sperry	100	Single & double	136	100	8,000			48		Experimental	
Sperry	150	Single	203	150						unit	
Sperry	400	Single		400							
Sperry	600	Single	676-1,356	500-1,000	3,000-6,000	1,356	1,000	175	31 X 41 X 33		
Sperry	1200	Single	813-2,712	600-2,000	2,610-6,700	2,712	2,000	200	31 X 41 X 23		
Sperry	4500	Double	6,101	4,500	6,500		200	500	48 X 48 dia	Experimental	NASA - Langley (Space Station Res)

Ref: CSDL-R-1499, An Investigation of Enabling Technologies for Large Precision Space Systems, September 1982, Vol. 3: R. Strunce, et. al.

3383-73
268.327-63

Table 16 - Maximum Torques Required from Actuators Using Active Control Alone

ACTUATOR #	MAXIMUM TORQUE (N-m)
1	936
2	1371
3	633
4	520
5	261
6	226
7	212
8	475
9	106

Table 17 - Actuator Types Selected for Active Control
Alone System and Associated Mass Properties

ACTUATOR #	ACTUATOR TYPE	MASS (kg)
1	Sperry 600	79.5
2	Sperry 600	79.5
3	Bendix MA 500 DC	65.9
4	Bendix MA 500 DC	65.9
5	Bendix MA 500 DC	65.9
6	Bendix MA 500 DC	65.9
7	Bendix MA 500 DC	65.9
8	Bendix MA 500 DC	65.9
9	Bendix MA 500 DC	<u>65.9</u>
	TOTAL	620.3

Table 18 - Maximum Torques Required from
Actuators for Passive/Active Design

ACTUATOR #	MAXIMUM TORQUE (N-m)
1	167
2	136

Table 19 - Mass Properties Associated with Damping
Devices in Passive/Active Final Design

DESCRIPTION	MASS (kg)
Passive Treatments	348
Actuator 1 (Bendix MA 500 DC)	65.9
Actuator 2 (Bendix MA 500 DC)	<u>65.9</u>
TOTAL	479.8

The total mass associated with passive and active control damping devices for the passive/active system would then be 480 kg as shown in Table 19. The additional mass of the passive/active system is 140 kg less than the mass associated with the actuators for the active control alone design. This mass comparison does not include any additional weight which may be required to eliminate outgassing or control temperature of the viscoelastic for the passive damping treatments, but these will most likely be small compared to the 140 kg difference between the two designs. The active control added mass estimate includes only actuator masses and not any additional mass for electronics required to operate the control system, or additional power or fuel needs.

The energy requirements of the active and passive/active systems can be compared by examination of Figure 7. The relative electrical energy required to drive the actuators for the passive/active system is less than 3.0% of that required for the active-alone system (this roughly corresponds to 75% maximum achievable damping on Figure 7). The actual comparison calculated from the slew maneuver of the final damped design is 2.6%. The passive/active system therefore has much lower requirements for a power source to drive the actuators. Of course, energy required for temperature control of the passive damping treatments, if necessary, should also be included in this comparison. Proper insulation and shielding of the treatments would probably make this power negligible.

It should be noted that in the previous comparison, the assumptions are biased in favor of the active components in the calculations. A damping factor of safety was used for the passive damping component in the final design, as the passive damping in the target and observable modes for the final design was at least 50% above the required value in each case. The active control damping component was allowed to achieve only slightly higher than the required damping levels in the target modes, although significant damping was obtained in several observable modes due to spillover. No factors of safety or gain margins were considered in the active control design.

The mass comparison of the two designs included only the mass of the actuators used for active control, while the larger power requirements of the active-alone system would surely result in a more massive power supply. Any additional wiring required for the larger number of sensors and actuators should also be included in the mass calculations, but was not. Also, control system electronics and redundant components which would be required for the active system were not included in the mass calculations.

Perhaps the largest effects not accounted for in the comparison were the effects on the modal parameters of the addition of the actuators and passive damping treatments. While the effects of the discrete box truss and equipment platform dampers on mode shapes and frequencies would be small, the addition of the constrained layer treatments to the tripod, antenna, and solar arrays would result in higher frequencies for the target modes since the structure would be stiffened in locations which have high strain energy in these modes. Alternatively, the addition of the large masses of the actuators at points of high modal deflections in the target modes (such as

at the equipment platform or antenna tips) would result in much lower frequencies since these masses would then have high generalized mass contributions. These effects would result in increased damping requirements for the active-alone system and decreased damping requirements for the passive/active system.

Conclusions

From the comparison of the active-alone system and the passive/active system, and the results of the RSA study, several conclusions may be drawn. These are:

- 1) Passive damping and/or active control will provide dramatic improvement in the performance of future space systems. For the RSA, a factor of 230 improvement in settling time after the slew maneuver was achieved.
- 2) Passive damping will be required for efficient implementation of vibration control technology on future space systems.
- 3) The passive/active RSA vibration control system, as compared to the active-alone RSA system, has much lower power requirements, higher reliability, lower active control system gains, and fewer electronic components.
- 4) Lower weight for overall systems will result from consideration of passive and active control together in an integrated damping methodology.
- 5) The fewer number of electronic components, lower overall weight and lower system power requirements of the passive/active system compared to the active-alone system are indicative of lower overall system costs.

Acknowledgement

This work was supported by the Air Force Wright Laboratories under the Passive and Active Control of Space Structures (PACOSS) program, contract number F33615-82-C-3222.

References

1. Morgenthaler, D. R. and Gehling, R. N., "Design and Analysis of the PACOSS Representative System," Damping 1986 Proceedings, May 1986 (AFWAL-TR-86-3059, Vol. 2), pp. DG-1-DG-31.
2. Gehling, R. N., "Active Augmentation of a Passively Damped Representative Large Space System," Damping 1986 Proceedings, May 1986, (AFWAL-TR-86-3059, Vol. 2), pp. EB-1-EB-18.

3. Gehling R. N., "Low Authority Control Through Passive Damping," Presented at the Annual AAS Guidance and Control Conference, Keystone, CO, February 1-5, 1986 (AAS 86-004).
4. Morgenthaler, D. R., "Design and Analysis of Passively Damped Large Space Structures," Presented at the 11th ASME Biennial Conference on Mechanical Vibration and Noise, Boston, Massachusetts, 27-30 September, 1987, (DE-Vol. 5), pp. 1-8.

A Damping Treatment for Resonant Test Fixtures¹

F. Cericola, J. D. Rogers, and D. J. Segalman
Sandia National Laboratories
Albuquerque, New Mexico 87185
(505) 846-3633

Abstract

The application of a synthetic putty as a vibration damping treatment has been investigated. The putty was applied to rod specimens of several lengths to obtain frequency characteristics of the treatment. Test results were compared with analyses for the various rod lengths and putty shapes.

Up to 1% damping was achieved with various combinations of viscoelastic plug and elastic rod. The analytic method, though simplistic, did provide guidance to interpreting the results. The analytic method and the experiments, together, established the inertial nature of the dissipative mechanism.

¹This work was supported by Sandia National Laboratories under contract to the U.S. Department of Energy (DE-AC04-76DP00789).

Contents

1 Introduction	KDA-3
2 Discussion of Testing	KDA-4
3 Analysis	KDA-5
4 Discussion of Results	KDA-8
5 Conclusions	KDA-9
6 Acknowledgments	KDA-9
References	KDA-10
7 Tables and Figures	KDA-11

1. Introduction

A common problem in vibration testing is the control of a test through a resonant test fixture. If the resonant mode of the test fixture is lightly damped, the control of the test near this frequency is difficult, if not impossible. Thus, methods for moving modal frequencies out of the test bandwidth or sufficiently damping these modes are of great interest to the test engineer. In many cases, it is not possible to remove the fixture resonances from the frequency bandwidth of the test, so one must attempt to damp the fixture sufficiently to allow control through the resonances.

One method for adding damping to a fixture is to apply a viscoelastic material to the surface of the fixture. The mechanical energy transmitted from the fixture to the viscoelastic material is partially dissipated, thus increasing the damping of the fixture.

In the current work, the effect of applying a synthetic putty to the surface of a rod specimen was considered. Aluminum rod specimens of varying lengths were used to obtain frequency dependent characteristics of the damping treatment. The rods had a plug of the putty attached to one end and were impacted at the other end with an instrumented hammer. The damping was identified by the logarithmic decrement from an attached accelerometer and by a modal curve fit. The plugs of putty were applied in two shapes to investigate shape effects and two volumes to investigate volume effects. Viscoelastic properties of the putty were obtained from rheological tests, and a computer code was written to predict the damping for the various plug shapes.

The damping material selected for this investigation was Scotch Seal 1279, a synthetic putty designed for use in sealing environmental test chambers. The damping properties of this material were not available from the manufacturer so tests were performed in the rheology laboratory at Sandia National Laboratories to obtain the master curve shown in Fig. 1. The complex elastic modulus was deduced from the shear storage and loss moduli, recognizing that the material was above its glass-transition at all frequencies. It is clear from the figure that the material's characteristics are a strong function of frequency. Under static loading, the elastic modulus becomes quite small and the material is soft, pliable, and "sticky" to the touch. This is not surprising since it was designed to seal environmental chambers. The frequency range of interest in this work, however, was the range from 2000 Hz to 4000 Hz. In this range, the material has an elastic modulus about one one-thousandth that of aluminum.

2. Discussion of Testing

The tests performed in this work utilized aluminum rod specimens varying from 24 to 48 inches in length, each rod with a 0.75 inch diameter. To these rods were added four different "plugs" of the synthetic putty. The plugs were of two masses, 6 grams and 19.1 grams, and two shapes, cylindrical and conical. The putty plugs were attached to one end of each rod and the rod was then struck at the other end with an instrumented hammer. The input force and the resulting acceleration of the rod were measured using piezoelectric transducers on the hammer and rod respectively. The test configuration is shown in Fig. 2.

The natural frequency and damping ratio were obtained from a modal analysis complex exponential curve fit. The damping ratio was also obtained from the logarithmic decrement technique applied to the measured accelerometer response. The values of the damping ratio obtained in these two manners compared quite well in all cases. The natural frequencies and damping ratios are given in Table 1.

The thrust of this work was to investigate the effect of adding synthetic putty on the damping of the aluminum rods so the natural frequency information appears to be superfluous. However, the natural frequency data provided a method for gaining an understanding of the physical mechanisms present. The initial assumption is that the putty will act as a lossy mass, i.e., a mass and damper combination. However, when Table 1 and Fig. 3 are considered this model is clearly not reasonable. The data show that the rods with 6 grams of putty added had lower natural frequencies than those with 19.1 grams of putty added. This result is not consistent with the lossy mass model, since by that model, increasing the mass should decrease the natural frequency.

If the putty plug is modeled as a spring-mass addition to the rod, the effective end condition on the rod is either mass-like or spring-like depending upon the natural frequencies of the rod and spring-mass system, as shown by Snowdon [5]. For example, if the natural frequency of the rod is much less than that of the spring-mass system then the end condition is mass-like. This concept extends to considering the plug as a viscoelastic addition to the aluminum rod. To gain some understanding of this, the cylindrical plugs were considered as elastic rods attached to the aluminum rods. The elastic properties were obtained from Fig. 1. The natural frequencies obtained from the closed form wave equation for the bi-material rod for the case of the 42 inch aluminum rod and cylindrical putty lengths encompassing all test cases are shown in Fig. 4. The figure also shows the predicted natural frequencies for the simple added mass model. Clearly, the putty plugs acted as rod-like additions in their effect on the natural frequency of the rods.

3. Analysis

The system under test was modeled as an elastic rod attached to a linearly viscoelastic rod of tapering cross-section. The tapering was assumed to be sufficiently gradual that only axial deformations would result.

The resulting computational problem is that of evaluating the dynamic impedance at the driving point of a rod of linearly viscoelastic material, and then finding the complex frequency at which the impedance matches that of the elastic rod to which the viscoelastic rod is attached.

Letting

$$u(x, t) = \text{Im}\{e^{i\lambda t} U(x, \lambda)\} \quad (1)$$

and

$$\sigma(x, t) = \text{Im}\{e^{i\lambda t} E^*(\lambda) U(x, \lambda),_x\} \quad (2)$$

the equation for extensional vibration of the viscoelastic rod becomes:

$$(A(x) E^*(\lambda) U(x, \lambda),_x),_x + A(x) \lambda^2 \rho U(x, \lambda) = 0 \quad (3)$$

subject to the no-stress boundary condition on the right:

$$E^*(\lambda) U(x, \lambda),_x |_{x=L} - M \lambda^2 U(x, \lambda)|_{x=L} = 0 \quad (4)$$

and the matched-displacement condition on the left:

$$U(x, \lambda)|_{x=0} = 1 \quad (5)$$

In the above, $u(x, t)$ is the axial rod displacement at time t and location x ;
 $\sigma(x, t)$ is the axial stress at t and x ;
 $A(x)$ is the cross-sectional area at x ;
 M is whatever mass is attached to the free end of the rod;
 λ is the complex frequency;
 $E^*(\lambda)$ and ρ are the complex Young's modulus and density;
and L is the length of the viscoelastic rod.

The notion of complex modulus is discussed in Ref. [2].

The solution, $U(x, \lambda)$, of Equation 3 subject to the boundary conditions of Equations 4 and 5 for a given complex frequency λ defines a dynamic impedance

$$F_v(\lambda) = E^*(\lambda) U(x, \lambda),_x|_{x=0} / U(x, \lambda)|_{x=0} \quad (6)$$

at the driving point of the rod. It is the matching of this impedance to a corresponding impedance of the attached elastic rod which defines the complex eigenfrequencies of the combined system.

Numerical solution of Equation 3 subject to its boundary conditions at $x = 0$ and $x = L$ at a given complex frequency λ is straight-forward provided that $E^*(\lambda)$ is known.

Using a standard Galerkin formulation to discretize Equation 3 where U is represented as

$$U(x, \lambda) = \sum_{\text{nodes } n} U_n(\lambda) h_n(x) \quad (7)$$

one obtains for each basis function $h_n(x)$:

$$0 = \int_0^L \{ h_n(x) (A(x) E^*(\lambda) U_{,x})_{,x} + h_n(x) \lambda^2 \rho U(\lambda) \} dx \quad (8)$$

(Ref. [1] contains a good discussion of these methods.) After substitution of Equation 7 into the above equation, and an integration-by-parts, the following system of equations involving the nodal variables U_m is obtained (one equation for each “n”):

$$\begin{aligned} 0 &= h_n(L) A(L) E^*(\lambda) U(x, \lambda)_{,x} |_{x=L} \\ &- h_n(0) A(0) E^*(\lambda) U(x, \lambda)_{,x} |_{x=0} \\ &+ \sum_{\text{nodes } m} \int_0^L \{ -E^*(\lambda) h_n(x)_{,x} (A(x) h_m(x))_{,x} U_m(\lambda) \\ &\quad + A(x) \lambda^2 \rho h_n(x) h_m(x) U_m \} dx \end{aligned} \quad (9)$$

The boundary conditions (Equations 4 and 5) are integrated into the above system of equations as follows: occurrences of $E^*(\lambda) U(x, \lambda)_{,x} |_{x=L}$ are replaced by $M \lambda^2 U(x, \lambda)_{,x} |_{x=L}$; and the equation associated with the node at $x = 0$ is replaced by the boundary condition of Equation 5. Occurrences of $U(x, \lambda)_{,x} |_{x=L}$ and $U(x, \lambda)_{,x} |_{x=0}$ are replaced by the corresponding sums of Equation 7.

In our numerical implementation of the above system of equations, the traditional tent-shaped basis functions are used and a tridiagonal system of equations with complex coefficients results. Solution of that system of equations provides the displacement field $U(x, \lambda)$ as represented in Equation 7, which when substituted into Equation 6, provides numerical values for $F_v(\lambda)$ for the complex frequency, λ , considered.

The impedance of the attached elastic rod is:

$$F_e(\lambda) = -(A_e E_e / L_e) (r \lambda) \tan(r \lambda) \quad (10)$$

where A_e is the cross-sectional area of the elastic rod;
 E_e is the Young's modulus of the elastic rod;
 L_e is the length of the elastic rod;
 $r = L_r \sqrt{\rho_e/E_e}$;
and ρ_r is the density of the elastic rod.

One would impose a force balance between the elastic rod and the viscoelastic plug by requiring that

$$F_e(\lambda) = F_v(\lambda) \quad (11)$$

and solving for the complex frequency λ that makes Equation 11 true. Such a frequency would be an eigen frequency of the combined system. In the above equation, $F_e(\lambda)$ is evaluated to make proper sense of the sign of the axial force.

At this point, it is necessary to introduce two serious assumptions.

- Since $E^*(\lambda)$ is known for only real λ , the following assumption is invoked:

$$F_v(\lambda) = F_v(Re\{\lambda\}) \quad (12)$$

(Note that though the argument in the above equation is real, the resulting impedance is still complex.)

- Since the mass of the plug is very small compared to that of the rod, we further assume that the system eigen frequency will be close enough to that of the rod alone(ω_{rod}), that we may assume that

$$F_v(\lambda) = F_v(\omega_{rod}) \quad (13)$$

The resulting approximate equation:

$$F_e(\lambda) = F_v(\omega_{rod}) \quad (14)$$

is solved for λ with a Newton iteration.

We hope to remove the above simplifications in future work, using analytic continuation to estimate complex moduli at complex frequencies from the storage and loss moduli of real frequencies.

It is emphasized that the above Fourier technique is not the damping matrix method of Ref. [4] in which a "small viscoelasticity" assumption is invoked.

4. Discussion of Results

The comparisons between the test and analysis results for both natural frequency and damping ratio are shown in Figures 5-10. The natural frequency results, shown in Figures 5 and 6, indicate that the analysis was very good in predicting the natural frequency except for the case of the 6 gram cone. The code predicted that the 6 gram putty cone would have a resonance at about 3000 Hz which the test did not reveal. The authors do not feel that this is due to a serious error in the modeling of the physical mechanism, but probably is an error in the geometric modeling of the cones. The modeling of the large cone was not as critical as the small cone since the large cone did not have a resonance in the frequency band of interest.

The test results for the damping ratio are shown in Figures 7 and 8. These figures compare equal masses of putty applied as cylinders and cones. In each case, the cones provided more damping than did an equal mass of putty shaped as a cylinder. The comparisons between test and analysis results for the damping ratios are shown in Figures 9 and 10. The analysis predicted the trends for all cases except for the 6 gram cone. Just as with the natural frequency comparison, the model predicted a resonance of the 6 gram cone at about 3000 Hz which was not observed in the tests. The analysis did predict the higher damping of the cones which was observed in the tests; however, a physical interpretation of this result has not been obtained. The analytically predicted damping ratios did not agree precisely in magnitude with the test results. The predictions were generally larger than the test values, occasionally by as much as a factor of three. These discrepancies can be attributed to uncertainties in the values of the material properties and to approximations in the modeling. We do not feel that they indicate severe errors in the analysis.

The damping of the aluminum rods without any putty was quite small. The damping ratios obtained for the bare aluminum rods were about 0.0001. This value is consistent with Zener Thermal Relaxation Theory [6] and with test data from Rogers [3]. Comparing this value with the damping ratios shown in Table 1, it is clear that the putty significantly increased the damping of the rods.

5. Conclusions

The current work may be summarized with a few conclusions. First, the addition of the synthetic putty does add damping to the aluminum rods, and the putty plug may be adequately modeled as a viscoelastic addition to the rod. Second, the shape of the putty plug is important for the amount of damping obtained. Conical shapes give greater damping for a given mass of putty than do cylindrical shapes.

This damping mechanism is distinct from methods such as the constrained layer method in that it depends on inertial loads to cause the strains in the viscoelastic material. The viscoelastic material is optimally placed at a location of maximal acceleration on the main structure, not necessarily at a location of high strain. Such a placement was demonstrated in the experiments described here.

That the viscoelastic plug is most effective as a damper when its natural frequency is close to that of the rod, and that the plug's impedance changes drastically with frequency near its own resonance, undermine the utility of the assumptions which are embodied in Equation 13. Future work will be aimed toward removing these assumptions, to solve the full nonlinearity of Equation 11.

6. Acknowledgments

The authors wish to thank Mr. Doug Adolph and Mr. Arlo Nord of Sandia National Laboratories for their efforts in obtaining the master curve for the synthetic putty and in the modal parameter extraction respectively.

References

- [1] Cook, R. D., *Concepts and Applications of Finite Element Analysis*, (Second Edition), John Wiley and Sons, New York, 1981, Chapter 18.
- [2] Ferry, J. D., *Viscoelastic Properties of Polymers*, (Third Edition), John Wiley and Sons, New York, 1980, p. 68, Equations 39 and 40.
- [3] Rogers, J. D., *A Method for Determining Material Damping from Driving Point Measurements*, Ph.D. Dissertation, Iowa State University, Ames, IA, 1986.
- [4] Segalman, D. J., "Calculation of damping matrices for linearly viscoelastic structures", *Journal of Applied Mechanics*, Vol. 109, September 1987, pp. 585-588.
- [5] Snowdon, J. C., *Shock in Damped Mechanical Systems*. John Wiley and Sons, New York, 1968.
- [6] Zener, C., *Elasticity and Anelasticity of Metals*, Univ. of Chicago Press, Chicago, 1948.

7. Tables and Figures

Rod Length (inches)	Mass of Putty (grams)	Shape of Putty	Natural Frequency (Hz)	Damping Ratio	Undamped Natural Freq. (Hz)
24	19.1	Cylinder	4086	0.011	4108
24	19.1	Cone	4076	0.0088	4108
24	6.0	Cylinder	4055	0.0065	4108
24	6.0	Cone	4058	0.0085	4108
30	19.1	Cylinder	3281	0.0102	3294
30	19.1	Cone	3275	0.0088	3294
30	6.0	Cylinder	3258	0.0027	3294
30	6.0	Cone	3259	0.0043	3294
36	19.1	Cylinder	2729	0.0084	2740
36	19.1	Cone	2726	0.0093	2740
36	6.0	Cylinder	2715	0.0022	2740
36	6.0	Cone	2716	0.0028	2740
42	19.1	Cylinder	2340	0.0080	2348
42	19.1	Cone	2336	0.0100	2348
42	6.0	Cylinder	2330	0.0015	2348
42	6.0	Cone	2331	0.0025	2348
48	19.1	Cylinder	2045	0.0085	2052
48	19.1	Cone	2042	0.0100	2052
48	6.0	Cylinder	2038	0.0010	2052
48	6.0	Cone	2038	0.0015	2052

Table 1. Test results for natural frequency and damping ratio.

Storage and Loss Shear Moduli for the synthetic putty

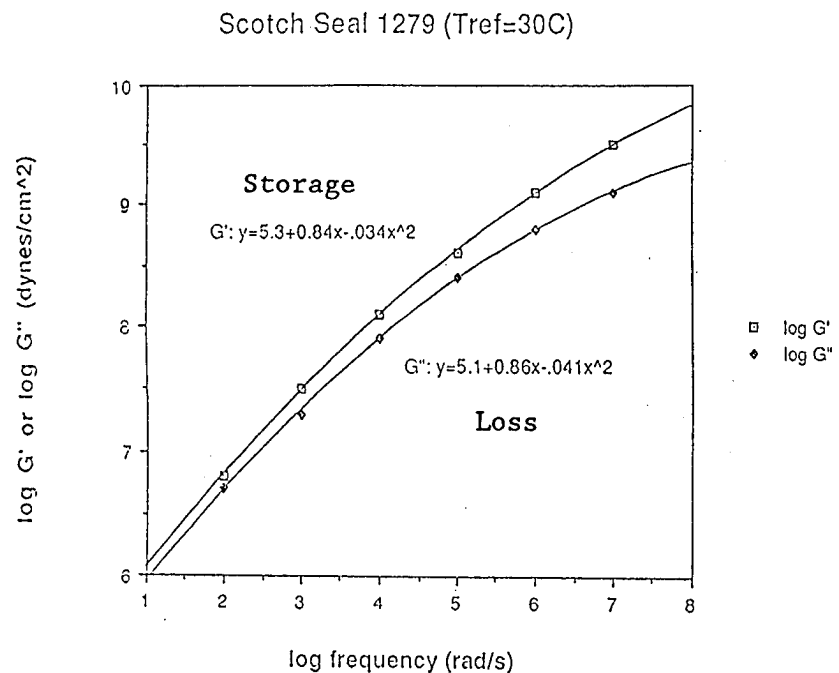


Figure 1. Master curve for the synthetic putty.

Test Setup

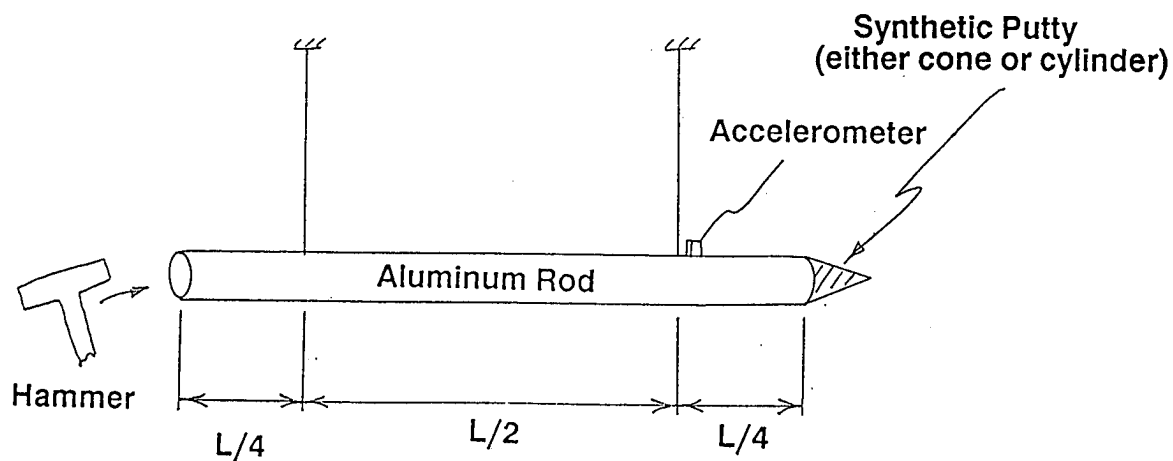


Figure 2. Test configuration.

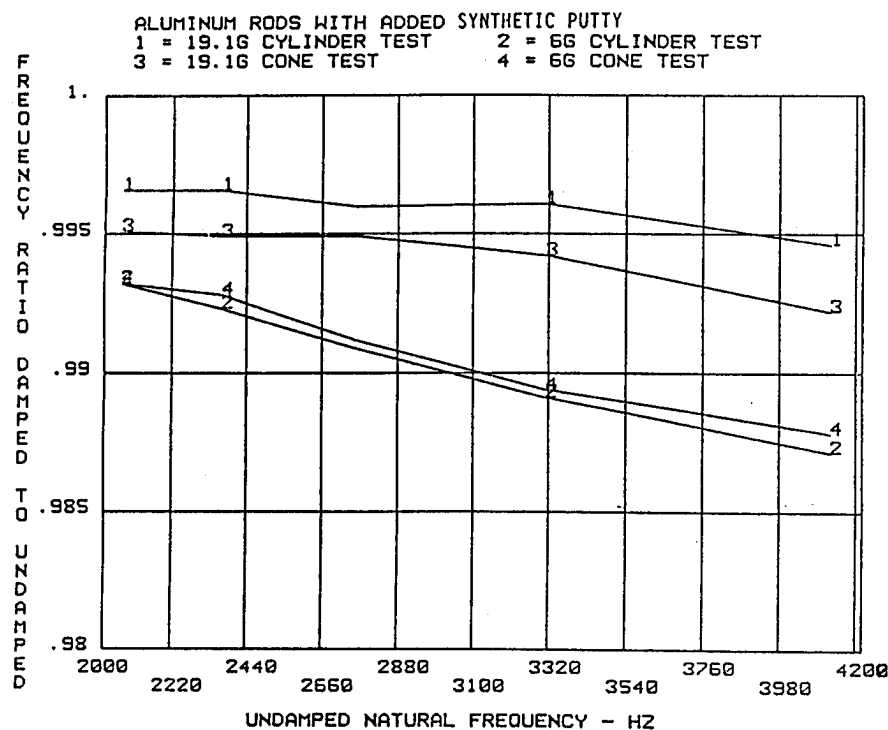


Figure 3. Natural frequency comparison for all tests.

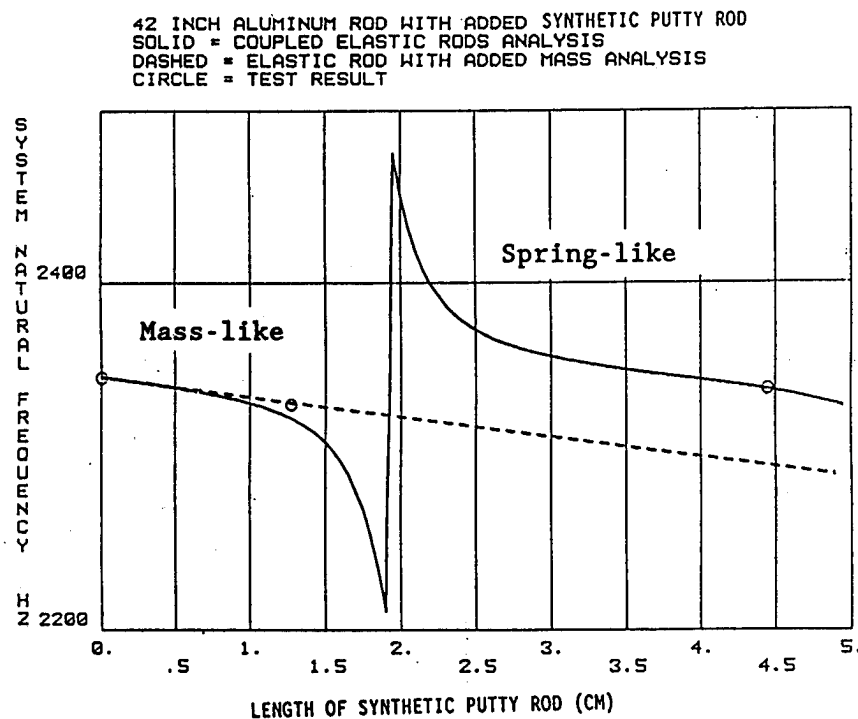


Figure 4. Natural frequencies for test, mass model, and elastic rod model.

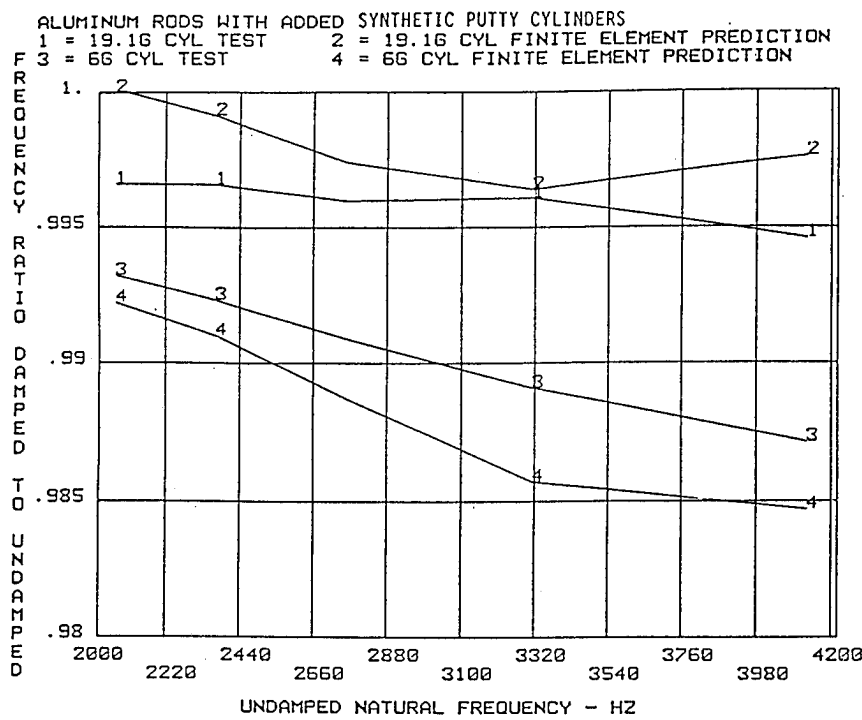


Figure 5. Comparison of frequency prediction of model with test for cylinders.

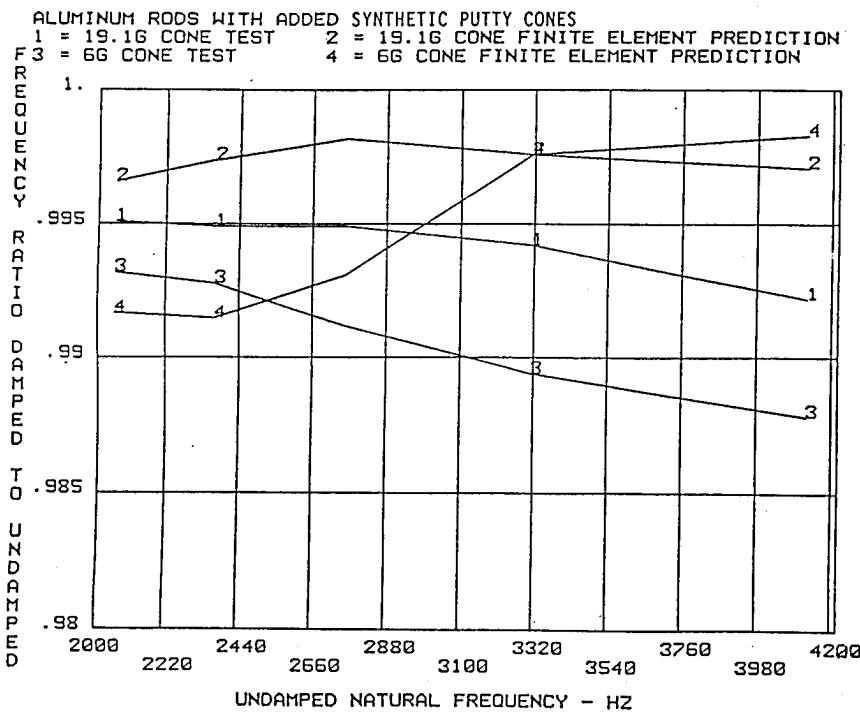


Figure 6. Comparison of frequency prediction of model with test for cones.

ALUMINUM RODS WITH SYNTHETIC PUTTY ADDED
 1 = 19.1G CYLINDER TEST 2 = 19.1G CONE TEST

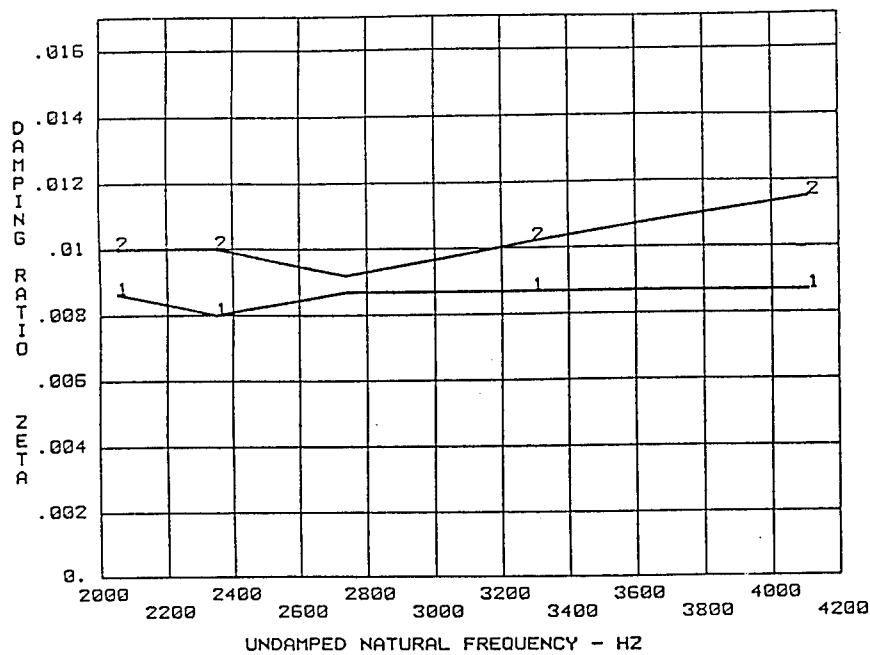


Figure 7. Damping ratios for rods with 19.1 grams of putty.

ALUMINUM RODS WITH SYNTHETIC PUTTY ADDED
 1 = 6G CYLINDER TEST 2 = 6G CONE TEST

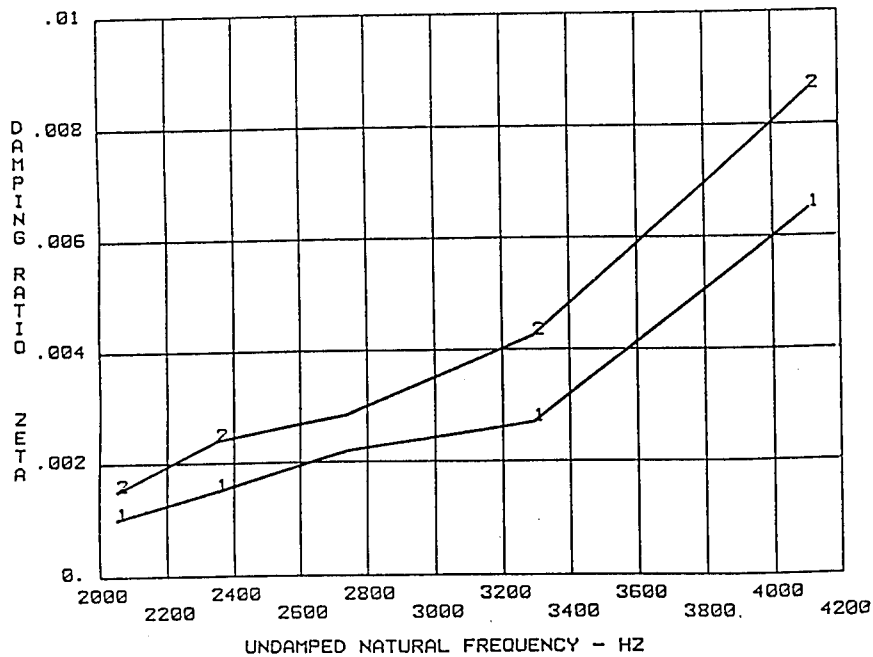


Figure 8. Damping ratios for rods with 6 grams of putty.

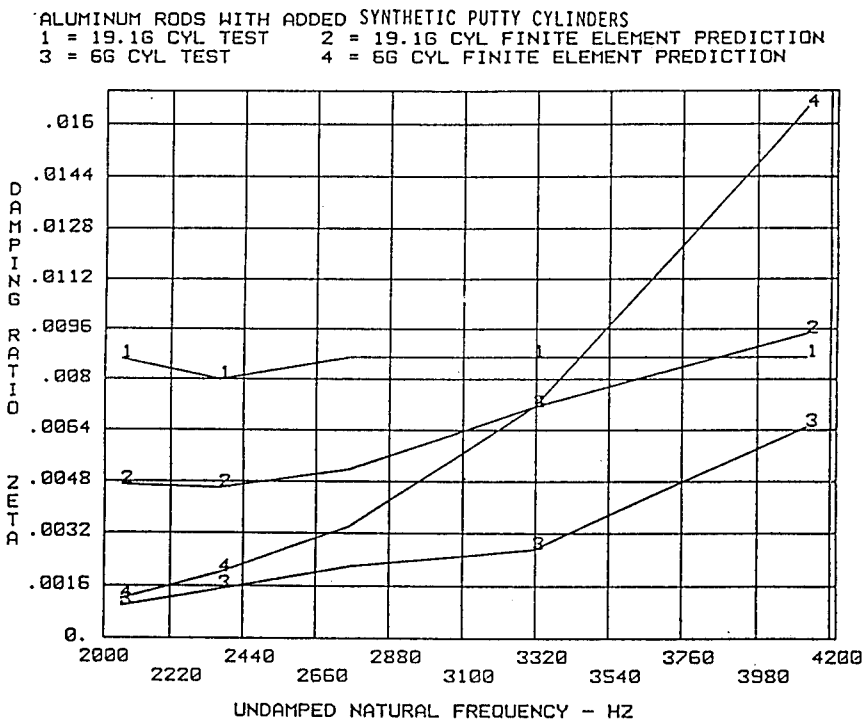


Figure 9. Comparison of damping ratios between test and model for cylinders.

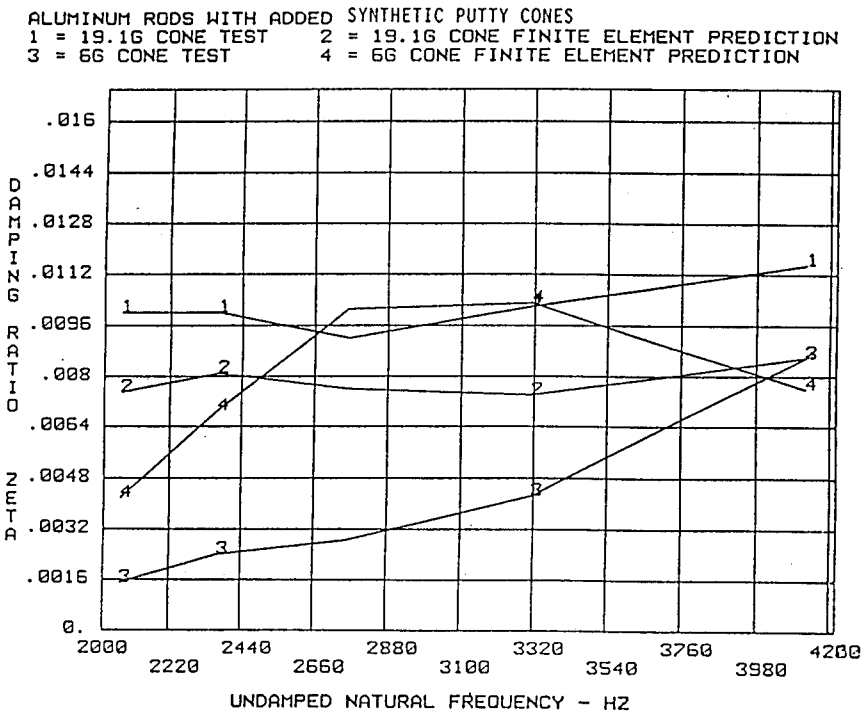


Figure 10. Comparison of damping ratios between test and model for cones.

Optimization of Dynamic Vibration Absorber -Case of Cantilever Boring Bar

E. I. Rivin, H. L. Kang
Department of Mechanical Engineering
Wayne State University
Detroit, MI 48202

Abstract

Passive dynamic vibration absorbers (DVAs) are very popular for vibration control/enhancement of effective damping in various structures. This paper describes techniques which allow one to substantially enhance the effectiveness of DVAs, specifically for long overhang cantilever structures (on the example of cantilever boring bar). A so-called combination structure is designed, in which the root segment is made of a high stiffness material, while the overhang segment is made of a light material. Optimization of such a structure results in a stiff but light system with greatly increased dynamic stiffness K_E . Optimal parameters of a DVA for main mass under self-excited vibration and random excitations are discussed. Test results are given for an optimized combination boring bar and DVA parameters with length-to-diameter ratio $L/D=15$.

1. Introduction

Passive dynamic vibration absorbers (DVAs) are very popular for vibration control/enhancement of effective damping in various structures. In boring bars, like in many other cantilever structures, vibrations are easily developed due to their weakness in both structural stiffness and damping, and thus DVAs are often used. But, due to the intrinsic limitations of the space available for installation of inertia mass, the mass ratio is limited and the DVAs often have curtailed efficiency. Thus, boring bars with length-to-diameter ratios exceeding $L/D=9-10$ were generally considered not feasible. This paper will describe several techniques which allow one to enhance effectiveness of a DVA for long overhang cantilever structures, specifically for cantilever boring bars.

A so-called combination cantilever bar was designed [1], in which the root segment is made of a high stiffness material, possibly having high specific density, while the overhang segment is made of a light material, possibly having a low Young modulus. Optimization of such a structure results in a rigid but light system, usually with greatly increased natural frequency and mass ratio of DVA, and with reduced usage of expensive materials.

Self-excited vibrations and random excitations are often encountered in structural vibrations, especially in the cutting processes, and they are the main factors of system instability. Classical (DenHartog [2]) optimization for DVAs' parameters is based on a case of harmonic external excitation applied to the main mass. Frequently, however, optimal parameters for this case are considered as a universal approach

for DVAs' design. It will be shown that for other practical cases, such as random excitation of the main mass and the case of self-excited vibrations, optimal parameters of a DVA are quite different.

Test results will be given which show that a boring bar designed as an optimized combination structure and furnished with a properly optimized DVA demonstrates substantially lower vibration amplitudes during cutting and can operate with L/D=15. The proposed concept are applicable for a wide range of cantilever structures.

2. DVA attached to the main mass which is under self-excitation conditions

In the self-excited vibrations case the alternating force that sustains the motion is created or controlled by the motion itself; when the motion stops the alternating force disappears. The general expression of the dynamic cutting force can be written as [3]:

$$F_x = -K_{cx}X_1 - C_{cx}\frac{dX_1}{dt} \quad (1)$$

where K_{cx} is stiffness coefficient and C_{cx} is damping coefficient, and K_{cx} , C_{cx} can be defined as "effective cutting stiffness" and "effective cutting damping", respectively. At some combinations of parameters, force (1) can lead to self-excitation of vibrations.

Dynamic vibration absorber can be modeled as a absorber mass M_2 attached by a spring with stiffness K_2 and a damper C_2 to the main system whose mass M_1 is subjected to the excitation force $F(t)$. A model of the main mass with a damped vibration absorber is given in Fig.1 where K_1 and C_1 are stiffness and damping of the main mass.

Equations of motion of this system can be written as:

$$\ddot{X}_1 + 2(\xi_1\omega_1 + \xi_2\omega_2\mu)\dot{X}_1 + (\omega_1^2 + \omega_2^2\mu)X_1 - 2\xi_2\omega_2\mu\dot{X}_2 - \omega_2^2\mu X_2 = \frac{F(t)}{M_1} \quad (2)$$

$$\ddot{X}_2 + 2\xi_2\omega_2\dot{X}_2 + \omega_2^2X_2 - 2\xi_2\omega_2\dot{X}_1 - \omega_2^2X_1 = 0 \quad (3)$$

with

$$\frac{K_1}{M_1} = \omega_1^2; \quad \frac{K_2}{M_2} = \omega_2^2; \quad \frac{M_2}{M_1} = \mu; \quad \frac{C_1}{\sqrt{K_1 M_1}} = 2\xi_1; \quad \frac{C_2}{\sqrt{K_2 M_2}} = 2\xi_2$$

where X_1 , X_2 are vibration amplitudes of the main mass and absorber, ω_1 , ω_2 are partial natural frequencies of the main mass and absorber subsystem, μ is the mass ratio of absorber mass to main mass, and ξ_1 , ξ_2 are damping ratios of the main mass and absorber subsystems, respectively.

By letting $F(t)=F_x$ for the exciting force in the equation (1), the system characteristic equation from the equations of motion becomes:

$$S^4 + B_3 S^3 + B_2 S^2 + B_1 S + B_0 = 0 \quad (4)$$

where

$$B_3 = 2(\xi_r \omega + \xi_2 \omega_2 (1 + \mu))$$

$$B_2 = \omega^2 + \omega_2^2 (1 + \mu) + 4\xi_r \xi_2 \omega \omega_2$$

$$B_1 = 2(\xi_r \omega \omega_2^2 + \xi_2 \omega_2 \omega^2)$$

$$B_0 = \omega^2 \omega_2^2$$

$$\frac{K_1 + K_{cx}}{M_1} = \omega^2;$$

$$\frac{C_1 + C_{cx}}{M_1} = 2\xi_r \omega$$

Here ω is the self-excited vibration frequency which is close to but different from the natural frequency of the main mass subsystem (due to addition of K_{cx}) and ξ_r is damping ratio of the main mass subsystem during cutting. Parameter ξ_r combines the damping of the main mass (always positive) and effective damping from the expression for the dynamic cutting force (1). The latter can be positive, thus assuring an unconditional dynamic stability of the system, or negative, which then should be compensated by the positive damping of the main mass and by the stabilizing effects of the absorber in order to achieve stable conditions. Thus, effectiveness of the absorber can be judged by the critical value of ξ_r , which corresponds to the stability boundary of the system. And the maximum effectiveness of the absorber can be characterized by the maximum magnitude of negative critical value of ξ_r , which the absorber can still compensate.

Routh stability criterion states that for a system to be stable, all the coefficients of the characteristic equation must be positive and also must satisfy inequalities [2]:

$$B_1 B_2 B_3 > B_1^2 + B_3^2 B_0 \quad (5)$$

From the former requirements, we arrive to conditions:

$$\xi_r > -r \xi_2 (1 + \mu) \quad (6)$$

$$\xi_r > -\left(\frac{1}{4\xi_2 r} + \frac{r(1 + \mu)}{4\xi_2} \right) \quad (7)$$

$$\xi_r > -\frac{\xi_2}{r} \quad (8)$$

where

$$r = \frac{\omega_2}{\omega}$$

is frequency ratio of the partial frequency of the absorber subsystem to the self-excited vibration frequency of the main mass.

The critical value of ξ_r can be obtained by replacing (6)-(8) with equalities, from which the largest value can be determined and then checked with equation (5). If the latter is not satisfied, the critical value of ξ_r can be determined by iterations to satisfy (5).

Fig.2 gives the critical value of ξ , at various mass and frequency ratios of the absorber. It can be seen that at a given mass ratio and damping ratio of absorber, there exists a optimal (tuning) frequency ratio ω_2/ω , at which critical negative value of ξ , has maximum magnitude (maximum effectiveness of the absorber).

The influence of absorber damping on system stability under optimal frequency ratio conditions can be seen in Fig.3. If the absorber damping is too low, it will result in a poor system stability because of small effectiveness of absorber. If the absorber damping is too high, it also gives poor system stability because the absorber mass is in fact locked together with main mass and low effectiveness will result. There is an optimal damping of the absorber which gives the maximum negative value of ξ , and results in the main mass remaining stable at higher magnitudes of negative damping induced by the cutting process for a given mass ratio.

Fig.4 gives the influence of mass ratios on system stability under both optimal frequency and optimal absorber damping ratio. It is obvious that the higher mass ratio, the better system stability.

The optimal frequency ratio at the optimal absorber damping condition will be called the global optimal frequency ratio. Since the absorber damping in practical designs may not be optimal, the optimal frequency ratio at this situation can be called a locally optimal, which means that if a value of absorber damping which is not optimum is used, the local optimal frequency ratio has to be chosen for absorber to be the most effective at this damping. Optimal absorber damping and global optimal frequency ratio for a given mass ratio are shown in Fig.5 and Fig.6 together with the results for random (see below) and sinusoidal [2] excitations.

3. DVA attached to the main mass which is under random excitation conditions

Here optimal tuning parameters will be discussed for a case of random excitation having white noise characteristics with a constant spectral density function S_0 and zero memory. In real circumstances random signal is rarely constant over the frequency range $0 - \infty$, but it is frequently constant over a wide frequency band. Thus white noise excitation is used in the analysis as an approximation of typical random signals. The frequency response method is used to get the mean square response of the system [4].

In order to get the frequency response functions $H_1(\omega)$ and $H_2(\omega)$, let:

$$\frac{F(t)}{M_1} = e^{i\omega t} \quad (9)$$

$$X_1 = H_1(\omega) e^{i\omega t} \quad (10)$$

$$X_2 = H_2(\omega) e^{i\omega t} \quad (11)$$

Then substituting above expressions and their derivatives into equations of motion (2) and (3), the frequency response functions can be written as follows:

$$H_1(\omega) = \frac{\omega_2^2 + 2\xi_2\omega_2(i\omega) + (i\omega)^2}{A_0 + A_1(i\omega) + A_2(i\omega)^2 + A_3(i\omega)^3 + (i\omega)^4} \quad (12)$$

where

$$A_3 = 2(\xi_1\omega_1 + \xi_2\omega_2(1 + \mu))$$

$$A_2 = \omega_1^2 + \omega_2^2(1 + \mu) + 4\xi_1\xi_2\omega_1\omega_2$$

$$A_1 = 2(\xi_1\omega_1\omega_2^2 + \xi_2\omega_2\omega_1^2)$$

$$A_0 = \omega_1^2\omega_2^2$$

and

$$H_2(\omega) = \frac{\omega_2^2 + 2\xi_2\omega_2(i\omega)}{(i\omega)^2 + 2\xi_2\omega_2(i\omega) + \omega_2^2} H_1(\omega) \quad (13)$$

The mean square response of the mass M_1 under the white noise excitation is then given as:

$$E(X_1^2) = \int_{-\infty}^{\infty} |H_1(\omega)|^2 S_o d\omega \quad (14)$$

which represent the total energy of the main system after attachment of a dynamic vibration absorber. For the main system without dynamic vibration absorber, the frequency response function is:

$$H_{10}(\omega) = \frac{1}{(i\omega)^2 + 2\xi_1\omega_1(i\omega) + \omega_1^2} \quad (15)$$

The mean square response can also be given by equation (14) in which $H_{10}(\omega)$ is used. A non-dimensional normalized mean square response of the main subsystem, i.e. the ratio of mean square response of M_1 with absorber to mean square response of M_1 without absorber, which reflects effect of the absorber on the main mass, is then defined as:

$$\frac{E(X_1^2)}{E(X_1^2)_0} = 2\xi_1\omega_1^3 \frac{A}{B} \quad (16)$$

where

$$A = -A_0A_1 - A_0A_3(4\xi_2^2\omega_2^2 - 2\omega_2^2) + \omega_2^4(A_1 - A_2A_3)$$

$$B = A_0(A_0A_3^2 + A_1^2 - A_1A_2A_3)$$

The calculation results of the normalized mean square response of the main mass are given in Fig.7 for a main system damping ratio $\xi_1 = 0.02$. Since the mean square response represents the total energy of the system over the entire frequency range, the normalized mean square response gives the total energy ratio of the response of the main mass M_1 but not the response itself. The larger the value of the normalized mean square response, the larger is response of the main mass and the lesser effect of the absorber on the main system behavior. Influence of mass ratio on the local optimal frequency ratio is similar to the case of self-excited vibration, but the different values of the optimal frequency ratios. Computed optimal global frequency ratio and optimal absorber damping ratio are plotted in Fig.5 and Fig.6.

A mass with dynamic vibration absorber under sinusoidal excitation has been analyzed by J. P. DenHartog [2] where he considered the case with zero main system damping which is a good approximation for the system: cantilever bar with damped vibration absorber.

Comparing optimal tuning and damping conditions under various excitations in Fig.5 and Fig.6, it can be seen that at the same mass ratios, the required optimal absorber damping values are the lowest for the case of white noise excitation, and the highest for the case of sinusoidal excitation. The required optimal frequency ratios are the lowest for the case of sinusoidal excitation and the highest for the case of self-excited vibrations. For the case of cantilever boring bar, since both self-excitation and random excitation exist during cutting process [5], the optimal tuning values for the frequency ratio and damping could be chosen in between of the optimal values shown in Figs.5,6 for cases of self-excitation and random white noise excitation.

4. Optimization of combination cantilever bar

A combination bar of length L with sintered carbide in the root segment (length L_1) and aluminum in the free end segment (solid part of length L_2 and hollow part of length L_3), shown in Fig.8, was analyzed. The absorber made of heavy machinable tungsten alloy is located in the hollow part of the free end as shown in Fig.9. An optimization procedure was applied to choose parameters L_1 , L_2 , and L_3 in order to have the highest dynamic stiffness $K\xi$ of the cantilever bar, where K is static stiffness and ξ is effective damping ratio of the main mass subsystem since both damping and stiffness are important for the system stability.

The Rayleigh expression for fundamental natural frequency of the system without absorber was used [1],

$$\omega_1^2 = \frac{\int_0^L E(z) I(z) \left(\frac{d^2 x}{dz^2} \right)^2 dz}{\int_0^L m(z) x^2 dz + M_t x_1^2} \quad (17)$$

where $E(z)$ is Young's modulus, $I(z)$ is moment of inertia of the cross section, $m(z)$ is mass per unit length, and all these parameters are considered as function of z (coordinate along the axis of the cantilever bar). M_t is mass at the free end, x is vibration amplitude of cantilever bar (a function of z), and x_1 is vibration amplitude at the free end of cantilever bar.

The effective mass at the length $L_0=L-L_3/2$ which is the midpoint of the absorber cavity L_3 is [1]:

$$M_1 = \frac{\int_0^L E(z) I(z) \left(\frac{d^2 x}{dz^2} \right)^2 dz}{x_0^2 \omega_1^2} \quad (18)$$

The effective stiffness at L_0 then is:

$$K_t = \omega_1^2 M_t \quad (19)$$

To determine the effective stiffness at the tool end, the effective mass at the length L should be determined. The approximate fundamental mode shape of the cantilever bar to be used in the Rayleigh formula (17) is assumed to be:

$$x(z) = 1 - \cos\left(\frac{\pi z}{2L}\right) \quad (20)$$

which satisfies the boundary conditions for this mode.

A combination cantilever bar and a steel bar were analyzed and compared. The parameters used for combination bar are: outside diameter $D=1.25$ in (31.75 mm), for carbide segment: $E=80,000,000$ lb/in (55 N/cm), specific gravity $\rho_c=0.516$ lb/in (0.01428 Kg/cm), for aluminum segment: inside diameter $d_3=1.0$ in (25.4 mm), $E=10,000,000$ lb/in (7 N/cm), specific gravity $\rho_a=0.09384$ lb/in (0.0028 Kg/cm); for steel bar: $E=28,600,000$ lb/in (19 N/cm), specific gravity $\rho_s=0.28$ lb/in (0.008 Kg/cm). Mass at the free end is $M_t=0.0004857$ lb-sec²/in (0.085 N-sec²/m), material for absorber mass is machinable tungsten with specific gravity $\rho_d=0.6497$ lb/in (0.01798 Kg/cm) and lengths $L_3=4,5,6$ in (0.1, 0.13, 0.15 m) were chosen for the cantilever bar with the overall length $L=18$ in (0.457 m).

By calculating stiffness values at tool end K_t and critical value of ξ_c of the combination boring bar with damped vibration absorber under optimal tuning and damping conditions, the performance index $K\xi_c$ vs L_1/L ratios can be obtained as shown in Fig.10. Since both higher stiffness K_t and more negative critical value of ξ_c give better cutting process stability, higher magnitudes of absolute value of the performance index (dynamic stiffness) are corresponding to a better stability of the system. It can be seen that L_1/L in the range 0.45–0.6 corresponds to the best stability of the boring bar. It has been shown [6] that for $L_1/L=0.45$, it corresponds to the highest natural frequency of the combination bar, and for $L_1/L=0.6$, the combination bar with damped vibration absorber has the minimum vibration amplitude under harmonic excitation.

The results of natural frequency f , stiffness at free end K_t , and mass ratio of absorber μ for the combination cantilever bar at $L_1/L=0.45$ and for the steel bar with the same dimension are given in Table-1. It can be seen that values of all this three parameters for the combination bar are about double of the values for the steel bar. Such increase in natural frequency and stiffness should improve dynamic performance of the cantilever structure, and the increase in absorber mass ratio makes the absorber more effective for a given limited absorber mass.

5. Cutting test using combination boring bar

A combination boring bar of 1.25 in (31.75 mm) diameter and 18.75 in (476 mm) long ($L/D=15$) was designed with parameters $L_3=6$ in (152 mm) and $L_1/L=0.6$. Rubber resilient elements were used which provide both necessary compliance and damping for the absorber. Absorber frequency tuning can be done by adjusting the screw

which results in preloading of the rubber elements. The absorber mass ratio is $\mu=1.07$. The damping ratio of the boring bar is $\xi_1=0.02$ and damping ratios of absorber ξ_2 are 0.07, 0.18, and 0.45 for three rubberlike materials used. Natural frequency of the boring bar is $f_1=173$ Hz. The recommended tuning frequencies for absorber are about 84 Hz in case of sinusoidal excitation, 105 Hz in case of random excitation, and 117 Hz in case of self-excited vibrations.

Vibration displacements of the boring bar in horizontal (x) directions were measured by LVDT at the distance 13.5 in (342 mm) from the clamp (since the measurement of the tool end vibration is impossible during the cutting). Deformations both at LVDT and at the tool end under static load were measured and it was shown that displacement at the tool end is about 1.91 times of displacement at the LVDT position. This factor was used as an approximation to get vibration displacements at the tool end from measured values from LVDT.

Table-2 gives maximum vibration peak-to-valley (p-v) values at the tool end for the boring bar without absorber and for the boring bar with damped vibration absorber having various absorber damping and tuning adjustments. The results show substantial improvements of cutting conditions while using boring bar with dynamic vibration absorber as compared with the original boring bar. The results show that if tuning at the local optimal frequency ratio at a given damping of rubber was realized according to the self-excitation and random white noise excitation case, smaller vibrations were observed (10-30% lower p-v values), as compared with cases of tuning as recommended for sinusoidal excitation [2]. It was also observed that when damping of the absorber is closer to the optimal damping values, the vibration amplitudes are smaller.

6. Conclusions

1. A combination cantilever bar with high rigidity material in the root segment and light weight material in the free end segment has much higher natural frequency, stiffness, and mass ratio of DVA compared with steel bar, which results in a higher dynamic stiffness (better dynamic performance) and higher effectiveness of dynamic vibration absorber.
2. The optimal tuning conditions and damping values of DVA are different for cases when the main mass is under self-excitation and under random excitation, than the classical case of sinusoidal excitation. Optimal tuning/damping parameters for actual cutting thus should be chosen accordingly. When absorber damping deviates from the obtained optimal values, the local optimal frequency ratios should be used for maximum effectiveness of absorber.
3. The cutting test results confirmed that the best results are obtained when absorber is tuned in accordance with the self-excitation/random excitation cases (smaller vibration amplitudes were recorded). The reasonably good results were obtained for a combination boring bar with length-to-diameter ratio L/D=15.

Acknowledgments

This research was supported by the Institute for Manufacturing Research (IMR) of Wayne State University and NSF Grant DMC-8718911. The supports are gratefully appreciated.

References:

1. E. I. Rivin, "A Chatter-resistant Cantilever Boring Bar", Proceedings of NAMRC-XI, SME, 1983, pp. 403-407
2. J. P. Den Hartog, "Mechanical Vibrations", McGraw-Hill, New York, 1956
3. S. A. Tobias, "Machine-Tool Vibration", John Wiley & Sons, Inc., New York, 1965
4. D. E. Newland, "An Introduction to Random Vibration and Spectral Analysis", Longman, 1975
5. S. M. Pandit, T. L. Subramaian, and S. M. Wu, "Modeling Machine Tool Chatter by Time Series", Transactions of the ASME, Journal of Engineering for Industry, 1975, pp. 211-215.
6. E. I. Rivin and H. L. Kang, "Optimized Boring Bar Design with Damped Vibration Absorber", Proceedings of the 15th National Science Foundation Conference on Production Research and Technology, 1989

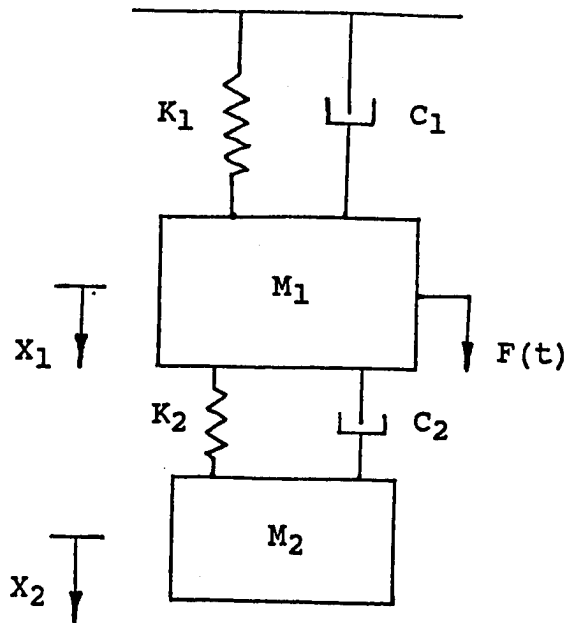


Fig.1 Model of boring bar with dynamic vibration absorber under an external excitation

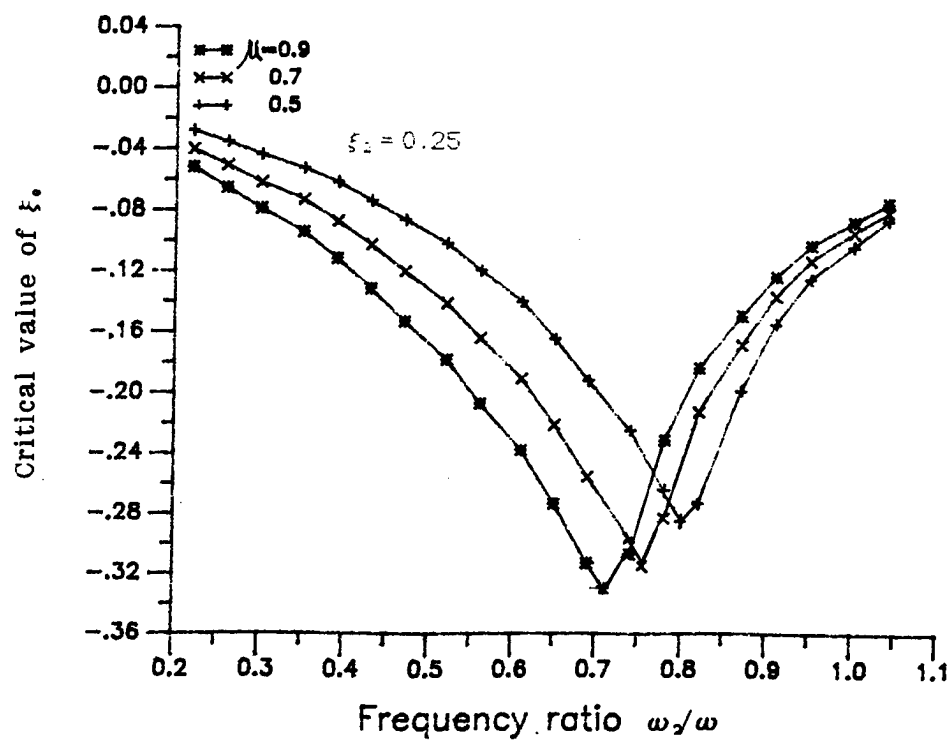


Fig.2 Critical value of ξ , vs frequency ratio of absorber at various mass ratios

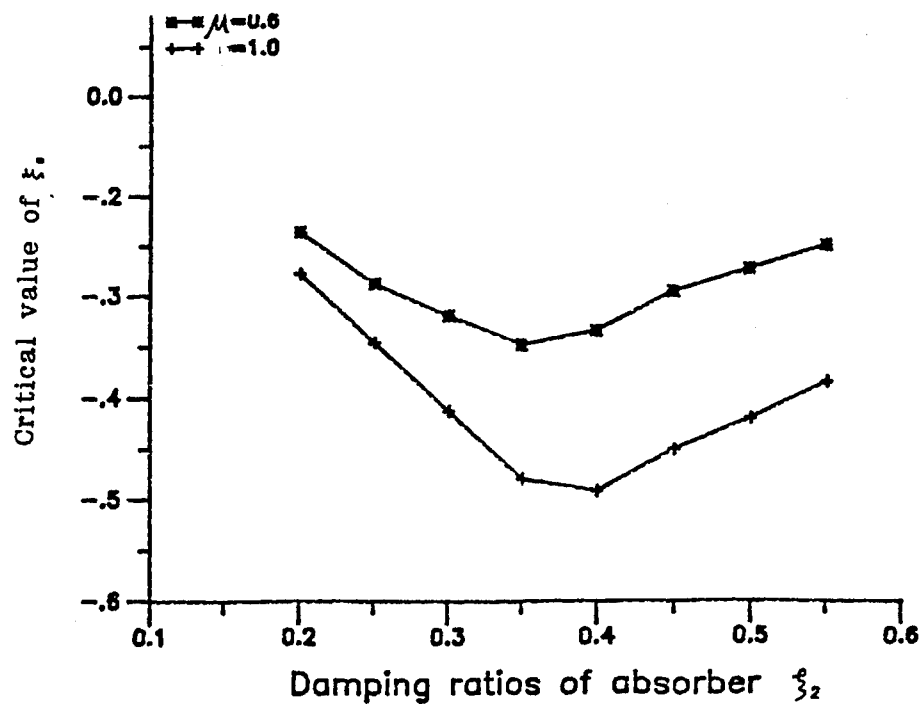


Fig.3 Critical value of ξ_0 vs absorber damping ratio
(optimal tuning condition)

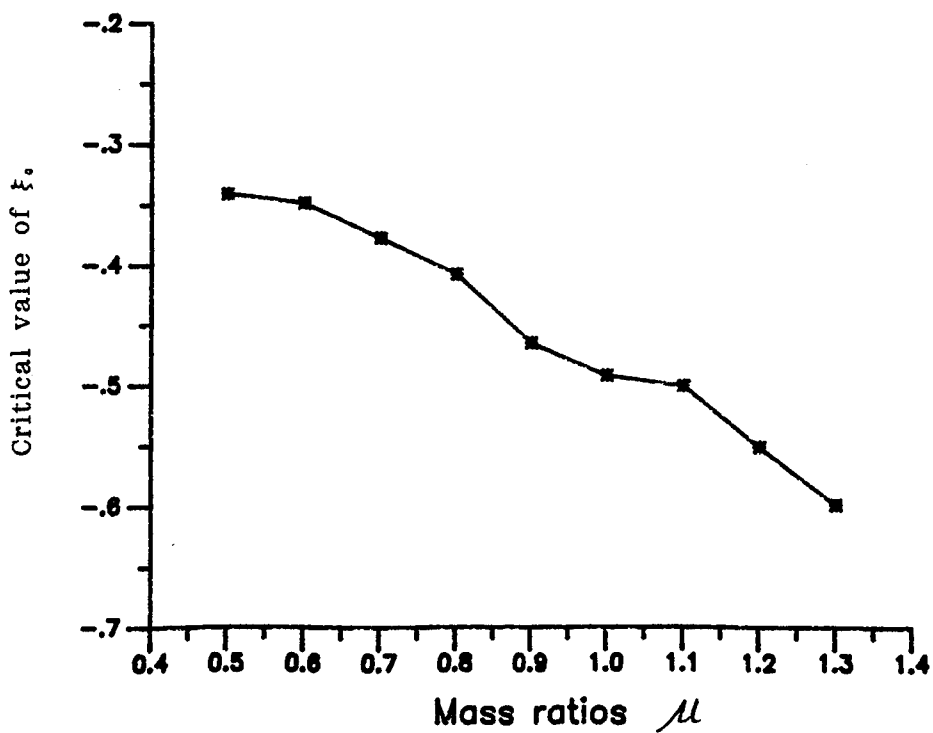


Fig.4 Critical value of ξ_0 vs mass ratio of absorber
(optimal tuning and damping condition)

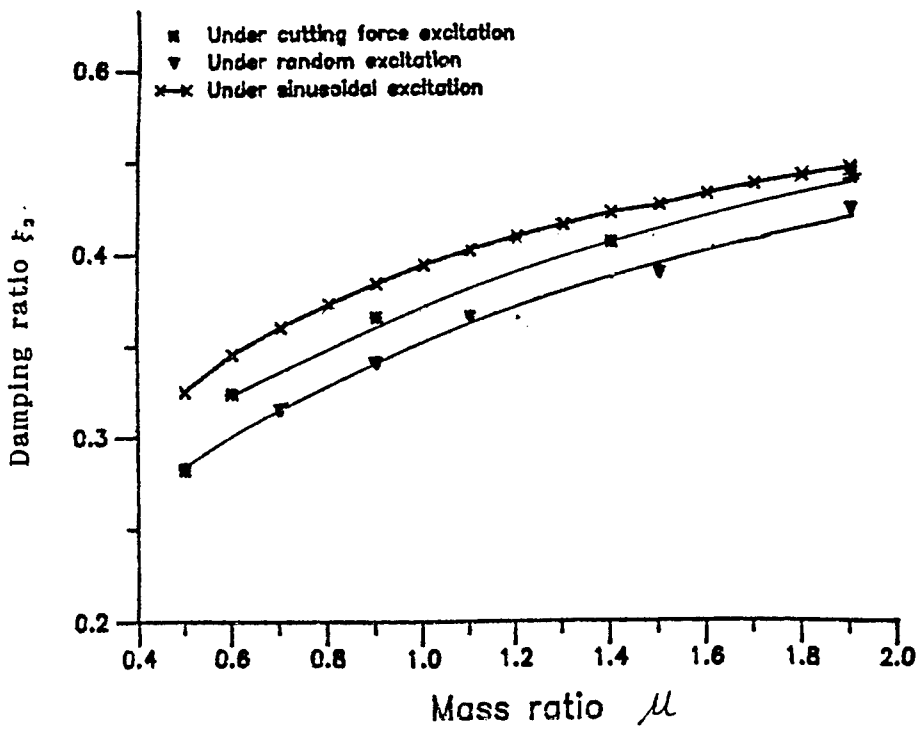


Fig.5 Optimal damping ratio of absorber vs mass ratio
(optimal tuning condition)

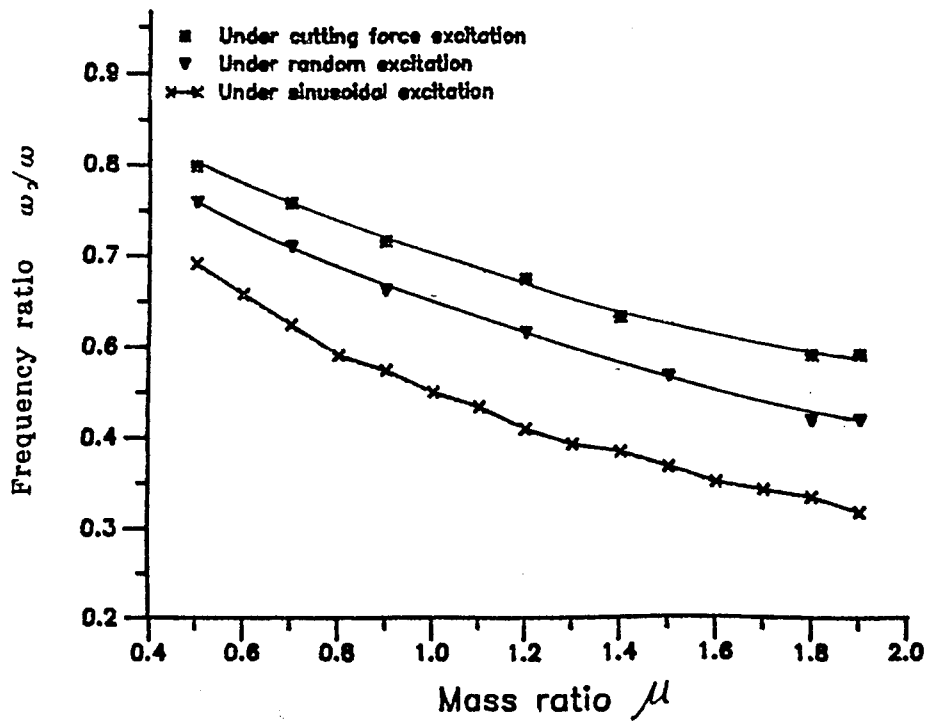


Fig.6 Optimal frequency ratio vs mass ratio
(optimal absorber damping condition)

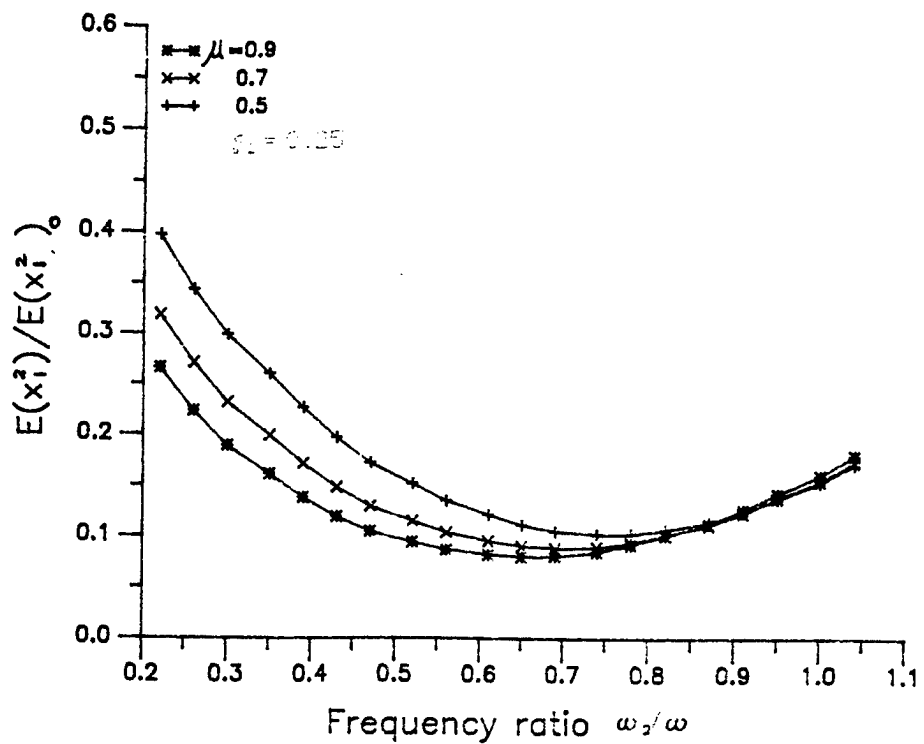


Fig.7 Normalized mean square response vs frequency ratio of absorber at various mass ratio

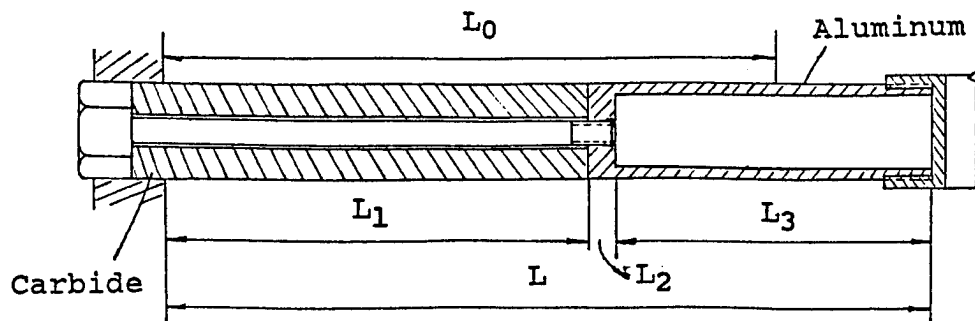


Fig.8 Combination boring bar design

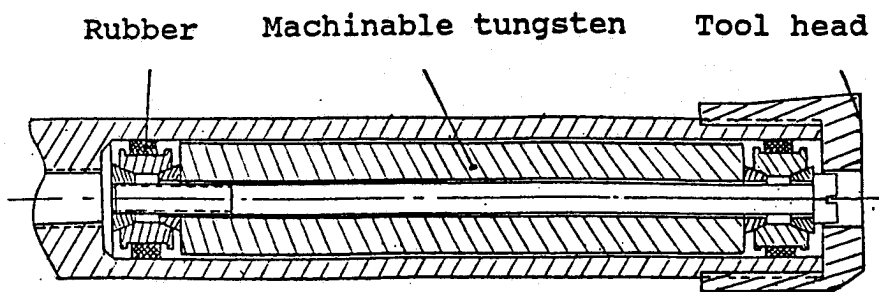


Fig.9 Dynamic vibration absorber design

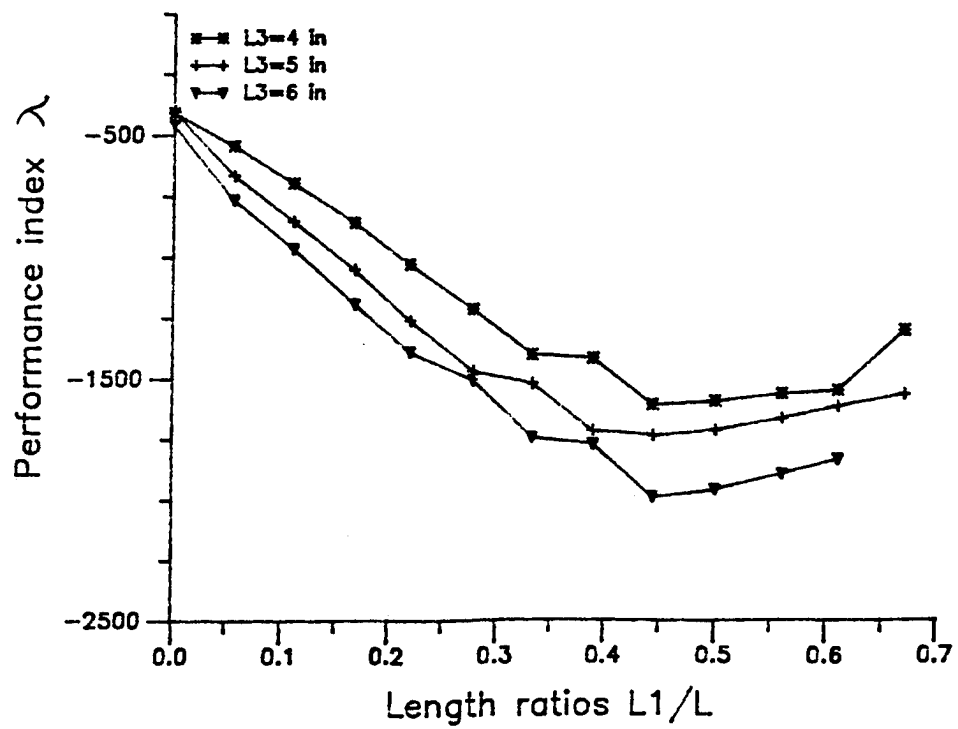


Fig.10 Performance index vs length ratio L_1/L
(combination cantilever structure)

L3 (in)	Bars	Frequency (Hz)	Stiffness (lb/in)	Mass ratio
4	Combination	275	3939	1.41
	Steel	133	1776	0.73
5	Combination	283	3935	1.77
	Steel	138	1764	0.94
6	Combination	289	3929	2.07
	Steel	143	1746	1.14

Table-1 Calculated natural frequency, stiffness, and mass ratio for combination bar ($L_1/L=0.45$) and steel bar

Absorber Damping Ratio	Spindle Speed (rpm)	Max. Peak under Se	-to-Vally Value (X- Direction)		
			Tuned under Ra	Tuned under Si	No Absorber
0.07	80	0.00177	0.00156	0.00192	0.00324
0.07	130	0.00184	0.00137	0.00241	0.00561
0.07	210	0.00265	0.00228	0.00371	0.00721
0.18	42	0.00079	0.00085	0.00114	
0.18	80	0.00104	0.0012	0.00121	
0.18	130	0.00118	0.00144	0.00167	

Se: Self-excited Vibration; Ra: Random Excitation;

Si: Sinusoidal Excitation

Table-2 Maximum p-v values (inches) of boring bar under various cutting speed, absorber damping, and tuning conditions